

*Supplementary Material (1) to accompany **The Maxwell-Stefan Description of Mixture
Diffusion in Nanoporous Crystalline Materials***

Maxwell-Stefan theory; CBMC simulation
methodology; Details of modeling of membrane
permeation, transient uptake, and transient
breakthroughs in fixed beds

Rajamani Krishna

Van 't Hoff Institute for Molecular Sciences, University of Amsterdam, Science Park 904,

1098 XH Amsterdam, The Netherlands

CORRESPONDING AUTHOR *Tel +31 20 6270990; Fax: + 31 20 5255604;

email: r.krishna@uva.nl

Table of Contents

1. Preamble to the Supplementary Material (1)	4
2. Introduction	4
3. The pioneers in the theory of diffusion, along with some historical perspective	5
4. Structural details for zeolites, MOFs, COFs, and ZIFs	6
5. Fickian formulation for diffusion	7
6. Maxwell-Stefan equations for n -component mixture diffusion	8
7. Maxwell-Stefan equations for unary diffusion.....	11
8. Maxwell-Stefan equations for binary mixture diffusion	12
9. Onsager formulation for binary mixture diffusion	16
10. Correlation effects in binary mixture permeation across membranes	17
11. Overshoot phenomena in transient membrane permeation	21
12. Simulations of transient unary uptake within crystals.....	25
13. Simulation methodology for transient mixture uptake in crystals.....	28
14. Transient uptake of N_2/CH_4 mixtures in LTA-4A and ETS-4.....	31
15. Transient uptake of CH_4/C_2H_6 mixtures in LTA-4A.....	33
16. Transient uptake of aromatic mixtures in MFI zeolite	33
17. Transient uptake of n -heptane/benzene mixtures in NaX zeolite.....	33
18. Transient uptake of propene/propane mixtures in ZIF-8 and CHA.....	34
19. Simulation methodology for transient breakthrough in fixed bed adsorbers	34
20. Transient breakthrough of CO_2/CH_4 , CO_2/H_2 , and CO_2/N_2 mixtures in Cu-TDPAT, MgMOF-74, NiMOF-74, NaX, EMC-1, and NOTT-300	39
21. Recovery of H_2 from steam-methane reformer off-gas (SMROG)	42
22. Fischer-Tropsch tail-gas separation.....	44
23. Recovery of helium from natural gas	44
24. Removal of Xe and Kr from off-gases from nuclear plants	45
25. Transient breakthrough of CO_2/CH_4 mixtures with KFI zeolite	46
26. Transient breakthrough of CO_2/CH_4 , CO_2/H_2 , and CO_2/N_2 mixtures with SIFSIX-2-Cu-i	48
27. Influence of increasing pressures on transient breakthrough of CO_2/CH_4 mixtures with amino-MIL-53(Al).....	48
28. Transient breakthrough of alkane isomers with ZIF-8	49
29. Transient breakthrough of C8 hydrocarbons with MOFs.....	50

30.	Separation of ethylbenzene and styrene mixtures	55
31.	Separation of aromatics/aliphatics mixtures.....	55
32.	Transient uptake and breakthrough of mixtures of 1-alcohols in SAPO-34 and CHA	57
33.	Transient uptake and breakthrough of alkene/alkane mixtures	61
34.	Separation of C ₂ H ₂ from hydrocarbons, and CO ₂	65
35.	Transient separation of mixtures of C ₄ hydrocarbons.....	67
36.	Separation of O ₂ /N ₂ mixtures	69
37.	Separation of chlorofluorocarbons	72
38.	Configurational-Bias Monte Carlo simulation methodology	73
39.	CBMC simulations of pure component adsorption isotherms in MFI, including experimental validation	75
40.	CBMC simulations of mixture adsorption equilibrium, including experimental validation.....	77
41.	Modeling mixture adsorption equilibrium using IAST	80
42.	Intersection blocking effects in MFI	82
43.	Transient breakthrough of alkane isomers.....	84
44.	Conclusions	98
45.	Notation	102
46.	References	128
47.	Caption for Figures.....	140

1. Preamble to the Supplementary Material (1)

This Supplementary Material (1), accompanying our main article *The Maxwell-Stefan Description of Mixture Diffusion in Nanoporous Crystalline Materials* includes (a) detailed derivation of the Maxwell-Stefan equations for mixture diffusion, (b) numerical procedures used for simulation of transient uptake within single crystals, transient breakthrough in fixed bed adsorbers, transient permeation across nanoporous membranes, (c) molecular simulation methodology and data for alkane isomers in MFI zeolite, and (d) detailed comparisons of experimental data on uptake, breakthrough and membrane permeation with simulation results.

More extensive references to the published literature are provided in the Supplementary Material in order to help researchers in this area.

2. Introduction

Ordered crystalline nanoporous materials such as zeolites (crystalline aluminosilicates), metal-organic frameworks (MOFs), zeolitic imidazolate frameworks (ZIFs), covalent organic frameworks (COFs), and porous aromatic frameworks (PAFs) offer considerable potential for separation of a wide variety of mixtures. The technologies used in such separations are either fixed bed adsorption units (some examples listed in Table 1), or membrane permeation devices (some examples are listed in Table 2). The separation performance is dictated by a combination of adsorption and diffusion characteristics, that can be manipulated by proper choice of pore size, pore topology, connectivity, and interactions (both van der Waals and electrostatic) of the guest molecules with the framework atoms. While membrane permeation units are commonly operated under steady-state conditions, the operations of fixed bed adsorption units are intrinsically transient in nature, i.e. the gas (or fluid) phase concentrations vary both with distance along the adsorber, z , and time, t .¹⁻³ The uptake within any crystallite in the fixed-bed adsorber also has a transient character. The description of transient mixture diffusion places a greater burden on process modeling than the corresponding description of steady-state characteristics.

The focus in this article is on proper and adequate modeling of intra-crystalline diffusion of mixtures of guest molecules within the pores of the nanoporous structures. The modeling of mixture diffusion needs to take due account of “coupling” effects, i.e. the flux of any species is influenced by the driving forces of *all* of the species in the mixture.⁴ During the last decade, there been a considerable amount of information and insights gained from Molecular Dynamics (MD) simulations to underscore the persuasive advantages in adopting the Maxwell-Stefan (M-S) diffusion equations in preference to either the Fickian or Onsager formulations.⁵⁻⁹ By a careful, detailed, analysis of a variety of published experimental data on membrane permeation, transient uptake and breakthrough, we identify conditions that demand the adoption of the rigorous Maxwell-Stefan (M-S) formulation to describe intra-crystalline mixture diffusion. We also identify situations in which the simpler diffusion models are of adequate accuracy for use in practice.

3. The pioneers in the theory of diffusion, along with some historical perspective

It is important to recognize the contributions of a few pioneers in the field of diffusion theory. Figure 1 provides pictures, culled from the web, of Adolf Fick, James Clerk Maxwell, and Josef Stefan, Irving Langmuir, Lars Onsager, Richard Barrer, Douglas Ruthven, and Jörg Kärger.

In 1855, Adolf Fick, a physiologist working as an anatomy demonstrator in Zürich, posited on the basis of analogy with conduction of heat or electricity, that the flux of matter is proportional to the gradient of its concentration. The majority of design methodologies and computational codes used in practice for separation and reaction equipment employ the Fickian formulation.

The derivation of the expression for description adsorption isotherms in Langmuir’s classic 1918 paper¹⁰ is essentially based on equating the kinetics of adsorption and desorption processes. Extension of the original Langmuir derivation using the quasi-chemical theory is useful in modeling the loading dependence of unary diffusivities.¹¹

Barrer made substantial, seminal, contributions to the theory of diffusion and described these in lucid terms in his classic book.¹²

The contemporary giants in the field of nanoporous crystalline diffusion are Ruthven and Kärger, whose monographs¹³⁻¹⁵ are a source of inspiration to many aspiring researchers in this field.

During the last three decades there has been increasing awareness of many pitfalls in using the Fickian formulation for describing diffusion in multicomponent mixtures, especially under circumstances in which additional driving forces such as electrostatic potential gradients are present.^{7, 8, 16, 17} Processes such as reverse osmosis, electrodialysis, ion exchange, and chemical vapor deposition demand the use of the more fundamentally based Maxwell-Stefan (M-S) diffusion equations, originating from the seminal contributions of James Clerk Maxwell¹⁸ and Josef Stefan.¹⁹ In a paper published in 1990, the Maxwell-Stefan approach was extended to describe intra-crystalline diffusion of multicomponent mixtures.²⁰ A key feature of the Maxwell-Stefan diffusion formulation is the use of chemical potential gradients as driving forces. Formally, the M-S formulation is equivalent to the Onsager formulation, and the Onsager symmetry relations are obeyed by the M-S diffusivities. The important advantages of the M-S formulation over the Onsager formulation have been underscored in previous work.⁹

Extensive sets of diffusivity data obtained from Molecular Dynamics (MD) simulations for a wide variety of guest molecules in several zeolites, MOFs, COFs, and ZIFs have been used to gain insights into the characteristics of the M-S diffusivities, and methods for their estimation.^{7-9, 21, 22} Supplementary Material (2) provides a summary of the estimation methods for M-S diffusivities.

4. Structural details for zeolites, MOFs, COFs, and ZIFs

The crystallographic data of zeolite structures are available at the website of the International Zeolite Association.²³ The structural details (unit cell dimension, pore volumes, pore landscapes, pore size distribution) of several zeolites, MOFs, COFs, and ZIFs are provided in the Supplementary materials accompanying our earlier publications.^{4, 8, 11, 24} To illustrate the type of information contained in our earlier works,^{4, 8, 11, 24} Figure 2 summarizes the salient structural details for MFI zeolite, also known as silicalite-1. The MFI structure consists of a set of two intersecting 10-ring channels of $5.4 \text{ \AA} \times 5.5 \text{ \AA}$

and $5.4 \text{ \AA} \times 5.6 \text{ \AA}$ size; see Figure 3. The pore volume, determined from molecular simulations using the helium insertion technique of Talu and Myers,²⁵ has a value of $0.165 \text{ cm}^3/\text{g}$.

Table 3 and Table 4 provide some salient structural information on various materials discussed in our article.

In comparison to traditionally used porous materials such as zeolites, MOFs and ZIFs offer significantly higher surface areas and porosities. This is underscored in the data presented in Figure 4 for surface areas, pore volumes, and characteristic dimensions of some representative zeolites, MOFs and ZIFs. The commonly used zeolite, FAU, for example, has a characteristic size (window aperture) of 7.4 \AA , a pore volume of $0.33 \text{ cm}^3/\text{g}$, and a surface area of $980 \text{ m}^2/\text{g}$. The accessible pore volumes of MOFs are commonly in the $0.5 - 2 \text{ cm}^3/\text{g}$ range. Furthermore, significantly higher surface areas are available with MOFs; for example MOF-177 has an area of $4800 \text{ m}^2/\text{g}$. The pore dimensions of MOFs are also often significantly larger; MgMOF-74 has one-dimensional (1D) hexagonal-shaped channels of approximately 11 \AA diameter.

5. Fickian formulation for diffusion

The Fickian formulation relates the component flux N_i , expressed as the number of moles of species i transported per m^2 of *crystalline material* per second, to the gradient of the molar loadings, q_i , or pore concentration, c_i

$$N_i = -\rho D_i \nabla q_i = -\phi D_i \nabla c_i \quad (1)$$

where ϕ is the fractional pore volume. Equation (1) defines the Fick diffusivity D_i , also termed “transport” diffusivity. The Fick diffusivity D_i can be determined by fitting transient uptake data and from chromatographic experiments.¹⁵

For a binary mixture consisting of species 1 and 2, each of the component fluxes N_1 and N_2 , are influenced by the gradients in the molar loadings, ∇q_1 , and ∇q_2 of both species in the mixture. In the

Fick formulation for mixture diffusion coupling effects are accounted for by defining a matrix of Fick

diffusivities $\begin{bmatrix} D_{11} & D_{12} \\ D_{21} & D_{22} \end{bmatrix}$.

$$\begin{pmatrix} N_1 \\ N_2 \end{pmatrix} = -\rho \begin{bmatrix} D_{11} & D_{12} \\ D_{21} & D_{22} \end{bmatrix} \begin{pmatrix} \nabla q_1 \\ \nabla q_2 \end{pmatrix}; \quad \text{Fick formulation} \quad (2)$$

The ratios D_{12}/D_{11} , and D_{21}/D_{22} reflect the extent of ‘‘coupling’’ in the species fluxes. Such couplings have two different origins, and to distinguish between these it is necessary to adopt the Maxwell-Stefan mixture diffusion formulations that use chemical potential gradients, $\nabla\mu_1$ and $\nabla\mu_2$, are used as driving forces of intra-crystalline diffusion.

An important shortcoming of the Fickian formulation (2) is that the $\begin{bmatrix} D_{11} & D_{12} \\ D_{21} & D_{22} \end{bmatrix}$ cannot be related simply to the data for unary Fick diffusivities of components 1 and 2, i.e. D_1 and D_2 .

6. Maxwell-Stefan equations for n -component mixture diffusion

The Maxwell-Stefan (M-S) equations for n -component diffusion inside porous crystalline materials can be written as^{5-9, 26}

$$-\phi \frac{c_i}{RT} \nabla\mu_i = \sum_{\substack{j=1 \\ j \neq i}}^n \frac{x_j N_i - x_i N_j}{D_{ij}} + \frac{N_i}{D_i}; \quad i = 1, 2, \dots, n \quad (3)$$

where ϕ represents the fractional pore volume and the c_i are the loadings, defined in terms of moles per m^3 of *accessible* pore volume, within the pore. It is to be noted that the ϕ appears in the M-S equations (3) because the c_i are defined in terms of pore volume and not the total volume of the crystals. The fluxes N_i defined in equation (3) are expressed in terms of the number of moles of species i transported per m^2 of *crystalline material* per second. In equation (3) the D_i is the M-S diffusivities of species i , portraying the interaction between component i in the mixture with the surface, or wall of the structure. An important advantage of the M-S formulation is that the D_i can be identified with the values for unary species i ; there are however exceptional circumstances where this advantage does not hold.^{11, 27} The D_{ij}

are M-S exchange coefficients representing interaction between component i with component j . At the molecular level, the D_{ij} reflect how the facility for transport of species i *correlates* with that of species j . The M-S equations (3) apply equally to meso-porous and micro-porous materials.^{28, 29} The Supplementary Material (2), provides procedures for estimating D_{ij} by relating these to the fluid phase M-S diffusivities for the binary pairs.

The pore concentrations c_i are related to the molar loadings q_i , expressed in terms of the number of moles of adsorbate per kg of material, by the expression

$$c_i = \frac{\rho q_i}{\phi} = \frac{q_i}{V_p} \quad (4)$$

where ρ represents the framework density, and V_p is the m³ accessible pore volume per kg of framework. The c_i are useful measures when comparing different materials. We will have occasion to use both c_i and the molar loadings q_i .

An equivalent formulation of the M-S equations uses the molar loadings q_i as concentration measures

$$-\rho \frac{q_i}{RT} \nabla \mu_i = \sum_{\substack{j=1 \\ j \neq i}}^n \frac{x_j N_i - x_i N_j}{D_{ij}} + \frac{N_i}{D_i}; \quad i = 1, 2, \dots, n \quad (5)$$

The x_i in (3) and (5) and represent the component mole fractions in the adsorbed phase within the pores and calculated from

$$x_i = q_i / q_t = c_i / c_t; \quad 1, 2, \dots, n \quad (6)$$

where q_t and c_t are the *total* mixture loadings and pore concentrations, respectively:

$$q_t = \sum_{i=1}^n q_i; \quad c_t = \sum_{i=1}^n c_i \quad (7)$$

The Onsager reciprocal relations require

$$D_{ij} = D_{ji} \quad (8)$$

The use of the pore concentrations c_i in equation (3) is particularly convenient for estimation of the exchange coefficients D_{ij} . To appreciate this, let us consider the limiting case of n -component mixture diffusion in the absence of any interactions, with the pore wall. In this case, we have $\phi = 1$, and equation (3) degenerates to the equation for describing bulk fluid phase mixture diffusion¹⁶

$$-\frac{c_i}{RT} \nabla \mu_i = \sum_{\substack{j=1 \\ j \neq i}}^n \frac{x_j N_i - x_i N_j}{D_{ij,\text{fl}}}; \quad i = 1, 2, \dots, n; \quad \text{bulk fluid mixture} \quad (9)$$

where $D_{ij,\text{fl}}$ represents the M-S diffusivity for the binary pair i - j in the n -component fluid mixture. Extensive MD simulations show that the D_{ij} can be related to $D_{ij,\text{fl}}$ provided the comparisons are made at the same total concentrations c_t .^{4, 28, 29} The Supplementary Material (2), accompanying this publication, provides detailed insights into the characteristics of the M-S diffusivities using MD simulation data.

By defining an n -dimensional square matrix $[B]$ with elements

$$B_{ii} = \frac{1}{D_i} + \sum_{\substack{j=1 \\ j \neq i}}^n \frac{x_j}{D_{ij}}; \quad B_{ij} = -\frac{x_i}{D_{ij}}; \quad i, j = 1, 2, \dots, n \quad (10)$$

we can recast equation (5) into the following form

$$-\rho \frac{q_i}{RT} \nabla \mu_i = \sum_{j=1}^n B_{ij} N_j; \quad i = 1, 2, \dots, n \quad (11)$$

The chemical potential gradients $\nabla \mu_i$ can be related to the gradients of the molar loadings, q_i , by defining thermodynamic correction factors Γ_{ij}

$$\frac{q_i}{RT} \nabla \mu_i = \sum_{j=1}^n \Gamma_{ij} \nabla q_j; \quad \Gamma_{ij} = \frac{q_i}{f_i} \frac{\partial f_i}{\partial q_j}; \quad i, j = 1, \dots, n \quad (12)$$

If the surface of the crystal is exposed to a bulk gas phase with partial fugacities, f_i , we can determine the chemical potential in the adsorbed phase

$$\mu_i = \mu_i^{\text{gas}} = \mu_i^0 + RT \ln f_i; \quad \text{thermodynamic equilibrium} \quad (13)$$

and the chemical potential gradients can be determined by differentiation

$$\nabla\mu_i = RT\nabla \ln f_i; \quad \text{chemical potential gradients} \quad (14)$$

In the special case in which each of the pure component adsorption isotherms is described by a single-site Langmuir model and a mixed gas Langmuir model is used to describe the mixture adsorption equilibrium we can derive the simple analytic expression²

$$\Gamma_{ij} = \delta_{ij} + \left(\frac{q_{i,sat}}{q_{j,sat}} \right) \left(\frac{\theta_i}{1 - \theta_1 - \theta_2 - \dots - \theta_n} \right); \quad i, j = 1, 2, \dots, n \quad (15)$$

where the fractional occupancies, θ_i , are defined by

$$\theta_i \equiv \Theta_i / \Theta_{i,sat} = q_i / q_{i,sat} \quad (16)$$

The elements of the matrix of thermodynamic correction factors Γ_{ij} are more precisely determined by numerical differentiation of the equations describing mixture adsorption equilibrium, using either IAST or RAST; this requires robust numerical procedures.

Equation (11) can be re-written in n -dimensional matrix notation as

$$(N) = -\rho[B]^{-1} [\Gamma]\nabla(q) \quad (17)$$

We denote the inverse of $[B]$ as $[\Delta]$:

$$[B]^{-1} \equiv [\Delta] \quad (18)$$

7. Maxwell-Stefan equations for unary diffusion

For unary diffusion of component i , the Maxwell-Stefan relations simplify to yield

$$N_i = -\rho D_i \nabla q_i = -\rho \mathcal{D}_i \Gamma_i \nabla q_i; \quad \Gamma_i = \frac{q_i}{f_i} \frac{\mathcal{F}_i}{\partial q_i}; \quad \text{unary system} \quad (19)$$

where the commonly used Fick diffusivity of species i is related to the unary Maxwell-Stefan diffusivity

$$D_i = \mathcal{D}_i \Gamma_i; \quad \text{unary system} \quad (20)$$

8. Maxwell-Stefan equations for binary mixture diffusion

For a binary mixture, the Maxwell-Stefan diffusion equations are^{5-9, 26},

$$-\rho \frac{q_1}{RT} \nabla \mu_1 = \frac{x_2 N_1 - x_1 N_2}{D_{12}} + \frac{N_1}{D_1}; \quad -\rho \frac{q_2}{RT} \nabla \mu_2 = \frac{x_1 N_2 - x_2 N_1}{D_{12}} + \frac{N_2}{D_2}; \quad \text{M-S formulation} \quad (21)$$

There are three M-S diffusivities that characterize binary mixture diffusion. The M-S diffusivities: D_1 and D_2 portray the interaction of species 1 and 2 with the pore walls. The exchange coefficient, D_{12} reflects *correlation* effects in binary mixture diffusion.^{5, 6, 21} The significance of correlation effects, quantified by (D_1/D_{12}) , that can be consider to be a measure of the *degree of correlations*. Values of (D_1/D_{12}) in the range of 1 - 20 can be regarded as reflecting a reasonably high degree of correlation.⁴

Generally speaking correlation effects are important to consider for a mixture consisting of more-mobile-less-strongly-adsorbed and tardier-more-strongly-adsorbed species e.g. H_2/CO_2 , $\text{CH}_4/\text{C}_2\text{H}_6$, $\text{CH}_4/\text{C}_3\text{H}_8$, and $\text{CH}_4/n\text{C}_4\text{H}_{10}$; this has been established on the basis of a careful analysis of available experimental data.⁴

Figure 5 shows MD data on D_1/D_{12} for diffusion of six different mixtures in a variety of host materials, expressed as a function of the total concentration, $c_t = (q_1 + q_2)/V_p$, of the adsorbed mixture within the pores. The use of pore concentrations c_t rather than the molar loadings affords a fairer comparison of different host materials as explained in previous works.²⁹ For any guest/host combination, D_1/D_{12} is seen to increase as the pore concentration increases; this implies that correlation effects are expected to be stronger for separations operating at higher pressures. Correlations are strongest in one-dimensional (1D) channel structures (e.g. MgMOF-74, NiMOF-74), intersecting channels (e.g. MFI), and “open” structures (e.g. IRMOF-1, FAU, NaX) consisting of large cages separated by wide windows. In such cases, the more mobile species is slowed down significantly by the tardier partner. Correlation effects are not of great significance for mixture permeation across ZIF-8, SAPO-34, DDR, and LTA structures; for these structures $(D_1/D_{12}) \rightarrow 0$, as an approximation.⁴ The

correlations are weak because molecules jump one-at-a-time across the narrow windows separating adjacent cages. The Supplementary Material (2), provides further details.

For a binary mixture, the chemical potential gradients can be related to the gradients in molar loadings

$$\frac{1}{RT} \begin{pmatrix} q_1 \nabla \mu_1 \\ q_2 \nabla \mu_2 \end{pmatrix} = \begin{bmatrix} \Gamma_{11} & \Gamma_{12} \\ \Gamma_{21} & \Gamma_{22} \end{bmatrix} \begin{pmatrix} \nabla q_1 \\ \nabla q_2 \end{pmatrix} \quad (22)$$

The elements Γ_{ij} can be determined from models describing mixture adsorption equilibrium, relating the component molar loadings q_1 and q_2 , to the partial gas phase fugacities f_1 and f_2 . Using the IAST or RAST calculations for the loadings Θ_i in Equations (15) and (16) is a reasonably good approximation

for calculating the elements of $\begin{bmatrix} \Gamma_{11} & \Gamma_{12} \\ \Gamma_{21} & \Gamma_{22} \end{bmatrix}$. The off-diagonal elements of the matrix $\begin{bmatrix} \Gamma_{11} & \Gamma_{12} \\ \Gamma_{21} & \Gamma_{22} \end{bmatrix}$ can have magnitudes significantly larger than unity.

For the simple case in which each species is described by a single-site Langmuir isotherm

$$q_i = \frac{q_{i,sat} b_i f_i}{1 + b_i f_i}; \quad \text{single - component Langmuir isotherm} \quad (23)$$

the partial gas phase fugacities are related to the component loadings by the mixed-gas Langmuir model:

$$\frac{q_i}{q_{i,sat}} = \theta_i = \frac{b_i f_i}{1 + b_1 f_1 + b_2 f_2}; \quad i = 1, 2; \quad \text{mixed - gas Langmuir} \quad (24)$$

Differentiation of equation (24) yields

$$\begin{bmatrix} \Gamma_{11} & \Gamma_{12} \\ \Gamma_{21} & \Gamma_{22} \end{bmatrix} = \frac{1}{1 - \theta_1 - \theta_2} \begin{bmatrix} 1 - \theta_2 & \frac{q_{1,sat}}{q_{2,sat}} \theta_1 \\ \frac{q_{2,sat}}{q_{1,sat}} \theta_2 & 1 - \theta_1 \end{bmatrix}; \quad \text{mixed - gas Langmuir model} \quad (25)$$

While, the mixed-gas Langmuir model is commonly used for describing mixture adsorption; in the more general case we need to use the Ideal Adsorbed Solution Theory (IAST) developed by Myers and Prausnitz.³⁰

For the special case of a binary mixture ($n = 2$) we obtain the explicit expression for $[\Delta]$

$$[\Delta] \equiv [B]^{-1} = \begin{bmatrix} \frac{1}{D_1} + \frac{x_2}{D_{12}} & -\frac{x_1}{D_{12}} \\ -\frac{x_2}{D_{12}} & \frac{1}{D_2} + \frac{x_1}{D_{12}} \end{bmatrix}^{-1} \quad (26)$$

The matrix inversion can be carried out explicitly to yield the following expression

$$[\Delta] \equiv [B]^{-1} = -\frac{1}{1 + \frac{x_1 D_2}{D_{12}} + \frac{x_2 D_1}{D_{12}}} \begin{bmatrix} D_1 \left(1 + \frac{x_1 D_2}{D_{12}}\right) & \frac{x_1 D_1 D_2}{D_{12}} \\ \frac{x_2 D_1 D_2}{D_{12}} & D_2 \left(1 + \frac{x_2 D_1}{D_{12}}\right) \end{bmatrix} \quad (27)$$

In the limiting case of $x_1 \rightarrow 1$; $x_2 \rightarrow 0$ we obtain

$$\Delta_{11} = \frac{D_1 \left(1 + \frac{x_1 D_2}{D_{12}}\right)}{1 + \frac{x_1 D_2 + x_2 D_1}{D_{12}}} \rightarrow D_1; \quad x_1 \rightarrow 1; \quad x_2 \rightarrow 0 \quad (28)$$

In the limiting case of $x_2 \rightarrow 1$; $x_1 \rightarrow 0$ we obtain

$$\Delta_{22} = \frac{D_2 \left(1 + \frac{x_2 D_1}{D_{12}}\right)}{1 + \frac{x_2 D_1 + x_1 D_2}{D_{12}}} \rightarrow D_2; \quad x_2 \rightarrow 1; \quad x_1 \rightarrow 0 \quad (29)$$

Equations (21), and (22) can be combined to yield explicit expression for the fluxes

$$\begin{pmatrix} N_1 \\ N_2 \end{pmatrix} = -\frac{\rho}{1 + \frac{x_1 D_2}{D_{12}} + \frac{x_2 D_1}{D_{12}}} \begin{bmatrix} D_1 \left(1 + \frac{x_1 D_2}{D_{12}}\right) & \frac{x_1 D_1 D_2}{D_{12}} \\ \frac{x_2 D_1 D_2}{D_{12}} & D_2 \left(1 + \frac{x_2 D_1}{D_{12}}\right) \end{bmatrix} \begin{bmatrix} \Gamma_{11} & \Gamma_{12} \\ \Gamma_{21} & \Gamma_{22} \end{bmatrix} \begin{pmatrix} \nabla q_1 \\ \nabla q_2 \end{pmatrix} \quad (30)$$

Comparison with the Fick formulation (2), we find the following explicit expression for the matrix of Fick diffusivities $[D]$

$$\begin{bmatrix} D_{11} & D_{12} \\ D_{21} & D_{22} \end{bmatrix} = \frac{\rho}{1 + \frac{x_1 D_2}{D_{12}} + \frac{x_2 D_1}{D_{12}}} \begin{bmatrix} D_1 \left(1 + \frac{x_1 D_2}{D_{12}} \right) & \frac{x_1 D_1 D_2}{D_{12}} \\ \frac{x_2 D_1 D_2}{D_{12}} & D_2 \left(1 + \frac{x_2 D_1}{D_{12}} \right) \end{bmatrix} \begin{bmatrix} \Gamma_{11} & \Gamma_{12} \\ \Gamma_{21} & \Gamma_{22} \end{bmatrix} \quad (31)$$

Equation (30) demonstrates that there are two different factors that contribute to strong coupling in mixture diffusion. Values of D_i/D_{12} in the range of 2 to 20 imply strong correlation effects; this results in significant contribution of the off-diagonal elements in the first right member of Equation (30). Often, but not always, strong correlation effects cause slowing-down of more-mobile-less-strongly-adsorbed molecules by tardier-more-strongly-adsorbed-partner species. Such is the case, for example, for diffusion of CO₂/H₂ mixtures in structures as MgMOF-74 and NaX zeolite.⁴

For the special case of *dominant* correlations, i.e. $\frac{D_1}{D_{12}} \rightarrow \infty$; $\frac{D_2}{D_{12}} \rightarrow \infty$, we can derive the following expressions³¹

$$\Delta_{11} = \Delta_{12} = \frac{D_1}{1 + \frac{x_2 D_1}{x_1 D_2}} = \frac{x_1}{\frac{x_1}{D_1} + \frac{x_2}{D_2}}; \quad \text{correlations dominant} \quad (32)$$

and

$$\Delta_{22} = \Delta_{21} = \frac{D_2}{1 + \frac{x_1 D_2}{x_2 D_1}} = \frac{x_2}{\frac{x_1}{D_1} + \frac{x_2}{D_2}}; \quad \text{correlations dominant} \quad (33)$$

The flux relations in the *dominant* correlations scenario are

$$\begin{pmatrix} N_1 \\ N_2 \end{pmatrix} = -\frac{\rho}{\frac{x_1}{D_1} + \frac{x_2}{D_2}} \begin{bmatrix} x_1 & x_1 \\ x_2 & x_2 \end{bmatrix} \begin{bmatrix} \Gamma_{11} & \Gamma_{12} \\ \Gamma_{21} & \Gamma_{22} \end{bmatrix} \begin{pmatrix} \nabla q_1 \\ \nabla q_2 \end{pmatrix}; \quad \text{correlations dominant} \quad (34)$$

The *dominant* correlations scenario provides an excellent description of mixture diffusion in carbon nanotubes.^{9, 31, 32}

Conversely, values of $D_i/D_{i2} \ll 1$, imply negligible influence of correlations; in this case, the first members on the right of Equation (21) can be ignored, yielding

$$\begin{pmatrix} N_1 \\ N_2 \end{pmatrix} = -\rho \begin{bmatrix} D_1 & 0 \\ 0 & D_2 \end{bmatrix} \begin{bmatrix} \Gamma_{11} & \Gamma_{12} \\ \Gamma_{21} & \Gamma_{22} \end{bmatrix} \begin{pmatrix} \nabla q_1 \\ \nabla q_2 \end{pmatrix}; \quad \text{negligible correlations} \quad (35)$$

Extensive Molecular Dynamics (MD) simulations have shown that correlation effects are of negligible importance for mixture diffusion across cage type zeolites such as ZIF-8, CHA, LTA, DDR, ERI that consist of cages separated by windows in the 3.4 Å – 4.2 Å size range;^{4, 7, 8, 22} molecules jump one-at-a-time across the narrow windows, and the assumption of negligible correlations is justified.

While there are a large number of publications that highlight the significance of correlation effects in mixture diffusion,^{5, 6, 33} far fewer publications are devoted to highlighting the influence of thermodynamic coupling, originating from sizable off-diagonal elements of $[\Gamma]$. One of our objectives is to underscore the contribution of thermodynamic coupling effects in mixture diffusion. In order to highlight the importance of thermodynamic coupling effects we also perform simulations ignoring thermodynamic coupling effects i.e. by taking $\Gamma_i = \delta_{ij}$, the Kronecker delta

$$\begin{pmatrix} N_1 \\ N_2 \end{pmatrix} = -\rho \begin{bmatrix} D_1 & 0 \\ 0 & D_2 \end{bmatrix} \begin{bmatrix} 1 & 0 \\ 0 & 1 \end{bmatrix} \begin{pmatrix} \nabla q_1 \\ \nabla q_2 \end{pmatrix}; \quad \text{negligible correlations; no thermo coupling} \quad (36)$$

The differences in the estimations using equations (35) and (36) can be attributed to the influence of thermodynamic coupling.

9. Onsager formulation for binary mixture diffusion

In the Onsager formulation, the fluxes are linearly related to the chemical potential gradients by defining a matrix of Onsager coefficients $[L]$

$$\begin{pmatrix} N_1 \\ N_2 \end{pmatrix} = -\frac{\rho}{RT} \begin{bmatrix} L_{11} & L_{12} \\ L_{21} & L_{22} \end{bmatrix} \begin{pmatrix} \nabla \mu_1 \\ \nabla \mu_2 \end{pmatrix}; \quad \text{Onsager formulation} \quad (37)$$

The Onsager Reciprocal Relations⁹ prescribes the symmetry,

$$L_{12} = L_{21} \quad (38)$$

Correlations in molecular jumps contribute to the off-diagonal elements of $[L]$.

The Onsager formulation is formally equivalent to the Maxwell-Stefan formulation, but suffers from the major disadvantage that the diagonal elements L_{11} and L_{22} cannot be identified with the corresponding values L_1 , and L_2 for unary transport of species 1 and 2.⁹

10. Correlation effects in binary mixture permeation across membranes

Generally speaking, intra-crystalline diffusion effects are of greater significance for membrane permeation than for transient breakthrough in fixed-bed adsorbers. The influence of correlations is best illustrated by considering the experimental data of Sandström et al.³⁴ for permeances of H₂ and CO₂ in a MFI membrane, determined both from unary and binary mixture permeation data; see Figure 6a. The permeance of species i is defined as the permeation flux N_i divided by the trans-membrane partial pressure difference, Δp_i

$$\Pi_i \equiv \frac{N_i}{\Delta p_i} \quad (39)$$

We note that the permeance of the tardier CO₂ in the mixture is practically the same as that for unary permeation for the entire range of upstream (feed) partial pressures. For H₂, the permeance in the mixture is about an order of magnitude lower than from unary experiments. This implies that mixture permeation is CO₂-selective, whereas the data based on unary permeation demonstrates H₂-selective performance. The reduction of the permeance of H₂ in the H₂/CO₂ mixtures is the consequence of two separate factors. Firstly, the mixture adsorption favors the more strongly adsorbed CO₂. Secondly, the mobility of H₂ in the mixture is reduced due to correlation effects in mixture diffusion. The more strongly adsorbed CO₂ does not vacate adsorption sites quick enough for H₂ to occupy. Consequently, there is a slowing-down of the more mobile H₂ in the mixture.

Calculations using equations (30), taking $D_1/D_{12} = 20$, along with the values of $\rho D_1/\delta = 80 \text{ kg m}^{-2} \text{ s}^{-1}$, $\rho D_2/\delta = 2.7 \text{ kg m}^{-2} \text{ s}^{-1}$, both determined from unary permeation data are shown in Figure 6b. There

is good agreement of model calculations with the experimentally determined permeances. At an upstream partial pressure of 1 MPa, for each component, the elements of the matrix $\frac{\rho[\Delta]}{\delta}$ are

$$\frac{\rho[\Delta]}{\delta} = \begin{bmatrix} 3.91 & 0.04 \\ 2.57 & 2.7 \end{bmatrix} \text{ kg m}^{-2} \text{ s}^{-1}; \text{ these values demonstrate the importance of correlations.}$$

In order to underscore the significant influence of correlations, Figure 6b also present the model calculations using equations (35), in which correlations are considered negligible. This simplified scenario, using equation (35), over-estimates the H₂ permeance by about an order of magnitude. In sharp contrast, the simplified model predictions for CO₂ are indistinguishable from those obtained taking correlations into account. Generally speaking, correlation effects have a strong *retarding* influence of the permeation of more-mobile-less-strongly-adsorbed molecules. Conversely, correlation effects are of lesser importance for tardier-more-strongly-adsorbed species.

If the *dominant* correlations scenario is chosen, then the H₂ permeance is estimated to be lower than the experimental values (solid black line). The *dominant* correlations scenario tends to overestimate the CO₂/H₂ permeation selectivity, defined by

$$S_{perm} = \frac{\Pi_1}{\Pi_2} = \frac{N_1/\Delta p_1}{N_2/\Delta p_2} \quad (40)$$

On the other hand, the *negligible* correlations scenario underestimates the CO₂/H₂ permeation selectivity; see Figure 6c. Membrane materials with high degrees of correlation are the best choices for enhancing the CO₂/H₂ permeation selectivity.

Consider the experimental data of van de Graaf et al.³⁵ for permeation of CH₄/C₂H₆, and CH₄/C₃H₈ mixtures across an MFI membrane at 303 K presented in Figure 7. The two sets of experimental permeance data are plotted as functions of the mole fraction of the tardier component in the feed gas mixture in the upstream compartment. Increasing the proportion of the tardier component in the feed mixture has the effect of progressively reducing the permeance of the more mobile CH₄ across the membrane. The reasons for the reduction in the permeance of CH₄ are two-fold: (a) due to mixture adsorption equilibrium that favors the heavier alkane, and (2) slowing-down of the mobility of CH₄ due

to correlation effects. Use of the flux equations (30) including correlation effects provides good estimates of the permeances of both species in the mixture.⁴ Ignoring correlation effects, and using the flux equations (35) severely overestimates the permeance of CH₄; see Figures 7a, and 7b. Consequently, the C₂H₆/CH₄ and C₃H₈/CH₄ permeation selectivities are overly pessimistic if correlations are considered to be negligible; Figures 7c, and 7d. Conversely, the dominant correlations scenario provides an overly optimistic picture of the permeation selectivities. Membrane materials with high degrees of correlation are the best choices for enhancing C₂H₆/CH₄ and C₃H₈/CH₄ permeation selectivities.

Figure 8a provides a comparison of the unary permeances of CH₄ and nC₄H₁₀ with those in equimolar CH₄/nC₄H₁₀ binary mixture across an MFI membrane as a function of the temperature.³⁶ Correlations effects cause the permeance of the more-mobile-less-strongly-adsorbed CH₄ to be significantly lower in the mixture when compared to the unary permeance. On the other hand, the permeance of the tardier-more-strongly-adsorbed nC₄H₁₀ is only influenced to a minor extent by correlation effects in the mixture.

Figure 8b provides a comparison of the unary permeances of H₂ and CO₂ with those in equimolar H₂/CO₂ binary mixture across an NH₂-MIL-53(Al) membrane as a function of the temperature.³⁷ Correlations effects cause the permeance of the more-mobile-less-strongly-adsorbed H₂ to be lower in the mixture when compared to the unary permeance. On the other hand, the permeance of the tardier-more-strongly-adsorbed CO₂ is only influenced to a minor extent by correlation effects in the mixture.

Baertsch et al.³⁸ have compared component permeances of o-xylene, m-xylene, p-xylene, ethylbenzene, toluene, and benzene across MFI membrane obtained from unary permeation experiments with those determined from a variety of binary mixture permeation data. The component permeances for mixed gas permeation was found to coincide with the permeance of the tardier species in the binary mixtures; this is clear demonstration of slowing-down of the more mobile partner species. Several other examples of the influence of correlations on mixture diffusion are provided in our earlier publications.⁴

Jeong et al.³⁹ report permeances of benzene and cyclohexane across a NaY zeolite membrane, obtained from both unary and mixture permeation experiments. The adsorption selectivity is strongly in favor of benzene, whereas the diffusion selectivity favors cyclohexane. The lower diffusivity of benzene is most likely attributable to the much stronger binding energy of benzene with the cations in NaY. From unary permeation data we note that the membrane is selective to cyclohexane. However, the mixture permeation is selective to benzene. Correlation effects tend to slow down the more mobile cyclohexane and the permeation selectivity is largely governed by adsorption selectivity that favors benzene.

Generally speaking, correlation effects are of minor significance for mixture permeation across SAPO-34, ZIF-7, ZIF-8, DDR, and LTA membranes.

Consider permeation of CO₂/CH₄ separation using a membrane made up of thin layers of SAPO-34 that consists of 316 Å³ sized cages separated by 3.8 Å × 4.2 Å sized windows. Experimental data on permeances Π_i of CO₂ and CH₄ determined from binary permeation experiments are compared in Figure 9, with the estimations of the M-S equations (36) ignoring correlations, and $(D_1/D_{12}) \rightarrow 0$ is a good assumption to make.

Figure 10 shows the experimental data of Li et al.⁴⁰ for the permeances of H₂ and CO₂ across a ZIF-7 membrane, determined as a function of the mole fraction of CO₂ in the gas phase in the upstream compartment. The magnitude of Π_i is hardly influenced by the mixture composition in the upstream compartment; correlation effects have negligible influences.

The separation of C₂H₄/C₂H₆, and C₃H₆/C₃H₈ mixtures using ZIF-8 membranes is primarily based on differences in the diffusivities of the alkenes and alkanes; such differences arise due to subtle differences in bond lengths and bond angles.²⁴ Experimental data on diffusivities of C₂H₄, and C₂H₆ show diffusion selectivities of the order of 5 in favor of C₂H₄; see Figure 11a.⁴¹ The ratio of the diffusivity of C₃H₆ propene to that of C₃H₈ in ZIF-8 has a value of 125 based on the uptake data of Li et al..⁴² A further confirmation of the subtle influence of bond lengths and bond angles on diffusivities of

alkenes and alkanes is provided by Ruthven and Reyes⁴³ who report diffusion selectivity values for C₃H₆/C₃H₈ mixtures in excess of 1000 for CHA and DDR zeolites.

The adsorption selectivities for C₂H₄/C₂H₆, and C₃H₆/C₃H₈ mixtures using ZIF-8 favor the saturated alkane; this implies that adsorption and diffusion do not proceed hand in hand. The diffusion selectivities over-ride the adsorption selectivities, yielding permeation selectivities in favor of the unsaturated alkene.

The experiments of Bux et al.⁴¹ for a ZIF-8 membrane show that the C₂H₄/C₂H₆ permeation selectivity is in the range of 2 – 3; see Figure 11b.

For C₃H₆/C₃H₈ permeation across ZIF-8 membrane, the permeation selectivities, S_{perm} , reported in the experiments of Pan et al.⁴⁴ (see Figure 12a), and Liu et al.⁴⁵ (see Figures 12b,c) show values in the range of 30 - 35. The values of S_{perm} are lower than the diffusion selectivity values of 125, because of adsorption favors propane.³ From the data in Figures 12a, and 12c we note that the magnitude of Π_i is hardly influenced by the mixture composition in the upstream compartment; correlation effects have negligible influence. The estimations of the component permeances for C₃H₆ and C₃H₈ across a ZIF-8 membrane are indicated by the solid continuous lines in Figures 12b,c; the M-S model is the simplified analytical model, ignoring correlations, described by Krishna and van Baten.⁴ There is reasonable agreement between the experimental data of Liu et al.⁴⁵ and the M-S model ignoring correlations.

11. Overshoot phenomena in transient membrane permeation

Diffusional coupling effects often lead to unusual phenomena such as overshoots in the flux of the more mobile partners during transient mixture permeation across nanoporous membranes. Geus et al.⁴⁶ report experimental data on transient permeation CH₄/nC₄H₁₀ mixture across MFI (cf. Figure 13a); the flux of the more mobile CH₄ exhibits a pronounced maximum.

In order to gain insights into this observed maximum in the flux of the more mobile partner, we carried out a set of simulations for transient permeation CH₄/nC₄H₁₀ mixture across MFI membranes using the data inputs used in an earlier publication⁴ using Equation (30). Correlation effects are taken using information contained in our earlier publication.⁴

For modeling purposes, the transient permeation fluxes are obtained by solving the set of partial differential equations

$$\frac{\partial q_i(z,t)}{\partial t} = -\frac{1}{\rho} \frac{\partial}{\partial z} (N_i) \quad (41)$$

where z is the distance coordinate along the direction of membrane thickness. The boundary conditions are the partial pressures and component molar loadings at the upstream ($z = 0$) and downstream ($z = \delta$) faces of the membrane; see schematic in Figure 14.

$$\begin{aligned} z = 0; \quad p_i &= p_{i0}; \quad q_i = q_{i0} \\ z = \delta; \quad p_i &= p_{i\delta}; \quad q_i = q_{i\delta} \end{aligned} \quad (42)$$

The simulation results for transient permeation $\text{CH}_4/\text{nC}_4\text{H}_{10}$ mixture are shown with continuous solid line in Figures 13b, c, and d for three different scenarios. In the simulations presented in Figure 13b we use the flux equations (30), including both correlations and thermodynamic coupling. The flux of the more mobile-less-strongly-adsorbed- CH_4 shows a pronounced maximum, whereas the tardier-more-strongly-adsorbed- nC_4H_{10} exhibits a monotonous approach to steady-state. In the simulations presented in Figure 13c we use the flux equations (35), ignoring correlations, but including thermodynamic coupling. In this scenario too, we note that the flux of CH_4 exhibits a maximum during the early phase of the transience. It is noteworthy that the maximum in the flux of CH_4 is more prominent when correlations are ignored. This is because correlations tend to slow down the more mobile CH_4 . Ignoring correlations, results in no slowing-down effects, and the steady-state flux of CH_4 is higher than for the scenario in which correlations are included. In the simulations presented in Figure 13d we use the flux equations (36) ignoring correlations and also ignoring thermodynamic coupling, with $\Gamma_{ij} = \delta_{ij}$. In this scenario too we note that the maximum in the CH_4 fluxes vanishes. The maximum in the transient CH_4 flux is traceable to thermodynamic coupling effects.

It should also be noted that the steady-state fluxes are different for each of the three scenarios, because the magnitudes of the driving forces are also altered in each case.

For nC4/iC4 mixture permeation across a MFI membrane, curious overshoots, and undershoots, in the transient retentate and permeate concentrations have been reported in the experiments of Courthial et al.⁴⁷; such phenomena are also ascribable to thermodynamic coupling effects. Figure 15a presents the elements Γ_{ij} of the thermodynamic corrector factor matrix $[\Gamma]$, obtained by differentiation of the IAST equations describing the nC4/iC4 adsorption equilibrium. We note that for $f_t < 100$ Pa, the off-diagonal elements are significantly smaller in magnitude than the corresponding diagonal elements. However, for $f_t > 100$ Pa, the contribution of the off-diagonal elements becomes increasingly significant. Figure 15b presents calculations of $(\Gamma_{12}\Theta_2/\Gamma_{11}\Theta_1)$ and $(\Gamma_{21}\Theta_1/\Gamma_{22}\Theta_2)$ and that signify the extent of thermodynamic coupling. We note that the driving force of iC4 is significantly influenced by that of nC4. Another interesting point to note is that $(\Gamma_{12}\Theta_2/\Gamma_{11}\Theta_1)$ exhibits a maximum. This maximum occurs at a total mixture loading of $\Theta_t = 4$ molecules per unit cell.

Figures 15c, 15d, and 15e present simulation of transient permeation of 5/95 nC4(1)/iC4(2) mixtures across a MFI membrane at 300 K for three different scenarios. In the simulations presented in Figure 15c we use the flux equations (30), including both correlations and thermodynamic coupling. The flux of the more mobile-more-strongly-adsorbed-nC4 shows a pronounced maximum, whereas the tardier-less-strongly-adsorbed-iC4 exhibits a monotonous approach to steady-state. In the simulations presented in Figure 15d we use the flux equations (35), ignoring correlations, but including thermodynamic coupling. In this scenario too, we note that the flux of nC4 exhibits a maximum during the early phase of the transience. In the simulations presented in Figure 15e we use the flux equations (36) ignoring correlations and also ignoring thermodynamic coupling, with $\Gamma_{ij} = \delta_{ij}$. In this scenario too we note that the maximum in the nC4 fluxes vanishes. The maximum in the transient nC4 flux is traceable to thermodynamic coupling effects. As in the case of CH₄/nC₄H₁₀ permeation, it should also be noted that the steady-state fluxes are different for each of the three scenarios, because the magnitudes of the driving forces are also altered in each case.

For permeation of nC6/2MP, and nC6/23DMB mixture across an MFI membrane, Matsufuji et al.⁴⁸ have reported transient data showing overshoots in the nC6 flux during transient approach to steady-

state; see Figures 16a, and 16b. As demonstrated in the two foregoing examples for CH₄/nC₄H₁₀ and nC₄(1)/iC₄(2) mixtures, the maximum in the flux of the more mobile nC₆ is ascribable to thermodynamic coupling effects. Figure 16c presents the elements Γ_{ij} of the thermodynamic corrector factor matrix for nC₆/2MP mixtures. We note that for $f_t < 1$ Pa, the off-diagonal elements are significantly smaller in magnitude than the corresponding diagonal elements. However, for $f_t > 1$ Pa, the contribution of the off-diagonal elements becomes increasingly significant. Figure 16d presents calculations of $(\Gamma_{12} \Theta_2 / \Gamma_{11} \Theta_1)$ and $(\Gamma_{21} \Theta_1 / \Gamma_{22} \Theta_2)$ and that signify the extent of thermodynamic coupling. We note that the driving force of 2MP is significantly influenced by that of nC₆. Another interesting point to note is that $(\Gamma_{12} \Theta_2 / \Gamma_{11} \Theta_1)$ exhibits a maximum at a total mixture loading of $\Theta_t = 4$ molecules per unit cell. This maximum is the direct cause of the observed maximum in the transient nC₆ flux for nC₆/2MP mixtures.

The experimental data of Matsufuji et al.⁴⁹ for transient permeation of (a) 50/50 m-xylene/p-xylene, and (b) 24/50/25 p-xylene/m-xylene/o-xylene mixtures across MFI membrane show a maximum in the flux of p-xylene which is the most mobile of the three isomers; see Figures 17a, and 17b. The most likely cause of this maximum is the influence of thermodynamic coupling. To verify this conclusion we carried out simulations of transient membrane for 50/50 m-xylene/p-xylene mixtures across an MFI membrane. O-xylene and m-xylene locate preferentially at the intersections of MFI, whereas the linear p-xylene molecules align the channels; see snapshots in Figure 17. The pure component isotherms, obtained from CBMC simulations,⁵⁰ show that, up to a loading of 4 molecules per unit cell the guest molecules are located at the channel intersections. At these locations, the adsorption strength of m-xylene is higher than that of p-xylene; this is due to more optimal interactions with the framework atoms. Transient uptake simulation results for two different scenarios are presented in Figures 17c, and 17d. Inclusion of thermodynamic coupling effects, and use of the flux equations (35) produces a maximum in the flux of the more mobile p-xylene during the early stages of the transience. Use the flux equations (36), ignoring thermodynamic coupling, with $\Gamma_{ij} = \delta_{ij}$, results in a monotonous approach to steady-state for both components. It must be remarked that Matsufuji et al.⁴⁹ offer the explanation that

the maximum in the flux of p-xylene is caused due to “blocking” of the transport of p-xylene in the later stages of the transience due to increasing occupation of the channels by the more strongly adsorbed m-xylene and o-xylene. Our belief, based on the presented simulations evidence, is that the maximum is ascribable to the influence of thermodynamic coupling.

For permeation of benzene/p-xylene mixtures across an MFI membrane, Kolvenbach et al.⁵¹ have reported an overshoot of the benzene flux during the early stages of the transience.

In the transient permeation experiments of Bennett et al.⁵² for C₂H₆/C₃H₈ , and N₂/CO₂ mixtures across an MFI membrane found maxima in the permeate concentrations of the more mobile partners C₂H₆, and N₂, in the respective mixtures. The flux maxima are most likely due to thermodynamic coupling effects.

Figures 18a,b present the fluxes of propene(1) and propane(2) for permeation across ZIF-8 membrane using two different simulation scenarios. Simulations taking thermodynamic coupling effects into account (cf. Figure 18a) show an overshoot in the flux of the more mobile propene. Neglect of thermodynamic coupling effects (cf. Figure 18b), shows that the fluxes of both propene and propane show a monotonous approach to steady-state. It is important to stress that while neglect of thermodynamic coupling has a significant influences on the transient permeation, the ratio of the fluxes at steady-state are practically identical. This implies that the steady-state permeation experiments (see Figure 11) can be modeled adequately using equations (36). A further point to note is that the steady-state permeation experiments of Pan et al.⁴⁴ confirm that the membrane permeation is propene selective; this selectivity is induced by diffusion, not by adsorption.

12. Simulations of transient unary uptake within crystals

For unary diffusion of species i in nanoporous materials, the Fickian formulation relating the molar flux N_i , expressed as the number of moles per m² of crystalline material, to the gradient in the molar loading is commonly written as

$$N_i = -\rho D_i \nabla q_i \quad (43)$$

Equation (43), which *defines* the Fick diffusivity D_i , is considered to be “practical” because it can be incorporated into the design equations for describing membrane permeation fluxes, and component uptakes within crystals packed in fixed beds.

For transient unary uptake within a crystal, the radial distribution of molar loadings, q_i , within a spherical crystallite, of radius r_c , is obtained from a solution of a set of differential equations describing the uptake

$$\frac{\partial q_i(r,t)}{\partial t} = -\frac{1}{\rho} \frac{1}{r^2} \frac{\partial}{\partial r} (r^2 N_i) \quad (44)$$

At any time t , during the transient approach to thermodynamic equilibrium, the spatially averaged molar loading within the crystallite r_c is obtained by integration of the radial loading profile

$$\bar{q}_i(t) = \frac{3}{r_c^3} \int_0^{r_c} q_i(r,t) r^2 dr \quad (45)$$

The $\bar{q}_i(t)$ can be compared directly with experimental transient uptake data. An analytical solution to equation (44) is only possible for the special case in which the Fick D_i can be considered to be independent of the loading.

The expression for fractional approach to equilibrium is ¹⁵

$$\frac{(\bar{q}_i(t) - q_i(r_c, 0))}{(q_i(r_c, t = \infty) - q_i(r_c, 0))} = 1 - \frac{6}{\pi^2} \sum_{m=1}^{\infty} \frac{\exp(-m^2 \pi^2 \frac{D_i}{r_c^2} t)}{m^2} \quad (46)$$

Equation (46) allows data on transient uptake to be fitted to obtain an average value of the Fick diffusivity D_i that is representative of the range of loadings encountered in the experiment.

Figure 19a shows the experimental data for transient adsorption and desorption profiles for C_2H_6 in LTA-4A zeolite. The adsorption branch can be fitted with $D_i/r_c^2 = 1.1 \times 10^{-3} \text{ s}^{-1}$, while the desorption branch yields a lower value $D_i/r_c^2 = 6 \times 10^{-4} \text{ s}^{-1}$. The asymmetry in the adsorption and desorption kinetics is not easy to interpret on the basis of the Fick formulation.

For a fundamental understanding of the observed asymmetry, we turn to the Maxwell-Stefan formulation that uses chemical potential gradients as the driving forces

$$N_i = -\rho D_i \frac{q_i}{RT} \nabla \mu_i \quad (47)$$

where the M-S diffusivity, D_i , is inter-related to the Fick diffusivity by

$$D_i = D_i \Gamma_i; \quad \Gamma_i \equiv \frac{q_i}{f_i} \frac{\partial f_i}{\partial q_i} \quad (48)$$

The thermodynamic correction factor, Γ_i , can be obtained by differentiation of the adsorption isotherm that relates the molar loadings to the bulk fluid phase pressure, or fugacity, surrounding the crystals. For the simplest case of a single-site Langmuir isotherm

$$\frac{q_i}{q_{i,sat}} = \theta_i = \frac{b_i f_i}{1 + b_i f_i} \quad (49)$$

the thermodynamic correction factor, Γ_i , is

$$\Gamma_i = \frac{1}{1 - q_i/q_{i,sat}} = \frac{1}{1 - \theta_i} \quad (50)$$

The inverse thermodynamic factor, $1/\Gamma_i$, decreases linearly with fractional occupancy (cf. Figure 19a). Both the adsorption and desorption cycles can be fitted with $D_i/r_c^2 = 2 \times 10^{-4} \text{ s}^{-1}$. This implies that that the asymmetry in the adsorption and desorption transience have their origin in the characteristics of $1/\Gamma_i$; the slower desorption kinetics is attributable to the decrease in $1/\Gamma_i$ during the desorption phase.

The strong imprint $1/\Gamma_i$ has on unary diffusion is highlighted by a wide variety of guest/host combinations^{11, 24}. For transient desorption of methanol from CuBTC, for example, the experimental data of Tsotsalas et al.⁵³ displays step-wise characteristics (cf. Figure 20a). The step-wise transience can be rationalized on the basis of the non-uniform variation of $1/\Gamma_i$ with occupancy (cf. Figure 20b), that is induced by molecular clustering effects.

The important message that emerges from the two examples on transient diffusion presented in Figures 19, and 20 is that the adsorption characteristics has a direct influence on the diffusion characteristics. The Fick formulation subsumes adsorption thermodynamic influences into the Fick diffusivity D_i . In the M-S formulation, thermodynamic effects are separately accounted for, and this results in a clearer understanding and description of diffusion.

13. Simulation methodology for transient mixture uptake in crystals

For most crystal geometries, representation as an equivalent sphere is an acceptable approximation, as argued by Ruthven.¹⁵ Indeed, most researchers report their uptake diffusivities in terms of a model that assumes uptake within a single spherical crystalline particle. The values thus obtained for the diffusivities within a spherical crystal can be translated to other crystal geometries by comparing values at the same characteristic dimension, defined as the ratio of the crystal volume to its external surface area. For a spherical shaped crystal of radius r_c , the ratio of the volume to the external surface area is

$\frac{\left(\frac{4}{3}\pi r_c^3\right)}{4\pi r_c^2} = \frac{r_c}{3}$. For a cylindrical shaped crystal of radius r_c and length L , the ratio of the volume to the

external surface area is $\frac{(\pi r_c^2 L)}{2\pi r_c L + 2\pi r_c^2}$, which reduces to $\frac{r_c}{2}$ for an infinitely long cylinder. For a cuboid

crystal of dimensions a , b , and c , the volume to surface area ratio is $\frac{(abc)}{2(ab + bc + ca)}$. The formula for

cuboids is applicable to coffin-shaped MFI crystals, that are often used in experimental studies on diffusion and adsorption. The mathematical analysis developed below for spherical crystals of radius r_c , may be applied to coffin-shaped MFI crystals by taking an equivalent radius of sphere to be

$$\frac{3(abc)}{2(ab + bc + ca)}.$$

The radial distribution of molar loadings, q_i , within a spherical crystallite, of radius r_c , is obtained from a solution of a set of differential equations describing the uptake

$$\frac{\partial q_i(r,t)}{\partial t} = -\frac{1}{\rho} \frac{1}{r^2} \frac{\partial}{\partial r} (r^2 N_i) \quad (51)$$

For uptake of a binary mixture within a spherical crystal, the flux expressions for r -coordinate radial diffusion of a binary mixture are summarized in matrix notation as follows

$$\begin{aligned} \begin{pmatrix} N_1 \\ N_2 \end{pmatrix} &= -\rho \begin{bmatrix} \Delta_{11} & \Delta_{12} \\ \Delta_{21} & \Delta_{21} \end{bmatrix} \begin{bmatrix} \Gamma_{11} & \Gamma_{12} \\ \Gamma_{21} & \Gamma_{21} \end{bmatrix} \frac{\partial \begin{pmatrix} q_1 \\ q_2 \end{pmatrix}}{\partial r} \\ &= \frac{\rho}{1 + \frac{x_1 D_2}{D_{12}} + \frac{x_2 D_1}{D_{12}}} \begin{bmatrix} D_1 \left(1 + \frac{x_1 D_2}{D_{12}} \right) & \frac{x_1 D_1 D_2}{D_{12}} \\ \frac{x_2 D_1 D_2}{D_{12}} & D_2 \left(1 + \frac{x_2 D_1}{D_{12}} \right) \end{bmatrix} \begin{bmatrix} \Gamma_{11} & \Gamma_{12} \\ \Gamma_{21} & \Gamma_{22} \end{bmatrix} \frac{\partial \begin{pmatrix} q_1 \\ q_2 \end{pmatrix}}{\partial r} \end{aligned} \quad (52)$$

The flux of each species is strongly coupled to its partner in the mixture due to two types of couplings: (a) correlation effects that contribute to finite contributions of non-diagonal elements in

$$\begin{bmatrix} \Delta_{11} & \Delta_{12} \\ \Delta_{21} & \Delta_{21} \end{bmatrix}, \text{ and (b) thermodynamic coupling due to the non-diagonal elements of } \begin{bmatrix} \Gamma_{11} & \Gamma_{12} \\ \Gamma_{21} & \Gamma_{21} \end{bmatrix}.$$

When correlation effects can be considered to be negligible, i.e. $D_i/D_{12} \rightarrow 0$, equations (52) reduce to

$$\begin{pmatrix} N_1 \\ N_2 \end{pmatrix} = -\rho \begin{bmatrix} D_1 & 0 \\ 0 & D_2 \end{bmatrix} \begin{bmatrix} \Gamma_{11} & \Gamma_{12} \\ \Gamma_{21} & \Gamma_{21} \end{bmatrix} \frac{\partial \begin{pmatrix} q_1 \\ q_2 \end{pmatrix}}{\partial r}; \quad \text{negligible correlations} \quad (53)$$

In order to demonstrate the importance of thermodynamic coupling effects in several examples that

are discussed below, we also report simulation results in which $\begin{bmatrix} \Gamma_{11} & \Gamma_{12} \\ \Gamma_{21} & \Gamma_{21} \end{bmatrix}$ is assumed to be the identity

matrix, and the following, simplified, flux relations apply

$$\begin{pmatrix} N_1 \\ N_2 \end{pmatrix} = -\rho \begin{bmatrix} D_1 & 0 \\ 0 & D_2 \end{bmatrix} \begin{bmatrix} 1 & 0 \\ 0 & 1 \end{bmatrix} \frac{\partial \begin{pmatrix} q_1 \\ q_2 \end{pmatrix}}{\partial r}; \quad \text{no thermodynamic coupling} \quad (54)$$

At time $t = 0$, i.e. the initial conditions, the molar loadings $q_i(r,0)$ at all locations r within the crystal are uniform. For all times $t \geq 0$, the exterior of the crystal is brought into contact with a bulk gas mixture at a different $p_i(r_c, t)$ that is maintained constant till the crystal reaches thermodynamic equilibrium with the surrounding gas mixture.

$$t \geq 0; \quad q_i(r_c, t) \text{ in equilibrium with the initial values } p_i(r_c, t) \quad (55)$$

At any time t , during the transient approach to thermodynamic equilibrium, the spatially averaged molar loading within the crystallites of radius r_c is calculated using

$$\bar{q}_i(t) = \frac{3}{r_c^3} \int_0^{r_c} q_i(r, t) r^2 dr \quad (56)$$

The $\bar{q}_i(t)$ can be compared directly with experimental transient uptake data.

An analytical solution to equation (51) is only possible for the special case of unary diffusion (cf. equation (19)) in which the Fick diffusivity, D_i , defined in equation (20), can be considered to be independent of the loading. The expression for fractional approach to equilibrium is²

$$\frac{(\bar{q}_i(t) - q_i(r_c, 0))}{(q_i(r_c, t = \infty) - q_i(r_c, 0))} = 1 - \frac{6}{\pi^2} \sum_{m=1}^{\infty} \frac{\exp(-m^2 \pi^2 \frac{D_i}{r_c^2} t)}{m^2} \quad (57)$$

There is no generally applicable analytical solution to describe transient diffusion of binary mixtures and the set of equations (51), (52) or (53) or (54), and (55) need to be solved numerically using robust computational techniques. Equations (51) are first subjected to finite volume discretization. The choice of the discretization scheme used is crucially important in obtaining accurate, converged results. Each crystallite, assumed to be spherical, is divided into equi-volume slices as sketched in Figure 21. The choice of equi-volume slices instead of equi-distant slices of the spherical particle is dictated by the fact that the gradients of the loadings are particularly steep nearer to $r = r_c$. Further details of the numerical procedures used in this work, are provided by Krishna and co-workers;^{2, 3, 54, 55} interested readers are referred to our website that contains the numerical details.⁵⁴

14. Transient uptake of N₂/CH₄ mixtures in LTA-4A and ETS-4

We now examine experimental data published in the literature where transient overshoot of the component loading of one of the components in a binary mixture has been reported.

The first example we consider is the separation of N₂(1)/CH₄(2) mixtures, that is important in the context of natural gas upgrading. For transportation purposes, the pipeline specifications usually demand that the amount of N₂ in natural gas is less than about 3%, because the presence of N₂ reduces the heating value. For purification of natural gas streams, that is commonly available at high pressures, it is desirable to use adsorbents in pressure swing adsorption (PSA) units that are selective to N₂, that is present in quantities that are often as high as 20%. For most known adsorbents, the adsorption selectivity favors CH₄. One practical solution to this problem is to rely on diffusion selectivities by using nanoporous materials that have significantly higher diffusivities of N₂, compared to that of CH₄.⁵⁶

57

The earliest study demonstrating the possibility of utilizing diffusion selectivities for separating N₂(1)/CH₄(2) mixtures is contained in the classic paper of Habgood⁵⁸ that presents experimental data on transient uptake of N₂(1)/CH₄(2) mixtures in crystallites of LTA-4A; their data measured at 194 K with partial pressures (a) $p_1 = 50.9$ kPa; $p_2 = 49.1$ kPa, and (b) $p_1 = 10$ kPa; $p_2 = 90$ kPa are shown in Figures 22a,b. The N₂(1)/CH₄(2) mixture constitutes a combination of more-mobile-less-strongly-adsorbed-N₂ and tardier-more-strongly-adsorbed-CH₄. The diffusivity of N₂ is a factor 22 higher than that of CH₄, but it has an adsorption strength that is a factor 2.2 lower. During the initial stages of the transient uptake, the pores of LTA-4A are predominantly richer in the more mobile N₂, but this is displaced by the more strongly adsorbed, tardier CH₄ molecules at longer times. This results in an overshoot in the N₂ uptake in both the experimental campaigns. The continuous solid lines in Figure 22 are the calculations of the Maxwell-Stefan model using the flux equation (53); this model successfully captures the overshoot in the uptake of the more mobile N₂. Extensive Molecular Dynamics (MD) simulations have confirmed that correlation effects are of negligible importance for mixture diffusion across cage type zeolites such as CHA, LTA, DDR, ERI that consist of cages separated by windows in

the 3.4 Å – 4.2 Å size range.^{4, 7, 8, 22} Molecules jump one-at-a-time across the narrow windows, and the assumption of negligible off-diagonal elements in the $[\Delta]$.

The calculations of the elements of the matrix of thermodynamic factors Γ_{ij} for $N_2(1)/CH_4(2)$ mixture within LTA-4A crystals demonstrate the significance of the off-diagonal elements at higher loadings; see Figure 23.

The dashed lines in Figure 22 are the Maxwell-Stefan model simulations using equation (54) in which the matrix of thermodynamic correction factors is assumed to be the identity matrix, i.e. taking $\Gamma_i = \delta_{ij}$,

i.e. $\begin{bmatrix} \Gamma_{11} & \Gamma_{12} \\ \Gamma_{21} & \Gamma_{21} \end{bmatrix} = \begin{bmatrix} 1 & 0 \\ 0 & 1 \end{bmatrix}$ Neglect of thermodynamic coupling results in uptake profiles that do not

exhibit an overshoot in N_2 uptake. The simulation results presented in Figures 22a,b confirm that thermodynamic coupling is the cause of the N_2 overshoot.

For a given set of adsorption parameters, the extent of overshoot of the more mobile species is governed by the ratio of the diffusivities. In order to demonstrate this, Figure 24 presents simulations for $p_1 = 50.9$ kPa; $p_2 = 49.1$ kPa in which the ratio of diffusivities D_1/D_2 is chosen to be a factor 1000, 22 (base case), 10, and 1 times that of CH_4 (whose diffusivity is maintained at the value for the base case). The necessary condition for the overshoot is that the diffusivity of N_2 be higher than that of CH_4 . When the diffusivity of N_2 is chosen to be a factor 1000 higher than that of CH_4 the extent of overshoot increases only slightly in comparison to the base case.

Based on his experimental results for transient uptake, Habgood filed a patent claiming that natural gas could be upgraded by removing the faster diffusing nitrogen using 4A zeolite and a kinetically controlled separation process at a low sub-atmospheric temperature.

By tuning the size of the microporous channels and using ETS-4 as adsorbent, both adsorption and diffusion characteristics favor the selective uptake of N_2 from $N_2(1)/CH_4(2)$ mixtures.^{56, 57, 59} The transient uptake data of Majumdar et al.⁵⁷ for Ba-ETS-4 are shown in Figures 25a, and 25b for (a) 10/90, and (b) 50/50 mixtures show overshoots in the uptake of the more mobile N_2 . Simulations of transient uptake for 10/90 mixture demonstrate that the overshoot is possible, provided thermodynamic

coupling effects are properly accounted using the flux equation (53). The dashed lines in Figure 25c are simulations using the simplified equation (54), neglecting thermodynamic coupling; in this case, the overshoot of N_2 disappears.

15. Transient uptake of CH_4/C_2H_6 mixtures in LTA-4A

For co-adsorption of a mixture of CH_4 and C_2H_6 in LTA-4A, the more mobile CH_4 is found to exhibit an overshoot in the experiments reported by Carlson and Dranoff;⁶⁰ see Figure 26. In this mixture we have a combination of more-mobile-less-strongly-adsorbed- CH_4 and tardier-more-strongly-adsorbed- C_2H_6 . Correlation effects are of negligible importance for the same reasons mentioned in the foregoing paragraph. Krishna⁶¹ has shown that use of the coupled flux equation (53) is necessary for capturing this CH_4 overshoot. Furthermore, he has also concluded that use of the simpler equation (54) neglecting the thermodynamic coupling, has the effect of anticipating a monotonic approach to equilibrium of both CH_4 and C_2H_6 .

16. Transient uptake of aromatic mixtures in MFI zeolite

Experimental data of Niessen and Karge^{62, 63} for transient uptake of (a) benzene(1)/ethylbenzene(2), and (b) benzene(1)/*p*-xylene(2) mixtures in MFI zeolite (H-ZSM-5) show overshoots in the benzene uptake; see Figure 27. Simulations of transient uptake for benzene(1)/ethylbenzene(2) mixture, presented in Figure 27c, demonstrate that the benzene overshoot can be captured provided thermodynamic coupling effects are included using the flux equation (53). The benzene overshoot disappears in simulations using the simplified equation (54), neglecting thermodynamic coupling.

17. Transient uptake of n-heptane/benzene mixtures in NaX zeolite

The experimental data of Kärger and Bülow⁶⁴ for transient uptake of n-heptane(1)/benzene(2) mixture in NaX zeolite at 359 K shows an overshoot in the uptake of the more mobile n-heptane; see Figure 28a. Benzene is much more strongly adsorbed due to electrostatic interactions with the Na^+ cations. The stronger binding energy of benzene, makes the mobility of benzene significantly lower than that of the non-polar n-heptane.²⁴ Our objective here is to examine the influence of thermodynamic

coupling on the transient uptake and n-heptane overshoot. The essential characteristics of the transient uptake can be captured qualitatively by the flux equation (53) in which correlation effects are ignored; see the continuous solid lines in Figure 28b; this model is able to capture the overshoot of n-heptane. The dashed lines are simulations using the simplified equation (54), neglecting thermodynamic coupling i.e. taking $\Gamma_{ij} = \delta_{ij}$; we note that the n-heptane overshoot has disappeared with neglect of the influence of thermodynamic coupling. The windows separating the adjacent cages of NaX are about 7.4 Å, and correlations effects need to be taken into consideration for quantitative modelling.^{4, 20} Inclusion of correlation effects will have the effect of slowing-down the more mobile n-heptane, leading to a less pronounced overshoot.

18. Transient uptake of propene/propane mixtures in ZIF-8 and CHA

The separation of alkene/alkane mixtures is important in practice, as we shall discuss in detail in a later section. Here, we consider the transient uptake of propene/propane mixtures in two different structures, ZIF-8 and CHA, that have cages separated by narrow windows. For both ZIF-8 and CHA, the adsorption strength of the saturated propane is higher than that of propene, whereas the diffusivities are significantly higher for the unsaturated propene. Figures 29a,b present simulations of transient uptake of propene(1)/propane(2) within crystals of (a) ZIF-8, and (b) CHA. In both cases the more mobile propene exhibits a maximum in the uptake. The overshoot is significantly lower for ZIF-8 for which $D_1/D_2 = 125$.⁴² The extent of overshoot is significantly higher for CHA for which the ratio of diffusivities of propene to propane, $D_1/D_2 = 5000$.⁶⁵ For both materials, neglect of thermodynamic coupling yields a monotonic approach to equilibrium for both species; see the dashed lines in Figure 29.

19. Simulation methodology for transient breakthrough in fixed bed adsorbers

Fixed bed, packed with crystals of nanoporous materials, are commonly used for separation of mixtures (see schematic in Figure 30); such adsorbers are commonly operated in a transient mode, and the compositions of the gas phase, and within the crystals, vary with position and time. Experimental

data on the transient breakthrough of mixtures across fixed beds are commonly used to evaluate and compare the separation performance of zeolites and MOFs.⁶⁶⁻⁷⁶ For a given separation task, transient breakthroughs provide more a realistic evaluation of the efficacy of a material, as they reflect the combined influence of adsorption selectivity, and adsorption capacity.⁷⁷

Furthermore, transient breakthroughs are influenced by both mixture adsorption equilibrium, and intra-crystalline diffusion. In order to determine the extent of the relative importance of adsorption and diffusion in determining the separation performance we perform transient breakthrough simulations, and compare these with experimental data. We describe below the simulation methodology used to perform transient breakthrough calculations.

Assuming plug flow of an n -component gas mixture through a fixed bed maintained under isothermal conditions, the partial pressures in the gas phase at any position and instant of time are obtained by solving the following set of partial differential equations for each of the species i in the gas mixture.^{1, 2,}

15, 78-81

$$\frac{1}{RT} \frac{\partial p_i(t, z)}{\partial t} = -\frac{1}{RT} \frac{\partial(v(t, z)p_i(t, z))}{\partial z} - \frac{(1-\varepsilon)}{\varepsilon} \rho \frac{\partial \bar{q}_i(t, z)}{\partial t}; \quad i = 1, 2, \dots, n \quad (58)$$

In equation (58), t is the time, z is the distance along the adsorber, ρ is the framework density, ε is the bed voidage, v is the interstitial gas velocity, and $\bar{q}_i(t, z)$ is the *spatially averaged* molar loading within the crystallites of radius r_c , monitored at position z , and at time t . The $\bar{q}_i(t, z)$ is determined by combining Equations (51), and (56) with the appropriate M-S model for the fluxes: Equation (30) (= Equation (52)) or Equation (35) (= Equation (53)) or Equation (36) (= Equation (54)). In other words, the uptake calculations need to be performed at every position along the adsorber.

Summing equation (56) over all n species in the mixture allows calculation of the *total average* molar loading of the mixture within the crystallite

$$\bar{q}_t(t, z) = \sum_{i=1}^n \bar{q}_i(t, z) \quad (59)$$

The *interstitial* gas velocity is related to the *superficial* gas velocity by

$$v = \frac{u}{\varepsilon} \quad (60)$$

In industrial practice, the most common operation is with to use a step-wise input of mixtures to be separation into an adsorber bed that is initially free of adsorbates, i.e. we have the initial condition

$$t = 0; \quad q_i(0, z) = 0 \quad (61)$$

At time, $t = 0$, the inlet to the adsorber, $z = 0$, is subjected to a step input of the n -component gas mixture and this step input is maintained till the end of the adsorption cycle when steady-state conditions are reached.

$$t \geq 0; \quad p_i(0, t) = p_{i0}; \quad u(0, t) = u_0 \quad (62)$$

where u_0 is the superficial gas velocity at the inlet to the adsorber.

Besides, the breakthrough simulations with a step-input (62), we also carried out simulations for a packed bed adsorber with injection of a short duration pulse of the mixture to be separated. This type of simulation is particularly useful to demonstrate the fractionating capability of adsorbents. For simulation of pulse chromatographic separations, we use the corresponding set of inlet conditions

$$0 \leq t \leq t_0; \quad p_i(0, t) = p_{i0}; \quad u(0, t) = u_0 \quad (63)$$

where the time for duration of the pulse is t_0 .

The breakthrough characteristics for any component is essentially dictated by two sets of parameters:

(a) The characteristic contact time $\frac{L}{v} = \frac{L\varepsilon}{u}$ between the crystallites and the surrounding fluid phase,

and (b) $\frac{D_i}{r_c^2}$, that reflect the importance of intra-crystalline diffusion limitations. It is common to use

the dimensionless time, $\tau = \frac{tu}{L\varepsilon}$, obtained by dividing the actual time, t , by the characteristic time, $\frac{L\varepsilon}{u}$

when plotting simulated breakthrough curves.⁷⁷

For most, but not all, of the breakthrough simulations reported here we use the parameter values: $L = 0.3$ m; voidage of bed, $\varepsilon = 0.4$; interstitial gas velocity, $v = 0.1$ m/s; superficial gas velocity, $u = 0.04$ m/s. Generally speaking, in pulse chromatographic simulations we take $t_0 = 10$ s.

When matching experimental data on breakthroughs, the parameter values used correspond to those relevant to the experiments being simulated.

For convenience, the set of equations describing the fixed bed adsorber are summarized in Figure 31. Typically, the adsorber length is divided into 100 – 200 slices. Combination of the discretized partial differential equations (PDEs) along with the algebraic IAST or RAST equilibrium model, results in a set of differential-algebraic equations (DAEs), which are solved using BESIRK.⁸² BESIRK is a sparse matrix solver, based on the semi-implicit Runge-Kutta method originally developed by Michelsen,⁸³ and extended with the Bulirsch-Stoer extrapolation method.⁸⁴ Use of BESIRK improves the numerical solution efficiency in solving the set of DAEs. The evaluation of the sparse Jacobian required in the numerical algorithm is largely based on analytic expressions.² Further details of the numerical procedures used in this work, are provided by Krishna and co-workers;^{2, 3, 54, 55} interested readers are referred to our website that contains the numerical details.⁵⁴

While most of the breakthrough simulations presented in the following sections refer to gas phase operations, a few simulations were also carried out for liquid phase operations. In this case we need to solve the following set of partial differential equations for each of the species i in the liquid mixture

$$\frac{\partial c_i(t, z)}{\partial t} = -\frac{\partial(v(t, z)c_i(t, z))}{\partial z} - \frac{(1-\varepsilon)}{\varepsilon} \rho \frac{\partial \bar{q}_i(t, z)}{\partial t}; \quad i = 1, 2, \dots, n \quad (64)$$

The intra-crystalline diffusion is described by the Maxwell-Stefan equations in the same manner as described earlier.

There are essentially four different scenarios to quantify the influence of intra-crystalline diffusion effects on breakthroughs. These are listed below in increasing order of complexity.

Scenario A. “Equilibrium” simulations, i.e. ignoring intra-crystalline diffusion limitations.

If the value of $\frac{D_i}{r_c^2}$ is large enough to ensure that intra-crystalline gradients are absent and the entire crystallite particle can be considered to be in thermodynamic equilibrium with the surrounding bulk gas phase at that time t , and position z of the adsorber

$$\bar{q}_i(t, z) = q_i(t, z) \quad (65)$$

The molar loadings at the *outer surface* of the crystallites, i.e. at $r = r_c$, are calculated on the basis of adsorption equilibrium with the bulk gas phase partial pressures p_i at that position z and time t . The adsorption equilibrium can be calculated on the basis of the IAST.

Scenario A is the one that is commonly adopted for screening different nanoporous materials for a given separation task.^{3, 77, 85, 86}

Scenario B. Intra-crystalline diffusion, ignoring both correlations and thermodynamic coupling.

In Scenario B, $\bar{q}_i(t, z)$ is determined by combining Equations (51), and (56) with flux calculations using Equation (35) (= Equation (54)). This Scenario B is perhaps the one most commonly used in cases where intra-crystalline diffusion is considered to be important.

Scenario C. Intra-crystalline diffusion, ignoring both correlations but including thermodynamic coupling.

In Scenario C, $\bar{q}_i(t, z)$ is determined by combining Equations (51), and (56) with flux calculations using Equation (36) (= Equation (53)). Scenario C is the one used in industrial practice of O₂/N₂ separations with LTA-4A or LTA-5A; see the monograph of Ruthven et al.¹

Scenario D. Intra-crystalline diffusion, including both correlations and including thermodynamic coupling.

In Scenario D, $\bar{q}_i(t, z)$ is determined by combining Equations (51), and (56) with flux calculations using Equation (30) (= Equation (52)). The use of Scenario D, though uncommon in practice, is used in the work of Krishna and Baur.²

We now analyse transient breakthrough experiments for a wide variety of guest/host combinations to determine which of the aforementioned scenarios afford the best representations of experiments. For any mixture separation, the influence of diffusion can be subdivided into four categories as follows.

Category A: Minor influence of intra-crystalline diffusion on breakthrough characteristics. The hierarchy of breakthroughs is not affected, but are more “diffuse” in nature when compared to equilibrium simulations.

Category B: Strong influence of intra-crystalline diffusion on breakthrough characteristics. The productivity or capture capacity is reduced due to diffusional influences. The hierarchy of breakthroughs, when compared to equilibrium simulations, is not affected.

Category C: Strong influence of intra-crystalline diffusion on breakthrough characteristics. The hierarchy of breakthroughs is altered; the components with lower diffusivities break through significantly earlier, when compared to equilibrium simulations.

Category D: Strong influence of intra-crystalline diffusion, and specifically thermodynamic coupling effects, on breakthrough characteristics. The productivity is enhanced by thermodynamic coupling effects.

Examples of the four categories are provided in Table 1.

Each of the examples in Table 1 are discussed in detail in the following sections.

20. Transient breakthrough of CO₂/CH₄, CO₂/H₂, and CO₂/N₂ mixtures in Cu-TDPAT, MgMOF-74, NiMOF-74, NaX, EMC-1, and NOTT-300

Figures 32a, 32b and 32c shows the experimental breakthrough data of Wu et al.⁸⁶ for 50/50 CO₂/CH₄, CO₂/H₂ and CO₂/N₂ mixtures in Cu-TDPAT that has an “open” structure. The continuous solid lines in Figure 32 represent our breakthrough simulations assuming thermodynamic equilibrium, i.e. invoking Equation (65). The simulations are able to reproduce the essential details of the experimental breakthroughs. It has also been demonstrated by Wu et al.⁸⁶ that inclusion of intra-crystalline diffusion effects, invoking the flux relations (36), leads to breakthroughs that are practically indistinguishable from those obtained using Equation (65).

With the aid of neutron diffraction measurements, Wu et al.⁸⁷ have established that CO₂ molecule attaches strongly, through one of its O atoms, to the Mg atoms of MgMOF-74, that has 1D channels of 11 Å size. The high CO₂ adsorption ability of MgMOF-74 is due to the strong Lewis acid and base interactions between metal ions and oxygen atom of CO₂. Diffusional effects are also of relatively minor importance for separation of CO₂/CH₄ mixtures through a fixed bed adsorber packed with MgMOF-74. This is demonstrated in the breakthrough simulations presented in Figure 33a, that compares the breakthroughs including diffusion with those assuming thermodynamic equilibrium, i.e. invoking Equation (65). The breakthrough times for both CO₂, and are hardly influenced by intra-crystalline diffusion. For CO₂, the approach to steady-state becomes more gradual due to intra-crystalline diffusional effects. The simulations including diffusion are in qualitative agreement with the experimental breakthrough data of Remy et al.⁸⁸

The diffusional effects for separation of CO₂/N₂ mixtures with NiMOF-74, the structural analog of MgMOF-74, are seen to be of negligible importance, as demonstrated in Figure 33b. The experimental breakthrough data of Liu et al.⁸⁹ provide some confirmation of the conclusion about the diffusional influences.

For choosing the appropriate adsorbent for post-combustion capture, attention needs to be given to the influence of water in the flue gas, and to the regeneration costs. Most adsorbents prefer the adsorption of H₂O over the adsorption of CO₂. Pirngruber et al.⁶⁶ presents a systematic study of a variety of zeolites for post-combustion CO₂ capture. Two of the best adsorbents were found to be NaX zeolite (Si/Al = 1.3; 9.68 wt% Na; $V_p = 0.34 \text{ cm}^3/\text{g}$), and EMC-1, also a Faujastite-type zeolite but with a higher Si/Al ratio (Si/Al = 3.9; 6.02 wt% Na; $V_p = 0.33 \text{ cm}^3/\text{g}$). Figure 34 compares the transient breakthroughs, assuming thermodynamic equilibrium and invoking Equation (65), of 50/50 CO₂/N₂ mixtures in fixed bed adsorber packed with (a) NaX zeolite, and (b) EMC-1 zeolite, operating at 303 K. The experimental data for breakthrough with EMCI-1 reported in Figure 5a of Pirngruber et al.⁶⁶ are in good agreement with the equilibrium simulations. This confirms that intra-crystalline diffusion effects are not of vital significance in determining the PSA performance. We note that the dimensionless breakthrough times

are 100 and 70, respectively, for NaX and EMC-1. The amount of CO₂ adsorbed, that is proportional to the breakthrough times, is about 30% higher with NaX as compared to EMC-1. While NaX zeolite has a higher adsorption capacity, and adsorption selectivity than EMC-1, the regeneration costs are higher because of the stronger binding energy of CO₂, reflected in the heats of adsorption of 40 kJ/mol and 25 kJ/mol, respectively. Pirngruber et al.⁶⁶ concludes that EMC-1 provides the optimum balance between adsorption capacity, regeneration costs, and sensitivity to the presence of water in the feed gas mixture.

In addition to capture of CO₂ from flue gases, other impurities such as SO₂ present in the flue gas mixture need to be removed along CO₂. Yang et al.⁹⁰ present isotherm adsorption data for NOTT-300; the hydroxyl groups within the 6.5 Å × 6.5 Å channels bind CO₂ and SO₂ selectively. Figure 35a presents simulation of transient breakthroughs (assuming thermodynamic and invoking Equation (65)), of 15/85/10 CO₂/N₂/SO₂ mixtures in fixed bed adsorber packed with NOTT-300. The breakthrough of SO₂ occurs much later than CO₂, indicating the much stronger binding of SO₂ as compared to CO₂. The isosteric heat of adsorption of CO₂ in NOTT-300 is in the range of 27 – 30 kJ/mol, significantly lower than materials such as MgMOF-74, Cu-TDPAT, and NaX zeolite, but slightly higher than that of EMC-1. Figure 35b compares the % CO₂ in the exit gas for 85/15 N₂/CO₂ mixture entering beds packed with NOTT-300, EMC-1, and NaX zeolite. The performance of NaX is best because it offers the longest breakthrough time; however the regeneration costs would be highest. Remarkably EMC-1 has a longer breakthrough time than NOTT-300, and also a slightly lower Q_{st} value. This comparison suggests that EMC-1 is superior in both performance and costs as compared to NOTT-300.

Vaesen et al.⁹¹ present adsorption isotherm data to demonstrate the potential of amino-MIL-125(Ti) for removal of both CO₂, and H₂S from natural gas. The isosteric heat of adsorption of CO₂ in amino-MIL-125(Ti) is 30 kJ/mol, significantly lower than materials such as MgMOF-74, Cu-TDPAT, and NaX zeolite; this is a desirable feature as it implies lower regeneration energy requirements. Simulation of transient breakthroughs in fixed bed adsorber with input of 35/60/5 CO₂/CH₄/H₂S mixtures operating at 2 MPa are shown in Figure 35c. The breakthrough of H₂S, occurs much later than CO₂ because of the stronger binding of H₂S.

21. Recovery of H₂ from steam-methane reformer off-gas (SMROG)

Pressure swing adsorption (PSA) is the most commonly used technology for recovery of pure hydrogen from a gaseous streams containing 60–90 mol% H₂.⁹² Steam-methane reformer off-gas (SMROG), after it has been further treated in a water-gas shift reactor, is a commonly used feed gas stream, with typical compositions 70–80% H₂, 15–25% CO₂, 3–6% CH₄, 1–3% CO, and also containing some N₂.⁹²⁻⁹⁴ In recent years there has been a considerable amount of research on the development of MOFs for use as adsorbents in PSA processes.^{86, 94-96} Breakthrough simulations, assuming thermodynamic equilibrium, i.e. invoking Equation (65), are particularly convenient for the comparative evaluation of adsorbents.

As illustration, Figure 36a presents the breakthrough characteristics a 5-component 73/16/3/4/4 H₂/CO₂/CO/CH₄/N₂ mixture in an adsorber packed with UiO-66(Zr)-Br and maintained at isothermal conditions at 298 K and total pressure of 0.7 MPa. The sequence of breakthroughs is H₂, N₂, CO, CH₄, and CO₂. For Cu-TDPAT, the sequence of breakthrough is somewhat different: H₂, N₂, CH₄, CO, and CO₂; see Figure 36b. The purity of H₂ in the product gas exiting the adsorber is primarily dictated by the presence of the less-strongly adsorbed N₂, CO, CH₄, rather than CO₂, that is the main impurity in the feed gas mixture. The N₂/H₂, CO/H₂, CH₄/H₂ adsorption selectivities are far more relevant than the CO₂/H₂ selectivity. Consequently, the only proper methodology for comparing different adsorbents is to perform breakthrough calculations; simple IAST calculations of mixture adsorption equilibrium do not present the complete picture on separation capabilities.

From breakthrough calculations of the type shown in Figure 36, we can compare different adsorbents by plotting the ppm (CO₂ + CO + CH₄ + N₂) in outlet gas as a function of the dimensionless time, τ , for various adsorbent materials. Figure 37a compares the performance of 8 different materials: UiO-66(Zr)-Br, UiO-66(Zr), UiO-67(Zr), ZrCl₂-AzoBDC, Activated Carbon, Cu-TDPAT, NaX, and CuBTC. We choose the impurity level to be 500 ppm (CO₂ + CO + CH₄ + N₂) in outlet gas; this is a typical value in industry. When this impurity level is reached, the corresponding dimensionless

breakthrough time, τ_{break} , can be determined. UiO-66(Zr)-Br has the highest value of τ_{break} , implying that the bed can be run for a longer time before shutting down for regeneration.

For each material we can determine the number of moles of 99.95%+ pure H₂ produced per L of adsorbent material that can be recovered during the time interval 0 – τ_{break} . This productivity value is linearly dependent on the corresponding values of τ_{break} ; see Figure 37b. The highest productivity for operation at the chosen total pressure of 0.7 MPa is obtained with UiO-66(Zr)-Br; this is also the best material in the study of Banu et al.⁹⁴ For UiO-66(Zr)-Br, the isotherm parameters are provided isotherms are based on GCMC simulations, as reported by Banu et al.,⁹⁴ and so the conclusions drawn here should be viewed with some degree of caution.

For recovery of H₂ from gaseous streams operating at pressures exceeding about 4 MPa, MOFs with more “open” structures, i.e. with high pore volumes, such as MgMOF-74, Cu-TDPAT, CuBTC, ZJU-35a, and ZJU-36a become more suitable and have higher productivities.^{86, 97} For pressures exceeding 2 MPa, UiO-66(Zr)-Br, UiO-66(Zr), UiO-67(Zr), ZrCl₂-AzoBDC, Activated Carbon, and NaX will suffer severe capacity limitations.

Besides productivity of 99.95%+ pure H₂, the economy of PSA operations is significantly influenced by the regeneration energy requirements, which is largely dictated by desorption of CO₂ with the highest binding energy. The isosteric heats of adsorption of CO₂ is plotted in Figure 38a as a function of the CO₂ loadings. Figure 38b presents a plot of the regeneration energy required, expressed per kg of adsorbent, plotted as function of the amount of CO₂ captured. We note that the highest regeneration requirements are for UiO-66(Zr)-Br that has the highest H₂ productivity. The important message conveyed by the results presented in Figures 37, and 38

Experimental confirmation that intra-crystalline diffusion effects are not of significant importance for H₂ purification processes is obtained by an analysis of the experimental data of Silva et al.⁹⁸ on the breakthrough characteristics of 3-component 35.5/47/17.5 H₂/CO₂/CH₄ mixture in adsorber packed with CuBTC at 303 K operating at a total pressure of 0.2 MPa; see Figure 39. The experimental data (symbols) are compared with breakthrough simulations (continuous solid lines) assuming

thermodynamic equilibrium, i.e. invoking Equation (65); the agreement is very good. Silva et al.⁹⁸ also present a detailed model for breakthrough that include: intra-crystalline diffusion, axial dispersion in the fixed bed, along with a rigorous energy balance. Their simulation results, presented in Figure 4a of their paper, are hardly distinguishable from our own simulations using invoking Equation (65) that assumes thermodynamic equilibrium.

22. Fischer-Tropsch tail-gas separation

The tail-gas from the Fischer-Tropsch process consists of a 5-component $\text{H}_2/\text{CO}_2/\text{CO}/\text{CH}_4/\text{N}_2$ mixture. Ideally, we would like to separate the mixture into three different fractions as indicated in Figure 40. Most of the commonly used adsorbents will have the hierarchy of adsorption strengths either $\text{CO}_2 > \text{CO} > \text{CH}_4 > \text{N}_2 > \text{H}_2$ or $\text{CO}_2 > \text{CH}_4 > \text{CO} > \text{N}_2 > \text{H}_2$. Consequently, it is perhaps difficult, if not impossible, to obtain the hierarchy required to obtain the three different fractions. To confirm this expectation, we carried out breakthrough simulations for 5-component equimolar $\text{H}_2/\text{CO}_2/\text{CO}/\text{CH}_4/\text{N}_2$ mixture in adsorber packed with Cu-TDPAT, CuBTC, NaX, LTA-5A, and MFI and maintained at isothermal conditions at 298 K and total pressure of 1 MPa; Figure 41. The sequence of breakthroughs is either $\text{H}_2, \text{N}_2, \text{CO}, \text{CH}_4, \text{and } \text{CO}_2$ (as for MFI) or $\text{H}_2, \text{N}_2, \text{CH}_4, \text{CO}, \text{and } \text{CO}_2$ (Cu-TDPAT, CuBTC, NaX, and LTA-5A). Neither hierarchy is capable of meeting the requirements of process scheme in Figure 40. The conclusion that we wish to draw is the separation required by industry requires out-of-the-box thinking. One option would be to shift the CO in the tail-gas ($\text{CO} + \text{H}_2 \rightarrow \text{CO}_2 + \text{H}_2$) and feeding the CO-free mixture to the adsorber so that we are now confronted with the separation of a 4-component $\text{H}_2/\text{CO}_2/\text{CH}_4/\text{N}_2$ mixture for which any adsorbent would yield the breakthrough hierarchy $\text{H}_2, \text{N}_2, \text{CH}_4, \text{and } \text{CO}_2$ making it a relatively simple task to obtain three fractions as indicated in Figure 40.

23. Recovery of helium from natural gas

Helium is an important industrial gas with a wide range of applications.^{99, 100} Helium is present in small concentrations of approximately 0.1% in natural gas, and pressure swing adsorption is a viable

technology for recovery of helium.^{99, 100} Breakthrough simulations, assuming thermodynamic equilibrium, i.e. invoking Equation (65), are particularly convenient for the comparative evaluation of adsorbents. To illustrate this Figure 42 presents pulse chromatographic simulations for breakthrough of 80/10/10 CO₂/CH₄/N₂ mixtures containing 0.1% Helium in packed beds of (a) MFI, and (b) CuBTC. Both these materials are seen to have the potential for recovering pure Helium during the initial stages of the breakthrough.

24. Removal of Xe and Kr from off-gases from nuclear plants

The removal and recovery of xenon (Xe) and krypton (Kr) from process off-gases from nuclear plants, typically present in concentrations of 400 ppm and 40 ppm, respectively, is an important problem.¹⁰¹ Liu et al.¹⁰¹ have presented isotherm and breakthrough data to demonstrate the efficacy of Ni₂(dobdc) (= NiMOF-74 = CPO-27-Ni; dobdc = 2,5-dioxido-1,4-benzenedicarboxylate) for use in this separation task. Ni₂(dobdc), that has 1D hexagonal-shaped channels of 11 Å size, is an excellent material for post combustion CO₂ capture. The breakthrough simulations for 15/85 CO₂/N₂ mixtures confirms this expectation; Figure 43a. These breakthrough simulations assume thermodynamic equilibrium, i.e. invoking Equation (65), because intra-crystalline diffusion is not expected to offer significant resistance. The breakthrough experiments reported by Liu et al.¹⁰¹ for a wide variety of mixtures show sharp, non-diffuse, near-vertical breakthroughs that characterize absence of intra-crystalline diffusion resistances.

Liu et al.¹⁰¹ have demonstrated the potency of Ni₂(dobdc) to separate a binary Xe/Kr mixture; this is confirmed by the breakthrough simulations in Figure 43b.

For a process gas containing predominantly N₂, and containing impurities such as Xe (400 ppm), Kr (40 ppm), and CO₂ (400 ppm), the breakthrough simulations in Figure 43b confirm that it is possible to recover Xe and Kr in nearly pure forms.

25. Transient breakthrough of CO₂/CH₄ mixtures with KFI zeolite

Introduction of intra-crystalline diffusional influences tends to produce more “diffuse” breakthroughs in beds containing materials in which the guest species are more strongly confined. This is illustrated by transient breakthrough of equimolar CO₂/CH₄ mixtures through a fixed bed adsorbers packed with (a) K-KFI, and (b) Na-KFI zeolites that consist of cages separated by narrow windows of about 0.4 nm size. Intra-cage hopping of both CO₂, and CH₄ are severely diffusion limited. The longer pencil-shaped CO₂ has a significantly higher diffusivity than the more spherical CH₄ molecule.²² The extent of diffusion limitations is different for K-KFI and Na-KFI because there are differences in the location of the cations within the framework. The assumption of thermodynamic equilibrium between the bulk gas and the crystals at any time t , and position z of the adsorber, i.e invoking equation (65), results in near-vertical breakthrough profiles, as indicated by the dotted lines in Figure 44.

Due to the “diffuse” nature of the breakthroughs for the case including intra-crystalline diffusion, the recovery, or productivity, of CH₄ with the required purity is lowered when compared to the case of equilibrium simulations. This is highlighted by the graphs showing the amount of CO₂ impurities in the exiting product gas. If the purity requirement is say < 500 ppm CO₂ in exit gas, there will be a significant reduction in the productivity of CH₄ with K-KFI.

Another point to stress is that the breakthrough simulation results presented in Figure 44 and Figure 44 use the simplified equation (54), neglecting thermodynamic coupling. For attempting to match experimental breakthrough data with simulations, there is no real need for using the more complete M-S model including thermodynamic coupling.

Figure 45 compares the experimental data of with breakthrough simulations that include intra-crystalline diffusion effects using the simplified equation (54), neglecting thermodynamic coupling. There is reasonably good agreement between the breakthrough simulations and the experimental results. The small differences in the precise breakthrough times is perhaps attributable to the fact that in the experiments, the x -axis relates to the times at which the exit gas mixture is analysed, somewhere downstream of the breakthrough tube. In our breakthrough simulations, the x -axis refers to the times

after injection of the mixture at the inlet. We need precise information on the delay times in the experimental set-up for a careful comparison. Such a careful comparison is provided in our earlier work.⁸⁶

For CO₂/CH₄ separations with KFI zeolite, the introduction of diffusional limitations serves to influence separations to a quantitative extent; they do not alter the principle of separation and the hierarchy of breakthroughs.

Yang et al.⁷⁵ have presented experimental data on transient breakthrough of 40/60 CO₂/CH₄ mixtures through fixed bed adsorber packed with K-KFI zeolite at flow rates of (a) 16.6 mL/min, and (b) 30 mL/min; see Figures 46a, and 46b. The experimental data are in good agreement with breakthrough simulations that assume thermodynamic equilibrium. In the experiments of Yang et al.⁷⁵ the size of the crystals packed into the breakthrough tube were in the 40-80 mesh range, corresponding to crystallite sizes in the range of 180 μm - 420 μm ; this size range is significantly lower than the size range of 500 μm - 650 μm that was used in the experiments of Remy et al.¹⁰² It must be borne in mind that the influence is diffusion scales with r_c^2 . A further reason that thermodynamic equilibrium is a good assumption in the experiments of Yang et al.⁷⁵ is that the contact times within the packed tubes are significantly higher, as compared to the breakthrough experiments of Remy et al.¹⁰² this is evidenced by the fact that the breakthroughs of CO₂ occurs at a significant later time in Figures 46a, and 46b in comparison to the data in Figure 45a. Longer contact times ensure that the component loadings within the crystals are closer to equilibrium conditions.

Figures 46c, and 46d present comparisons of CO₂ breakthroughs for 40/60 CO₂/CH₄ mixtures through fixed beds packed with K-KFI, NaX (=13 X zeolite), and LTA-5A zeolites. The longer breakthrough times with K-KFI indicate that K-KFI has a significantly higher CO₂ capture potential than commercially available NaX and LTA-5A zeolites.

26. Transient breakthrough of CO₂/CH₄, CO₂/H₂, and CO₂/N₂ mixtures with SIFSIX-2-Cu-i

The paper of Nugent et al.¹⁰³ presents breakthrough experimental data for separation of CO₂/CH₄, CO₂/N₂, and CO₂/H₂ mixtures using SIFSIX-2-Cu-i, with exceptionally high CO₂ uptake capacities. The experimental breakthroughs can be reproduced quantitatively by breakthrough simulations that include intra-crystalline diffusion effects using the simplified equation (54), neglecting thermodynamic coupling. Figures 47a,b,c compare the breakthrough simulations including diffusion with those assuming thermodynamic equilibrium. Intra-crystalline diffusion resistances have the effect of reducing the productivity of purified CH₄, N₂, and H₂; in this aspect there are similarities with the results presented in the foregoing section for K-KFI and Na-KFI zeolites.

Figure 47d presents the breakthrough simulations for 73/16/3/4/4 H₂/CO₂/O₂/CH₄/N₂ mixture in an adsorber packed with SIFSIX-2-Cu-i. It is clear that is impossible to obtain 99.95% pure H₂ because the N₂/H₂, O₂/H₂, and CH₄/H₂ adsorption selectivities are not high.

27. Influence of increasing pressures on transient breakthrough of CO₂/CH₄ mixtures with amino-MIL-53(Al)

The paper of Peter et al.¹⁰⁴ presents experimental data for transient breakthrough of 40/60 CO₂/CH₄ mixtures through a fixed bed adsorbers packed with amino-MIL-53(Al) operating at 303 K and pressures of 0.1 MPa, 0.5 MPa, and 3 MPa. The breakthroughs at 0.1 MPa, and 0.5 MPa are sharp, and indicative of absence of diffusional limitations, On the other hand, the experimental breakthroughs at 3 MPa are considerably less sharp, indicating that diffusional effects become increasingly important at higher pressures. In Figure 48, we compare simulations without intra-crystalline diffusion limitations with those that include intra-crystalline diffusion effects. For operation at 3 MPa, the breakthrough experiments are best represented by simulations that include intra-crystalline diffusion limitations. This indicates that the diffusivity decreases with increased pore concentrations. Extensive MD simulations for CO₂ and CH₄ diffusion in MIL-53 do confirm that strong reduction of the diffusivities with increased pore concentrations.^{7, 8, 11}

28. Transient breakthrough of alkane isomers with ZIF-8

Let us analyse, and simulate, the experimental data of Peralta et al.⁷¹ for breakthrough of nC6/3MP, nC6/22DMB, and 3MP/22DMB mixtures in a fixed bed adsorber packed with ZIF-8. The required pure component isotherm data are obtained from the work of Dubbeldam et al.¹⁰⁵ that uses CBMC simulations; Table 7 provides the dual-site Langmuir-Freundlich parameters.

In each case, two types of simulations were performed: (a) assuming thermodynamic equilibrium, i.e. invoking Equation (65) and (b) introducing intra-crystalline diffusion resistances in order to match their breakthrough experiments. The breakthrough simulation results with diffusion use the simplified equation (54), neglecting thermodynamic coupling. The diffusivity values used in the simulations are $D_{nC6}/r_c^2 = 0.004 \text{ s}^{-1}$; $D_{3MP}/r_c^2 = 2 \times 10^{-6} \text{ s}^{-1}$; $D_{22DMB}/r_c^2 = 8 \times 10^{-7} \text{ s}^{-1}$. There is no real justification for inclusion of thermodynamic coupling effects because the M-S diffusivities D_i are just fitted.

Figure 49 presents the breakthrough simulations for nC6/3MP mixture. The equilibrium simulations (cf. Figure 49a) show that nC6 breaks through earlier than 3MP, whereas the experiments show the reverse trend (cf. Figure 49b). The experimental breakthroughs can be reproduced nearly quantitatively by introducing diffusional influences, and by choosing the ratio $D_{nC6}/D_{3MP} = 1333$; see Figure 49b.

Figure 50 shows the breakthrough simulations for nC6/22DMB mixture. In this case, equilibrium simulations (cf. Figure 50a) predict the correct hierarchies of breakthrough as in the experiments but the quantitative agreement is poor. A near quantitative agreement in the breakthrough characteristics is obtained by accounting for intra-crystalline diffusion with the ratio $D_{nC6}/D_{22DMB} = 5000$; see Figure 50b.

Figure 51 shows the breakthrough simulations for 3MP/22DMB mixtures. The experimental breakthroughs are reproduced nearly quantitatively by introducing diffusional limitations and taking the ratio of diffusivities $D_{3MP}/D_{22DMB} = 3.75$.

The important conclusion that we wish to draw from the simulations of the breakthrough experiments of Peralta et al.⁷¹ is that the separation of alkane isomers using ZIF-8 is dominated by intra-crystalline

diffusion. The set of three different breakthroughs can be adequately modeled using the simplified equation (54), neglecting thermodynamic coupling.

29. Transient breakthrough of C8 hydrocarbons with MOFs

The separation of C8 hydrocarbons is of great importance in the petrochemical industries. Some mixed xylenes are used as solvents and in the printing, rubber, and leather industries. Mixed xylenes are also a desirable gasoline component, but are blended less often than toluene because there is greater demand and higher value in their chemical applications. However, most mixed xylenes are separated and the individual isomers consumed in specific end-uses. Para-xylene, the most valuable of the isomers, is primarily used as a feedstock with purity requirement of 99%+, for terephthalic acid or dimethyl terephthalate, whose end uses include polyester fibers and polyethylene terephthalate (PET) resins for beverage bottles. Ortho-xylene is oxidized to phthalic anhydride, a feedstock for plasticizers. Meta-xylene is oxidized to isophthalic acid that is used in resin manufacture.

The separation of C8 hydrocarbons by distillation is difficult because of the small differences in the boiling points; see Figure 52. There are, however, significant differences in the freezing points that allow fractional crystallization to be used for separations. The differences in the freezing points arise because of differences in the stacking efficiencies of molecules. Para-xylene has the highest freezing point because these molecules stack most efficiently; pure *p*-xylene crystals are the first to emerge from the solution. However, the energy requirements for fractional crystallization are high because of the need to cool to temperatures of about 220 K.

Selective adsorption of xylene isomers within the pores of ordered crystalline micro-porous materials is an energy-efficient alternative to fractional crystallization. In principle, it is possible to separate *p*-xylene from this mixture if *p*-xylene is either the most strongly or the most weakly adsorbed component. Because of the low *p*-xylene content of the feed it is often easier to reach a high productivity with *p*-xylene-selective adsorbents. Further informative discussions on this subject are provided by Peralta et al.⁶⁹

In current industrial practice Faujasite type zeolites, such as BaX, are used in the UOP Parex, and IFP Eluxyl technologies that employ simulated moving beds (SMB).^{69, 106, 107} The industrially used adsorbents (BaX and KBaY) are *p*-xylene-selective. The adsorption isotherms for *o*-xylene and *m*-xylene are nearly the same.¹⁰⁷ Figure 53 shows breakthrough simulations for C8 hydrocarbons in BaX. The large differences between the breakthrough times of *p*-xylene and the other components indicates strong adsorption selectivity in favor of *p*-xylene.

Differences in the stacking efficiency of C8 hydrocarbons can also be exploited by adsorption within channels of MOFs that have the appropriate channel geometry and dimensions. The height and width of the xylene isomers are: *o*-xylene: 8 Å × 7.5 Å; *m*-xylene: 8.6 Å × 7.4 Å; *p*-xylene: 9.2 Å × 6.7 Å; see dimensions provided in Figure 52. Depending on the channel dimensions and geometry of the MOF, the hierarchy of adsorption strengths, and component breakthroughs will be different.

Consider adsorption of ethyl benzene (EtBz), and *o*-, *m*-, *p*- xylenes within the one-dimensional, lozenge-shaped rhombohedral channels of C8 hydrocarbons. Figures 54, 55, 56, 57, 58, and 59 present snapshots showing the conformations of C8 hydrocarbons within the channels. Ethylbenzene is not a flat molecule; the ethyl branch is not in the same plane as the benzene ring. The xylene isomers are flat; these isomers can align themselves parallel to the channel walls, affording better van der Waals interactions with the framework atoms. Adsorption within the channels of MIL-47(V) favors *o*-xylene because the molecules can most effectively stack along the channel length; see Figure 54. Essentially, MIL-47(V) offers the appropriate “bookshelf” structure that is required to optimally stack *o*-xylene molecules. Note that the channel dimension of MIL-47(V) is not large enough to allow *p*-xylene to stack vertically; these molecules align obliquely along the channel length; the stacking of *p*-xylene is at an inclination; see Figure 56. Differences in the stacking efficiencies and van der Waals interactions with the framework leads to the hierarchy of adsorption isotherms as reported by Finsky et al.¹⁰⁸ for the pure components in Figure 60a. The differences in the polarities of the xylene isomers also contribute to the differences in the adsorption strengths. The sequence of breakthroughs in a fixed bed adsorber is *n*C8, ethylbenzene, *p*-xylene, *m*-xylene, and *o*-xylene if intra-crystalline diffusion effects are ignored; see

Figure 60b. Intra-crystalline diffusion limitations, taking $D_i/r_c^2 = 1 \times 10^{-4} \text{ s}^{-1}$ for each component, serve to make the breakthroughs more “diffuse” in character; compare Figures 60b, and 60c. The breakthrough simulations are in reasonably qualitative agreement with the experimental breakthrough reported by Finsy et al.¹⁰⁸ However, in the experiments of Finsy et al.,¹⁰⁸ m-xylene breaks through earlier than p-xylene; this reversal of the sequence, compared to our breakthrough simulations, is perhaps ascribable to a higher diffusivity of p-xylene compared to m-xylene.

The framework structures of MIL-53(Al) and MIL-53(Fe) are similar to that of MIL-47(V), and the hierarchy of breakthroughs is also similar to that of MIL-47(V); see Figures 61 and 62. Intra-crystalline diffusion influences do not influence the sequence of breakthroughs of individual isomers, as can be evidenced by comparing Figures 61b, and 61c. The experimental data of Remy et al.¹⁰⁹ appear to indicate that guest-induced structural changes of MIL-53(Al) are also to be considered in quantitative modeling of the breakthrough characteristics.

The experimental data on the pure component isotherms for xylene isomers in MIL-53(Fe), reported by El Costa et al.¹¹⁰ shows the adsorption hierarchy o-xylene > m-xylene > p-xylene. The adsorption hierarchy is reflected in the hierarchy of breakthroughs in the simulations presented in Figure 62. Diffusional influences do not alter the sequence of breakthroughs. The experimental breakthroughs are in reasonable agreement with the breakthrough simulations that include diffusional influences.

Configurational-Bias Monte Carlo (CBMC) simulations of the adsorption isotherms of C8 hydrocarbons in the hexagonal-shaped 1D channels of MgMOF-74 indicate that the adsorption strengths follow the hierarchy is o-xylene > m-xylene > p-xylene > Ethylbenzene > nC8. The sequence of breakthroughs in fixed adsorber is ethylbenzene, p-xylene, m-xylene, o-xylene; see Figure 63. This sequence suggests that it is possible to separate p-xylene from the xylenes with the required product purity. Introduction of intra-crystalline diffusion has a minor influence on the separation performance for MgMOF-74 that has channels of 11 Å size; compare the breakthroughs in Figure 63b (equilibrium) and Figure 63c (including diffusion).

The sequence of breakthroughs of C8 hydrocarbons in NiMOF-74, that is the structural analog of MgMOF-74, is similar in nature (cf. Figure 64), and this sequence is confirmed in the experiments of Peralta et al.⁶⁹

The experimental data of Peralta et al.⁶⁹ for transient breakthrough of m-xylene/p-xylene binary mixture in NiMOF-74 bed can be matched nearly quantitatively by accounting for intra-crystalline diffusion resistance, invoking the simplified equation (54), neglecting thermodynamic coupling; see Figure 65a. Ignoring intra-crystalline diffusion (i.e. invoking Equation (65)) results in sharper breakthroughs than that obtained with consideration of intra-crystalline diffusion; see comparison between the two sets in Figure 65b.

Nicolau et al.¹¹¹ report experimental breakthrough data for C8 hydrocarbons in beds packed with Zn(bdc)dabco, a framework that has two types of intersecting channels of about $7.5 \text{ \AA} \times 7.5 \text{ \AA}$ along the x-axis and channels of $3.8 \text{ \AA} \times 4.7 \text{ \AA}$ along y and z axes. The sequence of breakthrough of xylene isomers is p-xylene, m-xylene, o-xylene. Breakthrough simulations assuming thermodynamic equilibrium, i.e. invoking Equation (65) shown in Figures 66a, and 66b are able to reproduce the essential features of the observed experimental breakthroughs.

Bárcia et al.¹¹² and Moreira et al.¹¹³ report breakthrough data for C8 hydrocarbons in UiO-66(Zr). UiO-66(Zr) is a zirconium-based metal-organic framework (MOF) built up from hexamers of eight coordinated $\text{ZrO}_6(\text{OH})_2$ polyhedra and 1,4-benzene-dicarboxylate (BDC) linkers. Its cubic rigid 3D pores structure consists of an array of octahedral cavities of diameter 11 \AA , and tetrahedral cavities of diameter 8 \AA . The two types of cages are connected through narrow triangular windows of approximately 6 \AA . The sequence of experimental breakthroughs of xylene isomers is p-xylene, m-xylene, o-xylene. The adsorption selectivity is in favor of o-xylene; this is mostly likely due to the more compact configuration of o-xylene that allows preferential location in the smaller tetrahedral cages of UiO-66. The separation performance is most likely to be influenced strongly by intra-crystalline diffusion considerations because of the small windows at the entrance to the cages. We will demonstrate in a later

section that diffusional limitations are of significant importance in the separation of hexane isomers in UiO-66; this conclusion is likely to hold also for xylene isomers.

All the MOFs (MIL-47(V), MIL-53(Al), NiMOF-74, MgMOF-74, UiO-66, Zn(bdc)dabco) discussed in the foregoing paragraph are selective to the adsorption of o-xylene, and not suitable for use in industrial practice.

Let us turn our attention to MOFs that have the desired selectivity towards p-xylene.

MIL-125(Ti) comprises of two different types of cages: larger 12 Å octahedral cages, and smaller tetrahedral 6 Å cages. The two types of cages are connected through narrow triangular windows of 5 Å. Amino-functionalisation of the benzene linker yields MIL-125(Ti)-NH₂. Due to the protrusion of the amino groups in the pore space the pore space of MIL-125(Ti)-NH₂ are slightly smaller than in MIL-125(Ti). The thesis of Moghadam¹¹⁴ contains CBMC data on adsorption isotherms for the three xylene isomers, along with explanations regarding the hierarchy of adsorption strengths in both cages. The molecular simulation data indicate the adsorption hierarchy p-xylene > o-xylene > m-xylene. The experimental data of Vermoortele et al.¹¹⁵ and Moreira et al.^{116, 117} on breakthroughs of xylene isomers in titanium 1,4-benzenedicarboxylate (or terephthalate) MIL-125(Ti), along with the amino functionalized structure, and NH₂-MIL-125(Ti), appears to confirm that these materials have the desirable selectivity towards p-xylene. However, the breakthrough experiments also show that the selectivity towards p-xylene appears to depend on the concentration of ethylbenzene in the feed stream. Indeed, for a range of feed compositions p-xylene and ethylbenzene breakthrough at the same time. This indicates that MIL-125(Ti) is not a suitable adsorbent because industrial feed mixtures invariably contain a sizable proportion of ethylbenzene.

CBMC simulation data for adsorption C8 hydrocarbons with 10 Å square-shaped 1D channels of Co(BDP) show separation characteristics that are desirable from an industrial perspective. The channel dimension is large enough to allow the p-xylene molecules to align vertically; see snapshots in Figure 67. This allows the para isomer to be optimally packed within the 1D channels. CBMC simulations of the pure component isotherms (cf Figure 68a) clearly demonstrate a higher adsorption loading of p-

xylene than any of the other C8 hydrocarbons. Breakthrough simulations (cf. Figure 68b) confirm that good separation of p-xylene from the remaining components of a C8 hydrocarbons mixture is possible. Experimental confirmation of the promising separation capability of Co(BDP) is required.

Jin et al.¹¹⁸ have presented isotherm data for xylene isomers in JUC-77 which is a MOF that has rhombus-shaped channels running in two perpendicular directions. The size of the channels is such as to favor only p-xylene that has the smallest cross-section; this results in para-selectivity in separation.

30. Separation of ethylbenzene and styrene mixtures

The separation of ethylbenzene/styrene mixtures is of great importance in the petrochemical industry. Currently technology uses distillation; this separation is difficult because of the small, 9 K, difference in the boiling points (cf. Figure 52). Maes et al.¹¹⁹ and Remy et al.¹²⁰ have demonstrated that MIL-47 (V) and MIL-53 (Al) are also of potential use in the separation of mixtures of styrene and ethylbenzene. Styrene is a flat molecule, whereas ethylbenzene is not flat. Due to differences in the flatness, styrene has stronger interactions with the metal framework. Being flat styrene molecules stack more efficiently within the 1D channels. Figures 69a, and 69b compare breakthrough simulations for ethylbenzene/styrene mixtures in MIL-47(V) and MIL-53(Al) assuming (a) thermodynamic equilibrium, and (b) with inclusion of intra-crystalline diffusion. The sequence of breakthroughs is unaltered due to inclusion of diffusion limitations. Diffusional limitations lead to more diffuse, i.e. non-sharp, breakthroughs, in agreement with the liquid phase experimental breakthrough data of Maes et al.¹¹⁹ and the gas phase breakthrough experiments of Remy et al.¹²⁰

31. Separation of aromatics/aliphatics mixtures

There are several examples where it is required to separate mixtures of aromatics and aliphatic compounds.

Cyclohexane, and important industrial chemical, is produced by catalytic hydrogenation of benzene. The unreacted benzene is present in the effluent from the reactor must be removed from the desired

product. The separation of benzene and cyclohexane is difficult because the differences in the boiling points is only 0.6 K.

Currently technologies use extractive distillation with entrainers such as sulpholane, dimethylsulfoxide, N-methylpyrrolidone, and N-formylmorpholine; such processes are energy intensive. Adsorptive separations offer the energy-efficient alternatives to extractive distillation, especially for mixtures containing small percentage of benzene, as is commonly encountered.

Takahashi and Yang¹²¹ have presented pure component isotherm data for benzene and cyclohexane to show that cation-exchange Faujasites Na-Y, Pd-Y, and Ag-Y zeolites have high selectivity for adsorption of benzene, due to π -complexation; cyclohexane does not form π -complexes.

An alternative to the use of cation-exchange Faujasites, as suggested by Ren et al.¹²² is to use a porous aromatic framework, PAF-2. The pure component isotherm data for PAF-2 shows excellent selective sorption of benzene. The much higher uptake of benzene compared to cyclohexane is due to the π - π interaction between the benzene molecule and the aromatic framework of PAF-2.

Breakthrough simulations show that clear separations are achievable with both Ag-Y and PAF-2; see Figure 70. The productivity and regeneration costs will eventually dictate which adsorbent has a better potential for use in practice.

Hexane, used as solvent for oil seeds extraction has to conform to food grade specifications that stipulate a maximum of 1.3 wt% aromatics. The source for food grade hexane is straight run naphtha with a narrow 63 – 69 °C cut; this cut usually contains more than the stipulated maximum concentration of aromatics and is as high as 14% for Bombay High crude oil.¹²³ Krishna et al.¹²³ discuss the use of sulpholane and NMP as solvents for liquid extraction processes. PAF-2, Ag-Y, and NaX could perhaps be used for selective removal of benzene from the 63 – 69 °C naphtha cut.

Most ethylene cracker feeds contain 10 – 25% of aromatic components. The aromatic compounds are not converted to olefins. Aromatics reduce the capacity of the furnaces and increase the load on the separation section of the C5+ aliphatic compounds. Removal of the major part of the aromatic

compounds present in the feed to the ethylene crackers, i.e. upstream of the furnaces, offers several advantages: higher capacity, higher thermal efficiency and less fouling of the furnaces.

32. Transient uptake and breakthrough of mixtures of 1-alcohols in SAPO-34 and CHA

The overshoot phenomenon for transient uptake within crystals is particularly prominent for mixtures for which the differences in both mobilities and adsorption strengths are significantly large. This is best illustrated by the experimental data of Saint-Remi et al.¹²⁴ for transient uptake of ethanol/1-propanol mixtures within SAPO-34, that is the structural analog of CHA zeolite; see Figure 71a. The more mobile ethanol is found to exhibit a pronounced maximum in the uptake transience. For either component the uptake in the mixture is lower than that of the corresponding pure component. For uptake of methanol/1-propanol mixture, the more mobile methanol also exhibits a sharp maximum in the experimental uptake data reported by Saint-Remi et al.¹²⁴; see Figure 71b. For uptake of methanol/ethanol mixtures, no overshoot in the methanol uptake has been reported; see Figure 71c.

We now attempt to rationalize the experimentally observed overshoots in the uptake of the more mobile partners in mixtures of 1-alcohols. The uptake experiments of Saint-Remi et al.¹²⁴ for methanol/ethanol, methanol/1-propanol, and ethanol/1-propanol mixtures in SAPO-34 were conducted with under conditions that the bulk fluid phase surrounding the crystal is in the liquid state. The conditions in the uptake experiments of Saint-Remi et al.¹²⁴ are such that the adsorption favors the shorter 1-alcohol. We first try to understand why the shorter alcohol is preferred in mixture adsorption.

Towards this end we use the CBMC simulations of pure component 1-alcohols with C atoms in the 1 – 6 range in CHA at 300 K as reported in the work of Krishna and van Baten;¹²⁵ see Figure 72a. The CBMC simulated isotherms in CHA can be expected to be a fair representation of the corresponding isotherms in SAPO-34 for which no experimental data is available. The continuous solid lines in Figure 72a are fits using the dual-Langmuir-Freundlich model with parameters as specified in Table 11. The saturation capacities, $\Theta_{i,\text{sat}}$, decreases from 5.4 molecules per cage for methanol to 1 molecule per cage for 1-hexanol; see data in Figure 72b. Figure 72c presents snapshots of the location, and conformation,

of the 1-alcohols within the cages of CHA at saturation conditions. Except for methanol, the cage capacity at saturation has an integer value because no 1-alcohol can locate at the window region. A close examination of the CBMC data show that perhaps the loading for methanol would approach 6 per cage, had the simulations been performed to fugacities exceeding 1 MPa.

Figure 73 presents CBMC mixture simulation data for (a) methanol – ethanol, (b) ethanol - 1-propanol, (c) ethanol - 1-hexanol in CHA at 300 K. The partial fugacities in the bulk fluid phase are taken to be equal, i.e. $f_1=f_2$. The continuous solid lines represent calculations of the IAST³⁰ using dual-Langmuir-Freundlich fits of pure component isotherms. The range of liquid phase operation is indicated by the shaded region; the transition between vapor and liquid bulk phase is determined using the Peng-Robinson equation of state.

Consider adsorption of a fluid mixture of methanol and ethanol in CHA. The saturation capacities are 5.4 and 4 molecules per cage, respectively. CBMC simulations on the component loadings in equilibrium with equimolar ($f_1 = f_2$) methanol-ethanol mixtures is shown in Figure 73a for varying fluid phase partial fugacities, $f_i (= f_2)$. At $f_i < 5$ kPa, the selectivity is in favor of the component with the longer chain length, ethanol; this is “normal” behavior for mixture adsorption. However, for $f_i > 5$ kPa selectivity reversal occurs and methanol is preferentially adsorbed due to its higher packing efficiency.

The CBMC mixture simulations for ethanol - 1-propanol mixtures are shown in Figure 73b. For partial fugacities, $f_i < 100$ kPa, the adsorption selectivity is strongly in favor of the longer 1-propanol molecule. However, when the partial fugacities exceed 300 kPa, we find a reversal of selectivity. This selectivity is entropy based and is ascribable to the significantly higher saturation capacity of ethanol (4/cage) in comparison to that of 1-propanol (2/cage). The shaded region in Figure 73b indicates that the bulk fluid phase is in the liquid phase for the range of fugacities, f_i . This region has been estimated using the Peng-Robinson equation of state. The CBMC data for mixture adsorption indicates that selectivity reversal is ensured when adsorption is from the *liquid* phase mixture and under these conditions the adsorption favors the alcohol with the shorter chain length.

The CBMC mixture simulations for ethanol - 1-hexanol mixtures are shown in Figure 73c. For partial fugacities, $f_i < 60$ kPa, the adsorption selectivity is strongly in favor of the longer 1-hexanol molecule. However, when the partial fugacities exceed 100 kPa, we find a reversal of selectivity. This selectivity is entropy based and is ascribable to the significantly higher saturation capacity of ethanol (4/cage) in comparison to that of 1-hexanol (1/cage). The shaded region in Figure 73c indicates that the bulk fluid phase is in the liquid phase for the range of fugacities, f_i .

The continuous solid lines in Figures 73a,b,c are the predictions of the Ideal Adsorbed Solution Theory (IAST) of Myers and Prausnitz³⁰ using pure component isotherm fits. Table 11 provides the pure component fit dual-site Langmuir Freundlich parameters. The IAST calculations have been presented here to demonstrate that selectivity reversal is not an unexpected phenomenon, but is a natural result that is obtained for a mixture of two species having (1) lower adsorption strength, but higher saturation capacity, and (2) higher adsorption strength, but lower saturation capacity. When saturation conditions are approached the component with the higher saturation capacity is invariably preferred. This is due to the fact that vacant “sites” are more easily filled by the smaller molecule at near-saturation conditions. Though the predictions of the IAST are in general qualitative agreement with CBMC simulations, the agreement is not quantitatively perfect in all three cases.

To rationalize the experimental uptake data of Saint-Remi et al.¹²⁴, we choose conditions for the simulations with CHA zeolite such that partial fugacities in the fluid phase surrounding the crystal is in the liquid state. Specifically we choose:

$$f_1 = f_2 = 1 \text{ MPa for ethanol/1-propanol mixture}$$

$$f_1 = f_2 = 0.3 \text{ MPa for methanol/1-propanol mixture}$$

$$f_1 = f_2 = 0.5 \text{ MPa for methanol/ethanol mixture}$$

where the partial fugacities are chosen to match the molar loadings, albeit qualitatively, in the experiments.

The uptake simulation results are presented in Figures 74a,b,c for (a) ethanol/1-propanol, (b) methanol/1-propanol, and (c) methanol/ethanol mixtures within CHA crystals. The Maxwell-Stefan

diffusivities were chosen in the simulations to be: $D_{methanol}/r_c^2 = 6 \times 10^{-4} \text{ s}^{-1}$; $D_{ethanol}/r_c^2 = 1 \times 10^{-5} \text{ s}^{-1}$; $D_{1-propanol}/r_c^2 = 1 \times 10^{-8} \text{ s}^{-1}$. The continuous solid lines are the calculations of the Maxwell-Stefan model using flux equation (53). For all three mixtures we observe overshoots in the uptake of the more mobile partner species in the mixture. The simulated uptake characteristics are in qualitative agreement with the experimental uptake data of Saint-Remi et al.¹²⁴

The dashed lines are the calculations of the Maxwell-Stefan model simulations using equation (54) with $\Gamma_{ij} = \delta_{ij}$. Ignoring thermodynamic coupling does not produce a overshoot in the uptake of the more mobile partner.

As further confirmation that thermodynamic coupling effects are the root cause of the overshoots in the uptake of the more mobile partner species, Figure 75a presents the elements Γ_{ij} of the thermodynamic corrector factor matrix $[\Gamma]$. We note that for mixture loadings $q_t < 2 \text{ mol kg}^{-1}$, the off-diagonal elements are significantly smaller in magnitude than the corresponding diagonal elements. However, for $q_t > 2.7 \text{ mol kg}^{-1}$, the contribution of the off-diagonal elements becomes increasingly significant. Figure 75b presents calculations of $(\Gamma_{12} q_2 / \Gamma_{11} q_1)$, that signify the extent of thermodynamic coupling, for ethanol/1-propanol, methanol/1-propanol, and methanol/ethanol mixtures. We note that $(\Gamma_{12} q_2 / \Gamma_{11} q_1)$ displays maxima for the three mixtures at values of q_t in the range $2.8 - 3.8 \text{ mol kg}^{-1}$, in qualitative agreement with the experimental data of Saint-Remi et al.¹²⁴; cf. Figure 71.

Figure 76 presents data on the radial profiles of the loadings of ethanol and 1-propanol within CHA crystal, for ethanol/1-propanol mixture uptake at times (a) $t = 10^2 \text{ s}$, (b) $t = 10^3 \text{ s}$, (c) $t = 5 \times 10^3 \text{ s}$, (d) $t = 10^4 \text{ s}$, and (e) $t = 10^7 \text{ s}$. The component loading of ethanol displays a maximum close to surface of the crystal during the initial stages of the transient uptake process.

Figure 77 presents simulation results for transient desorption kinetics for ethanol/1-propanol mixture in CHA, subjected to a step decrease in total pressure of the surrounding gas phase. The desorption kinetics, at first sight, gives the impression of counter-current diffusion. The counter-current nature of the desorption kinetics is purely ascribable to the fact that the initial conditions, the mixture adsorption

equilibrium favors ethanol due to entropy effects¹²⁵ that are in play when conditions are near saturation conditions. However, the final equilibrated condition, the mixture adsorption equilibrium is in favor of 1-propanol, and not influenced by entropy effects.

The breakthrough experimental data of Remy et al.¹²⁶ for separation of (a) ethanol/1-propanol and (b) ethanol-1-hexanol mixtures in a fixed bed adsorber packed with SAPO-34, shown in Figure 78, are quite remarkable because the component that is eluted first from the adsorber is the alcohol with the longer chain length. The rationalization of these experimental data can be traced to the entropy effects that favor the shorter alcohols under conditions such that the bulk fluid phase is in the liquid state; cf. Figure 73. When operating under conditions such that the bulk fluid phase is a liquid mixture, both adsorption and diffusion favor the uptake of the shorter alcohol, and the longer alcohol is rejected in a fixed bed adsorber. Both adsorption and diffusion act synergistically in the such separations.

Breakthrough simulations for (a) ethanol/1-propanol and (b) ethanol-1-hexanol mixtures in a fixed bed adsorber packed with CHA (structural analog of SAPO-34), confirm that the longer alcohol can be eluted first from the adsorber; cf. Figure 79.

33. Transient uptake and breakthrough of alkene/alkane mixtures

Ethene is an important chemical used as feedstock in manufacture of polymers such as polyethylene, polyvinyl chloride, polyester, polystyrene as well as other organic chemicals. Propene is an important chemical used as feedstock in manufacture of polymers such as polypropene. Key processing steps in preparing feedstocks for polymer production are the separations of ethene/ethane, and propene/propane mixtures. The boiling points are below ambient temperatures: ethane (184.5 K), ethene (169.4 K), propane (225.4 K), propene (225.4 K). Due to the small differences in the boiling points, the separations of ethene/ethane, and propene/propane mixtures have low relative volatilities, in the range of 1.1 – 1.2. These separations are traditionally carried out by distillation columns that operate at high pressures and low temperatures. The purity requirement of the alkenes as feedstocks to polymerization reactors is 99.95%, and consequently the distillation columns are some of the largest and tallest distillation columns used in the petrochemical industries with about 150 - 200 trays, and operating at reflux ratios

of about 15. Distillation is energy intensive, and adsorptive separations offer an attractive, energy-efficient, alternative. Several nanoporous materials have potential for separation of ethene/ethane and propene/propane mixtures.^{3, 72}

Let us first consider the transient breakthrough characteristics of C₃H₆, and C₃H₈ mixtures in a packed bed of CuBTC crystallites as reported in the experiments of Yoon et al.¹²⁷ at $T = 313$ K; see Figure 80a. The unsaturated propene molecules bind more strongly with the Cu atoms than the saturated propane. The transient breakthrough characteristics are reasonably well represented by breakthrough simulations in which intra-crystalline diffusion effects are considered to be negligible and Equation (65) is invoked; witness the comparisons between experiments and simulations presented.

We now analyse in further detail the influence of intra-crystalline diffusion on the transient breakthrough characteristics with CuBTC. For this purpose we need the values of the intra-crystalline diffusivities. Wehring et al.¹²⁸ report experimental data on self-diffusivities of C₃H₆, and C₃H₈ within crystals of CuBTC in Table 2 of their paper. At a temperature of 313 K, the diffusivities for C₃H₆, and C₃H₈ are calculated to be $D_i = 1.7 \times 10^{-11} \text{ m}^2 \text{ s}^{-1}$, and $2 \times 10^{-10} \text{ m}^2 \text{ s}^{-1}$, respectively. It is also remarkable that the diffusivity value for C₃H₆ is lower than for C₃H₈. The reason for this can be traced to the higher binding energy of C₃H₆ compared to that for C₃H₈.^{11, 24} The isosteric heats of adsorption, Q_{st} , can be taken to be a measure of the binding energy can be taken to a reflection of the binding energy. The values of the isosteric heats of adsorption, Q_{st} , for C₃H₆ and C₃H₈ in CuBTC are 43 and 31 kJ mol⁻¹, respectively (see Table 2 of Wehring et al.¹²⁸).

In Figure 80b, two scenarios for breakthrough simulation results are compared. The first scenario is the same as the one presented in Figure 80a, represent breakthrough simulations assuming thermodynamic equilibrium, i.e. invoking Equation (65). The second scenario is one in which intra-crystalline diffusion effects (using the simplified equation (54), neglecting thermodynamic coupling) are accounted for with M-S diffusivities for C₃H₆, and C₃H₈ are taken to $D_i = 1.7 \times 10^{-11} \text{ m}^2 \text{ s}^{-1}$, and $2 \times 10^{-10} \text{ m}^2 \text{ s}^{-1}$, respectively. The crystallite radius r_c is assumed to be 400 μm ; this represents the largest crystallite size that is likely to be used in practice. The two sets of simulations yield virtually identical

values for breakthrough times. Inclusion of intra-crystalline diffusion makes the breakthrough of propene slightly more diffuse *after* breakthrough has occurred. The conclusion to be drawn here is that the assumption of thermodynamic equilibrium is a good one to make in practice, and invoking the assumption Equation (65) is sufficient to capture the separation performance of fixed bed adsorbers for hydrocarbons separations with MOFs that have “open” structures, i.e. with large pore volumes.

For FeMOF-74 (= Fe₂(dobdc)), Bloch et al.⁷² have established each alkene molecule attaches *side-on* to an Fe(II) atom in the FeMOF-74 framework. Breakthrough experiments were carried out by Bloch et al.⁷² in a 4 mm tube packed with FeMOF-74 crystallites; details of the experimental set-up and conditions are provided in the Supplementary Material accompanying their publication.⁷² The experimental breakthrough curves are in good agreement with simulations in which intra-crystalline diffusional effects are ignored, and equation (65) is invoked. The simulated transient gas composition profiles are in good agreement with the experimentally determined ones in Figure 81; this provides validation of the simulation methodology in which intra-crystalline diffusion effects are considered to be negligible.

Geier et al.¹²⁹ have measured the pure component isotherms for C₂H₄, C₂H₆, C₃H₆, and C₃H₈ for the six structural analogs M₂(dobdc) (M = Mg, Mn, Fe, Co, Ni, Zn), that indicate that the separation characteristics are of a similar nature to that of Fe₂(dobdc). The experimental data of Böhme et al.¹³⁰ for transient breakthrough of equimolar ethene/ethane, and propene/propane mixture in an adsorber bed packed with MgMOF-74, and CoMOF-74, provide confirmation that the separation characteristics are indeed of a similar nature; see Figure 82.

An important disadvantage of the alkane/alkene separations with CuBTC, FeMOF-74, MgMOF-74 and CoMOF-74 is that the desired alkene product, required for production of polymer grade polyethene and polypropene, can only be recovered in the desorption phase. It becomes necessary to operate with multiple beds involving five different steps; the alkene product of the desired purity is recovered in the final step by counter-current vacuum blowdown.^{131, 132} The energy requirements are high because of the

significantly higher binding energy of the alkenes; this is reflected in the isosteric heats of adsorption; see Figure 82.

From a practical view point it is much more advantageous to have the desired alkene product recovered in the adsorption phase. The experimental data of Böhme et al.¹³⁰ for transient breakthrough of equimolar C₂H₄/C₂H₆, and C₃H₆/C₃H₈ mixtures in an adsorber bed packed with ZIF-8 demonstrate that it is possible to recover pure alkene in the adsorption cycle; see Figure 83a. The adsorption selectivity in ZIF-8 favors the alkane, rather than the alkene.³ The essential characteristics of the experimental breakthroughs can be captured reasonably well with simulations using the using the simplified equation (54), neglecting thermodynamic coupling; see Figures 83b, and 83c.

The experimental breakthrough data of Gücüyener et al.⁷⁴ for C₂H₄/C₂H₆/H₂ mixtures in ZIF-7 show that pure ethene can be recovered in the adsorption phase; the separation characteristics are similar to that of ZIF-8. Gücüyener et al.⁷⁴ characterize the breakthrough characteristics as being “turned on its head”, with attendant practical advantages as already mentioned above. In Figures 84a, and 84b, the experimental data Gücüyener et al.⁷⁴ on transient breakthrough of C₂H₄/C₂H₆/H₂ mixtures in a fixed bed adsorber packed with ZIF-7 are compared with simulations (a) assuming thermodynamic equilibrium, and (b) inclusion of intra-crystalline diffusion effects taking $D_1/r_c^2 = 2 \times 10^{-4} \text{ s}^{-1}$; $D_1/D_2 = 1$ using the simplified equation (54), neglecting thermodynamic coupling. There is good agreement between the experimental data and simulations that include intra-crystalline diffusion effects. In Figures 84c, the two sets of simulations results are compared in order to highlight the strong influence of intra-crystalline diffusion on the breakthrough characteristics.

Figure 85 shows the simulations of the separation of C₃H₆/C₃H₈ mixtures in a fixed bed adsorber packed with ZIF-7 based on the pure component isotherm data are from Gücüyener et al.⁷⁴ Breakthrough simulations assuming thermodynamic equilibrium, i.e. invoking Equation (65), are indicated by the dashed lines. The continuous solid lines are simulations include diffusional effects but ignoring thermodynamic coupling effects and using uncoupled flux equations (36). We note that the strong influence of intra-crystalline diffusion that cause a significant reduction in the production of

99.95% pure propene. Indeed, with strong diffusional limitations, it will be impossible to produce product of the required purity. The experimental breakthroughs at 303 K, as reported by van den Bergh et al.¹³³ are in reasonable qualitative agreement with the breakthrough simulations that include intracrystalline diffusion effects.

It is also to be noted that the alkane diffusivity in ZIF-7 and ZIF-8 is expected to be lower than that of the corresponding alkenes, due to subtle differences in bond lengths and bond angles;²⁴ if the differences in the diffusivities are sufficiently large, then we should expect the alkanes to break through earlier.³ We need MOFs that display adsorption selectivity towards the alkanes, but do not suffer from strong diffusion limitations; this is a fruitful area for research.

JUC-103 is another MOF for which the separation of ethene/ethane mixture is “turned on its head” and C₂H₆ adsorbs more strongly than C₂H₄; witness the pure component isotherm data presented in Figure 3 of Jia et al.¹³⁴ But no experimental data on breakthroughs is available for JUC-103.

34. Separation of C₂H₂ from hydrocarbons, and CO₂

In steam cracking of ethane to produce ethene, one of the by-products is ethyne, more commonly referred to as acetylene. Ethyne has a deleterious effect on end-products of ethene, such as polyethene. Therefore recovery, or removal of ethyne from ethene streams is essential because the presence of ethyne at levels higher than 40 ppm will poison the catalyst. The selective removal of ethyne is conventionally carried out by absorption in DMF, which is energy-intensive. A typical processing scheme involves three steps: (1) acetylene absorption in a tray column, (2) stripping of ethene from the solvent DMF, and (3) DMF regeneration with recovery of ethyne. Selective C₂H₂ adsorption using microporous materials affords an energy-efficient alternative.

Typically, the C₂H₂ content of C₂H₂/C₂H₄ feed mixtures is 1%; this concentration has to be reduced to produce C₂H₄ containing less than 40 ppm C₂H₂. As illustration, Figure 86a presents a plot of the ppm C₂H₂ in the outlet gas of an adsorber bed packed with MgMOF-74, CoMOF-74, M'MOF-3a, M'MOF-4a; the simulation data are from He et al.³ The high C₂H₂ adsorption for M-MOF-74 is due to the strong complexation between the metal ions and the π orbital of C₂H₂. The breakthrough times, τ_{break}

corresponding to the exit gas containing 40 ppm C_2H_2 in the product gas can be determined. From a material balance on the adsorber, the number of moles of C_2H_2 , that is captured during the time interval $0 - \tau_{break}$ can be determined; this is plotted in Figure 86b. Materials such as MgMOF-74, and CoMOF-74 that have open structures with high uptake capacities for C_2H_2 , are able to capture the largest amounts of C_2H_2 .

From a material balance on the adsorber, we can also determine the production of C_2H_4 , with the specified purity level, can be determined by integrating during the time interval $0 - \tau_{break}$. Figure 86c presents a plot of the amount of C_2H_4 produced, containing less than 40 ppm of C_2H_2 , per L of adsorbent, during the time interval τ_{break} , plotted as a function of the time interval τ_{break} . The hierarchy of production capacities is $M'MOF-3a > M'MOF-4a > MgMOF-74 > CoMOF-74$. The superior productivity of $M'MOF-3a$ and $M'MOF-4a$ is ascribable to the higher C_2H_2/C_2H_4 adsorption selectivities.

Materials such as MgMOF-74, CoMOF-74, and FeMOF-74 are not only capable of separating C_2H_2/C_2H_4 mixtures but can fractionate a mixture containing C1, C2, and C3 hydrocarbons to recover each individual component into its relatively pure form. This is illustrated in Figures 87a, and 87b by transient breakthroughs of *equimolar* 6-component $CH_4/C_2H_2/C_2H_4/C_2H_6/C_3H_6/C_3H_8$ mixture with CoMOF-74, and FeMOF-74. For both CoMOF-74, and FeMOF-74, the sequence of breakthroughs, CH_4 , C_2H_6 , C_3H_8 , C_2H_4 , C_2H_2 , and C_3H_6 is dictated by a combination of chain length and degree of unsaturation.

He et al.¹³⁵ have underscored the potential of UTSA-35a ($V_p = 0.52 \text{ cm}^3/\text{g}$; $\rho = 1046 \text{ kg/m}^3$), a doubly interpenetrated metal-organic framework constructed from an aromatic tricarboxylate, for fractionation of a mixture containing C1, C2, and C3 hydrocarbons; see Figure 87c for breakthrough simulation results. The sequence of breakthroughs, CH_4 , C_2H_4 , C_2H_6 , C_2H_2 , C_3H_6 and C_3H_8 , is dictated by a primarily by the chain length. Though not stressed by the authors themselves, we note that the breakthrough of unsaturated C_2H_4 occurs earlier than that of the saturated C_2H_6 . This implies that the separation of ethene/ethane mixtures can be “turned on its head”, much in the same manner as

demonstrated for ZIF-7 and ZIF-8, discussed in the foregoing section. There is no experimental evidence of the desirable sequence of separation of ethene and ethane.

The separation of C₂H₂/CO₂ mixtures is important in industry for production of pure C₂H₂, that is required in for a variety of applications in the petrochemical and electronic industries.¹³⁶ The separation is particularly challenging in view of the similarity in the molecular dimensions.^{136, 137} Figure 88a provides a comparison of the adsorption selectivity for equimolar C₂H₂/CO₂ mixtures for three different MOFs: UTSA-30a (Ref: ¹³⁸, $V_p = 0.26 \text{ cm}^3/\text{g}$), UTSA-50a (Ref: ¹³⁹, $V_p = 0.35 \text{ cm}^3/\text{g}$), and CuBTC (Ref: ³, $V_p = 0.75 \text{ cm}^3/\text{g}$) with increasing pore volumes. The adsorption selectivities of UTSA-50a and CuBTC are nearly the same. The separation performance in fixed bed adsorbers is dictated not just by the adsorption selectivity, but by capacity considerations. CuBTC has the most open structure, and significantly higher uptake capacities. Higher uptake capacities lead to longer breakthrough times, and higher productivities. Figures 88b, 88c, and 88d present breakthrough simulations for the three materials. The productivity of pure C₂H₂ is proportional to the difference in the breakthrough times of C₂H₂, and CO₂. This leads us to conclude that the productivity of CuBTC is twice as high as that of UTSA-50a.

35. Transient separation of mixtures of C4 hydrocarbons

The separation of unsaturated alkenes from C4 hydrocarbon mixtures is important in petrochemical processing. The C4 hydrocarbons possess similar sizes and boiling points.

	Molar mass mol g ⁻¹	Boiling point K
iso-butane (2-methylpropane)	58.124	261.45
iso-butene (= 2-methylpropene)	56.108	266.25
1-butene	56.108	266.85
1,3 butadiene	54.092	268.75
normal butane	58.124	272.65

trans-2-butene	56.108	273.45
cis-2-butene	56.108	276.85

Consequently, distillation separations are energy-intensive operations. Butadiene is commonly removed by extractive distillation. Significant reductions in the energy requirements can be achieved by adopting one of the two strategies: (1) replacing distillation by adsorption, or (2) using a hybrid combination of distillation and adsorption processes.

We now examine some potential adsorption based separations of C4 hydrocarbons that could potentially be used in one of the aforementioned strategies.

Hartmann et al.¹⁴⁰ have presented breakthrough experimental data to demonstrate the separation of isobutane/isobutene mixtures using CuBTC; see Figure 89a. The adsorptive separation step exploits differences in the electronic properties due to the double bond of isobutene. Here the unsaturated molecules bond preferentially with the uncoordinated Cu atoms; this preferential binding is analogous to that observed earlier for propene/propane separations with CuBTC (cf. Figure 80). The breakthrough characteristics are sharp, and indicative of absence of intra-crystalline diffusion resistances. Breakthrough simulations assuming thermodynamic equilibrium, i.e. invoking Equation (65), shown in Figure 89b are capable of reproducing the essential characteristics of the experimental breakthroughs.

Tijsebaert et al.¹⁴¹ have demonstrated the potential of RUB-41 all-silica zeolite, that has the RRO structural topology, for separation of cis-2-butene and trans-2-butene from 1-butene; this separation is of industrial importance because 1-butene is needed in the production of e.g. linear low density polyethylene (LLDPE). RUB-41 comprises a 2-dimensional intersecting channel system consisting of an 8-membered ring channel (0.27×0.5 nm) along [001], and a 10-membered ring channel (0.4×0.65 nm) along [100]. The measured data on adsorption indicates that the adsorption equilibrium, and saturation capacities follow the hierarchy cis-2-butene > trans-2-butene \gg 1-butene. This hierarchy is, we believe, ascribable to length entropy effects such as that demonstrated for hexane isomer separation within 12-ring channels of AFI and MOR zeolites.¹⁴²⁻¹⁴⁴ The footprint of 1-butene is longer than that of either cis-2-butene or trans-2-butene. As a consequence it is possible to pack more molecules of either

cis-2-butene or trans-2-butene within a given length of the 10-ring channels. Differences in molecular lengths provides the rationale for the hierarchy of saturation loadings that follows cis-2-butene > trans-2-butene >> 1-butene. Breakthrough experiments, carried out in the liquid phase, indicate that 1-butene breaks through earlier than either cis-2-butene, or trans-2-butene. Using the fits of the pure component isotherms, the experimental breakthroughs can be reasonably well described by breakthrough simulations that include the influence of intra-crystalline diffusion. Figures 90a, and 90b demonstrate the influence of intra-crystalline diffusion on transient breakthroughs. The sequence is unaltered when diffusional influences are accounted for.

The selective adsorption of 1,3 butadiene from 1-butene using Ag-Y zeolite is suggested by Takahashi et al.¹⁴⁵

36. Separation of O₂/N₂ mixtures

The separation of air to produce N₂ and O₂ of high purities is one of the most important industrial processes that uses pressure swing adsorption technology.^{1, 146} The process technologies are geared to either production of purified O₂ or purified N₂. Cryogenic distillation has been the common technologies for this separation, but adsorptive separations offer energy efficient alternatives. Purified O₂ is required for a wide variety of applications that include portable adsorption units for medical applications and in space vehicles. Nitrogen is required in applications where it is desired or necessary to exclude oxygen. Typical industrial applications include laser cutting, food packaging, and nitrogen blanketing. N₂ is required for use in laboratory analytical equipment such as GC, LC, LCMS, FTIR, ICP, and in glove boxes.

For production of purified O₂, the adsorbents used are LTA-5A, NaX, CaX, and LiX can be used as selective adsorbents.¹⁴⁶⁻¹⁵⁰ The larger permanent quadrupole of N₂ compared to that of O₂ is responsible for the stronger adsorption strength of N₂ on these zeolites.¹⁴⁹ Both O₂, and N₂ have similar polarizabilities and magnetic susceptibilities. However, the quadrupole moment of N₂ is about 4 times that of O₂.

Figure 91a presents breakthrough calculations for separation of O₂/N₂ with LTA-5A. The O₂/N₂ separation essentially relies on the fact that the adsorption strength of N₂ is about 3.6 times that of O₂. The diffusion selectivity is in favor of O₂, with $D_{O_2}/D_{N_2}=2$. The cations within the framework do not block the window regions and diffusional limitations are adequately quantified by taking $D_{O_2}/r_c^2 = 0.01 \text{ s}^{-1}$.¹⁴⁶⁻¹⁴⁸ The continuous solid lines in Figure 91a are simulations that include diffusional effects but ignoring thermodynamic coupling effects. Inclusion of thermodynamic coupling effects leads to practically identically breakthrough characteristics; this is because the differences in the adsorption strengths of O₂ and N₂ in LTA-5A are small. The dashed lines in Figure 91a are breakthrough simulations in which diffusional influences are ignored, and thermodynamic equilibrium is assumed to prevail within the crystals. During the earlier stages of the transience nearly pure O₂ can be recovered at the exit of the adsorber. This technology is useful for medical applications in which enriched O₂ can be produced in portable units. Diffusional influences serve to produce more diffuse breakthrough characteristics and, as a consequence, the production capacity for pure O₂ is reduced. As illustration, let us say we need to enrich O₂ from 21% feed mixture to yield 85% O₂ in product gas. In absence of diffusional limitations the 85% pure O₂ productivity of LTA-5A is 1.58 mol L⁻¹. Taking intra-crystalline diffusion into account has the effect of reducing the productivity to 0.43 mol L⁻¹.

Diffusional effects are lesser importance of O₂/N₂ separations using LiX (with Si/Al = 1, referred to as LiLSX) that has wider 7.4 Å windows separating cages; cf. Figure 91b.¹⁵¹ The breakthrough characteristics are “less diffuse”, and breakthrough times are longer, than is the case with LTA-5A; this leads to higher productivities of purified O₂.

For production of pure N₂ from air, a different strategy is often employed using LTA-4A as adsorbent in fixed bed operations, and relying on diffusion selectivity.^{152, 153} Diffusion limitations are much more severe in LTA-4A because the window regions are partially blocked by the cations (see framework in Figure 92a). The production of pure N₂ relies on the significantly lower diffusivity of N₂ as compared to O₂. The continuous solid lines in Figure 92b are simulations that include diffusional effects with $D_{O_2}/r_c^2 = 2 \times 10^{-3} \text{ s}^{-1}$; $D_{O_2}/D_{N_2} = 100$, ignoring thermodynamic coupling effects.^{152, 153} Inclusion of

thermodynamic coupling effects leads to practically identically breakthrough characteristics; this is because the differences in the adsorption strengths of O₂ and N₂ in LTA-4A are small. N₂ of purity close to 100% can be recovered during the early stages of the breakthrough, albeit for a brief period. The dashed lines are breakthrough simulations in which diffusional influences are ignored, and thermodynamic equilibrium is assumed to prevail within the crystals. Introduction of strong diffusional limitations serves to reverse the hierarchy of breakthroughs.

Diffusion selectivity in favor of O₂ is also achievable by use of CMS (Carbon Molecular Sieve).¹⁵⁴ Purity levels up to 99.9995% N₂ are achievable in PSA processes. This nitrogen purity level can also be ensured by cryogenic systems, but they are considerably more complex. However, it is essential to stress that PSA processes can recover only oxygen or nitrogen as relatively pure streams, but not both from the same process at the same time.

A completely different strategy for N₂ production is to use Fe₂(dobdc) (= FeMOF-74 = CPO-27-Fe) as adsorbent; in this case O₂ binds selectively with the Fe atoms of the framework (cf. Figure 93a), that consists of hexagonal-shaped one-dimensional channels of 11 Å size.¹⁵⁵ The O₂ binding with Fe atoms has been demonstrated to be reversible up to temperatures of 211 K. At 211 K, O₂ uptake is fully reversible and the capacity corresponds to the adsorption of one O₂ molecule per iron center. Figure 93b shows breakthrough simulations for a fixed bed adsorber packed with Fe₂(dobdc) operating at a total pressure of 200 kPa and 211 K. In view of the large channel sizes, diffusional influences are of negligible importance and the breakthrough characteristics are practically unaltered when diffusional effects are ignored. This structure can be expected to have a significantly higher capacity to produce pure N₂ than LTA-4A. There is a need for further research on adsorbents similar to Fe₂(dobdc) that bind O₂ selectively and also allow operation at temperatures close to ambient conditions.

Mn₂(dobdc), the structural analog of Fe₂(dobdc) has also been shown to have the propensity for binding O₂ to the open Mn(II) coordination sites.¹⁵⁶ As is the case with Fe₂(dobdc), the desorption branch of the isotherm data at 298 K for Mn₂(dobdc), presented in Figure 6 of the paper of Wang et al.¹⁵⁶ indicates that the binding of O₂ is irreversible at 298 K; only at temperatures lower than 268 K is

the binding reversible. The isotherm data of Wang et al.¹⁵⁶ have also presented isotherm data for Mn₅(btac), a MOF first synthesized by Han et al.¹⁵⁷, that indicates that the binding of O₂ is irreversible at 298 K.

37. Separation of chlorofluorocarbons

Peng et al.¹⁵⁸ discuss the need for separation of CFC-115 (1-chloro-1,1,2,2,2-pentafluoroethane) and HFC-125 (1,1,1,2,2-pentafluoroethane). The boiling points of CFC-115 (234.1 K) and HFC-125 (224.7 K) are very close, and their mixtures can be nearly azeotropic. Therefore, cryogenic extractive distillation has been the dominant technology utilized to separate these mixtures. Adsorptive separations offer energy-efficient alternatives to distillation. Towards this end, Peng et al.¹⁵⁸ have reported the pure component isotherm data for CFC-115 and HFC-125 in MFI zeolite. CFC-115 locates preferentially at the intersections of MFI, and the pure component isotherms show inflections at loading of 4 molecules per unit cell. For total mixture loadings $\Theta_t < 4/\text{uc}$, the adsorption selectivity is in favour of CFC-115. However, due to configurational entropy effects, the adsorption selectivity is in favour of HFC-125 at higher loadings. The principle of separation is entirely analogous to that of the separation of hexane isomers discussed in detail in a later section.

Figure 94a present transient breakthrough simulations for equimolar CFC-115/HFC-125 mixture with MFI zeolite using three different scenarios for an adsorber operating at $p_t = 100$ kPa. As is to be expected, the reaktthrough simulations assuming thermodynamic equilibrium, i.e. invoking Equation (65), yield sharp breakthroughs; consequently the separation performance is “ideal”. Introduction of diffusion limitations produces diffuse breakthroughs, and, as a consequence, the productivities are significantly lowered. However, the choice of the diffusion model is quite important for MFI zeolite. Thermodynamic coupling effects have a significant influence on the breakthrough characteristics of the CFC-115; compare the continuous solids lines (simulations including the influence of thermodynamic coupling, Γ_{ij}), with the dotted lines (simulations assuming $\Gamma_{ij} = \delta_{ij}$).

A further point to note is that for $p_t = 100$ kPa the desired product HFC-125 is more strongly adsorbed in MFI; consequently it can only be recovered in the desorption (blowdown) cycle. This is not the ideal

adsorbent. If the chosen operating conditions are such that $p_t = 1$ kPa, then HFC-125 can be recovered in pure form during the adsorption cycle; see Figure 94b.

38. Configurational-Bias Monte Carlo simulation methodology

For analysis of the performance of various adsorbents for separation of mixtures of alkane isomers,^{105, 143, 159} we need accurate modelling of pure component and mixture isotherms. In earlier works,^{105, 143, 159} Configurational-Bias Monte Carlo (CBMC) simulations were carried out to determine the pure component and mixture isotherms in MFI zeolite, and other MOFs and ZIFs. We wish to establish the superiority of MFI zeolite over other materials for the task of producing high octane gasoline. Our analysis of the performance of MFI is based on CBMC simulations. For that reason, the accuracy of the CBMC simulations with MFI is established below by means of extensive comparisons with published experimental data.

Firstly, we summarize the CBMC simulation methodology. The linear and branched alkanes are described with a united-atom model, in which CH_3 , CH_2 , and CH groups are considered as single interaction centres. When these pseudo-atoms belong to different molecules or to the same molecule but separated by more than three bonds, the interaction is given by a Lennard-Jones potential. The Lennard-Jones parameters are chosen to reproduce the vapour-liquid curve of the phase diagram as shown in Siepmann et al.¹⁶⁰ For simulations with linear and branched alkanes with two or more C atoms, the beads in the chain are connected by harmonic bonding potentials. A harmonic cosine bending potential models the bond bending between three neighboring beads, a Ryckaert-Bellemans potential controls the torsion angle. Details for the alkane model can be found in Dubbeldam et al.^{105, 161}

Following Kiselev and co-workers¹⁶², we consider the MFI zeolite lattice to be rigid and we assume that interactions of an alkane with the zeolite are dominated by the dispersive forces between alkane pseudo atoms and the oxygen atoms of the zeolite. This is a very common approximation because the large oxygen atoms account for most of the potential energy and essentially shield the much smaller silicon atoms. The oxygen-adsorbate potential is an effective potential which implicitly includes the Si-

contribution. These interactions are described by a Lennard Jones potential, which parameters are given by Dubbeldam et al.^{105, 161} The Lennard-Jones potentials are shifted and cut at 12 Å.

The simulation box size was 2×2×4 unit cells for MFI; it was verified that the size of the simulation box was large enough to yield reliable data on adsorption isotherms. Periodic boundary conditions were employed.

Adsorption isotherms are conveniently computed using Monte Carlo simulations in the grand-canonical ensemble. In this ensemble the temperature and chemical potentials are imposed. The average number of adsorbed molecules per unit cell of the zeolite follows from the simulations. The characteristics of these type of simulations is that during the calculations attempts are made to change the total number of particles by making attempts to insert molecule into or remove molecules from the zeolite. To make these types of moves possible for the long chain alkanes, we use the Configurational-Bias Monte Carlo (CBMC) technique.^{163, 164} Instead of inserting a molecule at a random position, in a CBMC simulation, a molecule is grown atom by atom in such a way that the “empty spots” in the zeolite are found. This growing scheme gives a bias that is removed exactly by adjusting the acceptance rules.^{163, 164}

These simulations were performed in cycles and in each cycle, an attempt to perform one of the following moves was made:

- (1) displacement of a randomly selected chain. The maximum displacement was adjusted to an overall acceptance of 50%.
- (2) rotation of a chain around its center of mass. The chain is chosen at random and the maximum rotation angle is selected to accept 50% of the moves.
- (3) partly regrowing of a chain; a chain is selected at random and part of the molecule is regrown using the CBMC scheme. It is decided at random which part of the chain is regrown and with which segment the regrowing is started. For branched alkanes, the approach in Vlugt et al.¹⁶³
- (4) exchange with a reservoir; it is decided at random whether to add or to remove a molecule from the zeolite following the acceptance rules derived in Vlugt et al.¹⁶³

(5) change of identity (only in the case of mixtures); one of the components is selected at random and an attempt is made to change its identity.¹⁶³ The acceptance rules for these trial moves can be found in Frenkel and Smit .¹⁶⁴

Typically the number of MC cycles performed is 10^7 . Of these, 15% are displacements, 15% rotations, 15% partial re-growths, 50% exchanges with the reservoir and the remaining 5% of the moves were attempts to change the identity of a molecule.

39. CBMC simulations of pure component adsorption isotherms in MFI, including experimental validation

To establish the validity of CBMC simulations we performed a comprehensive test of CBMC simulations of pure component isotherm for linear and branched alkanes with 1 – 7 C atoms in MFI.

Figure 95 presents a comparison of CBMC simulations of pure component isotherms for CH₄ (= C1), C₂H₆ (= C3), C₃H₈ (= C3), and nC₄H₁₀ (= nC4) at a variety of temperatures with the experimental data of Sun et al.¹⁶⁵ The CBMC simulations are in good agreement with experimental isotherm data for the entire range of temperatures. The CBMC simulations for nC4 at 298 K are fitted with the dual-Langmuir-Freundlich model

$$\Theta_i = \Theta_{i,A,sat} \frac{b_{i,A} f_i^{V_A}}{1 + b_{i,A} f_i^{V_A}} + \Theta_{i,B,sat} \frac{b_{i,B} f_i^{V_B}}{1 + b_{i,B} f_i^{V_B}}; \quad q_i = q_{i,A,sat} \frac{b_{i,A} f_i^{V_A}}{1 + b_{i,A} f_i^{V_A}} + q_{i,B,sat} \frac{b_{i,B} f_i^{V_B}}{1 + b_{i,B} f_i^{V_B}} \quad (66)$$

with parameters specified in Table 5.

In equation (66), the loadings are expressed in two different ways. The loadings Θ_i are expressed in molecules per unit cell of MFI. The loadings q_i are expressed as mol per kg of MFI framework. The discussions of configurational entropy effects are much more convenient in terms of Θ_i . Experimental isotherm data are most commonly expressed in terms of q_i . The loadings in terms of Θ_i need to be multiplied by a factor 0.1734 in order to obtain the molar loading q_i . In the ensuing discussions, we will use both measures of component loadings: Θ_i and q_i .

The CBMC simulation results are presented in terms of the bulk phase gas fugacities, f_i . When comparing with experimental data from literature sources that are reported in terms of pressures, p_i , we have been meticulous in calculating the fugacity coefficients using the Peng-Robinson equation of state to ensure that the comparisons are made on a consistent basis. In all cases discussed in this work, the corrections for the fugacity coefficients were negligibly small.

Figure 96 presents a comparison of experimental isotherm data of Song and Rees¹⁶⁶ and Millot et al.^{167, 168} for nC6 with CBMC simulations; good agreement is again observed for a variety of temperatures. The nC6 isotherms exhibit a slight inflection in the adsorption isotherm at a loading $\Theta_i = 4$ molecules per unit cell, corresponding to $0.6935 \text{ mol kg}^{-1}$ and the reasons for this are explained by Vlugt et al.¹⁶³

The CBMC simulations for nC6 (cf. Figure 97) are fitted with the dual-Langmuir-Freundlich parameters specified in Table 6. Also shown in Figure 97 are snapshots showing the location of nC6 molecules within the straight and zig-zag channels of MFI. The length of the nC6 molecule is commensurate with the distance between intersections along the zig-zag channels and a maximum of 8 molecules in a unit cell can be accommodated in the straight and zig-zag channels.

The length of an n-heptane (nC7) molecule is slightly longer than the distance between adjacent intersections; see snapshot in Figure 98. The incommensurateness of the molecular length of nC7 with the periodicity of MFI causes the adsorption isotherms to exhibit an inflection at a loading $\Theta_i = 4/\text{uc}$; see Figure 98. The inflection characteristics, captured in CBMC simulations, are in accord with the experimental data of Sun et al.¹⁶⁹ and Eder.¹⁷⁰

Figure 99 presents a comparison of CBMC simulations of pure component isotherms for $i\text{C}_4\text{H}_{10}$ (= iC4) at a variety of temperatures compared with the experimental data of Sun et al.¹⁶⁵ and Zhu et al.¹⁷¹ For all temperatures, the adsorption isotherms for iC4 exhibit strong inflection characteristic due to the fact that iC4 locates preferentially at the intersections between straight and zig-zag channels; these intersection sites offer more “leg room”. There are 4 intersections per unit cell of MFI, and consequently the inflection is observed at a loading $\Theta_i = 4/\text{uc}$, corresponding to $q_i = 0.6935 \text{ mol kg}^{-1}$. To

obtain loadings higher than $\Theta_i = 4/\text{uc}$, an extra push is required to make the mono-branched locate within the channel interiors; this extra push is the cause of the inflection in the isotherm. The snapshot of adsorbed *i*C4 molecules at a loading $\Theta_i = 4/\text{uc}$ demonstrates that only the intersections are occupied. The CBMC simulations for *i*C4 at 300 K are fitted with the dual-Langmuir-Freundlich parameters specified in Table 5.

Figure 100 compares experimental isotherm data of Zhu et al.¹⁷² for 2-methylpentane (= 2MP) with the corresponding CBMC simulations. The strong inflection in the CBMC data at a loading of 4 molecules per unit cell is evident. Also shown is snapshot of 2MP molecules, again clearly indicating location at the intersection sites of MFI. The CBMC simulations for 2MP at 298 K are fitted with the dual-Langmuir-Freundlich parameters specified in Table 6.

A similar good agreement of CBMC simulations of the isotherm for 3MP with experimental data^{172, 173} is obtained for 3-methylpentane (= 3MP); see Figure 101 .

The di-branched isomers 2,2 dimethylbutane (= 22DMB) and 2,3 dimethylbutane (23DMB) are too bulky to locate within the channels, and therefore only the intersection sites can be occupied, yielding a saturation loading $\Theta_{i,\text{sat}} = 4/\text{uc}$ ($q_{i,\text{sat}} = 0.6935 \text{ mol kg}^{-1}$); see Figure 102.

Thus far we have considered each alkane individually. Figure 103a compares a comparison of CBMC simulations of pure component isotherms for *n*-pentane (*n*C5), 2-methylbutane (2MB), neopentane (neo-P), all at 433 K. Figure 103b compares the pure component isotherms for *n*C6, 3MP, and 23DMB in MFI at 433 K. Figure 103c compares the pure component isotherms for *n*C6, 2MP, 3MP, 22DMB, and 23DMB in MFI at 433 K. The continuous lines in Figure 103 are the dual-Langmuir-Freundlich fits of the isotherms with parameter values specified in Table 16. These fits will be used in IAST calculations to be presented later in this work.

40. CBMC simulations of mixture adsorption equilibrium, including experimental validation

The stark differences in the pure component adsorption behaviors of linear and branched alkanes, highlighted in the foregoing, can be exploited to separate mixtures containing linear from branched

alkanes with the same number of carbon atoms. To illustrate this separation principle, let us consider CBMC simulations of loadings in the adsorbed phase in equilibrium with equimolar binary gas phase containing a mixture of nC6 and 2MP with equal partial pressures $p_1 = p_2$ in the bulk gas phase; see Figure 104a. Up to total hydrocarbons pressures $p_t = p_1 + p_2 = 2$ Pa, the component loadings Θ_i of each component increases in an expected manner; increasing p_t leads to a corresponding increase in the component loading Θ_i . At 2 Pa pressure the total loading $\Theta_t = 4/\text{uc}$, signifying that all the intersection sites are fully occupied. To further adsorb 2MP we need to provide an extra “push”. Energetically, it is more efficient to obtain higher mixture loadings by "replacing" the 2MP with nC6; this *configurational entropy* effect is the reason behind the curious maxima in the 2MP loading in the mixture.

The separation potential of configurational entropy effects in separations is best quantified by the *adsorption selectivity* S_{ads} , defined by

$$S_{\text{ads}} = \frac{\Theta_1/\Theta_2}{p_1/p_2} = \frac{\Theta_1/\Theta_2}{f_1/f_2} \quad (67)$$

For equimolar binary gas phase mixtures, Equation (67) simplifies to yield

$$S_{\text{ads}} = \frac{\Theta_1}{\Theta_2} \quad (\text{for equimolar gas mixture with } p_1 = p_2) \quad (68)$$

The calculations of S_{ads} are shown in Figure 104b. We note that for total loadings $\Theta_t < 4/\text{uc}$, $S_{\text{ads}} \approx 1$, suggesting that adsorptive separations are not feasible in the pressures below $p_1 + p_2 < 2$ Pa. However, when the total loadings of the adsorbed phase Θ_t exceeds $4/\text{uc}$, the values of S_{ads} increase significantly to values by about one to two orders of magnitude. This implies that sharp separations of the linear and branched hexanes are possible provided the operating conditions correspond to total mixture loadings $\Theta_t > 4/\text{uc}$.

Configurational entropy effects can also be exploited for separation of linear nC6 from its di-branched isomers, 22DMB and 23DMB. To demonstrate this, Figure 105 presents CBMC simulation data for binary (a) nC6/23DMB, and (b) nC6/23DMB mixtures at 300 K. We note that the adsorption selectivity, S_{ads} , for both mixtures are in the range of 10 - 500 when $\Theta_t > 4/\text{uc}$.

The CBMC mixture simulation data presented thus far were for equal partial pressures or fugacities $f_1 = f_2$ in the bulk gas phase at 300 K. We now demonstrate that configurational entropy effects also manifest at higher temperatures and for different gas phase compositions. Figure 106a shows CBMC simulations of loadings in the adsorbed phase in equilibrium with binary nC6/22DMB mixture with partial fugacities $f_2 = 4 f_1$ in the bulk gas phase at 373 K. Up to a total hydrocarbons fugacity $f_t = 1$ kPa, the component loadings increase in an expected manner; increasing f_i leads to a corresponding increase in the component loading Θ_i . At $f_t \approx 2$ kPa, the total loading Θ_t in the zeolite $\approx 4/uc$. All the intersection sites are fully occupied; see snapshot in Figure 106. To further adsorb 22DMB, we need to provide an extra “push”. The configurational entropy effects, explained earlier in the context of nC6/2MP adsorption, are the root cause of the maximum in the 22DMB loading in the mixture at $f \approx 2$ kPa. For $f > 2$ kPa, we have unusual phenomenon that increasing the fugacity of 22DMB in the bulk fluid phase has the effect of reducing the loading in the adsorbed phase. Calculations of the adsorption selectivity, S_{ads} , using Equation (67) are shown in Figure 106b. We note that S_{ads} values increase by one to two orders of magnitude above unity when the conditions are such that the total mixture loading Θ_t exceeds $4/uc$.

Experimental confirmation of the maximum observed in the loading of the di-branched 22DMB in a binary mixture with nC6 is to be found in the MFI permeation experiments at 373 K reported by Gump et al.¹⁷⁴ The experimental data for permeation of a 20-80 nC6/22DMB mixture in the upstream compartment are shown in Figure 107. The 22DMB permeation flux exhibits a maximum at upstream pressure $p_t \approx 5$ kPa, at which the total loading in the adsorbed phase $\Theta_t \approx 4/uc$. This curious maximum in 22DMB permeation flux is therefore to be attributed to configurational entropy effects. The CBMC simulations in Figure 106 provide a qualitative explanation of the observed maximum in the 22DMB flux. For proper modeling of the permeation fluxes, we also need to account for diffusion of the individual species, as has been shown in earlier work.^{2, 175}

Configurational entropy effects also manifest for mixtures of linear, mono-branched, and di-branched alkanes. Figures 108a, b show CBMC simulations for adsorption of a ternary nC6/3MP/22DMB mixture

in MFI at 362 K. For total mixture loadings $\Theta_t > 4/\text{uc}$, we obtain the adsorption hierarchy nC6 \gg 3MP $>$ 22DMB, allowing the mixture to be separated into three individual fractions with different degrees of branching. Experimental evidence of the validity of the ternary mixture separation is provided by Santilli¹⁷⁶ and Calero et al;¹⁷⁷ see Figure 108c.

For nC4/iC4 mixture configurational entropy effects also cause the preferential adsorption of the linear nC4 molecule, but in this case the adsorption selectivities are not as high as those encountered earlier for nC6/2MP and nC6/22DMB mixtures; see Figure 109.

41. Modeling mixture adsorption equilibrium using IAST

We now examine how accurately configurational entropy effects in mixture adsorption are captured by calculations following the Ideal Adsorbed Solution Theory (IAST) of Myers and Prausnitz³⁰ using dual-Langmuir-Freundlich fits of the pure component isotherms. Briefly, the basic equation of IAST theory is the analogue of Raoult's law for vapour-liquid equilibrium, i.e.

$$p_i y_i = P_i^0(\Phi) x_i; \quad i = 1, 2, \dots, n \quad (69)$$

where x_i is the mole fraction in the adsorbed phase

$$x_i = \frac{q_i}{q_1 + q_2 + \dots + q_n} \quad (70)$$

and $P_i^0(\Phi)$ is the pressure for sorption of every component i , which yields the same surface potential,

Φ_i^0 for each of the pure components, as that for the mixture, Φ :

$$\frac{\Phi}{RT} = \rho \int_{f=0}^{f=P_1^0} \frac{q_1^0(f)}{f} df = \rho \int_{f=0}^{f=P_2^0} \frac{q_2^0(f)}{f} df = \rho \int_{f=0}^{f=P_3^0} \frac{q_3^0(f)}{f} df = \dots \quad (71)$$

where R is the gas constant, ρ is the framework density of MFI and $q_i^0(f)$ is the *pure* component adsorption isotherm given by eq. (66). The total amount adsorbed is calculated from

$$q_t \equiv q_1 + q_2 \dots + q_n = \frac{1}{\frac{x_1}{q_1(P_1^0)} + \frac{x_2}{q_2(P_2^0)} + \dots + \frac{x_n}{q_n(P_n^0)}} \quad (72)$$

The set of equations eq. (66), (69), (70), (71) and (72) need to be solved numerically to obtain the loadings, q_i , (or equivalently Θ_i) of the individual components in the mixture.

Figure 110 compares the IAST calculations with CBMC simulations of component loadings of binary nC4/iC4, and nC6/2MP mixtures. For both mixtures, the IAST estimations of the component loadings are of excellent accuracy for total mixture loadings $\Theta_t < 4/\text{uc}$. For modeling the uptake of nC6/2MP mixtures within MFI crystals exposed to bulk gas pressures lower than 2 Pa (Runs 1 and 2), we use IAST in the model calculations presented in the Manuscript.

While the correct qualitative trends are prediction for $\Theta_t > 4/\text{uc}$, the IAST estimations are not sufficiently accurate. The reasons for these deviations can be traced to the fact that the manifestation of configurational entropy effects at $\Theta_t < 4/\text{uc}$ implies strong segregation in the location of adsorbed molecules: branched molecules occupying only the intersections, while the linear molecules are located everywhere. A key assumption made in the derivation of the IAST is that there is a homogeneous distribution of the components in the adsorbed phase; this assumption is clearly violated for mixture adsorption of linear and branched alkanes in MFI. A detailed analysis, and quantification, of segregation effects for nC4/iC4 mixtures has been provided by Krishna and Paschek.¹⁷⁸

Figure 111a compares CBMC simulations of component loadings in a ternary of n-pentane(nC5)/2-methylbutane(2MB)/neopentane(neo-P) mixture at 433 K with IAST calculations. The CBMC data demonstrate the ability of MFI to separate pentane isomers into three fractions depending on the degree of branching. Up to a total hydrocarbons fugacities $f_t \approx 0.1$ MPa, the IAST calculations are of reasonable accuracy in predicting the mixture adsorption characteristics.

Figure 111b compares CBMC simulations of component loadings in a ternary mixture of ternary mixture of nC6/3MP/22DMB at 433 K with IAST calculations. The CBMC data show the ability of MFI to separate pentane isomers into three fractions depending on the degree of branching. Up to a total

hydrocarbons fugacities $f_i \approx 0.1$ MPa, the IAST calculations are of reasonable accuracy in predicting the mixture adsorption characteristics.

Figure 112a presents CBMC simulations of component loadings in a 5-component nC6/2MP/3MP/22DMB/23DMB mixture at 433 K as a function of the total hydrocarbons fugacity f_t . The plot of the component loading Θ_i as a function of the total mixture loading Θ_t (cf. Figure 112b), demonstrates that configurational entropy effects manifest at $\Theta_t > 4$, causing the hierarchy of component loadings to be nC6 > 2MP > 3MP > 23DMB > 22DMB. The total mixture loading of $\Theta_t = 4$ is attained at a total hydrocarbons fugacity $f_t \approx 0.3$ MPa. This suggests the efficacy of MFI for separating hexane isomers according to the degree of branching; we need to operate at $f_t > 0.3$ MPa.

For $f_t < 0.3$ MPa, the hierarchy of component loadings is nC6 \approx 2MP > 23DMB \approx 3MP > 22DMB. This implies that, on equilibrium considerations alone, a clear separation of mono-branched and di-branched isomers is not possible $f_t < 0.3$ MPa.

MFI appears in the long list of materials patented by Universal Oil Products (UOP) for separation of hexane isomers.^{142, 179-181} The UOP patents provide experimental data on pulsed chromatographic experiments, such as that plotted in Figure 112c. The hierarchy of breakthroughs in Figure 112c is precisely that obtained for MFI zeolite (cf. Figures 112a, and 112b). The UOP patents do not explicitly state that the pulsed chromatographic data in Figure 112c is obtained with MFI, but there are reasons to believe that this is indeed the case.^{142, 182}

42. Intersection blocking effects in MFI

As we have established earlier in this document, branched alkanes such as 2MP, 22DMB, 23DMB, iC4 locate preferentially at the intersections of the channel structures of MFI zeolite.¹⁸³ In the PFG NMR investigation of Fernandez et al.¹⁸⁴ the self-diffusivity of n-butane (nC4) in mixtures with isobutane (iC4), was found to decrease by about two orders of magnitude as the loading of iC4 is increased from $\Theta_{iC4} = 0$ to 2 molecules per unit cell; see Figure 113a. The reason for this strong decline can be understood on the basis of the preferential location of iC4 at the channel intersections of MFI. For Θ_{iC4}

= 2, half the total number of intersections are occupied by iC4, that has a diffusivity which is about three orders of magnitude lower than that of nC4. Since the occupancy of the intersections is distributed randomly, each of the straight channels has an iC4 molecule ensconced somewhere along the channels; this is evident from the snapshot in Figure 109c. This is tantamount to blockage and leads to severe reduction in the molecular traffic of the intrinsically more mobile nC4. Uptake experiments of Chmelik et al.¹⁸⁵ provide further evidence of the influence iC4 has on co-diffusion of nC4 in MFI crystals.

PFG NMR studies of Förste et al.¹⁸⁶ found that the self-diffusivity of CH₄ in MFI is significantly reduced as the loading of the co-adsorbed benzene increases; see Figure 113b. The explanation is again to be found in the hindering of CH₄ diffusion due to blocking of the intersections by benzene.^{183, 186}

Schuring et al.¹⁸⁷ have reported experimental data on the self-diffusivities of both nC6 and 2MP in C6/ 2MP mixtures. These measurements were made at a total loading that is kept nearly constant at 3.5 molecules per unit cell. Their data, that were measured at 433 K and re-plotted in Figure 113c, shows that *both* self-diffusivities are reduced with increasing loading of 2MP in the mixture. The preferential location of 2MP at the intersections causes blocking of molecular traffic in the intersecting channel system of MFI. MD simulations show that such intersection blocking effects also manifest in nC6/22DMB mixtures.¹⁸³ We also note that the linear nC6 has a diffusivity that is about an order of magnitude higher than that of the branched 2MP. MD simulations show that the results such as that in Figure 113c also hold for nC6/22DMB mixtures.¹⁸³

The right axis of Figure 113d presents the data on the ratio of the self-diffusivities. With increased 2MP loading, the diffusivity of nC6 increases far more significantly than that of 2MP. This implies that there are no slowing-down effects of nC6 due to the presence of the tardier 2MP. Rather, there is an enhancement of the mobility of nC6 with increased loading. Put another way, when analysing mixture diffusion of hexane isomer mixtures correlation effects can be ignored as a *conservative* estimate. The diffusion of nC6/2MP mixture in MFI has very special and unusual characteristics; nC6 is much more mobile, by about one order of magnitude. Furthermore, as a consequence of configurational entropy effects, the more strongly adsorbed species is also nC6. We therefore have a mixture of more-mobile-

more-strongly-adsorbed-nC6 and tardier-less-strongly-adsorbed-2MP. There is unusual synergy between adsorption and diffusion of alkane isomers in MFI zeolite.

43. Transient breakthrough of alkane isomers

Isomerization of alkanes, for the purposes of octane improvement, is a process of importance in the petroleum industry.^{71, 73, 105, 188, 189} Figure 114 shows an example of a process for isomerization of n-hexane (nC6). The product from the isomerization reactor, that commonly uses zeolite MOR as catalyst, consists of an equilibrium distribution of unreacted nC6, along with its mono-branched isomers 2-methylpentane (2MP), 3-methylpentane (3MP) and di-branched isomers 2,2-dimethylbutane (22DMB) and 2,3-dimethylbutane (23DMB). In current industrial practice the linear nC6 is separated from the branched isomers in an adsorption separation step that relies on molecular sieving.¹⁸⁹ The adsorbent is LTA-5A that consists of cages separated by 4.1 Å sized windows. The windows only allow the diffusion and adsorption of the linear isomer, and the branched isomers are rejected and removed as product. The unreacted nC6 is recycled back to the isomerization reactor.

The values of the Research Octane Number (RON) increases with the degree of branching; Table 15 lists the Research Octane Numbers (RON) of C5, and C6 alkanes.⁷³ For hexane isomers, we note that the RONs are: nC6 = 30, 2MP = 74.5, 3MP = 75.5, 22DMB = 94, 23DMB = 105. Therefore, di-branched isomers are preferred products for incorporation into the high-octane gasoline pool.

An improved process would require the recycle of both linear and mono-branched isomers to the reactor; see Figure 115. The separation of 22DMB and 23DMB from the remaining isomers is a difficult task because it requires distinguishing molecules on the *degree* of branching. Typically, in such a processing scheme the aim would be to produce a product stream from the separation step with RON value of 92. This requirement of 92+ RON implies that the product stream will contain predominantly the di-branched isomers 22DMB and 23DMB, while allowing a small proportion of 2MP and 3MP to be incorporated into the product stream. Sharp separations between mono- and di- branched isomers is not a strict requirement, but does help the performance of pressure swing adsorption (PSA) units.

Before proceeding with the examination of the separation of the 5-component hexane isomer mixture, we analyse the key separation of the mono-branched isomer and the di-branched isomers of hexane. For this purpose, we analyze, and simulate, a set of experimental breakthrough experiments reported by Jolimaître et al.¹⁹⁰ for binary and ternary mixtures containing 2-methylbutane (2MB), 2MP, and 22DMB mixtures at 473 K. Our analysis and simulations are for their data for MFI in the form of extrudate 2. The parameter values as input data for all the simulations presented here are specified in Table 17. The Maxwell-Stefan flux equations for ternary mixtures used is

$$\begin{pmatrix} N_1 \\ N_2 \\ N_3 \end{pmatrix} = -\rho \begin{bmatrix} D_1 & 0 & 0 \\ 0 & D_2 & 0 \\ 0 & 0 & D_3 \end{bmatrix} \begin{bmatrix} \Gamma_{11} & \Gamma_{12} & \Gamma_{13} \\ \Gamma_{21} & \Gamma_{22} & \Gamma_{23} \\ \Gamma_{31} & \Gamma_{32} & \Gamma_{33} \end{bmatrix} \frac{\partial}{\partial r} \begin{pmatrix} q_1 \\ q_2 \\ q_3 \end{pmatrix} \quad (73)$$

Equations (15) and (16) are used for calculations of the elements of the matrix of thermodynamic correction factors. In all the simulations of Jolimaître experiments presented below, we use the values $D_{2MB}/r_c^2 = 0.0075 \text{ s}^{-1}$; $D_{2MP}/r_c^2 = 0.005 \text{ s}^{-1}$; $D_{22DMB}/r_c^2 = 0.0000625 \text{ s}^{-1}$ in each of the total of seven experimental Runs. As already established in the foregoing section, the neglect of correlation effects is justified for MFI zeolite because of intersection blocking effects.

Figures 116a,b,c compare the breakthrough experiments for 2MB/2MP (Run 12), and 2MP/22DMB (Runs 17, and 18) binary mixtures with the Maxwell-Stefan model simulations using the flux equations(73). The essential characteristics such as component overshoots in the breakthrough experiments are captured, reasonably quantitatively, by the simulations.

Figures 117a,b,c,d compare the breakthrough experiments 2MB/2MP/22DMB ternary mixtures (Runs 19, 20, 21, and 22) with the M-S model simulations using the flux equations(73). . The M-S model including diffusional limitations is able to quantitatively reproduce the breakthrough characteristics, such as component overshoots, for a wide range of inlet partial pressures. In all four Runs, the sequence of breakthroughs is 22DMB, 2MB, and 2MP reflecting the combined influences of adsorption and

diffusion. The adsorption hierarchy is $2MP > 22DMB > 2MB$, whereas the diffusion hierarchy is $2MB > 2MP >> 22DMB$.

The important point to stress is that all seven breakthrough experimental runs for binary and ternary mixtures can be simulated reasonably quantitatively by using the same set of adsorption and diffusion parameters as specified in Table 17.

In order to demonstrate that diffusional effects within the MFI crystals serve to improve the separations, we also performed simulations for Runs 18, 20, and 21 in which the diffusional effects are ignored, and thermodynamic equilibrium is assumed; these simulations are indicated by the dotted lines in Figure 118. The breakthrough of 2MP and 22DMB are much sharper, near-vertical, and closer together; see Figure 118a. Introduction of diffusional effects tends to draw 2MP and 22DMB apart because the diffusivity of 22DMB is 80 times lower than that of 2MP.

If diffusional effects are ignored for Runs 20, and 21 with 2MB/2MP/22DMB ternary mixtures, the sequence of breakthroughs would be 2MB, 22DMB, and 2MP; this is demonstrated in the equilibrium simulations, shown by the dotted lines in Figures 118b,c. Ignoring diffusional limitations leads to the sequence of breakthrough that is dictated solely by adsorption strengths.

The alteration in the sequence of breakthroughs introduced by diffusional effects has a beneficial influence on the Research Octane Number (RON) value of the product stream exiting the adsorber. Figure 119 presents a comparison of the RON values of the exit gas stream for equilibrium simulations with those in which diffusional effects are taken into consideration. The earlier breakthrough of 22DMB (RON = 94) in the scenario including diffusion, results in higher RON values being attained in the earlier stages. The time interval during which $RON > 92$ is larger with diffusion. From a material balance on the adsorber the 92+ RON productivity increases from 0.2 mol per L of MFI adsorbent in the fixed bed, for the equilibrium case, to 0.25 mol L⁻¹ for the scenario including diffusion. Diffusional effects serve to enhance the productivity of 92 RON product.

We now examine the influence of thermodynamic coupling on the breakthrough characteristics. Towards this end we carried out a comparison of the breakthrough experimental data for Runs 18, 20

and 21 with simulations in which the thermodynamic correction factors Γ_{ij} are assumed to equal the Kronecker delta, δ_{ij} ; see Figure 120. Neglect of thermodynamic coupling (indicated by the dashed lines in Figure 120), does not alter the essential breakthrough characteristic for Runs 18, 20 and 21. However, the agreement with the experimental data is less good than for the corresponding simulations including thermodynamic coupling. This is particularly evident for experimental conditions for which high inlet partial pressures are used (Runs 18 and 20). For Run 21, the inlet partial pressures are relatively low and neglect of thermodynamic coupling has practically no influence on the breakthrough characteristics. For proper modeling of breakthrough characteristics diffusional influences need to be properly modeled with inclusion of thermodynamic coupling effects.

Having established the potency of our breakthrough simulation methodology for alkane isomer separations with MFI, we proceed further in comparing the performance of various nanoporous adsorbents for separation of 5-component hexane isomer mixtures.

Dubbeldam et al.¹⁰⁵ used Configurational-Bias Monte Carlo (CBMC) simulations of hexane mixture adsorption to screen more than 100 zeolites, metal-organic frameworks (MOFs), covalent-organic frameworks (COFs), and zeolitic imidazolate frameworks (ZIFs) to arrive at the best choice of adsorbent to meet the demands of the process scheme depicted in Figure 115. On the basis of the hierarchies in the component loadings of nC6, 2MP, 3MP, 22DMB, and 23DMB for 5-component mixture adsorption at $f_t = 0.1$ MPa and 433 K, the list of nanoporous crystalline materials was narrowed down to seven potential candidates for use in the process scheme of Figure 115:

Zeolites: MFI, CFI, ATS

MOFs: MgMOF-74, Co(BDP), UiO-66

ZIFs: ZIF-77

By comparison of the adsorption selectivities, S_{ads} , defined in a specific manner in their paper, Dubbeldam et al.¹⁰⁵ concluded that ZIF-77 is the best choice as adsorbent. The value of S_{ads} for MFI is 2.3, as compared to $S_{ads} = 320$ for ZIF-77. The low selectivity of MFI is because the CBMC simulations data presented in Figures 112a and Figure 112b, show that at $f_t = 0.1$ MPa the total loading $\Theta_t < 4$ and

configurational entropy effects are not yet in play; these effects manifest at $\Theta_t < 4$ and $f_t > 1$ MPa. On equilibrium considerations alone, at 0.1 MPa, MFI has the ability to separate 22DMB from the rest of the isomers; but a clean separation of 23DMB from the mono-branched 3MP is not possible.

The synthesis of ZIF-77 in milligram quantities was reported in 2008 by Banerjee et al.¹⁹¹ There is, however, no experimental data on isotherms or breakthroughs to confirm the superior separation performance of ZIF-77, highlighted by Dubbeldam. A further point to note is that the screening exercise of Dubbeldam et al.¹⁰⁵ does not take diffusional effects into consideration. In industrial separations that are normally conducted in fixed bed adsorbers, intra-crystalline diffusion effects could influence the separation characteristics, depending on the pore dimensions. ZIF-77 has a characteristic pore dimension of 4.5 Å significantly smaller than the 5.5 Å channel dimensions of MFI, and diffusional effects will undoubtedly influence the separation characteristics of ZIF-77.

In a recent and comprehensive investigation, Herm et al.⁷³ performed breakthrough experiments with $\text{Fe}_2(\text{BDP})_3$ for separating a 5-component hexane isomer mixture. This MOF, whose synthesis was tailored to separate hexane isomers, has one-dimensional channels that are triangular in shape, with a pore size of 4.9 Å. The linear nC6 can align optimally along the gutters, and have the best van der Waals interaction with the framework. The interactions of the mono- and di-branched isomers are less effective, leading considerably lower adsorption strengths. The breakthrough characteristics with $\text{Fe}_2(\text{BDP})_3$ revealed that diffusional influences are of importance; this was confirmed by comparing the breakthrough simulations taking account of diffusional influences.

The intra-crystalline diffusion model used in the study of Herm et al.⁷³ was the following extension the simplified equation (54) to 5-component hexane mixtures

$$\begin{pmatrix} N_{nC6} \\ N_{2MP} \\ N_{3MP} \\ N_{22DMB} \\ N_{23DMB} \end{pmatrix} = -\rho \begin{bmatrix} \mathcal{D}_{nC6} & 0 & 0 & 0 & 0 \\ 0 & \mathcal{D}_{2MP} & 0 & 0 & 0 \\ 0 & 0 & \mathcal{D}_{3MP} & 0 & 0 \\ 0 & 0 & 0 & \mathcal{D}_{22DMB} & 0 \\ 0 & 0 & 0 & 0 & \mathcal{D}_{23DMB} \end{bmatrix} \frac{\partial}{\partial r} \begin{pmatrix} q_{nC6} \\ q_{2MP} \\ q_{3MP} \\ q_{22DMB} \\ q_{23DMB} \end{pmatrix} \quad (74)$$

in which thermodynamic coupling is ignored. Herm et al proceeded further to demonstrate the superior performance of $\text{Fe}_2(\text{BDP})_3$ by performing breakthrough simulations for separation of 5-component hexane isomer mixtures at 433 K and 0.1 MPa in fixed bed adsorbers to compare the 92+ RON productivities of different zeolites, MOFs, and ZIFs.

To set the scene for the calculations to follow, we repeat the simulations for separations of 5-component nC6/2MP/3MP/22DMB/23DMB mixtures of hexane isomers in a fixed bed adsorber of length L , packed with $\text{Fe}_2(\text{BDP})_3$ crystals. The transient breakthrough profiles for the exiting gas mixture, assuming no diffusional influences, i.e invoking equation (65), is presented in Figure 121. The

x -axis is the dimensionless time, $\tau = \frac{tu}{L\epsilon}$, obtained by dividing the actual time, t , by the characteristic

time, $\frac{L\epsilon}{u}$. The sequence of breakthroughs is 22DMB, 23DMB, 2MP, 3MP, and nC6. The RON values

are highest, close to 100 near the start of the breakthrough when 22DMB and 23DMB emerge; see the

RON values plotted in (the RON values are plotted on the right y -axis). The RON of the mixture is

calculated from the pure component RON values in Table 15; no non-linear mixing rules are applied.

Appearance of 2MP and 3MP in the outlet gas has the effect of significantly lowering the product gas

RON to below the target level of 92. In this scenario of equilibrium adsorption, and no diffusional

limitations, the 92+ RON productivity is determined from a material balance on the adsorber to be 0.67

$\text{mol kg}^{-1} \equiv 0.77 \text{ mol L}^{-1}$; this is a cumulative value, averaged over the time interval that the desired

product gas is collected. The values coincide with those of Herm et al.⁷³, as they should because the

input data are identical.

Figure 122 presents breakthrough calculations with flux equations (74) in which intra-crystalline diffusion effects are quantified by $D_{nC6}/r_c^2 = 0.002 \text{ s}^{-1}$; $D_{nC6}/D_{2MP} = 5$; $D_{nC6}/D_{3MP} = 5$; $D_{nC6}/D_{22DMB} = 10$; $D_{nC6}/D_{23DMB} = 10$, and using the flux relations (74) ignoring thermodynamic coupling, following the Herm et al.⁷³ These diffusivity values yield breakthrough profiles that are in good agreement with the experimentally determined breakthroughs. Inclusion of diffusional effects results in breakthrough profiles that are less sharp. Furthermore, the breakthroughs of the branched isomers occurs earlier when compared to the results in Figure 121. Figure 123 compares the RON of the product gas exiting the adsorber packed with $\text{Fe}_2(\text{BDP})_3$ adsorber obtained for the two different scenarios. Inclusion of diffusion limitations results in a lowering of the productivity; the 92+ RON productivity reduces to $0.47 \text{ mol kg}^{-1} \equiv 0.54 \text{ mol L}^{-1}$. The two sets of productivity values for the two cases (a) and (b) are identical to the ones reported in the paper by Herm et al,⁷³ as is to be expected because an identical methodology is used in this work. The value of 0.54 mol L^{-1} is higher than obtained with any other nanoporous material in the comprehensive comparisons made by Herm et al.⁷³

Let us now examine the separation performance of MFI zeolite for separation of hexane isomers, and determine the separation performance of a fixed bed adsorber packed with MFI crystals operating at a total pressure $p_t = 0.1 \text{ MPa}$ and 433 K , with partial pressures of the components in the bulk gas phase at the inlet are $p_1 = p_2 = p_3 = p_4 = p_5 = 20 \text{ kPa}$. We first evaluate the situation in which intracrystalline diffusion effects are of negligible importance, i.e invoking equation (65). The CBMC mixture simulations for 5-component hexane mixtures (cf. Figure 112a) shows that at a total hydrocarbons pressure of 0.1 MPa , the hierarchy of component loadings is $nC6 \approx 2MP > 23DMB \approx 3MP > 22DMB$. For configurational entropy effects to significantly influence performance we need to operate at $p_t > 0.3 \text{ MPa}$. This implies that, on equilibrium considerations alone, a clear separation of mono-branched and di-branched isomers is not possible for operations at $p_t = 0.1 \text{ MPa}$. This expectation is confirmed in the breakthrough simulations presented in Figure 124. The sequence of breakthroughs is 22DMB, 3MP, 23DMB, 2MP, and nC6. This hierarchy is dictated primarily by the hierarchy of component loadings in the CBMC mixture simulations in Figure 112a. In the initial phase of the adsorption cycle, the exit gas

stream is richest in the 22DMB (RON = 94). This is followed by 3MP (RON = 75.5) and 23DMB (RON = 105).

The solid black line in Figure 124 are calculations of the RON of the hexane isomer mixture exiting the MFI adsorber as a function of the dimensionless time. The RON value of the product gas stream has the highest values near the early stages of the breakthrough when 22DMB is primarily in the gas phase. The RON value drops significantly due to appearance of the 3MP in the product gas. The RON value increases again when breakthrough of 23DMB occurs. However, the RON value does not exceed 92 because 23DMB is present in the gas phase along with 3MP. This means that the set target RON value of 92+ can only be achieved in the early stages of the breakthrough. A material balance on the adsorber yields information on the amount of 92 RON product that can be recovered. Note that this value of 92 is obtained by averaging over all isomers in the gas phase for the appropriate time interval. The 92 RON productivity, calculated on the basis of the amount of crystalline adsorbent MFI in the packed adsorber, is $0.114 \text{ mol kg}^{-1} \equiv 0.205 \text{ mol L}^{-1}$. The volumetric productivity is obtained by multiplying the gravimetric productivity by the framework density $\rho = 1.796 \text{ kg L}^{-1}$. The 92+ RON productivities are significantly lower than that obtained with $\text{Fe}_2(\text{BDP})_3$.

We now aim to show that inclusion of diffusional effects changes this picture dramatically for MFI. We need good estimates of the intra-crystalline diffusivities of all five isomers in MFI zeolite at 433 K. Let us first examine the relative values of the diffusivities. The self-diffusivity data of Schruing et al.¹⁸⁷ at 433 K suggests that $D_{nC6}/D_{2MP} \approx 5$ (cf. Figure 113c). For the fixed bed adsorber calculations, we assume value $D_{nC6}/D_{2MP} = 5$. We now try to get an estimate of the relative values of diffusivities of the branched isomers in MFI. On the basis of the experimental data on diffusivities of hexane isomers reported by Cavalcante and Ruthven¹⁹² and Jolimaître et al,¹⁷³ we note that the hierarchy of diffusivities is $2MP > 3MP \gg 23DMB \gg 22DMB$; see Figure 125.

The data in Figure 125 implies that inclusion of diffusional considerations will result in sharper separations with MFI between 3MP and 23DMB than is possible on the basis of equilibrium considerations alone. For a conservative evaluation of the separations we assume the ratios of

diffusivities as $D_{2MP}/D_{3MP}=1$; $D_{2MP}/D_{22DMB}=5$; $D_{22MB}/D_{23DMB}=1$; these values are also in agreement with those used in the work of Herm et al.⁷³ By fixing the value of D_{nC6}/r_c^2 , the diffusional characteristics are fully determined. Herm et al.⁷³ have taken the value of $D_{nC6}/r_c^2 = 0.002 \text{ s}^{-1}$ for MFI zeolite. This value of $D_{nC6}/r_c^2 = 0.002 \text{ s}^{-1}$ for nC6 is lower than the values of either 2MB and 2MP that are used to simulate the Jolimaître experiments. We therefore conclude that the value of $D_{nC6}/r_c^2 = 0.002 \text{ s}^{-1}$ is a conservative estimate.

Figures 126a show the transient breakthrough profiles with MFI zeolite for the scenario in which thermodynamic coupling effects are considered negligible, i.e. invoking the flux relations (74) ignoring thermodynamic coupling. The sequence of breakthroughs is seen to be 22DMB, 23DMB, 3MP, 2MP, and nC6; this is desirable from the point of view of the processing requirement of Figure 115. Of particular importance is the earlier breakthrough of 23DMB than 3MP, despite the fact that the adsorption strengths of 3MP and 23DMB are practically the same for $p_t < 0.1 \text{ MPa}$ (cf. Figure 112a). The ability of MFI to separate 3MP from 23DMB is a direct consequence of the differences in the diffusivities, a factor 5 in favor of 3MP. The net result is that the high RON value product can be recovered in the early stages of the breakthrough; see Figure 128. The 92+ RON productivity for scenario (a), determined from a material balance on the adsorber, is $0.28 \text{ mol kg}^{-1} \equiv 0.51 \text{ mol L}^{-1}$; this value is about a factor 2.5 higher than that achieved with the scenario in which diffusional effects are considered to be negligible. The value 0.51 mol L^{-1} is also identical to that reported for MFI in the study of Herm et al.⁷³; this is to be expected because the breakthrough simulations were carried out for the same set of input parameters.

In an earlier section, on the basis of simulations of the Jolimaître breakthrough experiments, we had clearly demonstrated that thermodynamic coupling effects are of significant importance for alkane isomer separations with MFI zeolite. The inclusion of thermodynamic coupling effects for MFI has been demonstrated to be required for quantitative agreement with the Jolimaître experiments. Therefore, we repeat the calculations for MFI zeolite, using the flux relations that include thermodynamic coupling.

$$\begin{pmatrix} N_{nC6} \\ N_{2MP} \\ N_{3MP} \\ N_{22DMB} \\ N_{23DMB} \end{pmatrix} = -\rho \begin{bmatrix} \mathcal{D}_{nC6} & 0 & 0 & 0 & 0 \\ 0 & \mathcal{D}_{2MP} & 0 & 0 & 0 \\ 0 & 0 & \mathcal{D}_{3MP} & 0 & 0 \\ 0 & 0 & 0 & \mathcal{D}_{22DMB} & 0 \\ 0 & 0 & 0 & 0 & \mathcal{D}_{23DMB} \end{bmatrix} \left[\Gamma \right] \frac{\partial}{\partial r} \begin{pmatrix} q_{nC6} \\ q_{2MP} \\ q_{3MP} \\ q_{22DMB} \\ q_{23DMB} \end{pmatrix} \quad (75)$$

The breakthrough simulations using the flux relations (75), including thermodynamic coupling, are shown in Figure 126b. A cursory comparison of Figures 126a, and 126b shows that the breakthrough characteristics appear to be significantly influenced by thermodynamic coupling effects. Inclusion of thermodynamic coupling causes the breakthroughs of all isomers to be delayed. Figure 126c compares the dimensionless breakthrough times, τ_{break} of each isomer for the two different scenarios; here τ_{break} is defined as the time at which the composition of the isomer at the outlet exceeds 1% of the value at the inlet, i.e. $(c_i/c_{i0}) > 0.01$. The differences in the breakthrough times for the mono-branched and di-branched isomers is crucial for this separation. If we ignore thermodynamic coupling, the values of τ_{break} for 3MP and 23DMB are 22.2 and 16.7, respectively. If we take proper account of thermodynamic coupling the values of τ_{break} for 3MP and 23DMB are 49 and 38.8. Consequently, inclusion of thermodynamic coupling has the effect of widening the gap between the breakthroughs of 3MP and 23DMB; this widening is beneficial for the producing high RON product.

The differences in the breakthrough characteristics can also be appreciated by comparing the corresponding uptake characteristics within a single MFI crystal exposed to a gas phase 5-component nC6/2MP/3MP/22DMB/23DMB mixture at a total pressure of 100 kPa and 433 K; see Figure 127. If thermodynamic coupling effects are ignored, the component loadings exhibit a monotonous approach to equilibrium; see Figure 127a. The component loadings during transient uptake for simulations that include thermodynamic coupling using the flux relations (75), are markedly different because the most mobile nC6 exhibits a sharp maximum during the early stages of the transience; see Figure 127b. The first paper to demonstrate the curious maximum¹⁸⁸ in the nC6 uptake is by Krishna¹⁸⁸ who performed

simulations for nC6/3MP and nC6/22DMB binary mixtures. The significantly higher nC6 loading within the crystal during the early stages of the transience contributes to a later breakthrough of nC6 witnessed in Figure 126b.

Inclusion of thermodynamic coupling effects results in higher RON values towards the latter stages of the breakthrough; see Figure 128, The 92+ RON productivity determined from a material balance on the adsorber is $0.36 \text{ mol kg}^{-1} \equiv 0.64 \text{ mol L}^{-1}$, about a factor 3 higher than that achieved with the scenario in which diffusional effects are considered to be negligible. Inclusion of thermodynamic coupling effects has a significant, enhancing, effect on the 92+ RON productivity of MFI zeolite, in agreement with the conclusions reached earlier on the basis of the Jolimaître breakthrough experiments; cf. Figure 119.

We now investigate the performance of ZIF-77, that emerged as the best material for hexane isomer separation in the computational screening study of Dubbeldam et al.¹⁰⁵. For evaluation of the performance of ZIF-77 we use the dual-Langmuir-Freundlich fits of the CBMC simulated pure component isotherms in the study of Dubbeldam et al;¹⁰⁵ the parameters are specified in Table 19. These parameters are used in the IAST calculations of mixture adsorption equilibrium.

Figure 129 shows the breakthrough simulations for the scenario assuming no diffusional influences, i.e invoking equation (65). The hierarchy of breakthroughs is 23DMB, 22DMB, 3MP, 2MP, and nC6, with a larger difference in the breakthrough times between the appearance of the di-branched and mono-branched isomers. Consequently, the product gas has a RON value close to 100 for a long time before 3MP starts breaking through; see right axis of Figure 129 that presents data on the RON of the product gas. From the transient concentrations of the exit gas, the 92+ RON productivity is determined from a material balance on the adsorber to be $0.88 \text{ mol kg}^{-1} \equiv 1.36 \text{ mol L}^{-1}$, significantly higher than that obtained for both MFI and $\text{Fe}_2(\text{BDP})_3$ with the same scenario. It must however be stressed that the performance evaluation of ZIF-77 is based purely on CBMC simulations for which there is no experimental verification. The evaluation of $\text{Fe}_2(\text{BDP})_3$ was on the basis of experimentally determined isotherms, backed by breakthrough experiments. For MFI, we have presented a wide range of experimental data on both adsorption isotherms and diffusivities to underpin and support the various

input parameter values. Be that as it may, we proceed to demonstrate that inclusion of realistic diffusivity estimates will markedly diminish the separation potential of ZIF-77.

Using the MD simulation data on self-diffusivities of hexane isomers in ZIF-77, presented in Supplementary Material accompany the paper of Dubbeldam et al,¹⁰⁵ we choose the following relative values of M-S diffusivities $D_{nC6}/D_{2MP}=5$; $D_{nC6}/D_{3MP}=5$; $D_{nC6}/D_{22DMB}=10$; $D_{nC6}/D_{23DMB}=10$. The characteristic pore size of ZIF-77 is 4.5 Å, significantly smaller than the 4.9 Å sized triangular channels of Fe₂(BDP)₃. We should therefore expect stronger diffusion limitations than with either MFI or Fe₂(BDP)₃. We choose $D_{nC6}/r_c^2 = 0.0004 \text{ s}^{-1}$ for a consistent comparison of the diffusional influences for MFI, Fe₂(BDP)₃, and ZIF-77 based on the pore dimensions. Figure 130 shows the transient breakthrough profiles for ZIF-77 with inclusion of diffusional influence for the scenario in which thermodynamic coupling effects are considered negligible, i.e. invoking the flux relations (74). Inclusion of diffusional influences has a significant effect on the 92+ RON productivity that is now reduced to 0.27 mol kg⁻¹ \equiv 0.42 mol L⁻¹, significantly poorer than obtained with either Fe₂(BDP)₃ or MFI zeolite.

Figure 131 presents a plot of 92+ RON productivities obtained with assumption of thermodynamic equilibrium (x-axis) vs that obtained with inclusion of diffusion limitations (y-axis) for MFI, Fe₂(BDP)₃, and ZIF-77. The inclusion of diffusional influences is beneficial for the 92 RON productivity of MFI. For both Fe₂(BDP)₃, and ZIF-77, inclusion of intra-crystalline diffusion results in a severe reduction in 92+ RON productivity. MFI distinguishes itself from both Fe₂(BDP)₃, and ZIF-77 in that diffusional effects serve to improve 92 RON productivities; this is a clear example of synergy between adsorption and diffusion.

We also carried out breakthrough simulations for determining the 92+RON productivity of other adsorbent materials that have been suggested in the literature for separation of hexane isomers. These include BEA¹⁹³ (see Figure 132), Zn(bdc)dabco¹⁹⁴ (see Figure 133), ZnHBDC¹⁹⁵ (see Figure 134), UiO-66¹¹² (see Figure 136), CFI¹⁹⁶ (see Figure 137), and ATS¹⁹⁷ (see Figure 138). Experimental data is available for demonstration of the propensity of for hexane isomer separation. We include CFI and ATS

because these materials have been patented by Chevron.^{196, 197} The materials UiO-66, CFI, and ATS have the “reverse” hierarchy i.e. the di-branched isomers are the most strongly adsorbed and the linear nC6 is the most weakly adsorbed. The reasons for this “reverse” adsorption hierarchy are not the same in every case.

UiO-66 is a zirconium-based metal-organic framework (MOF) built up from hexamers of eight coordinated $ZrO_6(OH)_2$ polyhedra and 1,4-benzene-dicarboxylate (BDC) linkers. Its cubic rigid 3D pores structure consists of an array of octahedral cavities of diameter 11 Å, and tetrahedral cavities of diameter 8 Å. The two types of cages are connected through narrow triangular windows of approximately 6 Å. For UiO-66, the di-branched isomers are preferentially lodged in the tetrahedral cages which provide “snug” fits and high adsorption strengths for the di-branched isomers.^{105, 112} In the papers by Denayer et al.¹⁹⁸ and B arcia et al.,¹¹² the stronger adsorption of the di-branched isomers in the octahedral cages is attributed to *rotational entropy* considerations. To illustrate the reverse hierarchy with UiO-66, Figure 135a presents pulse chromatographic simulations for 5-component nC6/2MP/3MP/22DMB/23DMB mixture in a fixed bed adsorber. The sequence of breakthrough times nC6 < 2MP < 3MP < 22DMB < 23DMB is a direct reflection of the hierarchy of adsorption strengths with 23DMB being the most strongly adsorbed isomer. In the pulse chromatographic experiments of Duerinck and Denayer,¹⁹⁹ the sequence of breakthrough times nC6 < 2MP < 3MP < 22DMB < 23DMB has been reported. The most likely explanation of the reversal of the breakthroughs observed for 22DMB and 23DMB is that 22DMB has a significantly lower diffusivity as compared to 23DMB.

Bozbiyik et al.²⁰⁰ have presented experimental pulse chromatographic data for binary mixtures of nC6 and cyclohexane (cC6) mixture in a fixed bed adsorber packed with UiO-66, operating at 473 K. In this case, the nC6 pulse breaks through significantly earlier than the pulse of cC6. Pulse chromatographic simulations of the breakthrough, assuming thermodynamic equilibrium, is able to capture the essential characteristics of the experimental breakthrough; see Figure 135b.

CFI and ATS zeolites, patented by Chevron for application in the alkane isomerization process,^{196, 197} have one-dimensional channels similar to that of AFI zeolite. The hierarchy of adsorption strengths is

nC6 < (2MP, 3MP) << (22DMB, 23DMB) is primarily dictated by the molecular footprints; see snapshots in Figures 137 and Figure 138 of the molecular conformations. The linear nC6 has a longer “footprint” and occupies a larger segment of the channel. 22DMB and 23DMB are the most compact molecules and have the smallest footprint; consequently, more di-branched isomers can be located within a given length of the channels when compared to nC6. 2MP and 3MP have footprints that have an intermediate character. *Molecular length entropy* effects dictates the sorption hierarchy in CFI, and ATS; a similar situation holds for MOR that has 0.65 nm × 0.7 nm sized 1D channels.^{142, 144, 159}

For materials with reverse hierarchy, the high-octane product can be recovered only in the desorption cycle. For UiO-66, CFI, and ATS we need to simulation the adsorption/desorption cycles, as discussed by Herm et al,⁷³ we follow the same methodology here.

Figure 142a compares the 92+RON productivity of MFI, Fe₂(BDP)₃ZIF-77, BEA, Zn(bdc)dabco, ZnHBDC, ZIF-8, and UiO-66, CFI, and ATS; materials that have reverse hierarchy are indicated with green color symbols. We conclude that MFI is the most effective adsorbent for separation of hexane isomers.

Can we improve on the performance of MFI? To answer this question, we carried out breakthrough simulations for Co(BDP) (see Figure 139), MgMOF-74 (see Figure 140), and ZnMOF-74 (see Figure 141) using CBMC simulation data for the pure component isotherms. Figure 142b presents the compares the 92+RON productivity of Co(BDP), MgMOF-74, and ZnMOF-74 with the other materials. For these three MOFs, intra-crystalline diffusion reduces the 92+RON productivity, but these are still higher than that of MFI mainly because they have capacity advantages because of their “open” structures. The capacity advantages of Co(BDP), MgMOF-74, and ZnMOF-74 have been stressed in the our earlier publications. We note that all these three materials have the ability to improve on the 92+RON productivity of MFI. For example, both Co(BDP) and ZnMOF-74 offers the potential of improving the 92+RON productivity of MFI. Experimental data on the isotherms and breakthrough characteristics of Co(BDP) and ZnMOF-74 is desirable.

44. Conclusions

The main objective of this review was to underscore the need to adopt the Maxwell-Stefan formulation for modeling intra-crystalline diffusion in ordered nanoporous materials. The major conclusions are summarized below.

(1) The M-S formulation is the most convenient one to use for describing binary mixture diffusion because the parameters D_1 and D_2 can, in most cases, be identified with those for unary transport. Furthermore, correlation effects are quantified by the exchange coefficient, D_{12} that can be estimated for different guest/host combinations on the basis of MD simulation data.⁴

(2) The M-S formulation clearly differentiates between two types of coupling: (a) coupling due to correlation effects modeled by the exchange coefficient D_{12} , and (b) thermodynamic coupling effects quantified by sizable off-diagonal elements of $\begin{bmatrix} \Gamma_{11} & \Gamma_{12} \\ \Gamma_{21} & \Gamma_{21} \end{bmatrix}$.

(3) Correlation effects need to be properly modeled for mixtures of more-mobile-less-strongly-adsorbed and tardier-more-strongly-adsorbed species as exemplified by permeation of H_2/CO_2 , CH_4/C_2H_6 , CH_4/C_3H_8 mixtures across MFI membranes; see Figures 6, 7, and 8. Correlation effects generally cause the slowing-down of the more mobile partner species.

(4) Generally speaking, correlation effects are of negligible importance when modeling permeation of mixtures across structures such as ZIF-8, SAPO-34, DDR, and LTA that consist of cages separated by narrow windows in the 3.4 Å – 4.1 Å range. Molecules hop one-at-a-time across the windows, and are largely uncorrelated. The experimental data for mixture permeation across SAPO-34 membrane (Figure 9), ZIF-7 membrane (Figure 10), and ZIF-8 membrane (cf. Figures 11, and 12) can be modeled adequately using equations (36) ignoring both correlations and thermodynamic coupling.

(5) For transient mixture permeation, thermodynamic coupling effects can lead to maxima in the fluxes of the more mobile partner species; Figures 13, 15, 16, 17, and 18.

- (6) For transient uptake of single components within a single crystalline particle, adsorption and desorption kinetics may be asymmetric; see Figure 19. Usually, the desorption kinetics is slower than the adsorption kinetics; this asymmetry is traceable to the influence of the thermodynamic correction factor, Γ .
- (7) The step-wise desorption kinetics for methanol in CuBTC, seen in Figure 20, can be rationalized on the basis of the characteristics of the inverse thermodynamic factor $1/\Gamma_i$ that is influenced by molecular clustering.
- (8) For transient uptake of binary mixtures within a nanoporous crystal, overshoots in the uptake of the more mobile partner species is traceable to the influence of thermodynamic coupling effects quantified by sizable off-diagonal elements of $\begin{bmatrix} \Gamma_{11} & \Gamma_{12} \\ \Gamma_{21} & \Gamma_{21} \end{bmatrix}$; see Figures 22, 25, 26, 27, 28 and 71.
- (9) Generally speaking, simulations of breakthroughs of mixtures in fixed-bed adsorbers assuming thermodynamic equilibrium and invoking Equation (65) lead to sharp breakthroughs, unless the adsorption selectivities are close to unity. Equilibrium simulations are adequate for modeling breakthroughs when the guest molecules are weakly confined within the pores of the framework. Examples include the breakthrough characteristics of CO₂/CH₄, CO₂/H₂, CO₂/CO/CH₄,H₂, and CO₂/N₂ mixtures in CuBTC, Cu-TDPAT, MgMOF-74, NiMOF-74, NaX zeolite, NOTT-300, MIL-125, UiO-66(Zr) that have “open” structures. Intra-crystalline diffusion effects do not have any significant influence on the separation performance.
- (10) Intra-crystalline diffusion effects lead to more “diffuse”, non-sharp, breakthrough characteristics. For breakthrough of CO₂/CH₄ mixtures in KFI beds, intra-crystalline diffusion effects do not influence the hierarchy of breakthroughs; see Figures 44, 45, and 46.
- (11) The separation of alkane isomers using ZIF-8 is dominated by intra-crystalline diffusion and in the case of nC₆/3MP mixtures, diffusional effects lead to alteration of the breakthrough hierarchy; see Figure 49.

- (12) The transient breakthrough of C8 hydrocarbons using MIL-47, MIL-53, MgMOF-74, NiMOF-74, and Zn(bdc)dabco can be predicted qualitatively assuming thermodynamic equilibrium and invoking Equation (65). Intra-crystalline diffusion effects need to be accounted for when attempting to match experimental data; see Figure 65. For matching a limited set of experimental breakthroughs, use of a simple model invoking the simplified equation (54) neglecting thermodynamic coupling is of sufficient accuracy.
- (13) The transient uptake of mixtures of 1-alcohols in SAPO-34 has special characteristics. Both adsorption and diffusion go hand-in-hand when operating under conditions such that the bulk fluid phase surrounding the crystals is a liquid mixture. In this case, entropy effects favor the adsorption of the shorter alcohol. Diffusion also favors the shorter alcohol. Overshoots of the shorter alcohol are observed in transient uptake in single crystals; see Figure 71. Simulations using the M-S model also anticipate a maximum in the profiles of the component loading of the shorter alcohol within the crystal; see. Figure 76. The breakthroughs of mixtures of 1-alcohols in fixed bed adsorbers is unusual in that the longer 1-alcohol is eluted first (cf. Figure 78); the Maxwell-Stefan model is able to predict the correct hierarchy of breakthroughs (cf. Figure 79).
- (14) The experimental data on transient breakthrough of alkene/alkane mixtures in “open” structures such as CuBTC (Figure 80), FeMOF-74 (Figure 81), MgMOF-74 (Figure 82a), and CoMOF-74 (Figure 82b) can be modeled reasonably quantitatively on the basis of a model that considers intra-crystalline diffusion to be of negligible importance. In all such structures, the desired alkene can only be recovered in the *desorption* phase.
- (15) The experimental data on transient breakthrough of alkene/alkane mixtures in ZIF-8 (Figure 83) show that the unsaturated alkene can be recovered in the *adsorption* phase in purities that are demanded as feedstock to polymerization reactors (99.95% purity). ZIF-7 has similar separation characteristics as ZIF-8 (Figures 84, and 85). For both ZIF-7 and ZIF-8, intra-crystalline diffusion effects are expected to be of importance.

- (16) LTA-5A can be used for production of pure O₂ from O₂/N₂ feed mixtures (Figure 91). The separation is primarily driven by adsorption that favors N₂. Intra-crystalline diffusion favors O₂ and, consequently, reduces the efficacy of the separation.
- (17) LTA-4A can be used for production of pure N₂ from O₂/N₂ feed mixtures (Figure 92). The separation is primarily driven by intra-crystalline diffusion that favors O₂.
- (18) FeMOF-74 appears to have potential for production of pure N₂ from O₂/N₂ feed mixtures (Figure 93). In this case, the separation is driven by adsorption, and intra-crystalline diffusion effects are of minor importance.
- (19) Configurational-Bias Monte Carlo (CBMC) simulations of the adsorption of alkane isomers in MFI zeolite demonstrate that configurational entropy effects can be utilized to separate linear isomers from mono-branched and di-branched isomers (Figure 104 to Figure 112). The IAST is able to capture configurational entropy effects in mixture adsorption, nearly quantitatively; see Figures 110 and 111.
- (20) An important aspect of this separation of alkane isomers with MFI zeolite is the synergy between adsorption and diffusion. The intra-crystalline diffusion also favors the linear isomer (Figure 113). The synergy between adsorption and diffusion of alkane isomers in MFI zeolite can be exploited in the process scheme for producing gasoline with higher RON (Figure 115). Confirmation of the synergistic effect is obtained from the experiments of Jolimaître (Figures 116, 117, 118, 119, and 120). One vital conclusion emerging from the simulations of the Jolimaître experiments is the importance of thermodynamic coupling. Diffusional effects, with inclusion of thermodynamic coupling effects serve to improve the productivity of MFI zeolite to produce high octane product in the adsorber (Figures 119, and 128). The 92+RON productivity of MFI is significantly higher than that obtained from Fe₂(BDP)₃, and ZIF-77 that emerged, respectively, as the best nanoporous material for use in the process scheme of Figure 115; see Figure 131.

45. Notation

b_A	dual-Langmuir-Freundlich constant for species i at adsorption site A, $\text{Pa}^{-\nu_i}$
b_B	dual-Langmuir-Freundlich constant for species i at adsorption site B, $\text{Pa}^{-\nu_i}$
$[B]$	matrix of inverse M-S coefficients, defined by eq. (10), $\text{m}^{-2} \text{s}$
c_i	pore concentration of species i , $c_i = q_i/V_p$, mol m^{-3}
c_t	total pore concentration in mixture, $c_t = q_t/V_p$, mol m^{-3}
c_i	molar concentration of species i in gas mixture, mol m^{-3}
c_{i0}	molar concentration of species i in gas mixture at inlet to adsorber, mol m^{-3}
D_i	Maxwell-Stefan diffusivity, $\text{m}^2 \text{s}^{-1}$
D_{ij}	M-S exchange coefficient, $\text{m}^2 \text{s}^{-1}$
D_{12}	M-S exchange coefficient for binary mixture, $\text{m}^2 \text{s}^{-1}$
D_i	Fick diffusivity of species i , $\text{m}^2 \text{s}^{-1}$
$D_{i,\text{self}}$	self-diffusivity of species i , $\text{m}^2 \text{s}^{-1}$
f_i	partial fugacity of species i , Pa
f_t	total fugacity of bulk fluid mixture, Pa
L	length of packed bed adsorber, m
m	summation index, dimensionless
n	number of species in the mixture, dimensionless
N_i	molar flux of species i , $\text{mol m}^{-2} \text{s}^{-1}$
p_i	partial pressure of species i in mixture, Pa
p_t	total system pressure, Pa
P_i^0	sorption pressure, Pa
q_i	component molar loading of species i , mol kg^{-1}
$q_i^0(f)$	pure component adsorption isotherm of species i , mol kg^{-1}
$q_{i,\text{sat}}$	molar loading of species i at saturation, mol kg^{-1}
q_t	total molar loading in mixture, mol kg^{-1}

$q_{\text{sat,A}}$	saturation loading of site A, mol kg ⁻¹
$q_{\text{sat,B}}$	saturation loading of site B, mol kg ⁻¹
$\bar{q}_i(t)$	<i>spatially averaged</i> component molar loading of species i , mol kg ⁻¹
Q_{st}	isosteric heat of adsorption, J mol ⁻¹
r	radial direction coordinate, m
r_c	radius of crystallite, m
R	gas constant, 8.314 J mol ⁻¹ K ⁻¹
S_{ads}	adsorption selectivity, dimensionless
S_{diff}	diffusion selectivity, dimensionless
t	time, s
T	absolute temperature, K
u	superficial gas velocity in packed bed, m s ⁻¹
v	interstitial gas velocity in packed bed, m s ⁻¹
x_i	mole fraction of species i in adsorbed phase, dimensionless
y_i	mole fraction of component i in bulk vapor phase, dimensionless
V_p	pore volume, m ³ kg ⁻¹
z	distance along the adsorber, and along membrane layer, m

Greek letters

δ	membrane thickness, m
δ_{ij}	Kronecker delta, dimensionless
$[\Delta]$	matrix defined of M-S diffusivities, m ² s ⁻¹
Δ_{ij}	elements of $[\Delta]$, m ² s ⁻¹
ε	voidage of packed bed, dimensionless
γ_i	activity coefficient of component i in adsorbed phase, dimensionless
Γ_{ij}	thermodynamic factors, dimensionless
$[\Gamma]$	matrix of thermodynamic factors, dimensionless
Φ	surface potential of adsorbed mixture, J m ⁻³
Φ_i^0	surface potential of pure component i in adsorbed phase i , J m ⁻³

μ_i	molar chemical potential, J mol ⁻¹
ν	exponent in dual-Langmuir-Freundlich isotherm, dimensionless
Π_i	permeance of species i in mixture, mol m ⁻² s ⁻¹ Pa ⁻¹
θ_i	fractional occupancy of component i , dimensionless
θ_v	fractional vacancy, dimensionless
Θ_i	loading of species i , molecules per unit cell
$\Theta_{i,\text{sat}}$	saturation loading of species i , molecules per unit cell
Θ_t	total molar loading of mixture, molecules per unit cell
ρ	framework density, kg m ⁻³
τ	time, dimensionless

Subscripts

fl	referring to site fluid phase
i	referring to component i
A	referring to site A
B	referring to site B
t	referring to total mixture

Table 1. Examples of PSA separations using ordered nanoporous crystalline materials.

Category A: Minor influence of intra-crystalline diffusion on breakthrough characteristics. The hierarchy of breakthroughs is not affected, but are more “diffuse” in nature when compared to equilibrium simulations.

Category B: Strong influence of intra-crystalline diffusion on breakthrough characteristics. The productivity or capture capacity is reduced due to diffusional influences. The hierarchy of breakthroughs, when compared to equilibrium simulations, is not affected.

Category C: Strong influence of intra-crystalline diffusion on breakthrough characteristics. The hierarchy of breakthroughs is altered; the components with lower diffusivities break through significantly earlier, when compared to equilibrium simulations.

Category D: Strong influence of intra-crystalline diffusion, and specifically thermodynamic coupling effects, on breakthrough characteristics. The productivity is enhanced by thermodynamic coupling effects.

Process	Mixtures	Category of materials	Literature
Natural gas purification	CH ₄ /CO ₂ CH ₄ /CO ₂ /H ₂ S CH ₄ /CO/CO ₂	A: NaX, Cu-TDPAT, MgMOF-74, NiMOF-74, CuBTC, UTSA-16, SIFSIX-2-Cu, MIL-47(V), amino-MIL-53, Amino-MIL-125(Ti), MIL-100(Cr), MIL-140(Zr) B: LTA-5A, SAPO-34, KFI	67, 68, 75, 85, 86, 89, 91, 95, 103, 104, 201-204
Natural gas upgrading for meeting pipeline specifications	N ₂ /CH ₄	C: LTA-4A, ETS-4, BaETS-4	56-59
Recovery of H ₂ from steam methane reformer off-gas (SMROG)	H ₂ /CO ₂ , H ₂ /CO/CH ₄ /CO ₂ H ₂ /CH ₄ /CO ₂	A: MgMOF-74, MOF-177, NaX, CuBTTri, Cu-TDPAT, SIFSIX-2-Cu, Cu-TDPAT, Zn(bdc)dabco, UiO-66, UiO-67, ZJU-35a, ZJU-36a B: LTA-5A	77, 85, 86, 94-97, 103
CO ₂ capture from flue gas	N ₂ /CO ₂ N ₂ /CO ₂ /CO/O ₂ N ₂ /CO ₂ /SO ₂	A: MFI, MgMOF-74, NiMOF-74 NaX, MOF-177, EMC-1, SIFSIX-2-Cu, PCP-1, NOTT-300 B: LTA-5A	66, 89, 90, 103, 205-207
CO ₂ capture from ambient air	CO ₂ /O ₂ /N ₂	A: mmen-CuBTTri, PPN-6, mmen-Mg ₂ (dobpdc)	208-210
Fischer-Tropsch tail gas separation	H ₂ /CO ₂ /CO/ CH ₄ /N ₂	A: Cu-TDPAT, CuBTC, NaX, MFI B: LTA-5A	
Recovery of He from	He/N ₂ /CH ₄ /CO ₂	A: CuBTC, MFI	

natural gas			
Recovery of Xe and Kr from process off-gases	Xe/Kr/N ₂ /CO ₂	A: NiMOF-74	101
Separation of hexane isomers for production of 92+ RON product	nC6/2MP/3MP/22DMB/23DMB	B: Fe ₂ (BDP) ₃ , ZIF-77, UiO-66, Zn(bdc)dabco, ATS, CFI, MWW, Co(BDP), ZnMOF-74, MgMOF-74 C: ZIF-8 D: MFI	73, 105, 143
Separation of C8 hydrocarbons	o-xylene/m-xylene/p-xylene/ethylbenzene	A: BaX, MIL-47, MIL-53, MgMOF-74, NiMOF-74, MIL-125, Amino-MIL-125(Ti) B: UiO-66, Zn(bdc)dabco	69, 108-110, 112, 113, 115-117
Separation of C8 hydrocarbons	ethylbenzene/styrene	A: MIL-47, MIL-53,	119, 120
Separation of aromatics from non-aromatics	benzene/cyclohexane benzene/n-hexane	A: Na-Y, Pd-Y, Ag-Y, H-USY, PAF-2	121, 122
Separation of alkene/alkane	C ₂ H ₄ /C ₂ H ₆ C ₃ H ₆ /C ₃ H ₈ 1-octene/nC8	A: CuBTC, MgMOF-74, NiMOF-74, CoMOF-74, NaX B: ZIF-7, ZIF-8	3, 72, 74, 127, 129, 130, 133, 211
Separation of C1, C2, C3 hydrocarbons	CH ₄ /C ₂ H ₂ / C ₂ H ₄ /C ₂ H ₆ / C ₃ H ₆ /C ₃ H ₈	A: M' MOFs, MgMOF-74, CoMOF-74, FeMOF-74, CuBTC, UTSA-30a, UTSA-35a	3, 72, 135, 138, 212
Production of C ₂ H ₂	CO ₂ /C ₂ H ₂	A: UTSA-30a, UTSA-50a, CuBTC	136-139
Separation of C4 hydrocarbons	nC4/iC4	A: CuBTC	140
Separation of butenes	is-2-butene/trans-2-butene/1-butene	B: RUB-41 zeolite	141
Removal of dienes from C4 gas stream	1,3 butadiene/1-butene	A: Ag-Y zeolite	145
Dehydration of alcohols	water/ethanol	B: LTA-K, LTA-Na, LTA-Ca, FAU-Na	213
Separation of 1-alcohols	methanol/ethanol/1-propanol/1-butanol/1-hexanol	D: SAPO-34	124-126
Production of pure O ₂	N ₂ /O ₂	A: LiX, LiLSX B: LTA-5A	146-149, 151
Production of pure N ₂	N ₂ /O ₂	A: FeMOF-74 C: LTA-4A	152, 153, 155
Separation of chlorofluorocarbons	CFC-115/HFC-125	D: MFI	158

Table 2. Examples of nanoporous membrane separations.

Category E: Correlation effects and thermodynamic coupling effects are both of importance.

Category F: Correlation effects are of minor significance

Process	Mixtures	Category of materials	Liter-ature
CO ₂ capture from flue gas	CO ₂ /N ₂	E: NaY, NaX, MFI, ZIF-69 F: SAPO-34, DDR	214-219
CO ₂ removal for natural gas purification	CO ₂ /CH ₄	E: MFI, NaY, NaX, MgMOF-74, amino-MIL-53, ZIF-69 F: SAPO-34, ZIF-8, DDR	4, 33, 55, 214, 215, 218, 220-224
N ₂ removal for natural gas purification	N ₂ /CH ₄	F: SAPO-34, DDR	214, 215
CO ₂ -selective purification of H ₂	H ₂ /CO ₂	E: MFI, NaX, MgMOF-74, F: SAPO-34	4, 33, 34, 55, 216
H ₂ -selective purification of H ₂	H ₂ /CO ₂	E: amino-MIL-53(Al) F: ZIF-7, ZIF-22	37, 40, 225
H ₂ -selective separation from hydrocarbons	H ₂ /CH ₄ H ₂ / C ₃ H ₈	E: amino-MIL-53(Al) F: ZIF-7, ZIF-8, ZIF-22, SAPO-34	37, 40, 214, 225-227
Alkene/alkane	C ₂ H ₄ /C ₂ H ₆ C ₃ H ₆ /C ₃ H ₈	E: NaY, FeMOF-74 F: ZIF-7, ZIF-8	41, 44, 45, 72, 228
Pervaporation	water/methanol water/ethanol water/2-propanol water/NMP	E: MFI F: LTA-4A, CHA, H-SOD, DDR, ZIF-8	229-232
Separation of light alkanes	CH ₄ /C ₂ H ₆ /C ₃ H ₈	E: MFI	35
Separation of C4 hydrocarbons	iC4/1-butene nC4/iC4	E: MFI	36, 49, 233
Separation of C5 hydrocarbons	nC5/isoprene	E: MFI	234
Separation of hexane isomers	nC6/2MP nC6/22DMB	E: MFI	48, 174, 188, 235, 236
Separation of C8 hydrocarbons	o-xylene/m-xylene/ p-xylene/ethylbenzene	E: MFI	49, 235
Separation of aromatics from aliphatics	Benzene/nC6 Benzene/nC7 benzene/cyclohexane	E: NaY, NaX	39, 237

Table 3. Salient structural information on zeolites.

Structure	Topology	Fractional pore volume, ϕ	Pore volume/ cm ³ /g	Framework density/ kg/m ³
AFI	12-ring 1D channels of 7.3 Å size	0.274	0.159	1730
BEA	Intersecting channels of two sizes: 12-ring of 6.1 Å - 6.8 Å and 10-ring of 5.6 Å - 6.7 Å	0.408	0.271	1509
BOG	Intersecting channels: 12-ring 6.8 Å -7.4 Å and 10-ring of 5.6 Å - 5.8 Å	0.374	0.241	1996
CHA	316 Å ³ cages separated by 3.77 Å × 4.23 Å size windows	0.382	0.264	1444
DDR	277.8 Å ³ cages separated by 3.65 Å × 4.37 Å size windows	0.245	0.139	1760
ERI	408 Å ³ cages separated by 3.8 Å - 4.9 Å size windows	0.363	0.228	1595
FAU-Si	790 Å ³ cages separated by 7.4 Å size windows	0.439	0.328	1338
FER	10-ring 1D main channels of 4.2 Å -5.4 Å size, connected with 8-ring side pockets of 3.5 Å -4.8 Å size	0.283	0.160	1772
ISV	Intersecting channels of two sizes: 12-ring of 6.1 Å -6.5 Å and 12-ring of 5.9 Å - 6.6 Å	0.426	0.278	1533
ITQ-29	678 Å ³ cages separated by 4 Å × 4.22 Å size windows	0.405	0.283	1433
LTL	12-ring 1D channels of 7.1 Å size	0.277	0.170	1627
LTA-Si	743 Å ³ cages separated by 4.11 Å × 4.47 Å size windows	0.399	0.310	1285
LTA-4A	694 Å ³ cages separated by 4 Å × 4.58 Å size windows	0.38	0.25	1530
LTA-5A	702 Å ³ cages separated by 4 Å × 4.58 Å size windows	0.38	0.25	1508
MFI	10-ring intersecting channels of 5.4 Å - 5.5 Å and 5.4 Å - 5.6 Å size	0.297	0.165	1796
MOR	12-ring 1D main channels of 6.5 Å -7 Å size, connected with 8-ring side pockets of 2.6 Å -5.7 Å size	0.285	0.166	1715
MTW	12-ring 1D channels of 5.6 Å -6 Å size	0.215	0.111	1935
NaY	790 Å ³ cages separated by 7.4 Å size windows	0.41	0.303	1347
NaX	790 Å ³ cages separated by 7.4 Å size windows	0.40	0.280	1421
TON	10-ring 1D channels of 4.6 Å -5.7 Å size	0.190	0.097	1969

Table 4. Salient structural information on MOFs, ZIFs, and COFs.

Structure	Topology	Fractional pore volume, ϕ	Pore volume/ cm ³ /g	Framework density/ kg/m ³
CuBTC	Large cages are inter-connected by 9 Å windows of square cross-section. The large cages are also connected to tetrahedral-shaped pockets of ca. 6 Å size through triangular-shaped windows of 4.6 Å size	0.759	0.863	879
IRMOF-1	Two alternating, inter-connected, cavities of 10.9 Å and 14.3 Å with window size of 8 Å.	0.812	1.369	593
Zn(bdc)dabco	There exist two types of intersecting channels of about 7.5 Å × 7.5 Å along the x-axis and channels of 3.8 Å × 4.7 Å along y and z axes.	0.662	0.801	826
Co(bdc)dabco	There exist two types of intersecting channels of about 7.6 Å × 7.6 Å along the x-axis and channels of 3.7 Å × 5.1 Å along y and z axes.	0.648	0.796	814
MOF-177	Six diamond-shaped channels (upper) with diameter of 10.8 Å surround a pore containing eclipsed BTB ³⁻ moieties.	0.840	1.968	427
Co(BDP)	1D square-shaped channels of 10 Å	0.67	0.927	721
MgMOF-74	1D hexagonal-shaped channels of 11 Å	0.708	0.782	905
NiMOF-74	1D hexagonal-shaped channels of 11 Å	0.695	0.582	1193
CoMOF-74	1D hexagonal-shaped channels of 11 Å	0.707	0.599	1180
ZnMOF-74	1D hexagonal-shaped channels of 11 Å	0.709	0.582	1219
FeMOF-74	1D hexagonal-shaped channels of 11 Å	0.705	0.626	1126
MIL-47	1D diamond-shaped channels of 8.5 Å	0.608	0.606	1004
MIL-53 (Cr)-lp	1D lozenge-shaped channels of 8.5 Å	0.539	0.518	1041
BTP-COF	1D hexagonal-shaped channels of 34 Å	0.752	1.79	420
COF-102	Cavity of size 8.9 Å	0.8	1.875	426
COF-103	Cavity of size 9.6 Å	0.82	2.040	400
COF-108	Two cavities, of sizes 15.2 Å and 29.6 Å	0.93	5.467	170
ZIF-7		0.277	0.223	1241
ZIF-8	1168 Å ³ cages separated by 3.26 Å size windows	0.476	0.515	924

Table 5. Dual-site Langmuir-Freundlich parameters for pure component isotherms for butanes in MFI at 300 K. Note that the saturation capacities are specified in molecules per unit cell; multiply these by 0.1734 to obtain the loading values in mol per kg framework.

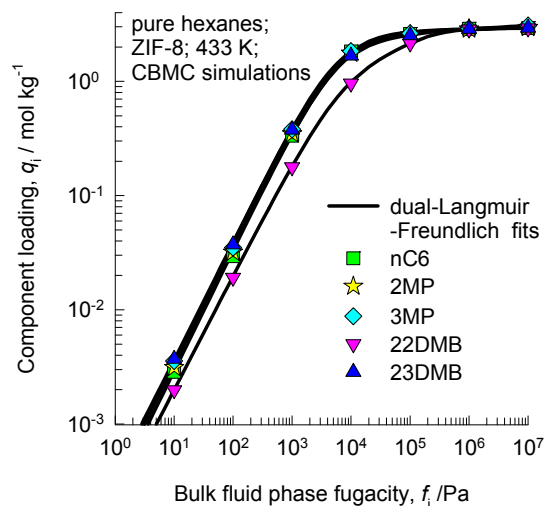
	Site A			Site B		
	$\Theta_{i,A,sat}$ molecules uc ⁻¹	$b_{i,A}$ Pa ^{-ν_i}	$\nu_{i,A}$ dimensionless	$\Theta_{i,B,sat}$ molecules uc ⁻¹	$b_{i,B}$ Pa ^{-ν_i}	$\nu_{i,B}$ dimensionless
CO ₂	19	6.12×10^{-6}	1	11	1.73×10^{-8}	1
CO	19	7.95×10^{-7}	1	14	7.64×10^{-10}	1
H ₂	30	3.57×10^{-8}	1	42	1.39×10^{-9}	1
N ₂	15	7×10^{-7}	1	15	5×10^{-9}	1
CH ₄	16	3.1×10^{-6}	1	7	5×10^{-9}	1
C ₂ H ₆	13	7.74×10^{-5}	1	3.3	4.08×10^{-7}	1
C ₃ H ₈	10.7	6.34×10^{-4}	1	1.4	3.35×10^{-4}	1
nC ₄ H ₁₀	1.5	2.24×10^{-3}	0.57	8.7	9.75×10^{-3}	1.12
iC ₄ H ₁₀	4	2.29×10^{-2}	1	6	2.87×10^{-5}	1
He	77	7.64×10^{-9}	1	120	7.95×10^{-11}	1

Table 6. Dual-site Langmuir-Freundlich parameters for pure component isotherms in MFI at 300 K. Note that the saturation capacities are specified in molecules per unit cell. Multiply these by 0.1734 obtain the loading values in mol per kg framework.

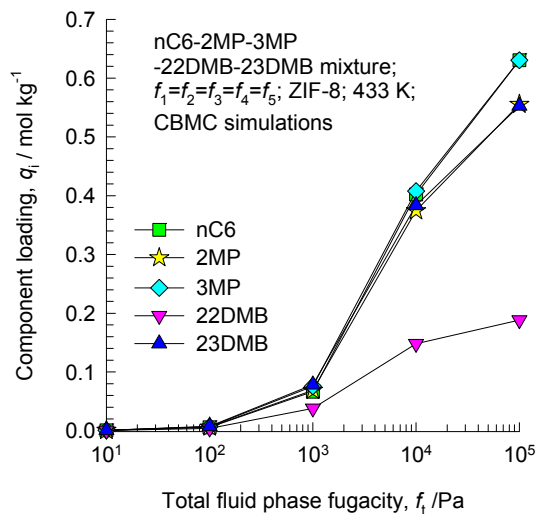
	Site A			Site B		
	$\Theta_{i,A,sat}$ molecules uc ⁻¹	$b_{i,A}$ Pa ^{-v_i}	$V_{i,A}$ dimensionless	$\Theta_{i,B,sat}$ molecules uc ⁻¹	$b_{i,B}$ Pa ^{-v_i}	$V_{i,B}$ dimensionless
nC6	6.6	0.708	0.83	1.4	16.6	1.5
2MP	4	4.51	1.05	4	7.92×10^{-6}	1.13
3MP	4	1.59	1.08	4	1.36×10^{-2}	0.53
22DMB	4	0.555	1			
23DMB	4	1.5	1			
nC6	4	114	1.15	3	0.0135	1.5

Table 7. Dual-site Langmuir-Freundlich parameters for pure component hexane isomers at 433 K in ZIF-8.

(a) Pure components



(b) 5-component mixture



	Site A			Site B		
	$q_{i,A,sat}$ mol kg ⁻¹	$b_{i,A}$ Pa ^{-v_{iA}}	$v_{i,A}$ dimensionless	$q_{i,B,sat}$ mol kg ⁻¹	$b_{i,B}$ Pa ^{-v_{iB}}	$v_{i,B}$ dimensionless
nC6	2.8	8.53×10^{-5}	1.07	0.44	5.59×10^{-5}	0.59
2MP	2.8	1.06×10^{-4}	1.04	1.0	8.08×10^{-6}	0.64
3MP	2.8	9.81×10^{-5}	1.07	1.2	2.98×10^{-5}	0.58
22DMB	1.82	1.09×10^{-4}	1.0	1.1	1.55×10^{-7}	1.34
23DMB	2.4	1.18×10^{-4}	1.06	0.6	1.11×10^{-4}	0.76

Table 8. Dual-site Langmuir-Freundlich parameters for pure component C8 hydrocarbons at 433 K in MgMOF-74. Note that the saturation capacities are specified in molecules per unit cell; multiply these by 0.4579 to obtain the values in mol per kg framework.

	Site A			Site B		
	$\Theta_{i,A,sat}$ molecules uc ⁻¹	$b_{i,A}$ Pa ^{-$v_{i,A}$}	$v_{i,A}$ dimensionless	$\Theta_{i,B,sat}$ molecules uc ⁻¹	$b_{i,B}$ Pa ^{-$v_{i,B}$}	$v_{i,B}$ dimensionless
n-octane (nC8)	4.1	4.64×10^{-5}	2.9	3.2	9.66×10^{-3}	1
Ethylbenzene	4.4	2.6×10^{-4}	2.8	4.8	2.01×10^{-2}	1
o-xylene	5.4	1.22×10^{-8}	9	4	8.84×10^{-2}	1.1
m-xylene	5.4	3.72×10^{-6}	5.6	4	5.66×10^{-2}	1.05
p-xylene	9	1.3×10^{-3}	2.28	0.4	3.62×10^{-1}	1.0

Table 9. Dual-site Langmuir-Freundlich parameters for pure component xylene isomers at 398 K in NiMOF-74. Note that the saturation capacities are specified in molecules per unit cell; multiply these by 0.356 to obtain the values in mol per kg framework.

	Site A			Site B		
	$\Theta_{i,A,sat}$ molecules uc ⁻¹	$b_{i,A}$ Pa ^{-v_{iA}}	$v_{i,A}$ dimensionless	$\Theta_{i,B,sat}$ molecules uc ⁻¹	$b_{i,B}$ Pa ^{-v_{iB}}	$v_{i,B}$ dimensionless
o-xylene	7.2	3.85×10^{-41}	41.5	2.7	5.11×10^{-2}	1.06
m-xylene	7.4	1.48×10^{-11}	10.9	2	2.98×10^{-2}	1.03
p-xylene	$\Theta_{i,A,sat}$	7.22×10^{-6}	4.33	1	2.76×10^{-2}	1.02

Table 10. Dual-site Langmuir-Freundlich parameters for pure component C8 hydrocarbons at 433 K in Co(BDP). Note that the saturation capacities are specified in molecules per unit cell; multiply these by 0.9362 to obtain the values in mol per kg framework.

	Site A			Site B		
	$\Theta_{i,A,sat}$ molecules uc ⁻¹	$b_{i,A}$ Pa ^{-$v_{i,A}$}	$v_{i,A}$ dimensionless	$\Theta_{i,B,sat}$ molecules uc ⁻¹	$b_{i,B}$ Pa ^{-$v_{i,B}$}	$v_{i,B}$ dimensionless
n-octane (nC8)	2.6	2.57×10^{-7}	3.3	1.8	3×10^{-3}	1
Ethylbenzene	3.5	3.93×10^{-12}	4.5	2.2	8.74×10^{-4}	1
o-xylene	3.9	1.12×10^{-7}	3.1	1.9	1.89×10^{-3}	1.1
m-xylene	3.8	1.36×10^{-8}	3.6	1.8	2.16×10^{-3}	1.05
p-xylene	4.2	6.52×10^{-12}	5.3	1.7	2.15×10^{-3}	1.0

Table 11. Dual-site Langmuir-Freundlich parameters for pure component 1-alcohols in CHA at 300 K. The fit parameters are based on the CBMC simulations of pure component isotherms presented in earlier work.¹²⁵ Note that the saturation capacities are specified in molecules per cage; multiply these by 1.387 to obtain the values in mol per kg framework.

	Site A			Site B		
	$\Theta_{i,A,sat}$ Molecules cage ⁻¹	$b_{i,A}$ Pa ^{-v_i}	$v_{i,A}$ dimensionless	$\Theta_{i,B,sat}$ molecules cage ⁻¹	$b_{i,B}$ Pa ^{-v_i}	$v_{i,B}$ dimensionless
methanol	2.7	6.77×10^{-11}	3.3	2.7	4.45×10^{-4}	1
ethanol	2	7.93×10^{-5}	0.87	2	3.6×10^{-3}	1.14
1-propanol	1	1.28×10^{-2}	1.8	1	9.11×10^{-2}	1
1-butanol	1	0.231	1.46	1	0.5066	1
1-pentanol	0.5	19.26	1.72	0.5	6.91	1
1-hexanol	0.5	2561	2.4	0.5	24.8	1

Table 12. 1-site Langmuir-Freundlich parameters for ethene, ethane, propene and propane in ZIF-8. The T -dependent parameters are obtained by fitting the combined sets of pure component isotherm data of Li et al.⁴² and Böhme et al.¹³⁰ determined for a variety of temperatures in the range 273 K to 408 K.

$$q = q_{sat} \frac{bp^\nu}{1 + bp^\nu} \quad b_A = b_0 \exp\left(\frac{E}{RT}\right)$$

	q_{sat} mol kg ⁻¹	b_0 Pa ^{-ν}	E kJ mol ⁻¹	ν dimensionless
ethene	12	9.37×10^{-11}	21.5	1.08
ethane	12	8.55×10^{-11}	23.2	1.08
propene	5.2	4.57×10^{-11}	33.9	1
propane	5.2	1.39×10^{-10}	31.3	1

Table 13. Dual-Langmuir-Freundlich $q = q_{A,sat} \frac{b_A p^{v_A}}{1 + b_A p^{v_A}} + q_{B,sat} \frac{b_B p^{v_B}}{1 + b_B p^{v_B}}$ fits for adsorption, and desorption branches of C₂H₄, C₂H₆, C₃H₆, and C₃H₈ at 298 K in ZIF-7. The fit parameters are obtained from the experimental data of Gücüyener et al.⁷⁴ The comparison of the experimental isotherm data and DLF fits are shown in Figures 84, and 85.

	Site A			Site B		
	$q_{i,A,sat}$ mol/kg	$b_{i,A}$ Pa ^{-v_i}	$v_{i,A}$ dimensionless	$q_{i,B,sat}$ mol/kg	$b_{i,B}$ Pa ^{-v_i}	$v_{i,B}$ dimensionless
C ₂ H ₄ , Adsorption branch	1.4	2.33×10 ⁻⁵⁵	11.85	3	8.12×10 ⁻⁷	1.06
C ₂ H ₄ , Desorption branch	1.5	5.34×10 ⁻⁶⁷	14.9	0.5	1.72×10 ⁻⁵	1.04
C ₂ H ₆ , Adsorption branch	1.5	3.16×10 ⁻⁵⁵	13.4	1.22	8.58×10 ⁻⁶	0.96
C ₂ H ₆ , Desorption branch	1.57	2.88×10 ⁻⁴⁹	12.5	0.4	2.06×10 ⁻⁸	1.7
C ₃ H ₆ , Adsorption branch	1.37	2.86×10 ⁻⁴⁹	14.2	0.64	2.13×10 ⁻¹¹	2.85
C ₃ H ₆ , Desorption branch	1.46	1.45×10 ⁻⁶³	19	1.15	5.24×10 ⁻²	0.27
C ₃ H ₈ , Adsorption branch	0.78	6.04×10 ⁻⁷²	24.3	0.98	1.61×10 ⁻³	0.92
C ₃ H ₈ , Desorption branch	0.76	5×10 ⁻⁶⁷	28	1.1	1.81×10 ⁻³	1

Table 14. Dual-site Langmuir-Freundlich parameters for pure component isotherms of isobutene and isobutane in CuBTC at 303 K. The fits are based on the experimental isotherms of Hartmann et al.¹⁴⁰

	Site A			Site B		
	$q_{i,A,sat}$ mol/kg	$b_{i,A}$ Pa^{-v_i}	$v_{i,A}$ dimensionless	$q_{i,B,sat}$ mol/kg	$b_{i,B}$ Pa^{-v_i}	$v_{i,B}$ dimensionless
isobutene	7.2	8.22×10^{-3}	1			
isobutane	3.4	1.95×10^{-17}	6.5	2.7	2.05×10^{-3}	1

Table 15. Research Octane Numbers (RON) of C5, C6 alkanes. Data is from Herm et al.⁷³

Alkane		Research Octane Number (RON)
Symbol	Chemical Name	
nC5	n-pentane	61.7
2MB	2-methyl butane	93.5
nC6	n-hexane	30
2MP	2-methyl pentane	74.5
3MP	3-methyl pentane	75.5
22DMB	2,2 dimethyl butane	94
23DMB	2,3 dimethyl butane	105

Table 16. Dual-site Langmuir-Freundlich parameters for pure component pentane and hexane isomers at 433 K in MFI zeolite.

	Site A			Site B		
	$\Theta_{i,A,sat}$ molecules uc^{-1}	$b_{i,A}$ $Pa^{-\nu_i}$	$\nu_{i,A}$ dimensionless	$\Theta_{i,B,sat}$ molecules uc^{-1}	$b_{i,B}$ $Pa^{-\nu_i}$	$\nu_{i,B}$ dimensionless
nC5	4	6.26×10^{-6}	1.12	4	1.94×10^{-4}	1
2MB	4	1.69×10^{-4}	1	2	4.93×10^{-7}	1
Neo-pentane	4	1.24×10^{-4}	1			
nC6	3.2	2.21×10^{-8}	1.6	4.3	7.42×10^{-4}	1
2MP	4	7.85×10^{-4}	1.03			
3MP	4	4.22×10^{-4}	1.02	1	9.88×10^{-7}	1
22DMB	4	2.55×10^{-4}	1.02			
23DMB	4	4.59×10^{-4}	1.02			

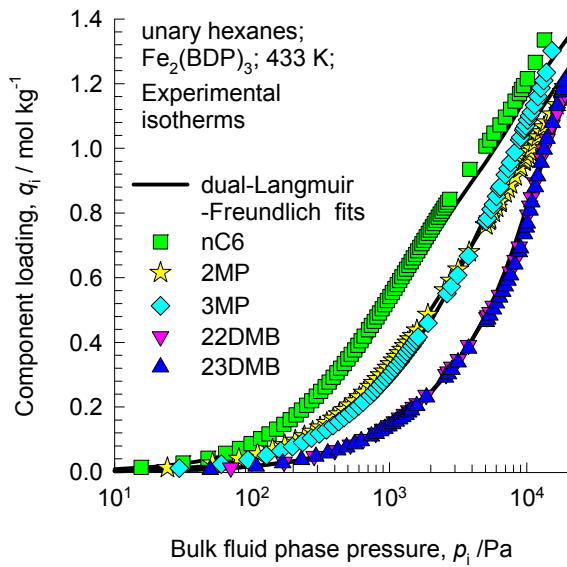
Table 17. Single-site Langmuir parameters, and M-S diffusivities D_i/r_c^2 , for pure component 2MB, 2MP, and 22DMB at 473 K in MFI zeolite. The parameters are based on the experimental data of Jolimaître et al.^{173, 190}. All simulations of the breakthrough experiments of Jolimaître et al.¹⁹⁰ were performed for extrudate 2 with the following fixed bed parameters: bed length, $L = 0.795$ m; bed voidage, $\varepsilon = 0.4$; density of extrudate 2, $\rho = 620.8$ kg m⁻³; The interstitial velocity v varied with each run and were taken from Table 6 of Jolimaître et al.¹⁹⁰ The partial pressures of each of the components 2MB, 2MP, and 22DMB at the inlet to the adsorber are specified using the data provided in Table 6 of Jolimaître et al.¹⁹⁰

	$\Theta_{i,\text{sat}}$ molecules uc ⁻¹	$b_{i,A}$ Pa ⁻¹	D_i/r_c^2 s ⁻¹
2MB	4	4.12×10^{-5}	0.0075
2MP	4	1.27×10^{-4}	0.005
22DMB	4	7.12×10^{-5}	0.0000625

Table 18. Dual-Langmuir-Freundlich parameter fits for $\text{Fe}_2(\text{BDP})_3$ based on the experimental data of Herm et al.⁷³ for isotherms at 403 K, 433 K, and 473 K. These isotherms were fitted with

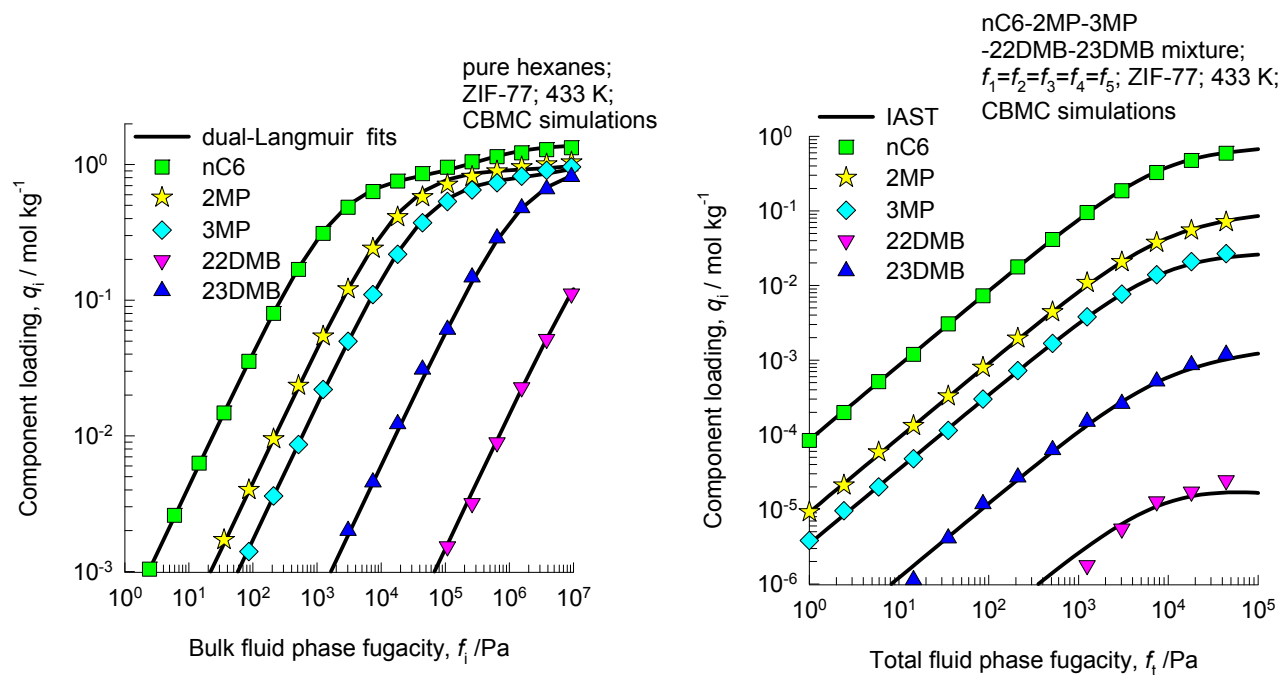
$$q = q_{A,\text{sat}} \frac{b_A p^{v_A}}{1 + b_A p^{v_A}} + q_{B,\text{sat}} \frac{b_B p^{v_B}}{1 + b_B p^{v_B}} \text{ with } T\text{-dependent parameters}$$

$$b_A = b_{A0} \exp\left(\frac{E_A}{RT}\right); \quad b_B = b_{B0} \exp\left(\frac{E_B}{RT}\right)$$



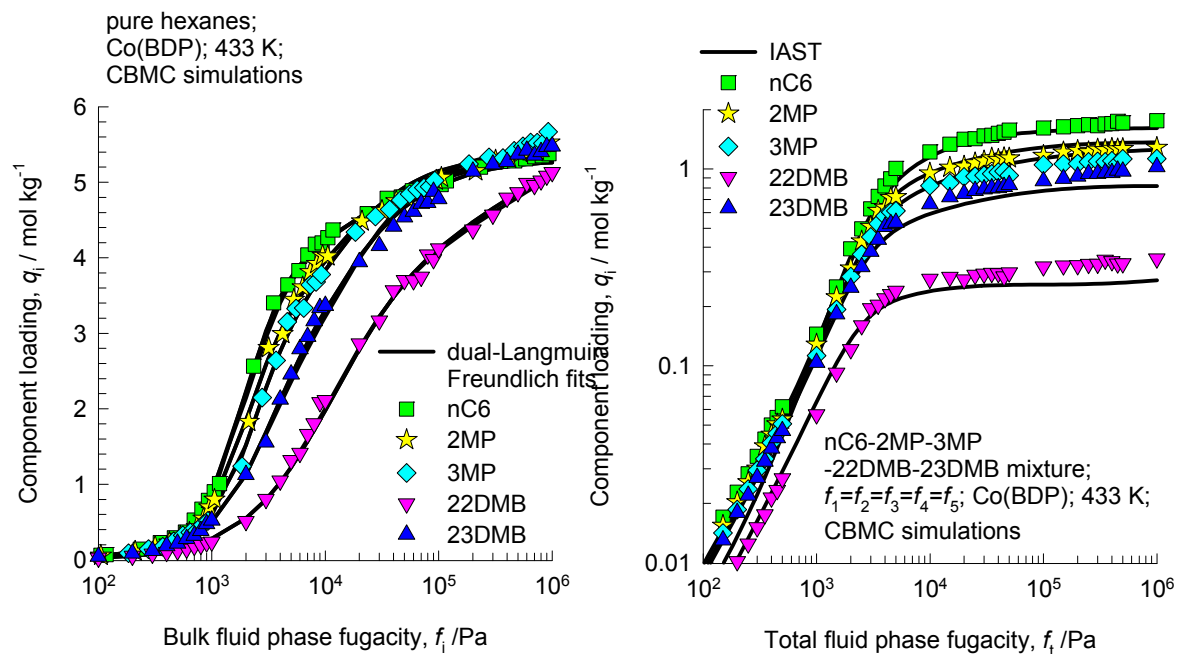
	Site A				Site B			
	$q_{A,\text{sat}}$ mol kg ⁻¹	b_{A0} Pa ^{-v_A}	E_A kJ mol ⁻¹	v_A dimensionless	$q_{B,\text{sat}}$ mol kg ⁻¹	b_{B0} Pa ^{-v_B}	E_B kJ mol ⁻¹	v_B dimensionless
nC6	0.28	2.74×10^{-26}	111	3	1.17	8.86×10^{-13}	73	1.02
2MP	0.78	2.13×10^{-13}	76	1.1	0.63	5.61×10^{-17}	89	1.36
3MP	0.36	4.62×10^{-13}	76	1.1	1.07	1.34×10^{-16}	89	1.36
22DMB	0.53	1.33×10^{-32}	167	2.9	0.94	1.42×10^{-12}	67	1
23DMB	0.61	9.74×10^{-33}	167	2.9	0.92	1.49×10^{-12}	67	1

Table 19. Dual-site Langmuir-Freundlich parameters for pure component hexane isomers at 433 K in ZIF-77.



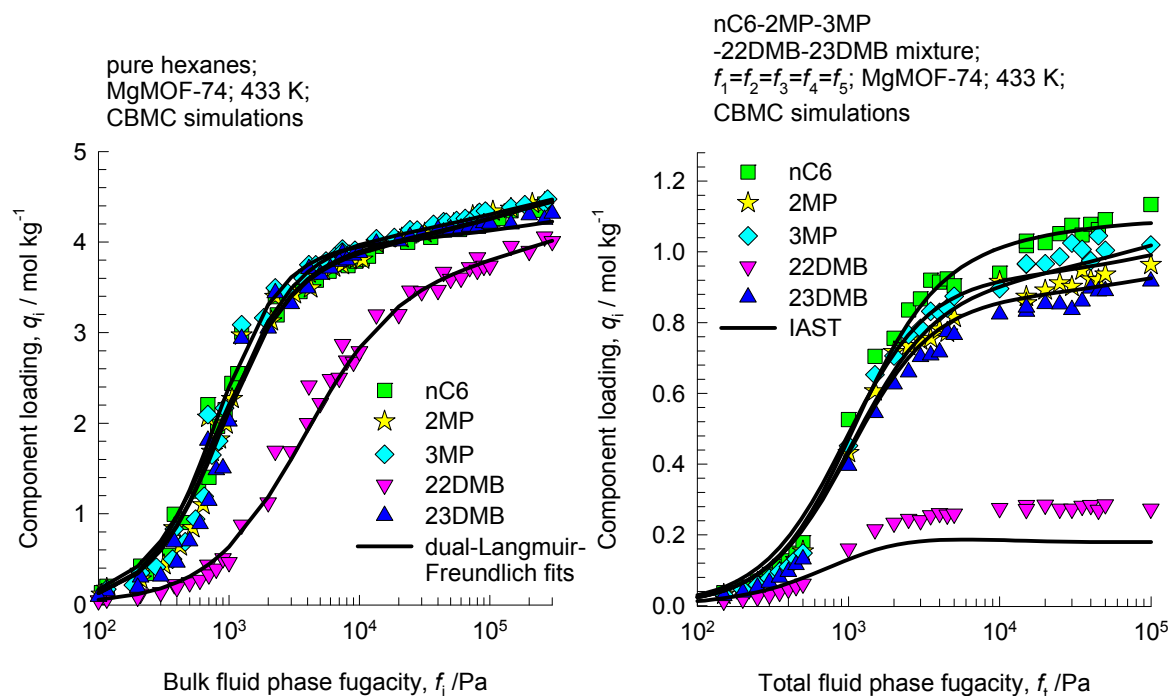
	Site A			Site B		
	$q_{i,A,sat}$ mol kg ⁻¹	$b_{i,A}$ Pa ^{-ν_i}	$\nu_{i,A}$ dimensionless	$q_{i,B,sat}$ mol kg ⁻¹	$b_{i,B}$ Pa ^{-ν_i}	$\nu_{i,B}$ dimensionless
nC6	0.81	5.25×10^{-4}	1	0.59	2.24×10^{-6}	1
2MP	0.92	4.95×10^{-5}	1	0.43	1.66×10^{-8}	1
3MP	0.8	2.15×10^{-5}	1	0.4	5.15×10^{-8}	1
22DMB	0.7	2.1×10^{-8}	1			
23DMB	0.96	6.31×10^{-7}	1	0.2	3.65×10^{-9}	1

Table 20. Dual-site Langmuir-Freundlich parameters for pure component hexane isomers at 433 K in Co(BDP). The fits are based on CBMC simulation data of Krishna and van Baten.¹⁵⁹



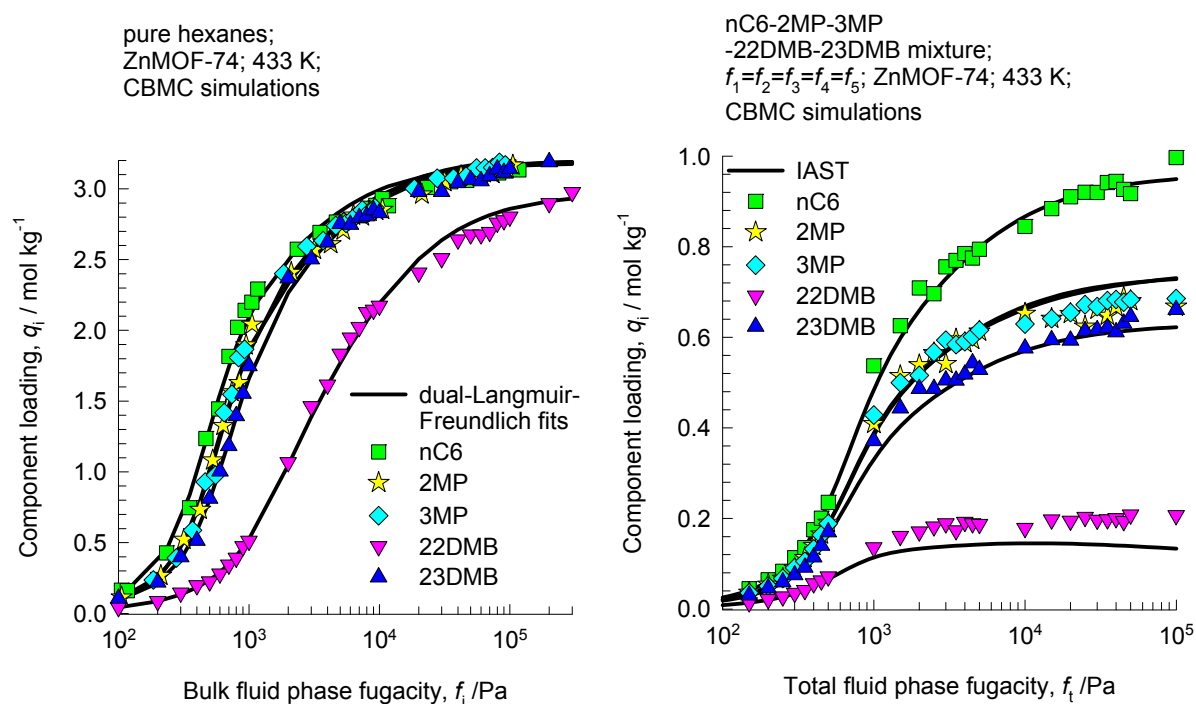
	Site A			Site B		
	$q_{i,A,sat}$ mol kg ⁻¹	$b_{i,A}$ Pa ^{-ν_i}	$\nu_{i,A}$ dimensionless	$q_{i,B,sat}$ mol kg ⁻¹	$b_{i,B}$ Pa ^{-ν_i}	$\nu_{i,B}$ dimensionless
nC6	1.7	3.65×10^{-4}	0.8	3.7	6.29×10^{-8}	2.2
2MP	3.3	1.49×10^{-4}	1	2	6.77×10^{-10}	2.8
3MP	3.5	1.3×10^{-4}	1	1.9	8.82×10^{-10}	2.7
22DMB	1.8	5.14×10^{-5}	0.74	4.1	3.42×10^{-5}	1.1
23DMB	4	1.07×10^{-4}	1	1.3	1.24×10^{-8}	2.3

Table 21. Dual-site Langmuir-Freundlich parameters for pure component hexane isomers at 433 K in MgMOF-74. The fits are based on CBMC simulation data of Krishna and van Baten.¹⁵⁹



	Site A			Site B		
	$q_{i,A,sat}$ mol kg ⁻¹	$b_{i,A}$ Pa ^{-ν_i}	$\nu_{i,A}$ dimensionless	$q_{i,B,sat}$ mol kg ⁻¹	$b_{i,B}$ Pa ^{-ν_i}	$\nu_{i,B}$ dimensionless
nC6	3.95	1.98×10^{-5}	1.66	1.1	1.41×10^{-3}	0.5
2MP	3.84	1.85×10^{-5}	1.66	1.2	1.39×10^{-3}	0.52
3MP	3.95	1.81×10^{-5}	1.66	1.1	1.43×10^{-3}	0.5
22DMB	3.5	4×10^{-5}	1.3	1.2	5×10^{-4}	0.6
23DMB	3.9	9.94×10^{-6}	1.73	1.04	1.57×10^{-3}	0.45

Table 22. Dual-site Langmuir-Freundlich parameters for pure component hexane isomers at 433 K in ZnMOF-74. The fits are based on CBMC simulation data of Krishna and van Baten.¹⁵⁹



	Site A			Site B		
	$q_{i,A,sat}$ mol kg ⁻¹	$b_{i,A}$ Pa ^{-v_i}	$v_{i,A}$ dimensionless	$q_{i,B,sat}$ mol kg ⁻¹	$b_{i,B}$ Pa ^{-v_i}	$v_{i,B}$ dimensionless
nC6	1.6	6.05×10^{-8}	2.7	1.6	7.57×10^{-4}	1
2MP	1.4	6.31×10^{-9}	3	1.83	5.54×10^{-4}	1
3MP	1.5	1.88×10^{-8}	2.8	1.7	5.81×10^{-4}	1
22DMB	0.77	7.53×10^{-8}	2.2	2.2	1.88×10^{-4}	1
23DMB	1.5	4.25×10^{-8}	2.6	1.7	5.04×10^{-4}	1

46. References

- (1) Ruthven, D. M.; Farooq, S.; Knaebel, K. S. Pressure swing adsorption; VCH Publishers: New York, 1994.
- (2) Krishna, R.; Baur, R. Modelling issues in zeolite based separation processes, *Sep. Purif. Technol.* **2003**, *33*, 213-254.
- (3) He, Y.; Krishna, R.; Chen, B. Metal-Organic Frameworks with Potential for Energy-Efficient Adsorptive Separation of Light Hydrocarbons, *Energy Environ. Sci.* **2012**, *5*, 9107-9120.
- (4) Krishna, R.; van Baten, J. M. Investigating the Influence of Diffusional Coupling on Mixture Permeation across Porous Membranes *J. Membr. Sci.* **2013**, *430*, 113-128.
- (5) Skoulidas, A. I.; Sholl, D. S.; Krishna, R. Correlation effects in diffusion of CH₄/CF₄ mixtures in MFI zeolite. A study linking MD simulations with the Maxwell-Stefan formulation, *Langmuir* **2003**, *19*, 7977-7988.
- (6) Chempath, S.; Krishna, R.; Snurr, R. Q. Nonequilibrium MD simulations of diffusion of binary mixtures containing short n-alkanes in faujasite, *J. Phys. Chem. B* **2004**, *108*, 13481-13491.
- (7) Krishna, R. Describing the diffusion of guest molecules inside porous structures, *J. Phys. Chem. C* **2009**, *113*, 19756-19781.
- (8) Krishna, R. Diffusion in Porous Crystalline Materials, *Chem. Soc. Rev.* **2012**, *41*, 3099-3118.
- (9) Krishna, R.; van Baten, J. M. Onsager coefficients for binary mixture diffusion in nanopores, *Chem. Eng. Sci.* **2008**, *63*, 3120-3140.
- (10) Langmuir, I. The adsorption of gases on plane surfaces of glass, mica and platinum, *J. Am. Chem. Soc.* **1918**, *40*, 1361-1403.
- (11) Krishna, R.; van Baten, J. M. Influence of Adsorption Thermodynamics on Guest Diffusivities in Nanoporous Crystalline Materials, *Phys. Chem. Chem. Phys.* **2013**, *15*, 7994-8016.
- (12) Barrer, R. M. Zeolites and Clay minerals as Sorbents and Molecular sieves; Academic Press: London, 1978.
- (13) Kärger, J.; Ruthven, D. M. Diffusion in zeolites and other microporous solids; John Wiley: New York, 1992.
- (14) Kärger, J.; Ruthven, D. M.; Theodorou, D. N. Diffusion in Nanoporous Materials; Wiley - VCH: Weinheim, 2012.
- (15) Ruthven, D. M. Principles of Adsorption and Adsorption Processes; John Wiley: New York, 1984.
- (16) Krishna, R.; Wesselingh, J. A. The Maxwell-Stefan approach to mass transfer, *Chem. Eng. Sci.* **1997**, *52*, 861-911.
- (17) Krishna, R. Problems and Pitfalls in the Use of the Fick Formulation for Intraparticle Diffusion, *Chem. Eng. Sci.* **1993**, *48*, 845-861.
- (18) Maxwell, J. C. On the dynamical theory of gases, *Phil. Trans. Roy. Soc.* **1866**, *157*, 49-88.
- (19) Stefan, J. Über das Gleichgewicht und die Bewegung insbesondere die Diffusion von Gasgemengen, *Sitzber. Akad. Wiss. Wien.* **1871**, *63*, 63-124.
- (20) Krishna, R. Multicomponent surface diffusion of adsorbed species - A description based on the generalized Maxwell-Stefan equations, *Chem. Eng. Sci.* **1990**, *45*, 1779-1791.
- (21) Krishna, R.; van Baten, J. M. Insights into diffusion of gases in zeolites gained from molecular dynamics simulations, *Microporous Mesoporous Mater.* **2008**, *109*, 91-108.
- (22) Krishna, R.; van Baten, J. M. A molecular dynamics investigation of the diffusion characteristics of cavity-type zeolites with 8-ring windows, *Microporous Mesoporous Mater.* **2011**, *137*, 83-91.

- (23) Baerlocher, C.; McCusker, L. B. Database of Zeolite Structures, <http://www.iza-structure.org/databases/>, International Zeolite Association, 10 January 2002.
- (24) Krishna, R.; van Baten, J. M. Investigating the Relative Influences of Molecular Dimensions and Binding Energies on Diffusivities of Guest Species Inside Nanoporous Crystalline Materials *J. Phys. Chem. C* **2012**, *116*, 23556-23568.
- (25) Talu, O.; Myers, A. L. Molecular Simulation of Adsorption: Gibbs Dividing Surface and Comparison with Experiment, *A.I.Ch.E.J.* **2001**, *47*, 1160-1168.
- (26) Hansen, N.; Keil, F. J. Multiscale modeling of reaction and diffusion in zeolites: from the molecular level to the reactor, *Soft Mater.* **2012**, *10*, 179-201.
- (27) Krishna, R.; van Baten, J. M. Hydrogen bonding effects in adsorption of water-alcohol mixtures in zeolites and the consequences for the characteristics of the Maxwell-Stefan diffusivities, *Langmuir* **2010**, *26*, 10854-10867.
- (28) Krishna, R.; van Baten, J. M. An investigation of the characteristics of Maxwell-Stefan diffusivities of binary mixtures in silica nanopores, *Chem. Eng. Sci.* **2009**, *64*, 870-882.
- (29) Krishna, R.; van Baten, J. M. Unified Maxwell-Stefan description of binary mixture diffusion in micro- and meso- porous materials, *Chem. Eng. Sci.* **2009**, *64*, 3159-3178.
- (30) Myers, A. L.; Prausnitz, J. M. Thermodynamics of mixed gas adsorption, *A.I.Ch.E.J.* **1965**, *11*, 121-130.
- (31) Krishna, R.; van Baten, J. M. Describing Mixture Diffusion in Microporous Materials under Conditions of Pore Saturation, *J. Phys. Chem. C* **2010**, *114*, 11557-11563.
- (32) Krishna, R.; van Baten, J. M. Describing binary mixture diffusion in carbon nanotubes with the Maxwell-Stefan equations. An investigation using molecular dynamics simulations, *Ind. Eng. Chem. Res.* **2006**, *45*, 2084-2093.
- (33) Krishna, R.; van Baten, J. M. Maxwell-Stefan modeling of slowing-down effects in mixed gas permeation across porous membranes, *J. Membr. Sci.* **2011**, *383*, 289-300.
- (34) Sandström, L.; Sjöberg, E.; Hedlund, J. Very high flux MFI membrane for CO₂ separation, *J. Membr. Sci.* **2011**, *380*, 232-240.
- (35) van de Graaf, J. M.; Kapteijn, F.; Moulijn, J. A. Modeling permeation of binary mixtures through zeolite membranes, *A.I.Ch.E.J.* **1999**, *45*, 497-511.
- (36) Vroon, Z. A. E. P.; Keizer, K.; Gilde, M. J.; Verweij, H.; Burggraaf, A. J. Transport properties of alkanes through ceramic thin zeolite MFI membranes, *J. Membr. Sci.* **1996**, *113*, 293-300.
- (37) Zhang, F.; Zou, X.; Gao, X.; Fan, S.; Sun, F.; Ren, H.; Zhu, G. S. Hydrogen Selective NH₂-MIL-53(Al) MOF Membranes with High Permeability, *Adv. Funct. Mater.* **2012**, *22*, 3583-3590.
- (38) Baertsch, C. D.; Funke, H. H.; Falconer, J. L.; Noble, R. D. Permeation of aromatic hydrocarbon vapors through silicalite- zeolite membranes, *J. Phys. Chem.* **1996**, *100*, 7676-7679.
- (39) Jeong, B. H.; Hasegawa, Y.; Kusakabe, K.; Morooka, S. Separation of benzene and cyclohexane mixtures using an NaY-type zeolite membrane, *Separ. Sci. Technol.* **2002**, *37*, 1225-1239.
- (40) Li, Y.; Liang, F.; Bux, H.; Yang, W.; Caro, J. Zeolitic Imidazolate Framework ZIF-7 Based Molecular Sieve Membrane for Hydrogen Separation, *J. Membr. Sci.* **2010**, *354*, 48-54.
- (41) Bux, H.; Chmelik, C.; Krishna, R.; Caro, J. Ethene/Ethane Separation by the MOF Membrane ZIF-8: Molecular Correlation of Permeation, Adsorption, Diffusion, *J. Membr. Sci.* **2011**, *369*, 284-289.
- (42) Li, K.; Olson, D. H.; Seidel, J.; Emge, T. J.; Gong, H.; Zeng, H.; Li, J. Zeolitic Imidazolate Frameworks for Kinetic Separation of Propane and Propene, *J. Am. Chem. Soc.* **2009**, *131*, 10368-10369.
- (43) Ruthven, D. M.; Reyes, S. C. Adsorptive separation of light olefins from paraffins, *Microporous Mesoporous Mater.* **2007**, *104*, 59-66.
- (44) Pan, Y.; Li, T.; Lestari, G.; Lai, Z. Effective Separation of Propylene/Propane Binary Mixtures by ZIF-8 Membranes, *J. Membr. Sci.* **2012**, *390-391*, 93-98.
- (45) Liu, D.; Ma, X.; Xi, H.; Lin, Y. S. Gas transport properties and propylene/propane separation characteristics of ZIF-8 membranes, *J. Membr. Sci.* **2014**, *451*, 85-93.

- (46) Geus, E. R.; van Bekkum, H.; Bakker, W. J. W.; Moulijn, J. A. High-temperature stainless steel supported zeolite (MFI) membranes: preparation, module construction, and permeation experiments, *Microporous Mater.* **1993**, *1*, 131-147.
- (47) Courthial, L.; Bandot, A.; Tayakout-Fayolle, M.; Jallut, C. Transient Method for Mass-Transfer Characterization Through Supported Zeolite Membranes: Extension to Two Components, *A.I.Ch.E.J.* **2013**, *59*, 959-970.
- (48) Matsufuji, T.; Watanabe, K.; Nishiyama, N.; Egashira, Y.; Matsukata, M.; Ueyama, K. Permeation of hexane isomers through an MFI membrane, *Ind. Eng. Chem. Res.* **2000**, *39*, 2434-2438.
- (49) Matsufuji, T.; Nishiyama, N.; Matsukata, M.; Ueyama, K. Separation of butane and xylene isomers with MFI-type zeolitic membrane synthesized by a vapor-phase transport method, *J. Membr. Sci.* **2000**, *178*, 25-34.
- (50) Chempath, S.; Snurr, R. Q.; Low, J. J. Molecular modeling of binary liquid-phase adsorption of aromatics in silicalite, *A.I.Ch.E.J.* **2004**, *50*, 463-469.
- (51) Kolvenbach, R.; Al-Yassir, N.; S.S. Al-Khattaf, S. S.; Gobin, O. C.; Ahn, J. H.; Jentys, A.; Lercher, J. A. A comparative study of diffusion of benzene/p-xylene mixtures in MFI particles, pellets and grown membranes, *Catal. Today* **2011**, *168*, 147-157.
- (52) Bennett, K. H.; Cook, K. D.; Falconer, J. L.; Noble, R. D. Time-dependent permeance of gas mixtures through zeolite membranes, *Anal. Chem.* **1999**, *71*, 1016-1020.
- (53) Tsotsalas, M.; Hejcik, P.; Sumida, K.; Kalay, Z.; Furukawa, S.; Kitagawa, S. Impact of Molecular Clustering inside Nanopores on Desorption Processes, *J. Am. Chem. Soc.* **2013**, *135*, 4608-4611.
- (54) Krishna, R.; Baur, R. Diffusion, Adsorption and Reaction in Zeolites: Modelling and Numerical Issues, <http://www.science.uva.nl/research/cr/zeolite/>, University of Amsterdam, Amsterdam, 11 November 2003.
- (55) Krishna, R.; van Baten, J. M. Investigating the potential of MgMOF-74 membranes for CO₂ capture, *J. Membr. Sci.* **2011**, *377*, 249-260.
- (56) Bhadra, S. J.; Farooq, S. Separation of Methane/Nitrogen Mixture by Pressure Swing Adsorption for Natural Gas Upgrading, *Ind. Eng. Chem. Res.* **2011**, *50*, 14030-14045.
- (57) Majumdar, B.; Bhadra, S. J.; Marathe, R. P.; Farooq, S. Adsorption and Diffusion of Methane and Nitrogen in Barium Exchanged ETS-4, *Ind. Eng. Chem. Res.* **2011**, *50*, 3021-3034.
- (58) Habgood, H. W. The kinetics of molecular sieve action. Sorption of nitrogen-methane mixtures by Linde molecular sieve 4A, *Canad. J. Chem.* **1958**, *36*, 1384-1397.
- (59) Kuznicki, S. M.; Bell, V. A.; Nair, S.; Hillhouse, H. W.; Jacobinas, R. M.; Braunbarth, C. M.; Toby, B. H.; Tsapatsis, M. A titanosilicate molecular sieve with adjustable pores for size-selective adsorption of molecules, *Nature* **2001**, *412*, 720-724.
- (60) Carlson, N. W.; Dranoff, J. S. Competitive adsorption of methane and ethane on 4A zeolite. Fundamentals of Adsorption; Edited by A.I. Liapis, AIChE: New York, 1986.
- (61) Krishna, R. Diffusion of binary mixtures in microporous materials: Overshoot and roll-up phenomena, *Int. Commun. Heat Mass Transf.* **2000**, *27*, 893-902.
- (62) Niessen, W.; Karge, H. G. Diffusion of p-xylene in single and binary systems investigated by FTIR spectroscopy, *Microporous Mater.* **1993**, *1*, 1-8.
- (63) Karge, H. G. Infrared spectroscopic investigation of diffusion, co-diffusion and counter-diffusion of hydrocarbon molecules in zeolites, *C.R. Chim.* **2005**, *8*, 303-319.
- (64) Kärger, J.; Bülow, M. Theoretical prediction of uptake behaviour in adsorption kinetics of binary gas mixtures using irreversible thermodynamics, *Chem. Eng. Sci.* **1975**, *30*, 893-896.
- (65) Khalighi, M.; Chen, Y. F.; Farooq, S.; Karimi, I. A.; Jiang, J. W. Propylene/Propane Separation Using SiCHA, *Ind. Eng. Chem. Res.* **2013**, *52*, 3877-3892.
- (66) Pirngruber, G. D.; Carlier, V.; Leinekugel-le-Cocq, D. Post-Combustion CO₂ Capture by Vacuum Swing Adsorption Using Zeolites – a Feasibility Study, *Oil Gas Sci. Technol.* **2013**, *XX*, XXX-XXX. <http://dx.doi.org/10.2516/ogst/2012067>.

- (67) Pirngruber, G. D.; Hamon, L.; Bourelly, S.; Llewellyn, P. L.; Lenoir, E.; Guillerm, V.; Serre, C.; Devic, T. A Method for Screening the Potential of MOFs as CO₂ Adsorbents in Pressure Swing Adsorption Processes, *ChemSusChem* **2012**, *5*, 762-776.
- (68) Hamon, L.; Jolimaître, E.; Pirngruber, G. D. CO₂ and CH₄ Separation by Adsorption Using Cu-BTC Metal-Organic Framework, *Ind. Eng. Chem. Res.* **2010**, *49*, 7497-7503.
- (69) Peralta, D.; Barthelet, K.; Pérez-Pellitero, J.; Chizallet, C.; Chaplais, G.; Simon-Masseron, A.; Pirngruber, G. D. Adsorption and Separation of Xylene Isomers: CPO-27-Ni vs HKUST-1 vs NaY, *J. Phys. Chem. C* **2012**, *116*, 21844-21855.
- (70) Peralta, D.; Chaplais, G.; Simon-Masseron, A.; Barthelet, K.; Chizallet, C.; Quoineaud, A.-A.; Pirngruber, G. D. Comparison of the behaviour Metal-Organic Frameworks and Zeolites for Hydrocarbon Separations, *J. Am. Chem. Soc.* **2012**, *134*, 8115-8126.
- (71) Peralta, D.; Chaplais, G.; Simon-Masseron, A.; Barthelet, K.; Pirngruber, G. D. Separation of C6 paraffins using Zeolitic Imidazolate Frameworks: comparison with zeolite 5A, *Ind. Eng. Chem. Res.* **2012**, *51*, 4692-4702.
- (72) Bloch, E. D.; Queen, W. L.; Krishna, R.; Zadrozny, J. M.; Brown, C. M.; Long, J. R. Hydrocarbon Separations in a Metal-Organic Framework with Open Iron(II) Coordination Sites, *Science* **2012**, *335*, 1606-1610.
- (73) Herm, Z. R.; Wiers, B. M.; Van Baten, J. M.; Hudson, M. R.; Zajdel, P.; Brown, C. M.; Maschicchi, N.; Krishna, R.; Long, J. R. Separation of Hexane Isomers in a Metal-Organic Framework with Triangular Channels *Science* **2013**, *340*, 960-964.
- (74) Gücüyener, C.; van den Bergh, J.; Gascon, J.; Kapteijn, F. Ethane/Ethene Separation Turned on Its Head: Selective Ethane Adsorption on the Metal-Organic Framework ZIF-7 through a Gate-Opening Mechanism, *J. Am. Chem. Soc.* **2010**, *132*, 17704-17706.
- (75) Yang, J.; Krishna, R.; Li, J.; Li, J. Experiments and Simulations on Separating a CO₂/CH₄ Mixture using K-KFI at Low and High Pressures, *Microporous Mesoporous Mater.* **2014**, *184*, 21-27.
- (76) Palomino, M.; Corma, A.; Rey, F.; Valencia, S. New Insights on CO₂-Methane Separation Using LTA Zeolites with Different Si/Al Ratios and a First Comparison with MOFs, *Langmuir* **2010**, *26*, 1910-1917.
- (77) Krishna, R.; Long, J. R. Screening metal-organic frameworks by analysis of transient breakthrough of gas mixtures in a fixed bed adsorber, *J. Phys. Chem. C* **2011**, *115*, 12941-12950.
- (78) Yang, R. T. Gas separation by adsorption processes; Butterworth: Boston, 1987.
- (79) Do, D. D. Adsorption analysis: Equilibria and kinetics; Imperial College Press: London, 1998.
- (80) van den Broeke, L. J. P.; Krishna, R. Experimental Verification of the Maxwell-Stefan Theory for Micropore Diffusion, *Chem. Eng. Sci.* **1995**, *50*, 2507-2522.
- (81) Walton, K. S.; LeVan, M. D. Consistency of Energy and Material Balances for Bidisperse Particles in Fixed-Bed Adsorption and Related Applications, *Ind. Eng. Chem. Res.* **2003**, *42*, 6938-6948.
- (82) Kooijman, H. A.; Taylor, R. A dynamic nonequilibrium model of tray distillation columns, *A.I.Ch.E.J.* **1995**, *41*, 1852-1863.
- (83) Michelsen, M. An efficient general purpose method of integration of stiff ordinary differential equations, *A.I.Ch.E.J.* **1976**, *22*, 594-597.
- (84) Bulirsch, R.; Stoer, J. Numerical treatment of ordinary differential equations by extrapolation methods, *Numer. Math.* **1966**, *8*, 1-14.
- (85) Krishna, R.; van Baten, J. M. A comparison of the CO₂ capture characteristics of zeolites and metal-organic frameworks, *Sep. Purif. Technol.* **2012**, *87*, 120-126.
- (86) Wu, H.; Yao, K.; Zhu, Y.; Li, B.; Shi, Z.; Krishna, R.; Li, J. Cu-TDPAT, an *rht*-type Dual-Functional Metal-Organic Framework Offering Significant Potential for Use in H₂ and Natural Gas Purification Processes Operating at High Pressures, *J. Phys. Chem. C* **2012**, *116*, 16609-16618.
- (87) Wu, H.; Simmons, J. M.; Srinivas, G.; Zhou, W.; Yildirim, T. Adsorption Sites and Binding Nature of CO₂ in Prototypical Metal-Organic Frameworks: A Combined Neutron Diffraction and First-Principles Study, *J. Phys. Chem. Lett.* **2010**, *1*, 1946-1951.

- (88) Remy, T.; Peter, S. A.; Van der Perre, S.; Valvekens, P.; De Vos, D. E.; Baron, G. V.; Denayer, J. F. M. Selective Dynamic CO₂ Separations on Mg-MOF-74 at Low Pressures: A Detailed Comparison with 13X, *J. Phys. Chem. C* **2013**, *117*, 9301-9310.
- (89) Liu, J.; Tian, J.; Thallapally, P. K.; McGrail, B. P. Selective CO₂ Capture from Flue Gas Using Metal–Organic Frameworks - A Fixed Bed Study, *J. Phys. Chem. C* **2012**, *116*, 9575-9581.
- (90) Yang, S.; Sun, J.; Ramirez-Cuesta, A. J.; Callear, S. K.; David, W. I. F.; Anderson, D. P.; Newby, R.; Blake, A. J.; Parker, J. E.; Tang, C. C.; Schröder, M. Selectivity and direct visualization of carbon dioxide and sulfur dioxide in a decorated porous host, *Nature Chemistry* **2012**, *4*, 887-894.
- (91) Vaesen, S.; Guillermin, V.; Yang, Q.; Wiersum, A. D.; Marszalek, B.; Gil, B.; Vimont, A.; Daturi, M.; Devic, T.; Llewellyn, P. L.; Serre, C.; Maurin, G.; De Weireld, G. A robust amino-functionalized titanium(IV) based MOF for improved separation of acid gases, *Chem. Commun.* **2013**, *49*, 10082-10084.
- (92) Sircar, S.; Golden, T. C. Purification of Hydrogen by Pressure Swing Adsorption, *Separ. Sci. Technol.* **2000**, *35*, 667-687.
- (93) Ribeiro, A. M.; Grande, C. A.; Lopes, F. V. S.; Loureiro, J. M.; Rodrigues, A. E. A parametric study of layered bed PSA for hydrogen purification, *Chem. Eng. Sci.* **2008**, *63*, 5258-5273.
- (94) Banu, A. M.; Friedrich, D.; Brandani, S.; Düren, T. A Multiscale Study of MOFs as Adsorbents in H₂ PSA Purification, *Ind. Eng. Chem. Res.* **2013**, *52*, 9946-9957.
- (95) Herm, Z. R.; Krishna, R.; Long, J. R. CO₂/CH₄, CH₄/H₂ and CO₂/CH₄/H₂ separations at high pressures using Mg₂(dobdc), *Microporous Mesoporous Mater.* **2012**, *151*, 481-487.
- (96) Herm, Z. R.; Swisher, J. A.; Smit, B.; Krishna, R.; Long, J. R. Metal-Organic Frameworks as Adsorbents for Hydrogen Purification and Pre-Combustion Carbon Dioxide Capture *J. Am. Chem. Soc.* **2011**, *133*, 5664-5667.
- (97) Kong, G. Q.; Han, Z. D.; He, Y.; Qu, S.; Zhou, W.; Yildirim, T.; Krishna, R.; Zou, C.; Wu, C. D.; Chen, B. Expanded Organic Building Units for the Construction of Highly Porous Metal-Organic Frameworks, *Chem. Eur. J.* **2013**, *19*, 14886-14894.
- (98) Silva, B.; Salomon, I.; Ribeiro, A. M.; Chang, J. S.; Loureiro, J. M.; Rodrigues, A. E. H₂ purification by Pressure Swing Adsorption using CuBTC, *Sep. Purif. Technol.* **2013**, *118*, 744-756.
- (99) Das, N. K.; Chaudhuri, H.; Bhandari, R. K.; Ghose, D.; Sen, P.; Sinha, B. Purification of helium from natural gas by pressure swing adsorption, *Curr. Sci.* **2008**, *95*, 1684-1687.
- (100) Das, N. K.; Kumar, P.; Mallik, C.; Bhandari, R. K. Development of a helium purification system using pressure swing adsorption, *Curr. Sci.* **2012**, *103*, 631-634.
- (101) Liu, J.; Thallapally, P. K.; Strachan, D. Metal–Organic Frameworks for Removal of Xe and Kr from Nuclear Fuel Reprocessing Plants, *Langmuir* **2012**, *28*, 11584-11589.
- (102) Remy, T.; Peter, S. A.; Van Tendeloo, V.; Van der Perre, S.; Lorgouilloux, Y.; Kirschhock, C. E. A.; Baron, G. V.; Denayer, J. F. M. Adsorption and Separation of CO₂ on KFI Zeolites: Effect of Cation Type and Si/Al Ratio on Equilibrium and Kinetic Properties, *Langmuir* **2013**, *29*, 4998-5012.
- (103) Nugent, P.; Belmabkhout, Y.; Burd, S. D.; Cairns, A. J.; Luebke, R.; Forrest, K.; Pham, T.; Ma, S.; Space, B.; Wojtas, L.; Eddaoudi, M.; Zaworotko, M. J. Porous materials with optimal adsorption thermodynamics and kinetics for CO₂ separation, *Nature* **2013**, *495*, 80-84.
- (104) Peter, S. A.; Baron, G. V.; Gascon, J.; Kapteijn, F.; Denayer, J. F. M. Dynamic desorption of CO₂ and CH₄ from amino-MIL-53(Al) adsorbent, *Adsorption* **2013**, *19*, 1235-1244.
- (105) Dubbeldam, D.; Krishna, R.; Calero, S.; Yazaydin, A. Ö. Computer-Assisted Screening of Ordered Crystalline Nanoporous Adsorbents for Separation of Alkane Isomers, *Angew. Chem. Int. Ed.* **2012**, *51*, 11867-11871.
- (106) Minceva, M.; Rodrigues, A. E. Adsorption of xylenes on Faujasite-type zeolite. Equilibrium and Kinetics in Batch Adsorber, *Chem. Eng. Res. Des.* **2004**, *82*, 667-681.
- (107) Minceva, M.; Gomes, P. S.; Meshko, V.; Rodrigues, A. E. Simulated moving bed reactor for isomerization and separation of p-xylene, *Chem. Eng. J.* **2008**, *140*, 305-323.

- (108) Finsy, V.; Verelst, H.; Alaerts, L.; De Vos, D.; Jacobs, P. A.; Baron, G. V.; Denayer, J. F. M. Pore-Filling-Dependent Selectivity Effects in the Vapor-Phase Separation of Xylene Isomers on the Metal-Organic Framework MIL-47, *J. Am. Chem. Soc.* **2008**, *130*, 7110-7118.
- (109) Remy, T.; Baron, G. V.; Denayer, J. F. M. Modeling the Effect of Structural Changes during Dynamic Separation Processes on MOFs, *Langmuir* **2011**, *27*, 13064-13071.
- (110) El Osta, R.; Carlin-Sinclair, A.; Guillou, N.; Walton, R. I.; Vermoortele, F.; Maes, M.; De Vos, D.; Millange, F. Liquid-Phase Adsorption and Separation of Xylene Isomers by the Flexible Porous Metal-Organic Framework MIL-53(Fe), *Chem. Mater.* **2012**, *24*, 2781-2791.
- (111) Nicolau, M. P. M.; Barcia, P. S.; Gallegos, J. M.; Silva, J. A. C.; Rodrigues, A. E.; Chen, B. Single- and Multicomponent Vapor-Phase Adsorption of Xylene Isomers and Ethylbenzene in a Microporous Metal-Organic Framework, *J. Phys. Chem. C* **2009**, *113*, 13173-13179.
- (112) Barcia, P. S.; Guimaraes, D.; Mendes, P. A. P.; Silva, J. A. C.; Guillerm, V.; Chevreau, H.; Serre, C.; Rodrigues, A. E. Reverse shape selectivity in the adsorption of hexane and xylene isomers in MOF UiO-66, *Microporous Mesoporous Mater.* **2011**, *139*, 67-73.
- (113) Moreira, M. A.; Santos, J. C.; Ferreira, A. F. P.; Loureiro, J.; Ragon, F.; Horcajada, P.; Shim, K. E.; Hwang, Y. K.; Lee, U. H.; Chang, J. S.; Serre, C.; Rodrigues, A. E. Reverse Shape Selectivity in the Liquid-Phase Adsorption of Xylene Isomers in Zirconium Terephthalate MOF UiO-66, *Langmuir* **2012**, *28*, 5715-5723.
- (114) Moghadam, P. Z. Molecular simulation studies of gas adsorption and separation in metalorganic frameworks, Ph.D. Dissertation, University of Edinburgh, Edinburgh, 2012
- (115) Vermoortele, F.; Maes, M.; Moghadam, P. Z.; Lennox, M. J.; Ragon, F.; Boulhout, M.; Biswas, S.; Laurier, K. G. M.; Beurroies, I.; Denoyel, R.; Roefsaers, M.; Stock, N.; Duren, T.; Serre, C.; De Vos, D. E. *p*-Xylene-Selective Metal-Organic Frameworks: A Case of Topology-Directed Selectivity, *J. Am. Chem. Soc.* **2011**, *133*, 18526-18529.
- (116) Moreira, M. A.; Santos, J. C.; Ferreira, A. F. P.; Loureiro, J.; Ragon, F.; Horcajada, P.; Yot, P. G.; Serre, C.; Rodrigues, A. E. Toward Understanding the Influence of Ethylbenzene in *p*-Xylene Selectivity of the Porous Titanium Amino Terephthalate MIL-125(Ti): Adsorption Equilibrium and Separation of Xylene Isomers, *Langmuir* **2012**, *28*, 3494-3502.
- (117) Moreira, M. A.; Santos, J. C.; Ferreira, A. F. P.; Loureiro, J.; Ragon, F.; Horcajada, P.; Yot, P. G.; Serre, C.; Rodrigues, A. E. Effect of ethylbenzene in *p*-xylene selectivity of the porous titanium amino terephthalate MIL-125(Ti)-NH₂, *Microporous Mesoporous Mater.* **2012**, *158*, 229-234.
- (118) Jin, Z.; Zhao, H. Y.; Zhao, X. J.; Fang, Q. R.; Long, J. R.; Zhu, G. S. A novel microporous MOF with the capability of selective adsorption of xylenes, *Chem. Commun.* **2010**, *46*, 8612-8614.
- (119) Maes, M.; Vermoortele, F.; Alaerts, L.; Couck, S.; Kirschhock, C. E. A.; Denayer, J. F. M.; De Vos, D. E. Separation of Styrene and Ethylbenzene on Metal-Organic Frameworks: Analogous Structures with Different Adsorption Mechanisms, *J. Am. Chem. Soc.* **2010**, *132*, 15277-15285.
- (120) Remy, T.; Ma, L.; Maes, M.; De Vos, D. E.; Baron, G. V.; Denayer, J. F. M. Vapor-Phase Adsorption and Separation of Ethylbenzene and Styrene on the Metal-Organic Frameworks MIL-47 and MIL-53(Al), *Ind. Eng. Chem. Res.* **2012**, *51*, 14824-14833.
- (121) Takahashi, A.; Yang, R. T. New Adsorbents for Purification: Selective Removal of Aromatics, *A.I.Ch.E.J.* **2002**, *48*, 1457-1468.
- (122) Ren, H.; Ben, T.; Wang, E.; Jing, X.; Xue, M.; Liu, B.; Cui, Y.; Qui, S.; Zhu, G. Targeted synthesis of a 3D porous aromatic framework for selective sorption of benzene, *Chem. Commun.* **2010**, *46*, 291-293.
- (123) Krishna, R.; Goswami, A. N.; Nanoti, S. M.; Rawat, B. S.; Khanna, M. K.; Dobhal, J. Extraction of aromatics from 63-69 °C Naphtha fraction for food grade hexane production using sulpholane and NMP as solvents, *Indian Journal of Technology* **1987**, *25*, 602-606.
- (124) Saint-Remi, J. C.; Baron, G. V.; Denayer, J. F. M. Non-Uniform Chain Length Dependent Diffusion of Short 1-Alcohols in SAPO-34 in Liquid Phase, *J. Phys. Chem. C* **2013**, *117*, 9758-9765.
- (125) Krishna, R.; van Baten, J. M. Entropy-based separation of linear chain molecules by exploiting differences in the saturation capacities in cage-type zeolites, *Sep. Purif. Technol.* **2011**, *76*, 325-330.

- (126) Remy, T.; Saint-Remi, J. C.; Singh, R.; Webley, P. A.; Baron, G. V.; Denayer, J. F. M. Adsorption and Separation of C1-C8 Alcohols on SAPO-34, *J. Phys. Chem. C* **2011**, *115*, 8117-8125.
- (127) Yoon, J. W.; Jang, I. T.; Lee, K.-Y.; Hwang, Y. K.; Chang, J.-S. Adsorptive Separation of Propylene and Propane on a Porous Metal-Organic Framework, Copper Trimesate, *Bull. Korean Chem. Soc.* **2010**, *31*, 220-223.
- (128) Wehring, M.; Gascon, J.; Dubbeldam, D.; Kapteijn, F.; Snurr, R. Q.; Stallmach, F. Self-Diffusion Studies in CuBTC by PFG NMR and MD Simulations, *J. Phys. Chem. C* **2010**, *114*, 10527-10534.
- (129) Geier, S. J.; Mason, J. A.; Bloch, E. D.; Queen, W. L.; Hudson, M. R.; Brown, C. M.; Long, J. R. Selective adsorption of ethylene over ethane and propylene over propane in the metal-organic frameworks M₂(dobdc) (M = Mg, Mn, Fe, Co, Ni, Zn), *Chem. Sci.* **2013**, *4*, 2054-2061.
- (130) Böhme, U.; Barth, B.; Paula, C.; Kuhnt, A.; Schwioger, W.; Alexander Mundstock, A.; Caro, J.; Hartmann, M. Ethene/Ethane and Propene/Propane Separation via the Olefin and Paraffin Selective Metal-Organic Framework Adsorbents CPO-27 and ZIF8, *Langmuir* **2013**, *29*, 8592-8600.
- (131) Da Silva, F. A.; Rodrigues, A. E. Propylene/Propane Separation by Vacuum Swing Adsorption Using 13X Zeolite, *A.I.Ch.E.J.* **2001**, *47*, 341-357.
- (132) Grande, C. A.; Poplow, F.; Rodrigues, A. E. Vacuum pressure swing adsorption to produce polymer-grade polypropylene, *Separ. Sci. Technol.* **2010**, *45*, 1252-1259.
- (133) Van den Bergh, J.; Gücüyener, C.; Pidko, E. A.; Hensen, E. J. M.; Gascon, J.; Kapteijn, F. Understanding the Anomalous Alkane Selectivity of ZIF-7 in the Separation of Light Alkane/Alkene Mixtures, *Chem. Eur. J.* **2011**, *17*, 8832-8840.
- (134) Jia, J.; Sun, F.; Ma, H.; Wang, L.; Cai, K.; Bian, Z.; Gao, L.; Zhu, G. S. Trigonal prism or octahedron: the conformational change of a dendritic six-node ligand in MOFs, *J. Mater. Chem. A* **2013**, *1*, 10112-10115.
- (135) He, Y.; Zhang, Z.; Xiang, S.; Fronczek, F. R.; Krishna, R.; Chen, B. A robust doubly interpenetrated metal-organic framework constructed from a novel aromatic tricarboxylate for highly selective separation of small hydrocarbons, *Chem. Commun.* **2012**, *48*, 6493-6495.
- (136) Matsuda, R.; Kitaura, R.; Kitagawa, S.; Kubota, Y.; Belosludov, R. V.; Kobayashi, T. C.; Sakamoto, H.; Chiba, T.; Takata, M.; Kawazoe, Y.; Mita, Y. Highly controlled acetylene accommodation in a metal-organic microporous material, *Nature* **2005**, *436*, 238-241.
- (137) Fischer, M.; Hoffmann, F.; Fröba, M. New Microporous Materials for Acetylene Storage and C₂H₂/CO₂ Separation: Insights from Molecular Simulations, *ChemPhysChem* **2010**, *11*, 2220-2229.
- (138) He, Y.; Xiong, S.; Zhang, Z.; Xiong, S.; Fronczek, F. R.; Krishna, R.; O'Keeffe, M.; Chen, B. A microporous lanthanide-tricarboxylate framework with the potential for purification of natural gas, *Chem. Commun.* **2012**, *48*, 10856-10858.
- (139) Xu, H.; He, Y.; Zhang, Z.; Xiang, S.; Xiong, S.; Cai, J.; Cui, Y.; Yang, Y.; Qian, G.; Chen, B. A microporous metal-organic framework with both open metal and Lewis basic pyridyl sites for highly selective C₂H₂/CH₄ and C₂H₂/CO₂ gas separation at room temperature, *J. Mater. Chem. A* **2013**, *1*, 77-81.
- (140) Hartmann, M.; Kunz, S.; Himsl, D.; Tangermann, O.; Ernst, S.; Wagener, A. Adsorptive Separation of Isobutene and Isobutane on Cu₃(BTC)₂, *Langmuir* **2008**, *24*, 8634-8642.
- (141) Tijsebaert, B.; Varszegi, C.; Gies, H.; Xiao, F. S.; Bao, X.; Tatsumi, T.; Müller, U.; De Vos, D. Liquid phase separation of 1-butene from 2-butenes on all-silica zeolite RUB-41, *Chem. Commun.* **2008**, 2480-2482.
- (142) Krishna, R.; Smit, B.; Calero, S. Entropy effects during sorption of alkanes in zeolites, *Chem. Soc. Rev.* **2002**, *31*, 185-194.
- (143) Krishna, R.; van Baten, J. M. Screening of zeolite adsorbents for separation of hexane isomers: A molecular simulation study, *Sep. Purif. Technol.* **2007**, *55*, 246-255.
- (144) van Baten, J. M.; Krishna, R. Entropy effects in adsorption and diffusion of alkane isomers in mordenite: An investigation using CBMC and MD simulations, *Microporous Mesoporous Mater.* **2005**, *84*, 179-191.

- (145) Takahashi, A.; Yang, R. T.; Munson, C. L.; Chinn, D. Influence of Ag Content and H₂S Exposure on 1,3-Butadiene/1-Butene Adsorption by Ag Ion-Exchanged Y-Zeolites (Ag-Y), *Ind. Eng. Chem. Res.* **2001**, *40*, 3979-3988.
- (146) Farooq, S.; Ruthven, D. M.; Boniface, H. A. Numerical-Simulation of a Pressure Swing Adsorption Oxygen Unit, *Chem. Eng. Sci.* **1989**, *44*, 2809-2816.
- (147) Rama Rao, V.; Farooq, S.; Krantz, W. B. Design of a Two-Step Pulsed Pressure-Swing Adsorption-Based Oxygen Concentrator, *A.I.Ch.E.J.* **2010**, *56*, 354-370.
- (148) Rama Rao, V. Adsorption based portable oxygen concentrator for personal medical applications, Ph.D. Dissertation, National University of Singapore, Singapore, 2011
- (149) Sircar, S.; Myers, A. L. Gas Separation by Zeolites, Chapter 22. Handbook of Zeolite Science and Technology; Edited by S.M. Auerbach, K.A. Carrado and P.K. Dutta, Marcel Dekker: New York, 2003.
- (150) Ritter, J. A. Development of Pressure Swing Adsorption Technology for Spaceflight Oxygen Concentrators, <http://www.dsls.usra.edu/meetings/hrp2010/pdf/Friday/Ritter.pdf>, NASA Human Research Program, Houston, 2010.
- (151) Rege, S. U.; Yang, R. T. Limits for Air Separation by Adsorption with LiX Zeolite, *Ind. Eng. Chem. Res.* **1997**, *36*, 5358-5365.
- (152) Farooq, S.; Rathor, M. N.; Hidajat, K. A Predictive Model for a Kinetically Controlled Pressure Swing Adsorption Separation Process, *Chem. Eng. Sci.* **1993**, *48*, 4129-4141.
- (153) Farooq, S. Sorption and Diffusion of Oxygen and Nitrogen in Molecular- Sieve RS-10, *Gas Sep. Purif.* **1995**, *9*, 205-212.
- (154) Yang, R. T. Adsorbents: Fundamentals and Applications; John Wiley & Sons, Inc.: Hoboken, New Jersey, 2003.
- (155) Bloch, E. D.; Murray, L.; Queen, W. L.; Chavan, S. M.; Maximoff, S. N.; Bigi, J. P.; Krishna, R.; Peterson, V. K.; Grandjean, F.; Long, G. J.; Smit, B.; Bordiga, S.; Brown, C. M.; Long, J. R. Selective Binding of O₂ over N₂ in a Redox-Active Metal-Organic Framework with Open Iron(II) Coordination Sites, *J. Am. Chem. Soc.* **2011**, *133*, 14814-14822.
- (156) Wang, W.; Yang, J.; Li, L.; Li, J. Research on the adsorption of O₂ in metal-organic frameworks with open Manganese(II) coordination sites, *Functional Materials Letters* **2013**, *6*, 1350004.
- (157) Han, Z. B.; Lu, R. Y.; Liang, Y. F.; Zhou, Y. L.; Chen, Q.; Zeng, M. H. Mn(II)-Based Porous Metal-Organic Framework Showing Metamagnetic Properties and High Hydrogen Adsorption at Low Pressure, *Inorg. Chem.* **2012**, *51*, 674-679.
- (158) Peng, Y.; Zhang, Z.; Zheng, X.; Wang, H.; Xu, C.; Xiao, Q.; Zhong, Y.; Zhu, W. Comparison Study on the Adsorption of CFC-115 and HFC-125 on Activated Carbon and Silicalite-1, *Ind. Eng. Chem. Res.* **2010**, *49*, 10009-10015.
- (159) Krishna, R.; van Baten, J. M. In silico screening of metal-organic frameworks in separation applications, *Phys. Chem. Chem. Phys.* **2011**, *13*, 10593-10616.
- (160) Siepmann, J. I.; Martin, M. G.; Mundy, C. J.; Klein, M. L. Intermolecular potentials for branched alkanes and the vapour-liquid phase equilibria of n-heptane, 2-methylhexane, and 3-ethylpentane, *Mol. Phys.* **1997**, *90*, 687-693.
- (161) Dubbeldam, D.; Calero, S.; Vlugt, T. J. H.; Krishna, R.; Maesen, T. L. M.; Smit, B. United Atom Forcefield for Alkanes in Nanoporous Materials, *J. Phys. Chem. B* **2004**, *108*, 12301-12313.
- (162) Bezus, A. G.; Kiselev, A. V.; Lopatkin, A. A.; Du, P. Q. Molecular statistical calculation of the thermodynamic adsorption characteristics of zeolites using the atom-atom approximation. Part 1. Adsorption of methane by zeolite sodium-X, *J. Chem. Soc., Faraday Trans. II* **1978**, *74*, 367-379.
- (163) Vlugt, T. J. H.; Krishna, R.; Smit, B. Molecular simulations of adsorption isotherms for linear and branched alkanes and their mixtures in silicalite, *J. Phys. Chem. B* **1999**, *103*, 1102-1118.
- (164) Frenkel, D.; Smit, B. Understanding molecular simulations: from algorithms to applications; 2nd Edition, Academic Press: San Diego, 2002.
- (165) Sun, M. S.; Shah, D. B.; Xu, H. H.; Talu, O. Adsorption equilibria of C₁ to C₄ alkanes, CO₂, and SF₆ on silicalite, *J. Phys. Chem. B* **1998**, *102*, 1466-1473.

- (166) Song, L.; Rees, L. V. C. Adsorption and transport of n-hexane in silicalite-1 by the frequency response technique, *J. Chem. Soc.-Faraday Trans.* **1997**, *93*, 649-657.
- (167) Millot, B.; Méthivier, A.; Jobic, H.; Clemenccon, I.; Rebours, B. Adsorption of branched alkanes in silicalite-1: A temperature- programmed-equilibration study, *Langmuir* **1999**, *15*, 2534-2539.
- (168) Millot, B.; Méthivier, A.; Jobic, H. Adsorption of n-alkanes on silicalite crystals. A temperature- programmed desorption study, *J. Phys. Chem. B* **1998**, *102*, 3210-3215.
- (169) Sun, M. S.; Talu, O.; Shah, D. B. Adsorption equilibria of C₅ - C₁₀ normal alkanes in silicalite crystals, *J. Phys. Chem.* **1996**, *100*, 17276-17280.
- (170) Eder, F. Thermodynamics and siting of alkane sorption in molecular sieves, Ph.D. Dissertation, Universiteit Twente, Enschede, 1996
- (171) Zhu, W.; Kapteijn, F.; Moulijn, J. A. Equilibrium adsorption of light alkanes in silicalite-1 by the inertial microbalance technique, *Adsorpt.-J. Int. Adsorpt. Soc.* **2000**, *6*, 159-167.
- (172) Zhu, W.; Kapteijn, F.; van der Linden, B.; Moulijn, J. A. Equilibrium adsorption of linear and branched C₆ alkanes on silicalite-1 studied by the tapered element oscillating microbalance, *Phys. Chem. Chem. Phys.* **2001**, *3*, 1755-1761.
- (173) Jolimaître, E.; Tayakout-Fayolle, M.; Jallut, C.; Ragil, K. Determination of mass transfer and thermodynamic properties of branched paraffins in silicalite by inverse chromatography technique, *Ind. Eng. Chem. Res.* **2001**, *40*, 914-926.
- (174) Gump, C. J.; Noble, R. D.; Falconer, J. L. Separation of hexane isomers through nonzeolite pores in ZSM-5 zeolite membranes, *Ind. Eng. Chem. Res.* **1999**, *38*, 2775-2781.
- (175) Krishna, R.; Paschek, D. Permeation of hexane isomers across ZSM-5 zeolite membranes, *Ind. Eng. Chem. Res.* **2000**, *39*, 2618-2622.
- (176) Santilli, D. S. Pore probe: A new technique for measuring the concentration of molecules inside porous materials at elevated temperatures, *J. Catal.* **1986**, *99*, 335-341.
- (177) Calero, S.; Smit, B.; Krishna, R. Configurational entropy effects during sorption of hexane isomers in silicalite, *J. Catal.* **2001**, *202*, 395-401.
- (178) Krishna, R.; Paschek, D. Molecular simulations of adsorption and siting of light alkanes in silicalite-1, *Phys. Chem. Chem. Phys.* **2001**, *3*, 453-462.
- (179) Dandekar, H. W.; Funk, G. A.; Gillespie, R. D.; Zinnen, H. A.; McGonegal, C. P.; Kojima, M.; Hobbs, S. H., Process for alkane isomerization using reactive chromatography, UOP, Des Plaines, Illinois, USA., *U.S. Pat.*, US 5763730, 1999.
- (180) Dandekar, H. W.; Funk, G. A.; Zinnen, H. A., Process for separating and recovering multimethyl-branched alkanes, UOP LLC, Des Plaines, Illinois, USA., *U.S. Pat.*, US 6069289, 2000.
- (181) Carr, R. W.; Dandekar, H. W. Adsorption with reaction. Reactive Separation Processes; Edited by S. Kulprathipanja, Taylor & Francis: New York, USA, 2001.
- (182) Smit, B.; Krishna, R. Molecular simulations in zeolitic process design, *Chem. Eng. Sci.* **2003**, *58*, 557-568.
- (183) Krishna, R.; van Baten, J. M. Diffusion of hydrocarbon mixtures in MFI zeolite: Influence of intersection blocking, *Chem. Eng. J.* **2008**, *140*, 614-620.
- (184) Fernandez, M.; Kärger, J.; Freude, D.; Pampel, A.; van Baten, J. M.; Krishna, R. Mixture diffusion in zeolites studied by MAS PFG NMR and molecular simulation, *Microporous Mesoporous Mater.* **2007**, *105*, 124-131.
- (185) Chmelik, C.; Heinke, L.; van Baten, J. M.; Krishna, R. Diffusion of n-butane/iso-butane mixtures in silicalite-1 investigated using infrared (IR) microscopy, *Microporous Mesoporous Mater.* **2009**, *125*, 11-16.
- (186) Förste, C.; Germanus, A.; Kärger, J.; Pfeifer, H.; Caro, J.; Pilz, W.; Zikánová, A. Molecular mobility of methane adsorbed in ZSM-5 containing co-adsorbed benzene, and the location of benzene molecules, *J. Chem. Soc., Faraday Trans. 1.* **1987**, *83*, 2301-2309.
- (187) Schuring, D.; Jansen, A. P. J.; van Santen, R. A. Concentration and chainlength dependence of the diffusivity of alkanes in zeolites studied with MD simulations, *J. Phys. Chem. B* **2000**, *104*, 941-948.

- (188) Krishna, R. Exploiting configurational entropy effects for separation of hexane isomers using silicalite-1, *Chem. Eng. Res. Des.* **2001**, *79*, 182-194.
- (189) Vermeiren, W.; Gilson, J.-P. Impact of Zeolites on the Petroleum and Petrochemical Industry, *Top Catal* **2009**, *52*, 1131-1161.
- (190) Jolimaître, E.; Ragil, K.; Tayakout-Fayolle, M.; Jallut, C. Separation of Mono- and Dibranched Hydrocarbons on Silicalite, *A.I.Ch.E.J.* **2002**, *48*, 1927-1937.
- (191) Banerjee, R.; Phan, A.; Wang, B.; Knobler, C.; Furukawa, H.; O’Keeffe, M.; Yaghi, O. M. High-Throughput Synthesis of Zeolitic Imidazolate Frameworks and Application to CO₂ Capture, *Science* **2008**, *319*, 939-943.
- (192) Cavalcante, C. L.; Ruthven, D. M. Adsorption of Branched and Cyclic Paraffins in Silicalite .2. Kinetics, *Ind. Eng. Chem. Res.* **1995**, *34*, 185-191.
- (193) Bárcia, P. S.; Silva, J. A. C.; Rodrigues, A. E. Separation by fixed-bed adsorption of hexane isomers in zeolite BETA pellets, *Ind. Eng. Chem. Res.* **2006**, *45*, 4316-4328.
- (194) Bárcia, P. S.; Zapata, F.; Silva, J. A. C.; Rodrigues, A. E.; Chen, B. Kinetic Separation of Hexane Isomers by Fixed-Bed Adsorption with a Microporous Metal-Organic Framework, *J. Phys. Chem. B* **2007**, *111*, 6101-6103.
- (195) Ling, Y.; Chen, Z. X.; Zhai, F. P.; Zhou, Y. M.; Weng, L. H.; Zhao, D. Y. A zinc(II) metal-organic framework based on triazole and dicarboxylate ligands for selective adsorption of hexane isomers, *Chem. Commun.* **2011**, *47*, 7197-7199.
- (196) Maesen, T.; Harris, T., Process for producing high RON gasoline using CFI zeolite, Chevron U.S.A. Inc, San Ramon, CA, US, *U.S. Pat.*, US 70374222 B2, 2006.
- (197) Maesen, T.; Harris, T., Process for producing high RON gasoline using ATS zeolite, Chevron U.S.A. Inc, San Ramon, CA, US, *U.S. Pat.*, US 7029572 B2, 2006.
- (198) Denayer, J. F. M.; Ocakoglu, R. A.; Arik, I. C.; Kirschhock, C. E. A.; Martens, J. A.; Baron, G. V. Rotational entropy driven separation of alkane/isoalkane mixtures in zeolite cages, *Angew. Chem. Int. Ed.* **2005**, *44*, 400-403.
- (199) Duerinck, T.; Denayer, J. F. M. Unusual chain length dependent adsorption of linear and branched alkanes on UiO-66, *Adsorption* **2013**, *XX*, XXX-XXX. <http://dx.doi.org/10.1007/s10450-013-9568-6>.
- (200) Bozbiyik, B.; Duerinck, T.; Lannoeye, L.; De Vos, D. E.; Baron, G. V.; Denayer, J. F. M. Adsorption and Separation of *n*-hexane and cyclohexane on the UiO-66 metalorganic framework, *Microporous Mesoporous Mater.* **2013**, *XXX*, XXX-XXX. <http://dx.doi.org/10.1016/j.micromeso.2013.07.035>.
- (201) Xiang, S. C.; He, Y.; Zhang, Z.; Wu, H.; Zhou, W.; Krishna, R.; Chen, B. Microporous Metal-Organic Framework with Potential for Carbon Dioxide Capture at Ambient Conditions, *Nat. Commun.* **2012**, *3*, 954. <http://dx.doi.org/doi:10.1038/ncomms1956>.
- (202) Belmabkhout, Y.; Pirngruber, G.; Jolimaître, E.; Methivier, A. A complete experimental approach for synthesis gas separation studies using static gravimetric and column breakthrough experiments, *Adsorption* **2007**, *13*, 341-349.
- (203) Krishna, R. Adsorptive separation of CO₂/CH₄/CO gas mixtures at high pressures, *Microporous Mesoporous Mater.* **2012**, *156*, 217-223.
- (204) Couck, S.; Denayer, J. F. M.; Baron, G. V.; Rémy, T.; Gascon, J.; Kapteijn, F. An Amine-Functionalized MIL-53 Metal-Organic Framework with Large Separation Power for CO₂ and CH₄, *J. Am. Chem. Soc.* **2009**, *131*, 6326-6327.
- (205) Mason, J. A.; Sumida, K.; Herm, Z. R.; Krishna, R.; Long, J. R. Evaluating Metal-Organic Frameworks for Post-Combustion Carbon Dioxide Capture via Temperature Swing Adsorption, *Energy Environ. Sci.* **2011**, *4*, 3030-3040.
- (206) Duan, J.; Higuchi, M.; Krishna, R.; Kiyonaga, T.; Tsutsumi, Y.; Sato, Y.; Kubota, Y.; Takata, M.; Kitagawa, S. High CO₂/N₂/O₂/CO Separation in a Chemically Robust Porous Coordination Polymer with Low Binding Energy, *Chem. Sci.* **2013**, *XX*, XXX-XXX. <http://dx.doi.org/10.1039/C3SC52177J>.

- (207) Delgado, J. A.; Uguina, M. A.; Sotelo, J. L.; Ruíz, B. Fixed-bed adsorption of carbon dioxide–helium, nitrogen–helium and carbon dioxide–nitrogen mixtures onto silicalite pellets, *Sep. Purif. Technol.* **2006**, *49*, 91-100.
- (208) Lu, W.; Sculley, J. P.; Yuan, D.; Krishna, R.; Zhou, H. C. Carbon Dioxide Capture from Air Using Amine-Grafted Porous Polymer Networks *J. Phys. Chem. C* **2013**, *117*, 4057-4061.
- (209) McDonald, T. M.; D'Alessandro, D. M.; Krishna, R.; Long, J. R. Enhanced carbon dioxide capture upon incorporation of *N,N'*- dimethylethylenediamine in the metal-organic framework CuBTri, *Chem. Sci.* **2011**, *2*, 2022-2028.
- (210) McDonald, T. M.; Lee, W. R.; Mason, J. A.; Wiers, B. M.; Hong, C. S.; Long, J. R. Capture of Carbon Dioxide from Air and Flue Gas in the Alkylamine-Appended Metal-Organic Framework mmen-Mg₂(dobpdc), *J. Am. Chem. Soc.* **2012**, *134*, 7056-7065.
- (211) Lamia, N.; Granato, M. A.; Gomes, P. S. A.; Grande, C. A.; Wolff, L.; Leflaive, P.; Leinekugel-le-Cocq, D.; Rodrigues, A. E. Propane/Propylene Separation by Simulated Moving Bed II. Measurement and Prediction of Binary Adsorption Equilibria of Propane, Propylene, Isobutane, and 1-Butene on 13X Zeolite, *Separ. Sci. Technol.* **2009**, *44*, 1485-1509.
- (212) Das, M. C.; Guo, Q.; He, Y.; Kim, J.; Zhao, C. G.; Hong, K.; Xiang, S.; Zhang, Z.; Thomas, K. M.; Krishna, R.; Chen, B. Interplay of Metalloligand and Organic Ligand to Tune Micropores within Isostructural Mixed-Metal Organic Frameworks (M²MOFs) for Their Highly Selective Separation of Chiral and Achiral Small Molecules, *J. Am. Chem. Soc.* **2012**, *134*, 8703-8710.
- (213) Yamamoto, T.; Kim, Y. H.; Kim, B. C.; Endo, A.; Thongprachan, N.; T., O. Adsorption characteristics of zeolites for dehydration of ethanol: Evaluation of diffusivity of water in porous structure, *Chem. Eng. J.* **2012**, *181-182*, 443-448.
- (214) Li, S.; Falconer, J. L.; Noble, R. D.; Krishna, R. Interpreting unary, binary and ternary mixture permeation across a SAPO-34 membrane with loading-dependent Maxwell-Stefan diffusivities, *J. Phys. Chem. C* **2007**, *111*, 5075-5082.
- (215) van den Bergh, J.; Zhu, W.; Gascon, J.; Moulijn, J. A.; Kapteijn, F. Separation and Permeation Characteristics of a DD3R Zeolite Membrane, *J. Membr. Sci.* **2008**, *316*, 35-45.
- (216) Liu, Y.; Zeng, G.; Pan, Y.; Lai, Z. Synthesis of highly c-oriented ZIF-69 membranes by secondary growth and their gas permeation properties, *J. Membr. Sci.* **2011**, *379*, 46-31.
- (217) Bernal, M. P.; Coronas, J.; Menendez, M.; Santamaria, J. Separation of CO₂/N₂ Mixtures Using MFI-Type Zeolite Membranes, *A.I.Ch.E.J.* **2004**, *50*, 127-135.
- (218) Hasegawa, Y.; Tanaka, T.; Watanabe, K.; Jeong, B. H.; Kusakabe, K.; Morooka, S. Separation of CO₂-CH₄ and CO₂-N₂ Systems Using Ion-exchanged FAU-type Zeolite Membranes with Different Si/Al Ratios, *Korean J. Chem. Eng.* **2002**, *19*, 309-313.
- (219) White, J. C.; Dutta, P. K.; Shqau, K.; Verweij, H. Synthesis of Ultrathin Zeolite Y Membranes and their Application for Separation of Carbon Dioxide and Nitrogen Gases, *Langmuir* **2010**, *26*, 10287-10293.
- (220) Li, S.; Falconer, J. L.; Noble, R. D.; Krishna, R. Modeling permeation of CO₂/CH₄, CO₂/N₂, and N₂/CH₄ mixtures across SAPO-34 membrane with the Maxwell-Stefan equations, *Ind. Eng. Chem. Res.* **2007**, *46*, 3904-3911.
- (221) Bux, H.; Chmelik, C.; Van Baten, J. M.; Krishna, R.; Caro, J. Novel MOF-Membrane for Molecular Sieving Predicted by IR-Diffusion Studies and Molecular Modeling, *Adv. Mater.* **2010**, *22*, 4741-4743.
- (222) van den Bergh, J.; Zhu, W.; Groen, J. C.; Kapteijn, F.; Moulijn, J. A.; Yajima, K.; Nakayama, K.; Tomita, T.; Yoshida, S. Natural Gas Purification with a DDR Zeolite Membrane; Permeation Modelling with Maxwell-Stefan Equations, *Stud. Surf. Sci. Catal.* **2007**, *170*, 1021-1027.
- (223) Tomita, T.; Nakayama, K.; Sakai, H. Gas separation characteristics of DDR type zeolite membrane, *Microporous Mesoporous Mater.* **2004**, *68*, 71-75.
- (224) Himeno, S.; Tomita, T.; Suzuki, K.; Nakayama, K.; Yoshida, S. Synthesis and Permeation Properties of a DDR-type zeolite membrane for Separation of CO₂/CH₄ Gaseous Mixtures, *Ind. Eng. Chem. Res.* **2007**, *46*, 6989-6997.

- (225) Huang, A.; Bux, H.; Steinbach, F.; Caro, J. Molecular-Sieve Membrane with Hydrogen Permselectivity: ZIF-22 in LTA Topology Prepared with 3-Aminopropyltriethoxysilane as Covalent Linker, *Angew. Chem. Int. Ed.* **2010**, *122*, 5078-5081.
- (226) Bux, H.; Feldhoff, A.; Cravillon, J.; Wiebcke, M.; Li, Y.-S.; Caro, J. Oriented Zeolitic Imidazolate Framework-8 Membrane with Sharp H₂/C₃H₈ Molecular Sieve Separation, *Chem. Mater.* **2011**, *23*, 2262-2269.
- (227) Diestel, L.; Liu, X. L.; Li, Y. S.; Yang, W. S.; Caro, J. Comparative permeation studies on three supported membranes: Pure ZIF-8, pure polymethylphenylsiloxane, and mixed matrix membranes, *Microporous Mesoporous Mater.* **2013**, *XXX*, XXX-XXX.
<http://dx.doi.org/10.1016/j.micromeso.2013.09.012>.
- (228) Giannakopoulos, I. G.; Nikolakis, V. Separation of Propylene/Propane Mixtures Using Faujasite-Type Zeolite Membranes, *Ind. Eng. Chem. Res.* **2005**, *44*, 226-230.
- (229) Hasegawa, Y.; Abe, C.; Nishioka, M.; Sato, K.; Nagase, T.; Hanaoka, T. Formation of high flux CHA-type zeolite membranes and their application to the dehydration of alcohol solutions, *J. Membr. Sci.* **2010**, *364*, 318-324.
- (230) Pera-Titus, M.; Fité, C.; Sebastián, V.; Lorente, E.; Llorens, J.; Cunill, F. Modeling Pervaporation of Ethanol/Water Mixtures within 'Real' Zeolite NaA Membranes, *Ind. Eng. Chem. Res.* **2008**, *47*, 3213-3224.
- (231) Khajavi, S.; Jansen, J. C.; Kapteijn, F. Application of hydroxy sodalite films as novel water selective membranes, *J. Membr. Sci.* **2009**, *326*, 153-160.
- (232) Kuhn, J.; Castillo-Sanchez, J. M.; Gascon, J.; Calero, S.; Dubbeldam, D.; Vlugt, T. J. H.; Kapteijn, F.; Gross, J. Adsorption and Diffusion of Water, Methanol, and Ethanol in All-Silica DD3R: Experiments and Simulation, *J. Phys. Chem. C* **2009**, *113*, 14290-14301.
- (233) Voß, H.; Diefenbacher, A.; Schuch, G.; Richter, H.; Voigt, I.; Noack, M.; Caro, J. Butene isomers separation on titania supported MFI membranes at conditions relevant for practice, *J. Membr. Sci.* **2009**, *329*, 11-17.
- (234) Arruebo, M.; Falconer, J. L.; Noble, R. D. Separation of binary C₅ and C₆ hydrocarbon mixtures through MFI zeolite membranes, *J. Membr. Sci.* **2006**, *269*, 171-176.
- (235) Keizer, K.; Burggraaf, A. J.; Vroon, Z. A. E. P.; Verweij, H. Two component permeation through thin zeolite MFI membranes, *J. Membr. Sci.* **1998**, *147*, 159-172.
- (236) Sommer, S.; Melin, T.; Falconer, J. F.; Noble, R. D. Transport of C₆ isomers through ZSM-5 zeolite membranes, *J. Membr. Sci.* **2003**, *224*, 51-67.
- (237) Jeong, B. H.; Hasegawa, Y.; Sotowa, K.; Kusakabe, K.; Morooka, S. Separation of mixtures of benzene and n-alkanes using an FAU-type zeolite membrane, *J. Chem. Eng. Japan.* **2002**, *35*, 167-172.
- (238) Krishna, R.; Li, S.; van Baten, J. M.; Falconer, J. L.; Noble, R. D. Investigation of slowing-down and speeding-up effects in binary mixture permeation across SAPO-34 and MFI membranes, *Sep. Purif. Technol.* **2008**, *60*, 230-236.
- (239) Garg, D. R.; Ruthven, D. M. Effect of the concentration dependence of diffusivity on zeolitic sorption curves, *Chem. Eng. Sci.* **1972**, *27*, 417-423.
- (240) Dietzel, P. D. C.; Besikiotis, V.; Blom, R. Application of metal-organic frameworks with coordinatively unsaturated metal sites in storage and separation of methane and carbon dioxide, *J. Mater. Chem.* **2009**, *19*, 7362-7370.
- (241) Yang, J.; Zhao, Q.; Xu, H.; Li, L.; Dong, J.; Li, J. Adsorption of CO₂, CH₄, and N₂ on Gas Diameter Grade Ion-Exchange Small Pore Zeolites, *J. Chem. Eng. Data* **2012**, *57*, 3701-3709.
- (242) Bárcia, P. S.; Nicolau, M. P. M.; Gallegos, J. M.; Chen, B.; Rodrigues, A. E. Modeling adsorption equilibria of xylene isomers in a microporous metal-organic framework, *Microporous Mesoporous Mater.* **2012**, *155*, 220-226.
- (243) Cavalcante, C. L.; Ruthven, D. M. Adsorption of Branched and Cyclic Paraffins in Silicalite .1. Equilibrium, *Ind. Eng. Chem. Res.* **1995**, *34*, 177-184.

47. Caption for Figures

Figure 1. Photographs, culled from various web sources, of Adolf Fick, James Clerk Maxwell, Josef Stefan, Irving Langmuir, Lars Onsager, Richard M. Barrer, Douglas Ruthven, and Jörg Kärger.

Figure 2. Salient crystallographic structural details for MFI zeolite, also known as silicalite-1. The pore landscape of MFI is also shown.

Figure 3. Channel dimensions of MFI zeolite.

Figure 4. Comparison of surface area, pore volumes, framework densities, fractional pore volumes, and characteristic dimensions of some representative zeolites, MOFs and ZIFs. This information is obtained from molecular simulations.^{7, 8, 24}

Figure 5. MD simulation data for the degree of correlations, D_1/D_{12} , for diffusion of equimolar binary mixtures ($c_1 = c_2$) (a) H₂/CO₂, (b) CO₂/CH₄, (c) H₂/CH₄, (d) CH₄/nC₄H₁₀, (e) CH₄/C₂H₆, and (f) CH₄/C₃H₈ at 300 K in a variety of host materials, as a function of the total pore concentration, $c_t = (q_1 + q_2)/V_p$. As explained in previous works, the comparisons of diffusivities in different host materials is best done in terms of pore concentrations, expressed in terms of the accessible pore volume

V_p .²⁹ Further background information on the degrees of correlations are available in the Supplementary Material 2, also accompanying this publication.

Figure 6. (a) Permeances of H₂ and CO₂ determined for unary and binary mixture permeation across MFI membrane. The graph is constructed using the data of Sandström et al.³⁴ (b) Experimental data on permeances of H₂ and CO₂ in the mixture, compared with the estimations of the M-S model for mixture permeation.⁴ (c) Comparison of experimental CO₂/H₂ permeation selectivities with M-S model, using three different scenarios for correlations. The model for calculation of the permeation fluxes and permeances is based on a simplified analytic solution as derived in our earlier work in which the data inputs are provided.⁴ The pure component isotherm fits are provided in Table 5.

Figure 7. Experimental data of van de Graaf et al.³⁵ for (a, b) component permeances and (c, d) permeation selectivities of (a, c) CH₄/C₂H₆, and (b, d) CH₄/C₃H₈ mixtures as a function of the mole fraction of the tardier component in the feed gas mixture at a total pressure at 101 kPa. The continuous solid lines in (a) and (b) are the Maxwell-Stefan model calculations for the permeance of CH₄ using equation (35) that ignores correlations. In (c) and (d) three different scenarios for correlations are compared with experimental data on permeation selectivities. The model for calculation of the permeation fluxes and permeances is based on a simplified analytic solution as derived in our earlier work in which the data inputs are provided.⁴ The pure component isotherm fits are provided in Table 5.

Figure 8. (a) Comparison of the unary permeances of CH₄ and nC₄H₁₀ with those in equimolar CH₄/nC₄H₁₀ binary mixture across MFI membrane as a function of the temperature.³⁶ (b) Comparison of the unary permeances of H₂ and CO₂ with those in equimolar H₂/CO₂ binary mixture across NH₂-MIL-53(Al) membrane as a function of the temperature.³⁷

Figure 9. (a, b, c) Experimental data^{214, 220, 238} on permeances of CO₂(1) and CH₄(2) determined for binary CO₂(1)/CH₄(2) mixture permeation across SAPO-34 membrane compared with the estimations based on the M-S model ignoring correlations. In (a, b) the upstream compartment consists of equimolar mixtures. In (c) the compositions in the upstream compartment are varied, keeping the total upstream pressure constant at 3.53 MPa. The continuous solid lines in (b) and (c) are the Maxwell-Stefan model calculations for the permeance of CH₄ using equation (35) that ignores correlations. Further details of the model calculations, including isotherm fits, are provided in our earlier work which also contains the data inputs.⁴

Figure 10. Permeances of H₂ and CO₂ across a ZIF-7 membrane, determined as a function of the mole fraction of CO₂ in the gas phase in the upstream compartment in the experiments reported by Li et al.⁴⁰

Figure 11. (a) IRM experimental data for diffusivities of C₂H₄ and C₂H₆ in ZIF-8.⁴¹ (b) Experimental data of Bux et al.⁴¹ for permeances of C₂H₄ and C₂H₆ for mixture permeation across a ZIF-8 membrane;

Figure 12. (a) Permeances of C₃H₆ and C₃H₈ across a ZIF-8 membrane, determined as a function of the mole fraction of propene in the gas phase in the upstream compartment in the experiments reported by Pan et al.⁴⁴ (b, c) Comparison of permeances of C₃H₆ and C₃H₈ for mixture permeation cross ZIF-8 membrane at 308 K, as reported by Liu et al.⁴⁵, with M-S model ignoring correlations. In (b) the upstream compartment consists of equimolar mixtures. In (c) the compositions in the upstream compartment are varied, keeping the total upstream pressure constant at 202 kPa. The M-S model is the simplified analytical model described by Krishna and van Baten.⁴ The estimations are based on the

values of $\rho D_1/\delta = 5 \times 10^{-4} \text{ kg m}^{-2} \text{ s}^{-1}$, and $\rho D_2/\delta = 1.6 \times 10^{-4} \text{ kg m}^{-2} \text{ s}^{-1}$, both determined from unary permeation data. The isotherm parameters are specified in Table 12.

Figure 13. (a) Experimental data of Geus et al.⁴⁶ for transient permeation $\text{CH}_4/\text{nC}_4\text{H}_{10}$ mixture across MFI membrane. (b, c, d) Simulations of transient permeation of $\text{CH}_4(1)/\text{nC}_4\text{H}_{10}(2)$ mixture across MFI membrane at 300 K. The input data are as follows. The Maxwell-Stefan diffusivities are: $\rho D_1/\delta = 0.036 \text{ kg m}^{-2} \text{ s}^{-1}$, $\rho D_2/\delta = 0.000718 \text{ kg m}^{-2} \text{ s}^{-1}$; the membrane thickness $\delta = 200 \text{ }\mu\text{m}$; partial pressures in upstream membrane compartment, $p_1 = p_2 = 50 \text{ kPa}$; $p_2 = 50 \text{ kPa}$. The downstream compartment is placed under vacuum. Three different scenarios are used in (b), (c), and (d). In (b) we use the flux equations (30), including both correlations and thermodynamic coupling. In (c) we use the flux equations (35), ignoring correlations, but including thermodynamic coupling. In (d) we use the flux equations (36) ignoring both correlations and also ignoring thermodynamic coupling, with $\Gamma_{ij} = \delta_{ij}$. The pure component isotherm fits are provided in Table 5.

Figure 14. Schematic of membrane permeation device.

Figure 15. (a) Calculations of the elements Γ_{ij} of the thermodynamic corrector factor matrix $[\Gamma]$ for nC_4/iC_4 mixture as a function of the bulk gas phase fugacity at 300 K, with partial pressures $p_1 = p_2$. (b) Calculations of $(\Gamma_{12} \Theta_2/\Gamma_{11} \Theta_1)$, and $(\Gamma_{21} \Theta_1/\Gamma_{22} \Theta_2)$, as a function of the total mixture loading, $(\Theta_1 + \Theta_2)$. The calculations of the elements Γ_{ij} are obtained using the simplified Equations (15) that should serve as reasonable approximations. (c, d, e) Simulations of transient permeation of $\text{nC}_4(1)/\text{iC}_4(2)$ mixture across MFI membrane at 300 K. The input data are as follows. The Maxwell-Stefan diffusivities at zero-loading: $\rho D_1/\delta = 1.8 \times 10^{-3} \text{ kg m}^{-2} \text{ s}^{-1}$, $\rho D_2/\delta = 4.5 \times 10^{-4} \text{ kg m}^{-2} \text{ s}^{-1}$; the membrane thickness $\delta = 200 \text{ }\mu\text{m}$; partial pressures in upstream membrane compartment, $p_1 = 5 \text{ kPa}$, $p_2 = 95 \text{ Pa}$.

The downstream compartment is placed under vacuum. Three different scenarios are used in (c), (d), and (e). In (c) we use the flux equations (30), including both correlations and thermodynamic coupling. In (d) we use the flux equations (35), ignoring correlations, but including thermodynamic coupling. In (e) we use the flux equations (36) ignoring correlations and also ignoring thermodynamic coupling, with $\Gamma_{ij} = \delta_{ij}$. The pure component isotherm fits are provided in Table 5.

Figure 16. (a, b) Experimental data of Matsufuji et al.⁴⁸ for transient permeation of (a) nC6(1)/2MP(2), and (b) nC6(1)/23DMB(3) mixtures across MFI membrane. (c) Calculations of the elements Γ_{ij} of the thermodynamic corrector factor matrix $[\Gamma]$ for nC6/2MP mixture as a function of the bulk gas phase fugacity at 300 K, with partial pressures $p_1 = p_2$. (d) Calculations of $(\Gamma_{12} \Theta_2 / \Gamma_{11} \Theta_1)$, and $(\Gamma_{21} \Theta_1 / \Gamma_{22} \Theta_2)$, for nC6/2MP mixture as a function of the total mixture loading, $(\Theta_1 + \Theta_2)$. The calculations of the elements Γ_{ij} are obtained using the simplified Equations (15) that should serve as reasonable approximations. The pure component isotherm fits are provided in Table 6.

Figure 17. (a, b) Experimental data of Matsufuji et al.⁴⁹ for transient permeation of (a) 50/50 m-xylene/p-xylene, and (b) 24/50/25 p-xylene/m-xylene/o-xylene mixtures across MFI membrane at 303 K. (c, d) Simulations of transient membrane for 50/50 m-xylene/p-xylene mixtures across MFI membrane. The pure component isotherms are obtained from the molecular simulation data (for the orthorhombic (often denoted as ORTHO) MFI framework) of Chempath et al.⁵⁰ Two different scenarios are used in (c), and (d). In (c) we use the flux equations (35), ignoring correlations, but including thermodynamic coupling. In (d) we use the flux equations (36) ignoring correlations and also ignoring thermodynamic coupling, with $\Gamma_{ij} = \delta_{ij}$.

Figure 18. Simulation of transient permeation of propene(1)/propane(2) mixture across ZIF-8 membrane at 303 K. The isotherm parameters are specified in Table 12. The diffusivities data, obtained from Li et al.⁴², are as follow: $\rho D_1/\delta = 1.39 \times 10^{-3} \text{ kg m}^{-2} \text{ s}^{-1}$, $\rho D_2/\delta = 1.11 \times 10^{-5} \text{ kg m}^{-2} \text{ s}^{-1}$; $D_1/D_2 = 125$; ratio of single-site Langmuir parameter $b_2/b_1 = 1.07$; membrane thickness $\delta = 5 \text{ }\mu\text{m}$; partial pressures in upstream membrane compartment, $p_1 = p_2 = 50 \text{ kPa}$; $p_2 = 50 \text{ kPa}$. The downstream compartment is placed under vacuum. The continuous solid lines using the flux equations (35), neglecting correlation effects. The dashed lines are the calculations using uncoupled flux equations (36) with $\Gamma_{ij} = \delta_{ij}$.

Figure 19. (a) Transient adsorption and desorption profiles for C_2H_6 in LTA-4A zeolite at 298 K. Experimental data of Garg and Ruthven.²³⁹ (b) Variation of the inverse thermodynamic correction factor with fractional occupancy.

Figure 20. (a) Transient desorption profiles for methanol in CuBTC at 298 K. Experimental data of Tsotsalas et al.⁵³ (b) Variation of the inverse thermodynamic correction factor with fractional occupancy.

Figure 21. Discretization scheme for a single spherical crystallite.

Figure 22. Experimental data of Habgood⁵⁸ on transient uptake of $\text{N}_2(1)/\text{CH}_4(2)$ mixture within LTA-4A crystals, exposed to binary gas mixtures at partial pressures (a) $p_1 = 50.9 \text{ kPa}$; $p_2 = 49.1 \text{ kPa}$, and (b) $p_1 = 10 \text{ kPa}$; $p_2 = 90 \text{ kPa}$ at 194 K. The pure component isotherms were fitted to the experimental data using the single-site Langmuir parameters: N_2 : $q_{1,\text{sat}} = 3.6 \text{ mol kg}^{-1}$; $b_1 = 9.4 \times 10^{-5} \text{ Pa}^{-1}$; CH_4 : $q_{2,\text{sat}} = 3.6 \text{ mol kg}^{-1}$; $b_1 = 2.08 \times 10^{-4} \text{ Pa}^{-1}$; Maxwell-Stefan diffusivities: $D_1/r_c^2 = 1.56 \times 10^{-5} \text{ s}^{-1}$; $D_2/r_c^2 = 7.2 \times 10^{-9}$

s^{-1} . The continuous solid lines are the calculations using equation (53). The dashed lines are the calculations using uncoupled flux equations (54) with $\Gamma_{ij} = \delta_{ij}$.

Figure 23. Elements of the matrix of thermodynamic factors Γ_{ij} for $N_2(1)/CH_4(2)$ mixture adsorption in LTA-4A crystals, exposed to equimolar binary gas mixtures.

Figure 24. Influence of diffusivity ratios D_1/D_2 on the overshoot of N_2 for $N_2(1)/CH_4(2)$ mixture within LTA-4A crystals, exposed to binary gas mixtures at partial pressures (a) $p_1 = 50.9$ kPa; $p_2 = 49.1$ kPa.

Figure 25. (a, b) Experimental data of Majumdar et al.⁵⁷ for transient uptake of (a) 10/90, and (b) 50/50 mixtures of $N_2(1)/CH_4(2)$ mixtures in Ba-ETS-4 at 283 K and total pressure of 0.7 MPa. (c) Simulations of transient uptake for 10/90 mixture. Input data simulation: $D_1/r_c^2 = 1 \times 10^{-3} s^{-1}$; $D_2/r_c^2 = 3 \times 10^{-6} s^{-1}$. The mixture thermodynamics equilibrium is determined using the IAST. The continuous solid lines using the flux equations (53), neglecting correlation effects. The dashed lines are simulations using the simplified equation (54), neglecting thermodynamic coupling. Note that the y -axes represent the fractional uptake of each component; this is obtained by dividing each of the component loadings by the the final equilibrated loading within the crystal.

Figure 26. Experimental data of Carlson and Dranoff⁶⁰ on the fractional approach to equilibrium during the co-adsorption of methane and ethane in LTA-4A zeolite.

Figure 27. Experimental data of Niessen and Karge^{62, 63} for uptake of (a) benzene(1)/ethylbenzene(2), and (b) benzene(1)/*p*-xylene(2) mixtures in MFI zeolite (H-ZSM-5). (c) Simulations of transient uptake for benzene(1)/ethylbenzene(2) mixture. Input data simulation: $D_1/r_c^2 = 4 \times 10^{-3} \text{ s}^{-1}$; $D_2/r_c^2 = 8 \times 10^{-4} \text{ s}^{-1}$. The mixture thermodynamics equilibrium is determined using the IAST. The continuous solid lines using the flux equations (53), neglecting correlation effects. The dashed lines are simulations using the simplified equation (54), neglecting thermodynamic coupling.

Figure 28. (a) Experimental data of Kärger and Bülow⁶⁴ for transient uptake of n-heptane(1)/benzene(2) mixture in NaX zeolite at 359 K. (b) Simulations of transient uptake using $D_1/D_2 = 40$; ratio of single-site Langmuir parameter $b_2/b_1 = 6$. The continuous solid lines using the flux equations (53), neglecting correlation effects. The dashed lines are simulations using the simplified equation (54), neglecting both thermodynamic coupling and correlation effects.

Figure 29. (a, b) Simulations of transient uptake of $C_3H_6(1)/C_3H_8(2)$ within crystals of (a) ZIF-8, and (b) CHA. The simulations for ZIF-8 are at 303 K using the isotherm parameters specified in Table 12, along with $D_1/r_c^2 = 1.5 \times 10^{-2} \text{ s}^{-1}$; $D_1/D_2 = 125$; ratio of single-site Langmuir parameter $b_2/b_1 = 1.07$. The simulations for CHA are at 353 K and based on the data provided by Khalighi et al.⁶⁵: $D_1/r_c^2 = 1.73 \times 10^{-4} \text{ s}^{-1}$; $D_1/D_2 = 5000$; ratio of single-site Langmuir parameter $b_2/b_1 = 2.67$. The continuous solid lines using the flux equations (53), neglecting correlation effects. The dashed lines are simulations using the simplified equation (54), neglecting thermodynamic coupling.

Figure 30. Schematic of a packed bed adsorber.

Figure 31. Summary of model equations describing packed bed adsorber, along with discretization scheme.

Figure 32. Experimentally determined breakthrough curves obtained for 50/50 (a) CO₂/CH₄, (b) CO₂/H₂, and (c) CO₂/N₂ mixtures using activated and regenerated samples of Cu-TDPAT.⁸⁶ The smooth lines represent our breakthrough simulations assuming thermodynamic equilibrium, i.e. invoking Equation (65). The experimental breakthrough times are corrected for the time delay between the exit of the packed bed and the entrance to the mass-spectrometer detection unit.

Figure 33. Influence of intra-crystalline diffusion on transient breakthrough of (a) equimolar CO₂/CH₄ mixtures through fixed bed adsorber packed with MgMOF-74 operating at 308 K, and (b) 15/85 CO₂/N₂ mixtures through fixed bed adsorber packed with NiMOF-74 operating at 298 K,. Simulations without intra-crystalline diffusion limitations (i.e. equilibrium between bulk gas and crystal at any location and invoking Equation (65) (indicated by dotted lines) are compared with breakthrough simulations (continuous solid lines) that include intra-crystalline diffusion effects using the simplified equation (54), neglecting thermodynamic coupling (diffusivity values specified in the Figure). For (a) MgMOF-74, the column dimensions, and operating conditions are those used in the experiments of Remy et al.;⁸⁸ the pure component isotherm data are those provided by He et al.¹⁰² For (b) NiMOF-74, the parameter values are: $L = 0.3$ m; voidage of bed, $\varepsilon = 0.4$; interstitial gas velocity, $v = 0.1$ m/s; the pure component data fit parameters are those presented by Krishna and van Baten²⁴ based on the isotherm data of Dietzel et al.²⁴⁰

Figure 34. Comparison of transient breakthroughs (assuming thermodynamic and invoking Equation (65)), of 50/50 CO₂/N₂ mixtures in fixed bed adsorber packed with (a) NaX zeolite, and (b) EMC-1 zeolite, operating at 303 K. The parameter values are: $L = 0.05$ m; voidage of bed, $\varepsilon = 0.775$; interstitial gas velocity, $v = 0.1$ m/s. Also shown in (b) are the experimental breakthroughs for EMC-1 reported by Pirngruber et al.⁶⁶ The isotherm fit parameters used are those reported in Table 3 of Pirngruber et al.⁶⁶

Figure 35. (a, b) Simulation of transient breakthroughs in fixed bed adsorber with input of (a) 15/85/10 CO₂/N₂/SO₂ mixture using NOTT-300, and (b) 85/15 N₂/CO₂ mixtures entering beds packed with NOTT-300, EMC-1, and NaX zeolite. The breakthrough simulations assume thermodynamic and invoke Equation (65). The parameter values are: $L = 0.3$ m; voidage of bed, $\varepsilon = 0.4$; interstitial gas velocity, $v = 0.1$ m/s. The isotherm data for NOTT-300 are from Yang et al.⁹⁰ The isotherm data for EMC-1 and NaX are those reported in Table 3 of Pirngruber et al.⁶⁶

(c) Simulation of transient breakthroughs in fixed bed adsorber with input of 35/60/5 CO₂/CH₄/H₂S mixture using amino-MIL-125(Ti). The breakthrough simulations assume thermodynamic and invoke Equation (65). The parameter values are: $L = 0.3$ m; voidage of bed, $\varepsilon = 0.4$; interstitial gas velocity, $v = 0.1$ m/s. The isotherm data for amino-MIL-125(Ti) are from Vaesen et al.⁹¹

Figure 36. Breakthrough characteristics of 5-component 73/16/3/4/4 H₂/CO₂/CO/CH₄/N₂ mixture in adsorber packed with (a) UiO-66(Zr)-Br, and (b) Cu-TDPAT and maintained at isothermal conditions at 298 K and total pressure of 0.7 MPa. The breakthrough simulations assume thermodynamic equilibrium, i.e. invoking Equation (65). For UiO-66(Zr)-Br, the isotherm parameters are provided by Banu et al;⁹⁴ these isotherms are based on GCMC simulations. Other parameter values are: $L = 0.3$ m; voidage of bed, $\varepsilon = 0.4$; interstitial gas velocity, $v = 0.1$ m/s. It is to be noted that in Banu et al.⁹⁴ the parameters used are $L = 1$ m; voidage of bed, $\varepsilon = 0.38$; superficial gas velocity, $u = 0.1078$ m/s. We

verified that their breakthrough simulations can be reproduced almost precisely using Equation (65) and our simulation methodology. The isotherm data for CuBTC, NaX, and Cu-TDPAT are culled from the literature.^{3, 86, 97, 203}

Figure 37. (a) Ppm ($\text{CO}_2 + \text{CO} + \text{CH}_4 + \text{N}_2$) in outlet gas as a function of the dimensionless time for various adsorbent materials. The data plotted here are on the basis of breakthrough simulations, assuming thermodynamic equilibrium, i.e. invoking Equation (65) for each adsorbent material. The isotherm data for UiO-66(Zr)-Br, UiO-66(Zr), UiO-67(Zr), ZrCl_2 -AzoBDC, and Activated Carbon are from Banu et al.⁹⁴ UiO-66(Zr)-Br, UiO-66(Zr), UiO-67(Zr), ZnCl_2 -AzoBDC, the isotherm parameters are provided isotherms are based on GCMC simulations. Other parameter values are: $L = 0.3$ m; voidage of bed, $\varepsilon = 0.4$; interstitial gas velocity, $v = 0.1$ m/s. (b) The number of moles of 99.95%+ pure H_2 produced per L of adsorbent material during the time interval $0 - \tau_{\text{break}}$ for separation plotted as a function of the dimensionless breakthrough time, τ_{break} , correspond to those when the outlet gas contains less than 500 ppm of impurity.

Figure 38. (a) Comparison of the isosteric heats of adsorption of CO_2 in different materials. (b) Regeneration energy required per kg of material plotted as a function of the number of moles of CO_2 captured per L of adsorbent material during the time interval $0 - \tau_{\text{break}}$.

Figure 39. Adsorption/desorption breakthrough characteristics of 3-component 35.5/47/17.5 $\text{H}_2/\text{CO}_2/\text{CH}_4$ mixture in adsorber packed with CuBTC at 303 K operating at a total pressure of 0.2 MPa. The desorption phase is initiated at time $t = 6550$ s, the 3-component mixture is switched to pure H_2 . The experimental data of Silva et al.⁹⁸ (symbols) are compared with breakthrough simulations (continuous solid lines) assuming thermodynamic equilibrium, i.e. invoking Equation (65). The

experimental conditions correspond to Run 5 of Silva et al⁹⁸: $L = 0.31$ m; voidage of bed, $\varepsilon = 0.52$; interstitial gas velocity, $v = 0.0305$ m/s. The isotherm data for CuBTC are from the Silva paper.

Figure 40. The separation requirements for Fischer-Tropsch tail-gas stream.

Figure 41. Breakthrough characteristics of 5-component equimolar $H_2/CO_2/CO/CH_4/N_2$ mixture in adsorber packed with Cu-TDPAT, CuBTC, NaX, LTA-5A, and MFI and maintained at isothermal conditions at 298 K and total pressure of 1 MPa. Other parameter values are: $L = 0.3$ m; voidage of bed, $\varepsilon = 0.4$; interstitial gas velocity, $v = 0.1$ m/s.

Figure 42. Pulse chromatographic simulations for breakthrough of 80/10/10 $CO_2/CH_4/N_2$ mixtures containing 0.1% Helium in packed beds of (a) MFI, and (b) CuBTC. The total operating pressures is 0.5 MPa and temperature is 298 K. Other parameter values are: $L = 0.3$ m; voidage of bed, $\varepsilon = 0.4$; interstitial gas velocity, $v = 0.1$ m/s. The duration of the pulse is 10 s.

Figure 43. Breakthrough characteristics of (a) 15/85 CO_2/N_2 , (b) 80/20 Xe/Kr, and (c) 400/400/40/10⁶ $CO_2/Xe/Kr/N_2$ mixtures in $Ni_2(dobdc)$ at 298 K. The total pressure at the inlet is 100 kPa in all three cases. The breakthrough simulations, assume thermodynamic equilibrium, i.e. invoking Equation (65). The pure component isotherm data for CO_2 , and N_2 in $Ni_2(dobdc)$ are those reported by Krishna and van Baten²⁴, based on the data of Dietzel et al.²⁴⁰ The pure component isotherm data for Xe and Kr are from Liu et al.¹⁰¹ Other parameter values are: $L = 0.3$ m; voidage of bed, $\varepsilon = 0.4$; interstitial gas velocity, $v = 0.1$ m/s.

Figure 44. Influence of intra-crystalline diffusion on transient breakthrough of equimolar CO₂/CH₄ mixtures through a fixed bed adsorber packed with (a) K-KFI, and (b) Na-KFI zeolites. Simulations without intra-crystalline diffusion limitations (i.e. equilibrium between bulk gas and crystal at any location and invoking Equation (65) (indicated by dotted lines) are compared with breakthrough simulations (continuous solid lines) that include intra-crystalline diffusion effects using the simplified equation (54), neglecting thermodynamic coupling (values specified in the Figure). The column dimensions, operating conditions are those used in the experiments of Remy et al.¹⁰² The pure component isotherm data are those provided by Remy et al.¹⁰²

Figure 45. Transient breakthrough of equimolar CO₂/CH₄ mixtures through fixed bed adsorber packed with (a) K-KFI, and (b) Na-KFI zeolites. The experimental data (shown by dotted lines) of Remy et al.¹⁰² are compared with breakthrough simulations (continuous solid lines) that include intra-crystalline diffusion effects (values specified in the Figure). The simulations use the simplified equation (54), neglecting thermodynamic coupling. The pure component isotherms data, column dimensions, and operating conditions are those used in the experiments of Remy et al.¹⁰²

Figure 46. (a, b) Experimental data of Yang et al.⁷⁵ for transient breakthrough of 40/60 CO₂/CH₄ mixtures through fixed bed adsorber packed with K-KFI zeolite. The experimental data (symbols) of Yang et al.⁷⁵ at flow rates of (a) 16.6 mL/min, and (b) 30 mL/min are compared with breakthrough simulations that assume thermodynamic equilibrium, i.e. invoking Equation (65). (c, d) Experimental data of Yang et al.⁷⁵ comparing the CO₂ breakthroughs for 40/60 CO₂/CH₄ mixtures through fixed beds packed with K-KFI, NaX (=13 X zeolite), and LTA-5A zeolites at flow rates of (c) 16.6 mL/min, and

(d) 30 mL/min. It is to be noted that the simulations presented here use the high pressure isotherm data provided by Yang et al.²⁴¹; these isotherm data are not entirely compatible with the low pressure isotherm data reported by Remy et al.¹⁰²

Figure 47. Transient breakthrough of (a) 50/50 CO₂/CH₄, (b) 10/90 CO₂/N₂, and (c) 30/70 CO₂/H₂ mixtures through fixed bed adsorber packed with SIFSIX-2-Cu-i. Simulations without intra-crystalline diffusion limitations (i.e. equilibrium between bulk gas and crystal at any location and invoking Equation (65) (indicated by dashed lines) are compared with breakthrough simulations (continuous solid lines) that include intra-crystalline diffusion effects using the simplified equation (54), neglecting thermodynamic coupling. The pure component isotherm data of Nugent et al.¹⁰³, after fitting, were used for the IAST calculations. The column dimensions, operating conditions are those used in the experiments of Nugent et al.¹⁰³ (d) Breakthrough characteristics of 5-component 73/16/3/4/4 H₂/CO₂/CO/CH₄/N₂ mixture in adsorber packed with SIFSIX-2-Cu-i and maintained at isothermal conditions at 298 K and total pressure of 0.7 MPa. In (d) the parameter values are: $L = 0.3$ m; voidage of bed, $\varepsilon = 0.4$; interstitial gas velocity, $v = 0.1$ m/s.

Figure 48. Transient breakthrough of 40/60 CO₂/CH₄ mixtures through fixed bed adsorber packed with amino-MIL-53(Al) operating at 303 K and pressures of, (a) 0.1 MPa, (b) 0.5 MPa, and (c) 3 MPa. Simulations without intra-crystalline diffusion limitations (i.e. equilibrium between bulk gas and crystal at any location and invoking Equation (65) are indicated by dashed lines. Breakthrough simulations that include intra-crystalline diffusion effects using the simplified equation (54), neglecting thermodynamic coupling are shown by the continuous solid lines in (c). The adsorption phase of the pure component isotherms reported in the paper of Peter et al.¹⁰⁴ were fitted for the simulations presented here.

Figure 49. Breakthrough simulations for nC6/3MP mixture using ZIF-8 adsorbent, both (a) assuming thermodynamic equilibrium, i.e. invoking Equation (65), and (b) with inclusion of diffusional influences using the simplified equation (54), neglecting thermodynamic coupling. (b) Experimentally determined breakthrough reported in Figure 6 of Peralta et al.⁷¹ compared with the simulations including diffusional limitations. The diffusivity values used in the simulations are $D_{nC6}/r_c^2 = 0.004 \text{ s}^{-1}$; $D_{3MP}/r_c^2 = 2 \times 10^{-6} \text{ s}^{-1}$; $D_{nC6}/D_{3MP} = 1333$. The pure component isotherms, along with fit parameters (cf. Table 7), are from the CBMC simulations of Dubbeldam et al.¹⁰⁵

Figure 50. Breakthrough simulations for nC6/22DMB mixture using ZIF-8 adsorbent, both (a) assuming thermodynamic equilibrium, i.e. invoking Equation (65), and (b) with inclusion of diffusional influences using the simplified equation (54), neglecting thermodynamic coupling. (b) Experimentally determined breakthrough reported in Figure 8 of Peralta et al.⁷¹ compared with the simulations including diffusional limitations. The diffusivity values used in the simulations are $D_{nC6}/r_c^2 = 0.004 \text{ s}^{-1}$; $D_{22DMB}/r_c^2 = 8 \times 10^{-7} \text{ s}^{-1}$; $D_{nC6}/D_{22DMB} = 5000$. The pure component isotherms, along with fit parameters (cf. Table 7), are from the CBMC simulations of Dubbeldam et al.¹⁰⁵

Figure 51. Breakthrough simulations for 3MP/22DMB mixture using ZIF-8 adsorbent, both (a) assuming thermodynamic equilibrium, i.e. invoking Equation (65), and (b) with inclusion of diffusional influences using the simplified equation (54), neglecting thermodynamic coupling. (b) Experimentally determined breakthrough reported in Figure 9 of Peralta et al.⁷¹ compared with the simulations including diffusional limitations. The diffusivity values used in the simulations are $D_{3MP}/r_c^2 = 2 \times 10^{-6} \text{ s}^{-1}$; $D_{22DMB}/r_c^2 = 8 \times 10^{-7} \text{ s}^{-1}$; $D_{3MP}/D_{22DMB} = 3.75$. The pure component isotherms, along with fit parameters (cf. Table 7), are from the CBMC simulations of Dubbeldam et al.¹⁰⁵

Figure 52. Boiling points, and freezing points of C8 hydrocarbons.

Figure 53. Breakthrough simulations for C8 hydrocarbons in BaX assuming thermodynamic equilibrium, i.e. invoking Equation (65). The isotherm data are from Minceva and Rodrigues.¹⁰⁶ The adsorption isotherms for *o*-xylene and *m*-xylene are nearly the same, and the breakthroughs of these isomers will occur at nearly the same times.¹⁰⁷

Figure 54. Snapshot showing the location and orientation of *o*-xylene inside the lozenge-shaped channels of MIL-47(V).

Figure 55. Snapshot showing the location and orientation of *m*-xylene inside the lozenge-shaped channels of MIL-47(V).

Figure 56. Snapshot showing the location and orientation of *p*-xylene inside the lozenge-shaped channels of MIL-47(V).

Figure 57. Snapshot showing the location and orientation of Ethylbenzene inside the lozenge-shaped channels of MIL-47(V).

Figure 58. Snapshot showing the location and orientation of nC8 inside the lozenge-shaped channels of MIL-47(V).

Figure 59. Snapshot showing the location and orientation of Styrene inside the lozenge-shaped channels of MIL-47(V).

Figure 60. (a) Experimental data on pure component isotherms for C8 hydrocarbons in MIL-47(V) at 383 K, as reported by Finsy et al.¹⁰⁸ (b) Breakthrough simulations for C8 hydrocarbons in MIL-47(V) assuming thermodynamic equilibrium, i.e. invoking Equation (65). (c) Breakthrough simulations with inclusion of intra-crystalline diffusion using the simplified equation (54), neglecting thermodynamic coupling.

Figure 61. (a) Experimental data of Remy et al.¹⁰⁹ on pure component isotherms for C8 hydrocarbons in MIL-53(Al) at 383 K. (b) Breakthrough simulations for xylene isomers in MIL-53(Al) assuming thermodynamic equilibrium, i.e. invoking Equation (65). (c) Breakthrough simulations for C8 hydrocarbons in MIL-53, with inclusion of intra-crystalline diffusion using the simplified equation (54), neglecting thermodynamic coupling.

Figure 62. (a) Pure component isotherm data of El Costa et al.¹¹⁰ that has been fitted with the dual-site Langmuir-Freundlich model. Note that the x-axis is in terms of the molar concentrations, not pressures. (b). Breakthrough simulations for xylene isomers in MIL-53(Fe) assuming thermodynamic equilibrium, i.e. invoking Equation (65). (c, d, e, f) Breakthrough simulations for (c) ternary, and (d, e, f) binary xylene isomer mixtures in MIL-53(Fe), with inclusion of intra-crystalline diffusion using the simplified equation (54), neglecting thermodynamic coupling.

Figure 63. (a) CBMC simulations of pure component isotherms for C8 hydrocarbons in MgMOF-74. The isotherm parameter fits are provided in Table 8. (b) Breakthrough simulations for C8 hydrocarbons in MgMOF-74 assuming thermodynamic equilibrium, i.e. invoking Equation (65). (c) Breakthrough simulations for C8 hydrocarbons in MgMOF-74, with inclusion of intra-crystalline diffusion using the simplified equation (54), neglecting thermodynamic coupling.

Figure 64. (a) CBMC simulations of pure component isotherms for xylene isomers in NiMOF-74; the pure component isotherm fit parameters are provided in Table 9. (b) Pulse chromatographic simulations of o-xylene/m-xylene/p-xylene ternary mixture in NiMOF-74 bed. These simulations assume thermodynamic equilibrium. It is to be noted that pulse chromatographic simulations reflect the hierarchy of adsorption strengths in the Henry regime of adsorption

Figure 65. Transient breakthrough of m-xylene/p-xylene binary mixture in NiMOF-74 bed. (a) Comparison of the experimental breakthrough data of Peralta et al.⁶⁹ with breakthrough simulations including intra-crystalline diffusion, using the simplified equation (54), neglecting thermodynamic coupling. (b) Comparison breakthrough simulations assuming thermodynamic equilibrium, i.e. invoking Equation (65) with the corresponding simulations including intra-crystalline diffusion, using the simplified equation (54), neglecting thermodynamic coupling.

Figure 66. Transient breakthrough of 4-component C8 hydrocarbons in Zn(bdc)dabco bed at partial pressures of (a) 400 Pa, and (b) 2750 Pa corresponding, respectively the Runs q1 and q2 of Nicolau et

al.¹¹¹. The breakthrough simulations assume thermodynamic equilibrium, i.e. invoking equations (59). The pure component isotherm parameters are obtained from the publication of Barcia et al.²⁴²

Figure 67. Snapshots showing the location and conformations of *o*-xylene, *m*-xylene, *p*-xylene, nC8, and ethylbenzene within the channels of Co(BDP).

Figure 68. (a) CBMC simulations of the pure component isotherms for C8 hydrocarbons in Co(BDP) at 433 K.¹⁵⁹ The continuous solid lines are the dual-Langmuir-Freundlich fits of the pure component isotherms using the parameter values specified in Table 10. (b) Breakthrough simulations for C8 hydrocarbons in Co(BDP) assuming thermodynamic equilibrium, i.e. invoking Equation (65). Further details of the CBMC simulations, along with additional snapshots, are available in our earlier work.¹⁵⁹

Figure 69. (a, b) Breakthrough simulations for ethylbenzene/styrene mixtures in (a) MIL-47(V), and (b) MIL-53(AI) at 298 K. The operations are in the liquid phase, with step inputs of feed concentrations $c_{i0} = 0.47 \text{ mol L}^{-1}$ in both cases. The dotted lines are simulations assuming thermodynamic equilibrium, i.e. invoking Equation (65). The continuous solid lines represent breakthrough simulations with inclusion of intra-crystalline diffusion using the simplified equation (54), neglecting thermodynamic coupling. The isotherms used in the simulations are the experimental data reported by Maes et al.¹¹⁹

Figure 70. Breakthrough simulations for benzene/cyclohexane mixtures in fixed beds of (a) Ag-Y zeolite at 393 K, and (b) PAF-2 at 298 K. The simulations assume thermodynamic equilibrium, i.e.

invoking Equation (65). The pure component isotherm data are from Takahashi and Yang,¹²¹ and Ren et al.¹²²

Figure 71. Experimental data of Saint-Remi et al.¹²⁴ for transient uptake of (a) ethanol/1-propanol, (b) methanol/1-propanol, and (c) methanol/ethanol mixtures within SAPO-34, that is the structural analog of CHA zeolite. In (a, b, c) the component uptakes in mixtures are compared with the pure component uptakes.

Figure 72. (a) CBMC simulations of pure component adsorption isotherms for 1-alcohols in CHA at 300 K. (b) Saturation capacities for adsorption of 1-alcohols in CHA at 300 K. (c) Snapshots showing the conformations of 1-alcohols in CHA at saturation conditions.

Figure 73. CBMC mixture simulations for (a) methanol – ethanol, (b) ethanol - 1-propanol, (c) ethanol -1-hexanol in CHA at 300 K. The partial fugacities in the bulk fluid phase are taken to be equal, i.e. $f_1=f_2$. The continuous solid lines represent calculations of the IAST³⁰ using dual-Langmuir-Freundlich fits of pure component isotherms. Table 11 provides the pure component isotherm fit parameters. The range of liquid phase operation is indicated by the shaded region; the transition between vapor and liquid bulk phase is determined using the Peng-Robinson equation of state.

Figure 74. Simulations of transient uptake of (a) ethanol/1-propanol, (b) methanol/1-propanol, and (c) methanol/ethanol mixtures within CHA crystals, exposed to binary gas mixtures at partial fugacities at 300 K: (a) $f_{\text{ethanol}} = f_{1\text{-propanol}} = 1$ MPa; (b) $f_{\text{methanol}} = f_{1\text{-propanol}} = 0.3$ MPa; (c) $f_{\text{methanol}} = f_{\text{ethanol}} = 0.5$ MPa.

The pure component isotherms were fitted to the experimental data using the dual-site Langmuir-Freundlich parameters as specified in Table 11. The Maxwell-Stefan diffusivities: $D_{methanol}/r_c^2 = 6 \times 10^{-4} \text{ s}^{-1}$; $D_{ethanol}/r_c^2 = 1 \times 10^{-5} \text{ s}^{-1}$; $D_{1-propanol}/r_c^2 = 1 \times 10^{-8} \text{ s}^{-1}$. The continuous solid lines are the calculations of the Maxwell-Stefan model using equation (53). The dashed lines are the calculations of the Maxwell-Stefan model simulations using equation (54) with $\Gamma_{ij} = \delta_{ij}$.

Figure 75. (a) Calculations of the elements Γ_{ij} of the thermodynamic corrector factor matrix $[\Gamma]$ for ethanol(1)/1-propanol(2) mixture as a function of the bulk gas phase fugacity at 300 K, with partial pressures $f_1 = 5f_2$. (b, c) Calculations of $(\Gamma_{12}q_2/\Gamma_{11}q_1)$ for ethanol/1-propanol, methanol/1-propanol, and methanol/ethanol mixtures, expressed as a function of the total mixture loading $q_t = q_1 + q_2$. The calculations of the elements Γ_{ij} are obtained using the simplified Equations (15) that should serve as reasonable approximations.

Figure 76. (a, b, c, d, e, f) Radial profiles of the loadings of ethanol and 1-propanol within CHA crystal, for ethanol/1-propanol mixture uptake for the conditions specified in the legend to Figure 74, monitored at times (a) $t = 10^2 \text{ s}$, (b) $t = 10^3 \text{ s}$, (c) $t = 5 \times 10^3 \text{ s}$, (d) $t = 10^4 \text{ s}$, and (e) $t = 10^7 \text{ s}$.

Figure 77. Transient desorption kinetics for ethanol(1)/1-propanol(2) mixture in CHA at 300 K. Initially the crystal is equilibrated by exposing to an equimolar gas phase mixture with partial fugacities of 1 MPa. At time $t = 0$, the bulk gas phase is maintained with partial fugacities of 1 kPa. The mixture thermodynamics equilibrium is determined using the IAST. The continuous solid lines using the flux equations (53), neglecting correlation effects. The dashed lines are simulations using the simplified equation (54), neglecting thermodynamic coupling.

Figure 78. Breakthrough experimental data of Remy et al.¹²⁶ for separation of (a) ethanol/1-propanol and (b) ethanol-1-hexanol mixtures in a fixed bed adsorber packed with SAPO-34.

Figure 79. Breakthrough simulations for (a) ethanol/1-propanol and (b) ethanol-1-hexanol mixtures in a fixed bed adsorber packed with CHA. The adsorption equilibrium is calculated using the IAST, using the pure component fit parameters in Table 11.

Figure 80. (a) Comparison of experimentally determined transient breakthrough for equimolar mixtures of C₃H₆, and C₃H₈ in packed bed adsorber operating at a total pressure of 100 kPa and 313 K, packed with CuBTC crystallites with *equilibrium based* simulations. The experimental data and chosen conditions are those presented by Yoon et al.¹²⁷ The inlet partial pressures of C₃H₆, and C₃H₈ are 2.5 kPa each; the remainder of the gas is made up of helium. In the breakthrough simulations the intra-crystalline diffusion is considered to be negligible and the assumption specified by Equation (65) is invoked. (b) Here two scenarios for breakthrough simulation results are compared. The first scenario is the same as the one presented in (a), corresponding to equilibrium behaviors, without the influence of intra-crystalline diffusion. The second scenario is one in which the intra-crystalline diffusion is accounted for, but ignoring thermodynamic coupling effects. The M-S diffusivities for C₃H₆, and C₃H₈ are taken to $D_i = 1.7 \times 10^{-11} \text{ m}^2 \text{ s}^{-1}$, and $2 \times 10^{-10} \text{ m}^2 \text{ s}^{-1}$, respectively. The isotherm fit parameters are from He et al.³ The crystallite radius r_c is assumed to be 400 μm .

Figure 81. Comparison of experimentally determined transient breakthrough of an equimolar propene/propane mixture in an adsorber bed packed with FeMOF-74 at 318 K and a total pressure of

100 kPa with simulations in which the assumption specified by Equation (65) is invoked; only the adsorption cycle of the simulations are shown here. The isotherm fit parameters are from He et al.³ Breakthrough experiments, reported by Bloch et al.⁷² were carried out in a 4 mm tube packed with 375 mg of FeMOF-74 crystallites. The crystallites were packed within 120 mm of the tube length, i.e. $L = 0.12$ m. The x -axis is the dimensionless time, obtained by dividing the actual time by the characteristic contact time, $\frac{L\varepsilon}{u_0}$.

Figure 82. Experimental data on transient breakthrough of equimolar ethene/ethane, and propene/propane mixture in an adsorber bed packed with (a) MgMOF-74, and (b) CoMOF-74 at 298 K and a total pressure of 100 kPa. The graph is re-drawn using the experimental data of Böhme et al.¹³⁰

Figure 83. (a) Transient breakthrough of equimolar C_2H_4/C_2H_6 , and C_3H_6/C_3H_8 mixtures in an adsorber bed packed with ZIF-8 at 298 K and a total pressure of 100 kPa. The graph is re-drawn using the experimental data of Böhme et al.¹³⁰ (b, c) Comparison of the experimental breakthroughs (dashed lines) for C_2H_4/C_2H_6 , and C_3H_6/C_3H_8 mixtures with breakthrough simulations (continuous solid lines) using the simplified equation (54), including intra-crystalline diffusion but neglecting thermodynamic coupling. The isotherm parameters are specified in Table 12.

Figure 84. (a, b) The experimental data Gücüyener et al.⁷⁴ on transient breakthrough of $C_2H_4/C_2H_6/H_2$ mixtures in a fixed bed adsorber packed with ZIF-7 are compared with simulations (a) assuming thermodynamic equilibrium, and (b) inclusion of intra-crystalline diffusion effects with $D_1/r_c^2 = 2 \times 10^{-4}$ s⁻¹; $D_1/D_2 = 2$ using the simplified equation (54), neglecting thermodynamic coupling. The column dimensions, and operating conditions correspond to those used in the experiments. The simulations

were performed with the adsorption phase of the isotherms, rather than the desorption phase with the parameters specified in Table 13. In (c) the two sets of simulations results are compared in order to highlight the strong influence of intra-crystalline diffusion on the breakthrough characteristics.

Figure 85. Separation of C_3H_6/C_3H_8 mixtures in a fixed bed adsorber packed with ZIF-7. The pure component isotherm data are from Gücüyener et al.⁷⁴ The isotherm parameters are specified in Table 13. The simulations were performed with the adsorption phase of the isotherms, rather than the desorption phase. Breakthrough simulations assuming thermodynamic equilibrium, i.e. invoking Equation (65), are indicated by the dashed lines. The continuous solids lines are simulations include diffusional effects using the simplified equation (54), neglecting thermodynamic coupling. Other parameter values are: $L = 0.3$ m; voidage of bed, $\varepsilon = 0.4$; interstitial gas velocity, $v = 0.1$ m/s.

Figure 86. (a) Ppm C_2H_2 in the outlet gas of an adsorber bed packed with MgMOF-74, CoMOF-74, M'MOF-3a, and M'MOF-4a. The total bulk gas phase is at 296 K and 100 kPa. The partial pressures of C_2H_2 , and C_2H_4 in the inlet feed gas mixture are, respectively, $p_1 = 1$ kPa, $p_2 = 99$ kPa. (b) Plot of C_2H_2 captured per L of adsorbent, during the time interval τ_{break} , plotted as a function of the time interval τ_{break} . This is the corrected plot of Figure 23 of He et al.³ The y-axis should represent the number of moles of C_2H_2 captured, and not C_2H_4 produced as indicated in Figure 23 of He et al.³. (c) Plot of C_2H_4 produced, containing less than 40 ppm of C_2H_2 , per L of adsorbent, during the time interval τ_{break} , plotted as a function of the time interval τ_{break} .

Figure 87. Transient breakthrough of *equimolar* 6-component $CH_4/C_2H_2/C_2H_4/C_2H_6/C_3H_6/C_3H_8$ mixture with (a) CoMOF-74, (b) FeMOF-74, and (c) UTSA-35a. The isotherm input data are those provided by

He et al.^{3, 135} Other parameter values are: $L = 0.12$ m; voidage of bed, $\varepsilon = 0.75$; interstitial gas velocity, $v = 0.003$ m/s.

Figure 88. (a) IAST calculations for adsorption selectivity, and (b, c, d) transient breakthrough simulations for separation of equimolar C_2H_2/CO_2 mixtures and 296 K using (b) UTSA-30a (Ref: ¹³⁸, $V_p = 0.26$ cm³/g), (c) UTSA-50a (Ref: ¹³⁹, $V_p = 0.35$ cm³/g), and (d) CuBTC (Ref: ³, $V_p = 0.75$ cm³/g).

Figure 89. (a) Breakthrough experiments for 50/50 isobutene/isobutane mixture in adsorber packed with CuBTC and maintained at isothermal conditions at 303 K.¹⁴⁰ (b) Breakthrough simulations for total pressure of 1.6 kPa, assuming thermodynamic equilibrium, i.e. invoking Equation (65). Other parameter values are: $L = 0.3$ m; voidage of bed, $\varepsilon = 0.4$; interstitial gas velocity, $v = 0.1$ m/s. Table 14 provides the pure component isotherm parameters.

Figure 90. Influence of diffusional limitations on the breakthrough characteristics of (a) cis-2-butene/1-butene, and (b) trans-2-butene/1-butene mixtures using RUB-41 zeolite. The simulations are carried out using the experimental isotherm data of Tijsebaert et al.¹⁴¹ Breakthrough simulations assuming thermodynamic equilibrium, i.e. invoking Equation (65), are indicated by the dashed lines. The continuous solid lines are simulations include diffusional effects but ignoring thermodynamic coupling effects and using uncoupled flux equations (36). The diffusivities for cis-2-butene and trans-2-butene are chosen using the data provided by Tijsebaert et al.¹⁴¹ We take the diffusivity of 1-butene to be twice that of trans-2-butene.

Figure 91. (a, b) Influence of diffusional limitations on the breakthrough characteristics of O₂(1)/N₂(2) mixture in a fixed bed adsorbers packed with (a) LTA-5A, and (b) LiX operating at a total pressure of 200 kPa and 298 K. The partial pressures of the components in the bulk gas phase at the inlet are $p_1 = 42$ kPa, $p_2 = 158$ kPa. Other parameter values are: $L = 0.3$ m; voidage of bed, $\varepsilon = 0.4$; interstitial gas velocity, $v = 0.1$ m/s. The continuous solids lines are simulations that include diffusional effects while ignoring thermodynamic coupling effects and using uncoupled flux equations (36). The dashed lines are breakthrough simulations in which diffusional influences are ignored, and thermodynamic equilibrium is assumed to prevail within the crystals. For LiX, the isotherm data are from Rege and Yang.¹⁵¹

Figure 92. (a) Pore landscape of LTA-4A. (b) Influence of diffusional limitations on the breakthrough characteristics of O₂(1)/N₂(2) mixture in a fixed bed adsorber packed with LTA-4A operating at a total pressure of 200 kPa and 298 K. The partial pressures of the components in the bulk gas phase at the inlet are $p_1 = 42$ kPa, $p_2 = 158$ kPa. Other parameter values are: $L = 0.3$ m; voidage of bed, $\varepsilon = 0.4$; interstitial gas velocity, $v = 0.1$ m/s. The continuous solids lines are simulations include diffusional effects with $D_{O_2}/r_c^2 = 2 \times 10^{-3} \text{ s}^{-1}$, and $D_{O_2}/D_{N_2} = 100$, ignoring thermodynamic coupling effects. The adsorption and diffusion data used here are for RS-10 that is a modified version of LTA-4A that affords higher diffusion selectivity in favor of O₂; the data are taken from Farooq et al.^{152, 153} The dashed lines are breakthrough simulations in which diffusional influences are ignored, and thermodynamic equilibrium is assumed to prevail within the crystals.

Figure 93. (a) Structural framework of Fe₂(dobdc). (b) Simulations of the breakthrough characteristics of O₂(1)/N₂(2) mixture in a fixed bed adsorber packed with Fe₂(dobdc) operating at a total pressure of 200 kPa and 211 K. The partial pressures of the components in the bulk gas phase at the inlet are $p_1 = 42$ kPa, $p_2 = 158$ kPa. Other parameter values are: $L = 0.3$ m; voidage of bed, $\varepsilon = 0.4$; interstitial gas

velocity, $v = 0.1$ m/s. The isotherm fit parameters are from Bloch et al.¹⁵⁵ The continuous solids lines are breakthrough simulations in which diffusional influences are ignored, and thermodynamic equilibrium is assumed to prevail within the crystals.

Figure 94. Transient breakthrough simulations for equimolar CFC-115/HFC-125 mixture with MFI zeolite at 298 K and total pressures of (a) 100 kPa, and (b) 1 kPa. Three different scenarios are used in the simulations Breakthrough simulations assuming thermodynamic equilibrium, i.e. invoking Equation (65), are indicated by the dashed lines. The dotted lines are simulations include diffusional effects but ignoring thermodynamic coupling effects and using uncoupled flux equations (36). Simulations that include both diffusion and thermodynamic coupling are indicated by the continuous solid lines. The isotherm data are from Peng et al.¹⁵⁸

Figure 95. CBMC simulations of pure component isotherms for CH_4 (= C1), C_2H_6 (= C3), C_3H_8 (= C3), and nC_4H_{10} (= nC4) at a variety of temperatures compared with the experimental data of Sun et al.¹⁶⁵ The CBMC simulations for nC4 at 298 K are fitted with the dual-Langmuir-Freundlich parameters specified in Table 5. Also shown is snapshot of nC4 molecules within the straight and zig-zag channels of MFI at a total loading of 4 molecules per unit cell.

Figure 96. Comparison of experimental isotherm data of Song and Rees¹⁶⁶ and Millot et al.^{167, 168} with CBMC simulations for nC6 at a variety of temperatures.

Figure 97. CBMC simulations for nC6 isotherm; the CBMC data are fitted with the dual-Langmuir-Freundlich parameters specified in Table 6. Also shown are snapshots showing the location of nC6 molecules within the straight and zig-zag channels of MFI.

Figure 98. Comparison of CBMC simulations of pure component isotherm for n-heptane (= nC7) compared with the experimental data of Sun et al.¹⁶⁹ and Eder.¹⁷⁰ Also shown is snapshot of nC7 molecules at a total loading of 4 molecules per unit cell.

Figure 99. Comparison of CBMC simulations of pure component isotherms for iC₄H₁₀ (= iC4) at a variety of temperatures compared with the experimental data of Sun et al.¹⁶⁵ and Zhu et al.¹⁷¹ The CBMC simulations for iC4 at 298 K are fitted with the dual-Langmuir-Freundlich parameters specified in Table 5. Also shown is snapshot of iC4 molecules at a total loading of 4 molecules per unit cell.

Figure 100. CBMC simulations of pure component isotherm for 2-methylpentane (= 2MP) compared with experimental isotherm data of Zhu et al.¹⁷² at 303 K. The CBMC simulations for 2MP are fitted with the dual-Langmuir-Freundlich parameters specified in Table 6. Also shown is snapshot of 2MP molecules.

Figure 101. Comparison of CBMC simulations of pure component isotherm for 3-methylpentane (= 3MP) with the experimental data of Zhu et al.¹⁷² and Jolimaître et al.¹⁷³ Also shown is snapshot of 3MP molecules.

Figure 102. CBMC simulations of pure component isotherms for 2,2 dimethylbutane (= 22DMB) and 2,3 dimethylbutane (23DMB). Also shown are comparisons with the experimental data of Cavalcante and Ruthven.²⁴³ Also shown are snapshots of 22DMB molecules adsorbed in MFI. The CBMC simulations for 22DMB are fitted with the dual-Langmuir-Freundlich parameters specified in Table 6.

Figure 103. CBMC simulations of pure component isotherms for (a) n-pentane (nC5), 2-methylbutane (2MB), neopentane (neo-P), (b) nC6, 3MP, and 22DMB and (c) nC6, 2MP, 3MP, 22DMB, and 23DMB in MFI at 433 K. The continuous lines in Figure 103 are the dual-Langmuir-Freundlich fits of the isotherms with parameter values specified in Table 16.

Figure 104. (a) CBMC simulations of loadings in the adsorbed phase in equilibrium with binary nC6/2MP mixture with partial pressures $p_1 = p_2$ in the bulk gas phase at 298 K. (b) Calculations of the adsorption selectivity, S_{ads} , using Equation (67). (c) Snapshot showing the location of nC6 ($\Theta_1 = 2/uc$) and 2MP ($\Theta_2 = 2/uc$) molecules at a total loading $\Theta_t = 4/uc$.

Figure 105.(a, b) CBMC simulations of loadings in the adsorbed phase in equilibrium with binary (a) nC6/22DMB, and (b) nC6/23DMB mixtures with partial fugacities $f_1 = f_2$ in the bulk gas phase at 300 K. (c, d) Calculations of the adsorption selectivity, S_{ads} , using Equation (67).

Figure 106. (a) CBMC simulations of loadings in the adsorbed phase in equilibrium with binary nC6/22DMB mixture with partial fugacities $f_2 = 4 f_1$ in the bulk gas phase at 373 K. (b) Calculations of the adsorption selectivity, S_{ads} , using Equation (67). (c) Snapshot showing the location of nC6 ($\Theta_1 = 2/uc$) and 22DMB ($\Theta_2 = 2/uc$) molecules at a total loading $\Theta_t = 4/uc$.

Figure 107. Fluxes of binary nC6/22MB mixture permeation across MFI membrane at 373 K. The experimental data are from Gump et al.¹⁷⁴. The partial pressures in the upstream membrane compartment are such that $p_2 = 4 p_1$.

Figure 108. (a, b) CBMC simulations of loadings in the adsorbed phase in equilibrium with ternary fluid phase containing nC6(1)/3MP(2)/22DMB(3) in MFI at 362 K, with partial fugacities $f_1 = f_2 = f_3$. (c) Experimental data of Santilli¹⁷⁶ for nC6/3MP/22DMB adsorption in MFI, as re-interpreted by Calero et al.¹⁷⁷

Figure 109. (a) CBMC simulations of loadings in the adsorbed phase in equilibrium with binary nC4/iC4 mixture with partial pressures $p_1 = p_2$ in the bulk gas phase at 298 K. (b) Calculations of the adsorption selectivity, S_{ads} , using Equation (67). (c) Snapshot showing the location of nC4 ($\Theta_1 = 2/\text{uc}$) and iC4 ($\Theta_2 = 2/\text{uc}$) molecules at a total loading $\Theta_t = 4/\text{uc}$.

Figure 110. Comparison of the estimations using the Ideal Adsorbed Solution Theory (IAST) with CBMC simulations of component loadings of binary (a) nC4/iC4, and (b) nC6/2MP mixtures.

Figure 111. CBMC simulations of component loadings in (a) ternary mixture of n-pentane (nC5), 2-methylbutane (2MB), neopentane (neo-P), (b) ternary mixture of nC6, 3MP, and 22DMB and (c, d) 5-component mixture containing nC6, 2MP, 3MP, 22DMB, and 23DMB in MFI at 433 K. The continuous lines are IAST calculations using the pure component isotherm fits with parameter values specified in Table 16.

Figure 112. (a, b) CBMC simulations of component loadings in 5-component nC6/2MP/3MP/22DMB/23DMB mixture in MFI at 433 K. (c) Elution profiles in a pulsed chromatographic experiment.^{142, 179-181}

Figure 113. (a) PFG NMR experimental data¹⁸⁴ on self-diffusion coefficients of nC4 in nC4/iC4 mixtures in MFI as a function of the loading of iC4. The total loading in the experiments is $\Theta_t = 4/\text{uc}$. (b) PFG NMR experimental data¹⁸⁶ on self-diffusion coefficients of CH₄ in CH₄/Benzene mixtures in MFI as a function of the loading of Benzene in the mixture. (c, d) Experimental data¹⁸⁷ on self-diffusivities of nC6 and 2-methylpentane (2MP) as a function of the loading of 2MP, keeping the total loading $\Theta_t = 3.5/\text{uc}$.

Figure 114. Conventional process flow scheme for isomerization of n-hexane.

Figure 115. Suggested improved process for nC6 isomerization.

Figure 116. (a, b, c) Breakthrough experiments of Jolimaître et al.¹⁹⁰ for (a) 2MB/2MP, and (b, c) 2MP/22DMB binary mixtures at 473 K. The experimental data correspond to Run 12 (a), Run 17 (b), and Run 18 (b). The continuous solid lines are the breakthrough simulations using Equation (73). The input data are specified by Table 17.

Figure 117. (a, b, c, d) Breakthrough experiments of Jolimaître et al.¹⁹⁰ for 2MB/2MP/22DMB ternary mixtures at 473 K. The experimental data correspond to Run 19 (a), Run 20 (b), Run 21 (c) and Run 22 (d). The continuous solid lines are the breakthrough simulations using Equation (73). The input data are specified by Table 17.

Figure 118. Breakthrough experiments of Jolimaître et al.¹⁹⁰ for (a) 2MP/22DMB, and (b, c) 2MB/2MP/22DMB ternary mixtures at 473 K. The experimental data correspond to Run 18 (a), Run 20 (b), and Run 21 (c). The dotted lines are breakthrough simulations in which diffusional influences are ignored, and thermodynamic equilibrium is assumed to prevail within the crystals. The input data are specified by Table 17.

Figure 119. Influence of diffusional limitations on the RON of product gas exiting the MFI adsorber. The conditions correspond to Run 20 of Jolimaître et al.¹⁹⁰.

Figure 120. Breakthrough experiments of Jolimaître et al.¹⁹⁰ for (a) 2MP/22DMB, and (b, c) 2MB/2MP/22DMB ternary mixtures at 473 K. The experimental data correspond to Run 18 (a), Run 20 (b), and Run 21 (c). The dashed lines are the breakthrough simulations using equation (54) with $\Gamma_{ij} = \delta_{ij}$. The input data are specified by Table 17.

Figure 121. Simulations of breakthrough characteristics for 5-component nC6/2MP/3MP/22DMB/23DMB mixture in a fixed bed adsorber packed with $\text{Fe}_2(\text{BDP})_3$, (framework density $\rho = 1.145 \text{ kg L}^{-1}$), operating at a total pressure of 100 kPa and 433 K. The partial pressures of

the components in the bulk gas phase at the inlet are $p_1 = p_2 = p_3 = p_4 = p_5 = 20$ kPa. Other parameter values are: $L = 0.3$ m; voidage of bed, $\varepsilon = 0.4$; interstitial gas velocity, $v = 0.1$ m/s. In these simulations diffusional limitations are considered to be of negligible importance, i.e invoking equation (65). The IAST calculations of mixture adsorption equilibrium is based on the experimentally determined pure component isotherms; the parameters are available in the Supplementary Material of the paper by Herm et al.⁷³ The parameter sets are provided in Table 18. The solid black line represents the calculations of the RON of the product gas mixture exiting the adsorber; the RON values are on the right y-axis.

Figure 122. Breakthrough characteristics, that include diffusional limitations, for 5-component nC6/2MP/3MP/22DMB/23DMB mixture in a fixed bed adsorber packed with $\text{Fe}_2(\text{BDP})_3$ a total pressure of 100 kPa and 433 K. The partial pressures of the components in the bulk gas phase at the inlet are $p_1 = p_2 = p_3 = p_4 = p_5 = 20$ kPa. Other parameter values are: $L = 0.3$ m; voidage of bed, $\varepsilon = 0.4$; interstitial gas velocity, $v = 0.1$ m/s. These simulations include diffusional effects with $D_{nC6}/r_c^2 = 0.002$ s⁻¹; $D_{nC6}/D_{2MP} = 5$; $D_{nC6}/D_{3MP} = 5$; $D_{nC6}/D_{22DMB} = 10$; $D_{nC6}/D_{23DMB} = 10$ and invoking the flux relations (74) ignoring thermodynamic coupling. These diffusivity values limitations are the same as for $\text{Fe}_2(\text{BDP})_3$ in the paper by Herm et al.⁷³ The parameter sets are provided in Table 18. The IAST calculations of mixture adsorption equilibrium is based on the experimentally determined pure component experimental isotherm data of Herm et al.⁷³

Figure 123. Influence of diffusional limitations on the RON of product gas exiting the $\text{Fe}_2(\text{BDP})_3$ adsorber.

Figure 124. Simulations of breakthrough characteristics for 5-component nC6/2MP/3MP/22DMB/23DMB mixture in a fixed bed adsorber packed with MFI (framework density $\rho = 1.796$ kg L⁻¹) operating at a total pressure of 100 kPa and 433 K. The partial pressures of the

components in the bulk gas phase at the inlet are $p_1 = p_2 = p_3 = p_4 = p_5 = 20$ kPa. Other parameter values are: $L = 0.3$ m; voidage of bed, $\varepsilon = 0.4$; interstitial gas velocity, $v = 0.1$ m/s. In these simulations the chosen crystallite size is such that diffusional limitations are of negligible importance, i.e. invoking equation (65). The IAST calculations of mixture adsorption equilibrium is based on the CBMC determined pure component isotherm with parameters specified in Table 16. The solid black line represents the calculations of the RON of the product gas mixture exiting the adsorber; the RON values are as indicated on the right y -axis.

Figure 125. Arrhenius plot of diffusivities of 2MB, 2MP, 3MP, 22DMB, and 23DMB in MFI zeolite. The data are re-plotted from the experimental results of (a) Cavalcante and Ruthven,¹⁹² and (b) Jolimaître et al.¹⁷³

Figure 126. Influence of diffusional limitations on the breakthrough characteristics for 5-component nC6/2MP/3MP/22DMB/23DMB mixture in a fixed bed adsorber packed with MFI operating at a total pressure of 100 kPa and 433 K. The partial pressures of the components in the bulk gas phase at the inlet are $p_1 = p_2 = p_3 = p_4 = p_5 = 20$ kPa. Other parameter values are: $L = 0.3$ m; voidage of bed, $\varepsilon = 0.4$; interstitial gas velocity, $v = 0.1$ m/s. (a) These simulations include diffusional effects with $D_{nC6}/r_c^2 = 0.002$ s⁻¹; $D_{nC6}/D_{2MP} = 5$; $D_{nC6}/D_{3MP} = 5$; $D_{nC6}/D_{22DMB} = 25$; $D_{nC6}/D_{23DMB} = 25$ and invoking the flux relations (74) ignoring thermodynamic coupling. (b) These simulations include diffusional effects with $D_{nC6}/r_c^2 = 0.002$ s⁻¹; $D_{nC6}/D_{2MP} = 5$; $D_{nC6}/D_{3MP} = 5$; $D_{nC6}/D_{22DMB} = 25$; $D_{nC6}/D_{23DMB} = 25$ with inclusion of thermodynamic coupling using the flux relations (75). The IAST calculations of mixture adsorption equilibrium is based on the CBMC determined pure component isotherm with parameters specified in Table 16. (c) Comparison of dimensionless breakthrough times for each hexane isomer.

Figure 127. Transient uptake inside MFI crystal exposed to a gas phase 5-component nC6/2MP/3MP/22DMB/23DMB mixture at a total pressure of 100 kPa and 433 K. The partial pressures of the components in the bulk gas phase at the inlet are $p_1 = p_2 = p_3 = p_4 = p_5 = 20$ kPa. (a) These uptake simulations ignore thermodynamic coupling. (b) These uptake simulations include thermodynamic coupling using the flux relations (75). The diffusivity data inputs are as in Figure 126.

Figure 128. Influence of diffusional limitations on the RON of product gas exiting the MFI adsorber.

Figure 129. Simulations of breakthrough characteristics for 5-component nC6/2MP/3MP/22DMB/23DMB mixture in a fixed bed adsorber packed with ZIF-77 (framework density $\rho = 1.552$ kg L⁻¹) operating at a total pressure of 100 kPa and 433 K. The simulation details are the same as the ones provided by Herm et al.⁷³ The partial pressures of the components in the bulk gas phase at the inlet are $p_1 = p_2 = p_3 = p_4 = p_5 = 20$ kPa. Other parameter values are: $L = 0.3$ m; voidage of bed, $\varepsilon = 0.4$; interstitial gas velocity, $v = 0.1$ m/s. In these simulations the chosen crystallite is such that diffusional limitations are of negligible importance, i.e invoking equation (65). The simulation details are the same as the ones provided by Herm et al.⁷³ The IAST calculations of mixture adsorption equilibrium is based on the CBMC determined pure component isotherm with parameters specified in Table 19. The solid black line represents the calculations of the RON of the product gas mixture exiting the adsorber; the RON values are on the right y -axis.

Figure 130. Breakthrough characteristics, with inclusion of diffusional limitations, for 5-component nC6/2MP/3MP/22DMB/23DMB mixture in a fixed bed adsorber packed with ZIF-77 a total pressure of 100 kPa and 433 K. The partial pressures of the components in the bulk gas phase at the inlet are $p_1 = p_2 = p_3 = p_4 = p_5 = 20$ kPa. Other parameter values are: $L = 0.3$ m; voidage of bed, $\varepsilon = 0.4$; interstitial gas

velocity, $v = 0.1$ m/s. These simulations include diffusional effects with $D_{nC6}/r_c^2 = 0.0004$ s⁻¹; $D_{nC6}/D_{2MP} = 5$; $D_{nC6}/D_{3MP} = 5$; $D_{nC6}/D_{22DMB} = 10$; $D_{nC6}/D_{23DMB} = 10$ and invoking the flux relations (74) ignoring thermodynamic coupling. The IAST calculations of mixture adsorption equilibrium is based on the CBMC determined pure component isotherm with parameters specified in Table 19.

Figure 131. Comparison of 92+ RON productivities of ZIF-77, Fe₂(BDP)₃, and MFI. The productivity values plotted on the x-axis are obtained from breakthrough simulations with assumption of thermodynamic equilibrium i.e. invoking Equation (65). The productivity values on the y-axis are those obtained from breakthrough simulations taking intra-crystalline diffusion into account. For MFI, the productivity values are obtained using both flux equations (36), ignoring thermodynamic coupling, and equation (35) that includes thermodynamic coupling.

Figure 132. Influence of diffusional limitations on the breakthrough characteristics for 5-component nC6/2MP/3MP/22DMB/23DMB mixture in a fixed bed adsorber packed with BEA. The simulation details are the same as the ones provided by Herm et al.⁷³

Figure 133. Influence of diffusional limitations on the breakthrough characteristics for 5-component nC6/2MP/3MP/22DMB/23DMB mixture in a fixed bed adsorber packed with Zn(bdc)dabco. The simulation details are the same as the ones provided by Herm et al.⁷³

Figure 134. Breakthrough characteristics for 5-component nC6/2MP/3MP/22DMB/23DMB mixture in a fixed bed adsorber packed with ZnHBDC, including diffusional limitations. The simulation details are the same as the ones provided by Herm et al.⁷³

Figure 135. (a) Pulse chromatographic simulations for 5-component nC6/2MP/3MP/22DMB/23DMB mixture in a fixed bed adsorber packed with UiO-66. Other parameter values are: $L = 1$ m; voidage of bed, $\varepsilon = 0.4$; interstitial gas velocity, $v = 0.1$ m/s. The duration of the pulse is 10 s. The simulation details are the same as the ones provided by Dubbeldam et al et al.¹⁰⁵ (b) Pulse chromatographic simulations for binary nC6/cC6 mixture in a fixed bed adsorber packed with UiO-66; the isotherm data are from Bozbiyik et al.²⁰⁰

Figure 136. Influence of diffusional limitations on the breakthrough characteristics for 5-component nC6/2MP/3MP/22DMB/23DMB mixture in a fixed bed adsorber packed with UiO-66. The simulation details are the same as the ones provided by Herm et al.⁷³

Figure 137. Influence of diffusional limitations on the breakthrough characteristics for 5-component nC6/2MP/3MP/22DMB/23DMB mixture in a fixed bed adsorber packed with CFI. The simulation details are the same as the ones provided by Herm et al.⁷³

Figure 138. Influence of diffusional limitations on the breakthrough characteristics for 5-component nC6/2MP/3MP/22DMB/23DMB mixture in a fixed bed adsorber packed with ATS. The simulation details are the same as the ones provided by Herm et al.⁷³

Figure 139. Influence of diffusional limitations on the breakthrough characteristics for 5-component nC6/2MP/3MP/22DMB/23DMB mixture in a fixed bed adsorber packed with Co(BDP). The CBMC simulated pure component isotherms are fitted with the parameters specified in Table 20.

Figure 140. Influence of diffusional limitations on the breakthrough characteristics for 5-component nC6/2MP/3MP/22DMB/23DMB mixture in a fixed bed adsorber packed with MgMOF-74. The CBMC simulated pure component isotherms are fitted with the parameters specified in Table 21.

Figure 141. Influence of diffusional limitations on the breakthrough characteristics for 5-component nC6/2MP/3MP/22DMB/23DMB mixture in a fixed bed adsorber packed with ZnMOF-74. The CBMC simulated pure component isotherms are fitted with the parameters specified in Table 22.

Figure 142. (a) Comparison of 92+ RON productivities of MFI, $\text{Fe}_2(\text{BDP})_3\text{ZIF-77}$, BEA, Zn(bdc)dabco, ZnHBDC, ZIF-8, and UiO-66, CFI, and ATS. The productivity values plotted on the x -axis are obtained from breakthrough simulations with assumption of thermodynamic equilibrium i.e. invoking Equation (65). The productivity values on the y -axis are those obtained from breakthrough simulations taking intra-crystalline diffusion into account. For MFI, the productivity values are obtained using both flux equations (35) that includes thermodynamic coupling. For all other materials, thermodynamic coupling is ignored. The structures marked in black have “normal” adsorption hierarchies. The structures marked in green have “reverse” hierarchies. (b) This presents the same set of data as in (a) but also includes data for Co(BDP), MgMOF-74, and ZnMOF-74.

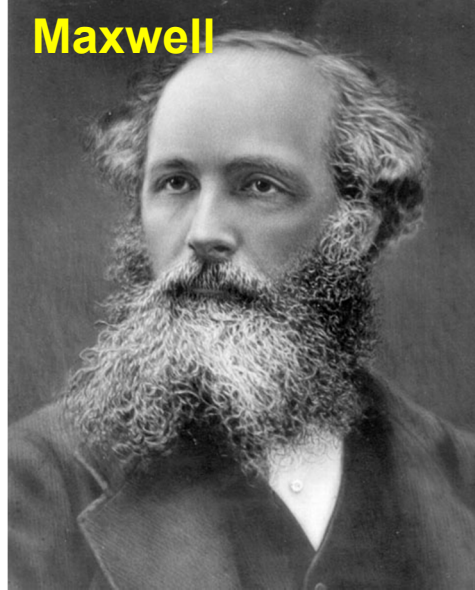
Figure 1

The pioneers

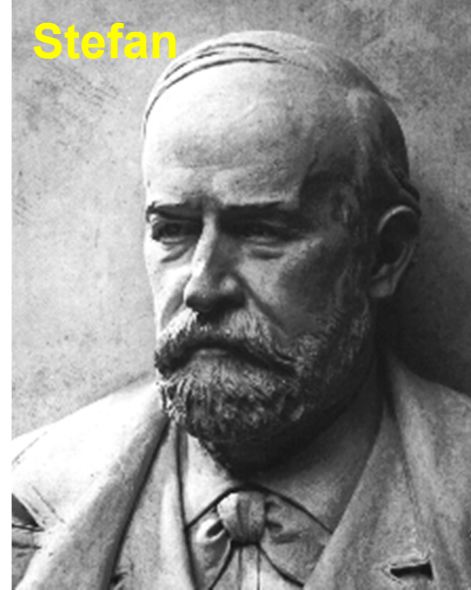
Fick



Maxwell



Stefan



Langmuir



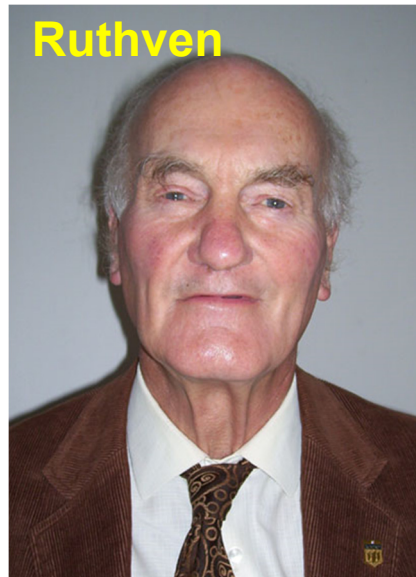
Onsager



Barrer



Ruthven



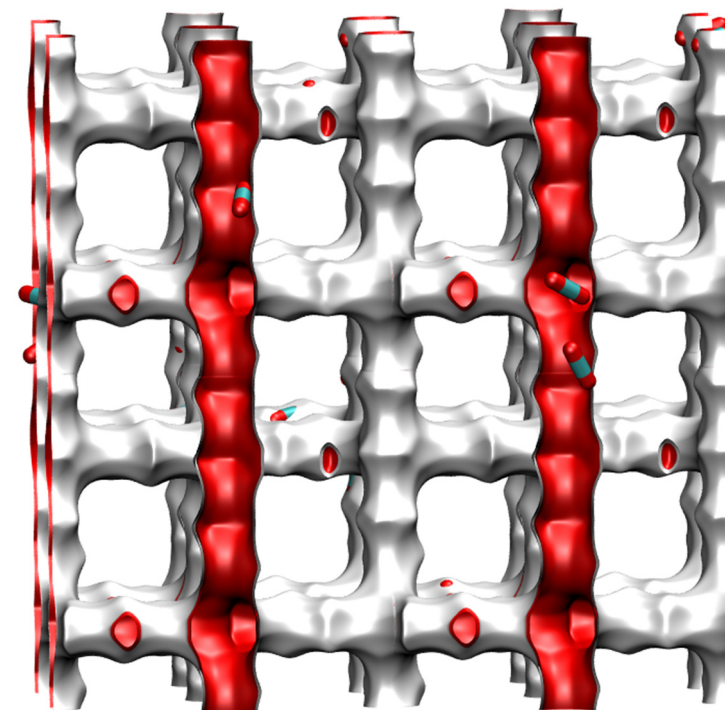
Kärger



Figure 2

MFI structure

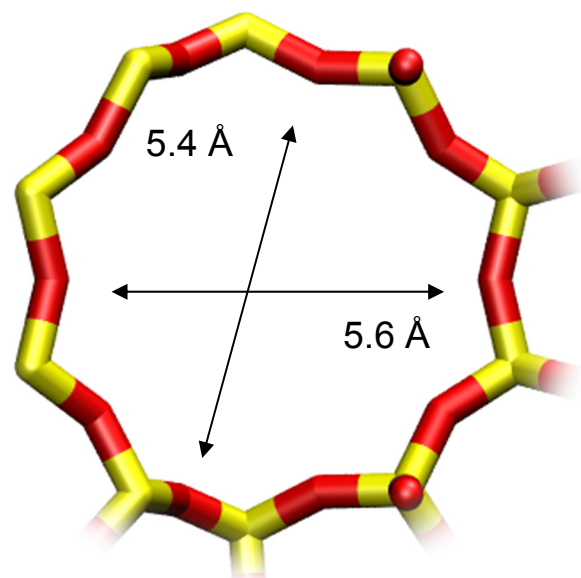
	MFI
$a / \text{\AA}$	20.022
$b / \text{\AA}$	19.899
$c / \text{\AA}$	13.383
Cell volume / \AA^3	5332.025
conversion factor for [molec/uc] to [mol per kg Framework]	0.1734
conversion factor for [molec/uc] to [kmol/m ³]	1.0477
ρ [kg/m ³]	1796.386
MW unit cell [g/mol(framework)]	5768.141
ϕ , fractional pore volume	0.297
open space / $\text{\AA}^3/\text{uc}$	1584.9
Pore volume / cm ³ /g	0.165
Surface area / m ² /g	487.0
DeLaunay diameter / \AA	5.16



Structural information from: C. Baerlocher, L.B. McCusker, Database of Zeolite Structures, International Zeolite Association, <http://www.iza-structure.org/databases/>

MFI structure

10 ring channel
of MFI viewed
along [100]



10 ring channel
of MFI viewed
along [010]

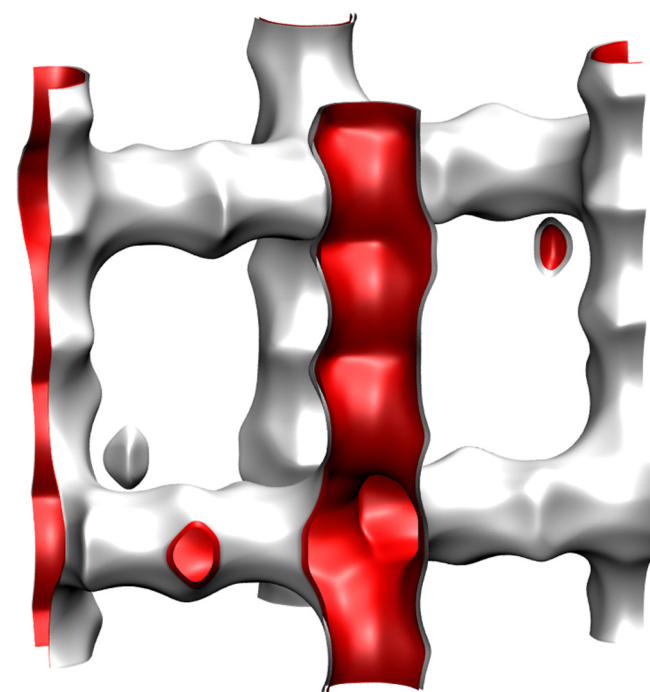
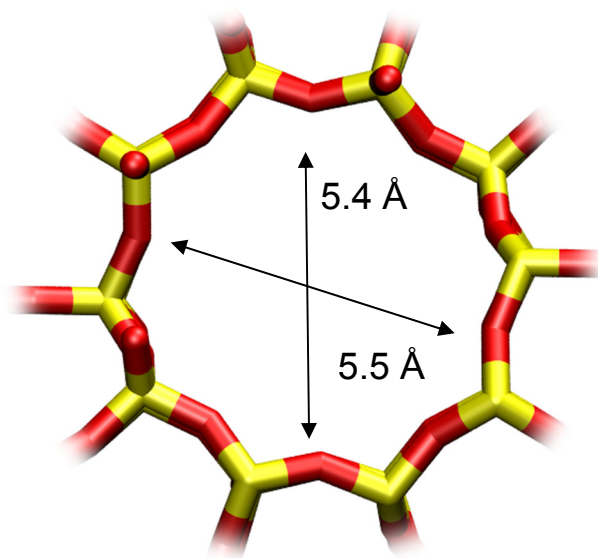


Figure 4

Comparing MOFs, ZIFs and Zeolites

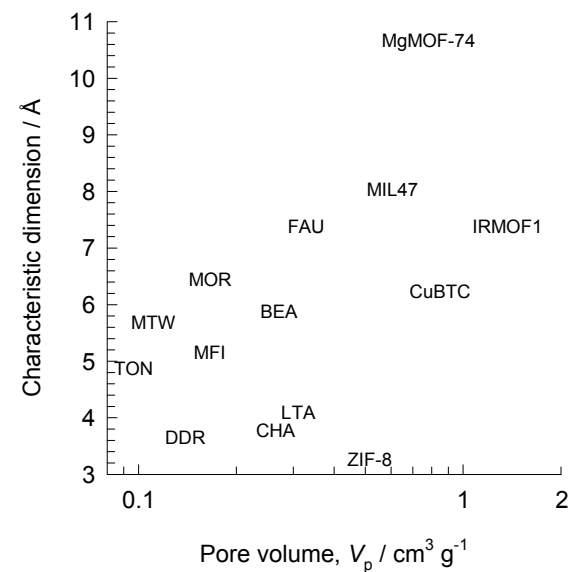
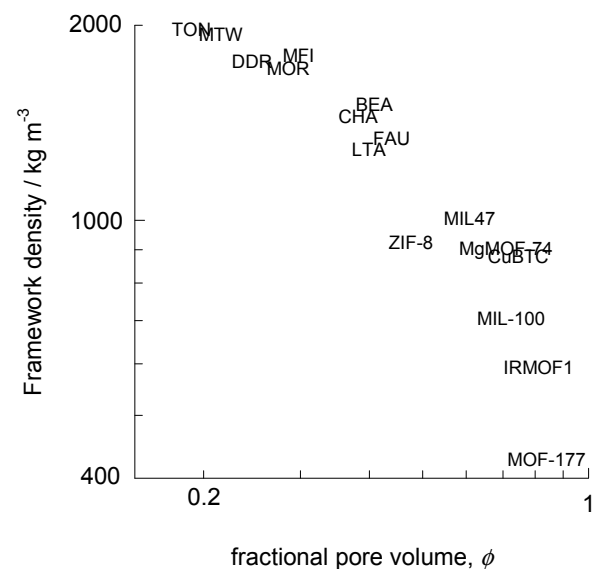
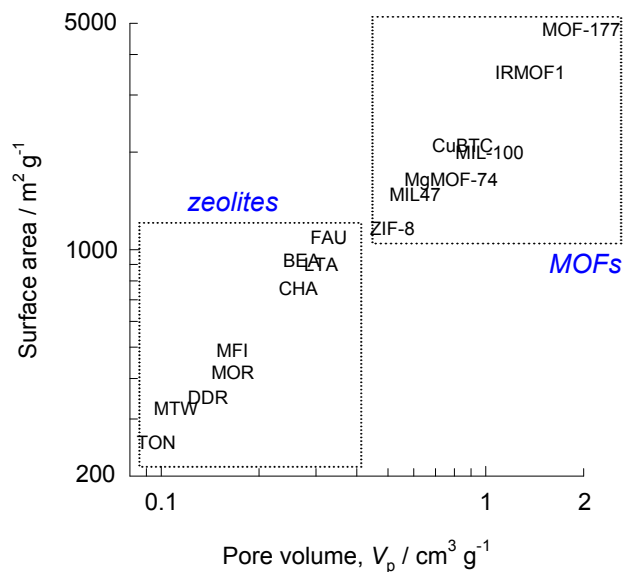
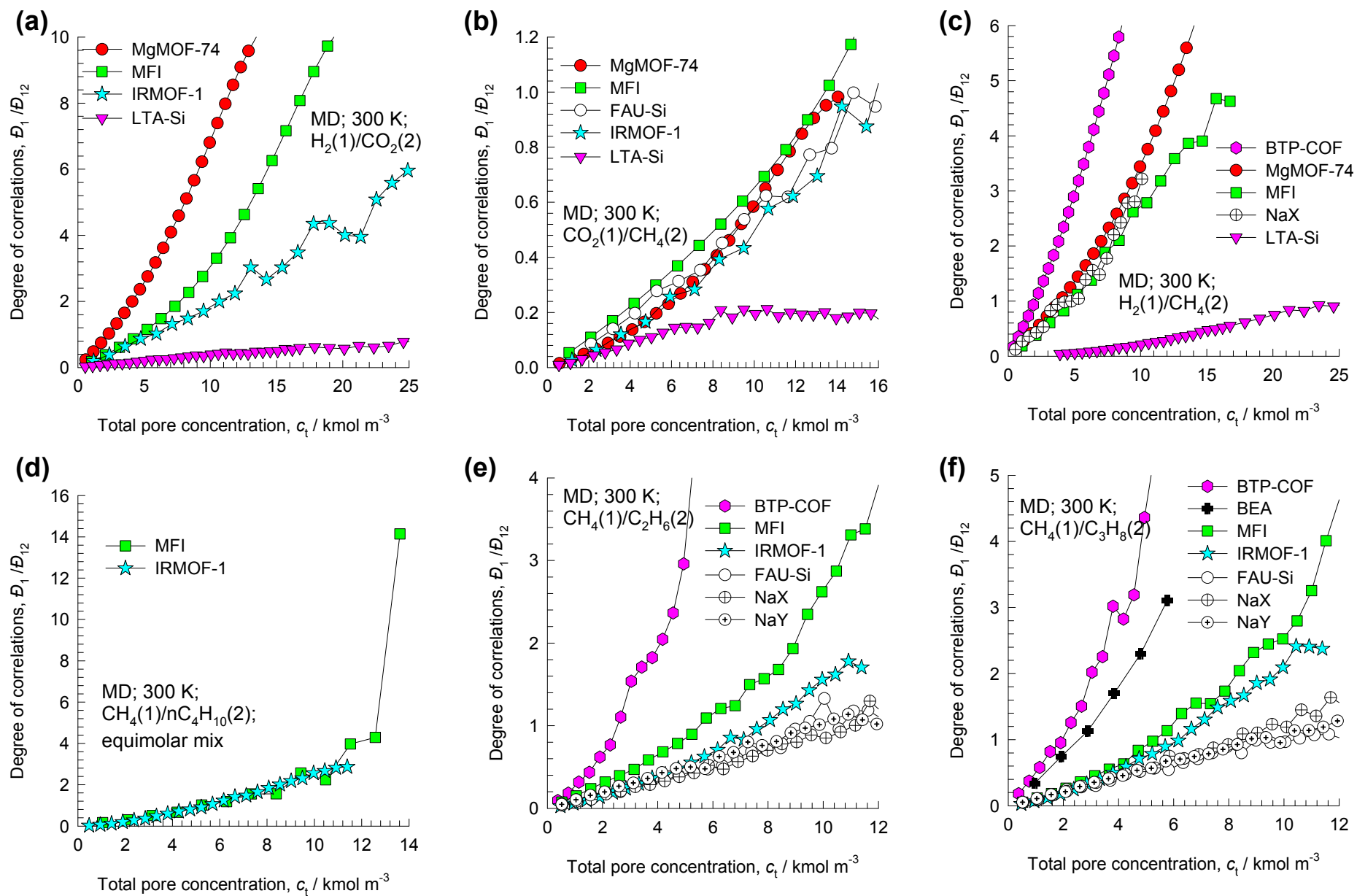
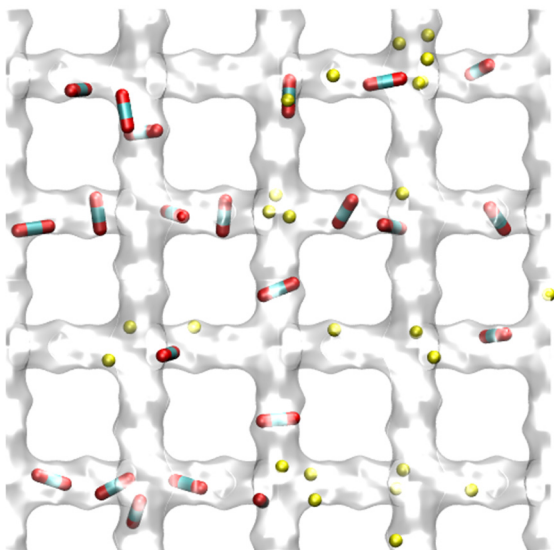


Figure 5

Degree of correlations



MFI zeolite



The mobility of H₂ is hindered by the presence of strongly adsorbed CO₂ within the 5.5 Å channels of MFI zeolite

(a)

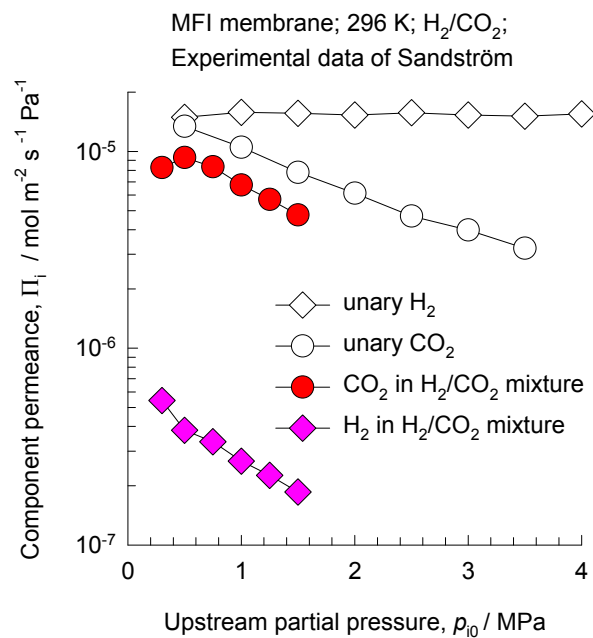
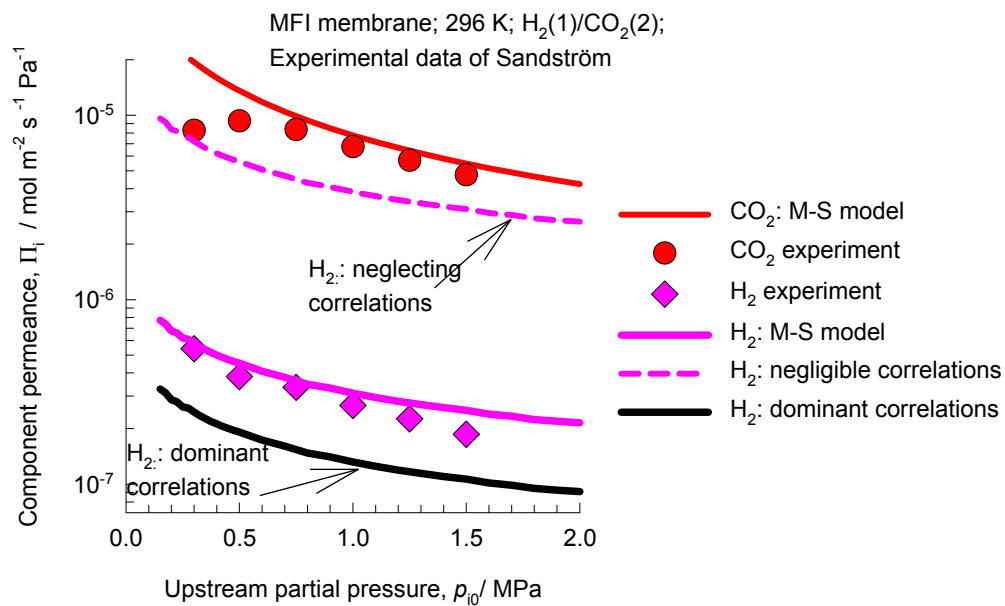
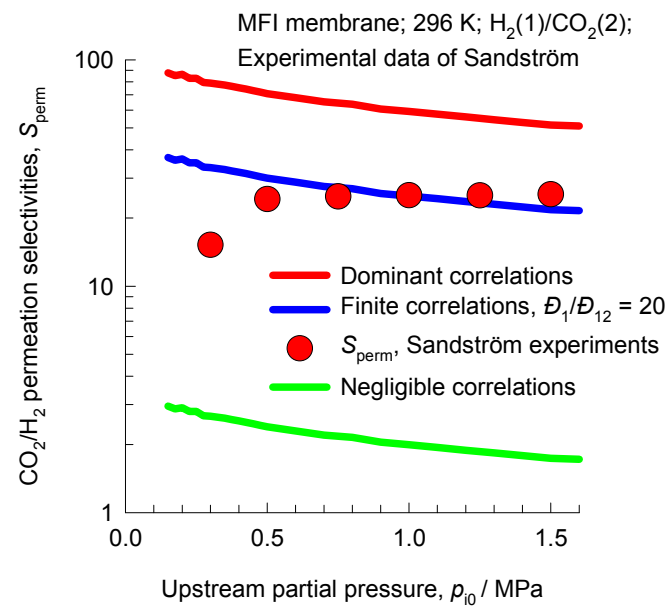


Figure 6

(b)



(c)



MFI zeolite

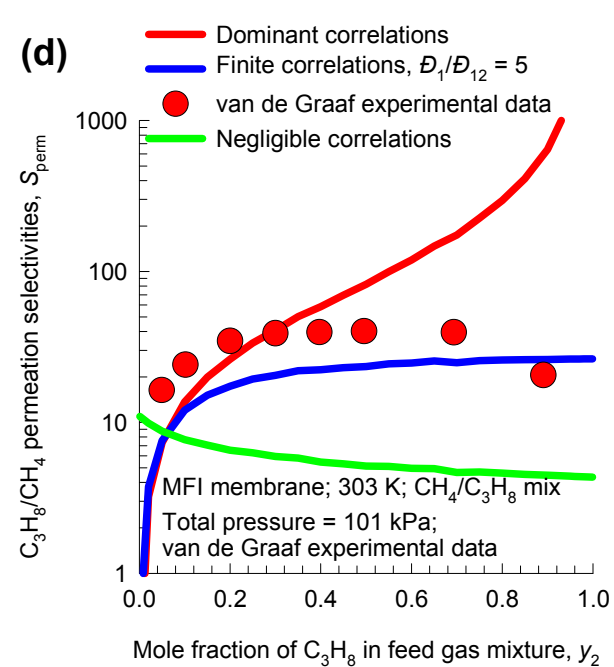
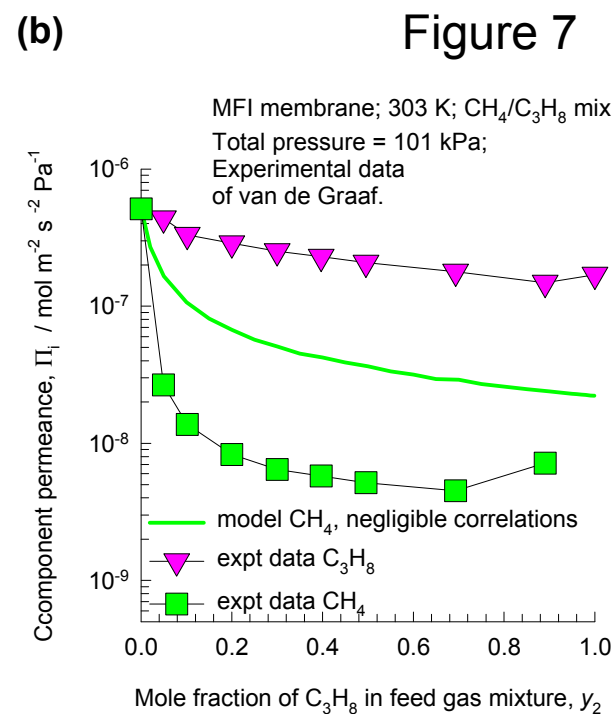
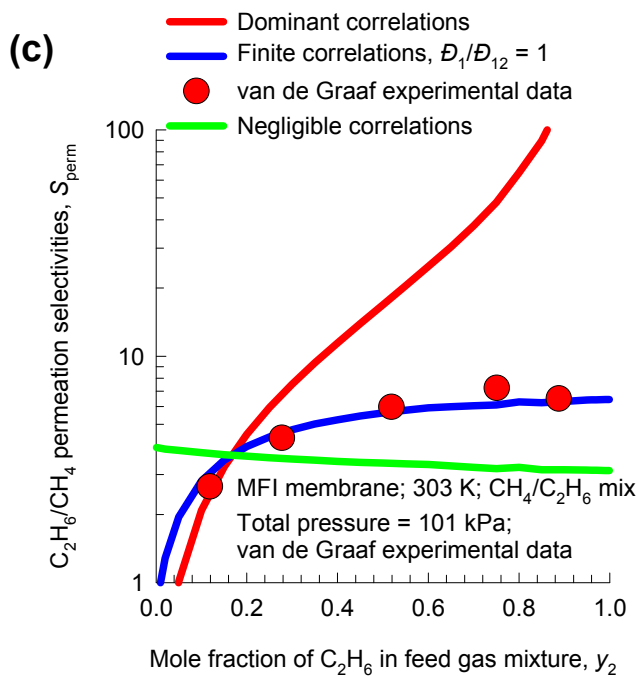
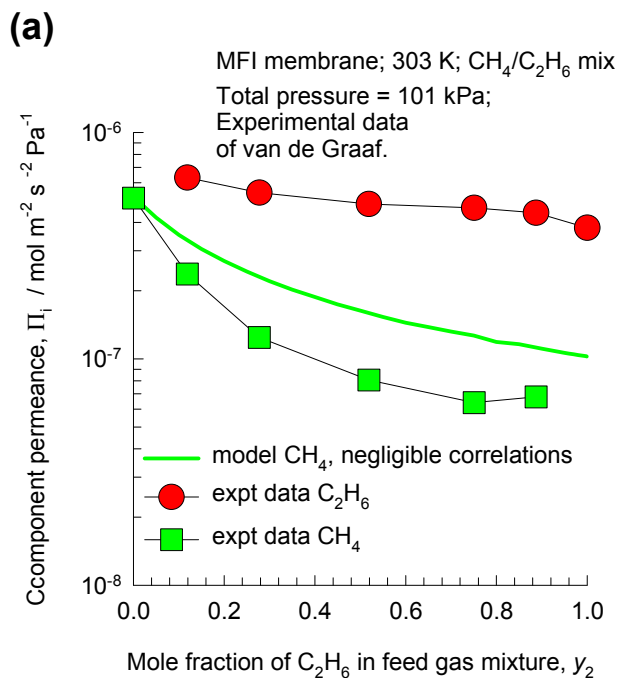
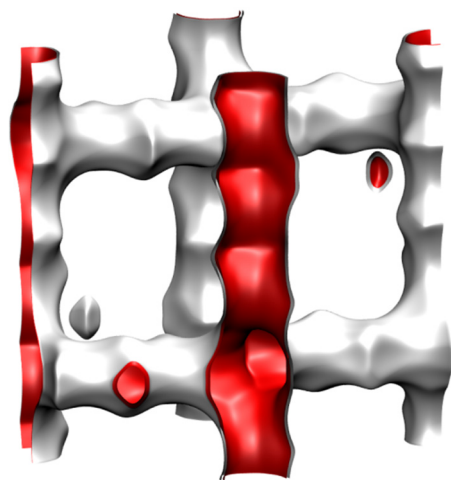
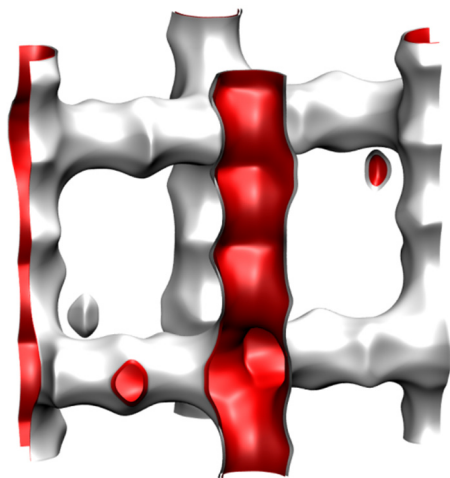


Figure 7

MFI membrane

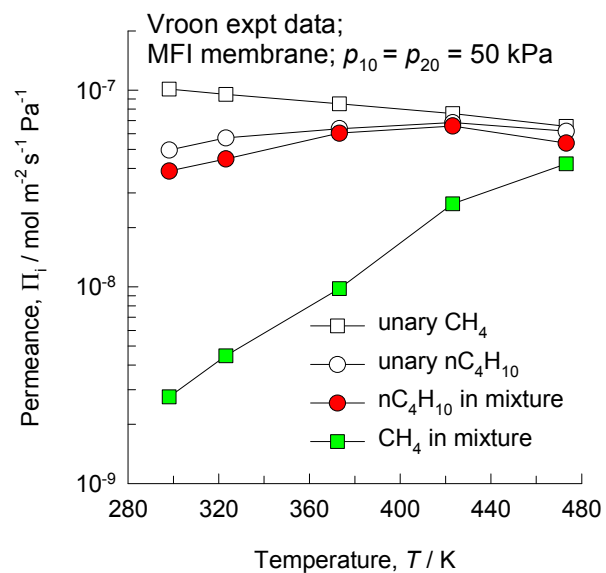


NH₂-MIL-53(Al) membrane

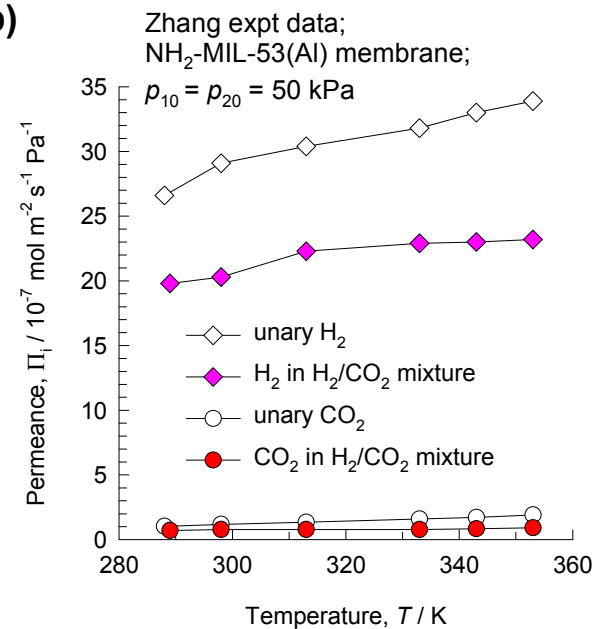
Figure 8



(a)



(b)



SAPO-34 membrane

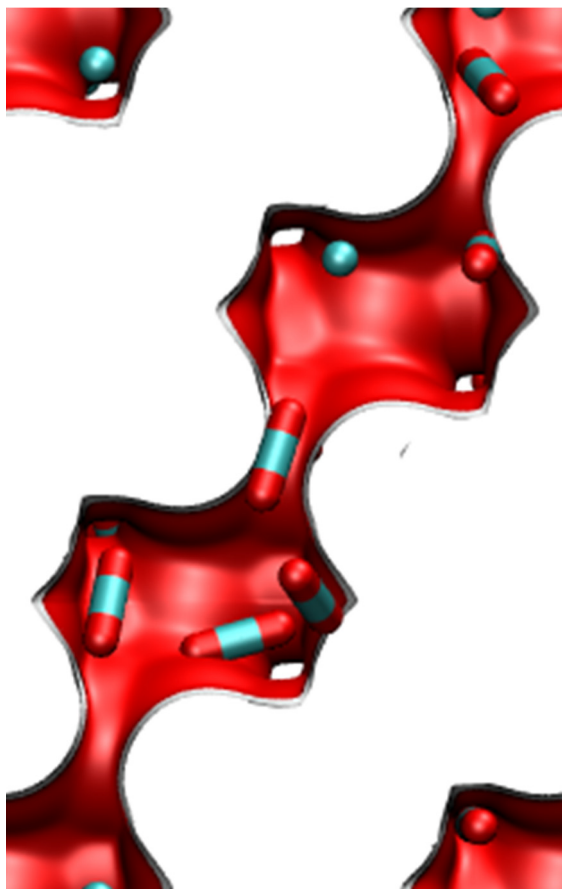
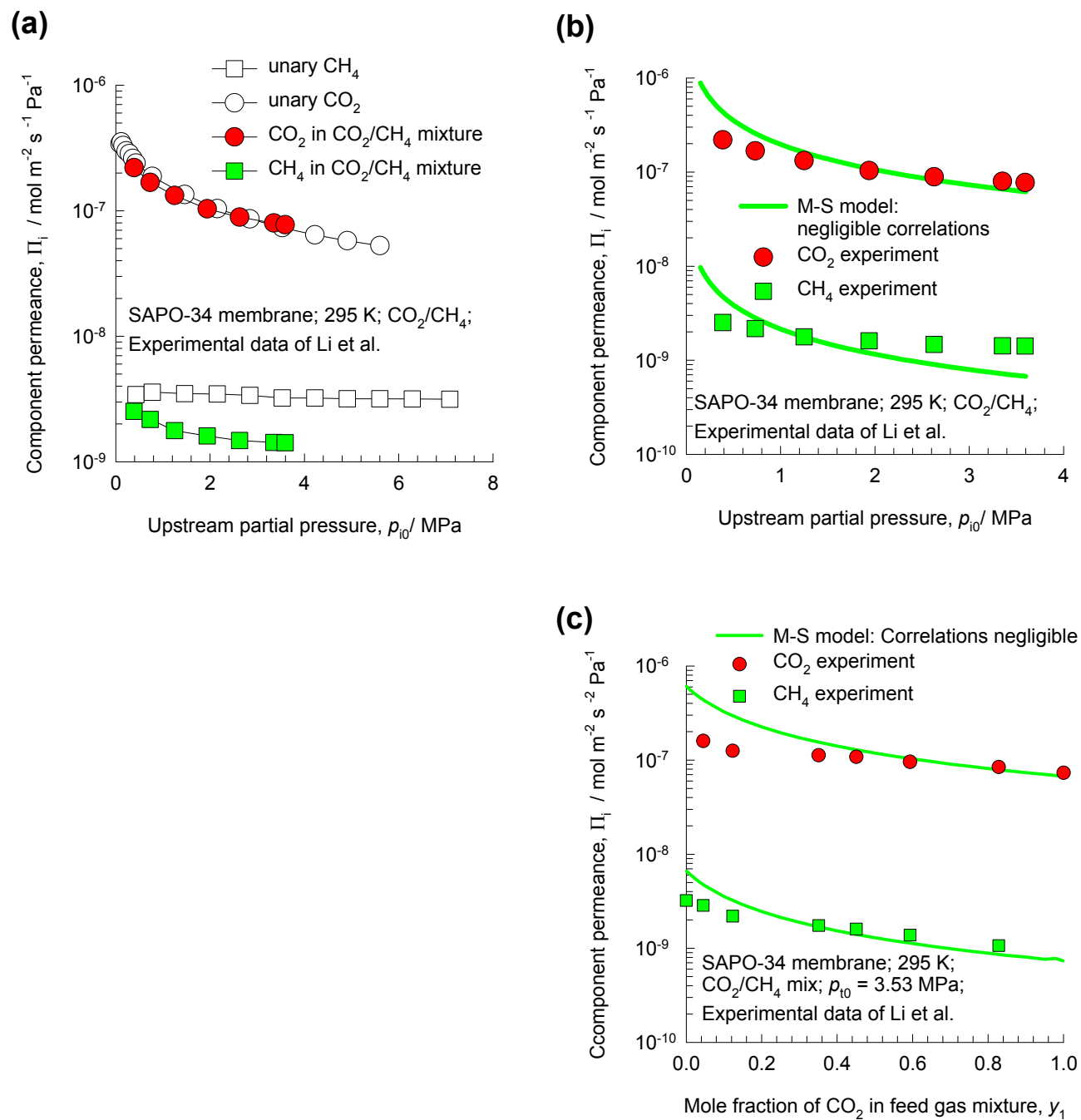
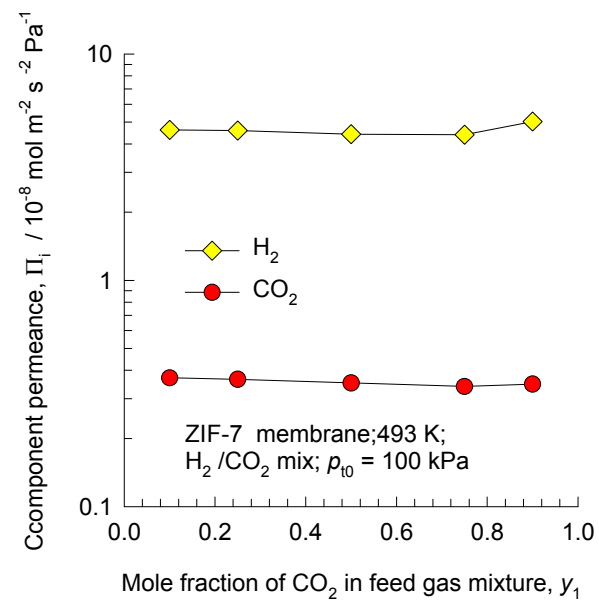
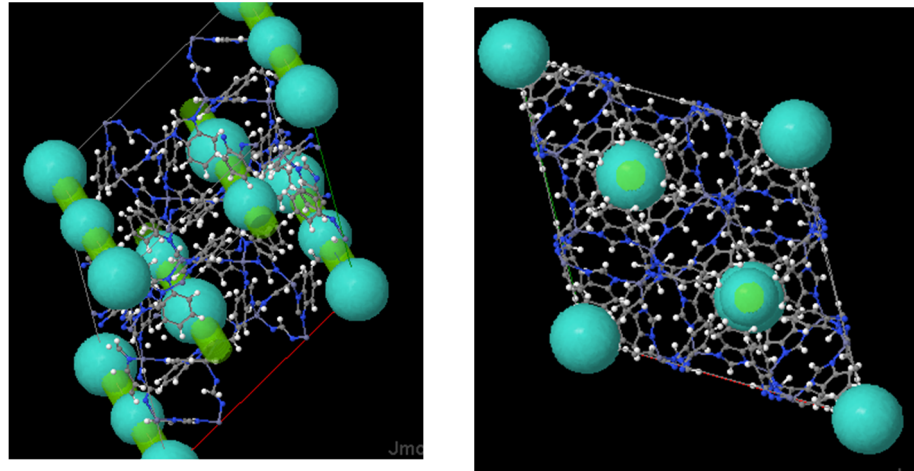


Figure 9



H₂/CO₂ permeation: ZIF-7 membrane

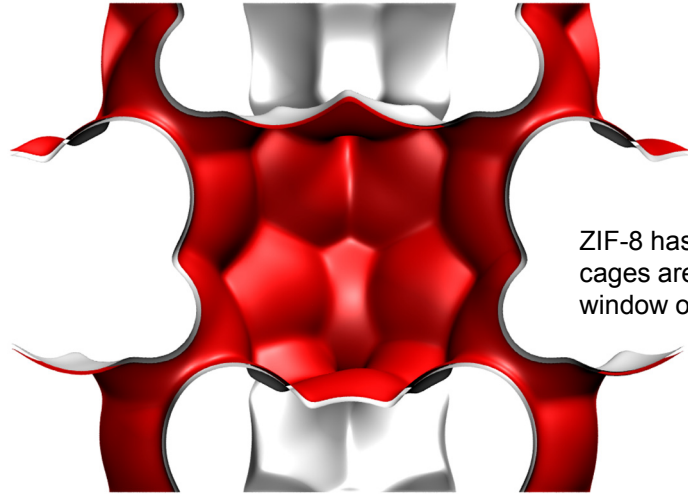
ZIF-7 is formed by combining Zn metal clusters through benzimidazole (BIM) linkers. It has a sodalite topology. 6 Å cages are connected by window openings of about 3 Å.



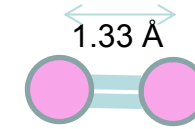
Ethene/ethane: ZIF-8 membrane

Figure 11

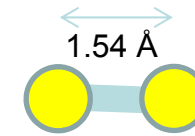
The ZIF-8 = $\text{Zn}(\text{methylimidazole})_2$



ZIF-8 has a sodalite topology. 13 Å cages are connected by flexible window openings of about 3.3 Å.

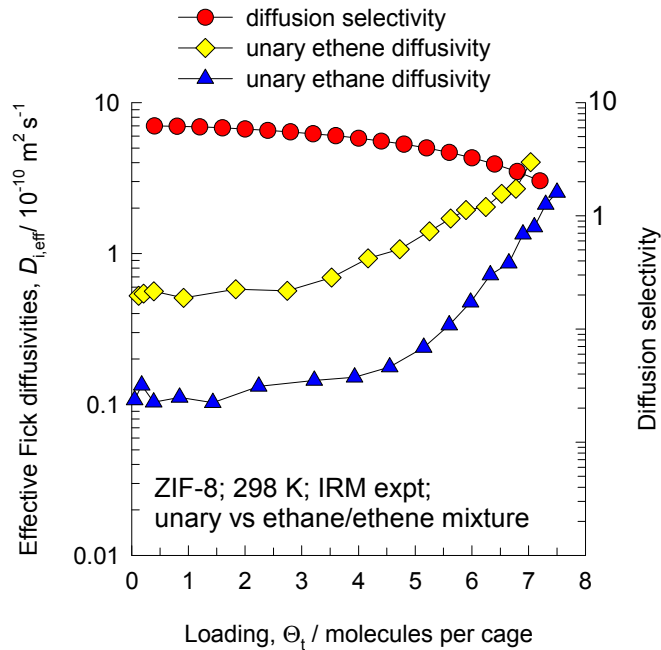


ethene

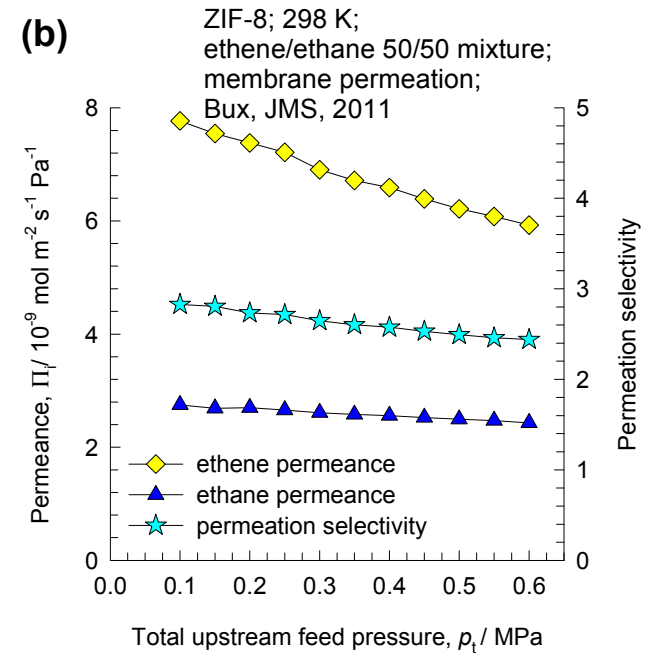


ethane

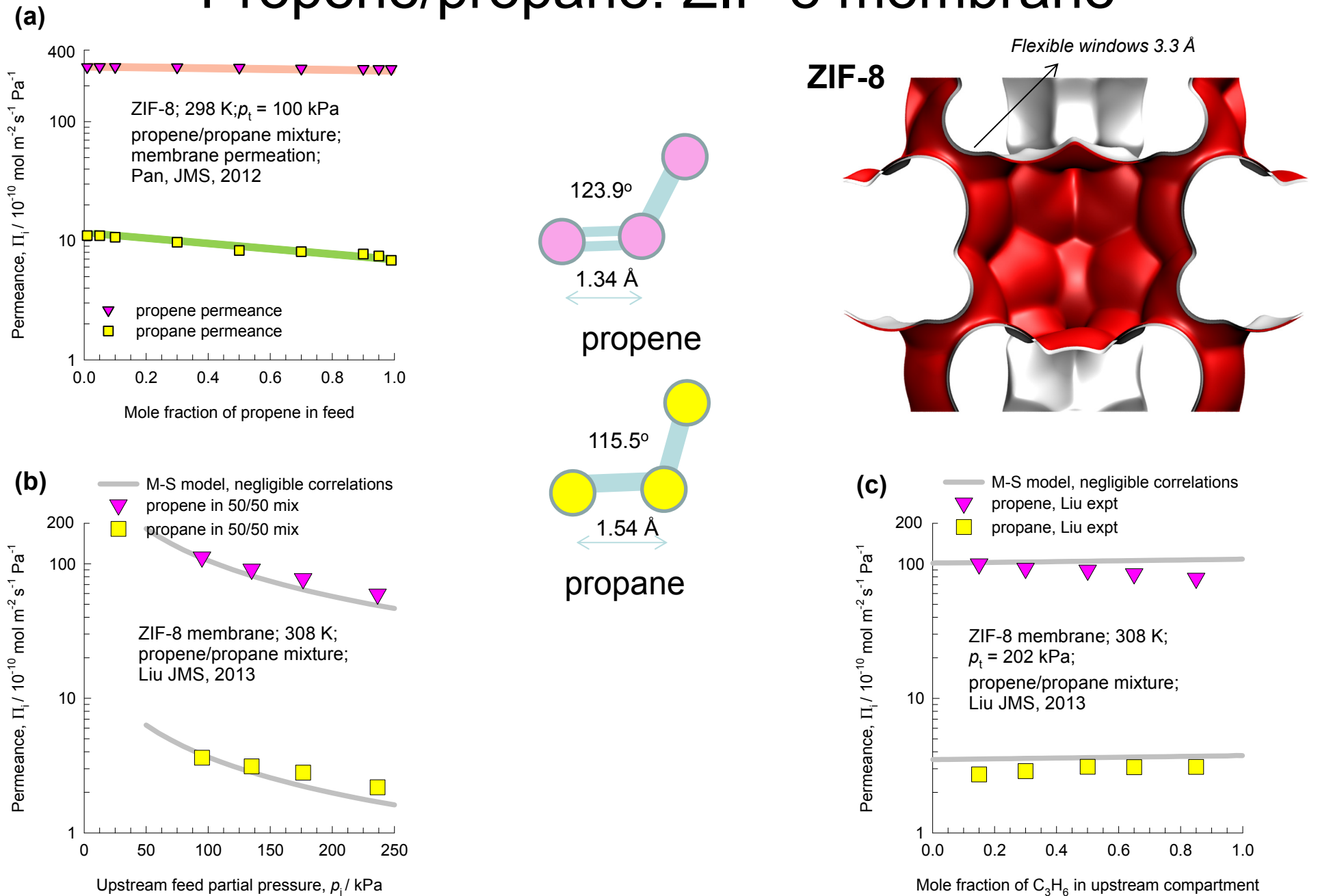
(a)



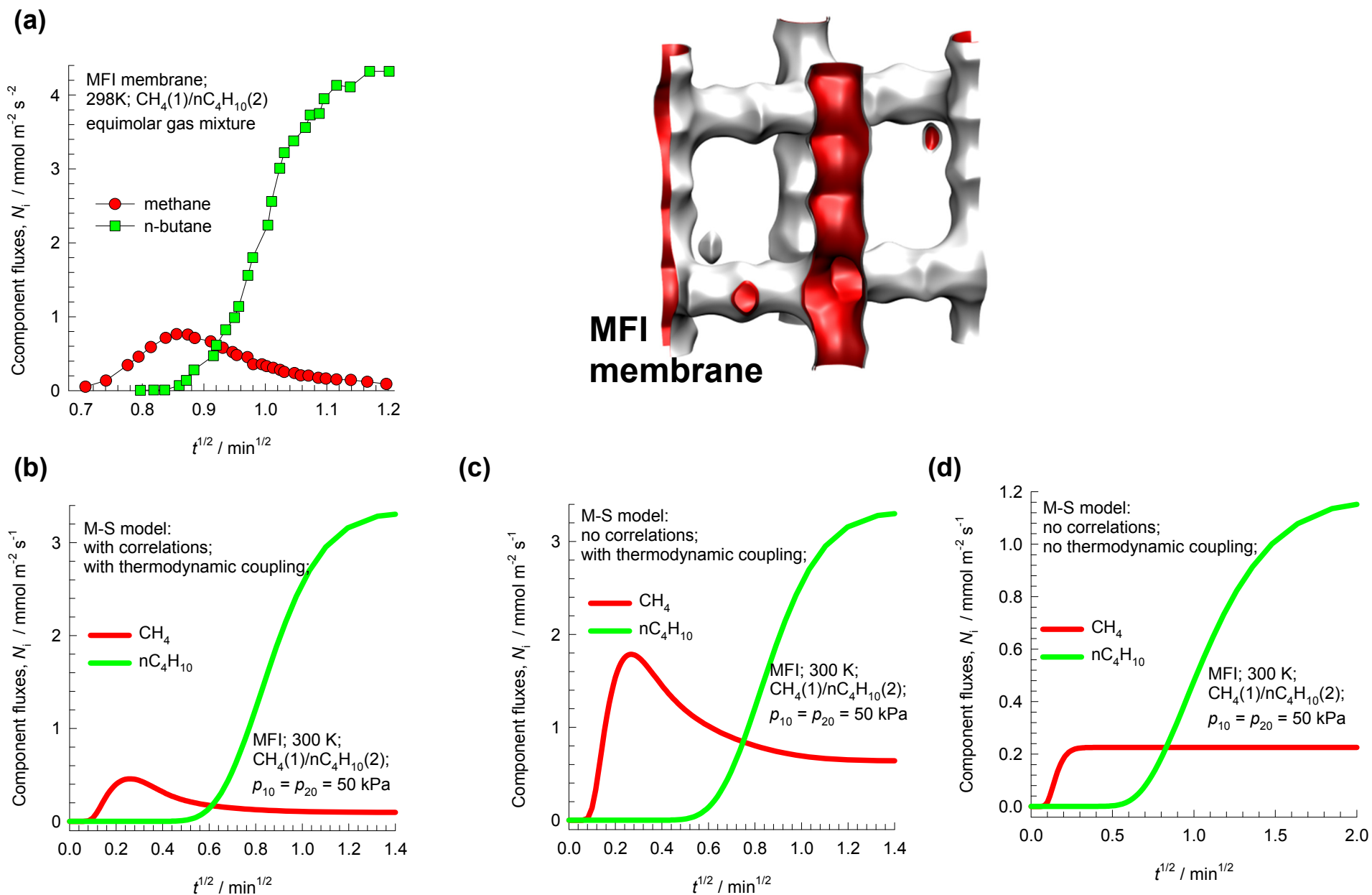
(b)



Propene/propane: ZIF-8 membrane Figure 12



C1/nC4 permeation: MFI membrane



Model for membrane permeation

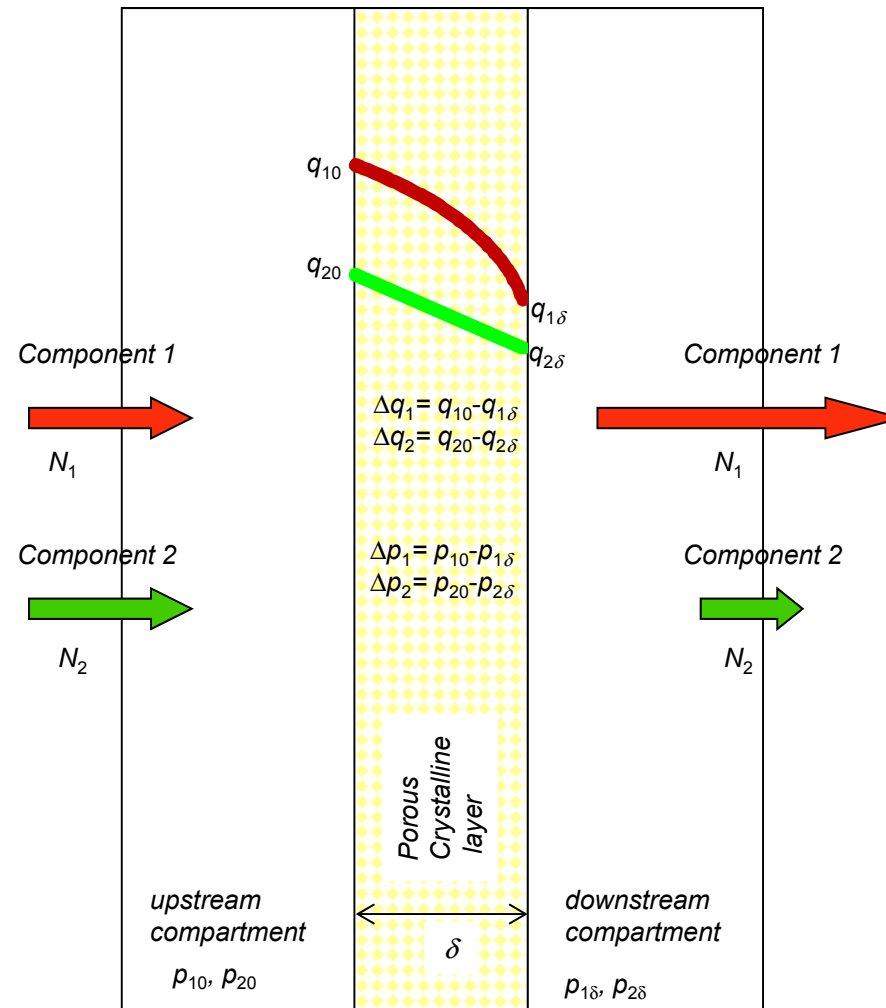


Figure 15

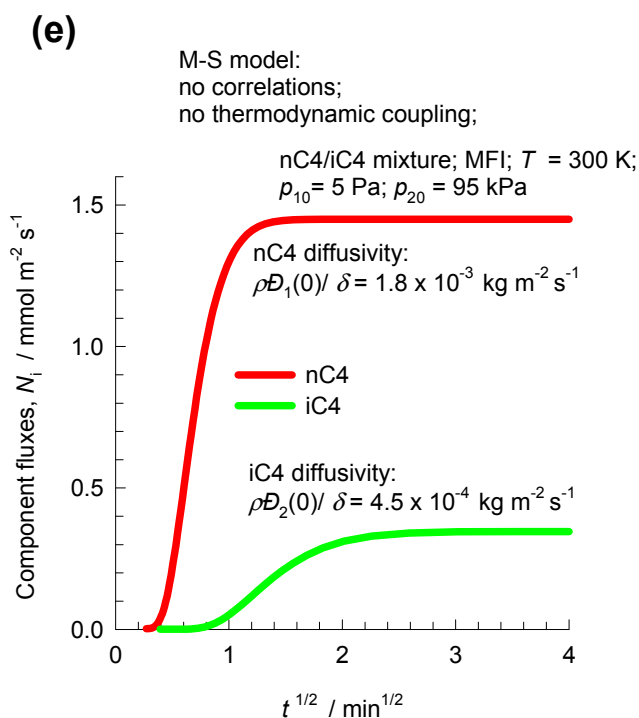
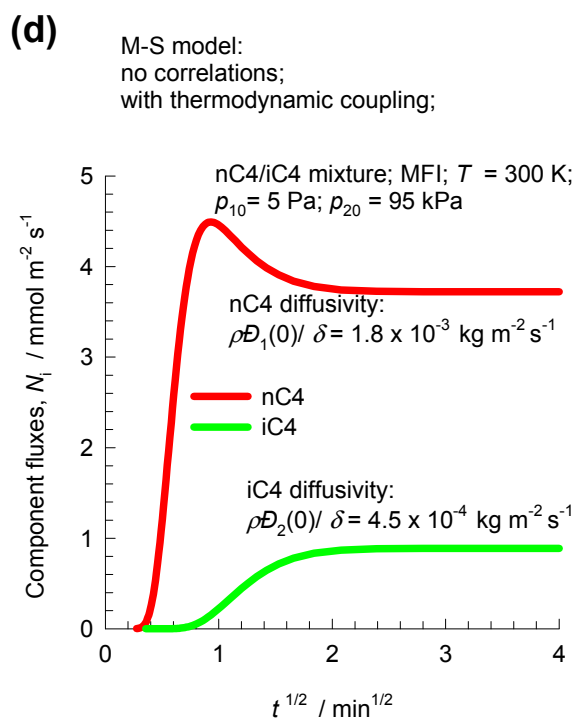
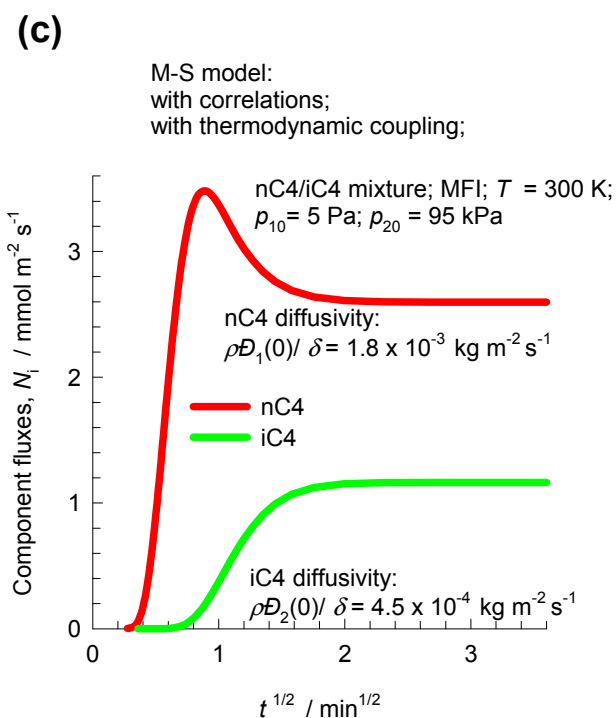
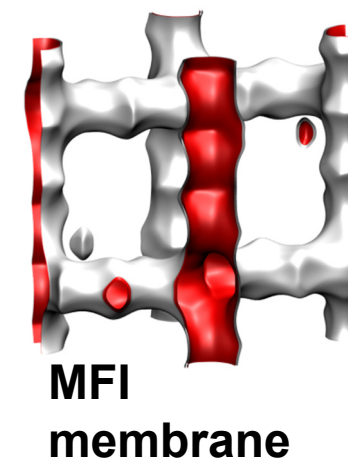
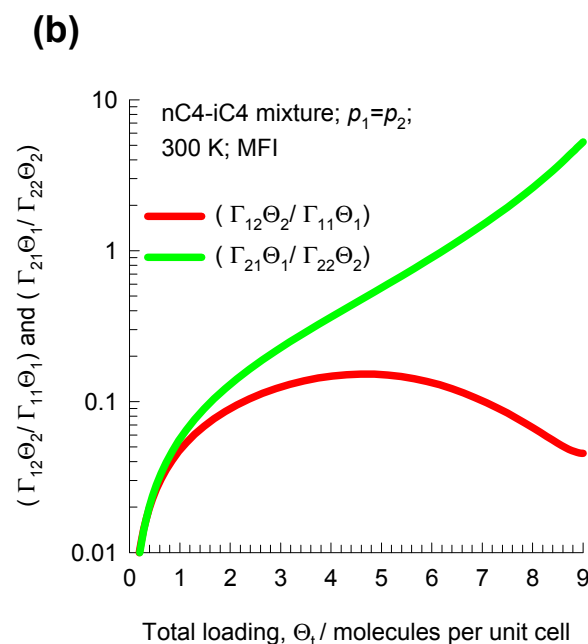
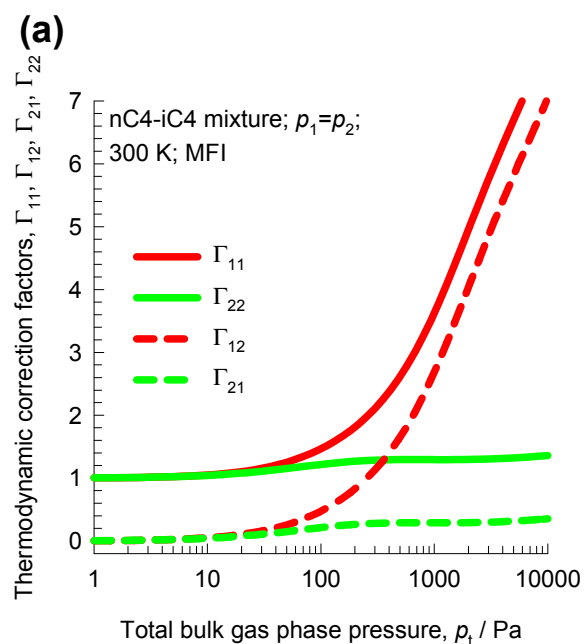
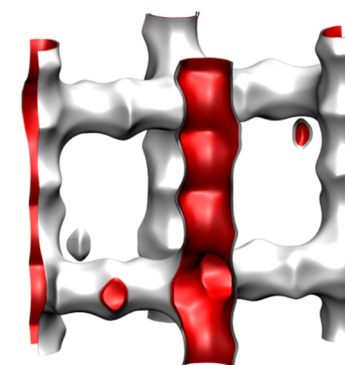
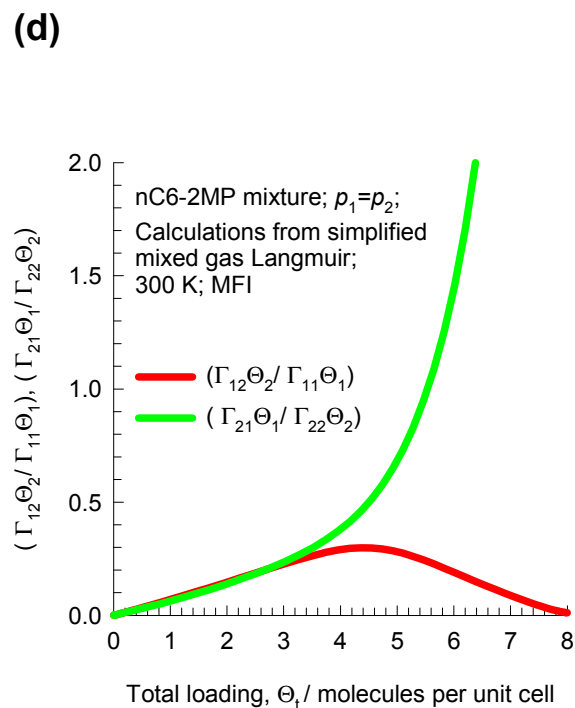
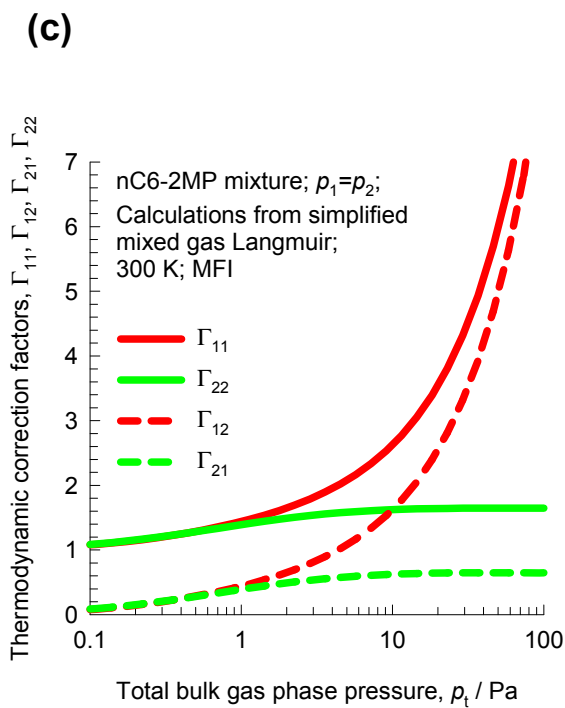
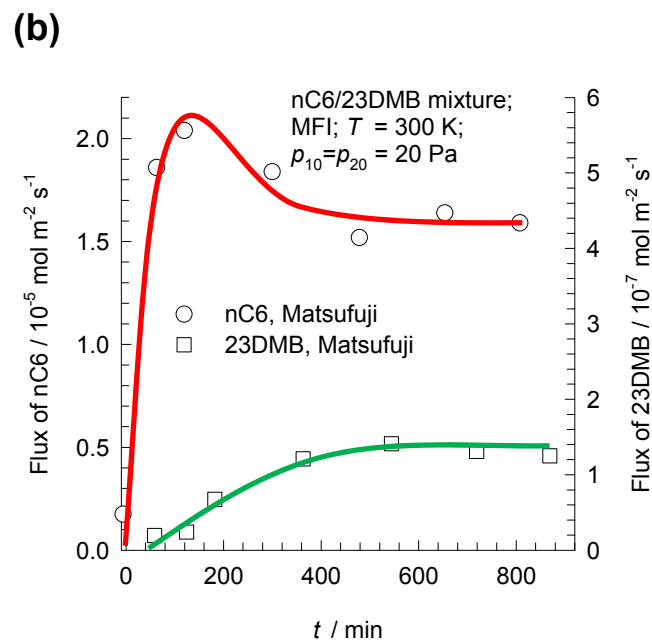
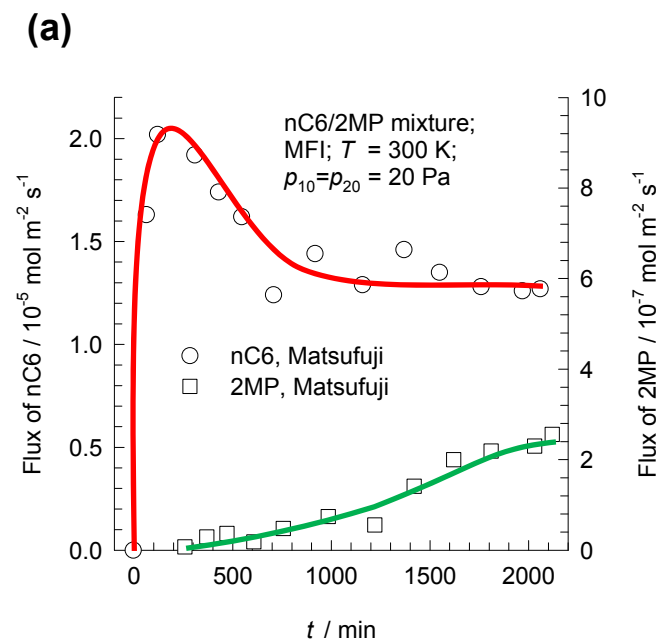
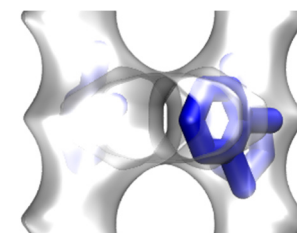
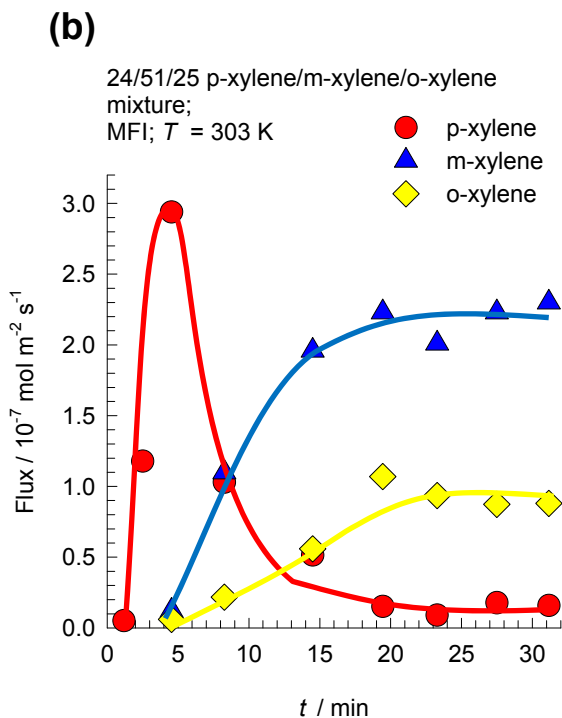
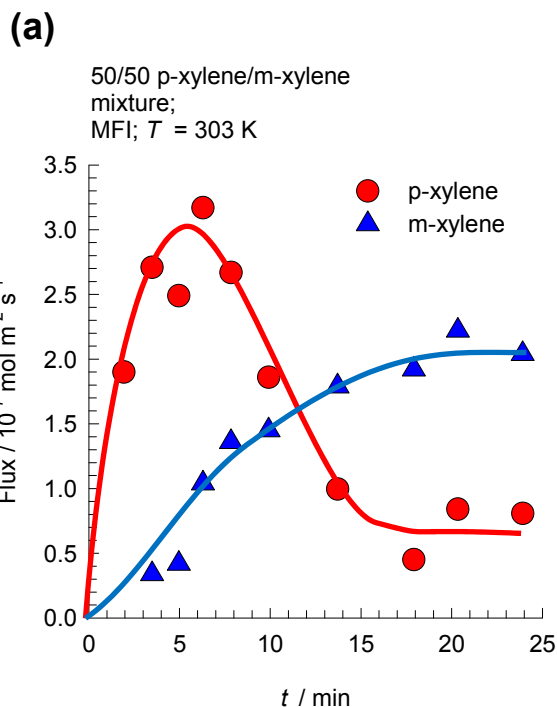


Figure 16

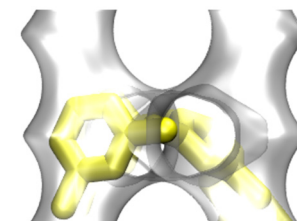


**MFI
membrane**

Figure 17

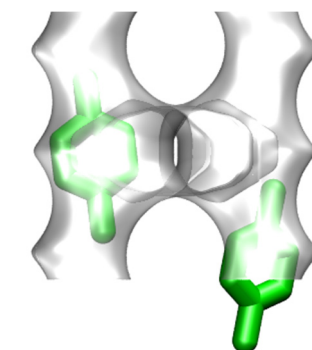
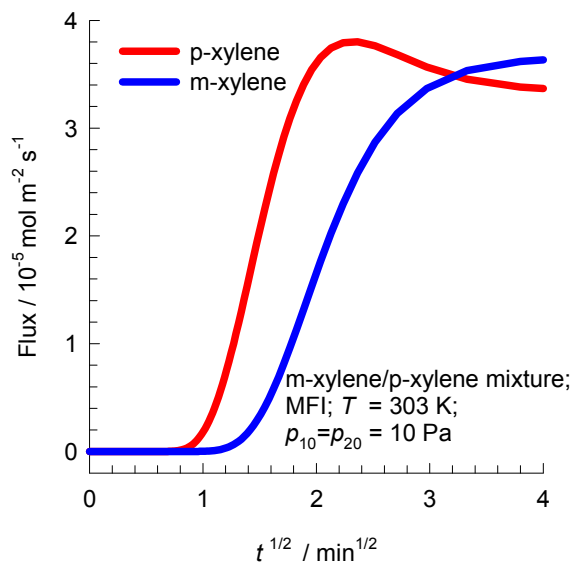


o-xylene, and m-xylene are preferentially located at the intersections of MFI



(c) With thermodynamic coupling

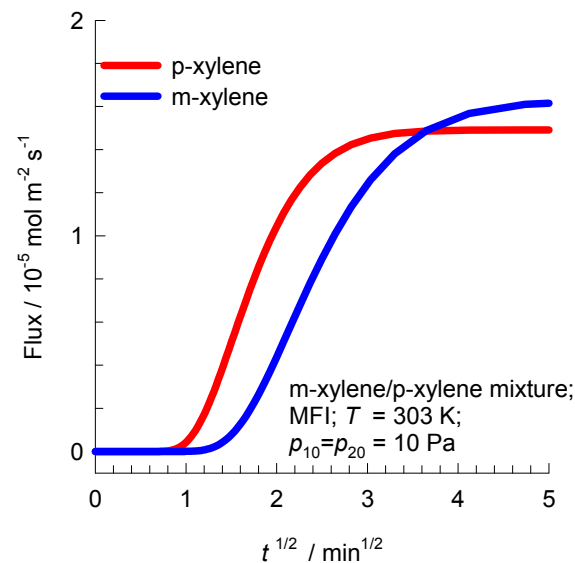
p-xylene diffusivity: $\rho D_2(0) \delta = 7.18 \times 10^{-5}$ kg m^{-2} s^{-1}
 m-xylene diffusivity: $\rho D_1(0) \delta = 3.59 \times 10^{-5}$ kg m^{-2} s^{-1}



p-xylene can locate along the channels MFI

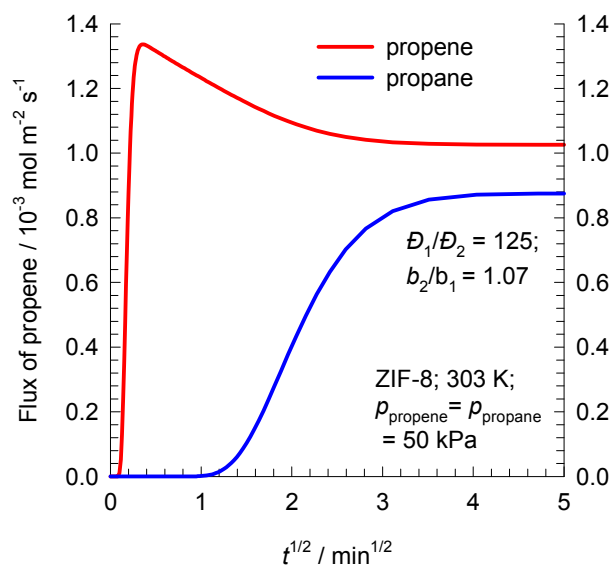
(d) Ignoring thermodynamic coupling

p-xylene diffusivity: $\rho D_2(0) \delta = 7.18 \times 10^{-5}$ kg m^{-2} s^{-1}
 m-xylene diffusivity: $\rho D_1(0) \delta = 3.59 \times 10^{-5}$ kg m^{-2} s^{-1}

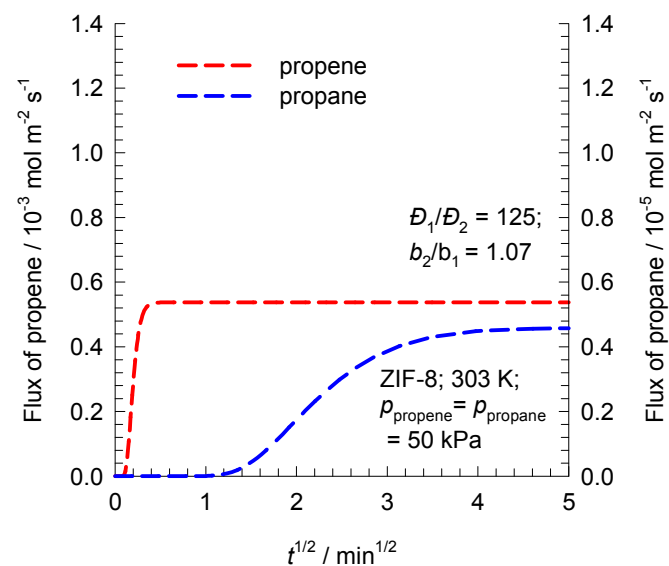
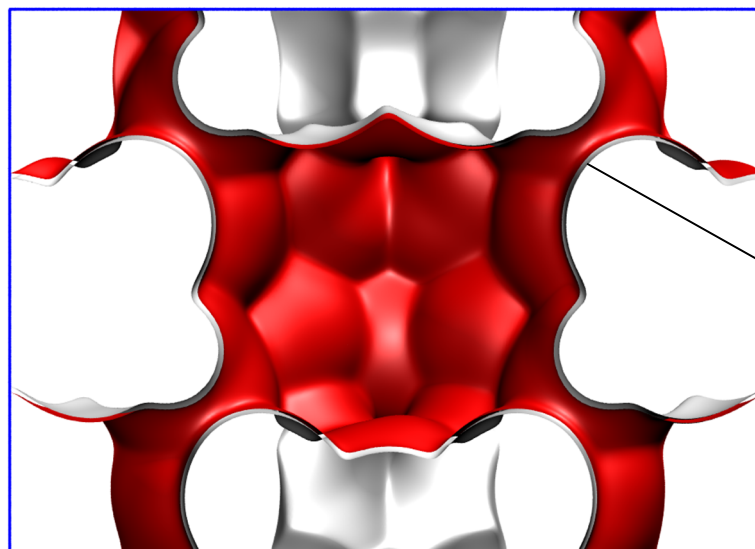


Propene/propane permeation across ZIF-8

(a)



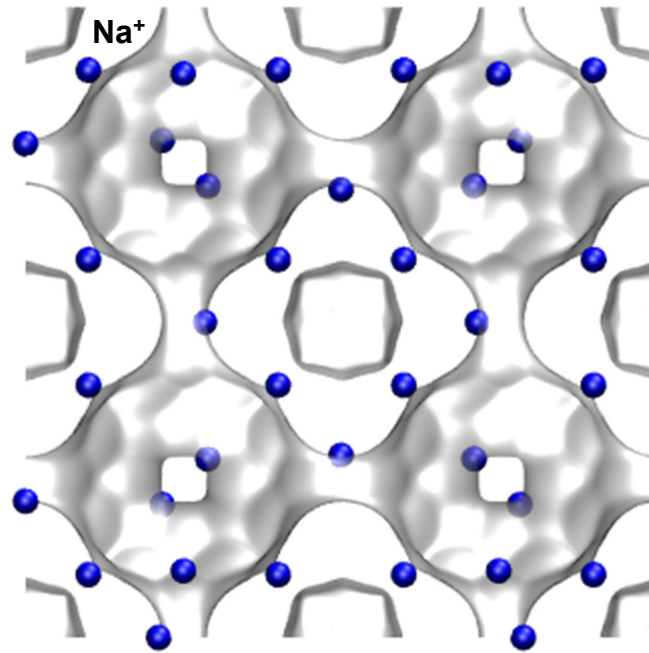
(b)

**ZIF-8**

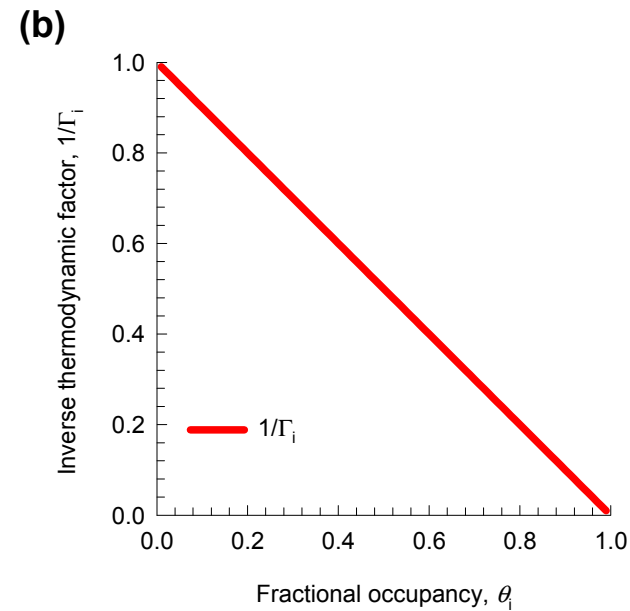
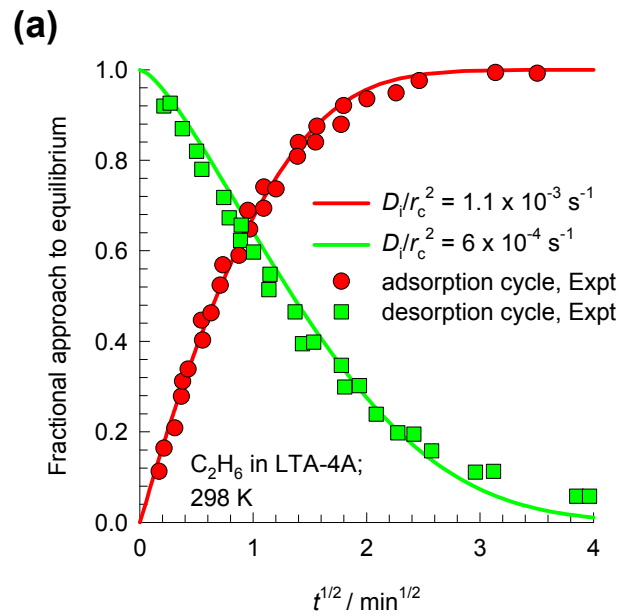
Flexible windows 3.3 Å

Adsorption/Desorption asymmetry

Figure 19



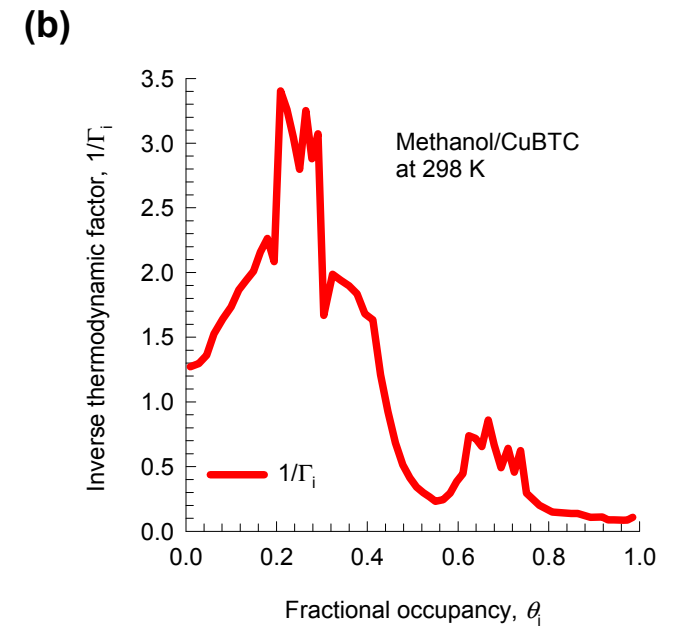
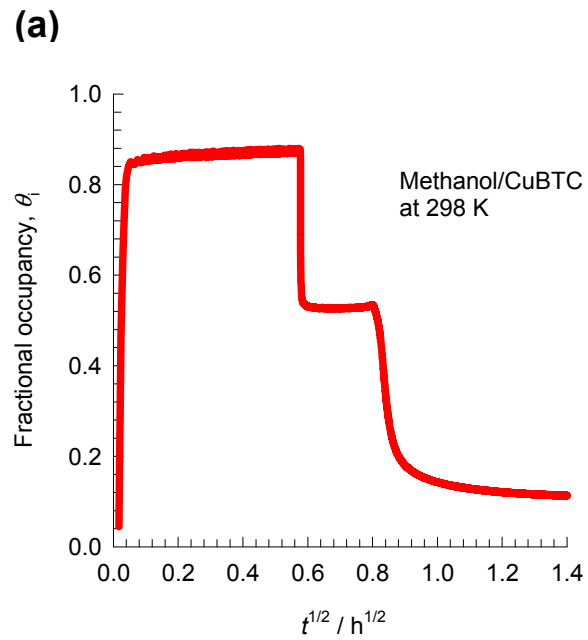
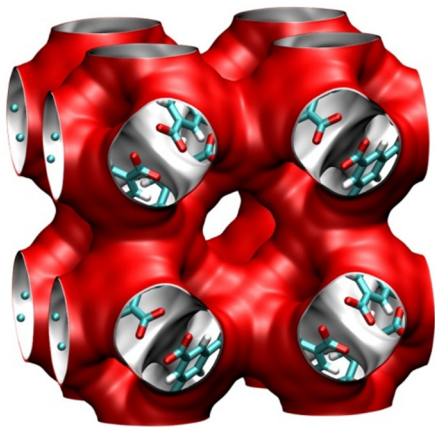
LTA-4A
(96 Na⁺)



Unary desorption transience

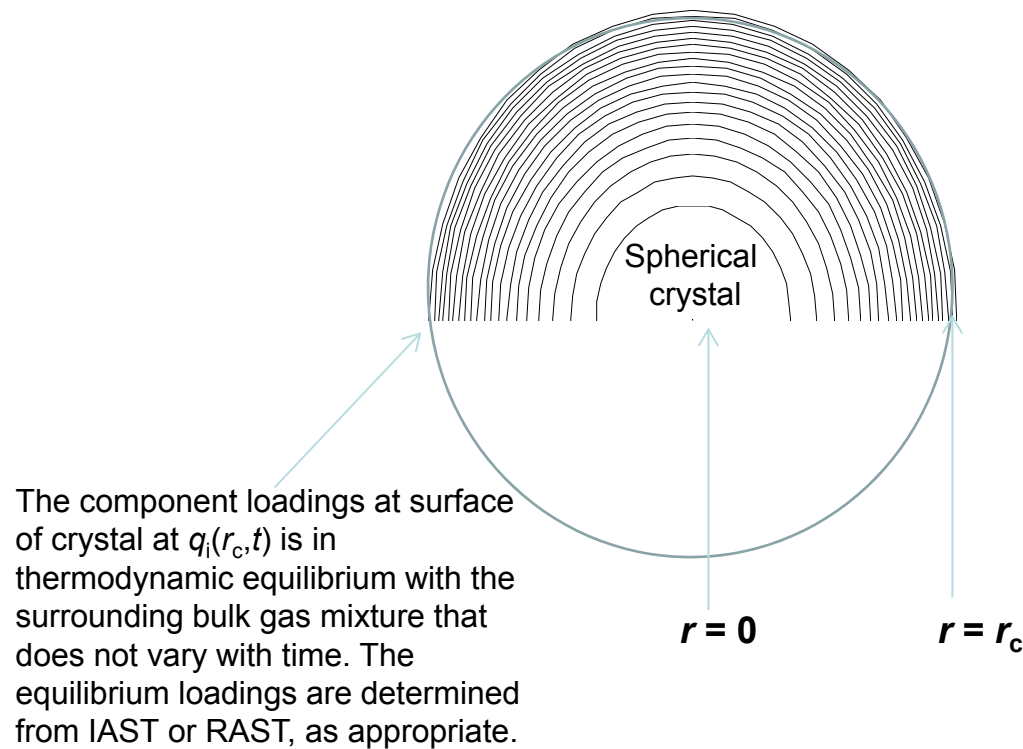
Figure 20

CuBTC



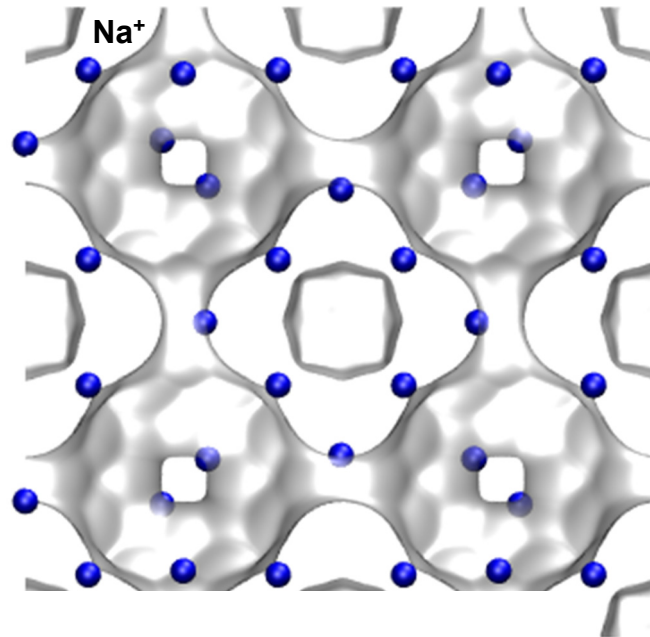
Discretization spherical crystal

Figure 21

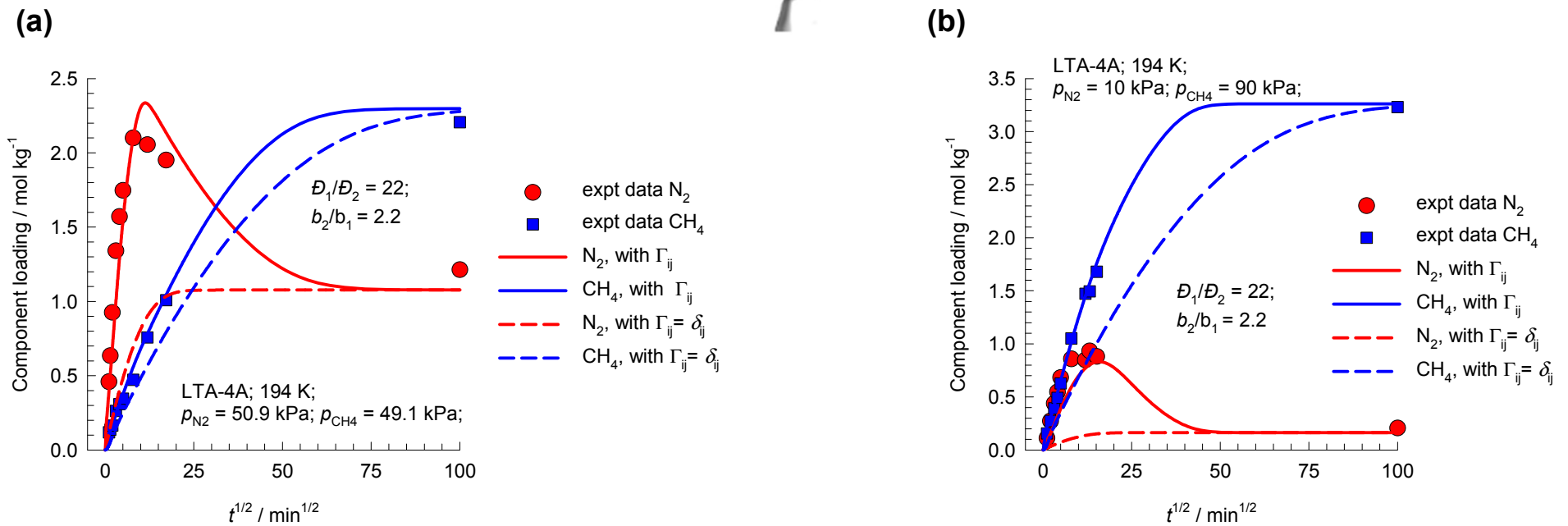


N₂/CH₄ mixture uptake LTA-4A

Figure 22



**LTA-4A
(96 Na⁺)**



Thermodynamic factors N_2/CH_4 in LTA-4A

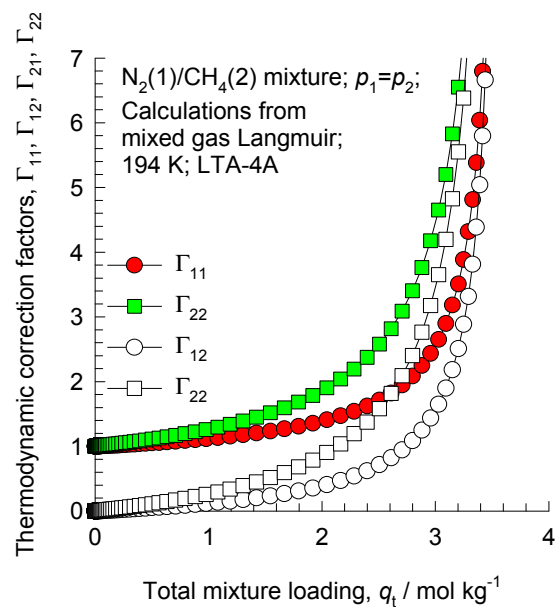


Figure 24

Overshoots for N₂/CH₄ in LTA-4A

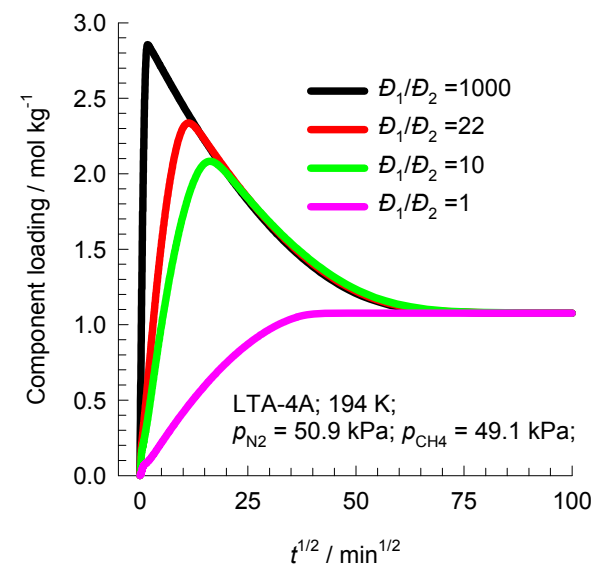
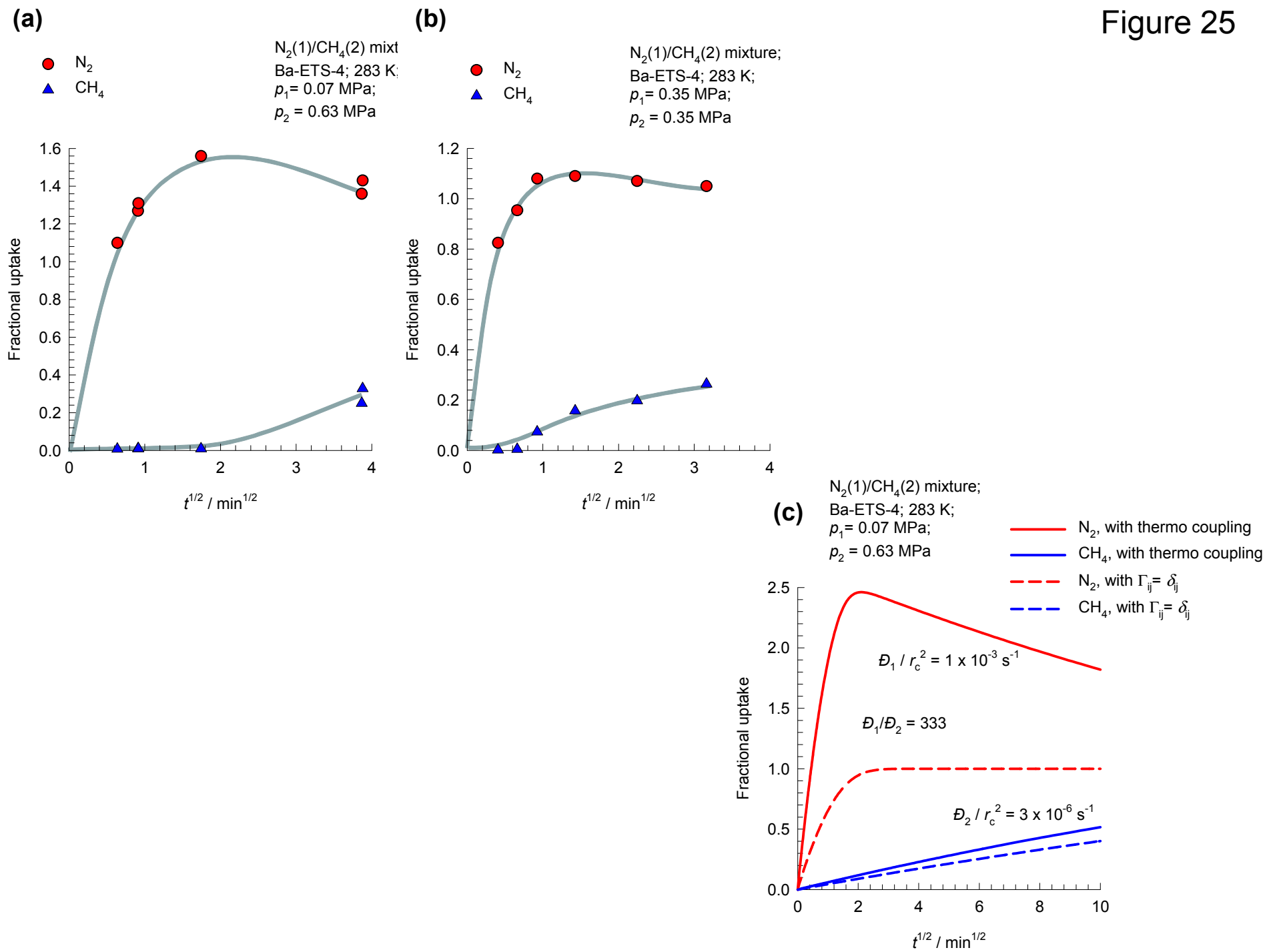
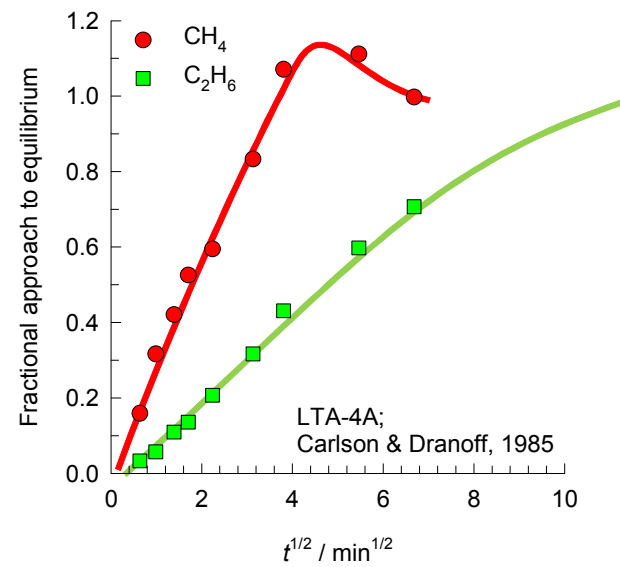
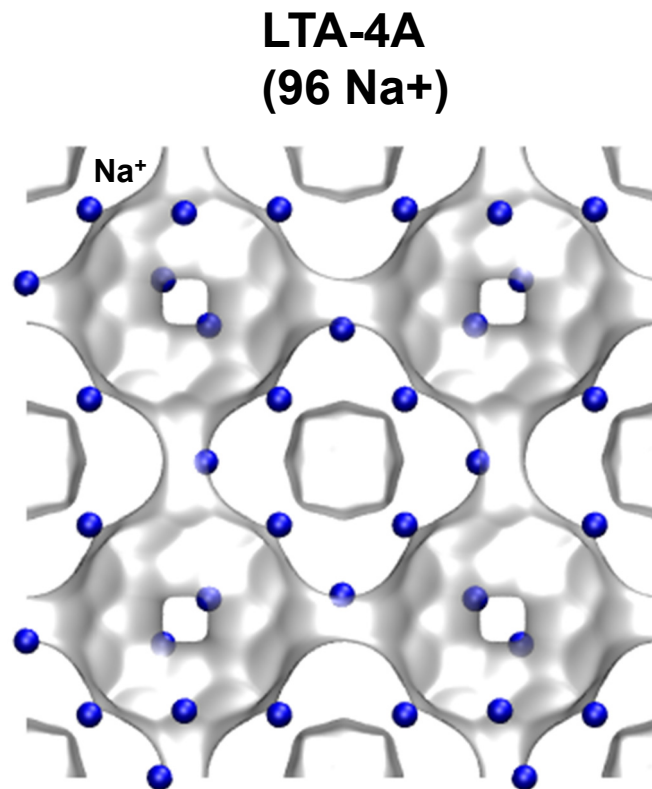
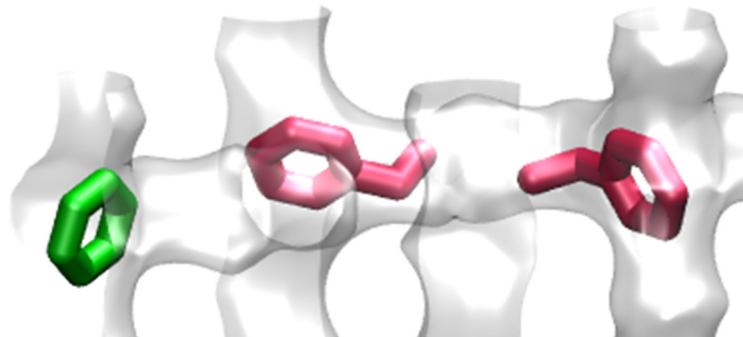
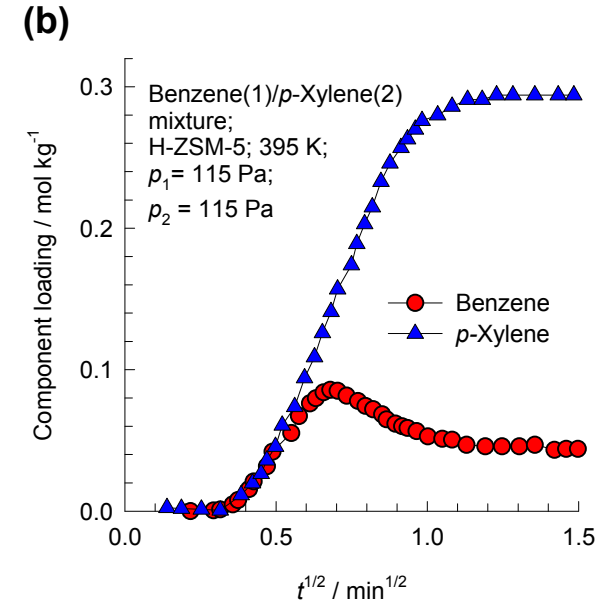
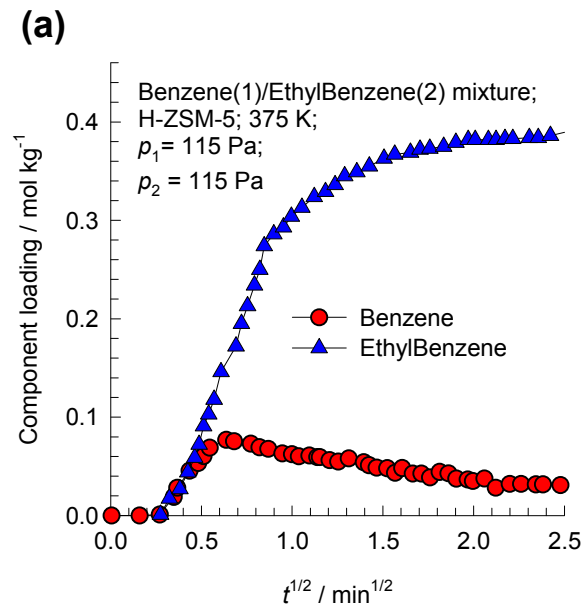


Figure 25



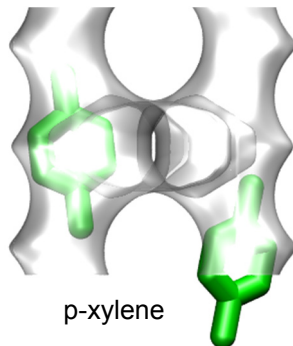
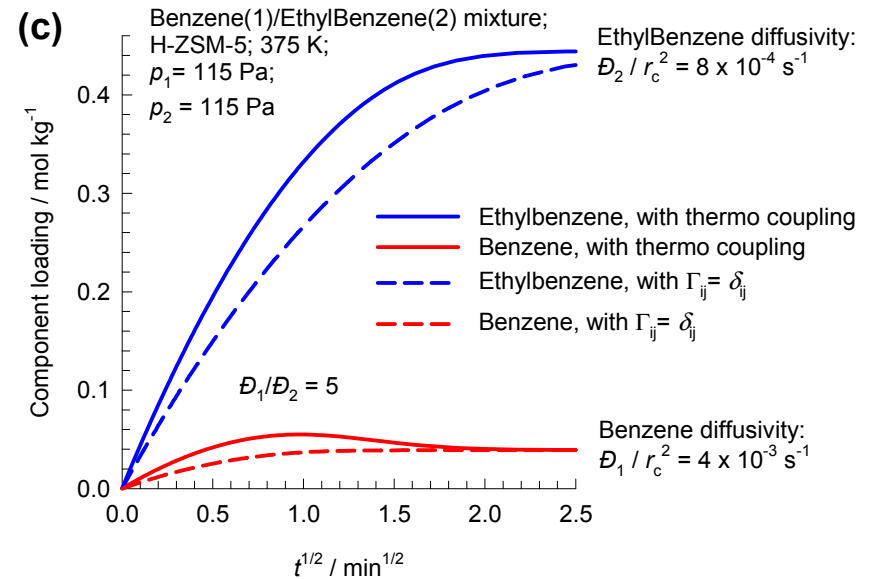
Transient uptake C1/C2 in LTA-4A





benzene

ethylbenzene

*p*-xylene

Transient nC7/Benzene uptake in NaX

NaX
zeolite

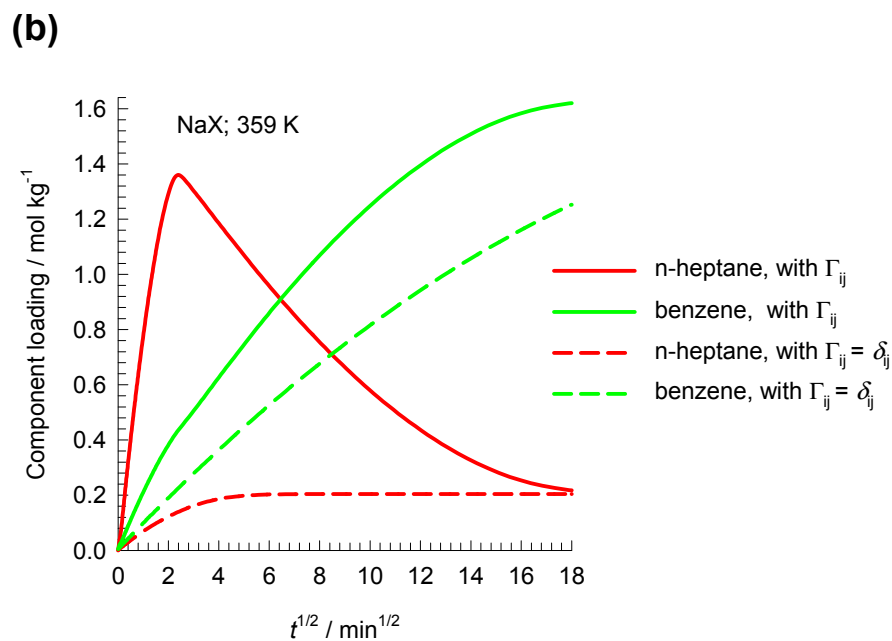
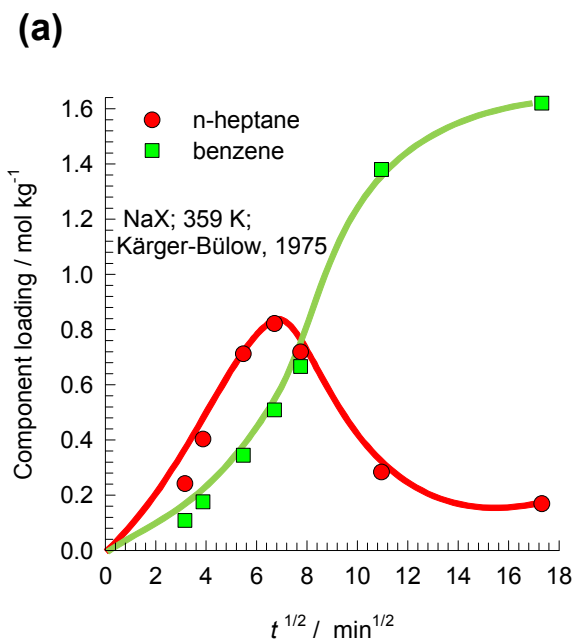
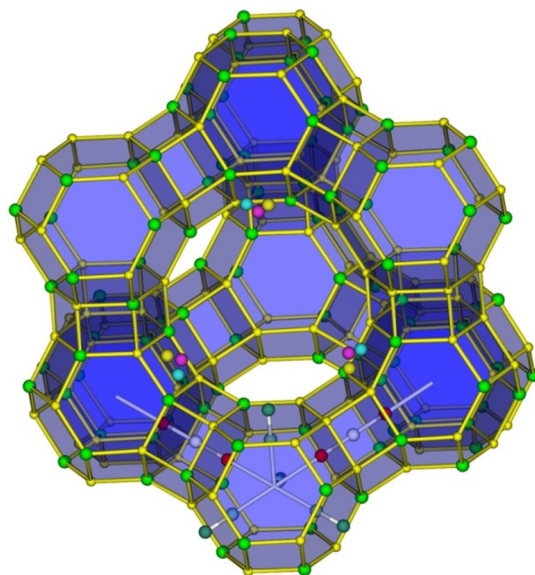
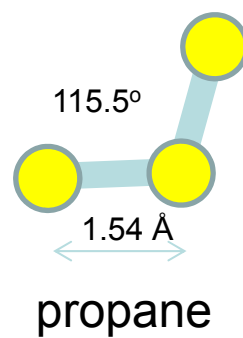
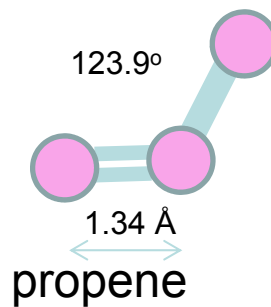
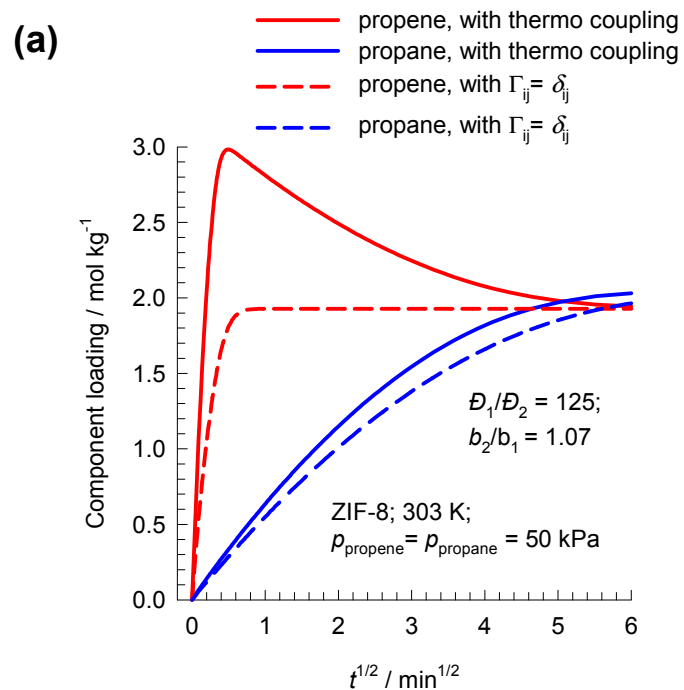
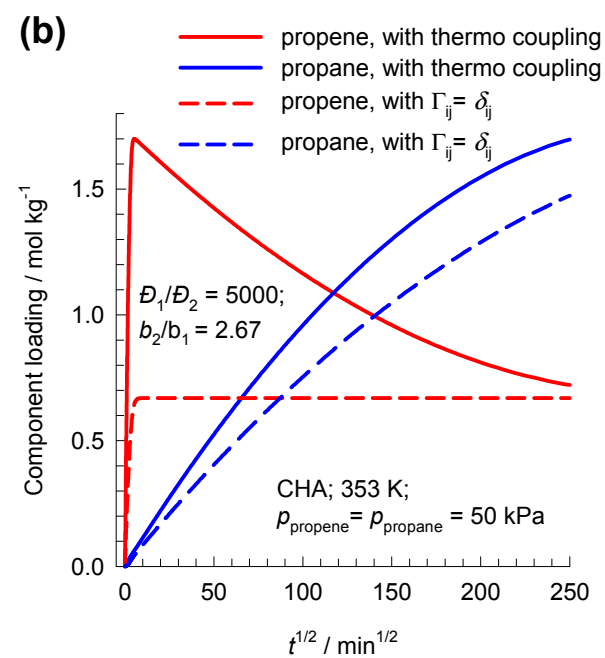
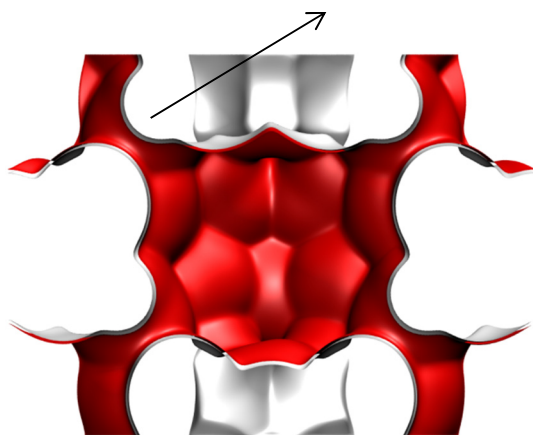


Figure 29



ZIF-8 Flexible windows 3.26 Å



CHA

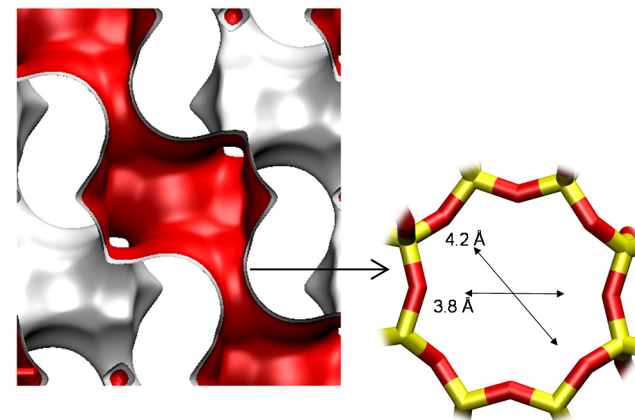
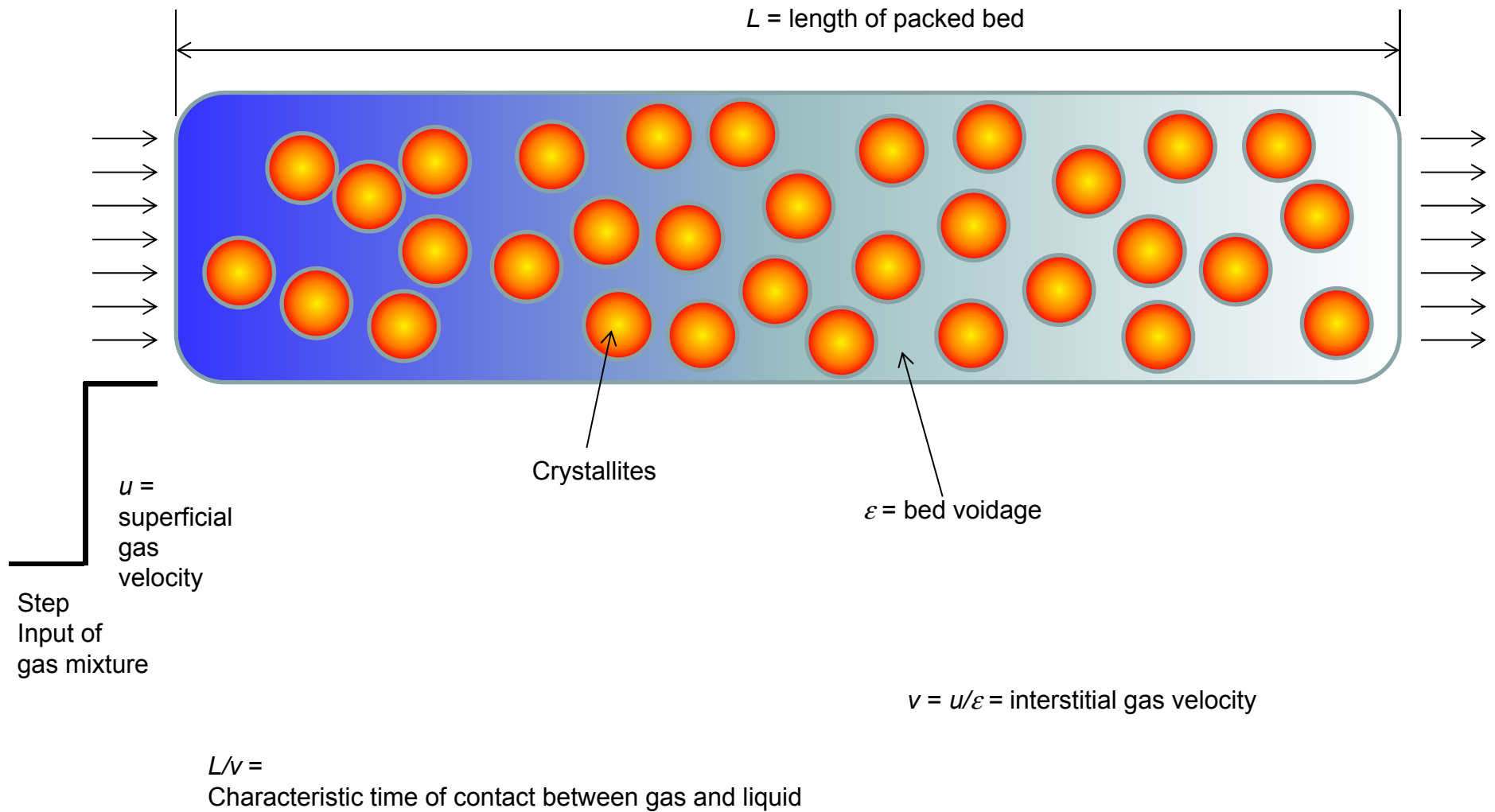


Figure 30

Fixed bed adsorber with step input



Fixed bed breakthrough model

Figure 31

Component balance

$$\frac{1}{RT} \frac{\partial p_i}{\partial t} = -\frac{1}{RT} \frac{\partial(v p_i)}{\partial z} - \frac{(1-\varepsilon)}{\varepsilon} \rho \frac{\partial \bar{q}_i}{\partial t}, \quad i=1,2,\dots,n$$

Balance for mixture

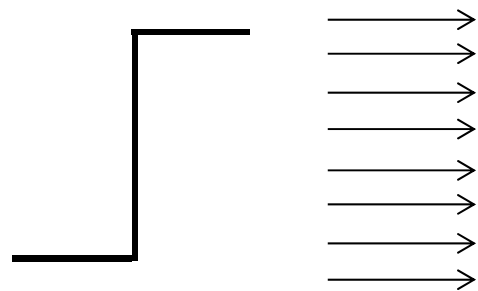
$$\frac{1}{RT} p_t \frac{\partial(v(t,z))}{\partial z} = -\frac{(1-\varepsilon)}{\varepsilon} \rho \frac{\partial \bar{q}_i(t,z)}{\partial t}$$

Average loading within crystal

$$\bar{q}_i = \frac{3}{r_c^3} \int_0^{r_c} q_i r^2 dr$$

$L =$ length of packed bed

100-200 slices



$$t = 0; \quad q_i(0, z) = 0$$

$$t \geq 0; \quad p_i(0, t) = p_{i0}; \quad u(0, t) = u_0$$

Uptake within crystal

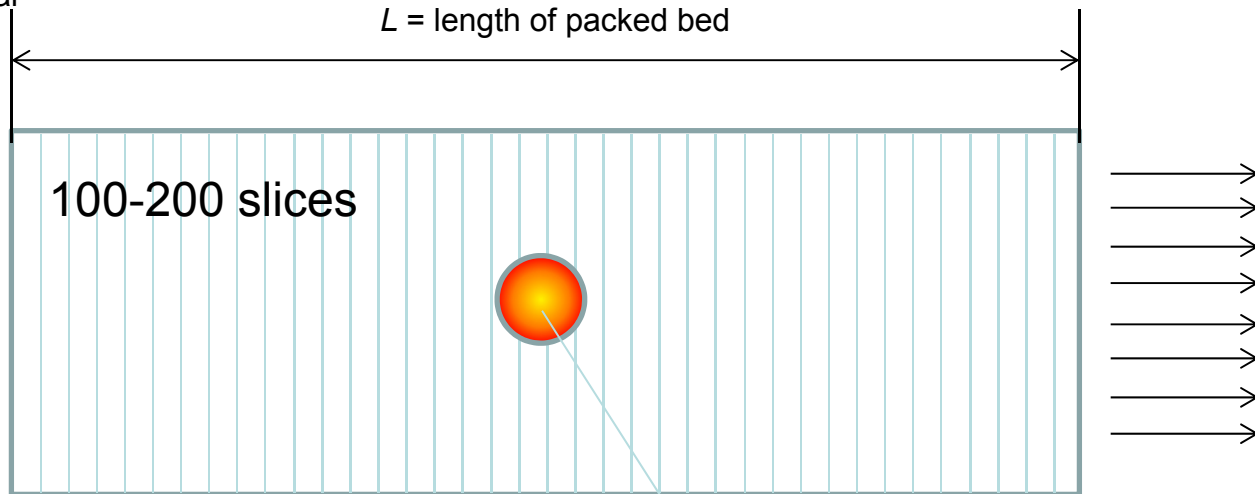
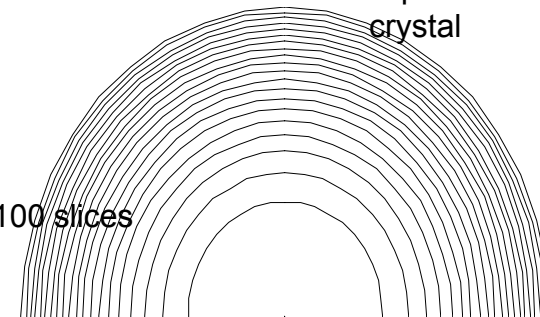
$$\frac{\partial q_i}{\partial t} = -\frac{1}{\rho} \frac{1}{r^2} \frac{\partial}{\partial r} (r^2 N_i)$$

Maxwell-Stefan equations

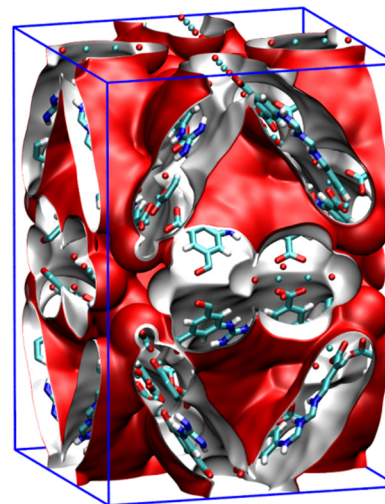
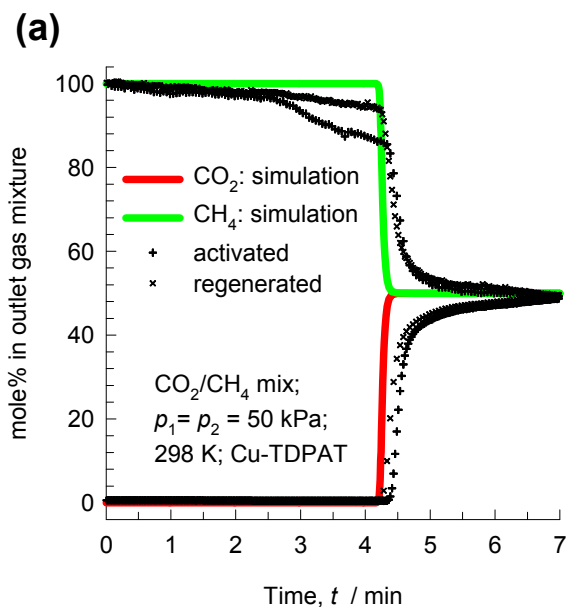
$$-\rho \frac{q_i}{RT} \nabla \mu_i = \sum_{\substack{j=1 \\ j \neq i}}^n \frac{x_j N_i - x_i N_j}{D_{ij}} + \frac{N_i}{D_i}; \quad i=1,2,\dots,n$$

Equi-volume grid within crystal

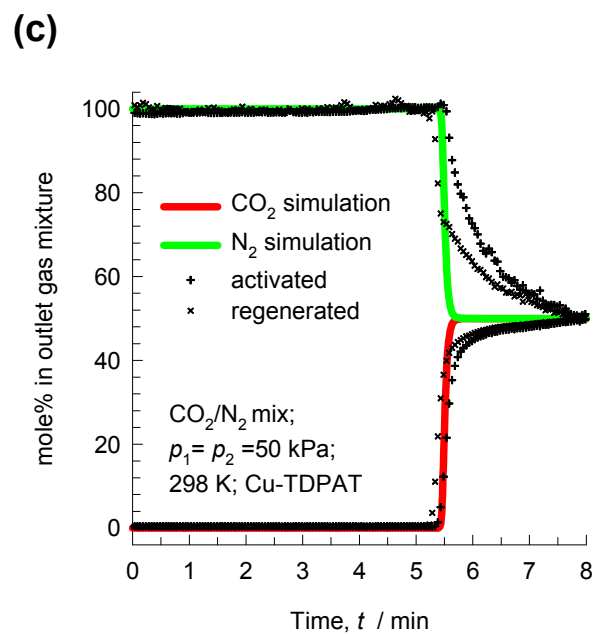
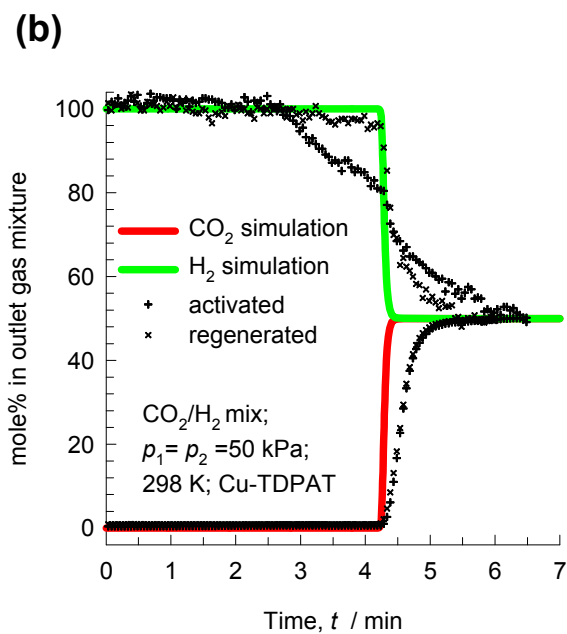
50-100 slices



Transient breakthrough in Cu-TDPAT

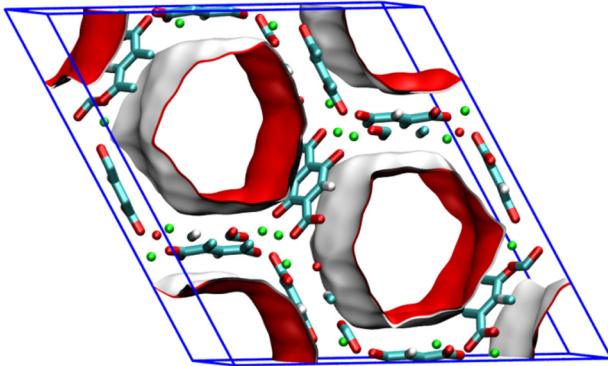


**Cu-TDPAT,
an *rht* type MOF**

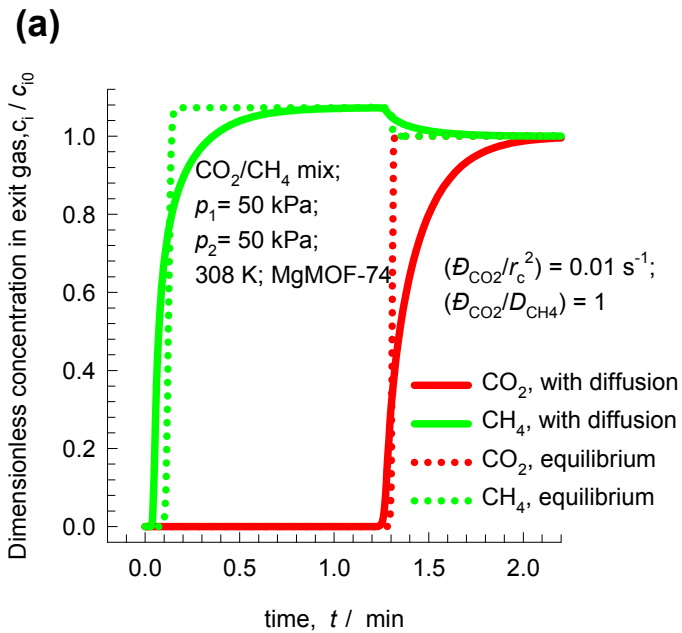
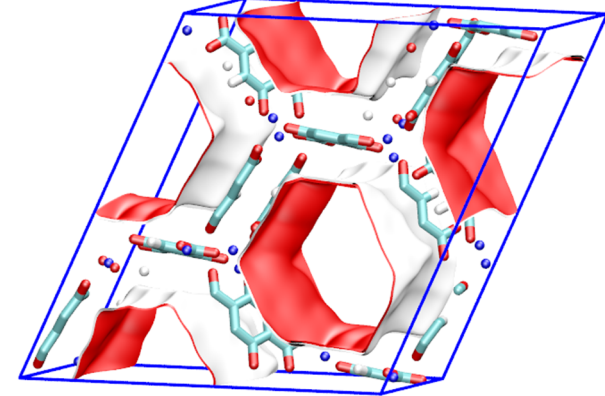


Transient breakthrough in M-MOF-74

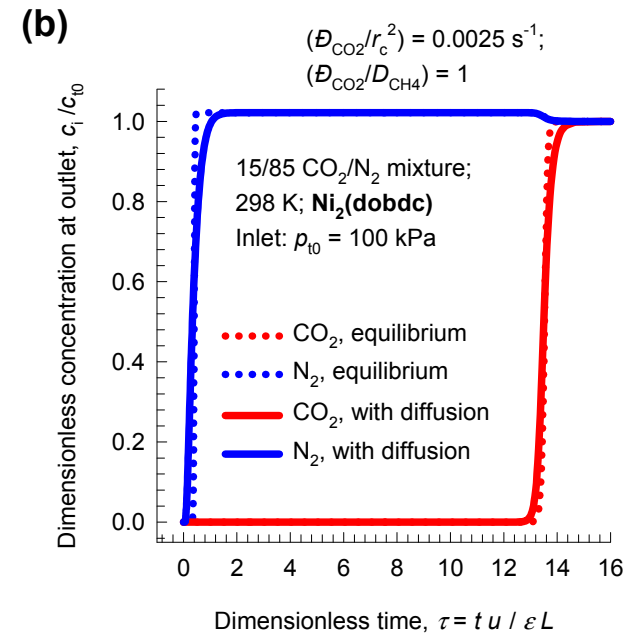
MgMOF-74



NiMOF-74



The breakthrough simulations including diffusion are in reasonable agreement with the experimental data of Remy et al.

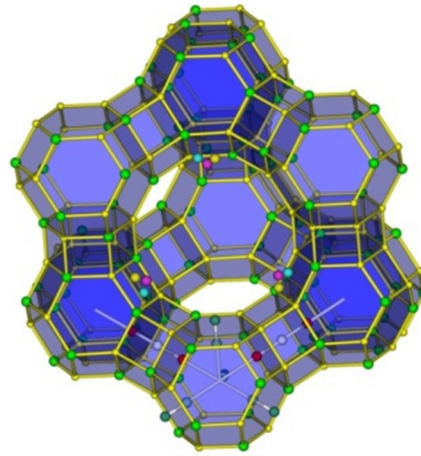


The breakthrough simulations including diffusion are in reasonable agreement with the experimental data of Liu et al.

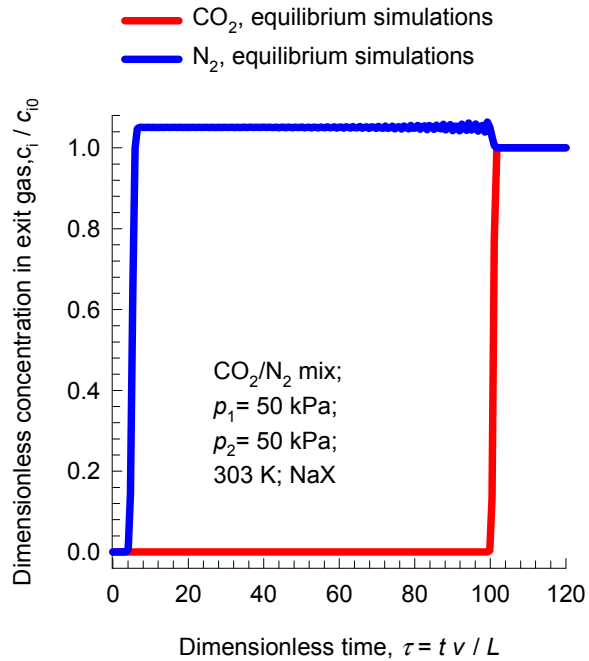
CO₂/N₂: Faujasites: NaX vs EMC-1

NaX

Si/Al = 1.3; 9.68 wt% Na; V_p = 0.34 cm³/g



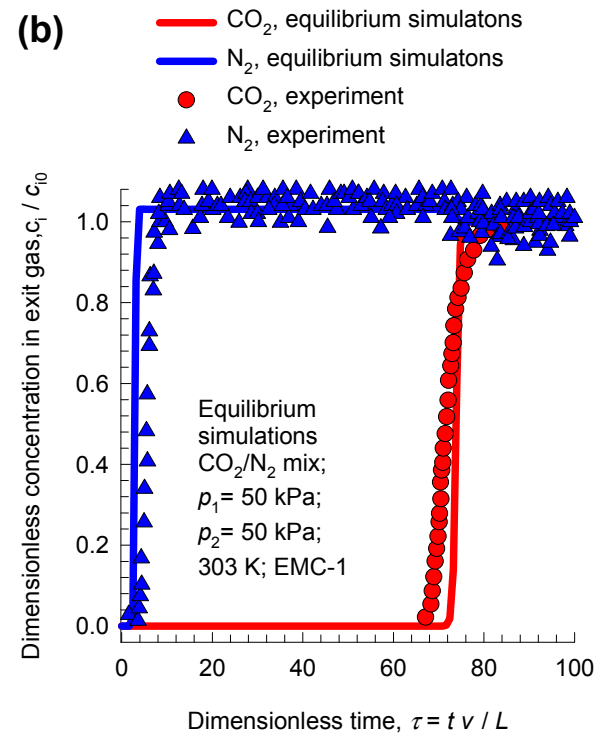
(a)



EMC-1

Si/Al = 3.9; 6.02 wt% Na; V_p = 0.33 cm³/g

(b)

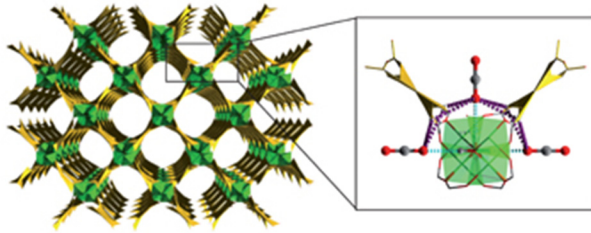


The equilibrium breakthrough simulations are in reasonable agreement with the experimental data of Pirngruber et al.

Removal of CO₂ and SO₂ or H₂S

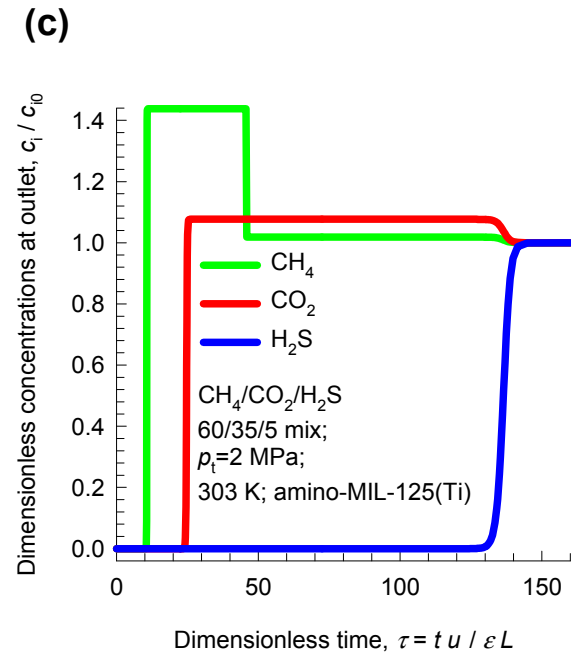
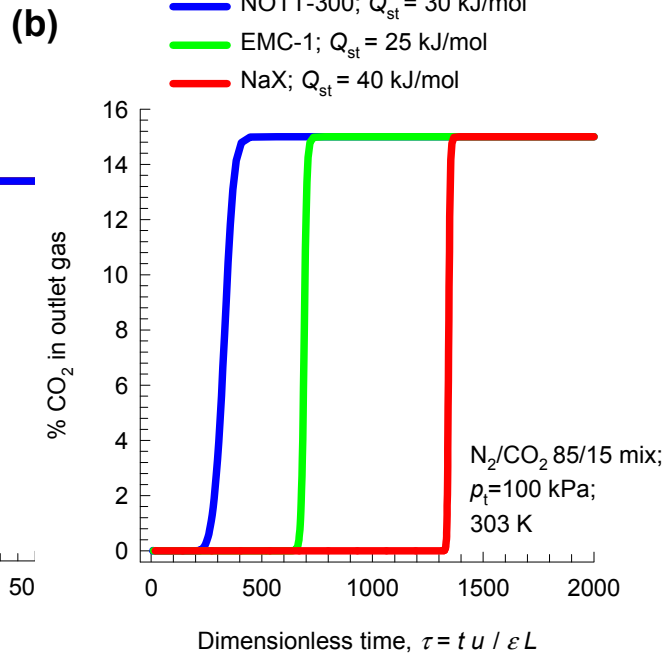
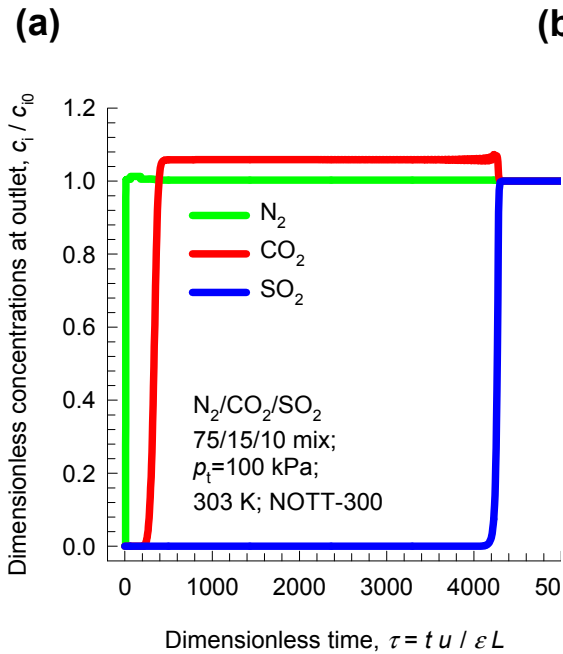
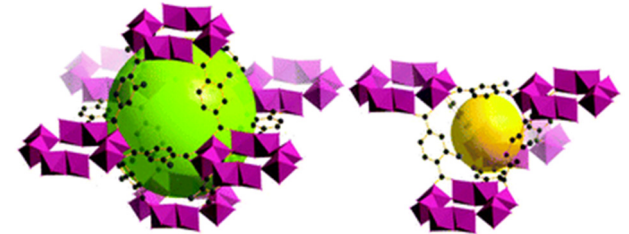
NOTT-300

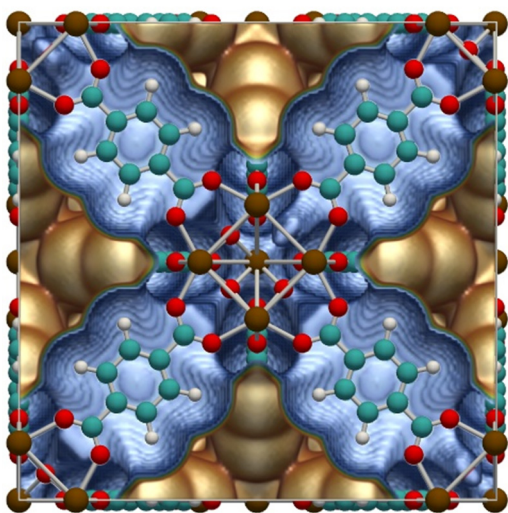
6.5 Å x 6.5 Å channels; V_p = 0.375 cm³/g



amino-MIL-125(Ti)

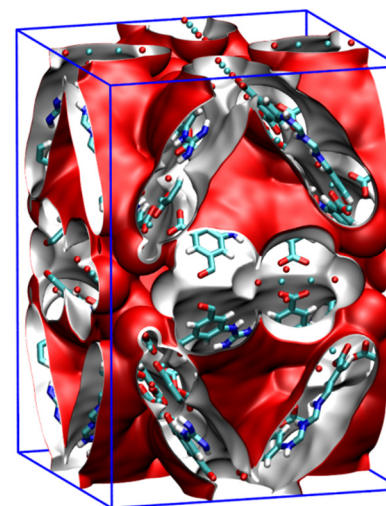
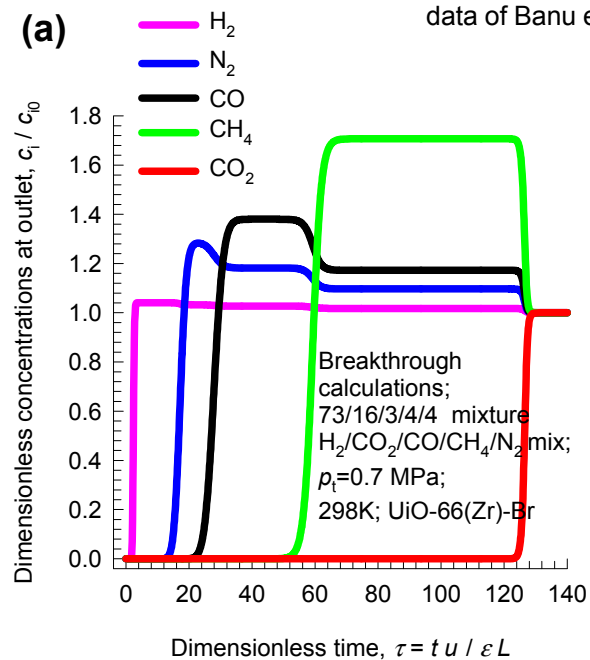
V_p = 0.54 cm³/g





UiO-66(Zr)-Br

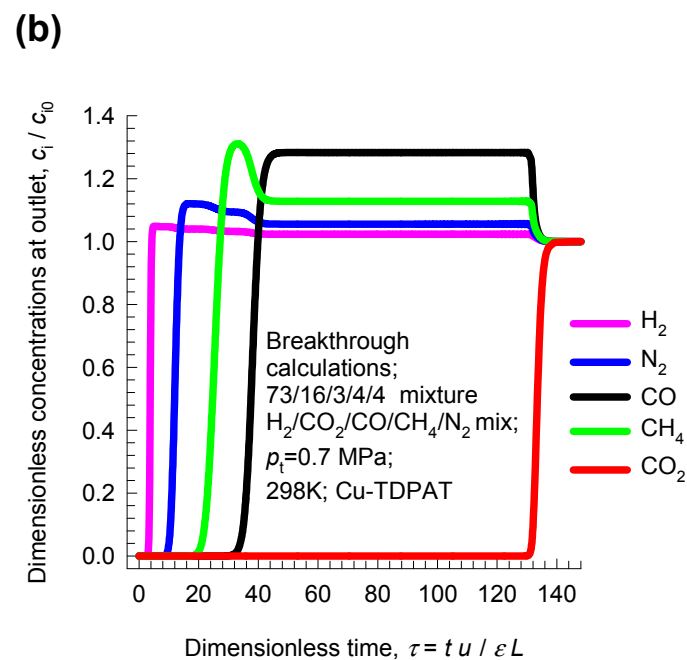
The pure component isotherms for UiO-66(Zr)-Br are based on GCMC molecular simulations as per the data of Banu et al.



Cu-TDPAT, an *rht* type MOF

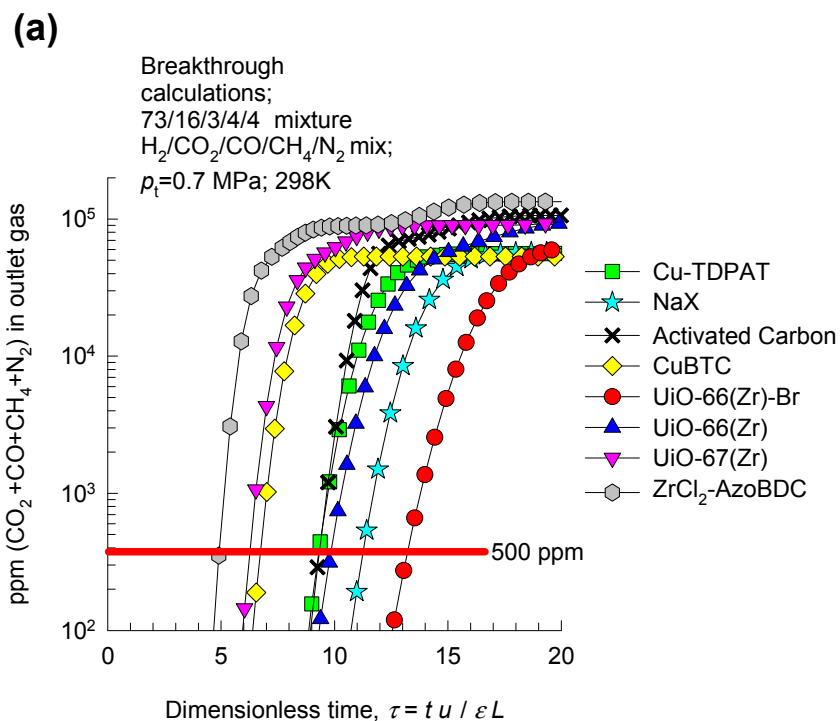
Figure 36

The pure component isotherms for Cu-TDPAT are from the experiments of Wu et al.



Breakthrough comparison H₂ purification

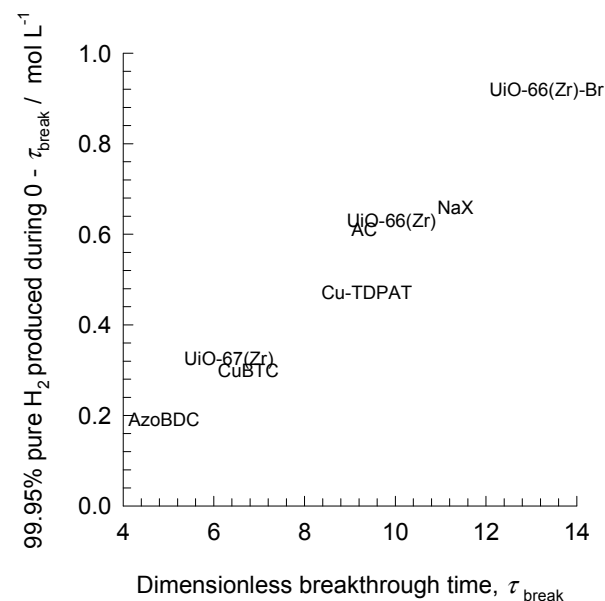
The pure component isotherms for
 UiO-66(Zr)
 UiO-66(Zr)-Br
 UiO-67(Zr)
 ZrCl₂-AzoBDC
 are based on GCMC molecular simulations as per the
 data of Banu et al.



The pure component isotherms for Cu-TDPAT are from the experiments of Wu et al.

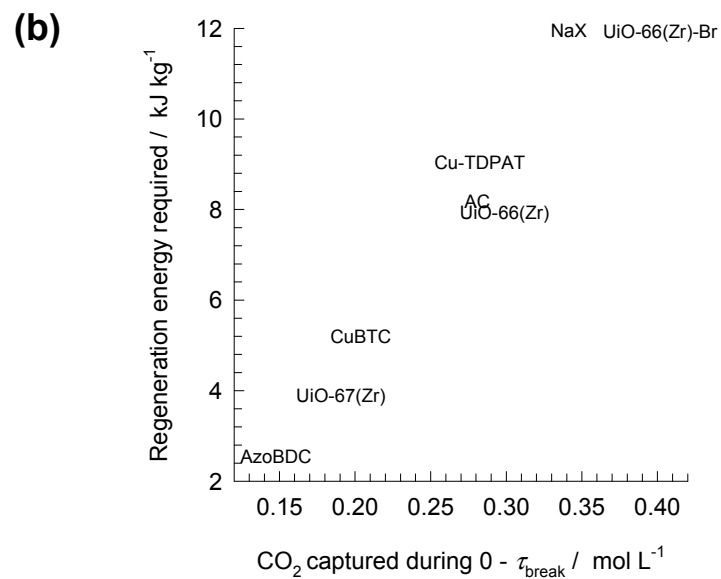
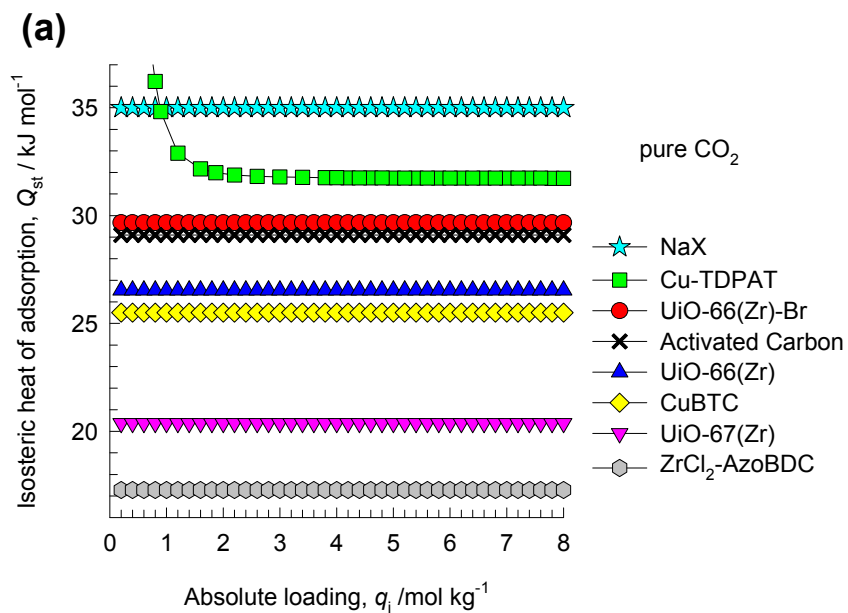
(b)

73/16/3/4/4 mixture
 H₂/CO₂/CO/CH₄/N₂ mix;
 $p_t=0.7$ MPa; 298K;
 < 500 ppm (CO₂+CO+CH₄) in H₂ product



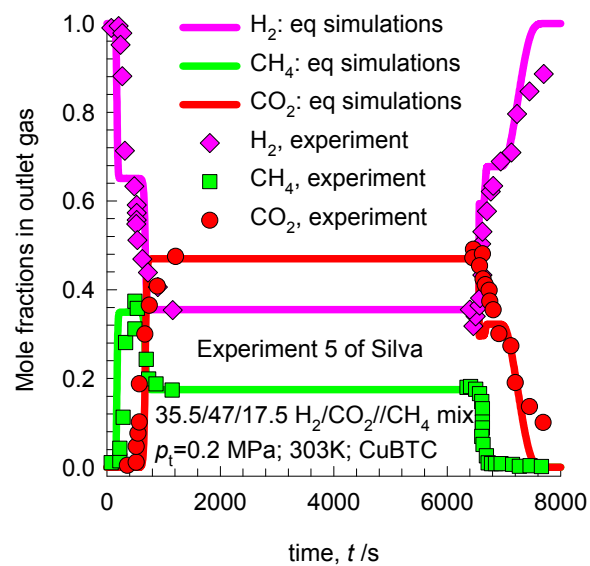
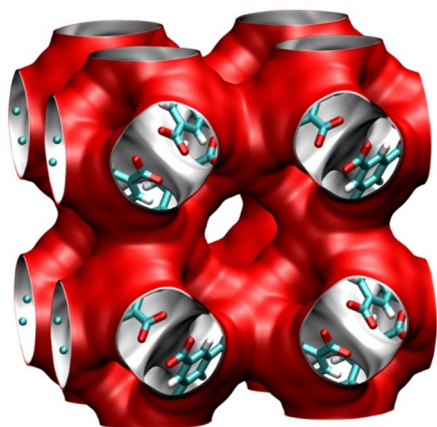
Regeneration requirements H₂ purification

73/16/3/4/4 mixture
 H₂/CO₂/CO/CH₄/N₂ mix;
 p₁=0.7 MPa; 298K;
 < 500 pmm (CO₂ +CO+CH₄) in H₂ product



Breakthrough H₂ purification CuBTC

CuBTC



Fischer Tropsch Tail Gas Separation

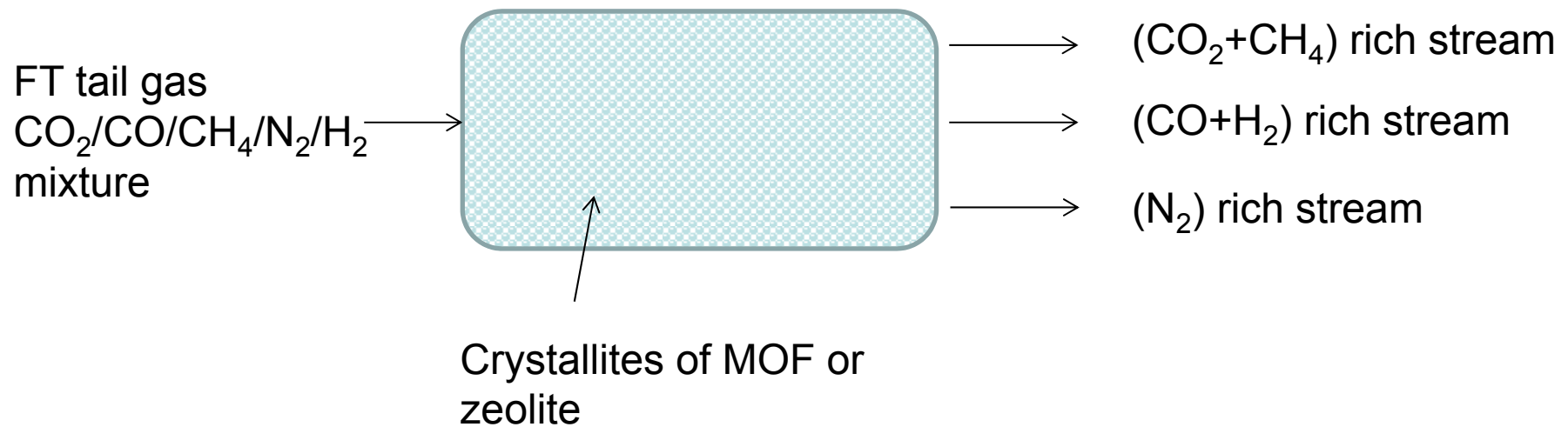
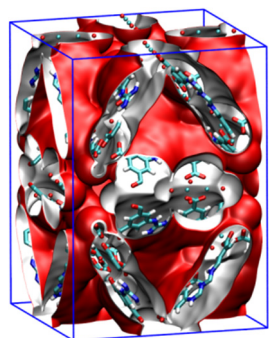
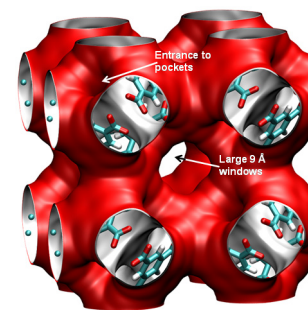
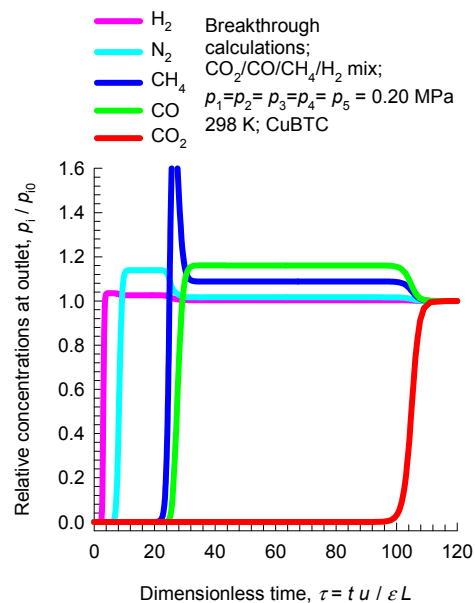
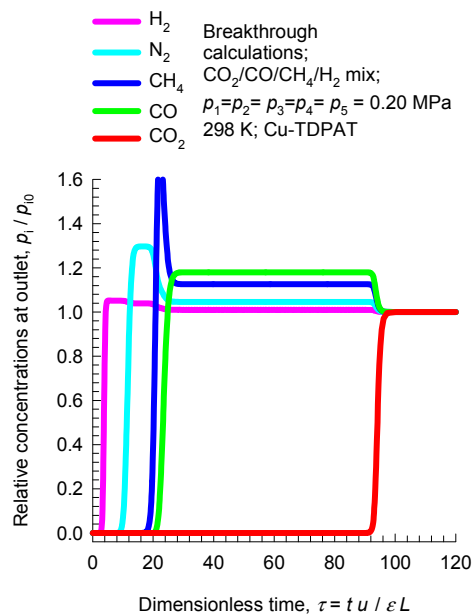


Figure 41

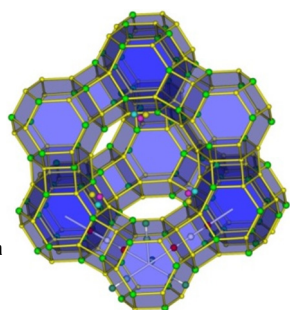
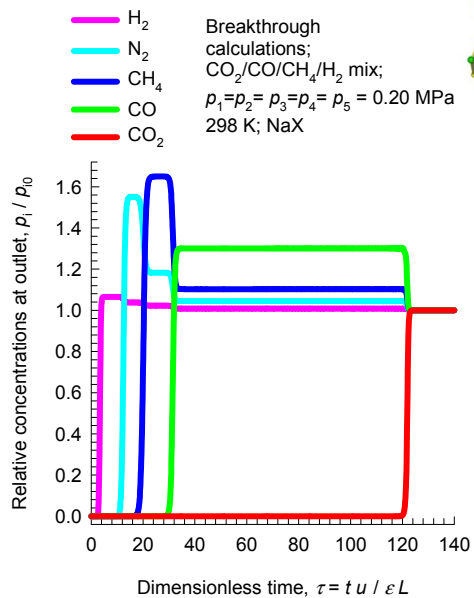


Cu-TDPAT

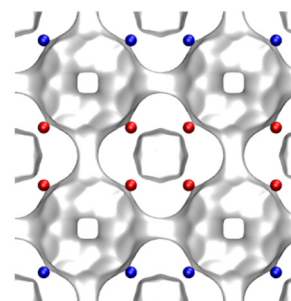
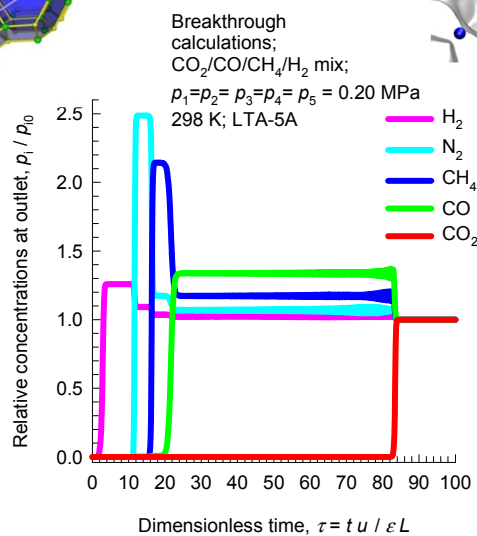


CuBTC

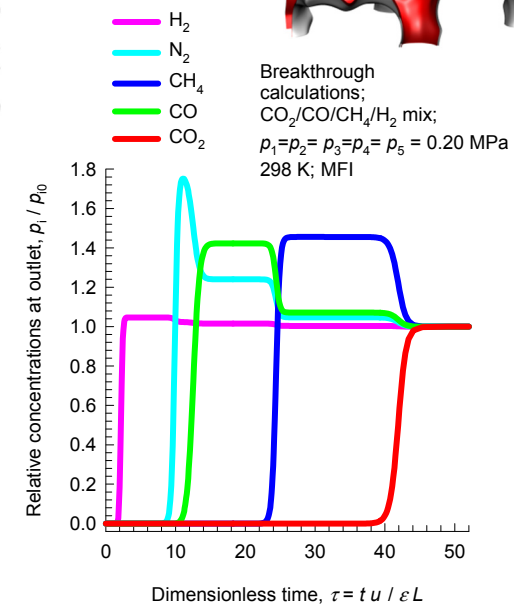
NaX zeolite



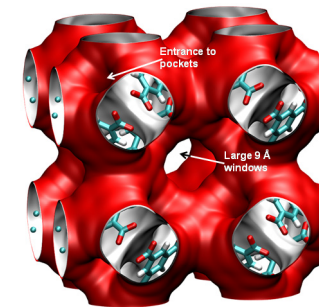
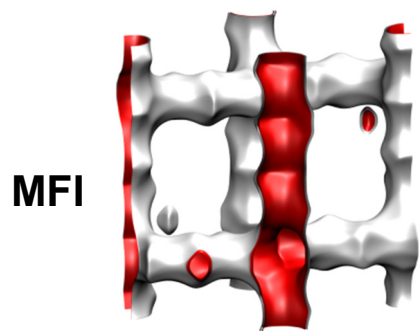
LTA-5A



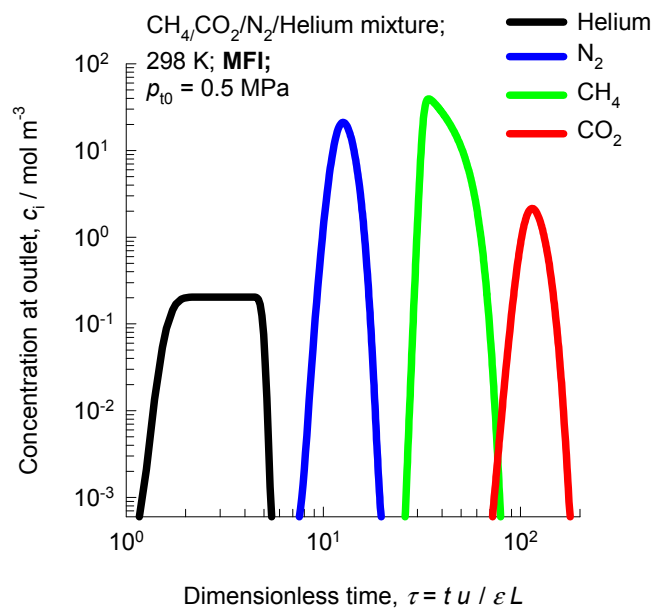
MFI



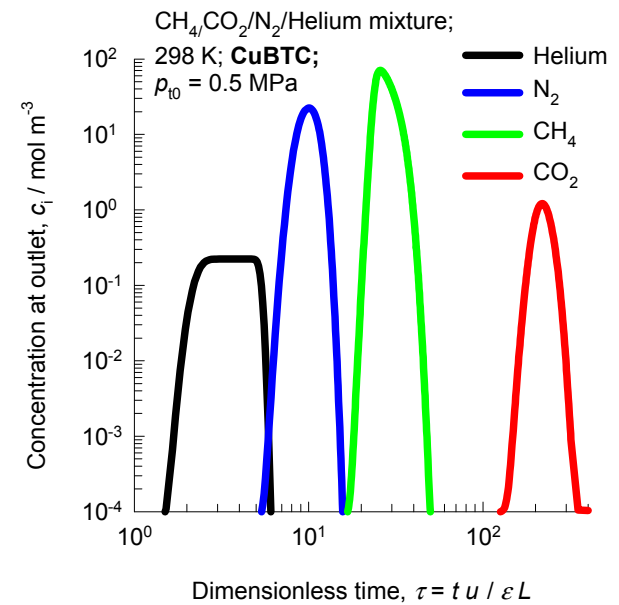
Helium recovery from Natural gas



(a)

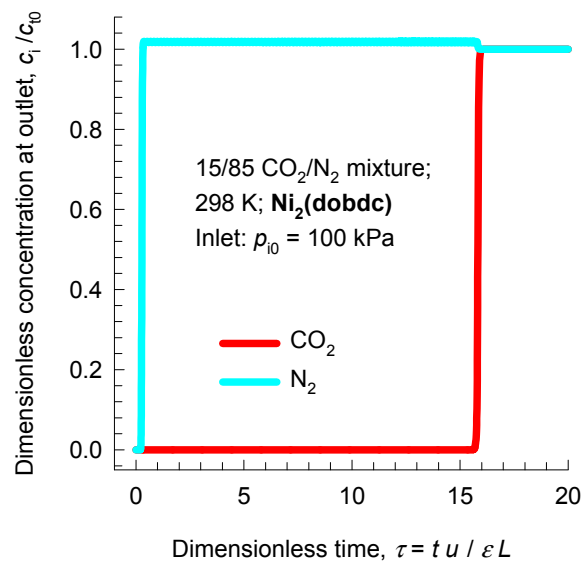
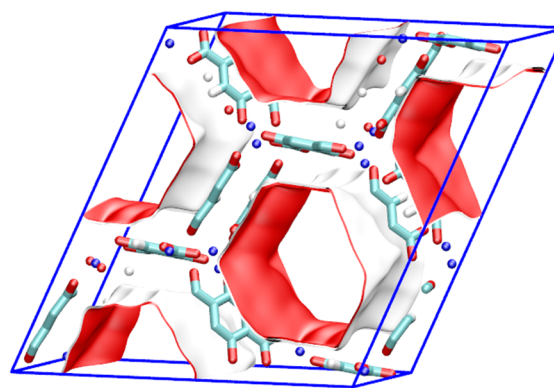


(b)



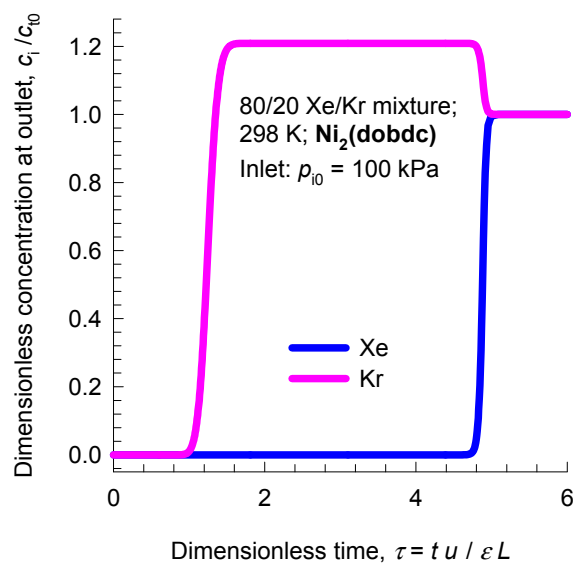
Xe/Kr recovery with NiMOF-74

(a)

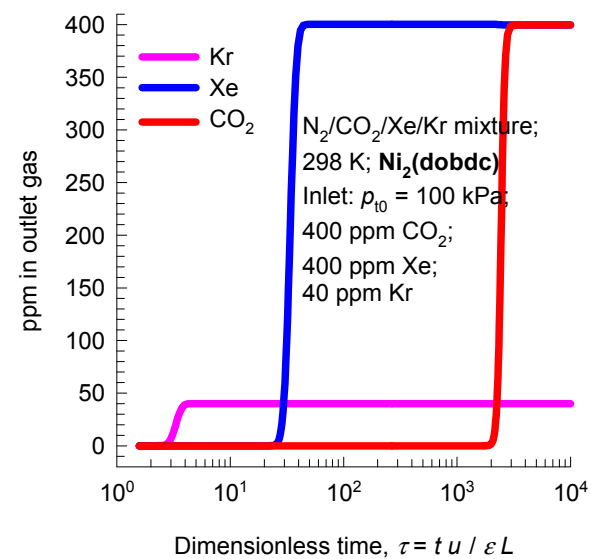
Ni₂(dobdc)

1D channels of 11 Å

(b)

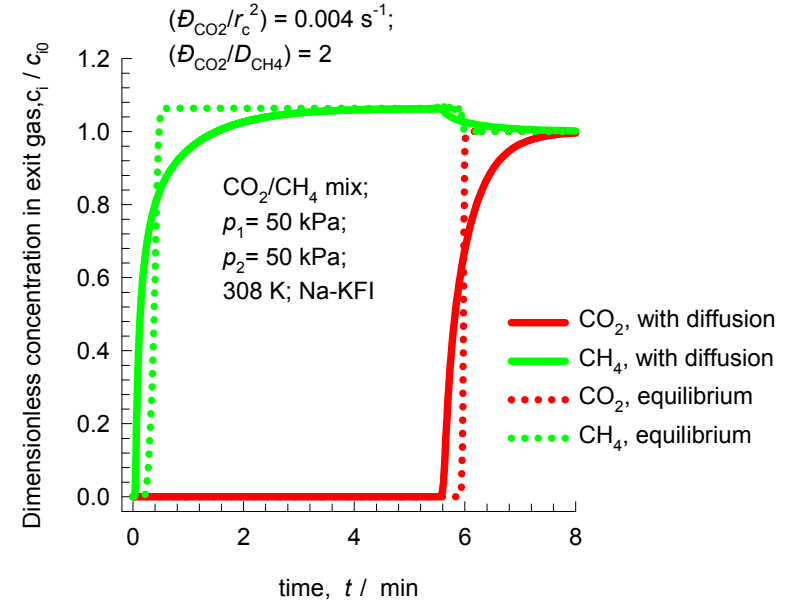
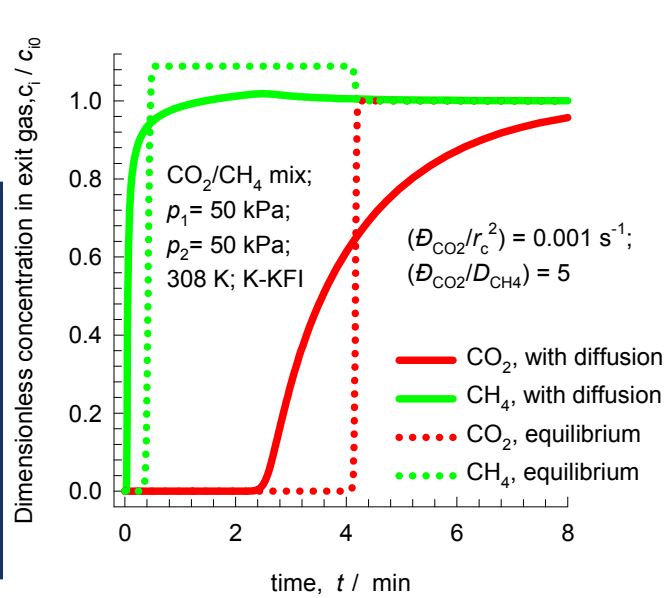
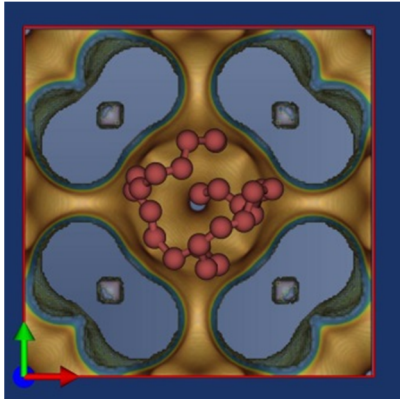


(c)

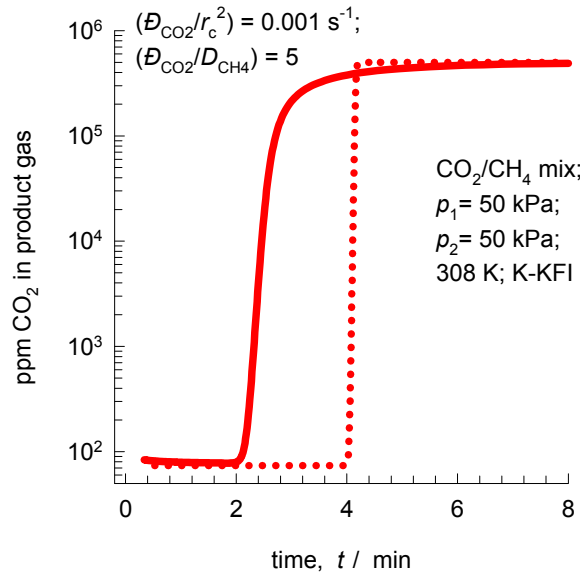


Influence of diffusion on breakthrough

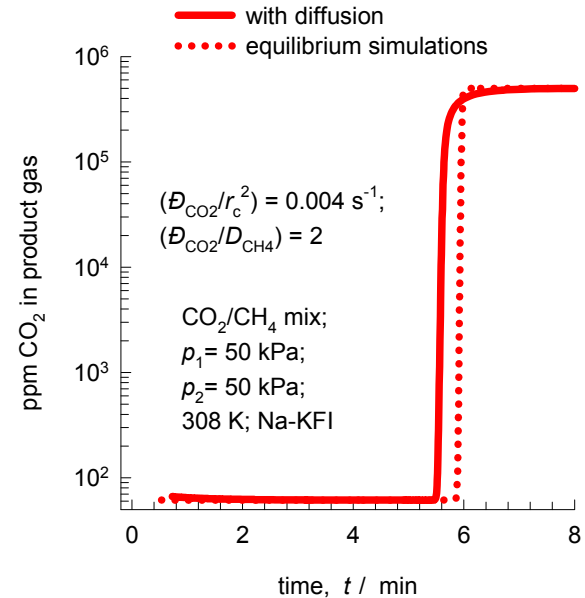
KFI



(a) — with diffusion
 equilibrium simulations



(b)

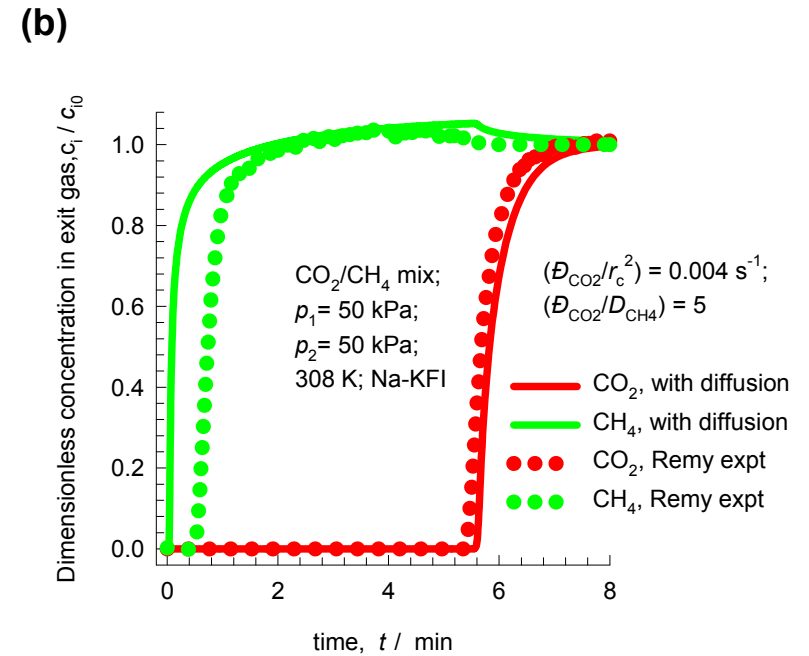
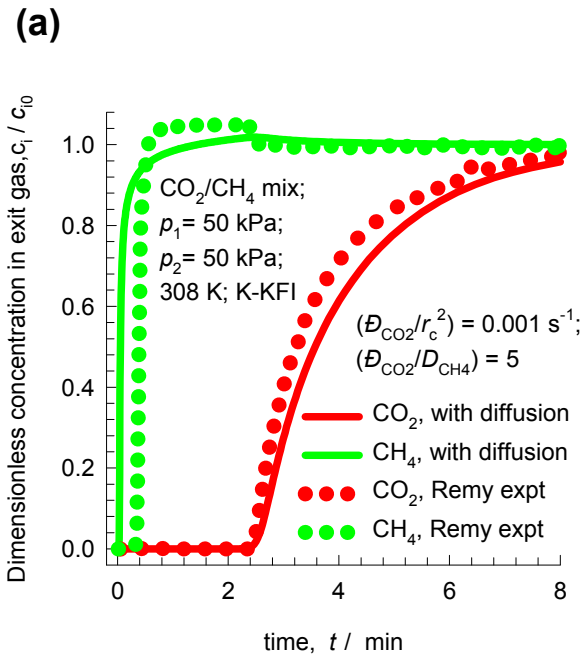
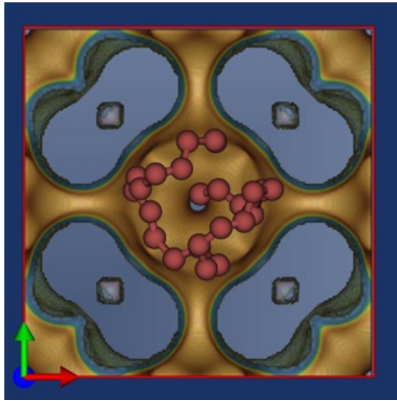


Experiment vs Simulation

CO₂/CH₄ separation with KFI

Figure 45

KFI

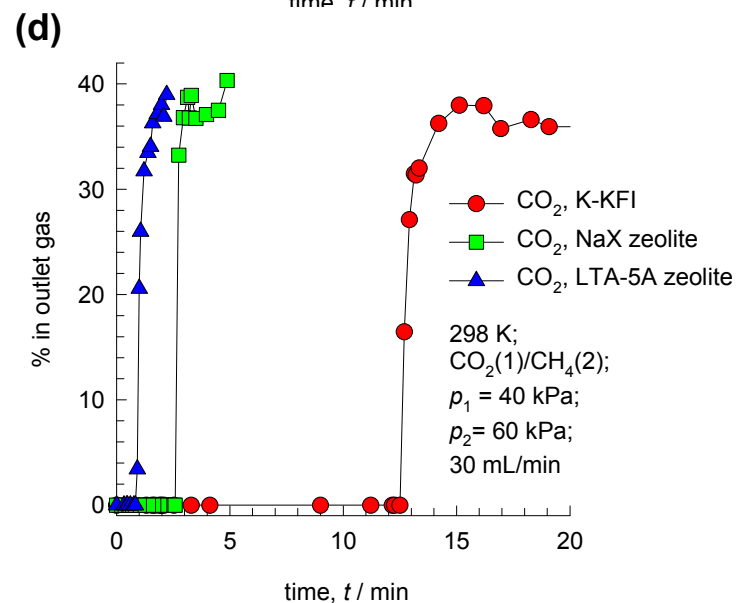
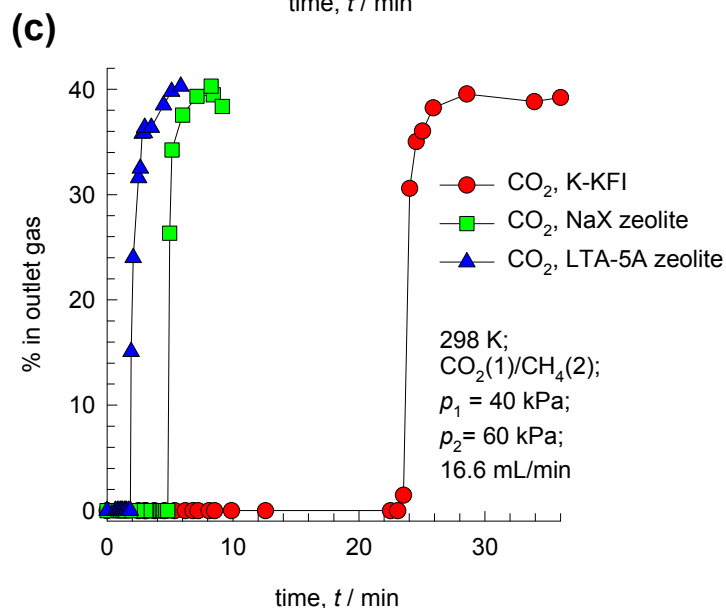
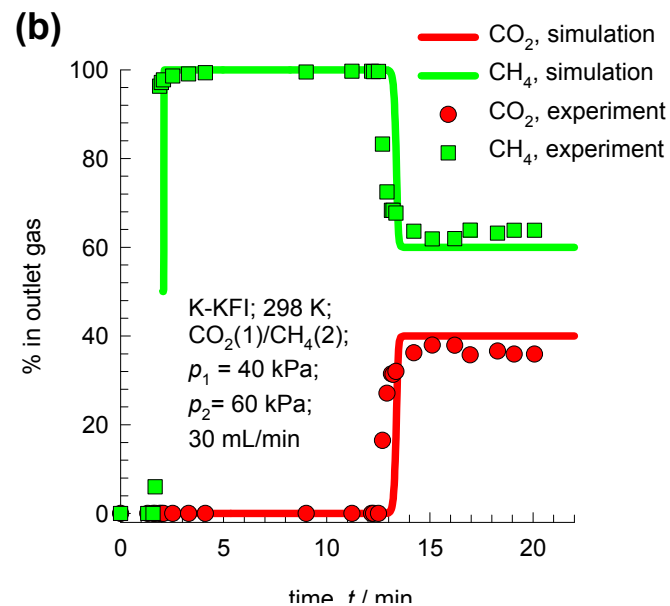
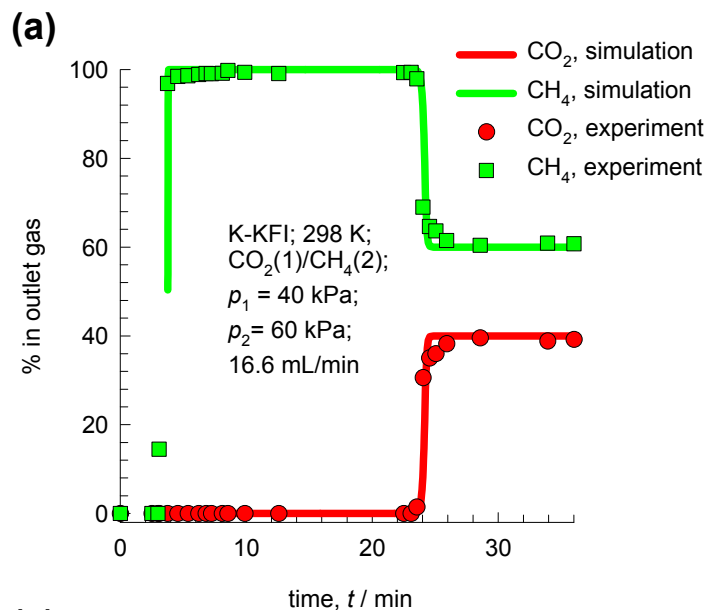
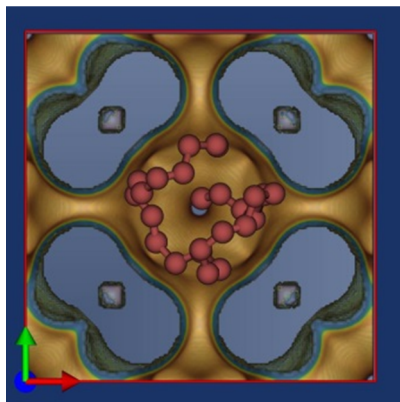


Experiment vs Simulation

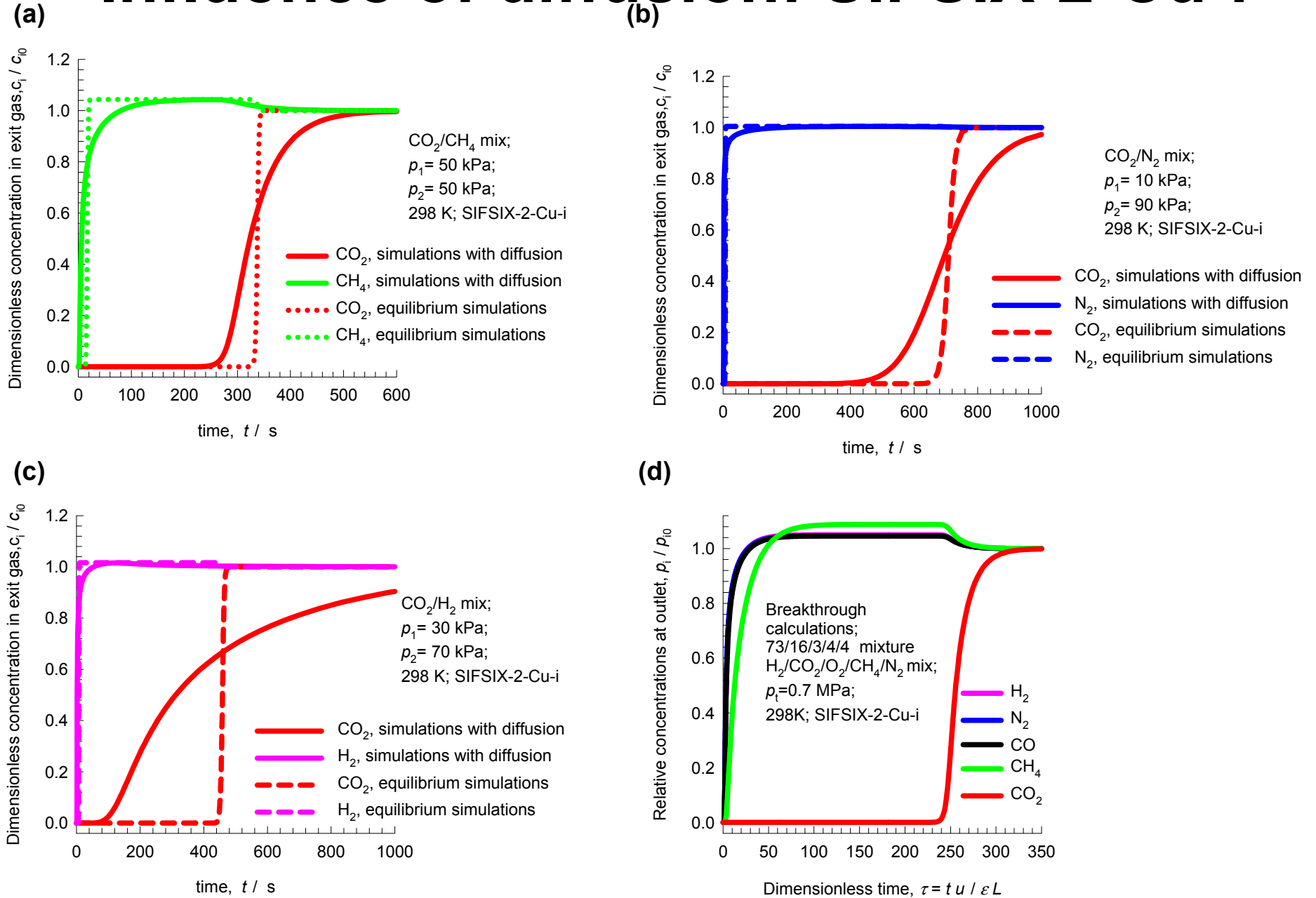
CO₂/CH₄ separation with K-KFI

Figure 46

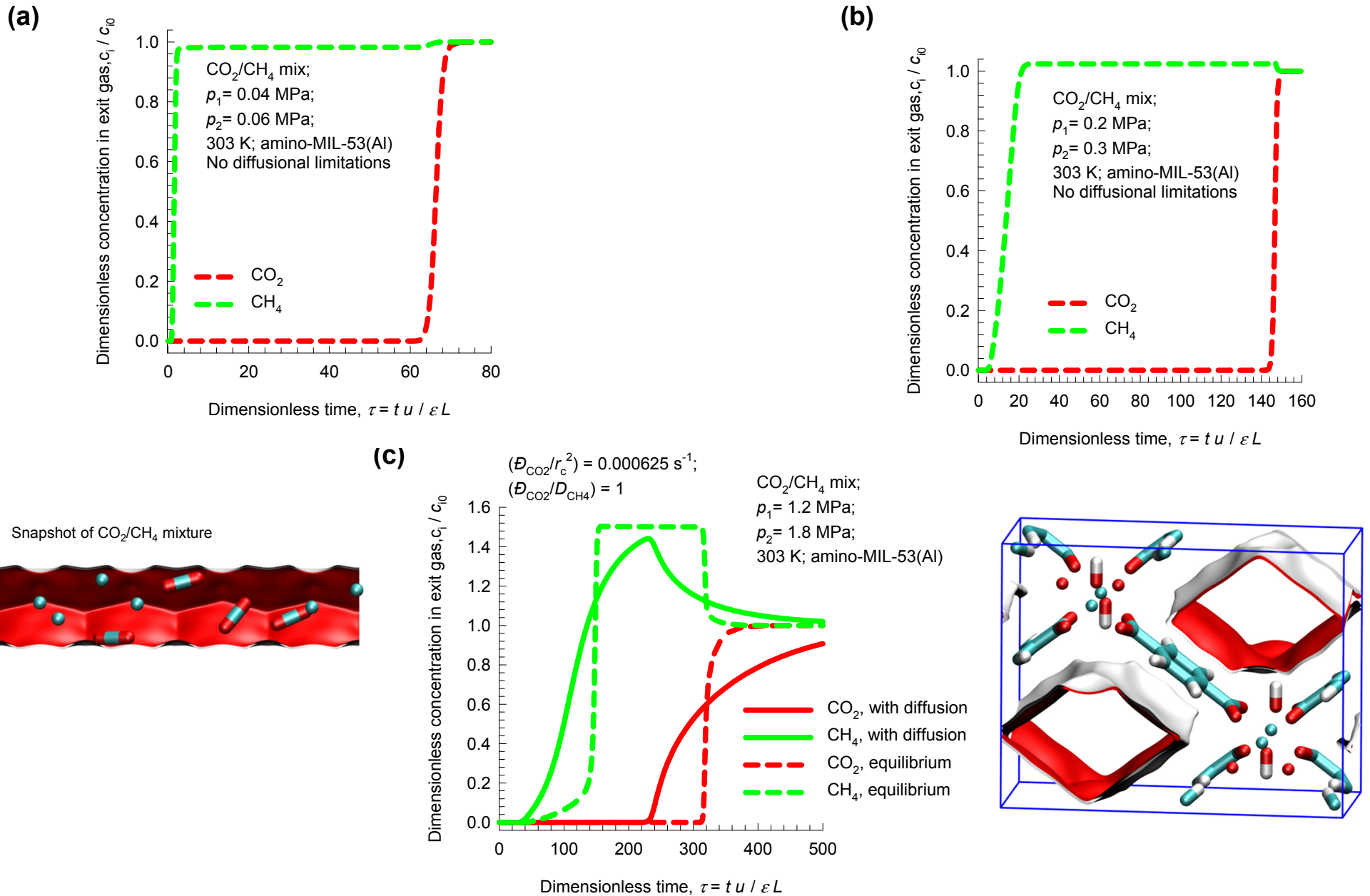
KFI



Influence of diffusion: SIFSIX-2-Cu-i

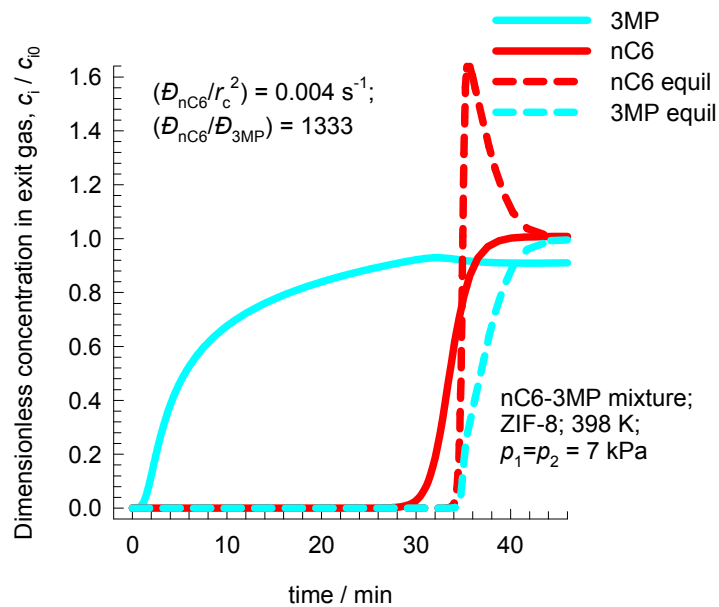


Influence of diffusion: amino-MIL53(AI)

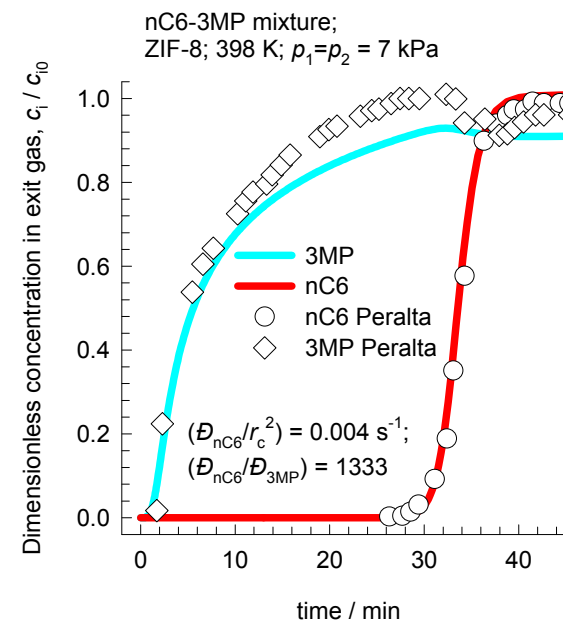


ZIF-8: compare with Fig 6 of Peralta

(a) Equilibrium simulations vs Diffusion

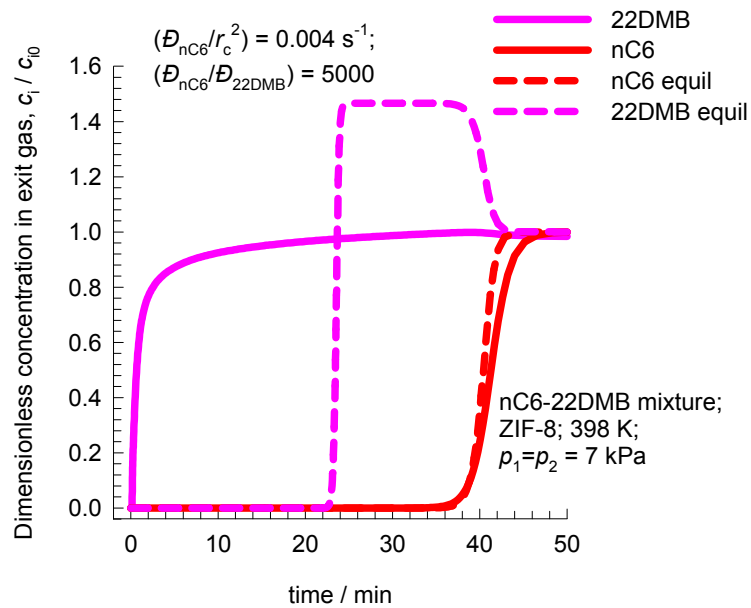


(b) Experiments vs Simulations with diffusion

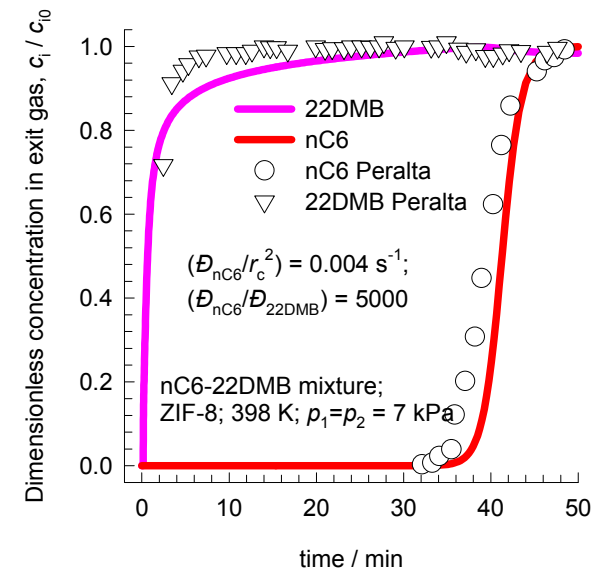


ZIF-8: compare with Fig 8 of Peralta

(a) Equilibrium simulations vs Diffusion

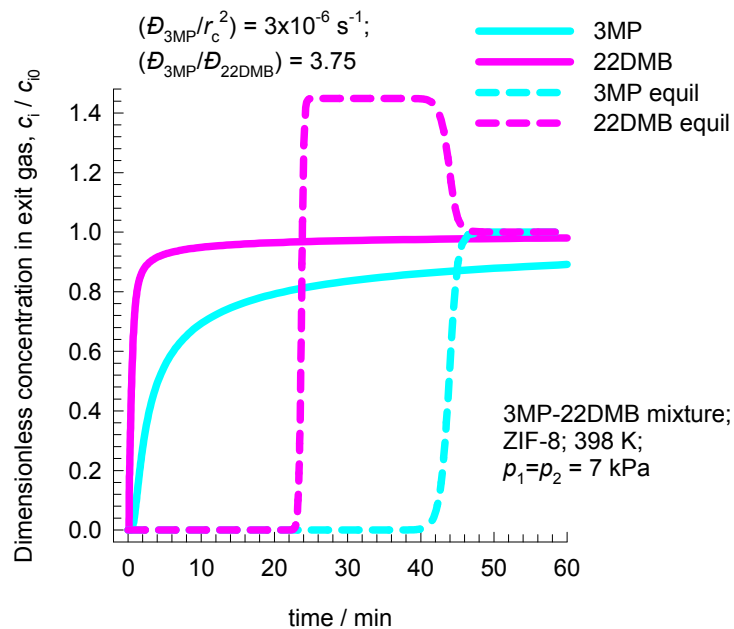


(b) Experiments vs Simulations with diffusion



ZIF-8: compare with Fig 9 of Peralta

(a) Equilibrium simulations vs Diffusion



(b) Experiments vs Simulations with diffusion

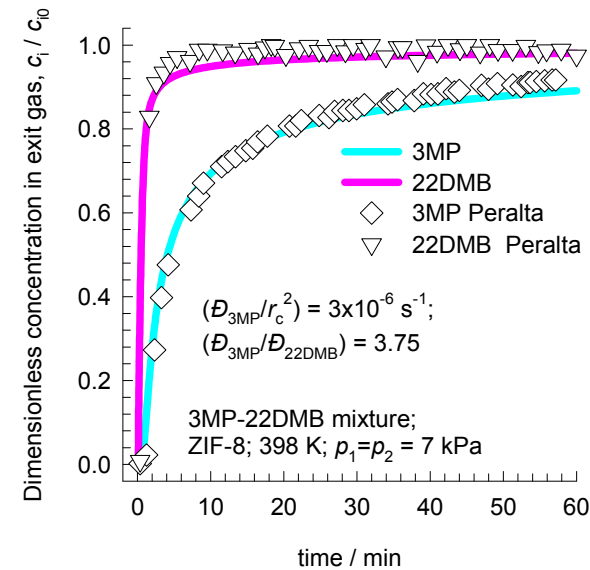
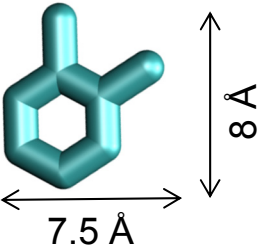
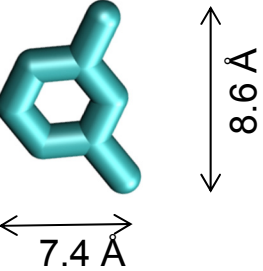
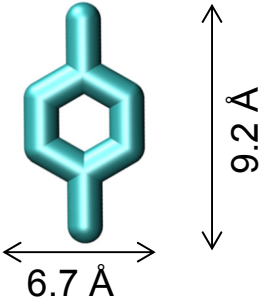
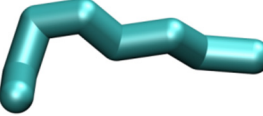
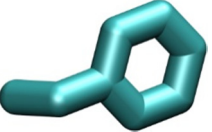
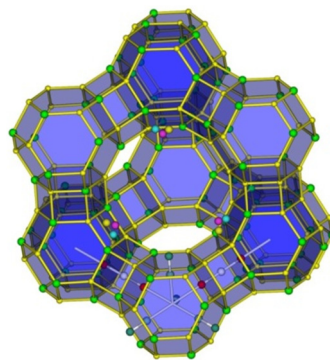


Figure 52

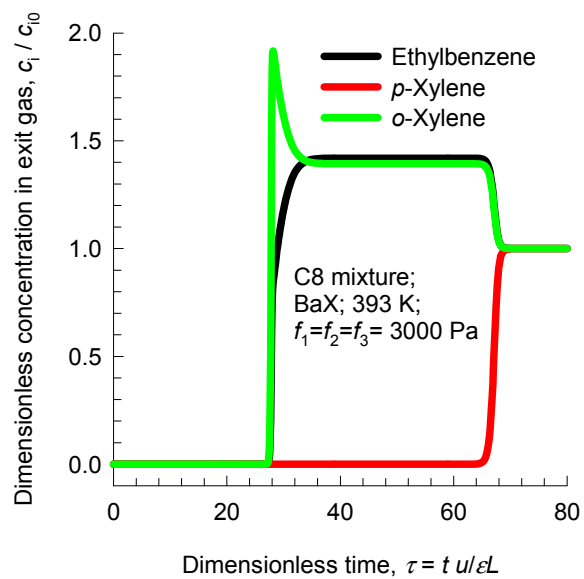
		Boiling point / K	Freezing point / K
o-xylene (oX)		417.6	248
m-xylene (mX)		412.3	222.5
p-xylene (pX)		411.5	286.4
n-octane (nC8)		398.8	216.4
Ethylbenzene (EtBz)		409.3	178.2
Styrene (St)		418.3	242.5

BaX breakthrough simulations for 3-component xylenes mixture

Figure 53



(a)



(b)

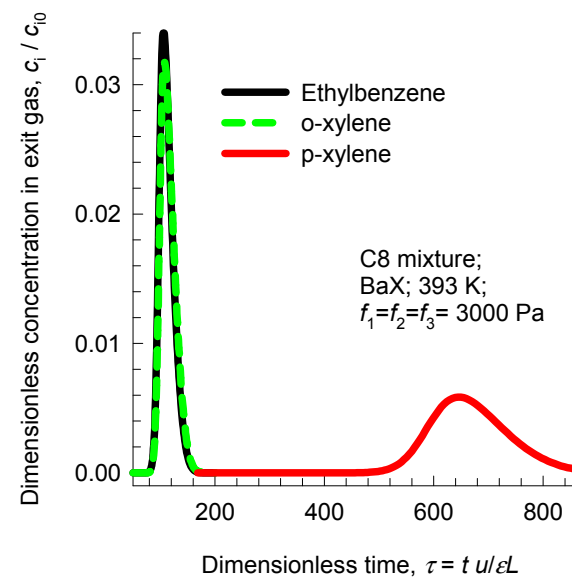
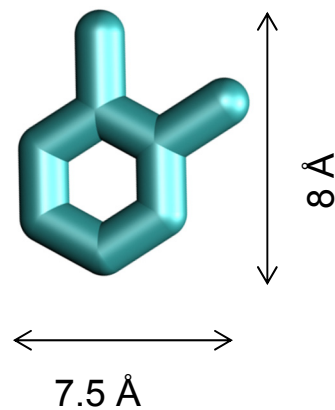
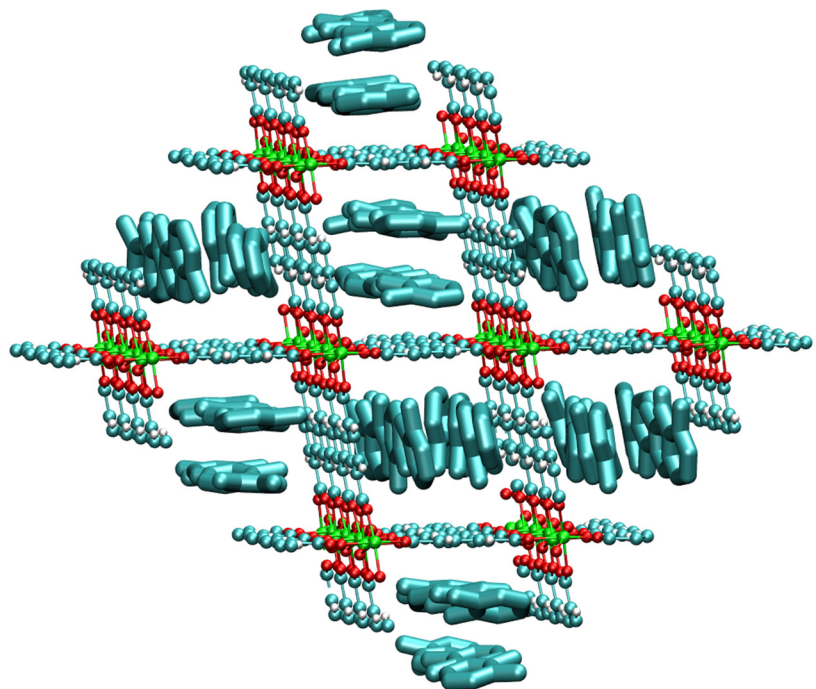


Figure 54



o-xylene adsorption in MIL-47

Stacking of o-xylene along channels

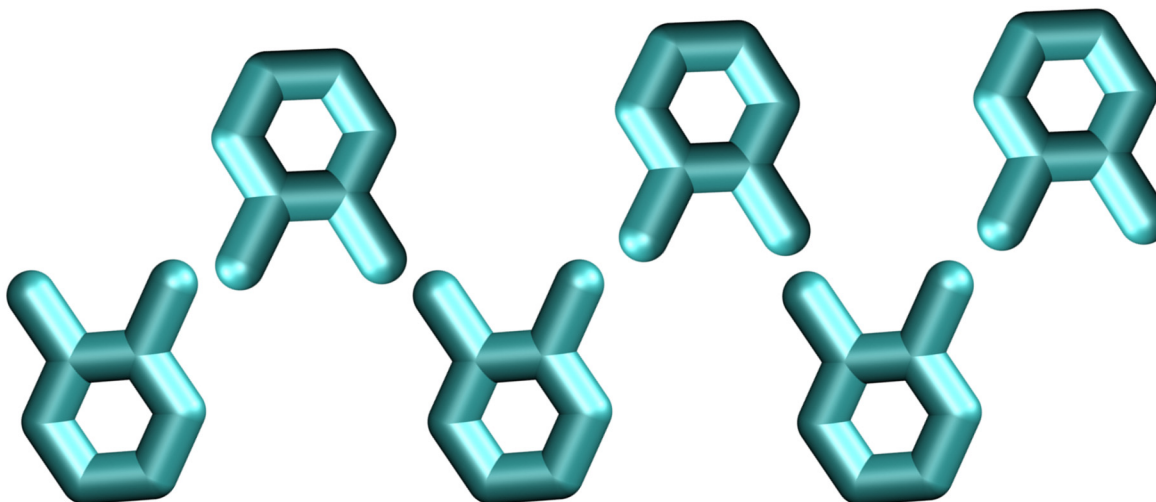
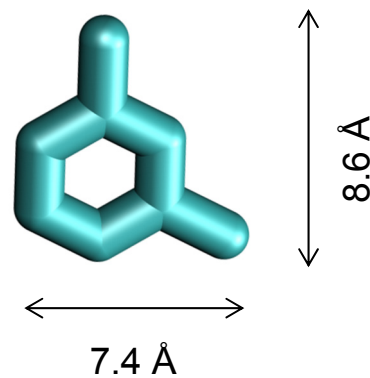
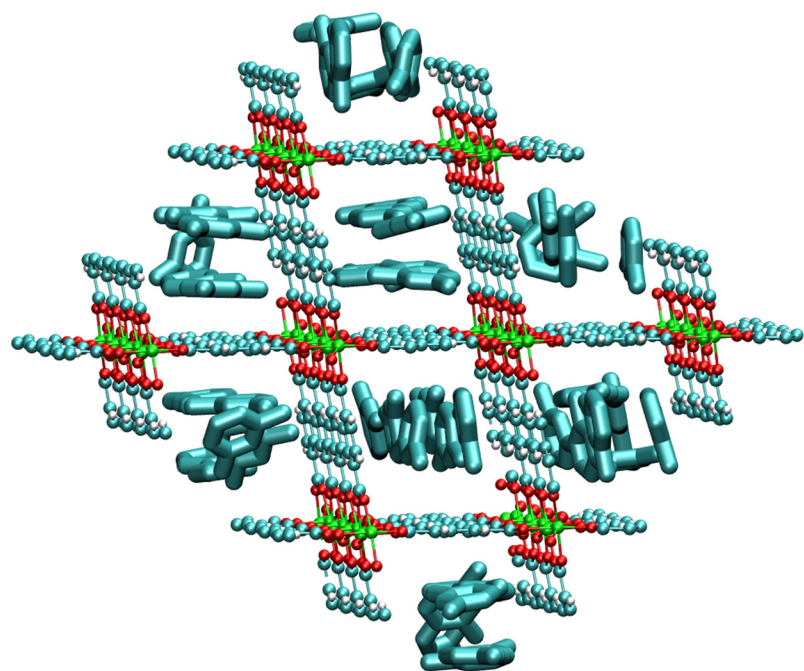


Figure 55



Stacking of m-xylene along channels

***m*-xylene
adsorption in
MIL-47**

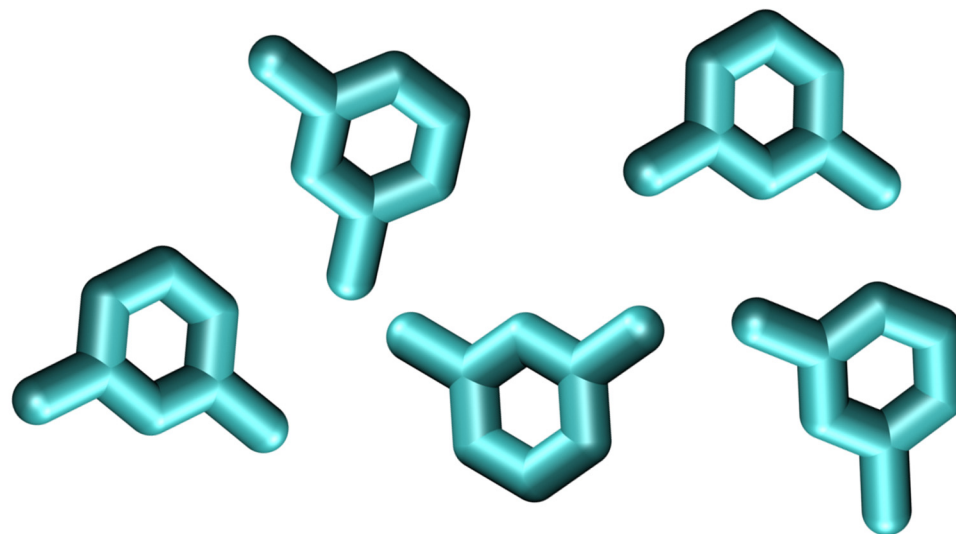
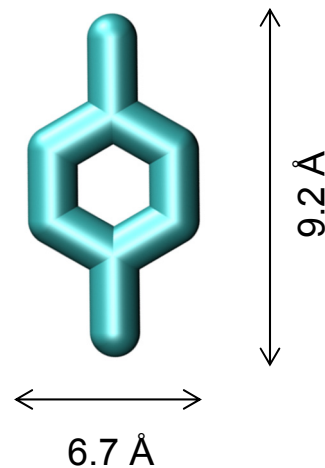
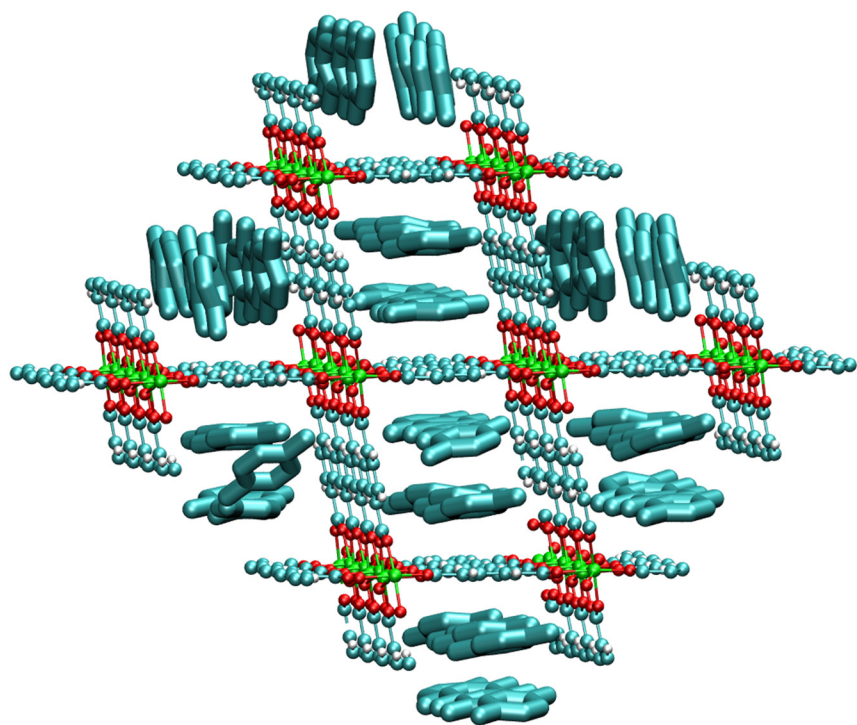


Figure 56



Stacking of p-xylene along channels

***p*-xylene
adsorption in
MIL-47**

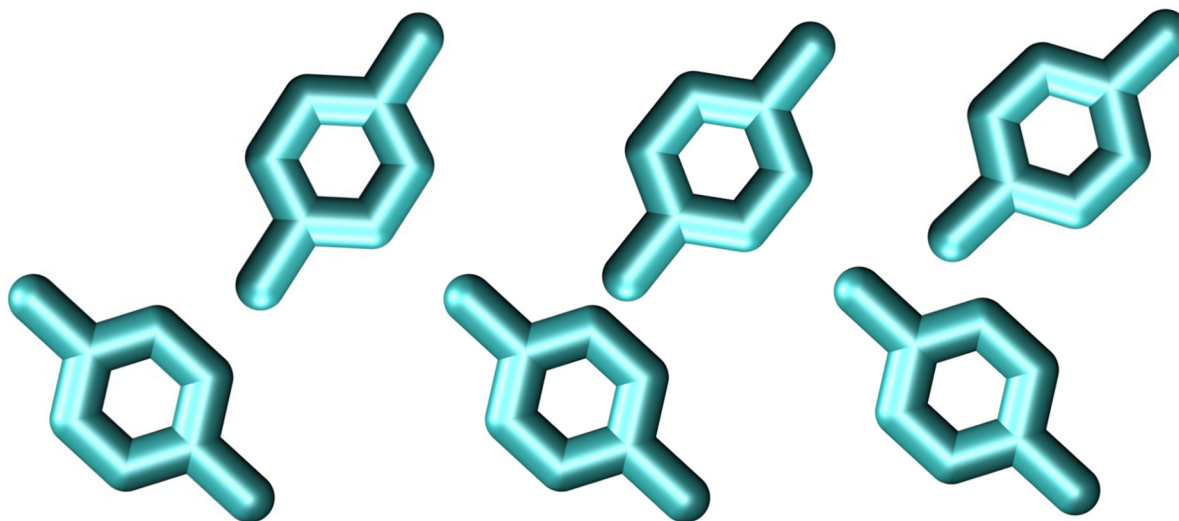
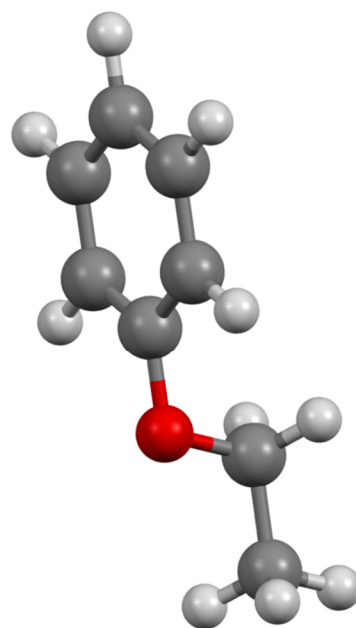
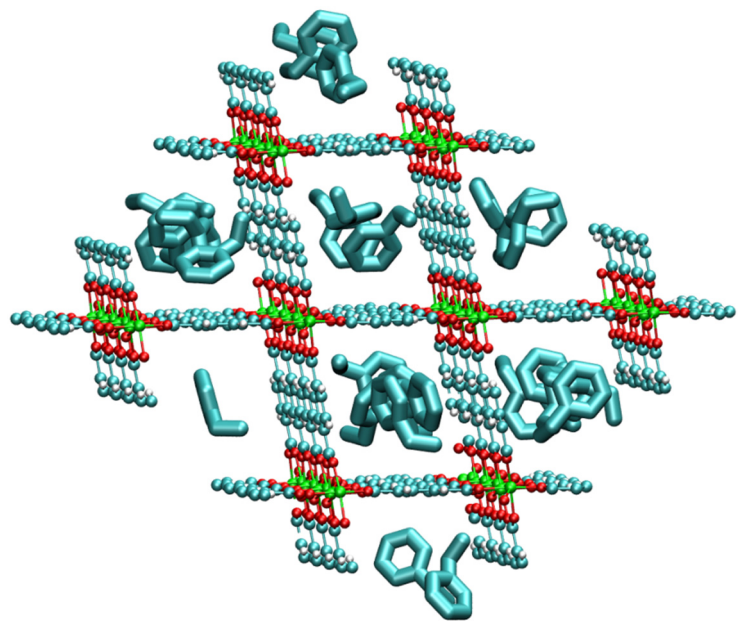


Figure 57



Ethylbenzene is not a flat molecule; the ethyl branch is not in the same plane as the benzene ring

Ethylbenzene adsorption in MIL-47

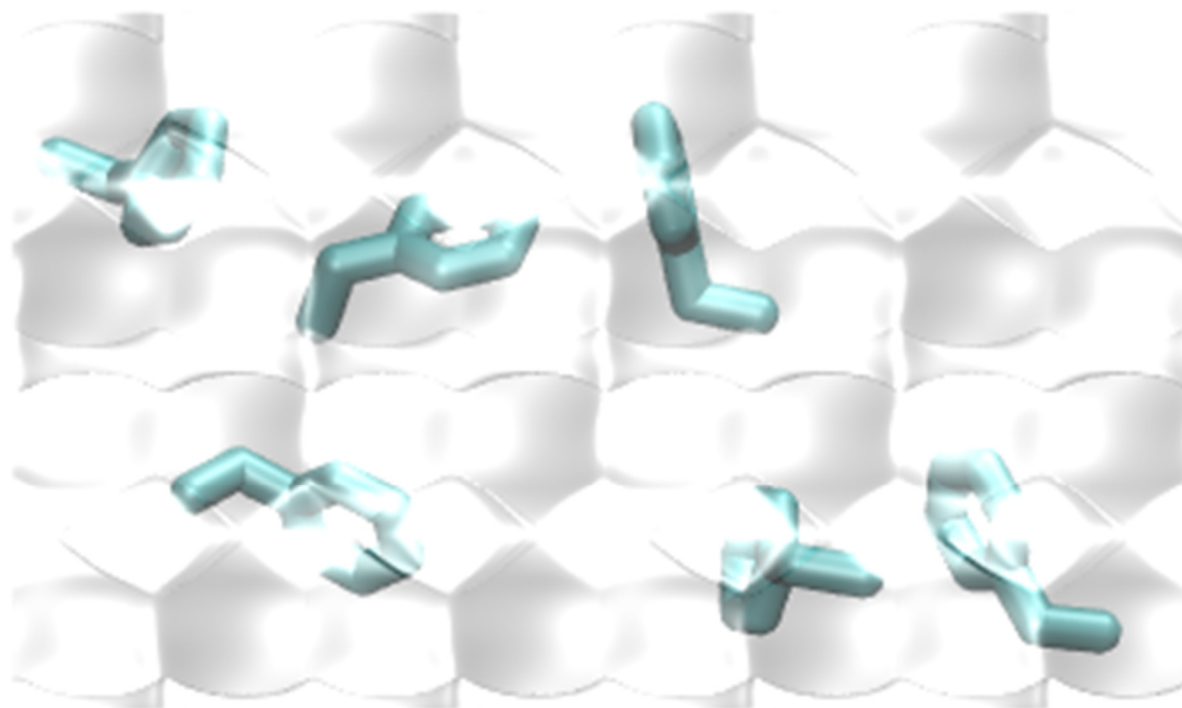
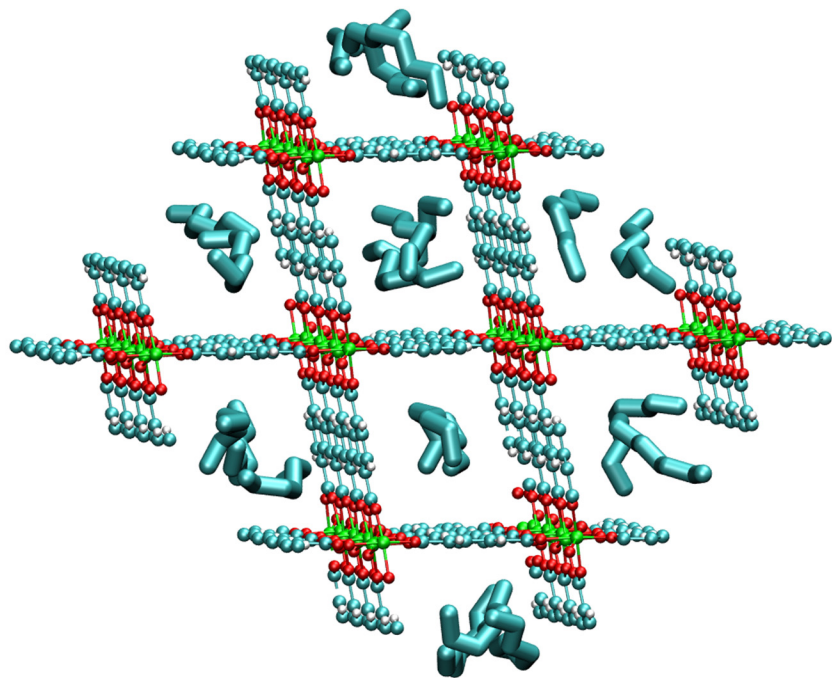


Figure 58



**nC8
adsorption in
MIL-47**

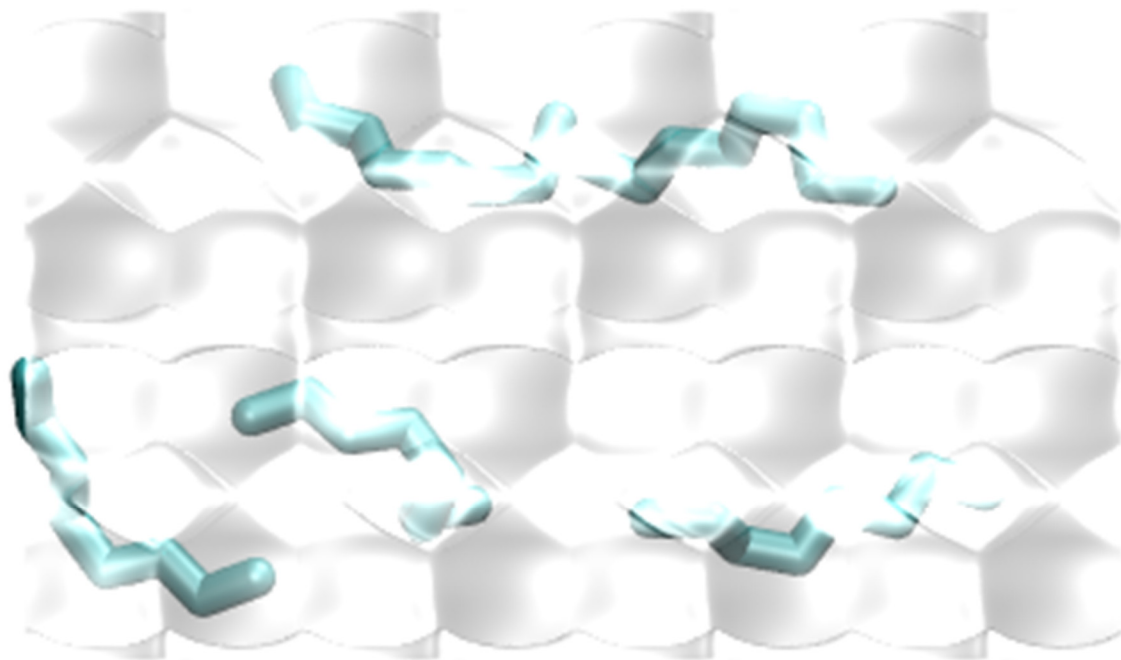
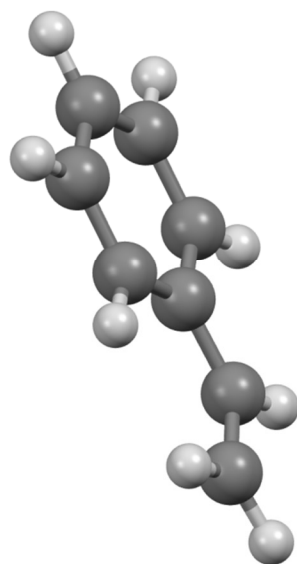
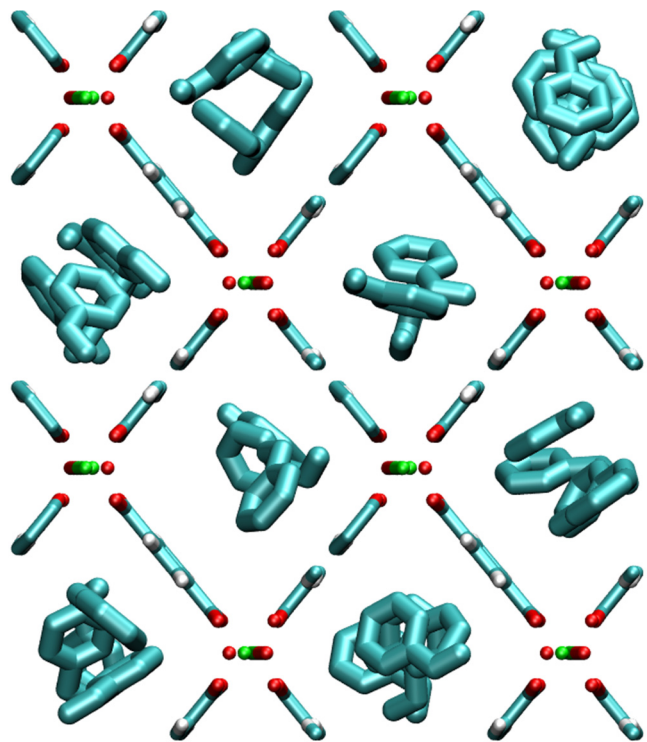
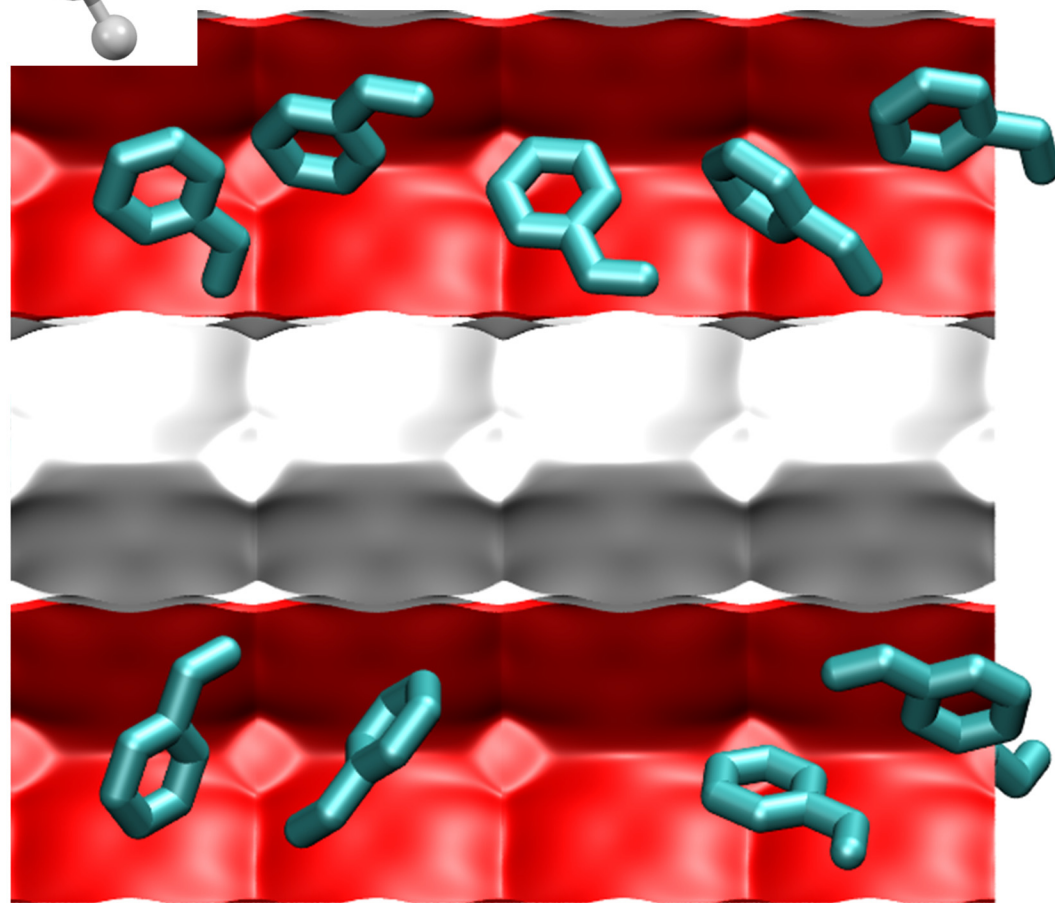


Figure 59



Styrene is a flat molecule; the branch is in the same plane as the benzene ring

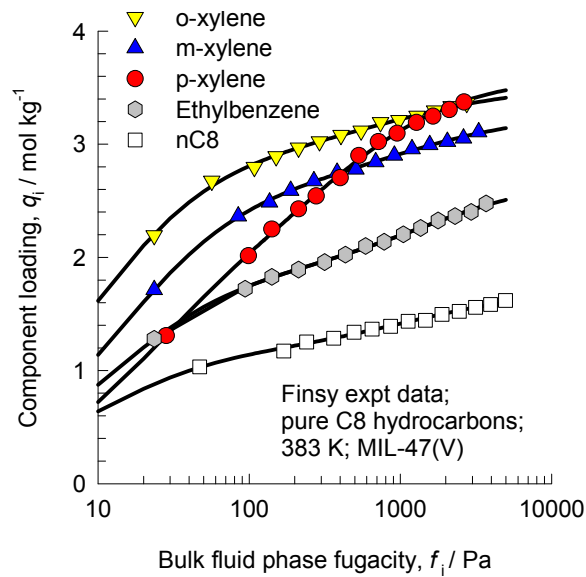
Styrene adsorption in MIL-47



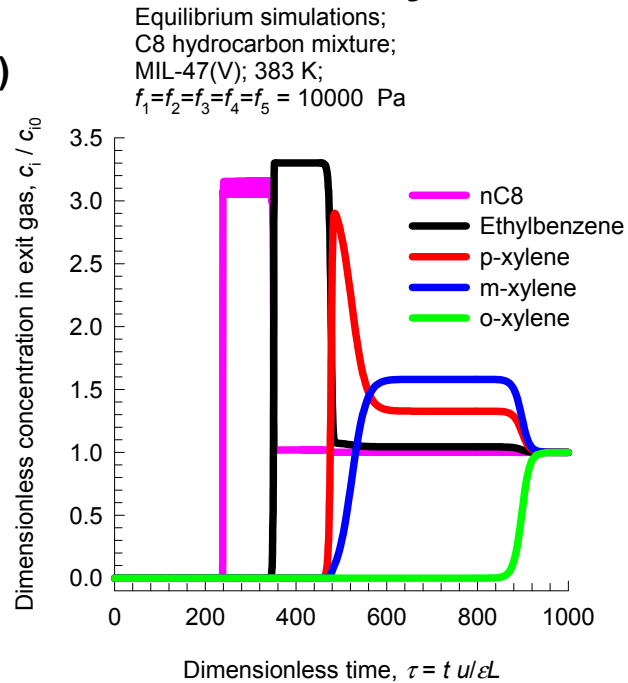
MIL-47(V) breakthrough simulations for xylenes mixture

Figure 60

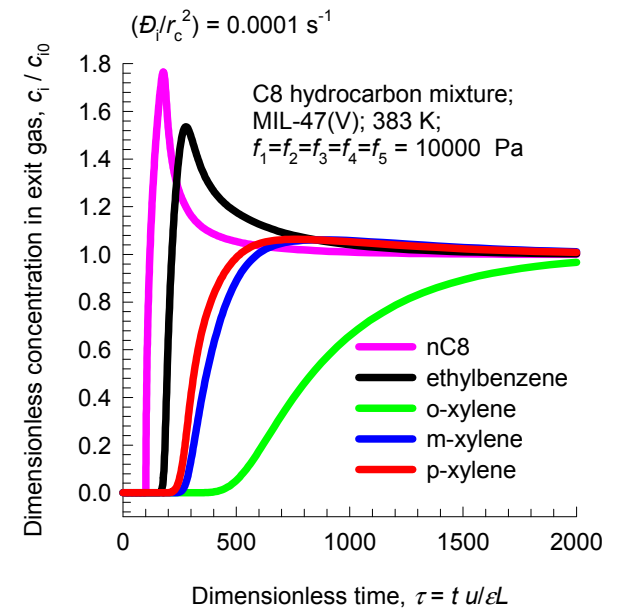
(a)



(b)

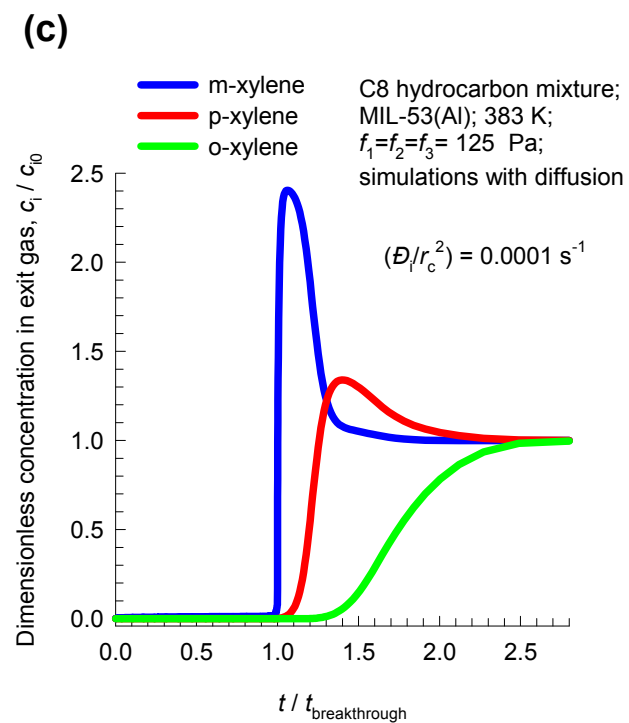
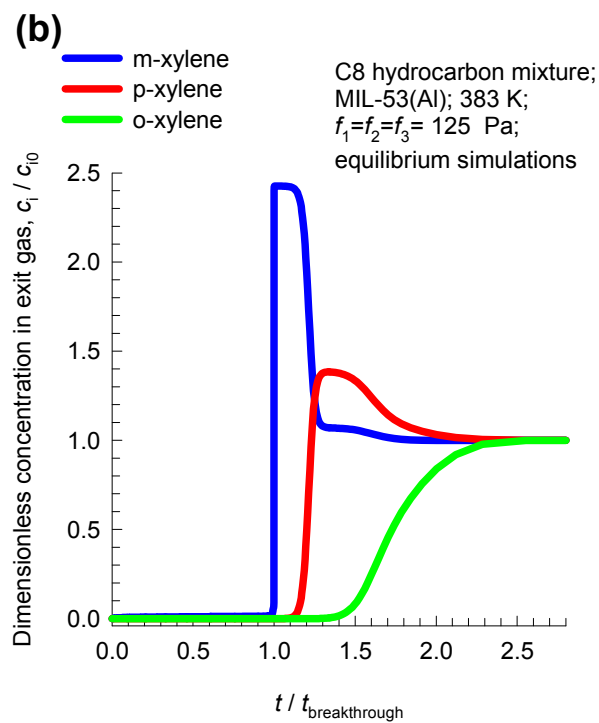
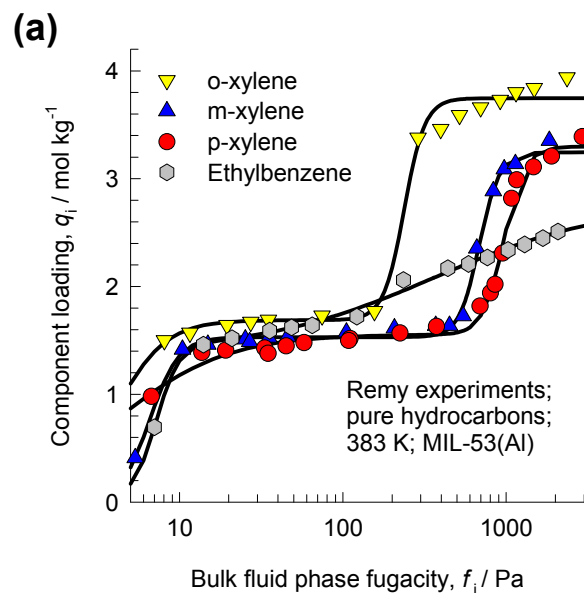


(c)



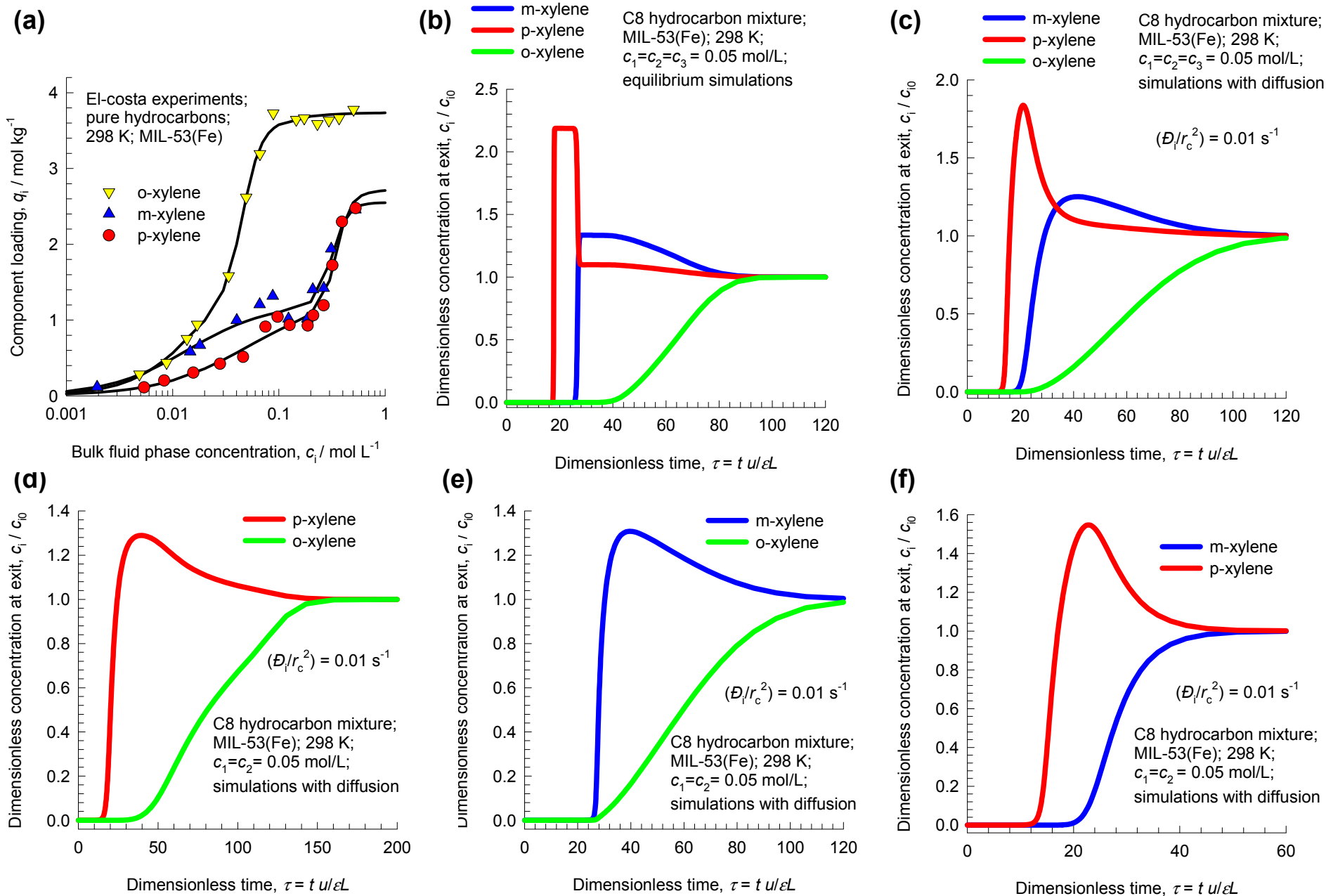
MIL-53(AI) breakthrough simulations for xylenes mixture

Figure 61



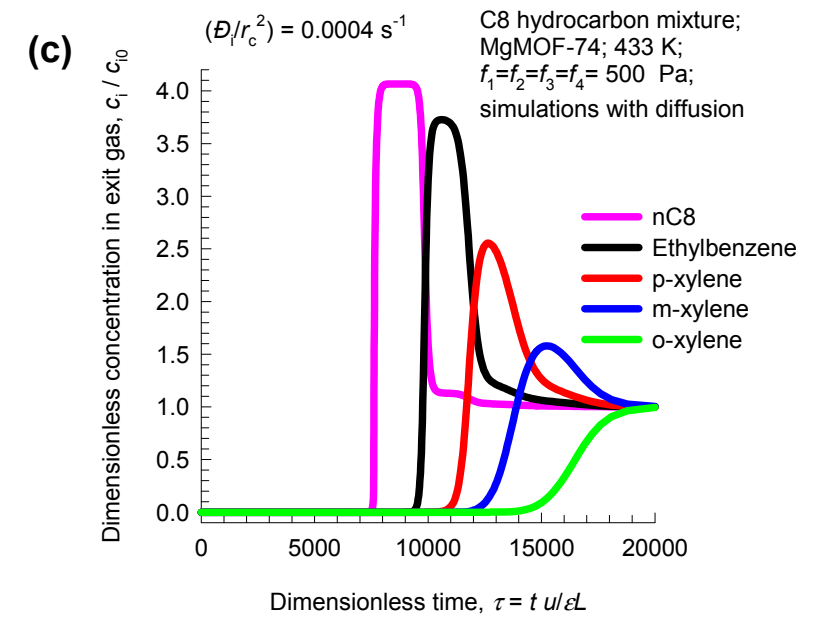
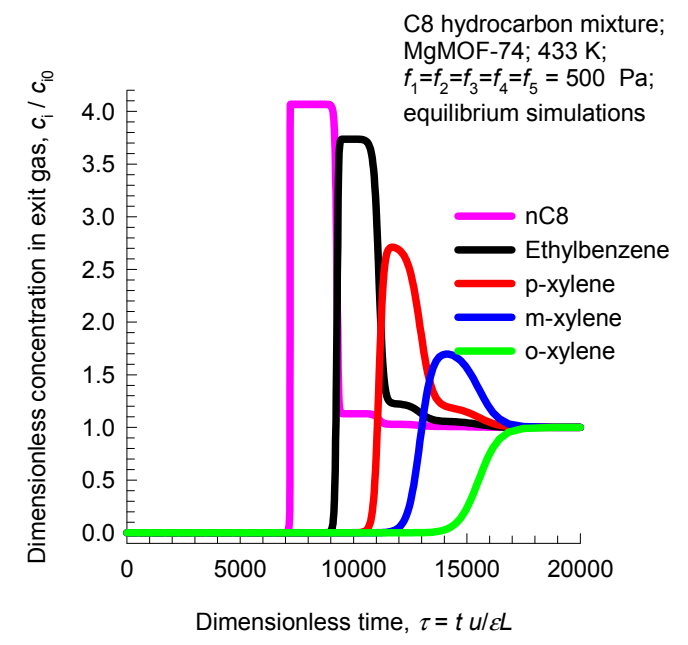
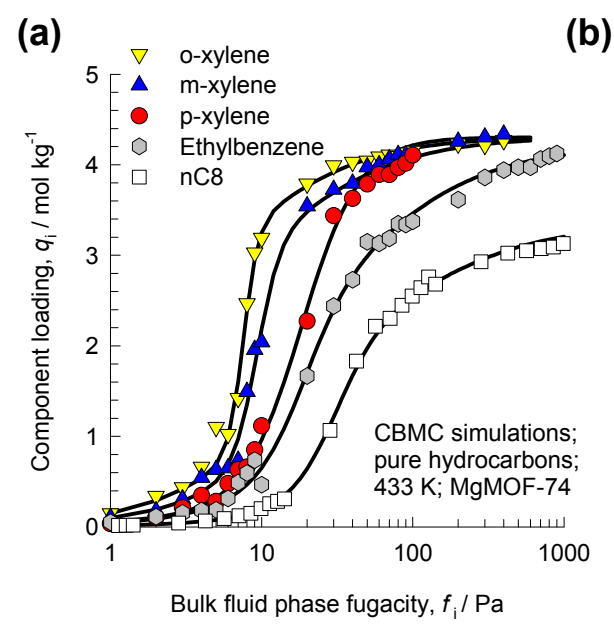
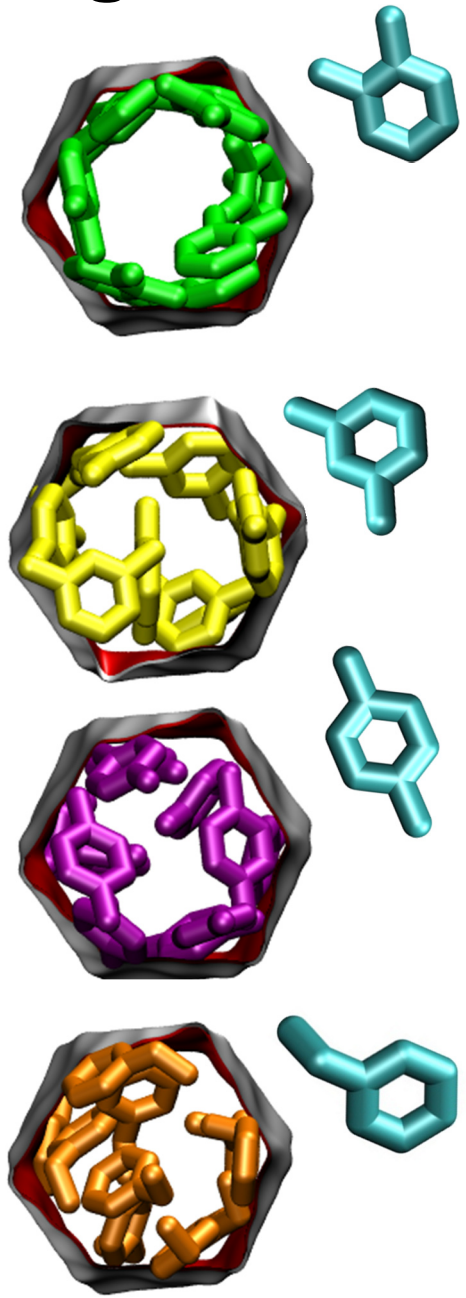
MIL-53(Fe) breakthrough simulations for xylenes mixture

Figure 62



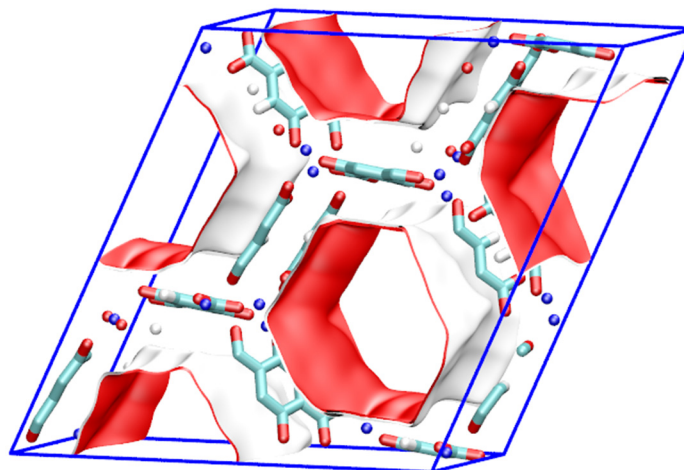
MgMOF-74 Separation of C8 hydrocarbons mixture

Figure 63

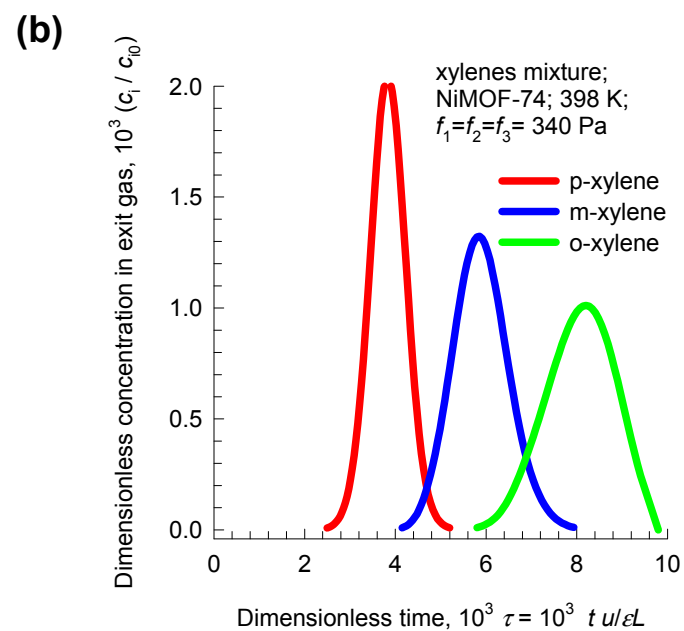
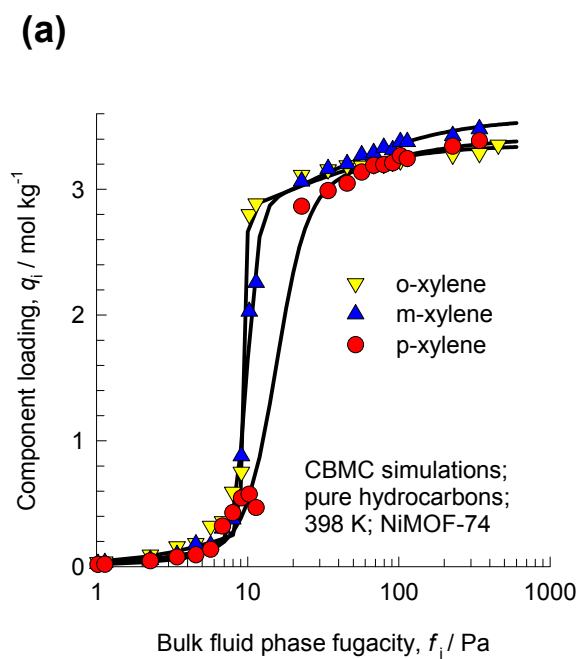


NiMOF-74: separation of xylenes

Figure 64



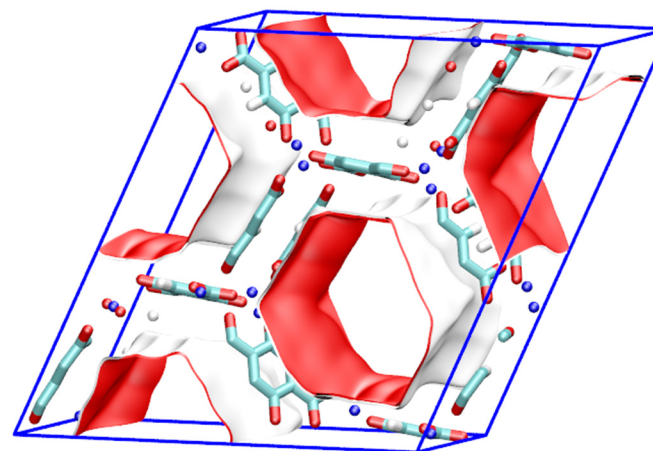
NiMOF-74



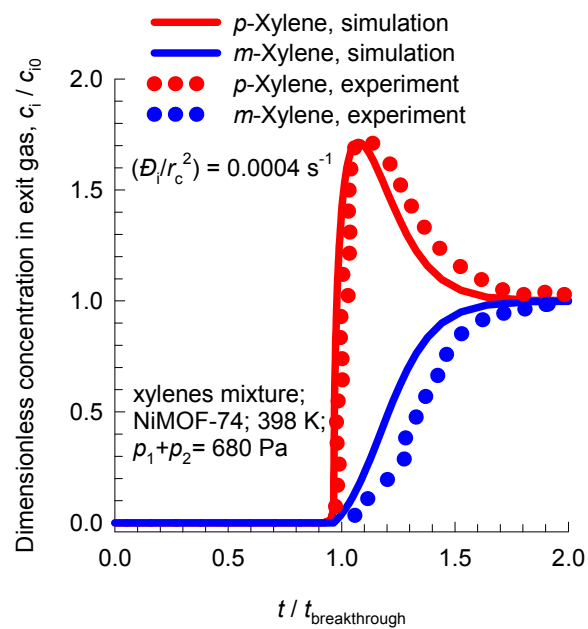
NiMOF-74: separation of xylenes

Figure 65

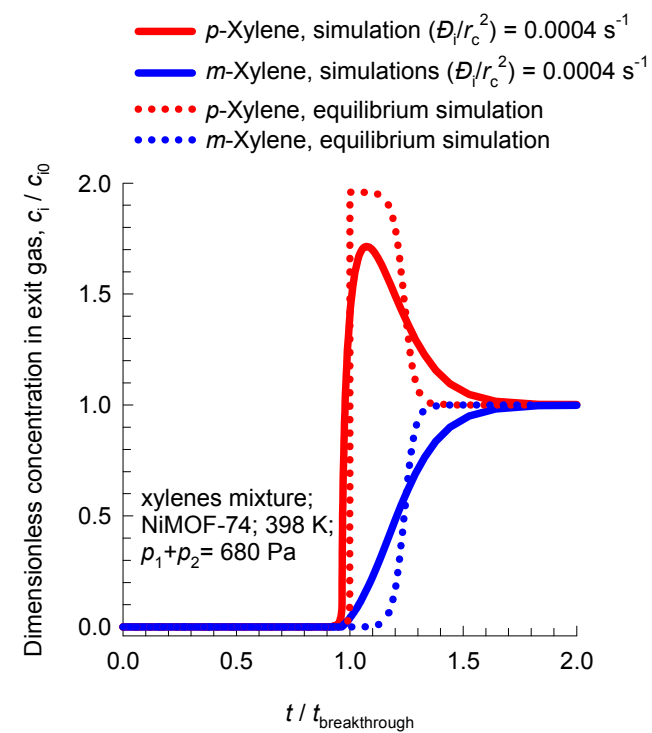
NiMOF-74



(a)

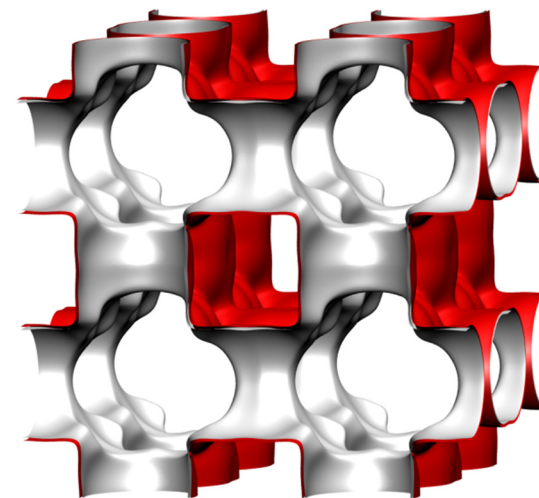


(b)

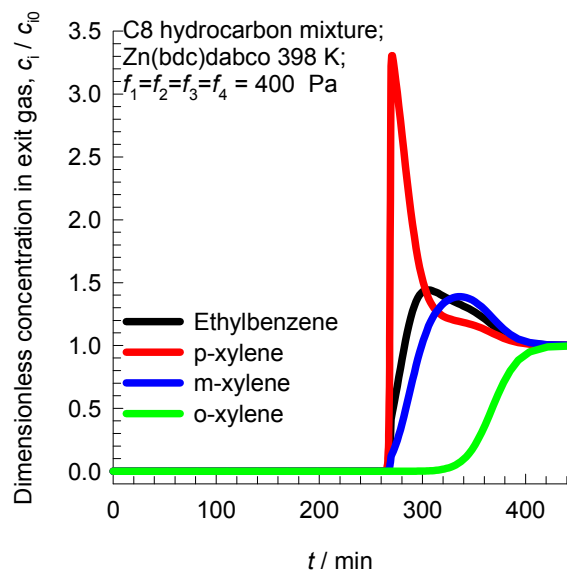


Zn(bdc)dabco: separation of xylenes

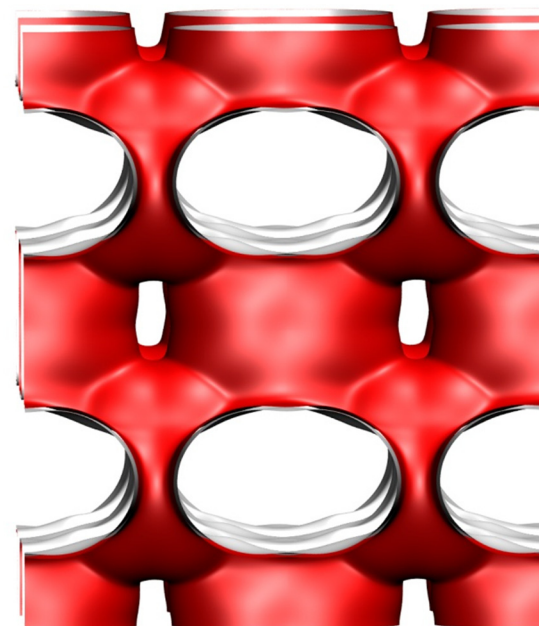
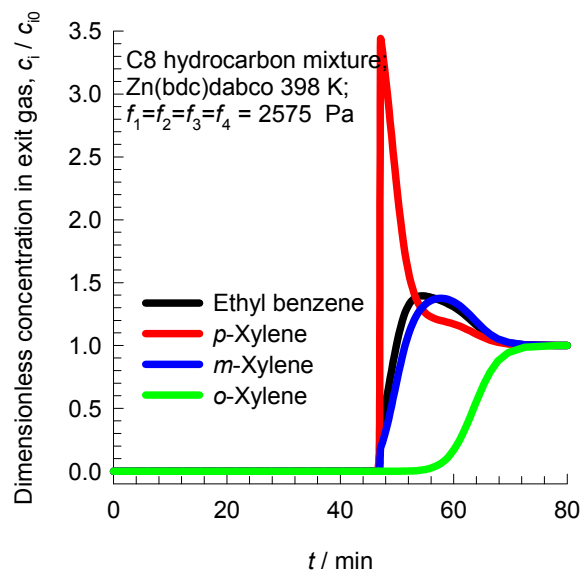
Figure 66



(a)

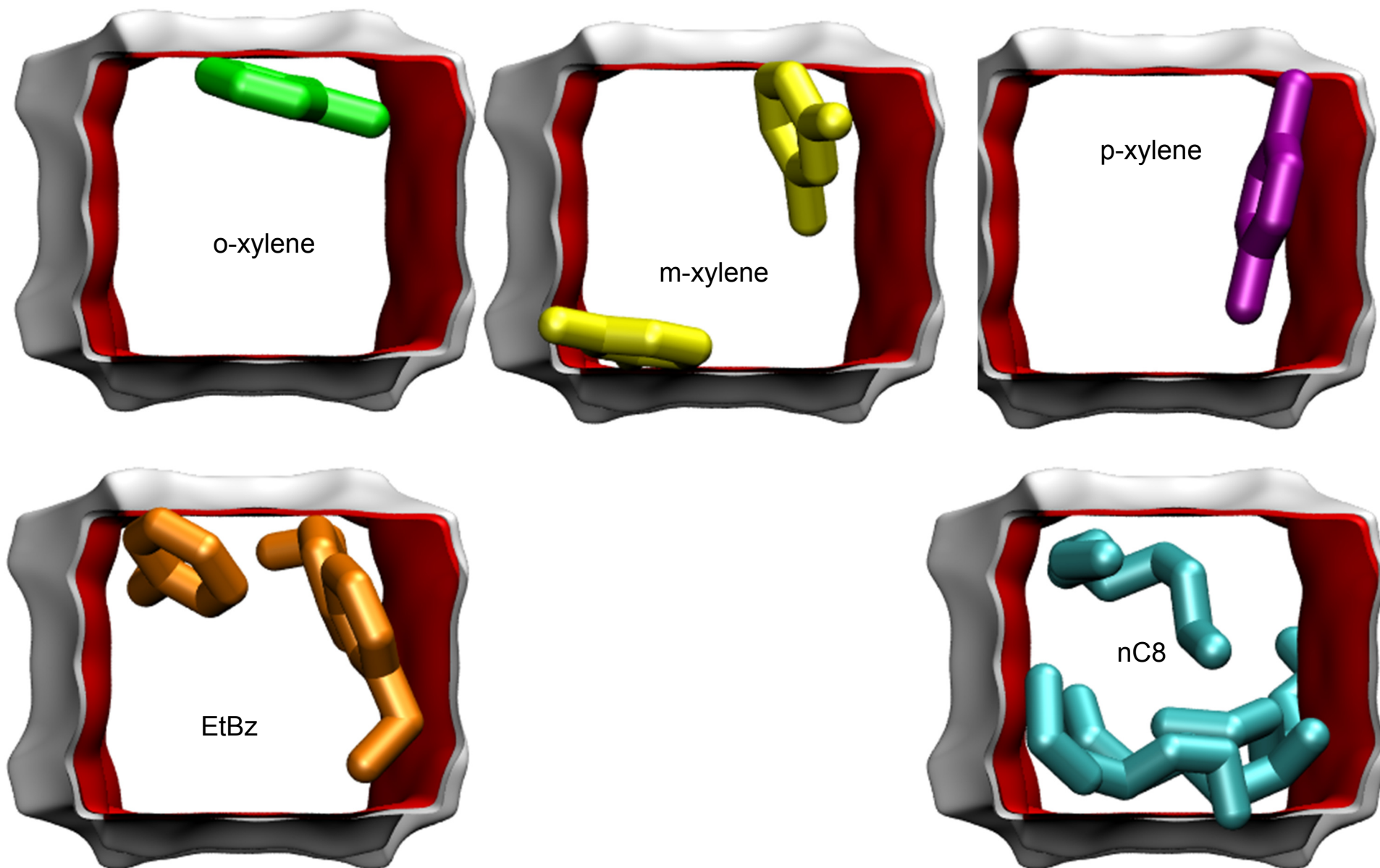


(b)



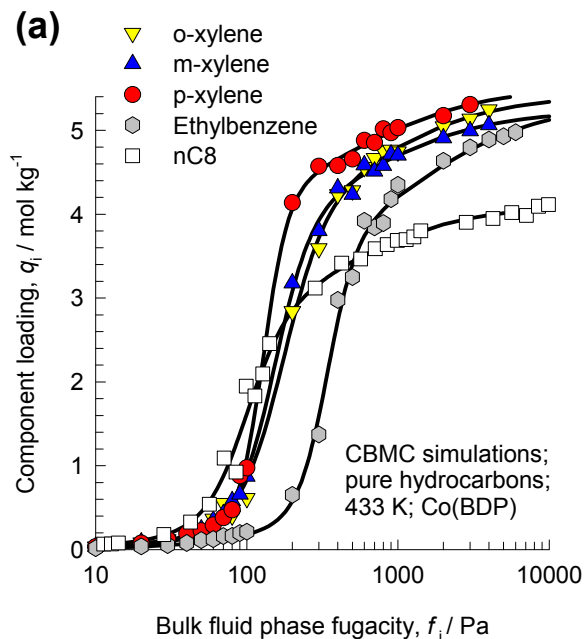
Co(BDP) snapshots of C8 hydrocarbons

Figure 67

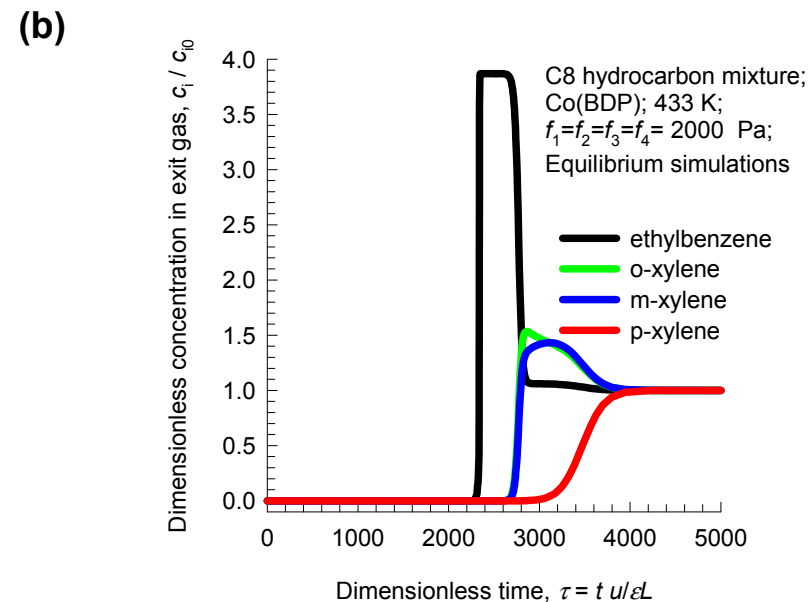


Co(BDP) separation of C8 hydrocarbons

Figure 68



Of the xylene isomers, the hierarchy of adsorption strengths is:
 $p\text{-xylene} > o\text{-xylene} > m\text{-xylene}$.

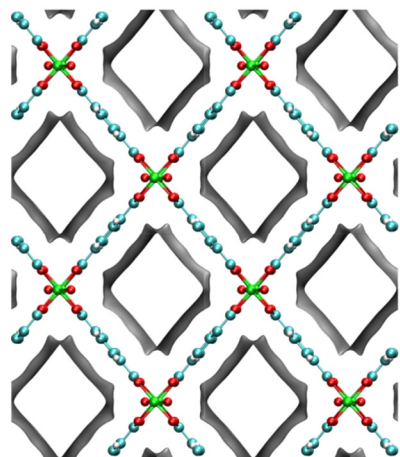


The sequence of breakthroughs is desirable from a practical point of view because $p\text{-xylene}$ is the most strongly adsorbed.

The desired $p\text{-xylene}$ can be recovered in the desorption cycle.

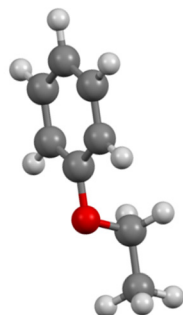
Breakthrough simulations for Ethylbenzene/Styrene mixture

Figure 69



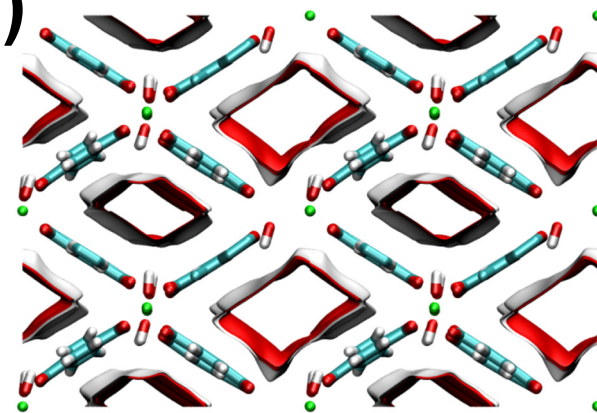
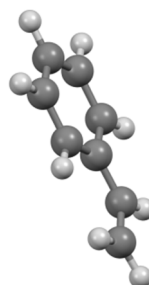
MIL-47(V)

Ethylbenzene
is not flat



MIL-53(Al)

Styrene
is flat

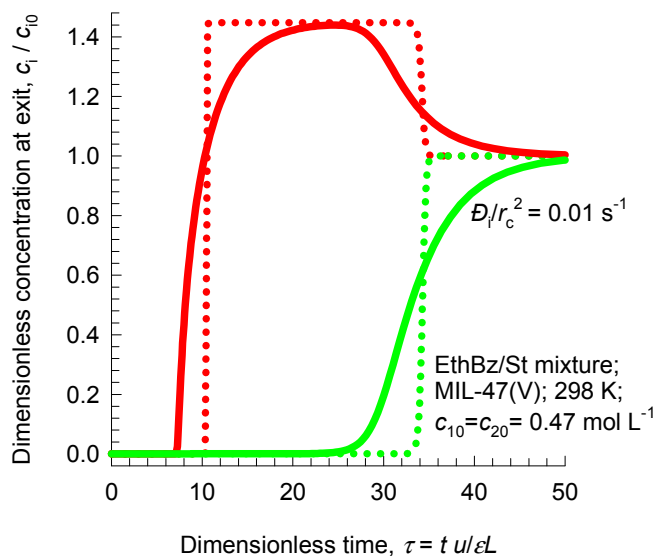


(a)

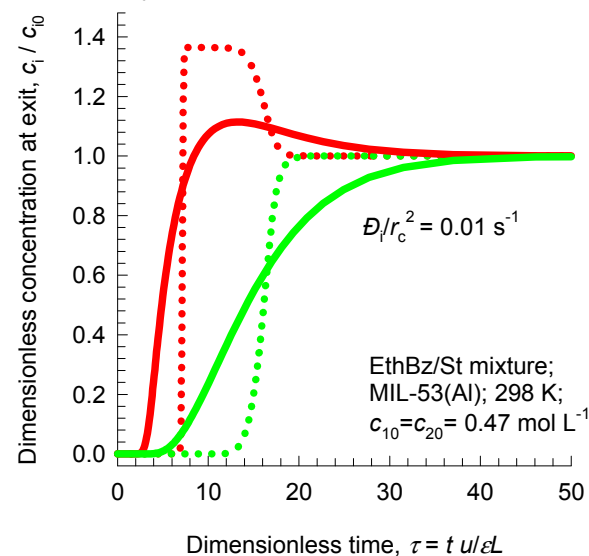
(b)

- Ethylbenzene, equilibrium simulations
- Styrene, equilibrium simulations
- Ethylbenzene, with diffusional limitations
- Styrene, with diffusional limitations

- Ethylbenzene, equilibrium simulations
- Styrene, equilibrium simulations
- Ethylbenzene, with diffusion
- Styrene, with diffusion

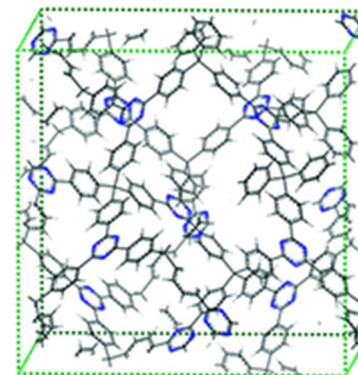


Essentially we are
exploiting differences in
the flatness of molecules

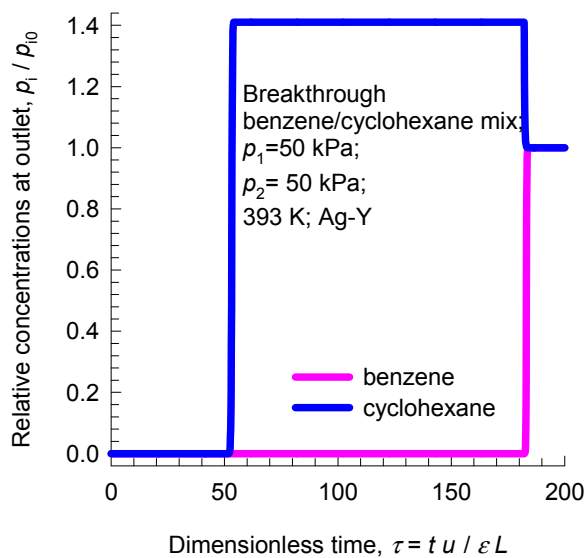


Ag-Y zeolite

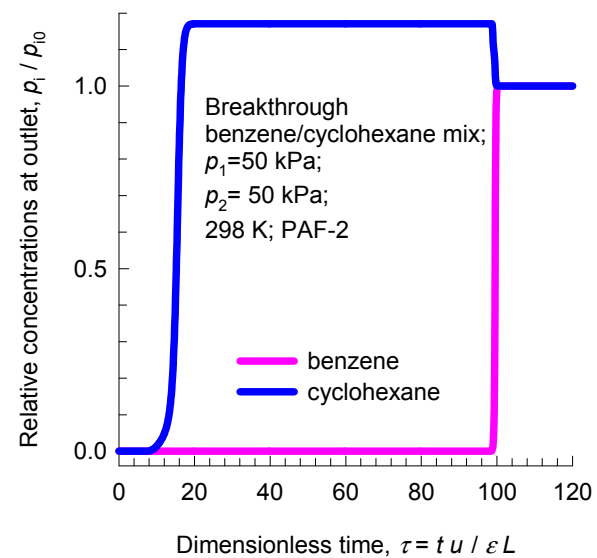
PAF-2



(a)



(b)



SAPO-34: Transient uptake of 1-alcohols

Figure 71

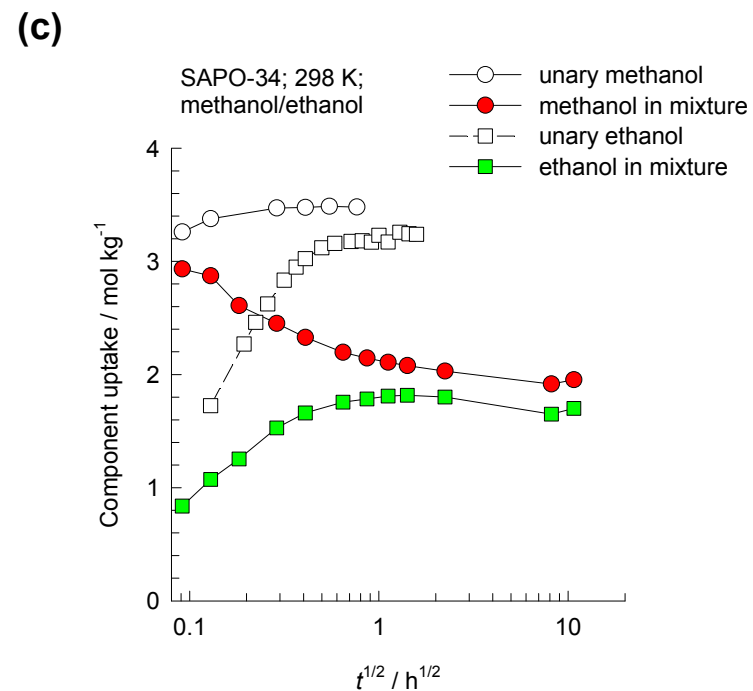
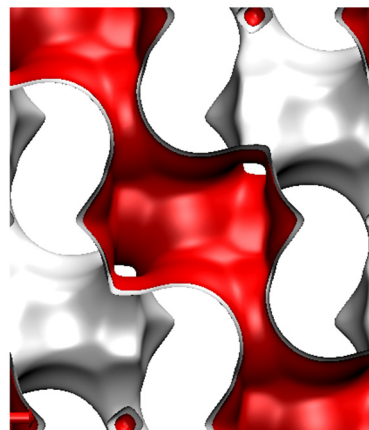
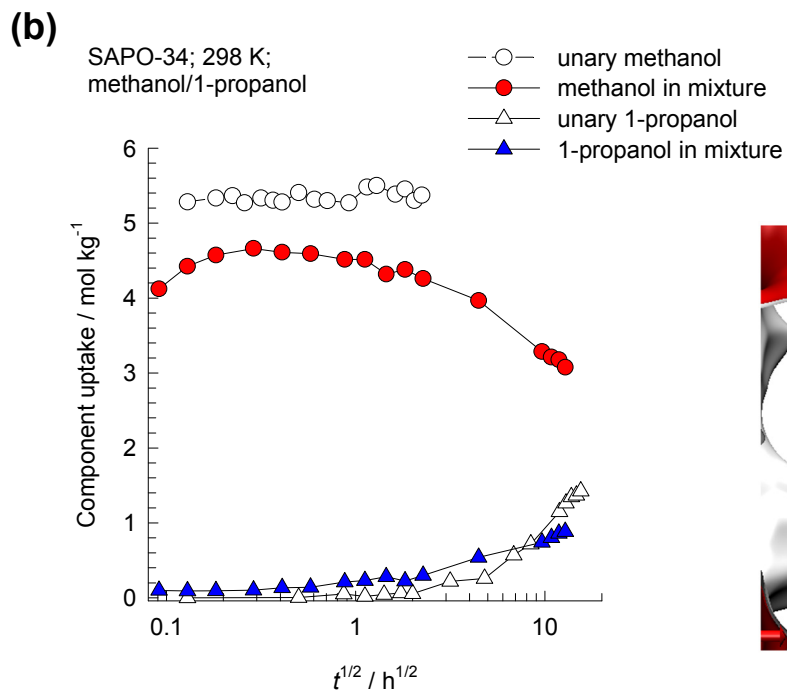
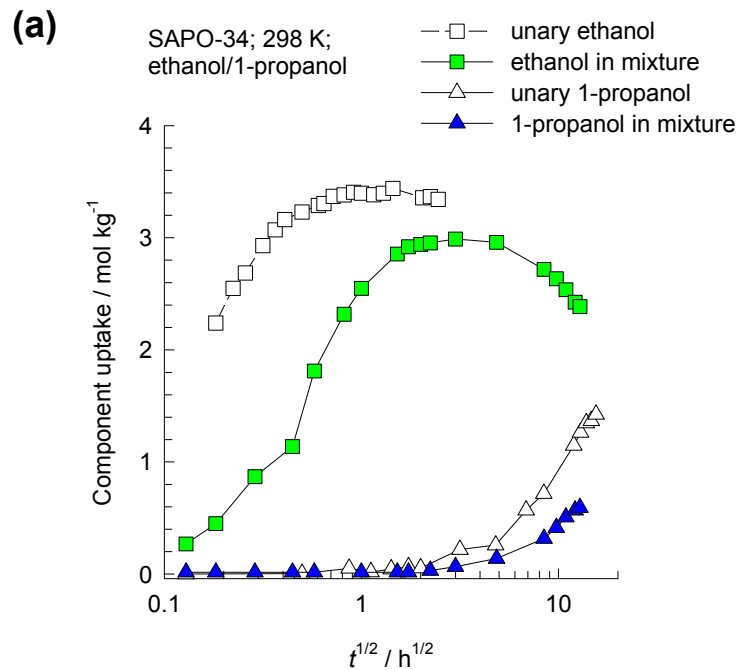


Figure 72

Isotherms for 1-alcohols in CHA

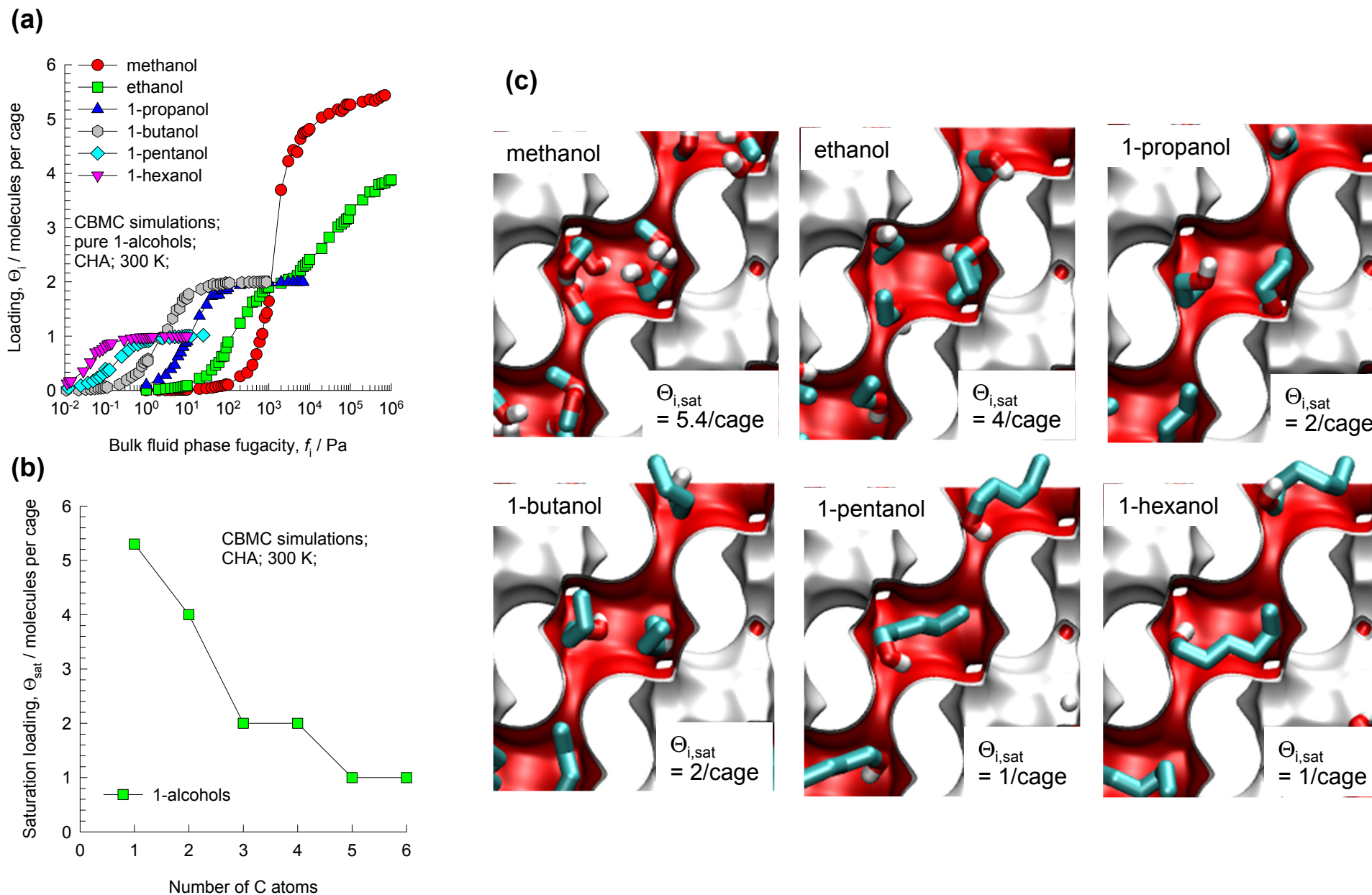
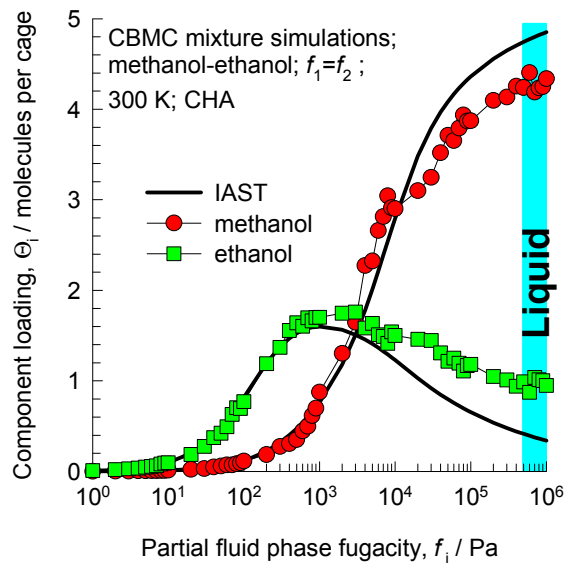
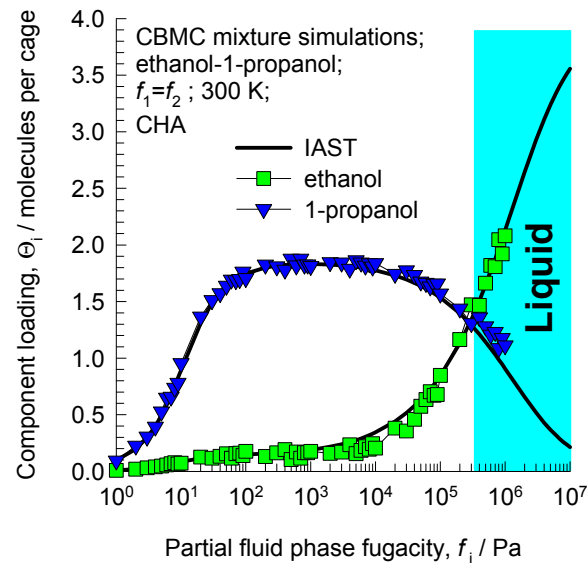


Figure 73

(a)



(b)



(c)

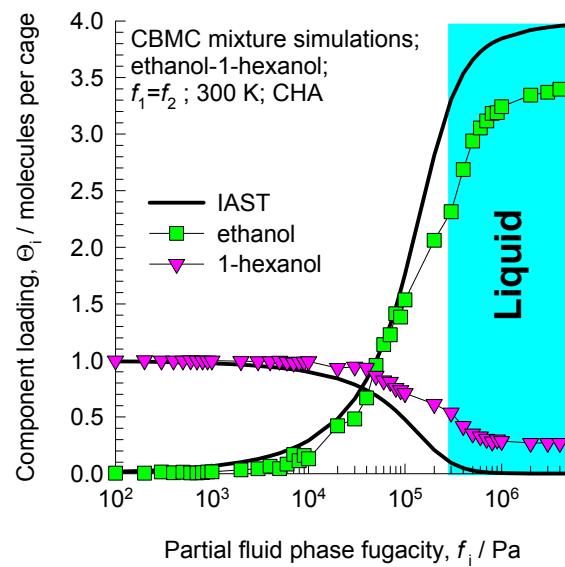


Figure 74

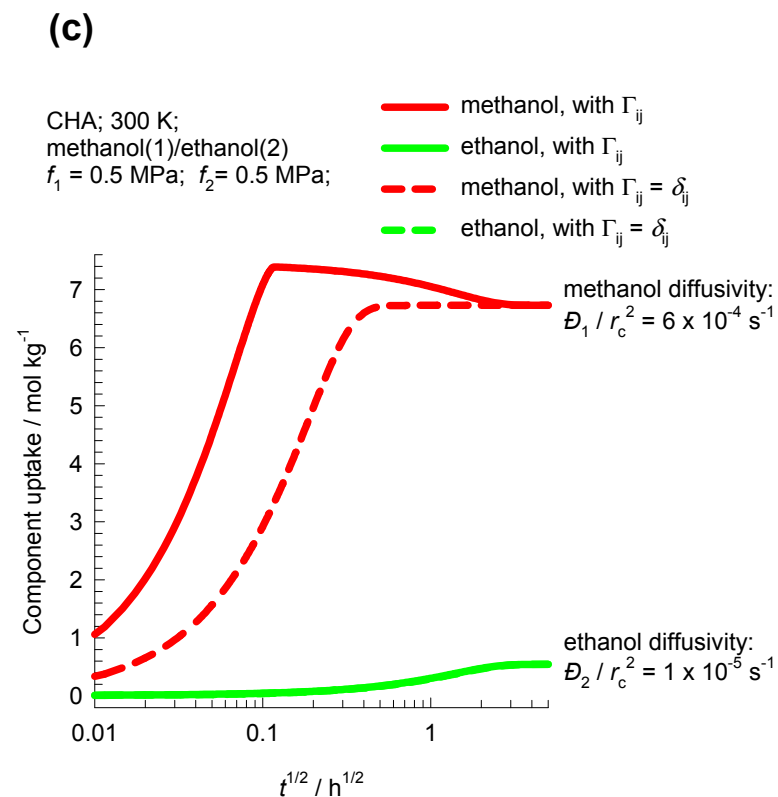
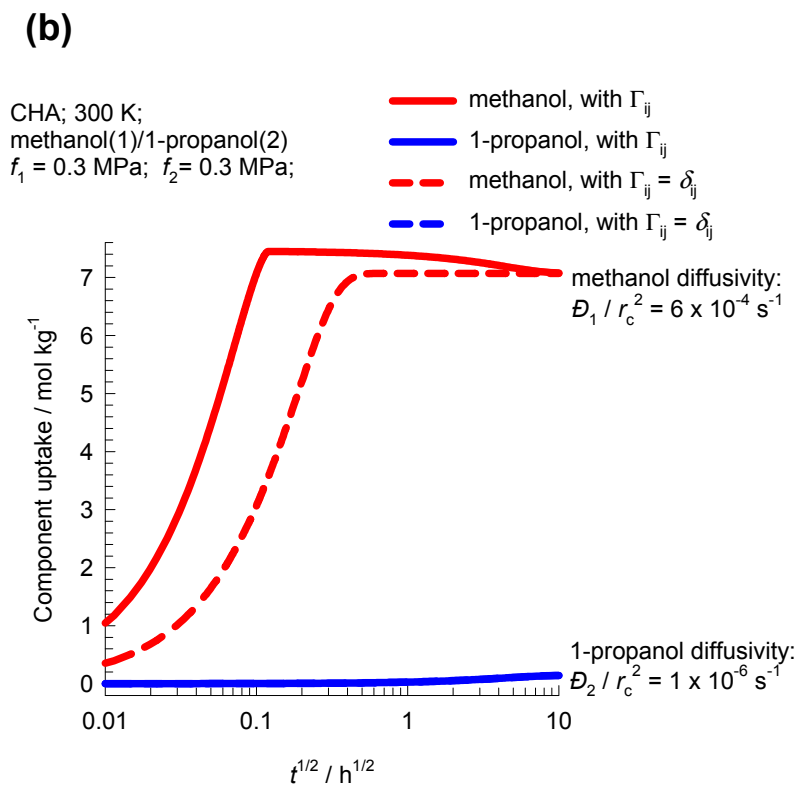
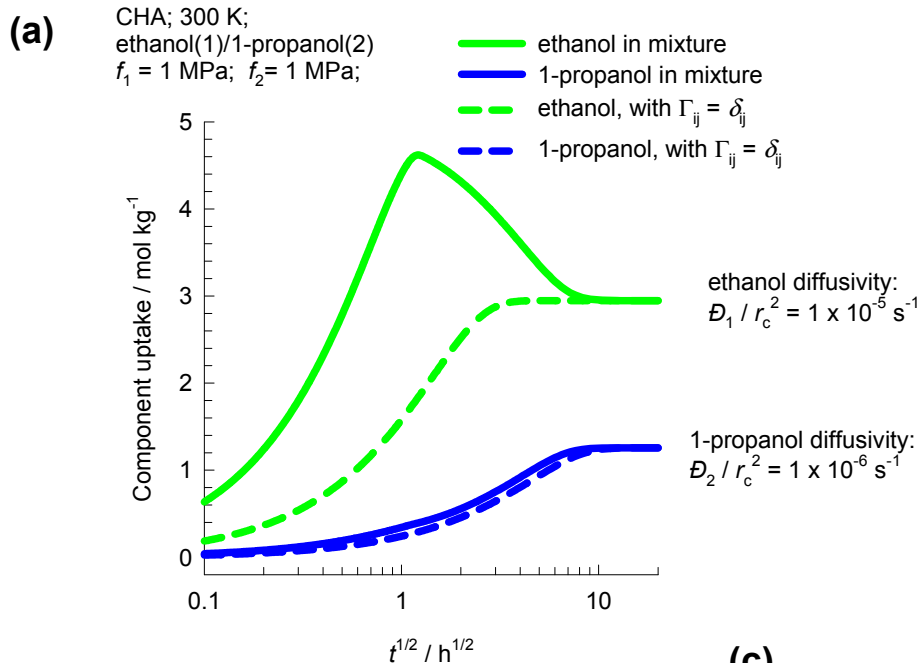
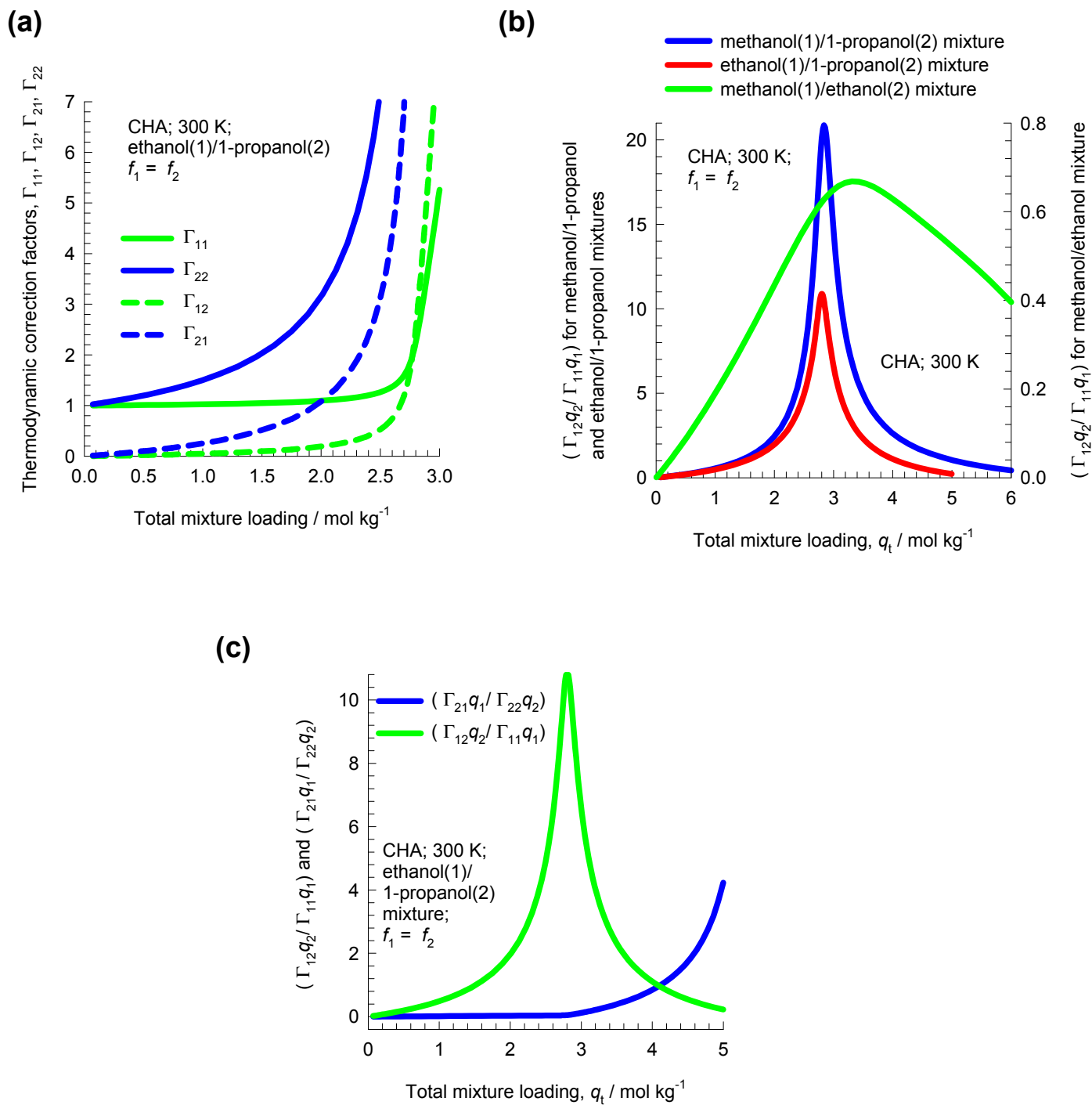
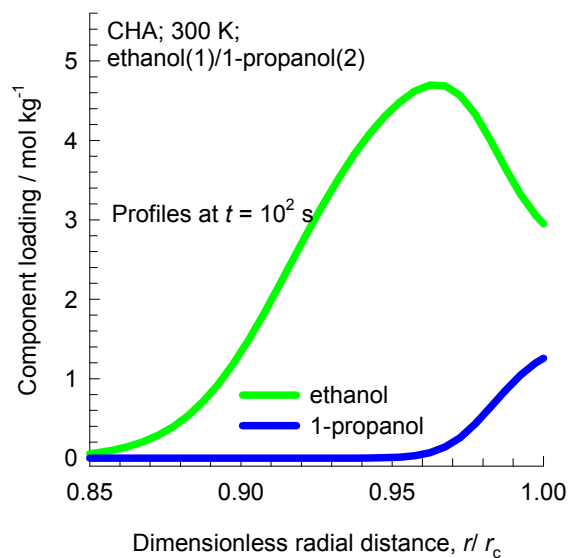
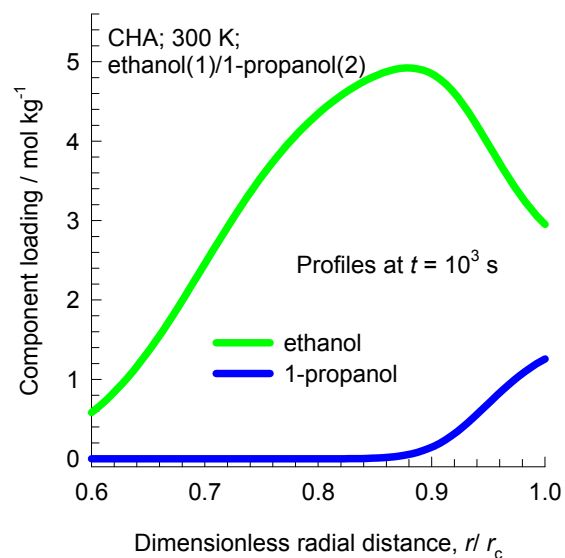
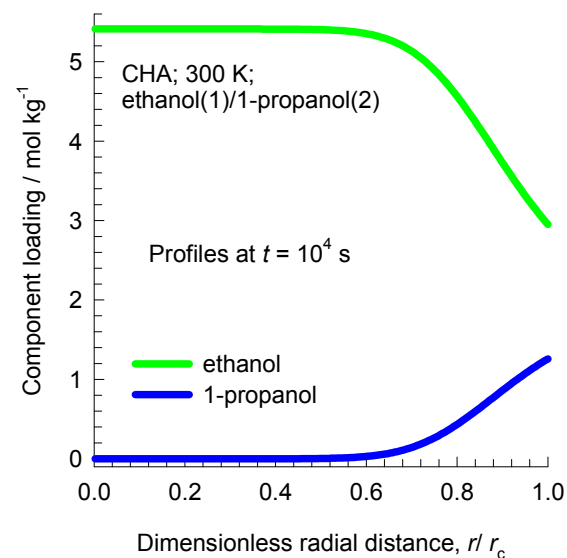
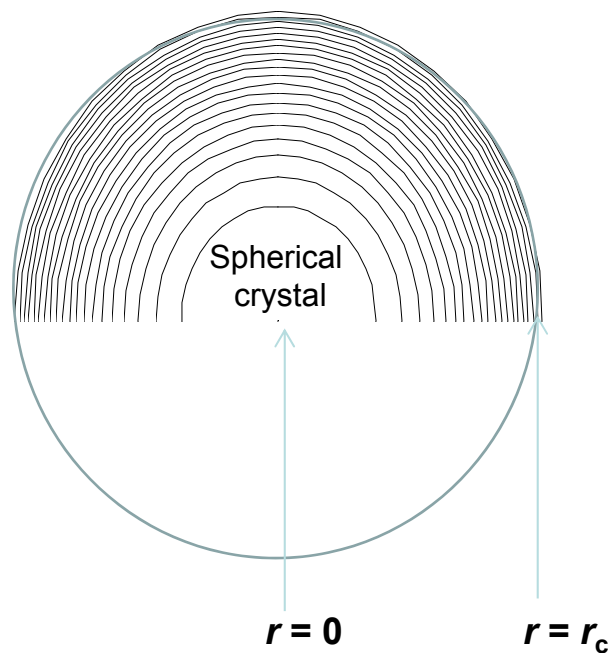
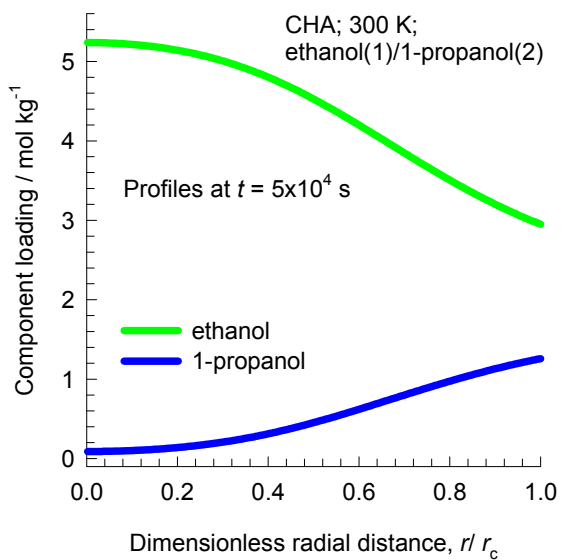
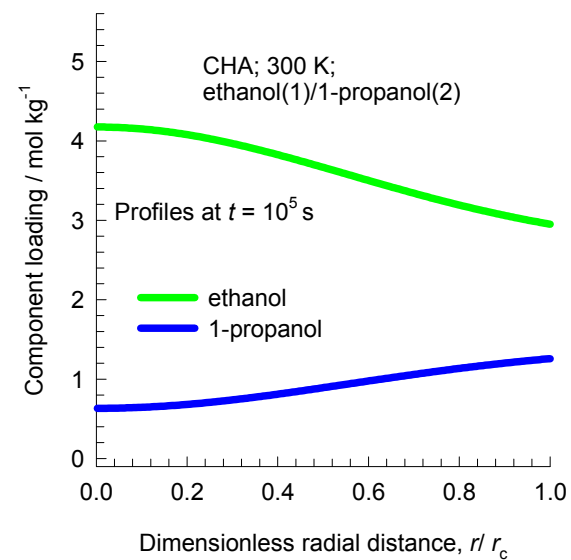


Figure 75



(a)**(b)****(c)****(d)****(e)**

Transient desorption of 1-alcohols in CHA

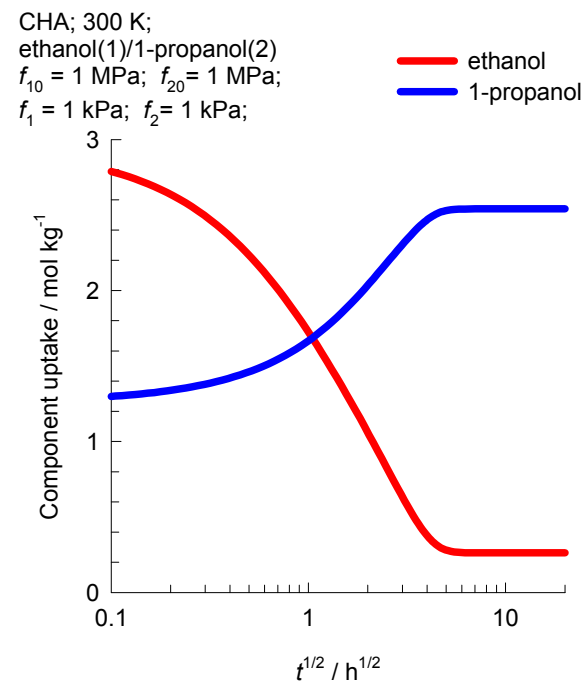
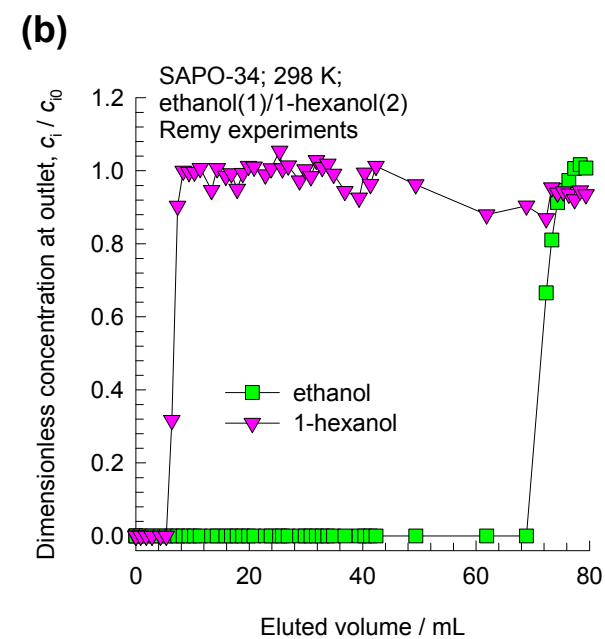
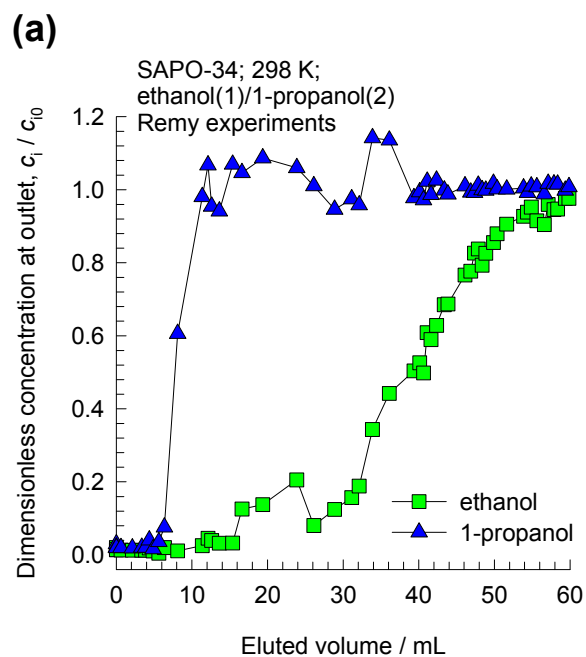
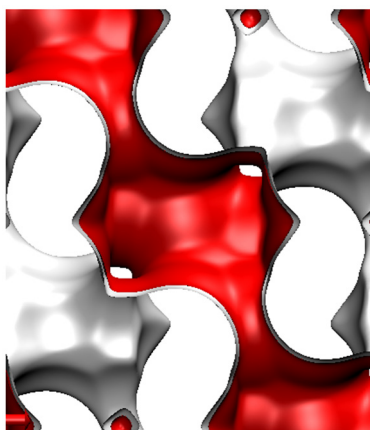


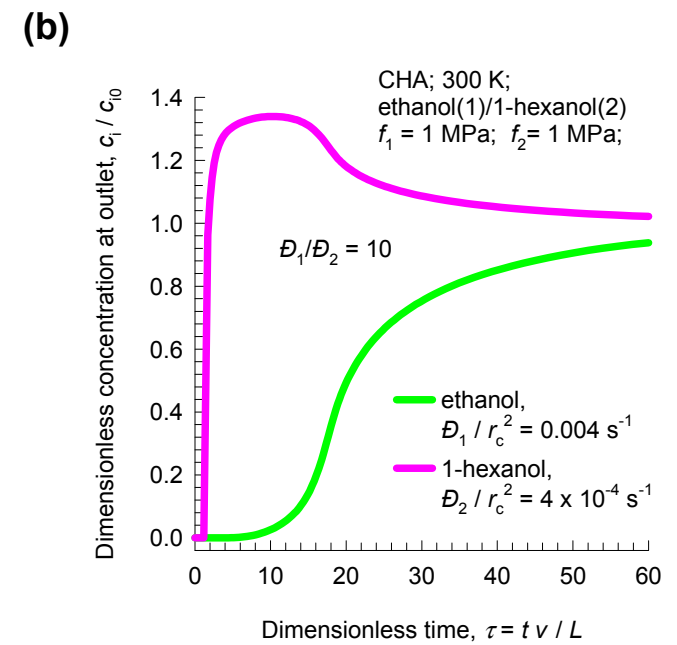
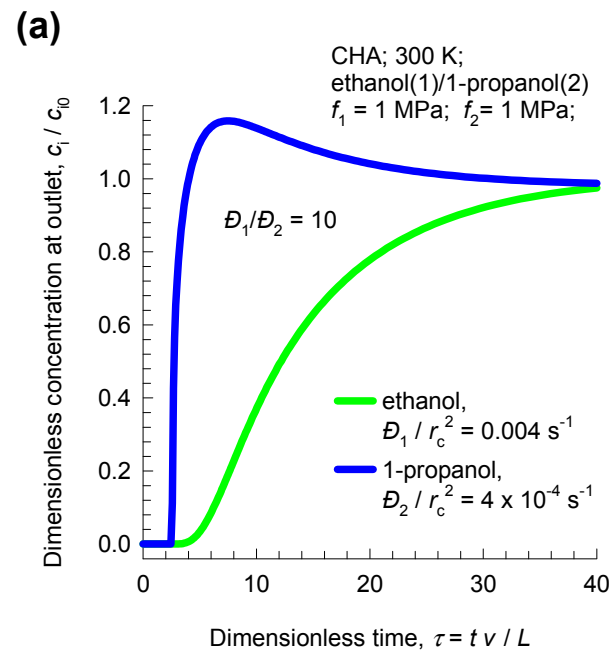
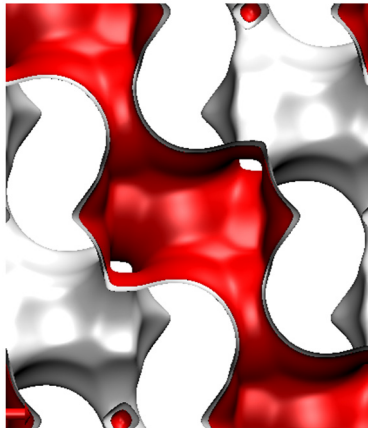
Figure 78

Transient breakthrough of 1-alcohols in SAPO-34

SAPO-34

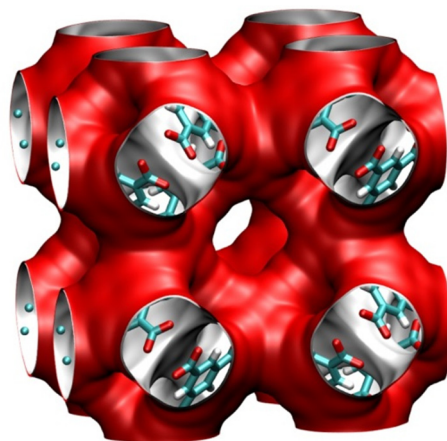
Transient breakthrough of 1-alcohols in CHA

CHA

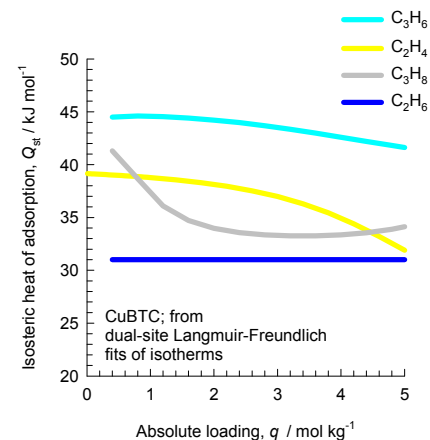


Transient breakthrough of propene/propane in CuBTC

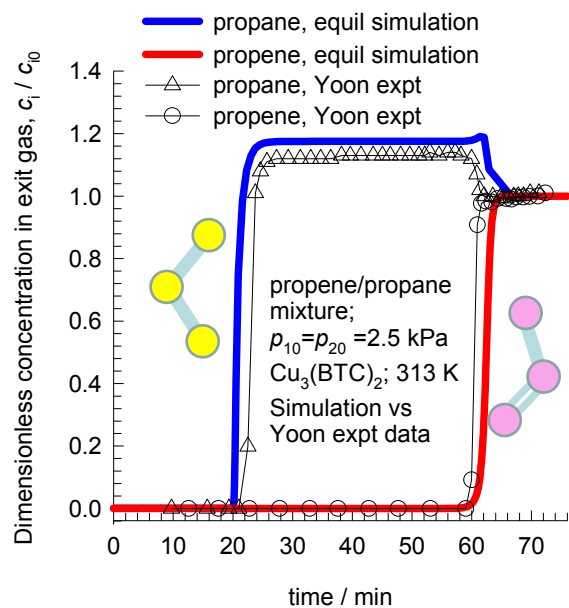
CuBTC



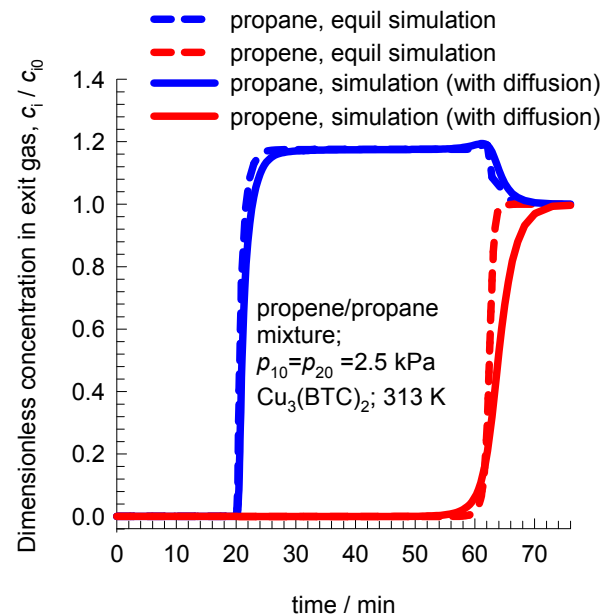
Alkenes bind more strongly with Cu than alkanes



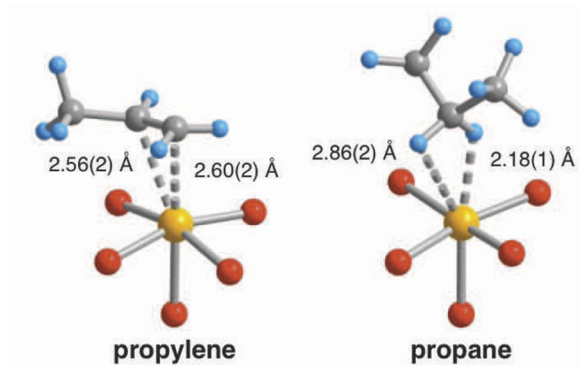
(a)



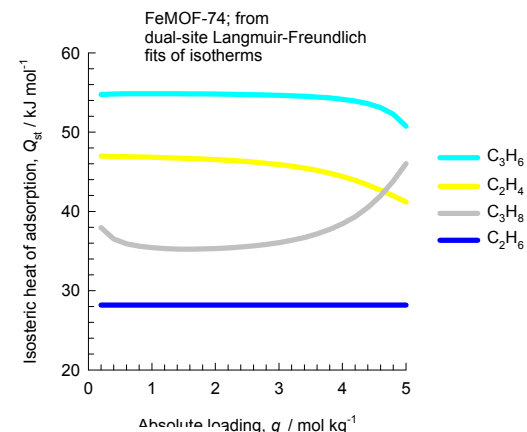
(b)



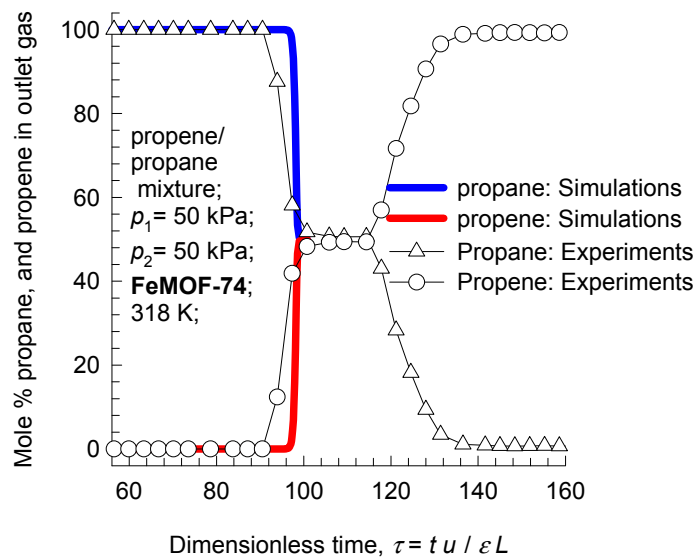
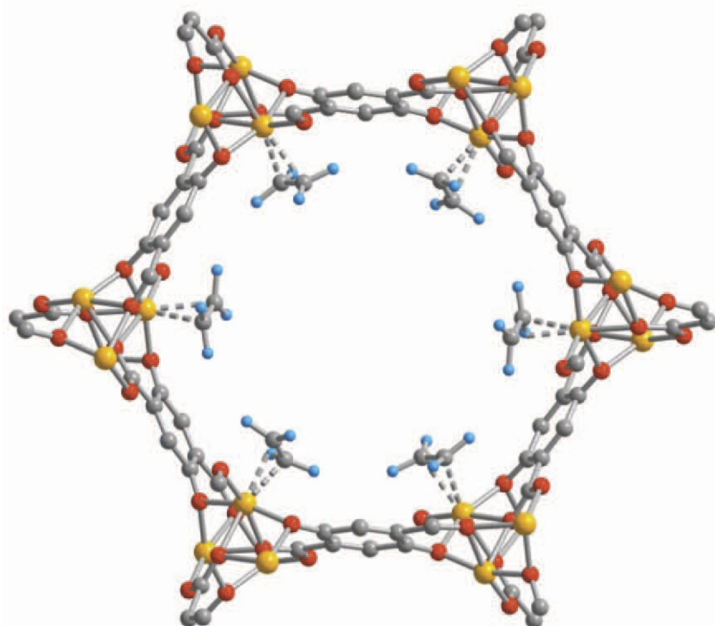
Transient breakthrough of propene/propane in FeMOF-74



Alkenes bind more strongly with Fe(II) than alkanes

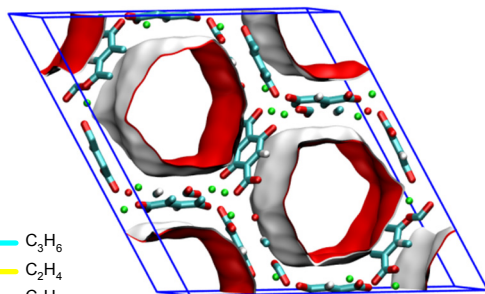


FeMOF-74

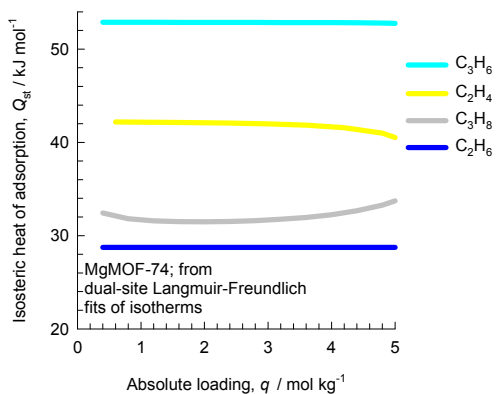


Transient breakthrough of alkene/alkane Figure 82

MgMOF-74

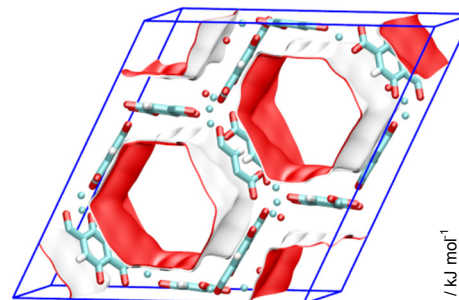


Alkenes bind more strongly with Mg than alkanes

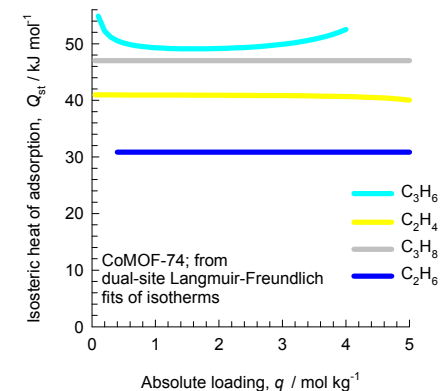


(a)

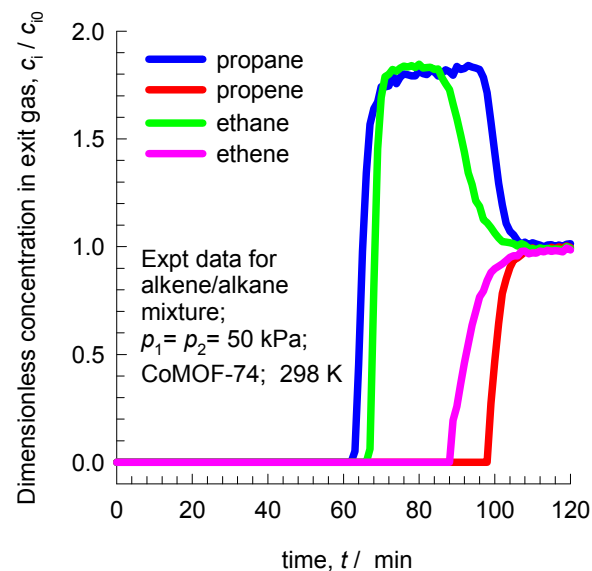
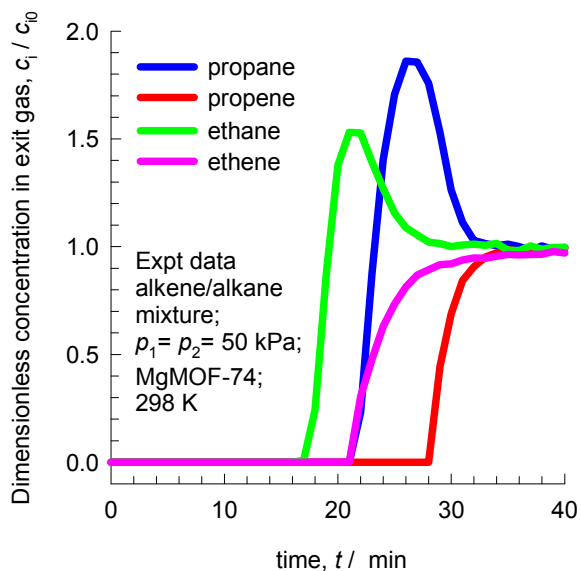
CoMOF-74



Alkenes bind more strongly with Co than alkanes

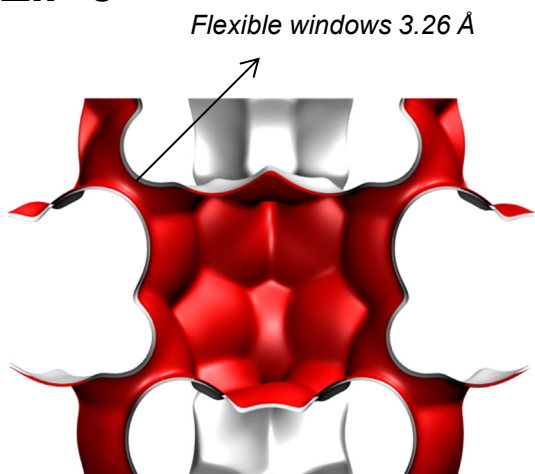


(b)

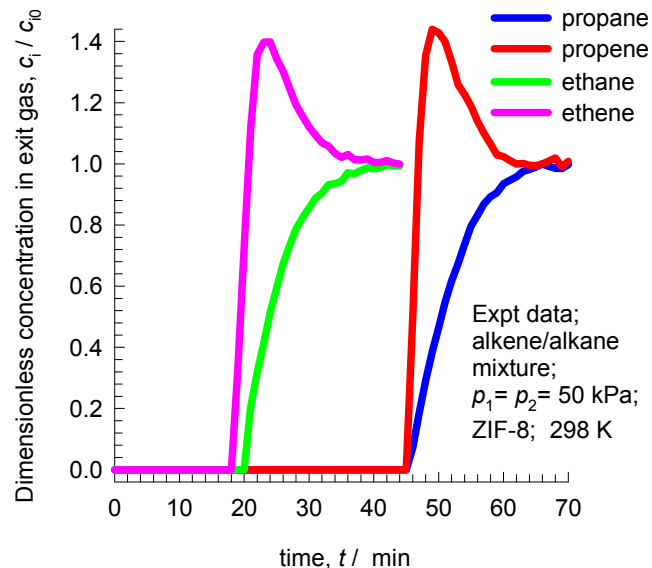


Transient breakthrough of alkene/alkane in ZIF-8 Figure 83

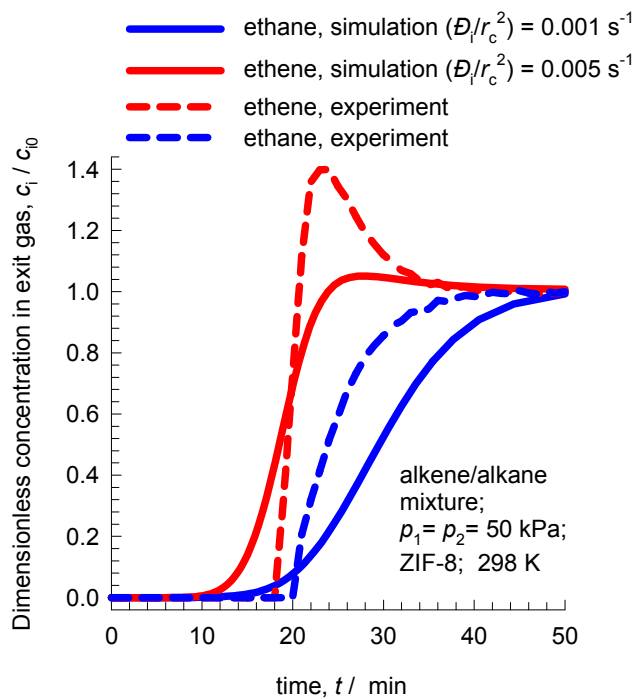
ZIF-8



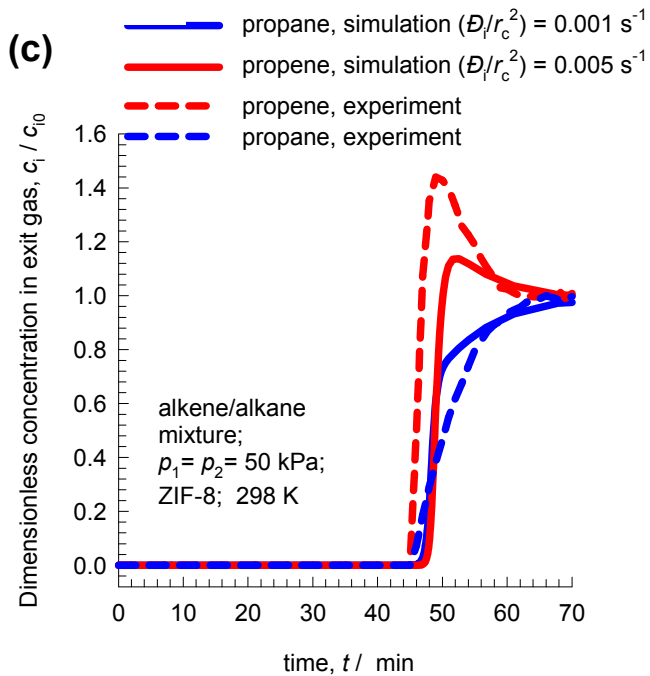
(a)



(b)

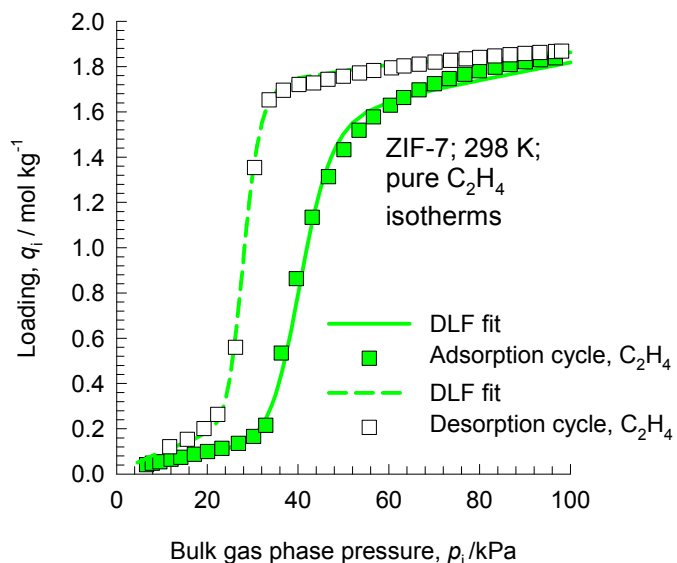


(c)

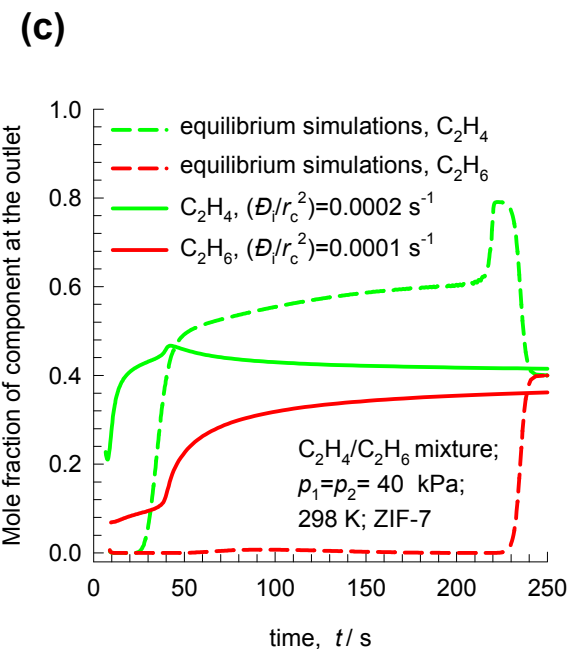
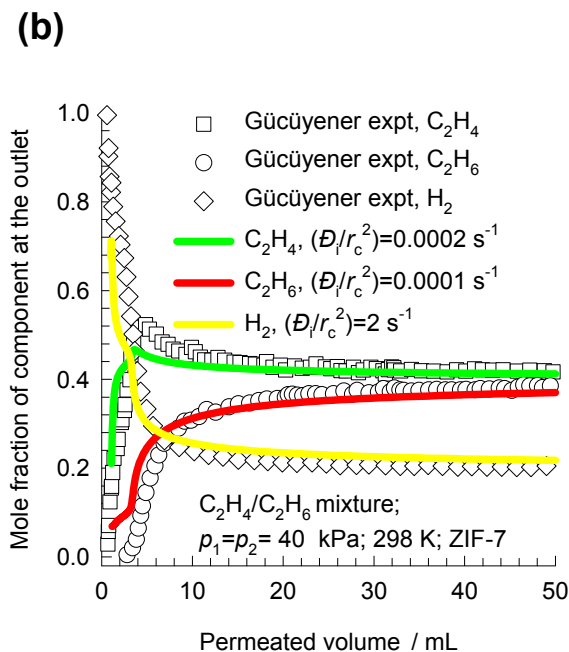
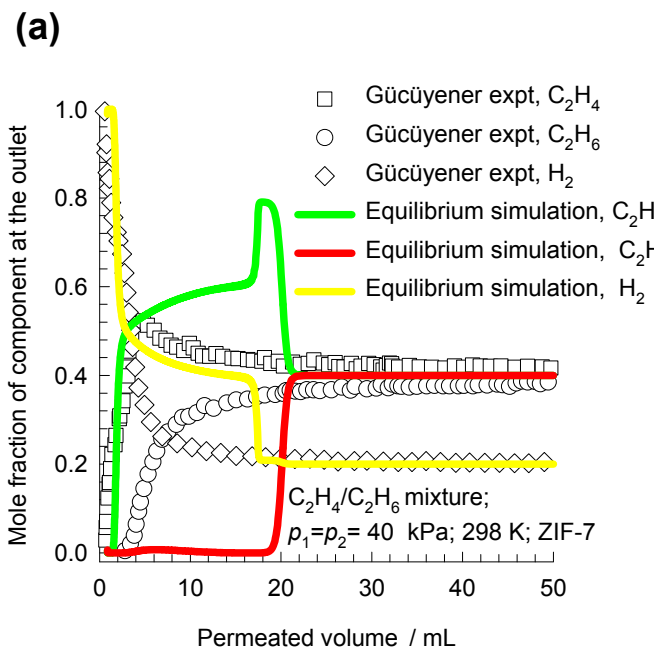
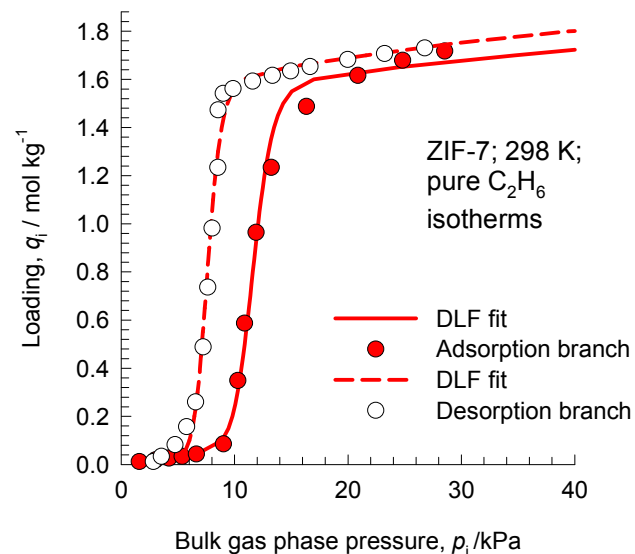


ethene/ethane in ZIF-7

Figure 84

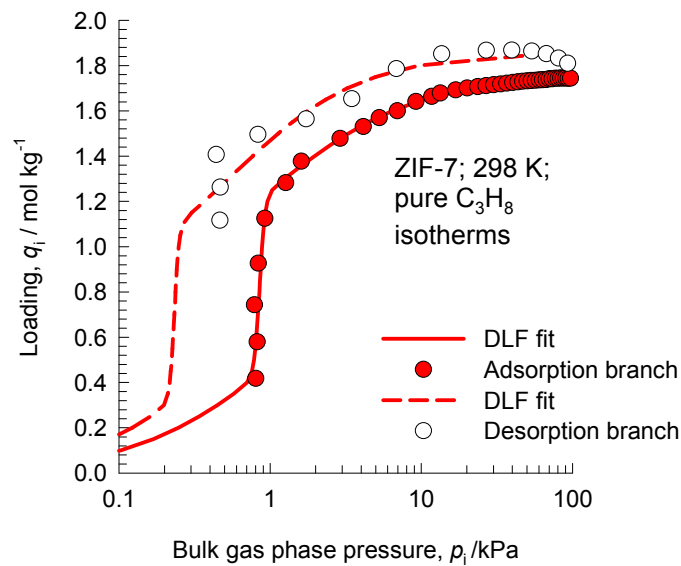
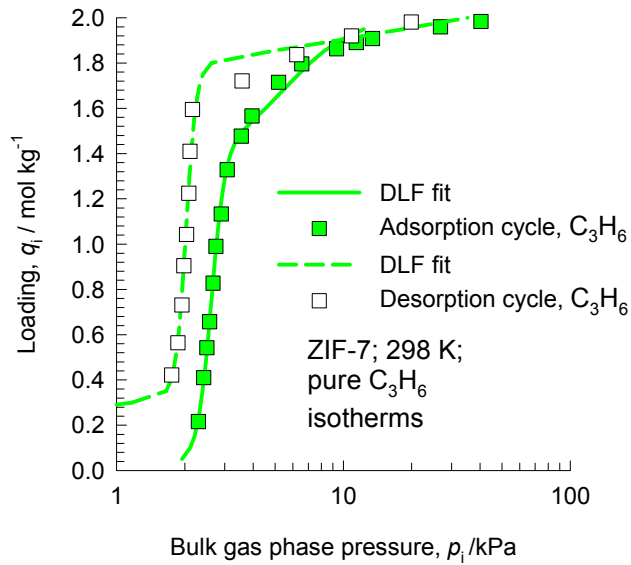


The breakthrough simulations use the fits of the adsorption cycle of the isotherms



Propene/propane in ZIF-7

Figure 85



The breakthrough simulations use the fits of the adsorption cycle of the isotherms

ZIF-7 is formed by combining Zn metal clusters through benzimidazole (BIM) linkers. It has a sodalite topology. 6 Å cages are connected by window openings of about 3 Å.

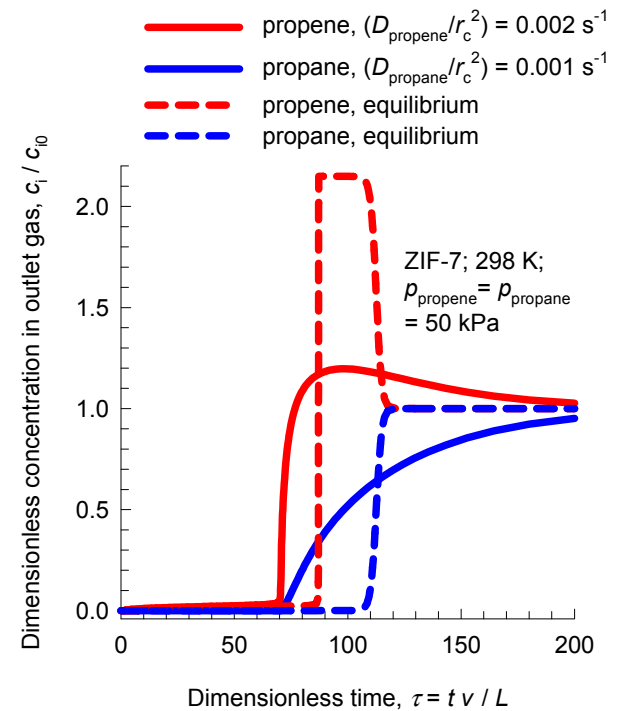
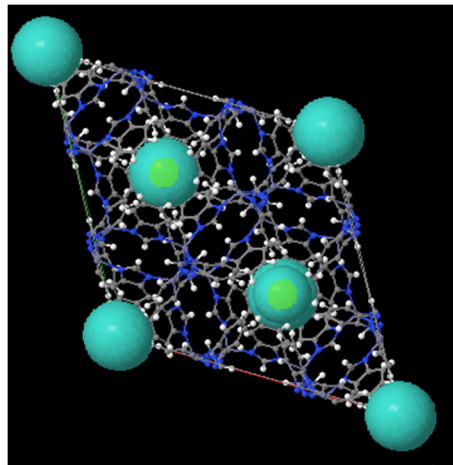
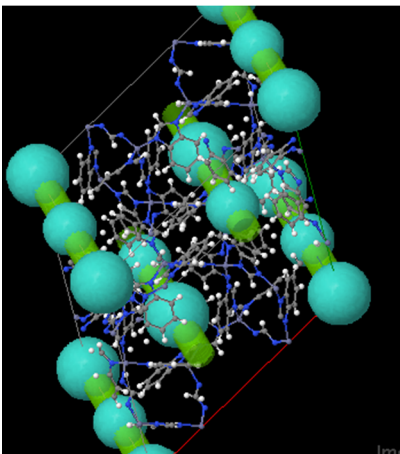
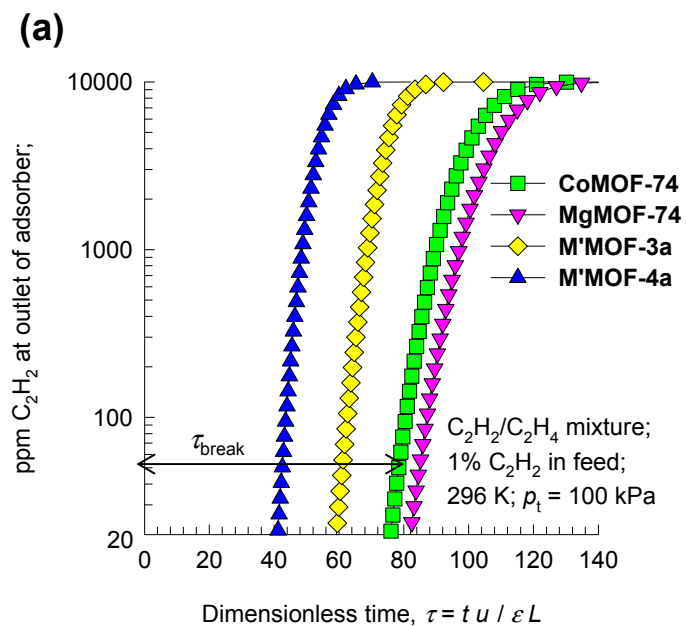
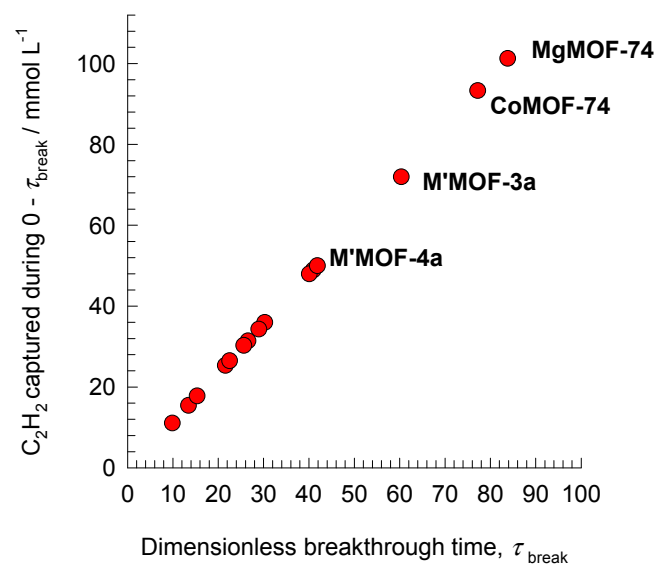


Figure 86

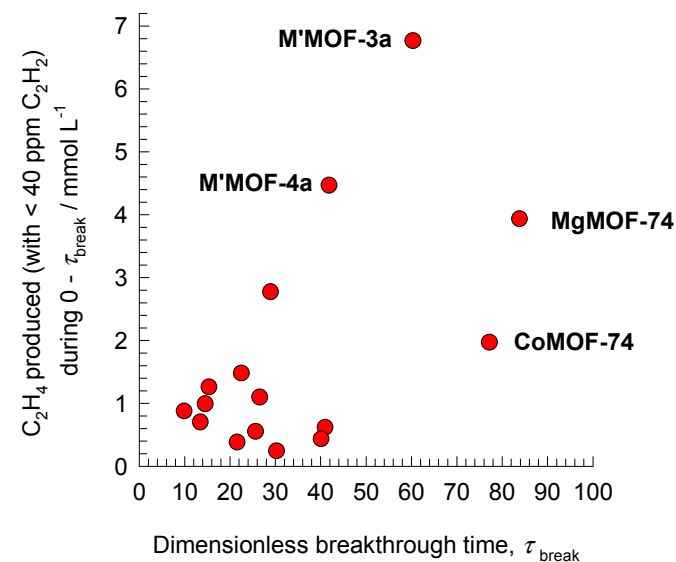
Separation of C_2H_2/C_2H_4 mixtures



(b) C_2H_2/C_2H_4 mixture;
1% C_2H_2 in feed;
296 K; $p_t = 100$ kPa;
< 40 ppm C_2H_2 in outlet gas

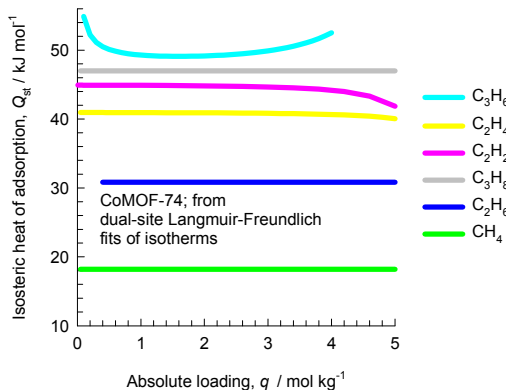


(c) C_2H_2/C_2H_4 mixture;
1% C_2H_2 in feed;
296 K; $p_t = 100$ kPa;
< 40 ppm C_2H_2 in outlet gas

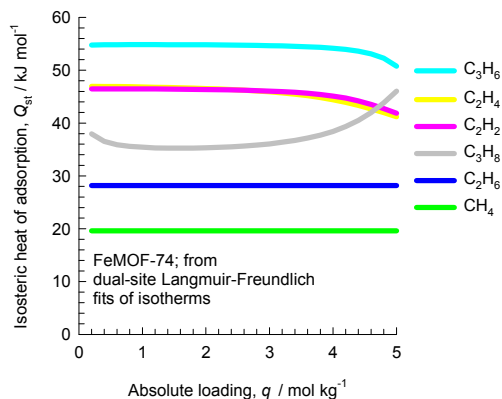


Fractionation of C1-C2-C3 hydrocarbons Figure 87

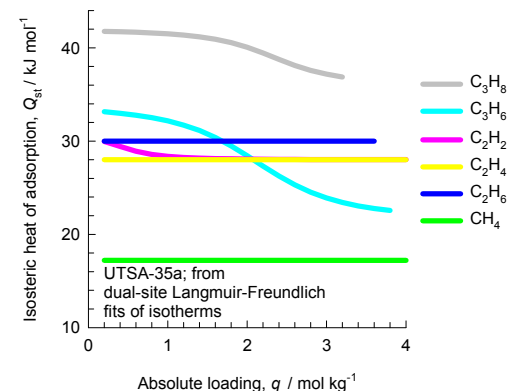
CoMOF-74



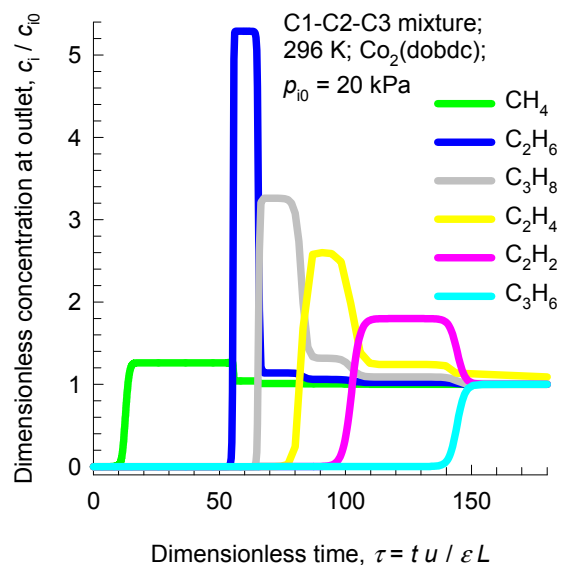
FeMOF-74



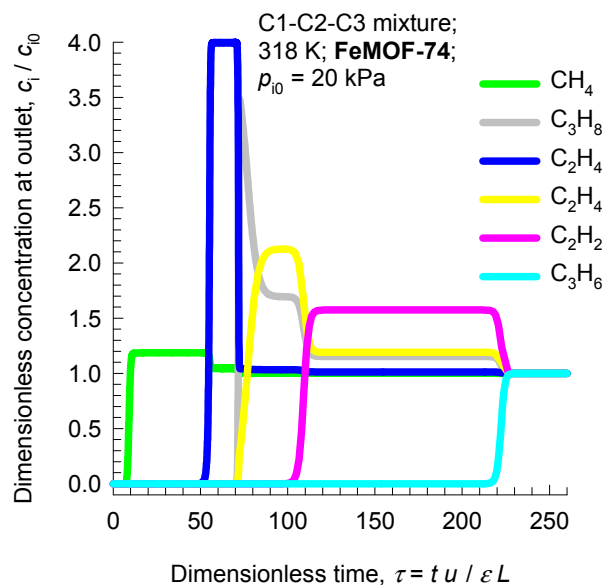
UTSA-35a



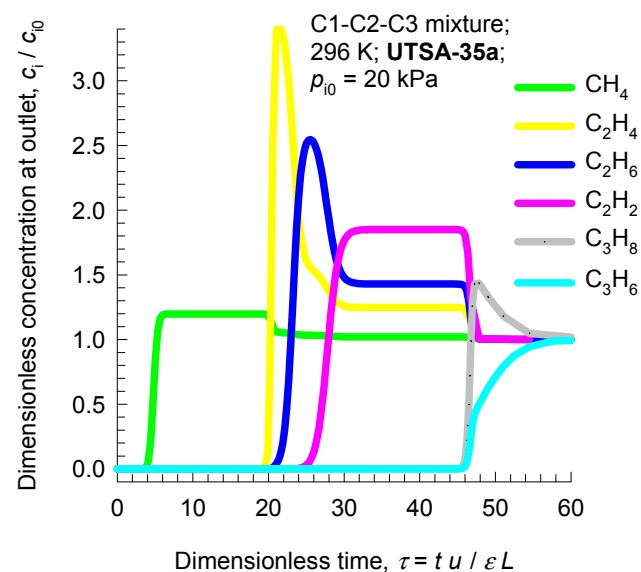
(a)



(b)

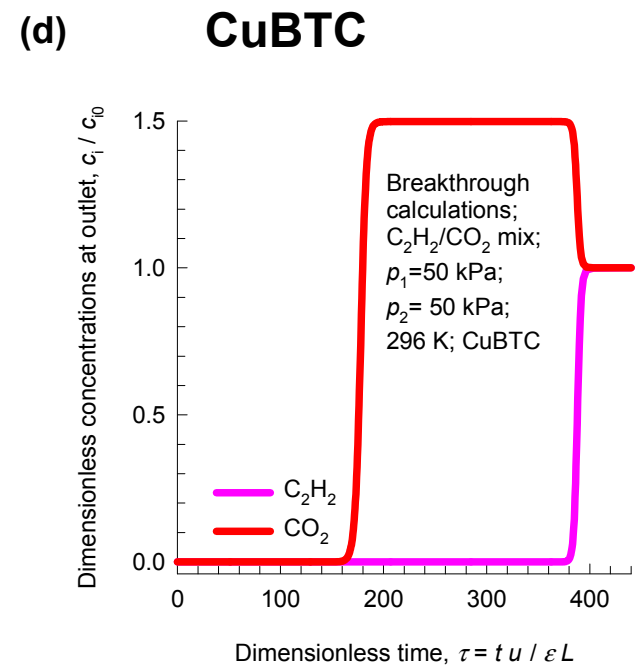
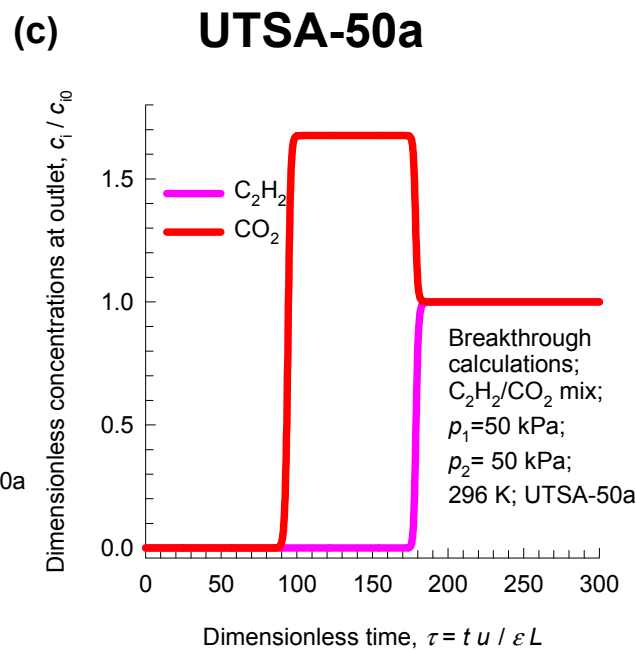
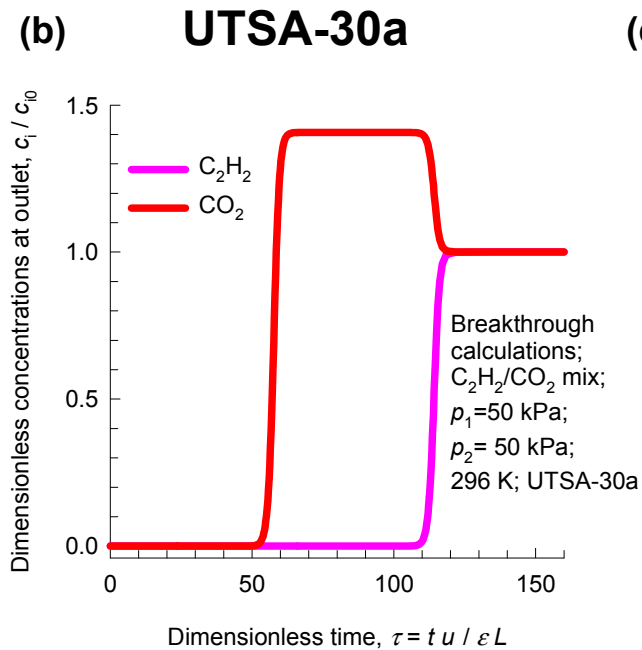
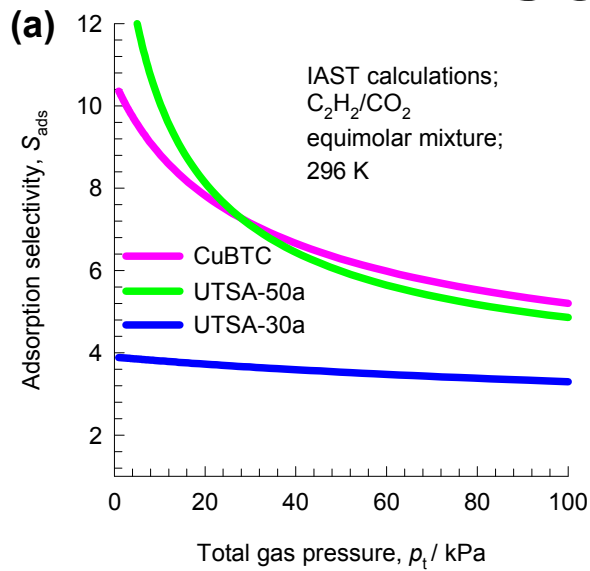


(c)



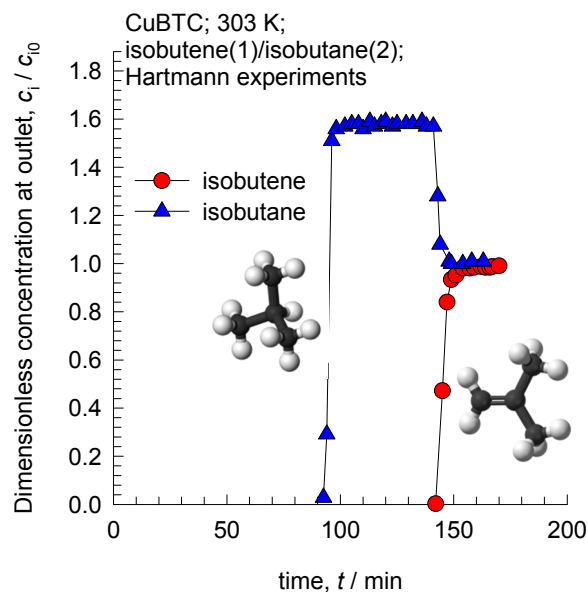
Separation of C_2H_2/CO_2

Figure 88

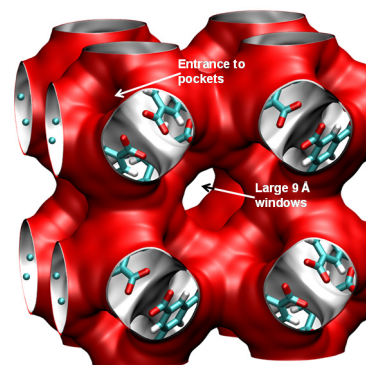


Separation of isobutene/isobutane

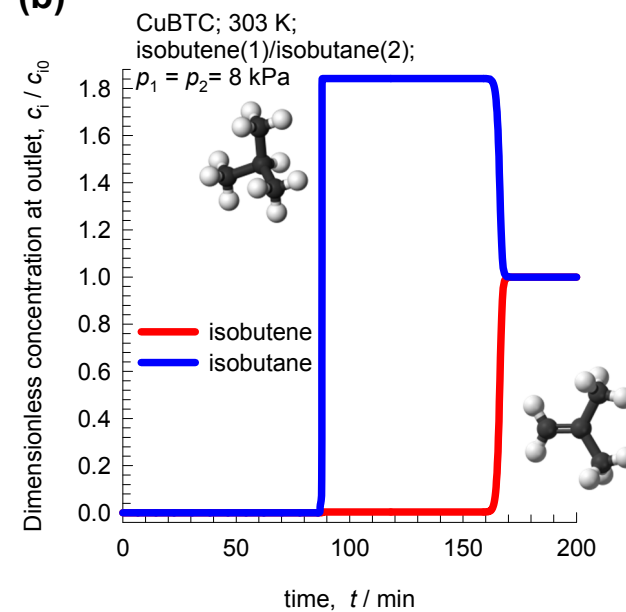
(a)



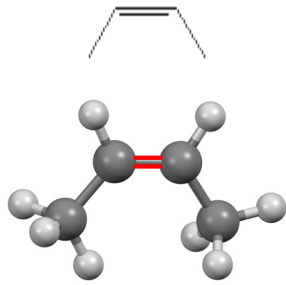
CuBTC



(b)

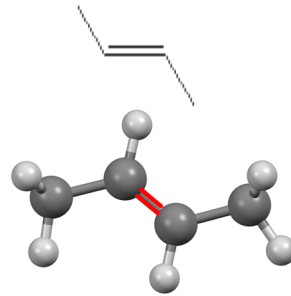


Separation of 2-butenes from 1-butene



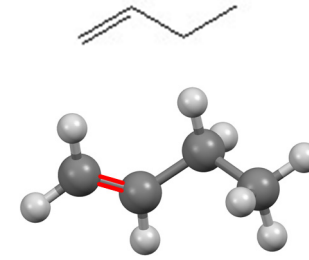
Shortest footprint

cis-2-butene



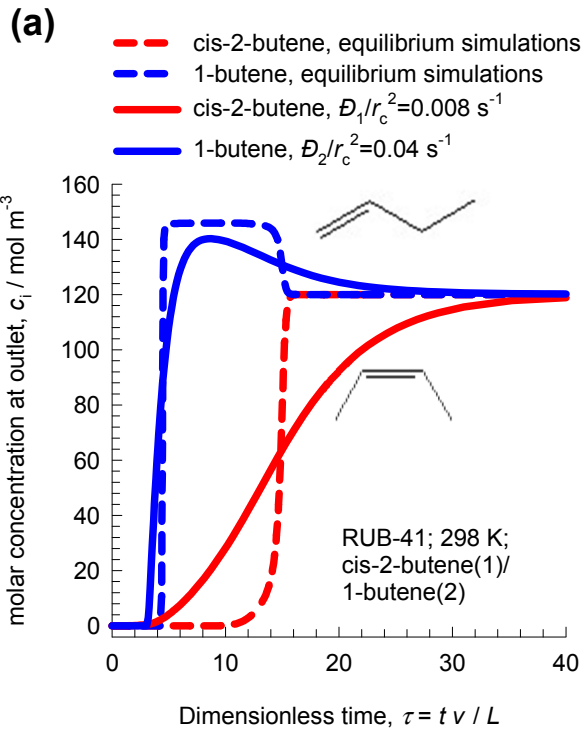
Intermediate footprint

trans-2-butene



Longest footprint

1-butene

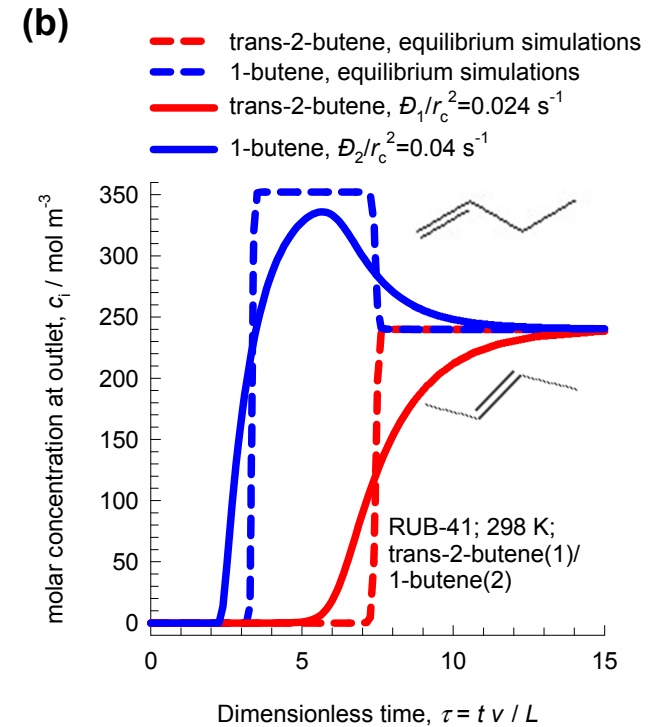


Within the 1D 10-ring channels of RUB-41 (= RRO zeolite topology), the optimal stacking is obtained with cis-2-butene that has the shortest footprint.

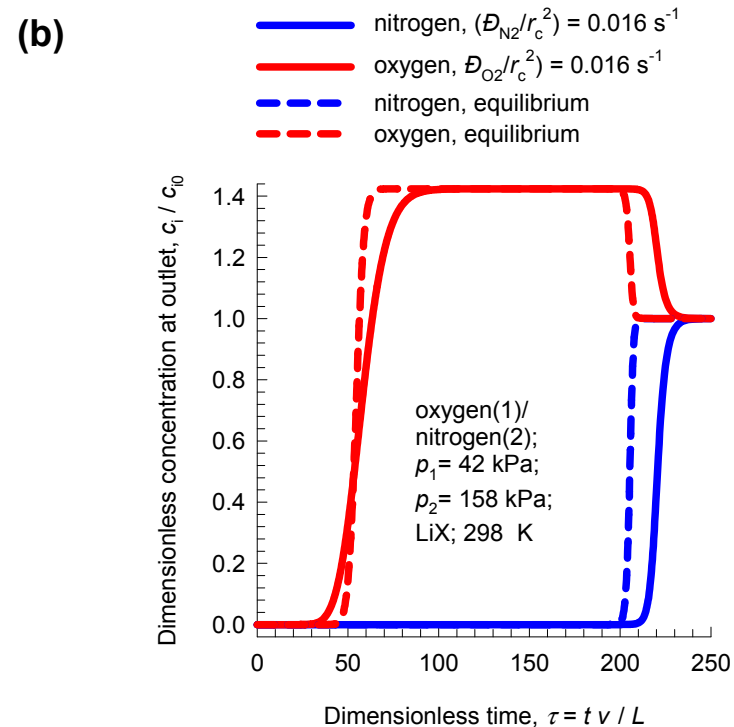
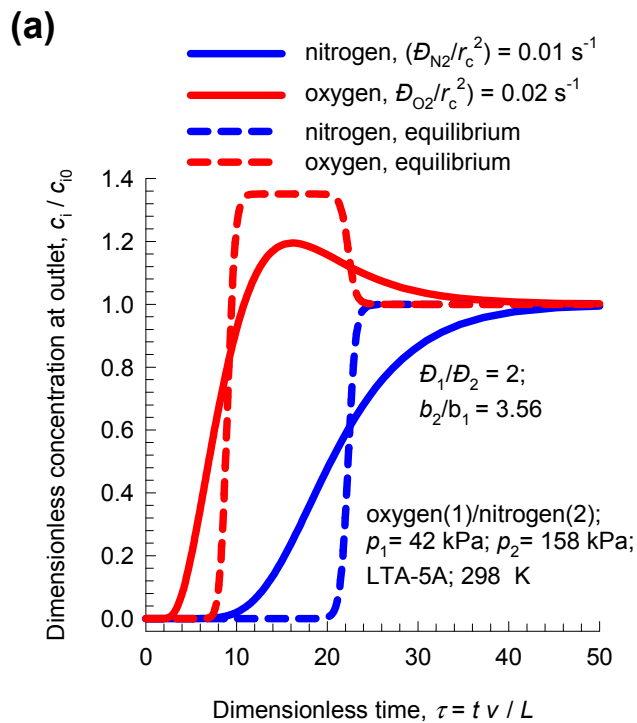
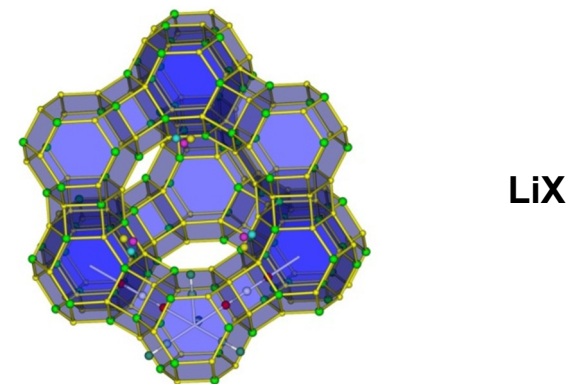
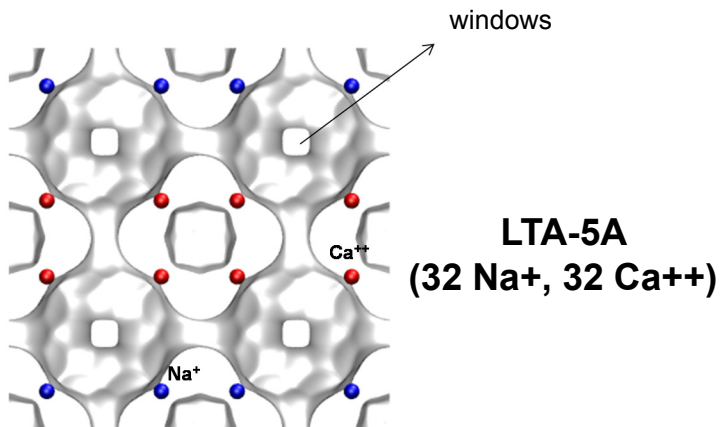
1-butene has the longest footprint and has the lowest capacity at saturation

The simulations on the left are in qualitative agreement with Figure 4a of Tijsebaert et al.

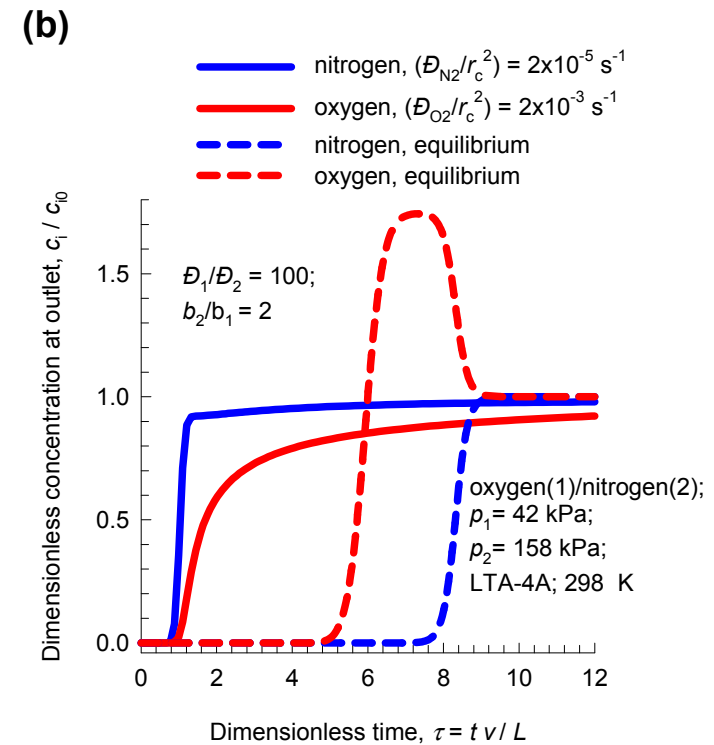
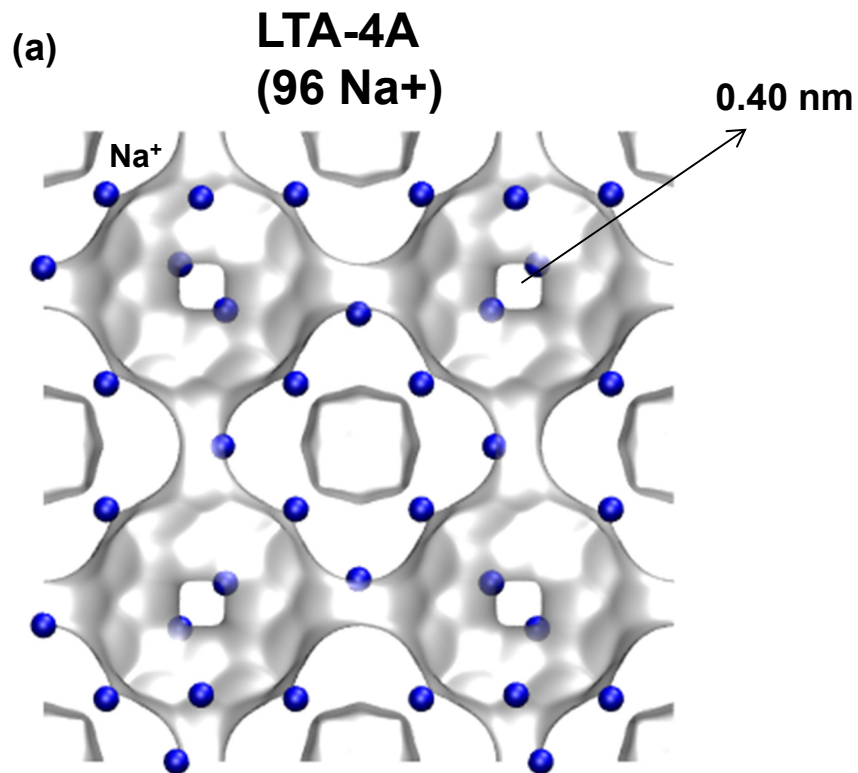
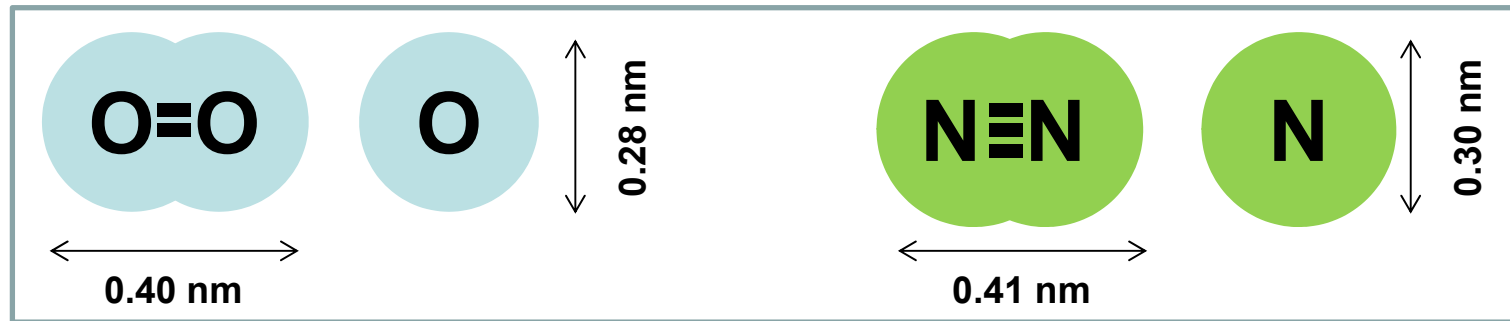
The simulations on the right are in qualitative agreement with Figure 4b of Tijsebaert et al.



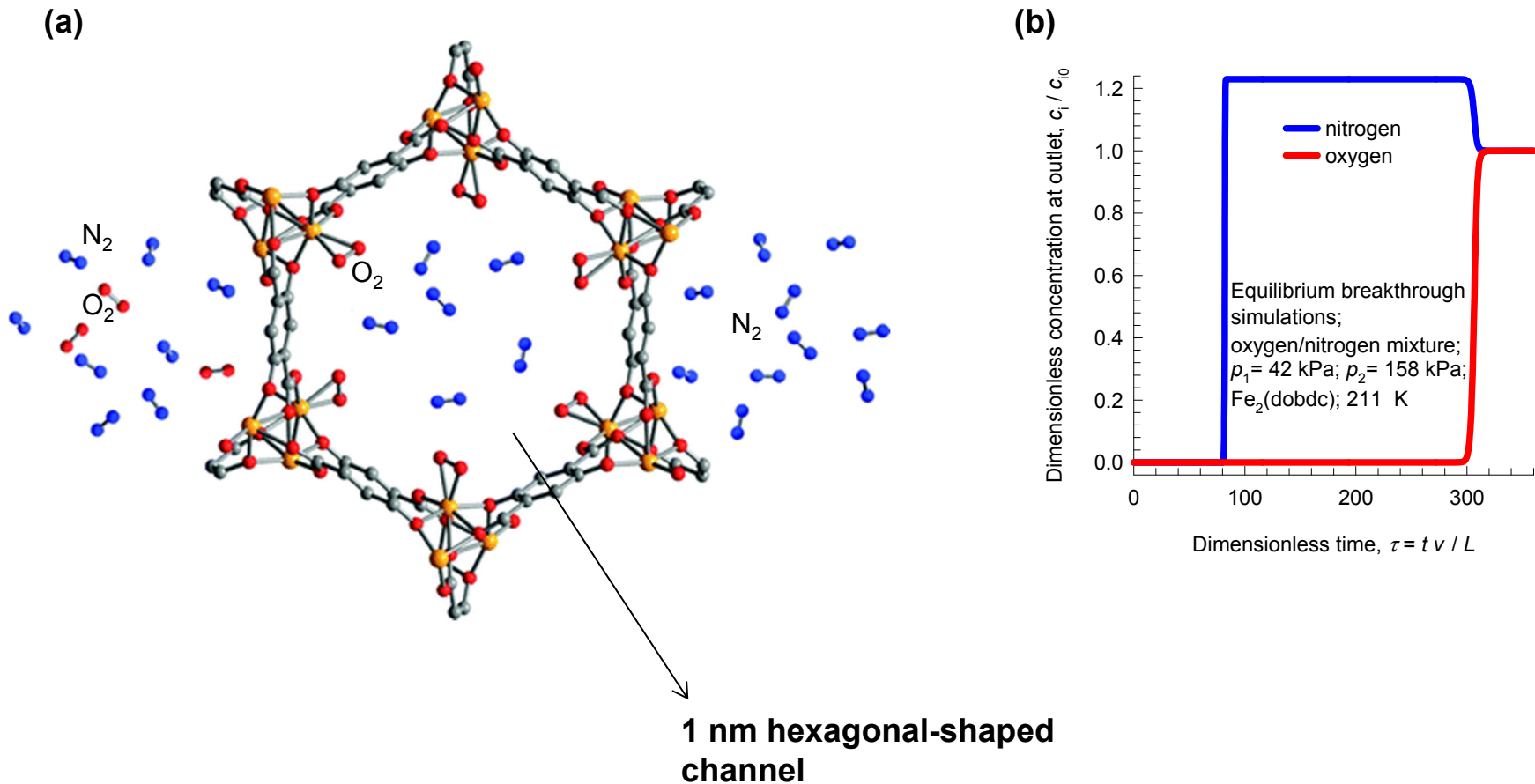
LTA-5A and LiX for O₂ production



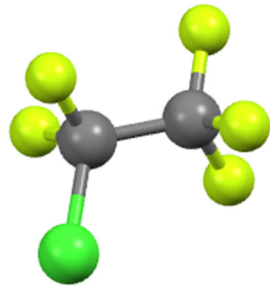
LTA-4A for N₂ production



Fe₂(dobdc) for N₂ production Figure 93



Separation of chlorofluorocarbons



CFC-115

(1-chloro-1,1,2,2,2-pentafluoroethane)

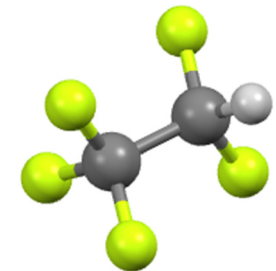
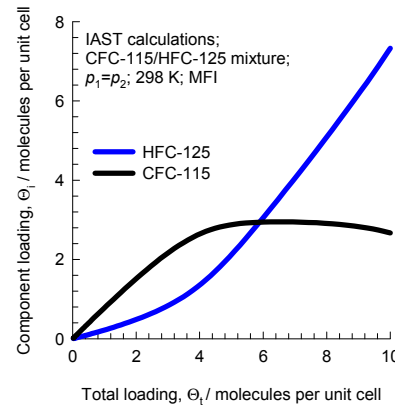
MW = 154.47 g mol⁻¹

Boiling point = 234.1 K

Critical temperature = 353.2 K

Critical pressure = 3.229 MPa

Enthalpy of vaporization = 14.62 kJ mol⁻¹



HFC-125

(1,1,1,2,2-pentafluoroethane)

MW = 120.02 g mol⁻¹

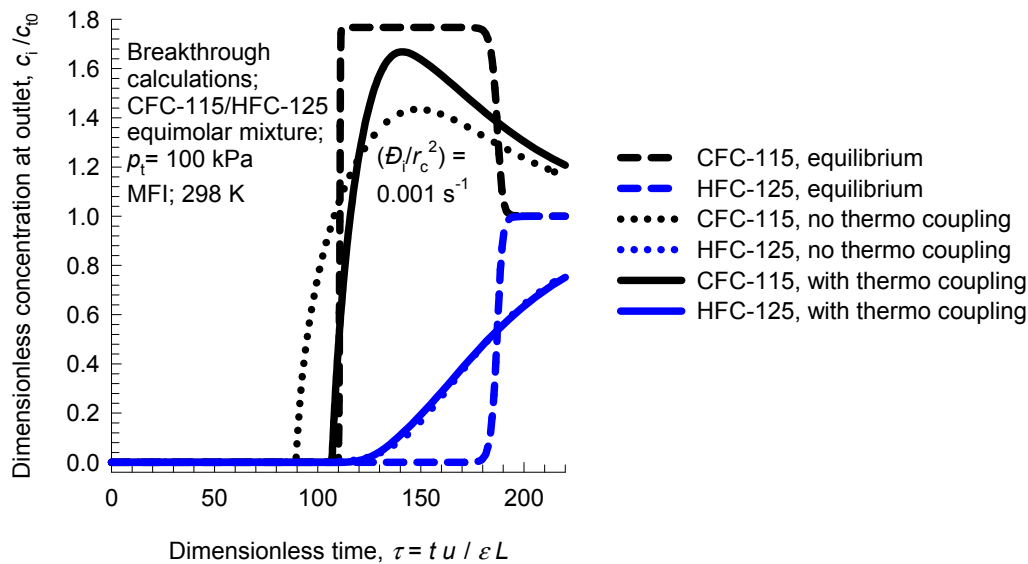
Boiling point = 224.7 K

Critical temperature = 339.2 K

Critical pressure = 3.617 MPa

Enthalpy of vaporization = 13.19 kJ mol⁻¹

(a)



(b)

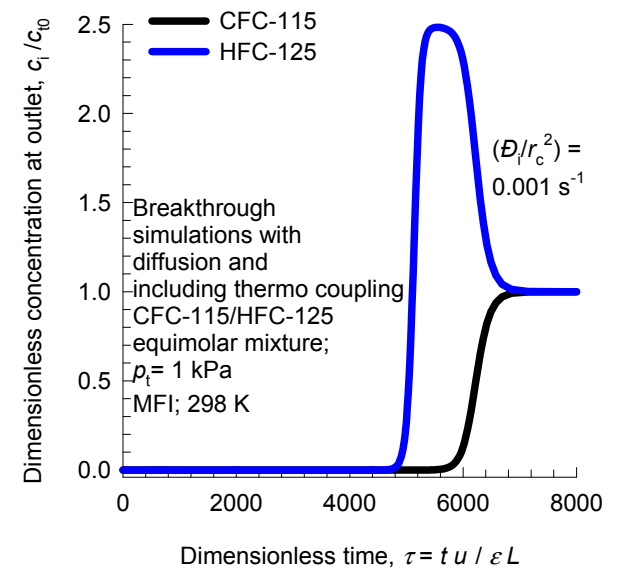


Figure 95

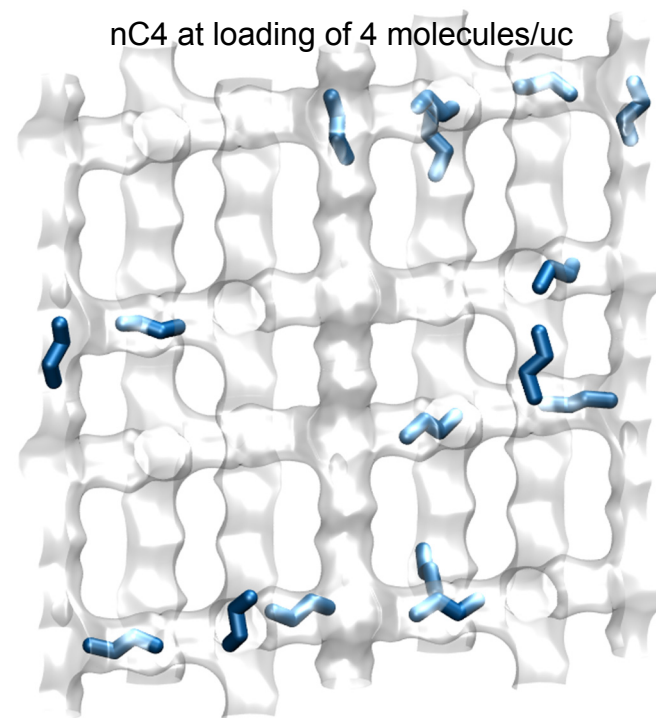
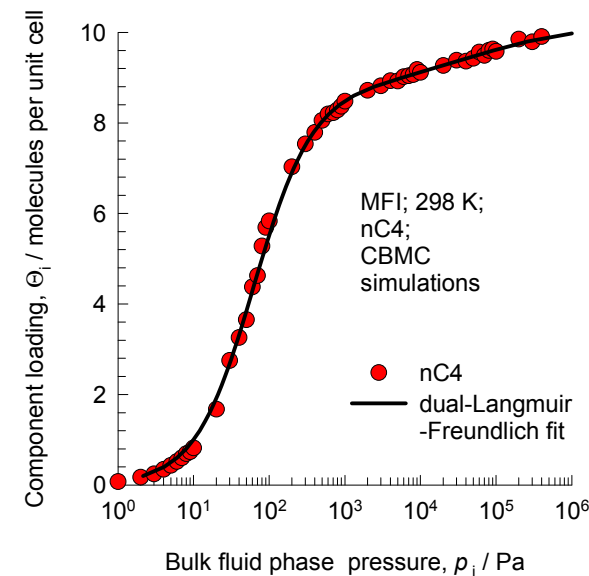
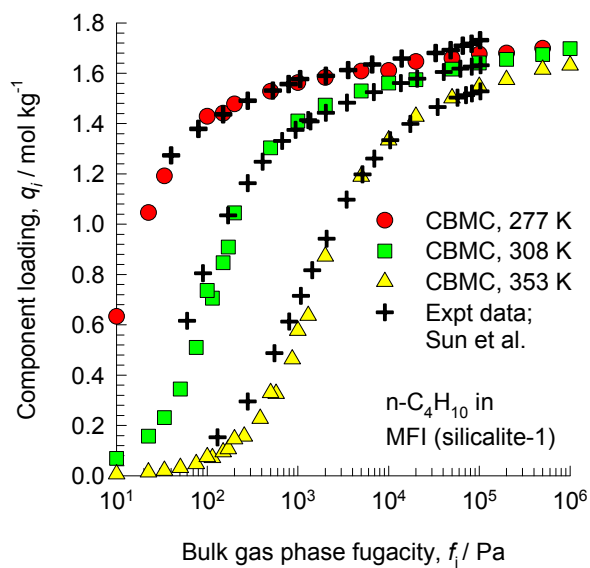
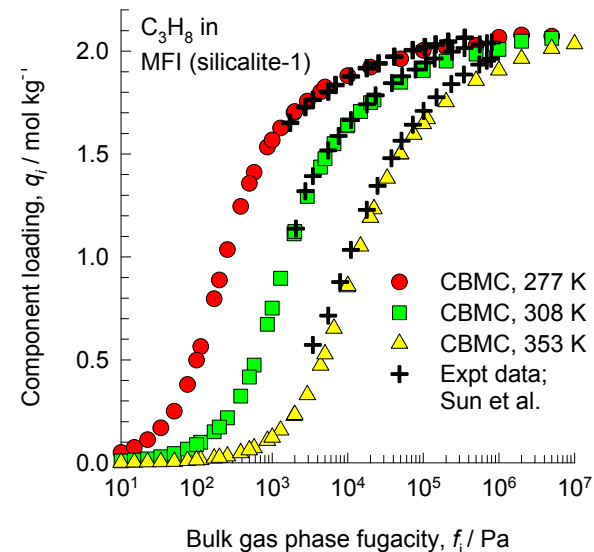
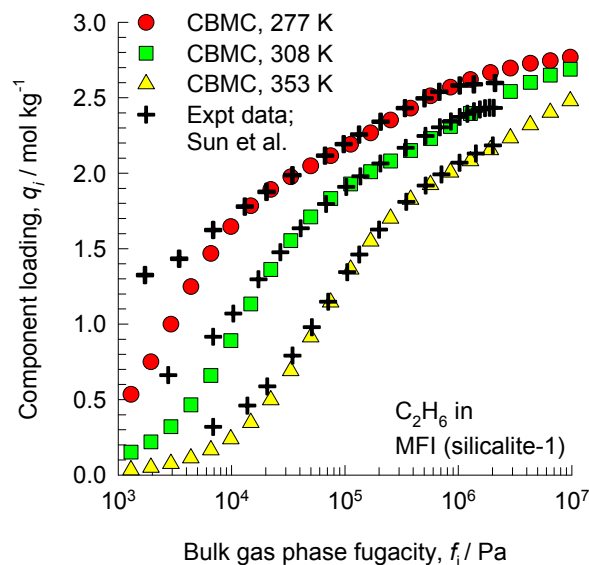
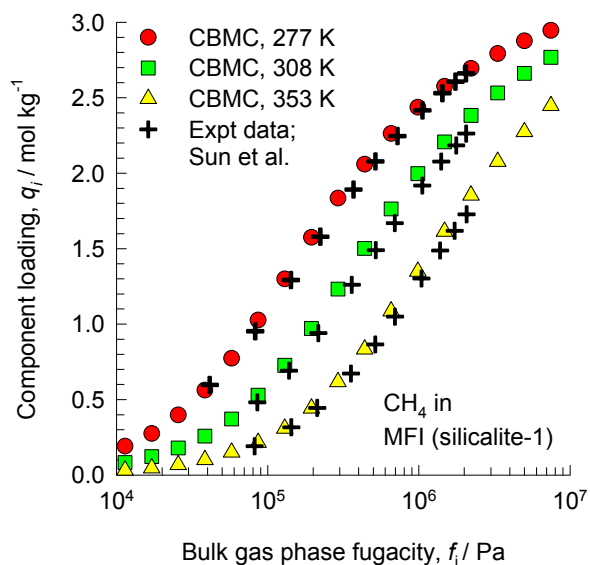
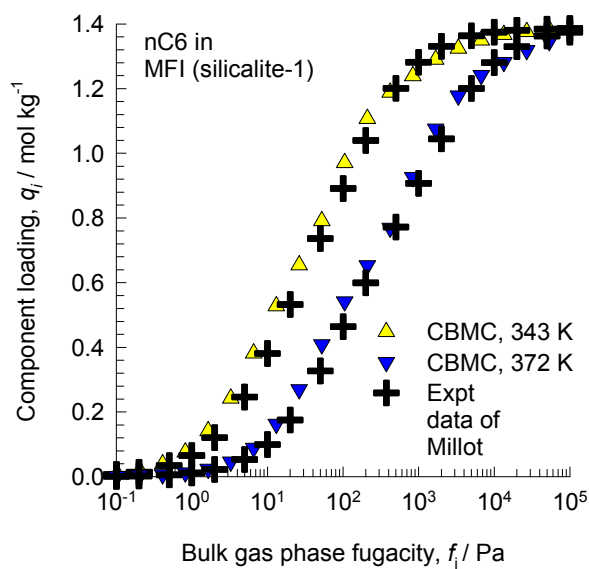
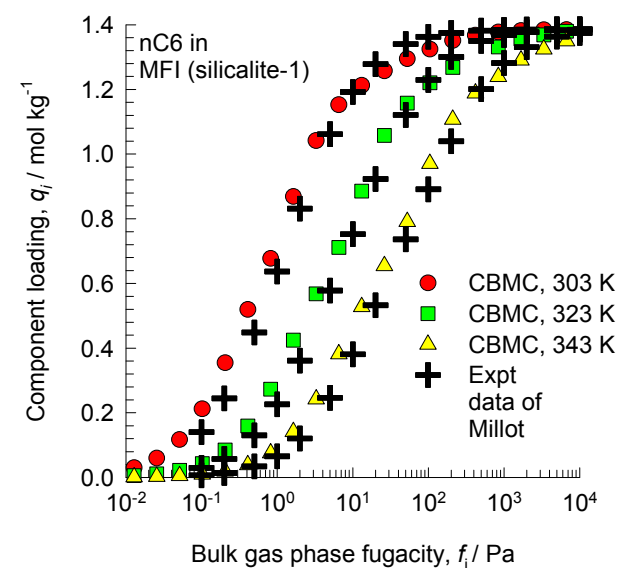
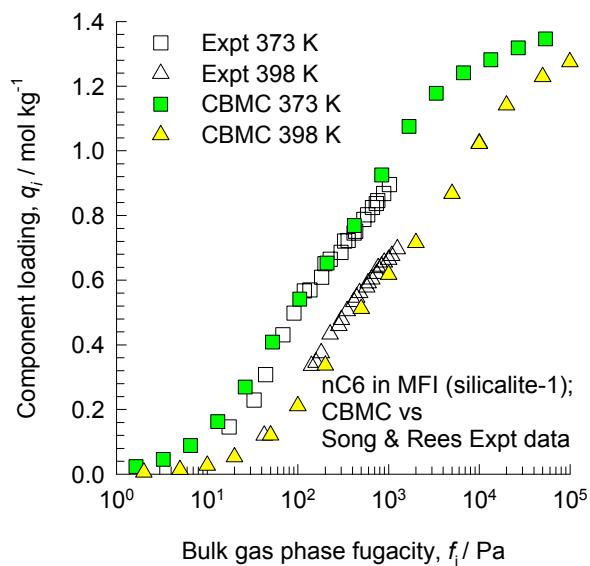
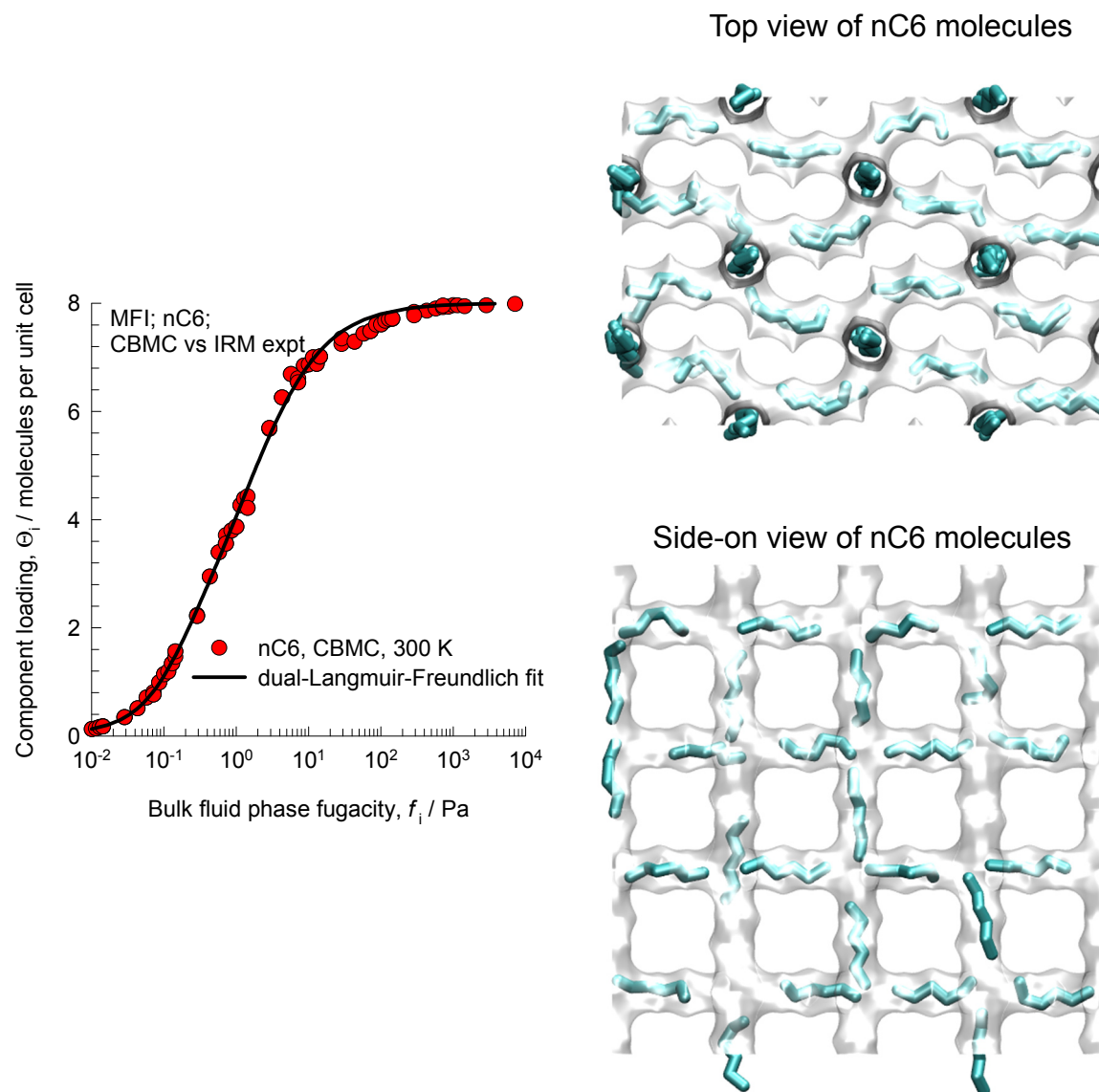


Figure 96

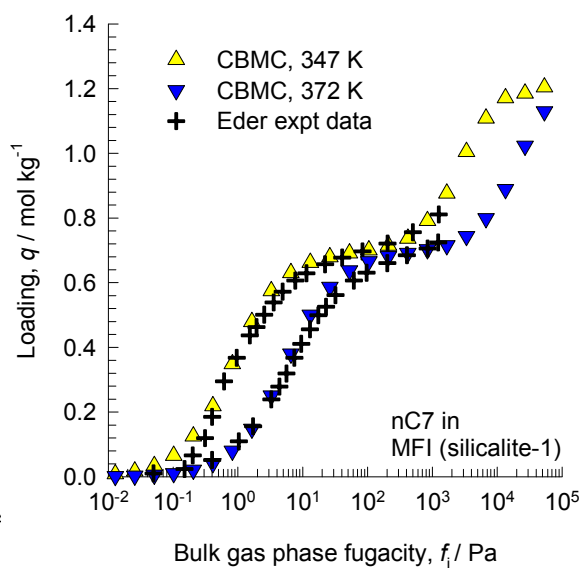
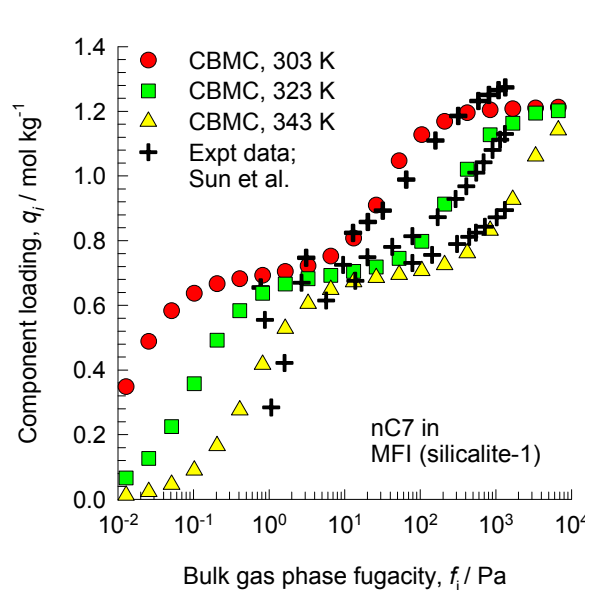
CBMC for unary alkanes in MFI



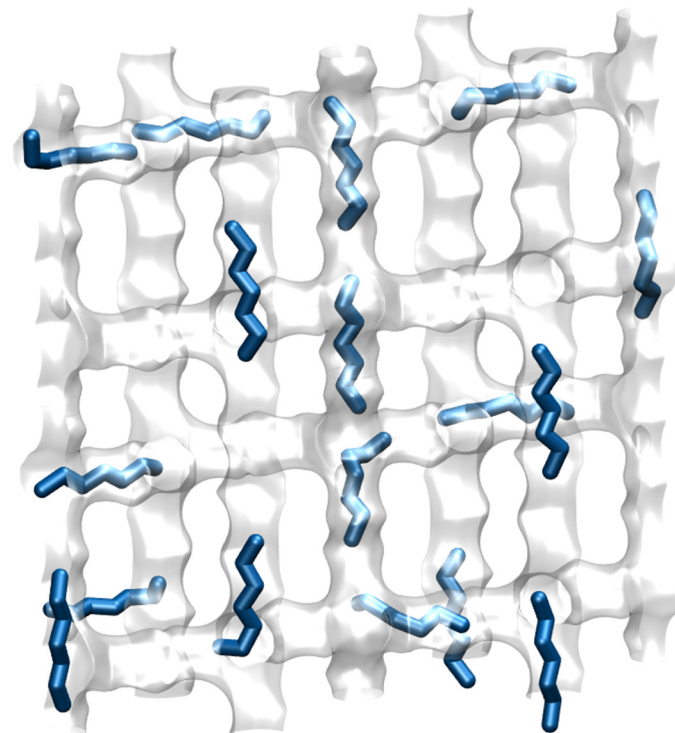
CBMC for unary alkanes in MFI



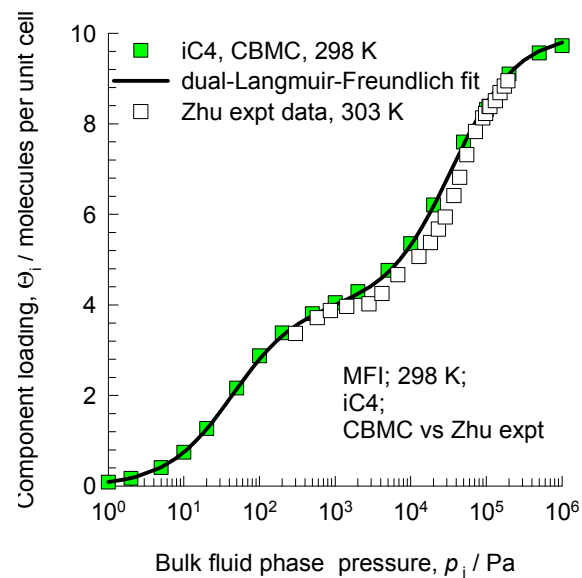
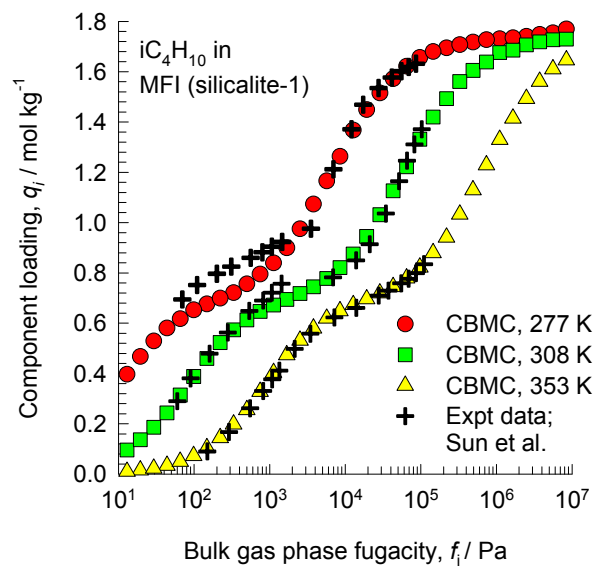
CBMC for unary alkanes in MFI



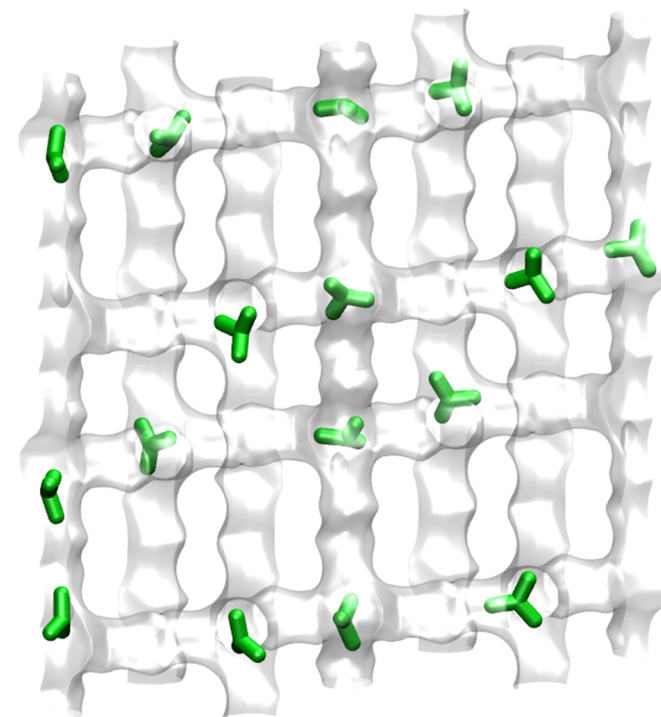
nC7 at loading of 4 molecules/uc



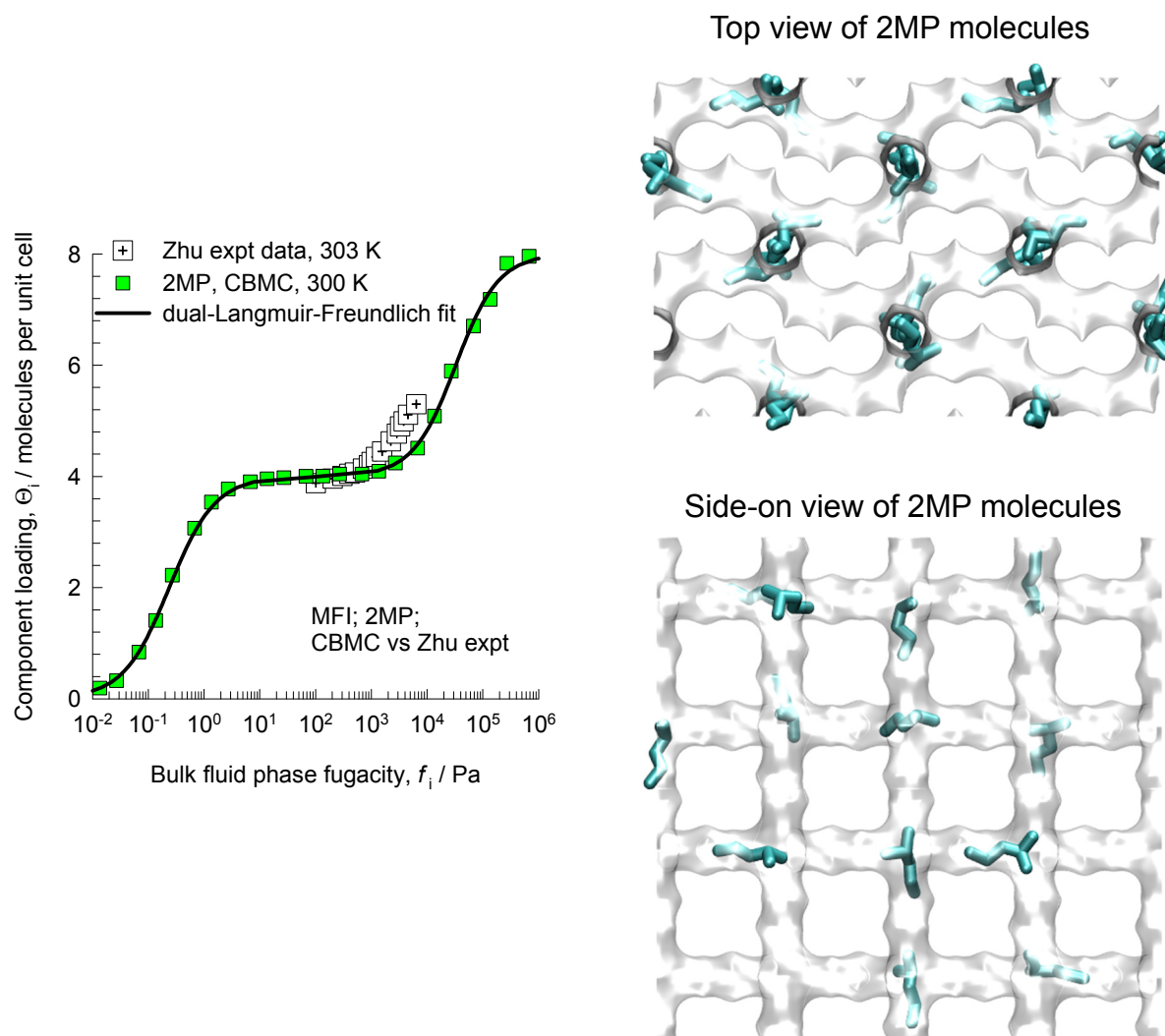
CBMC for unary alkanes in MFI



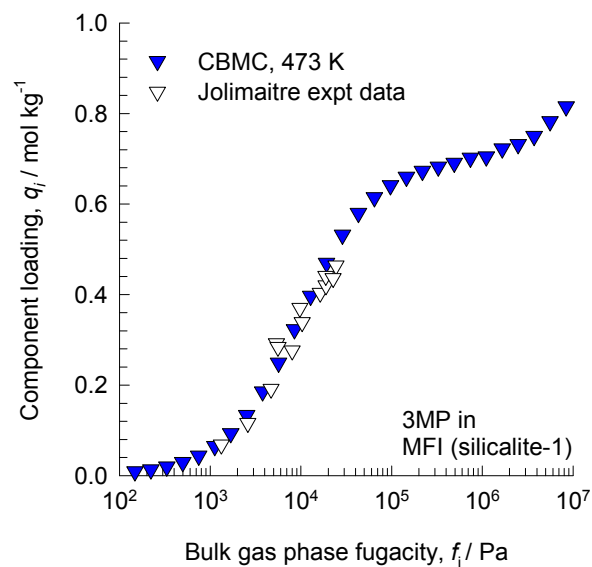
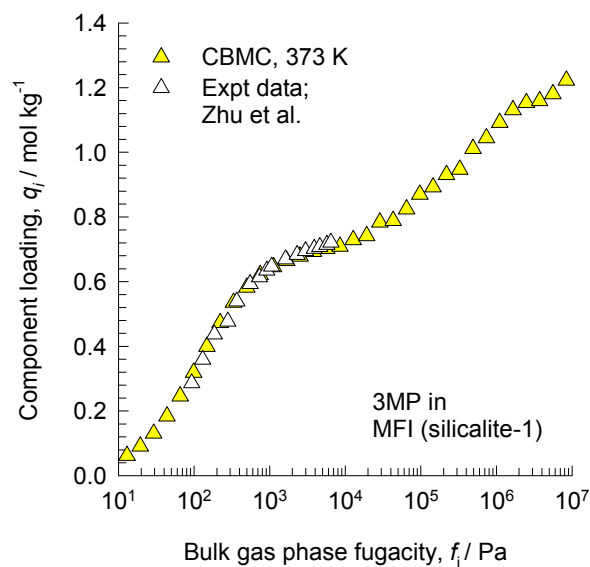
iC_4 at a loading of 4/uc



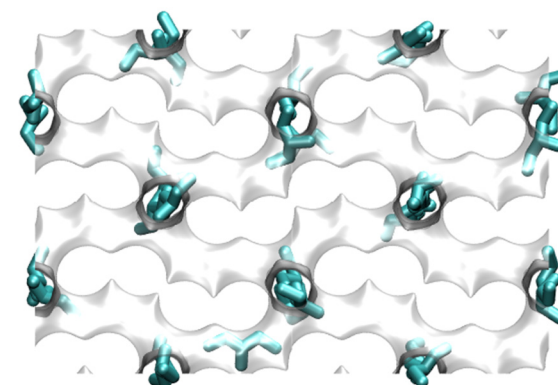
CBMC for unary alkanes in MFI



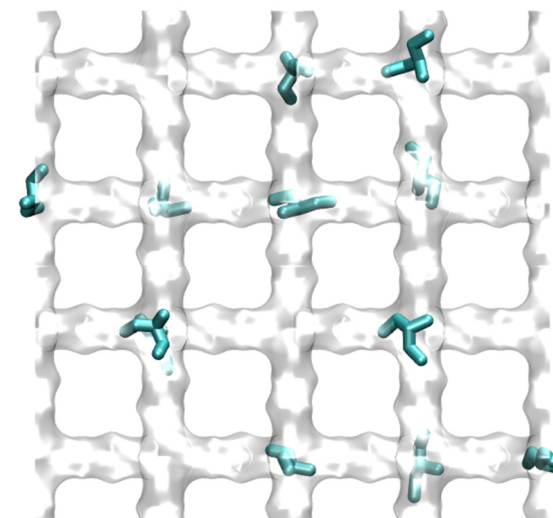
CBMC for unary alkanes in MFI



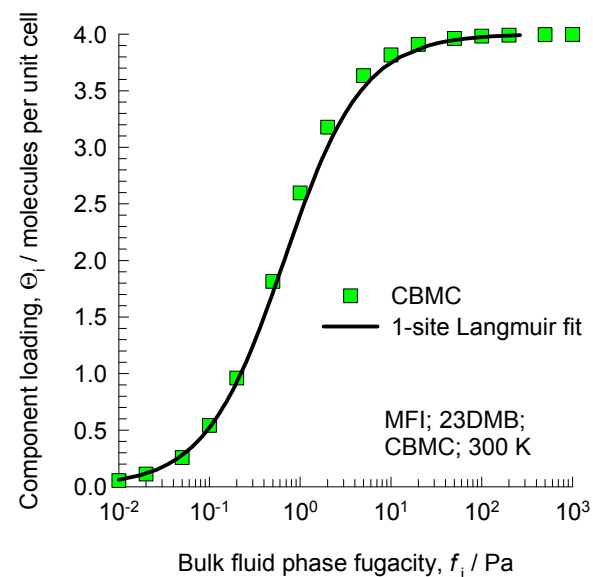
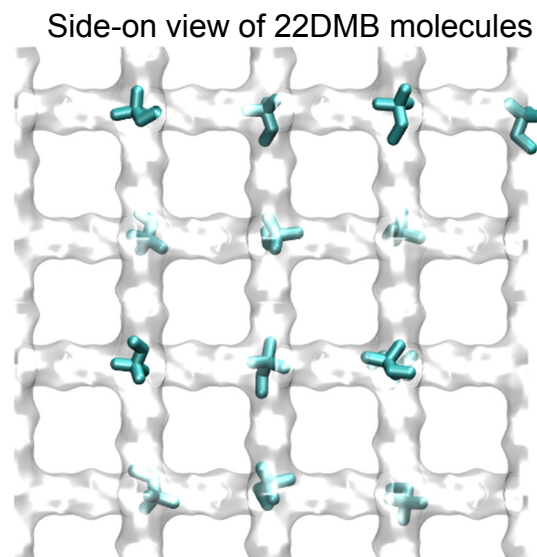
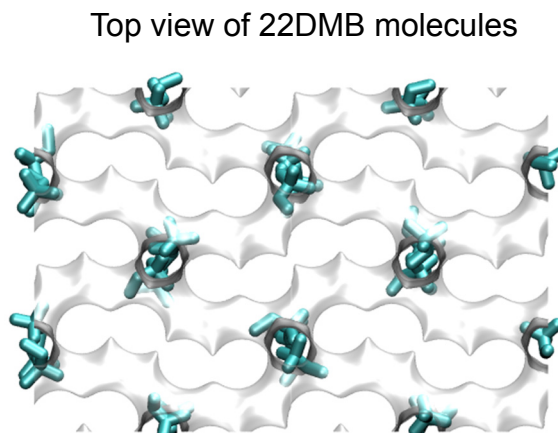
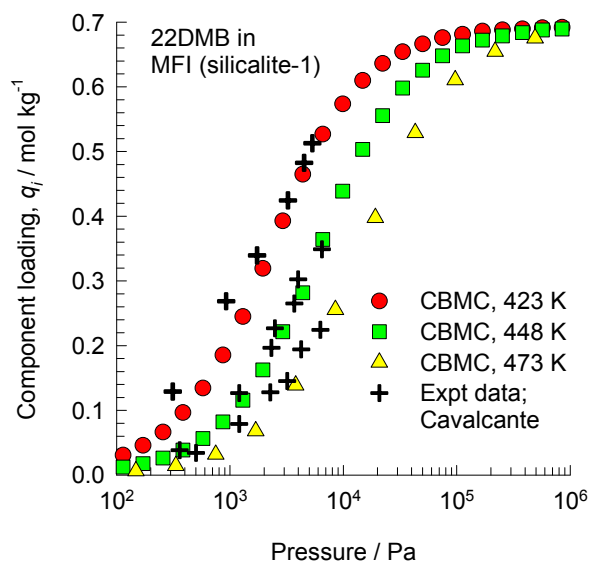
Top view of 3MP molecules



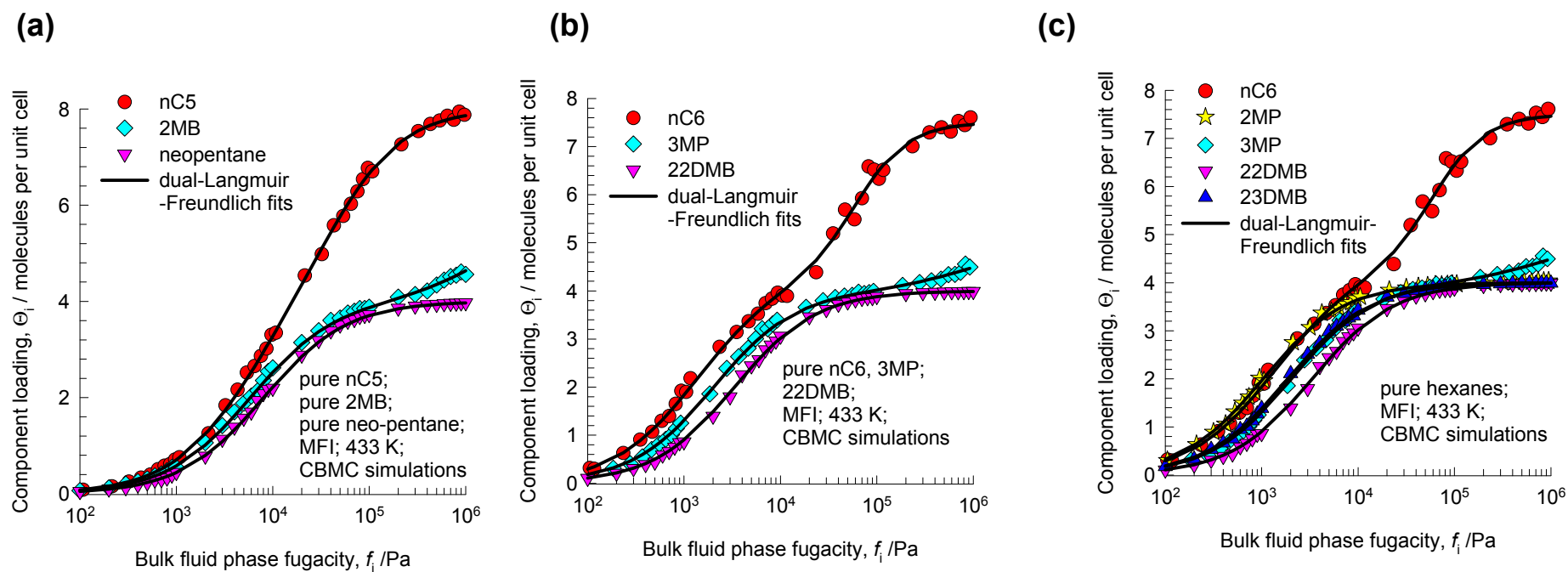
Side-on view of 3MP molecules

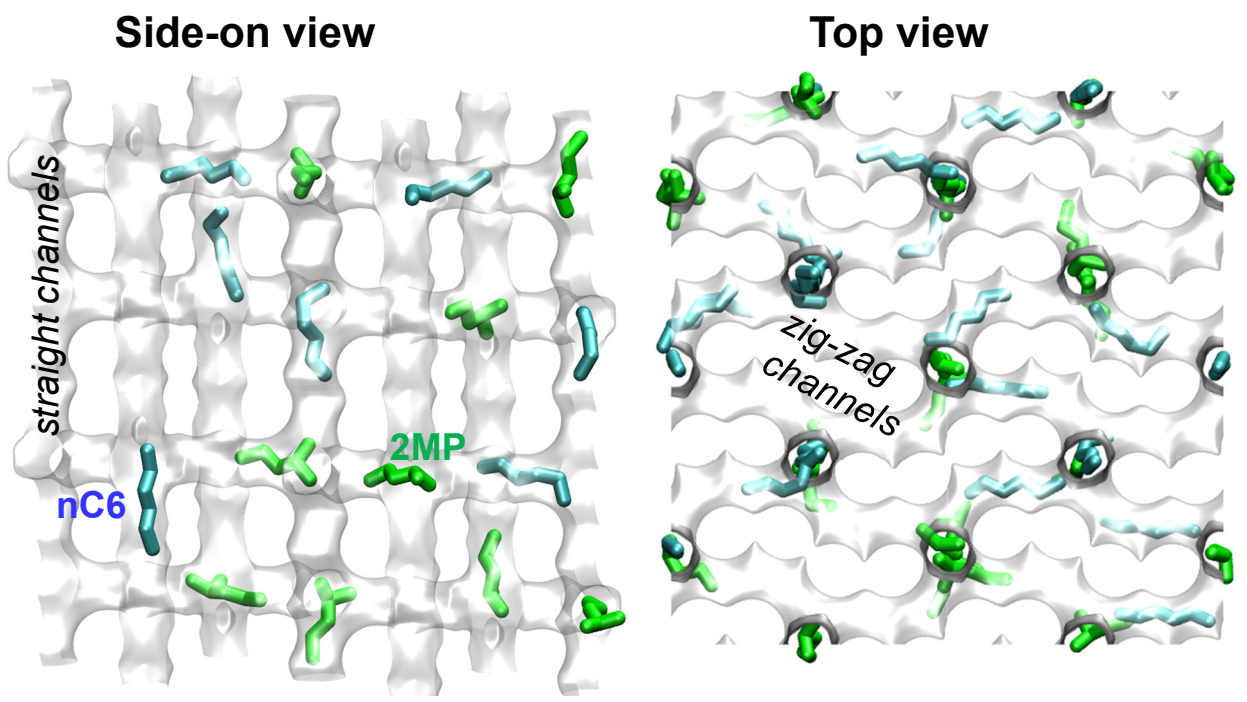
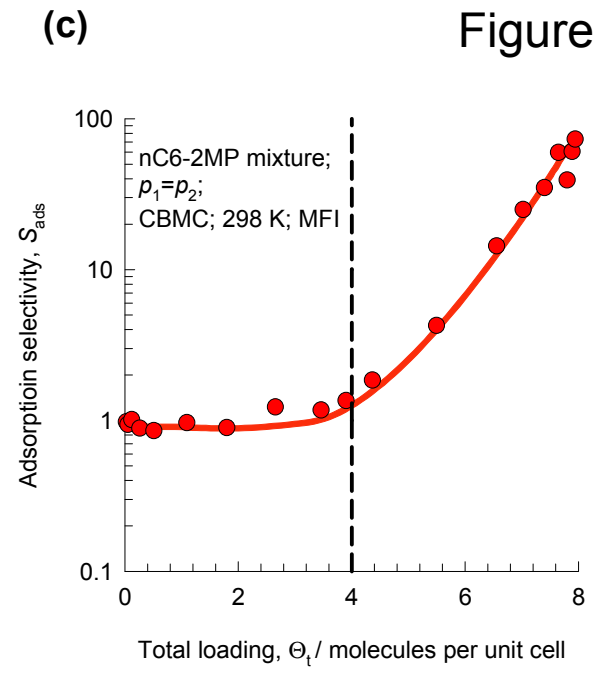
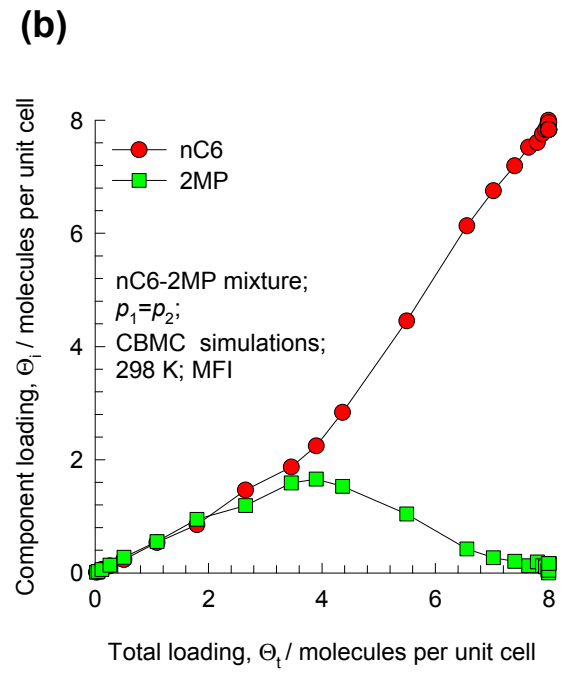
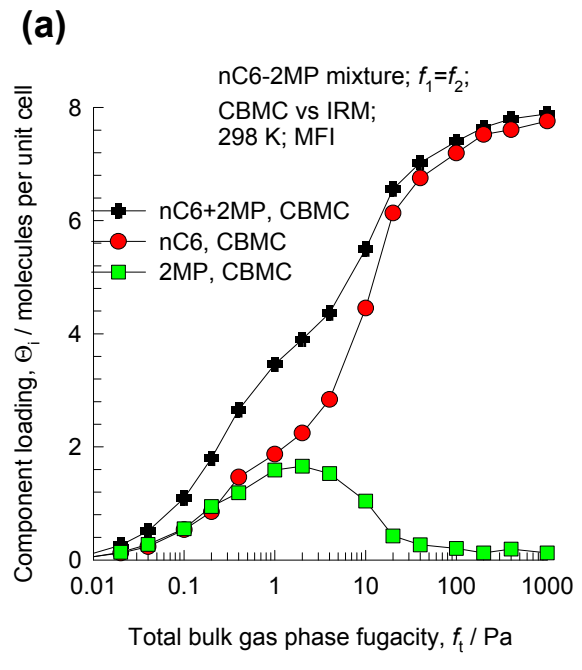


CBMC for unary alkanes in MFI

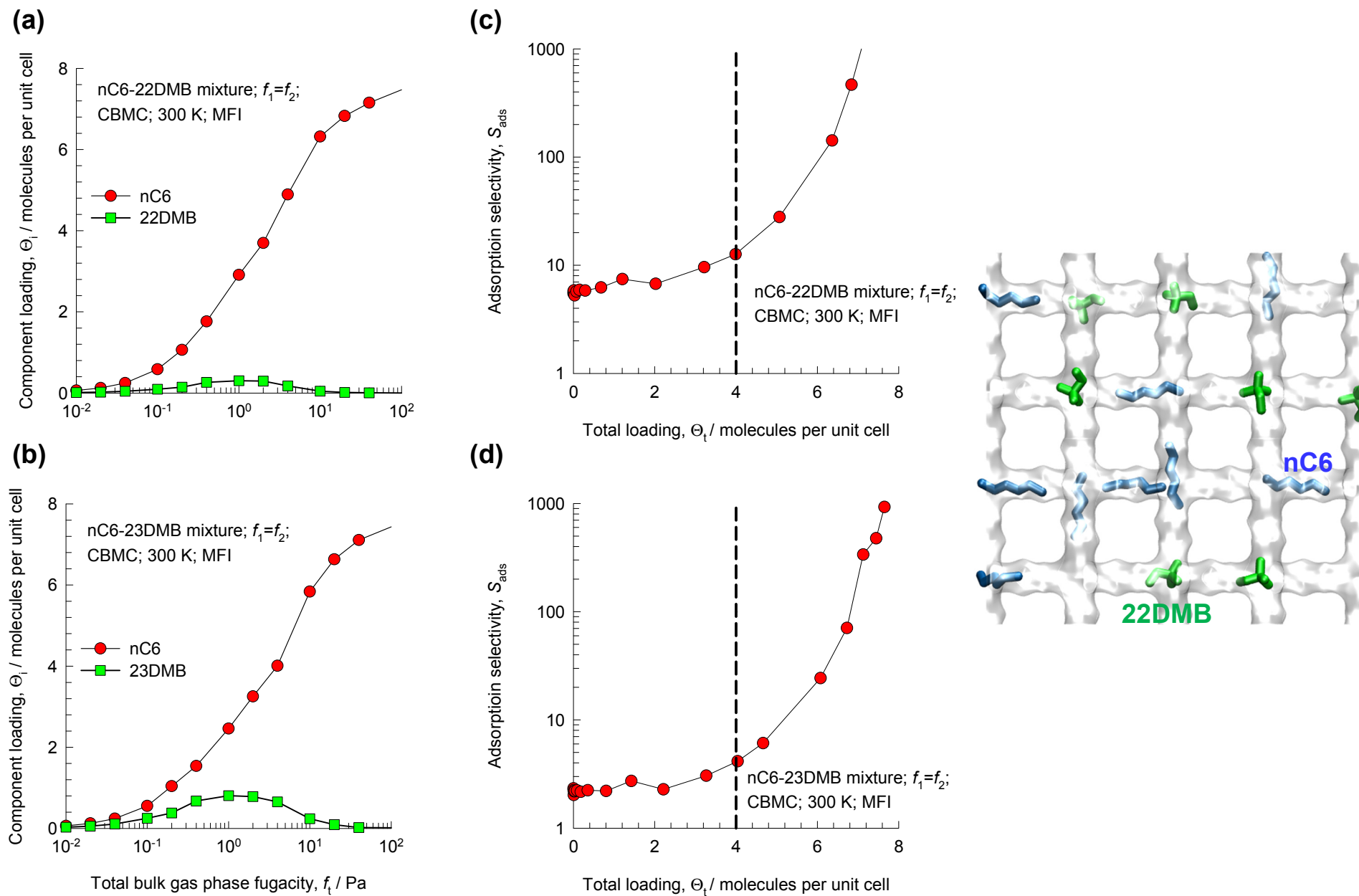


CBMC for unary alkanes in MFI



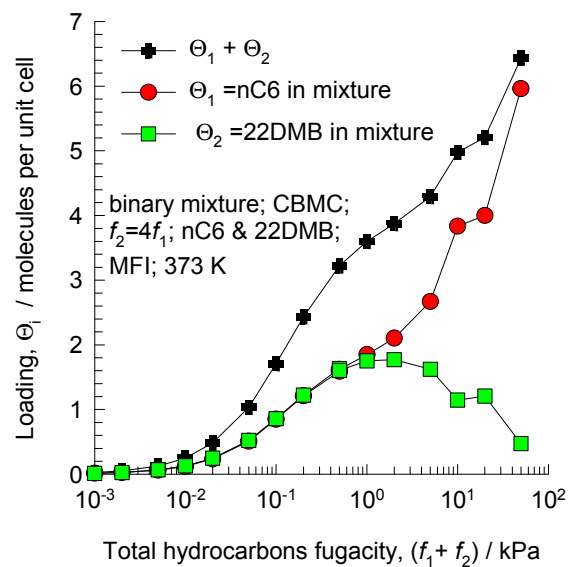


CBMC for alkane mixtures in MFI

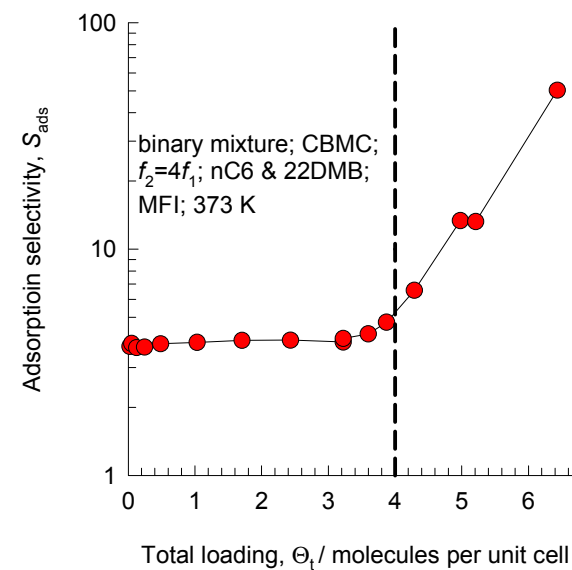


CBMC for alkane mixtures in MFI

(a)



(b)



(c)

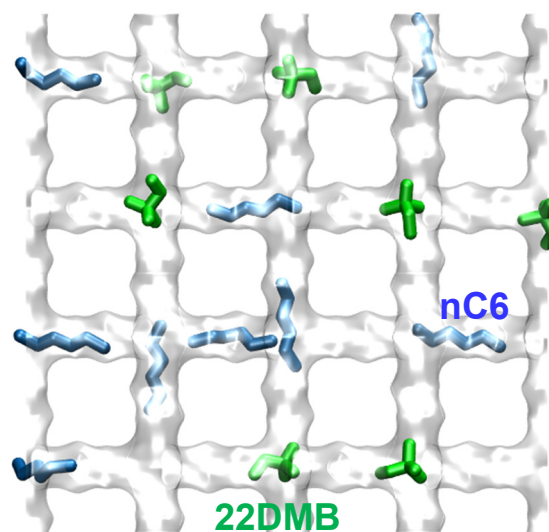
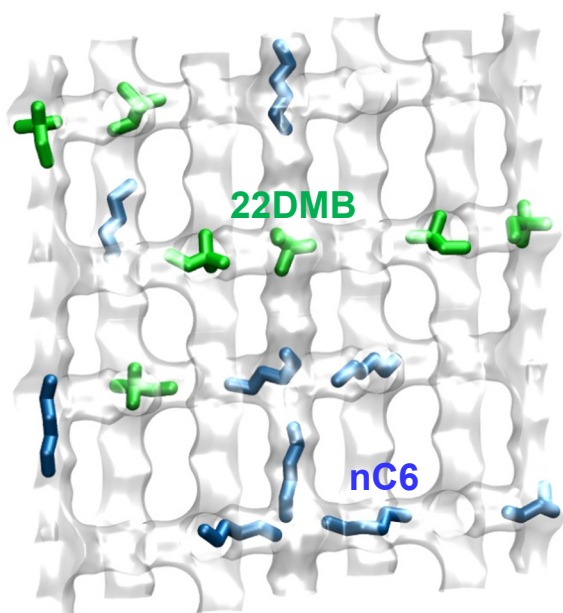
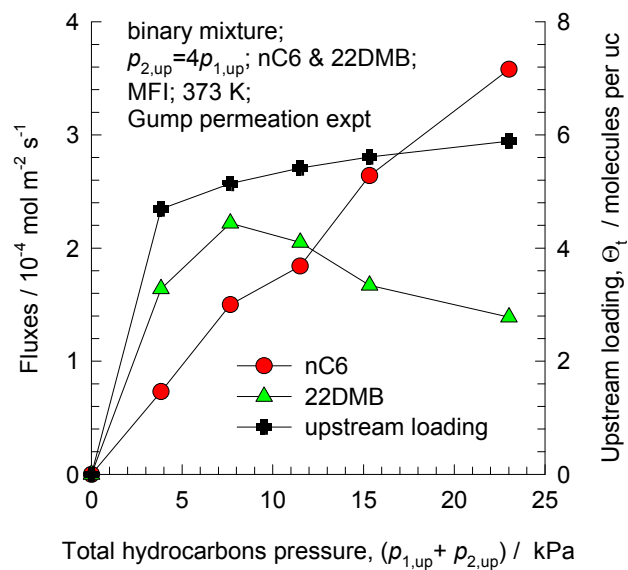
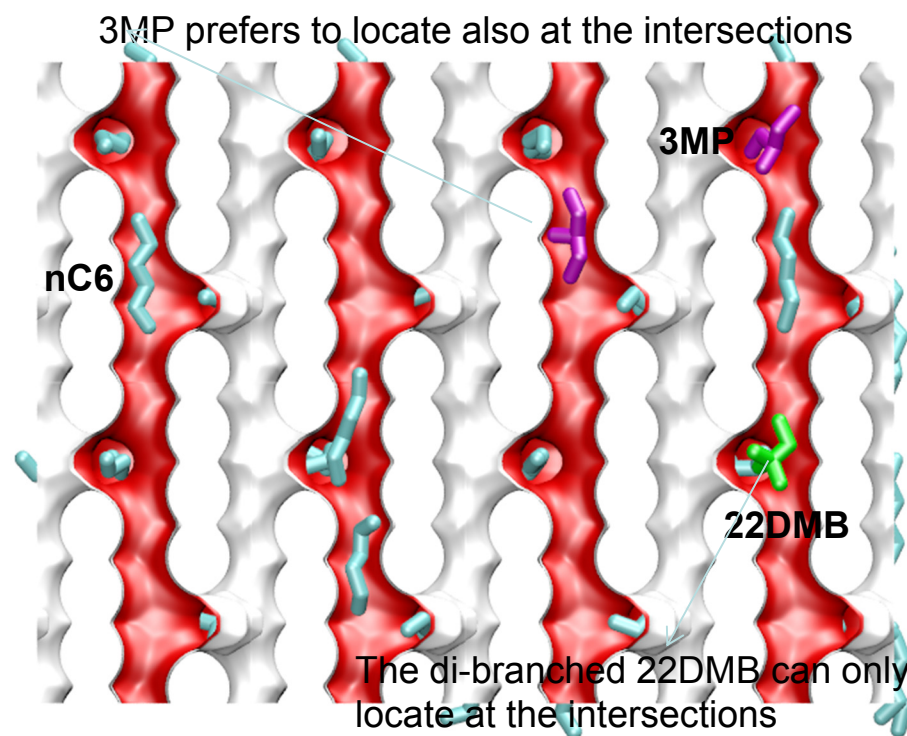
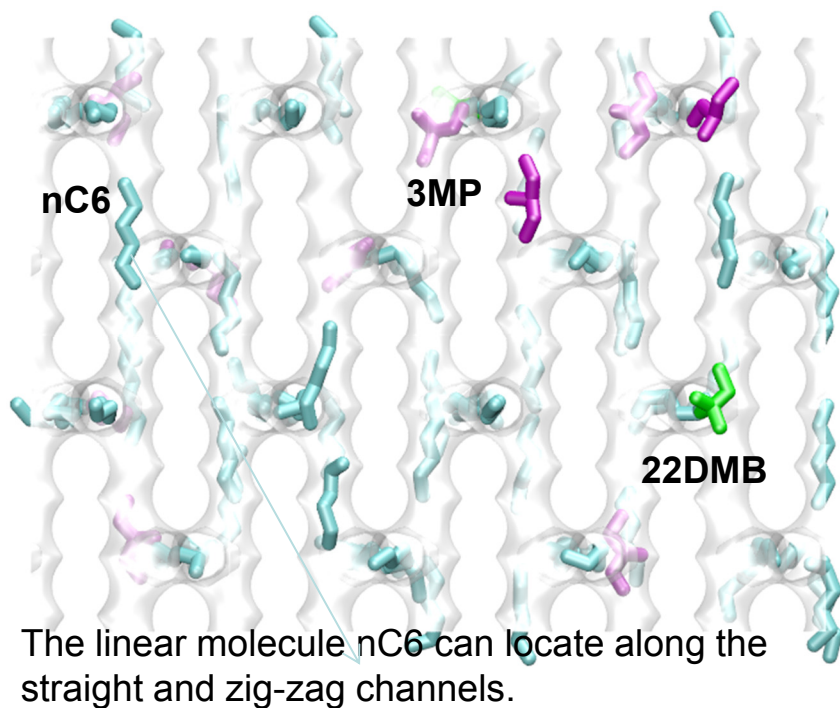
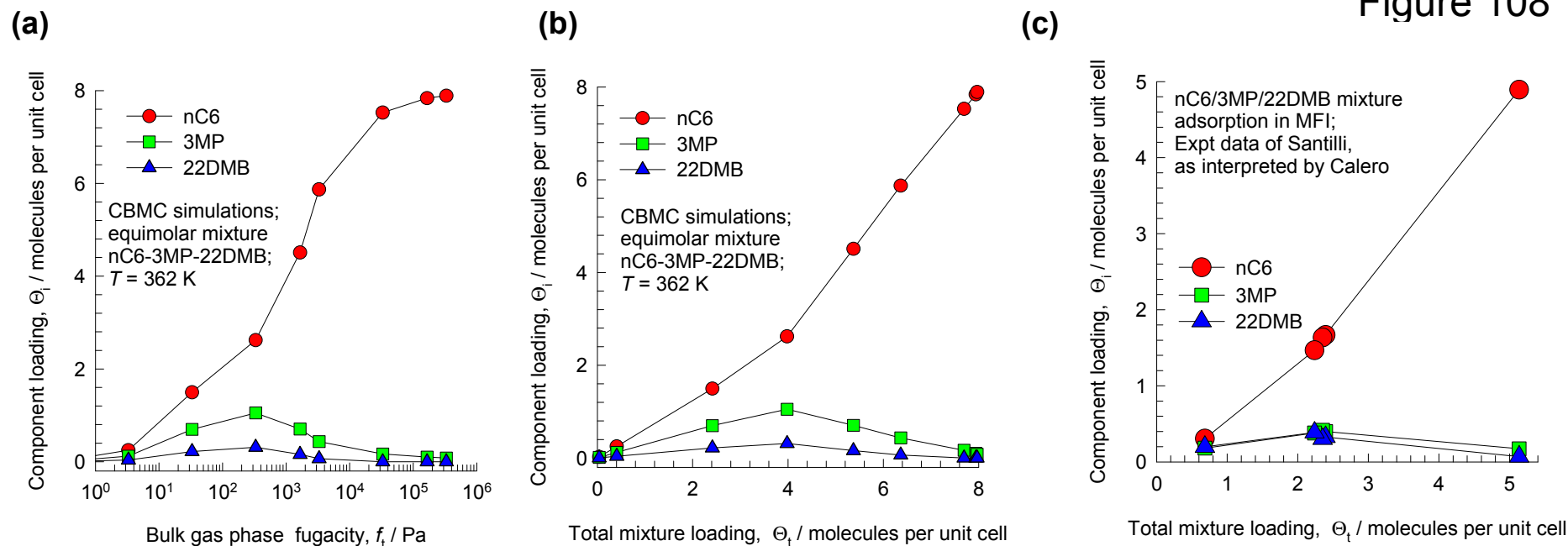


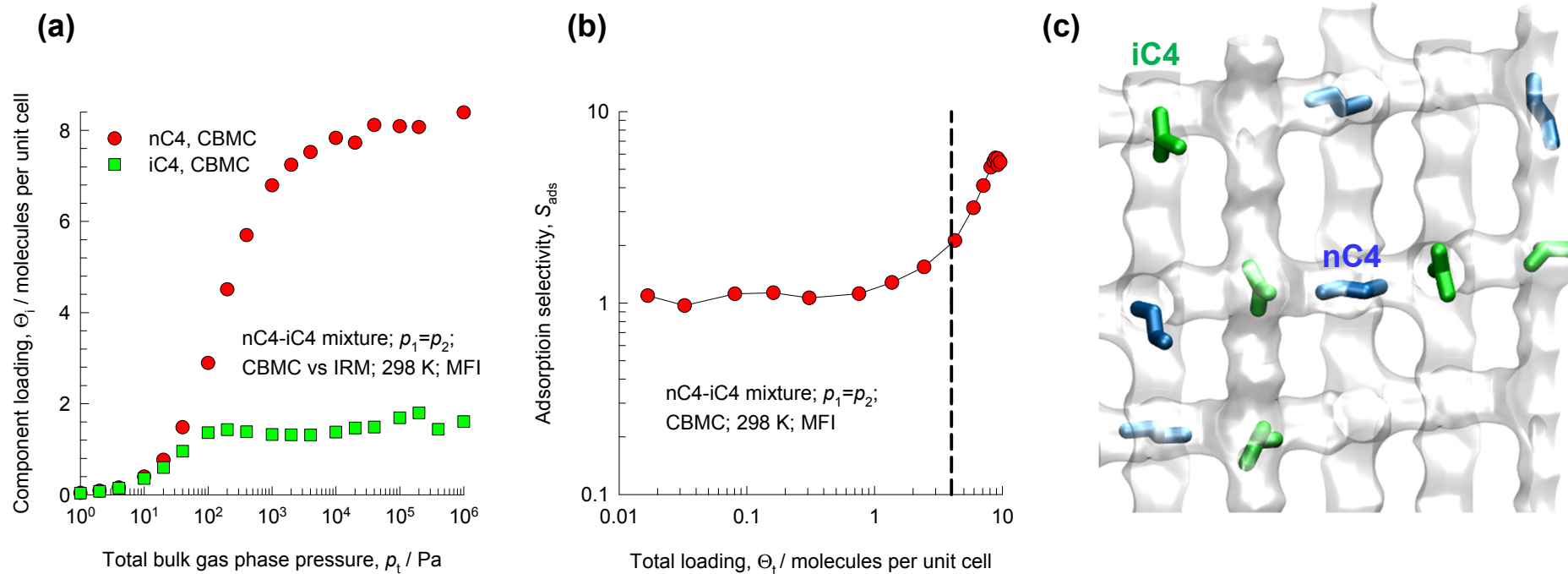
Figure 107

nC6/22DMB permeation across MFI



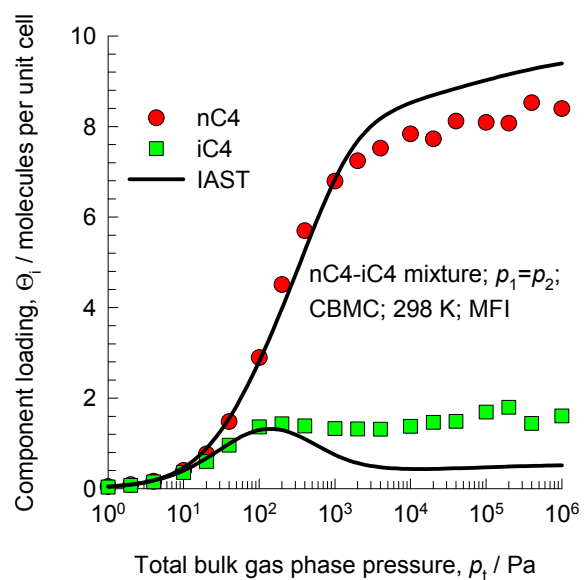


CBMC for nC4/iC4 mixture in MFI

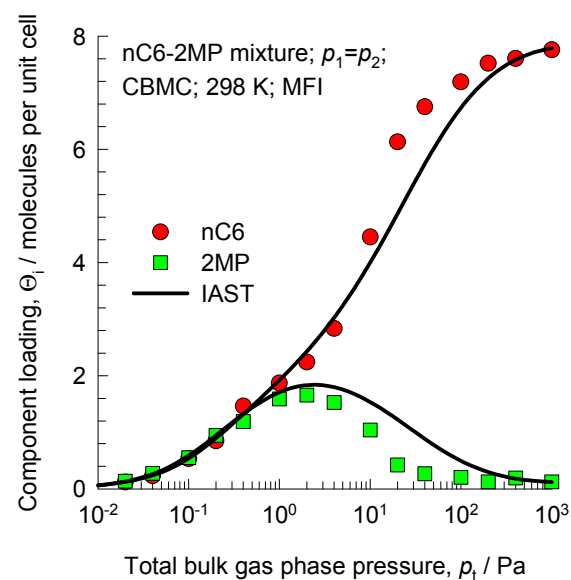


CBMC mixture vs IAST

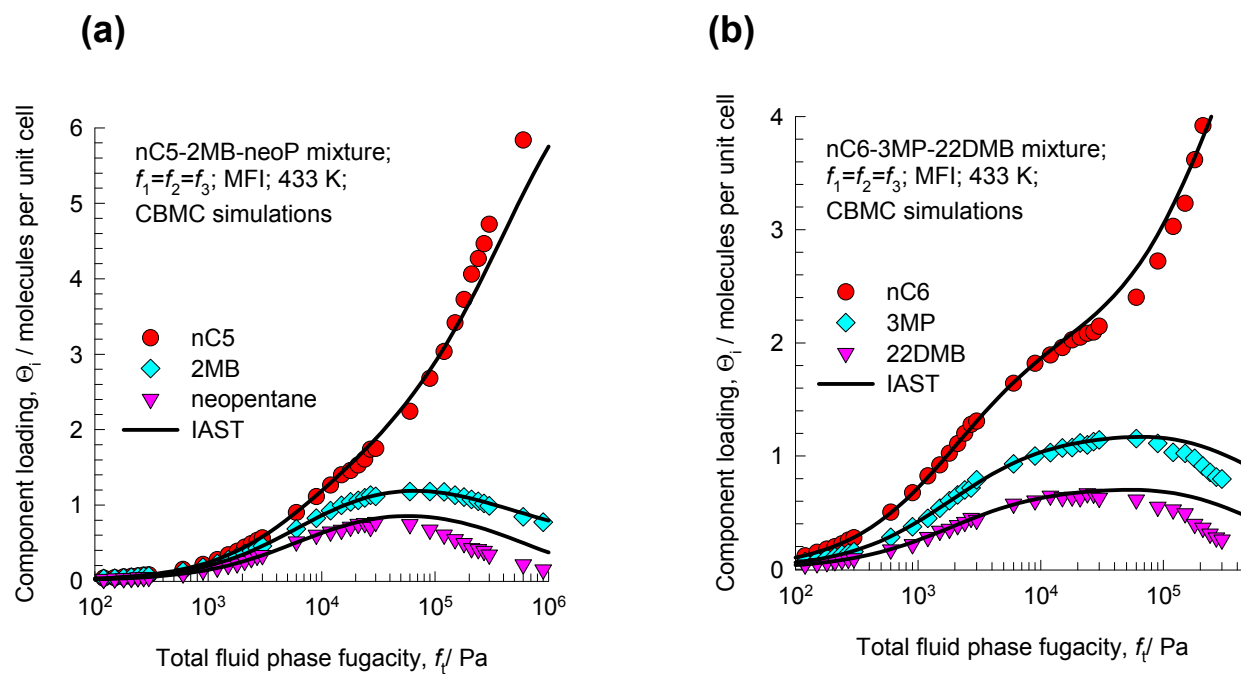
(a)



(b)



CBMC mixture vs IAST



CBMC for alkane mixtures in MFI

Figure 112

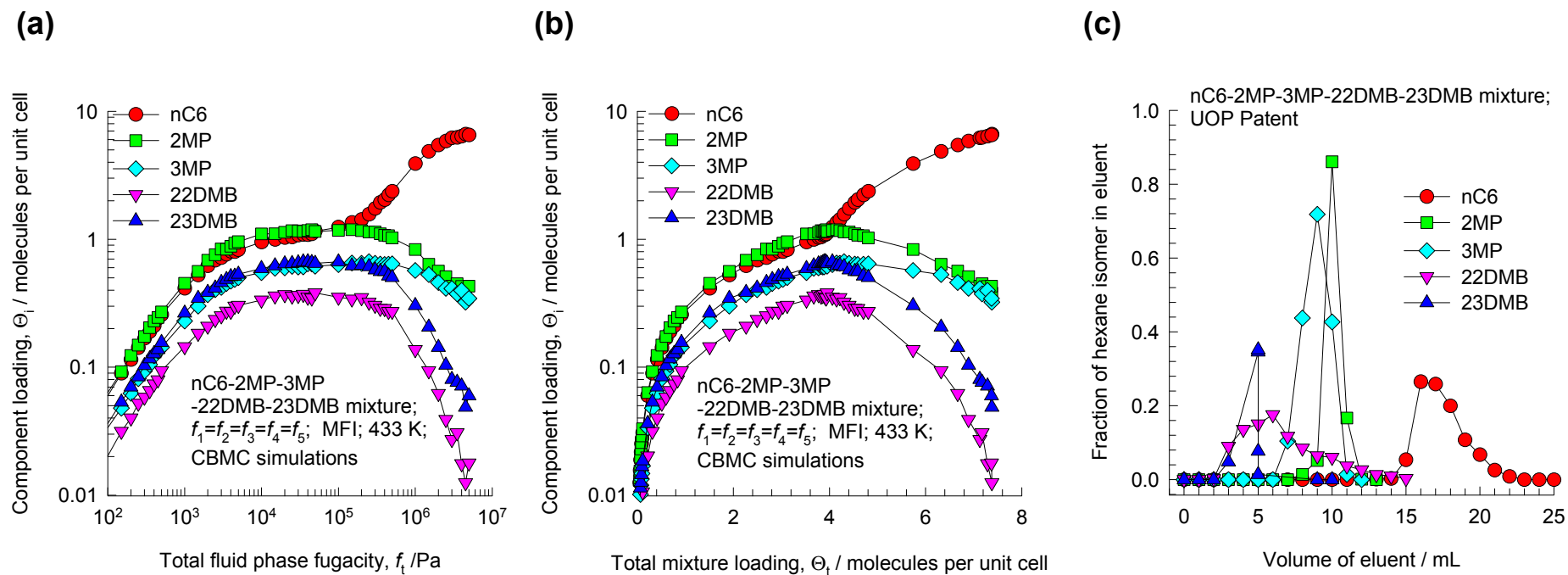
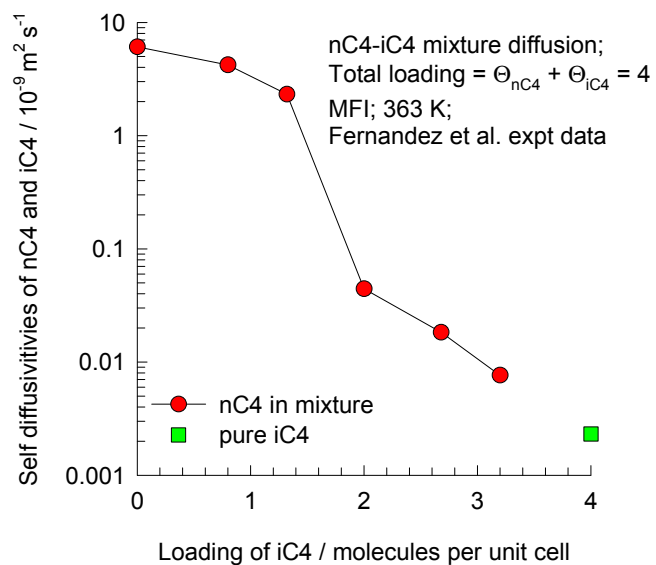


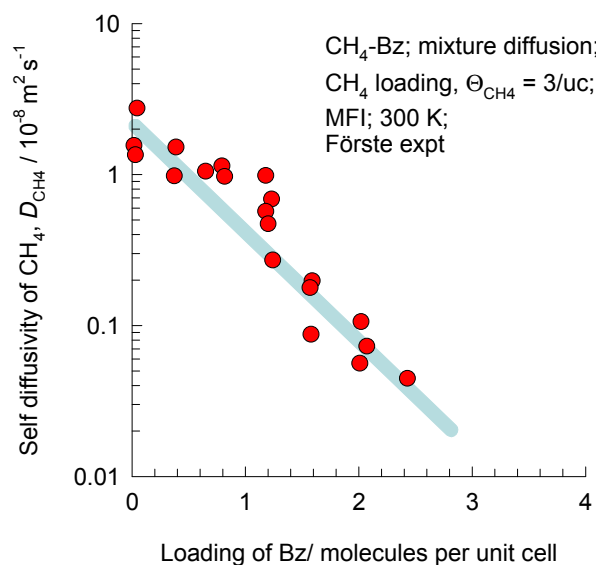
Figure 113

Traffic junction effects in MFI

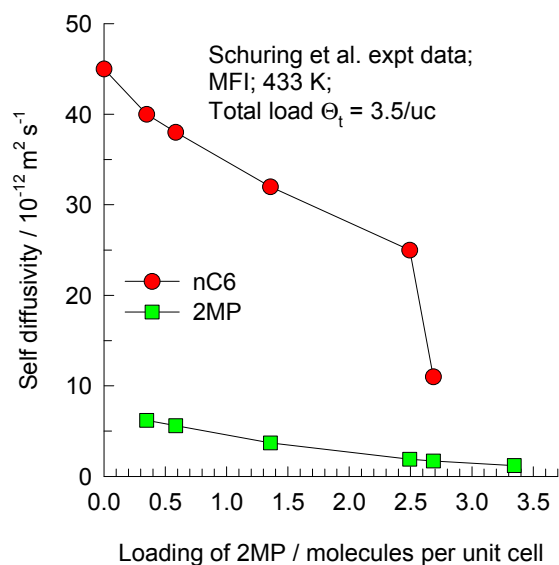
(a)



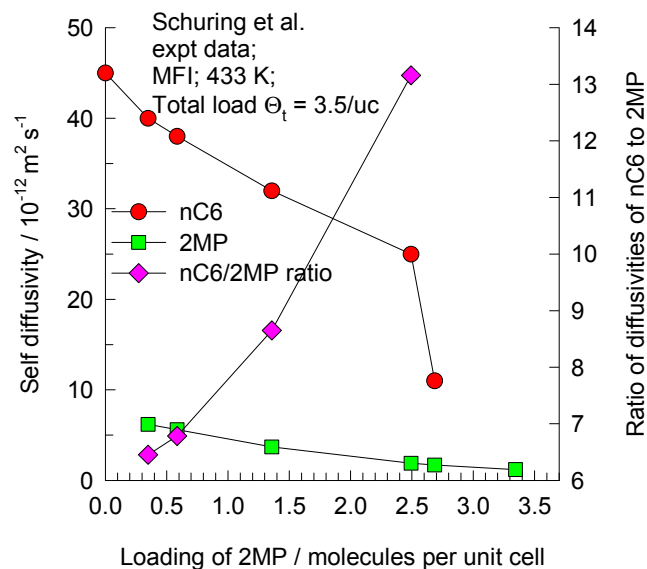
(b)



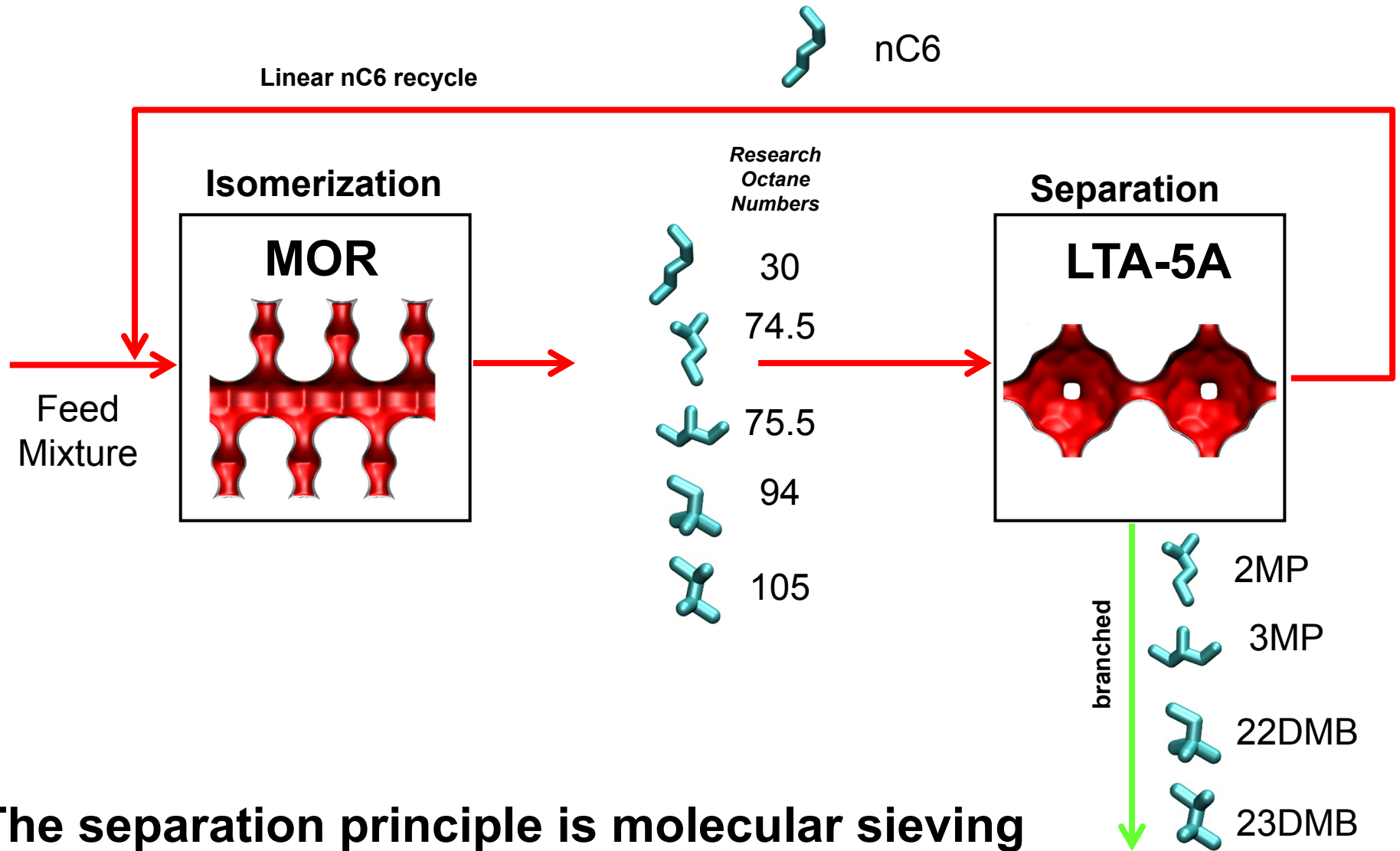
(c)



(d)

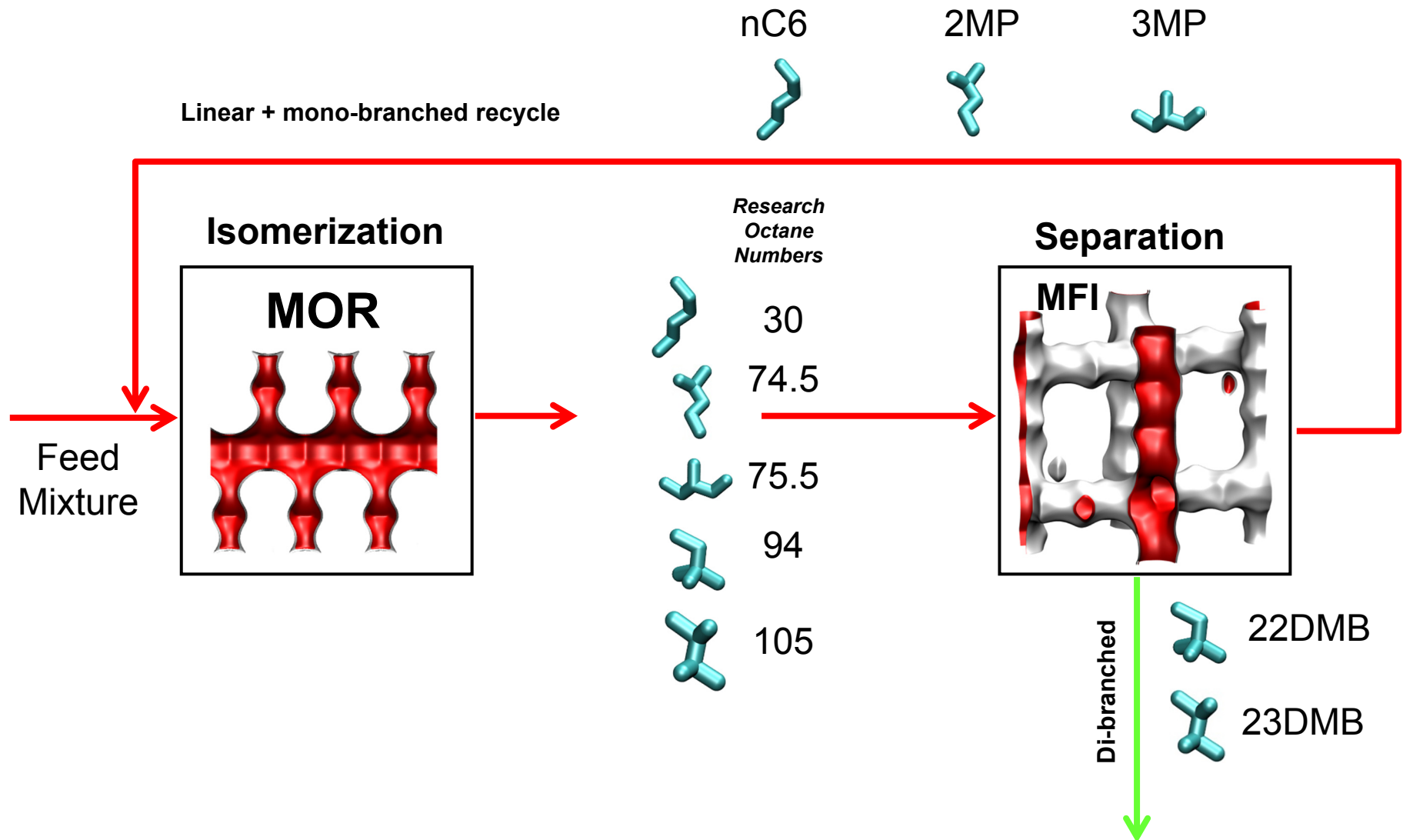


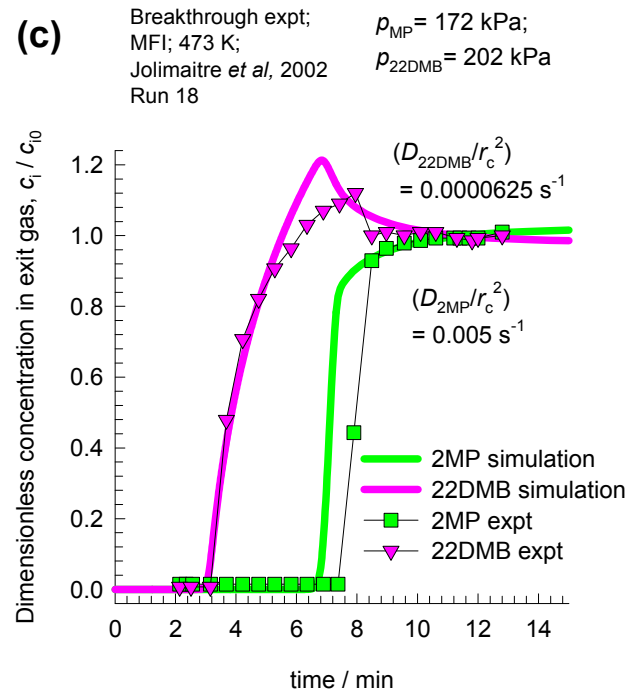
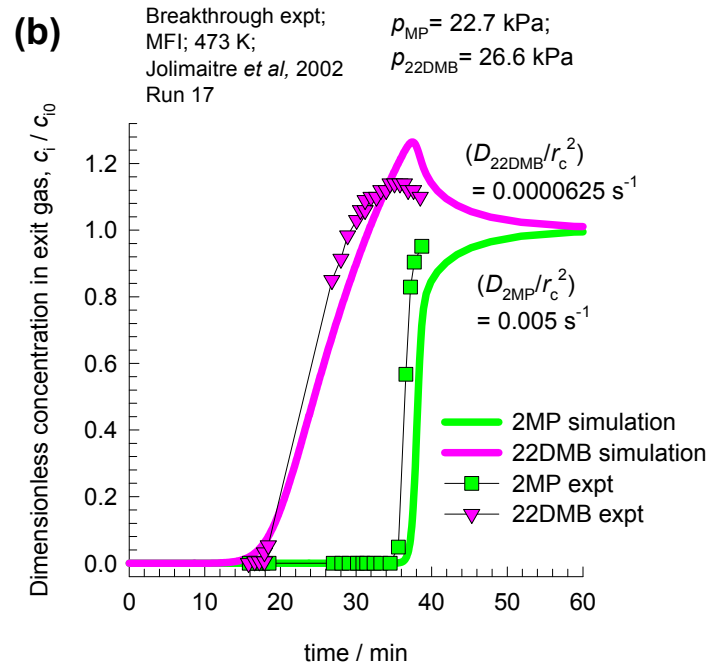
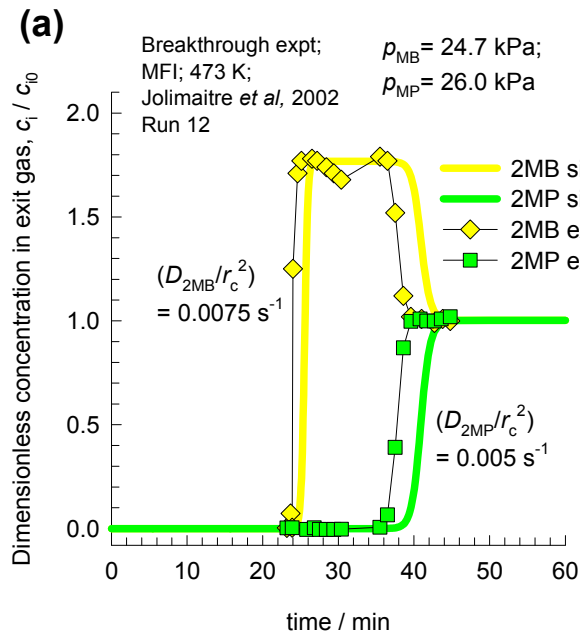
Conventional hexane isomerization process

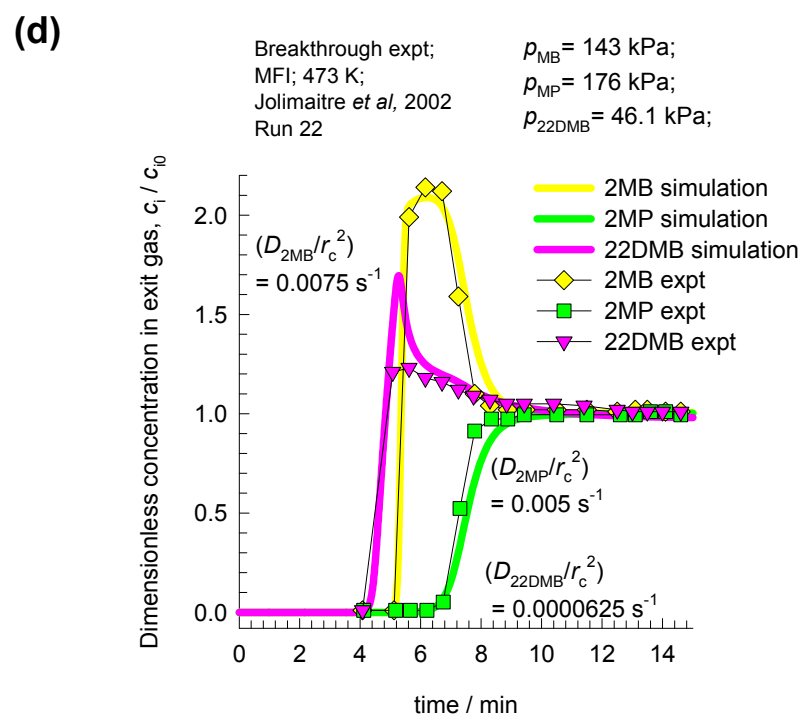
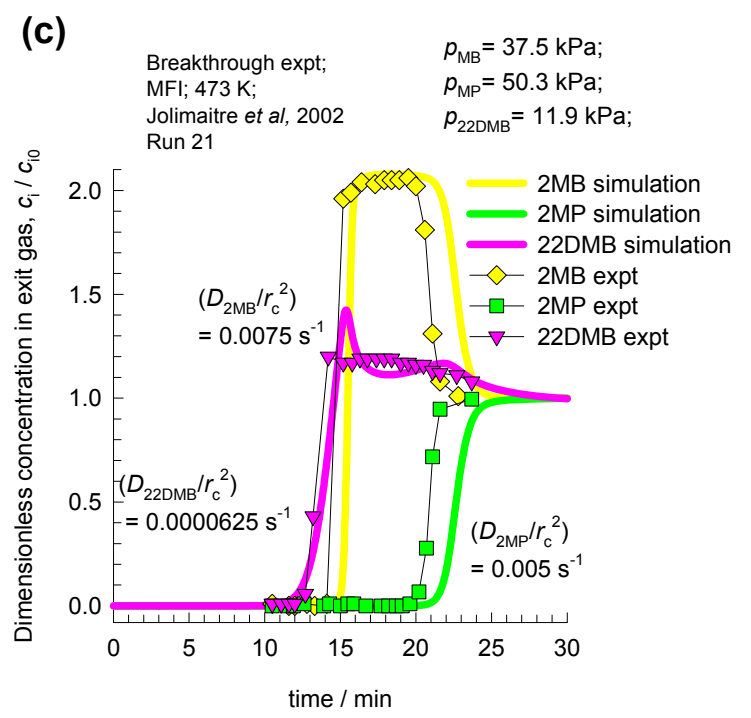
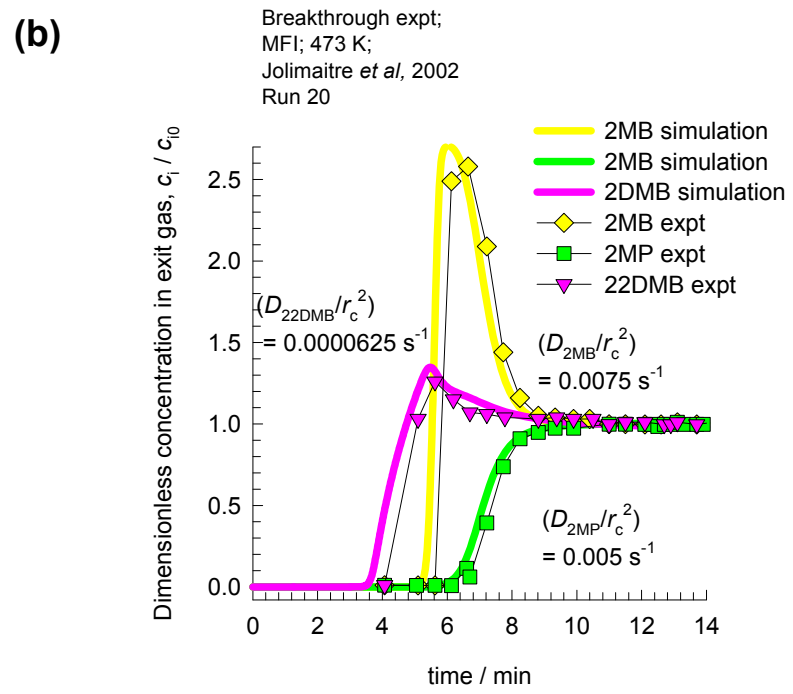
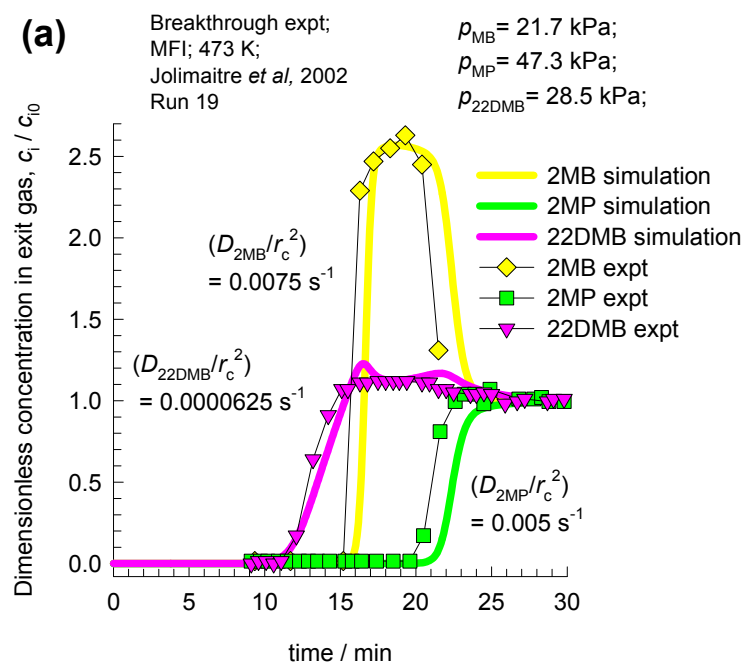


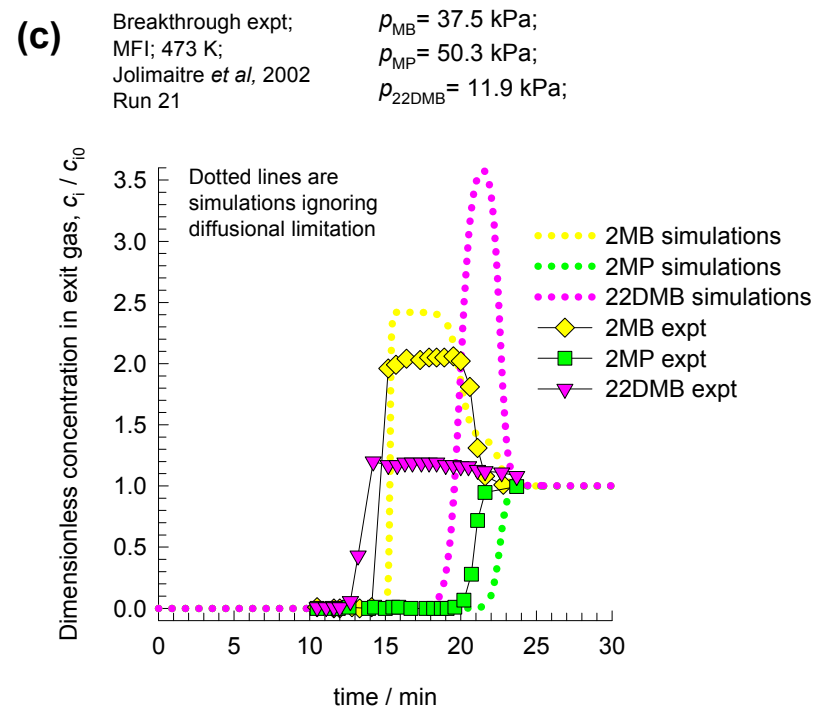
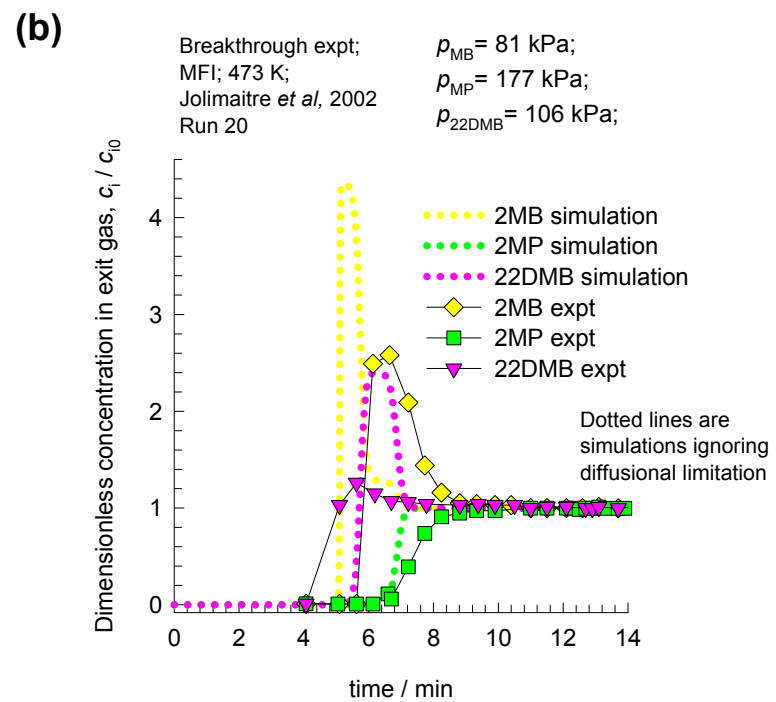
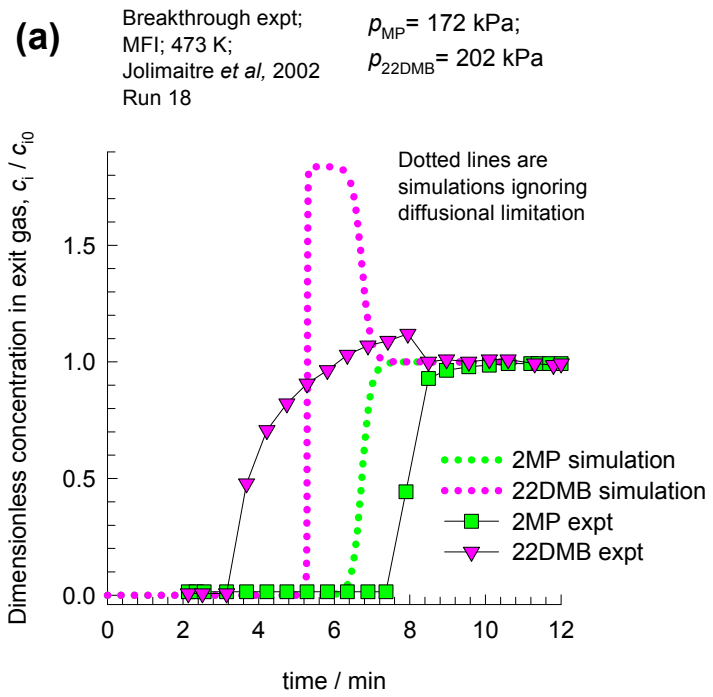
The separation principle is molecular sieving

Improved hexane isomerization process

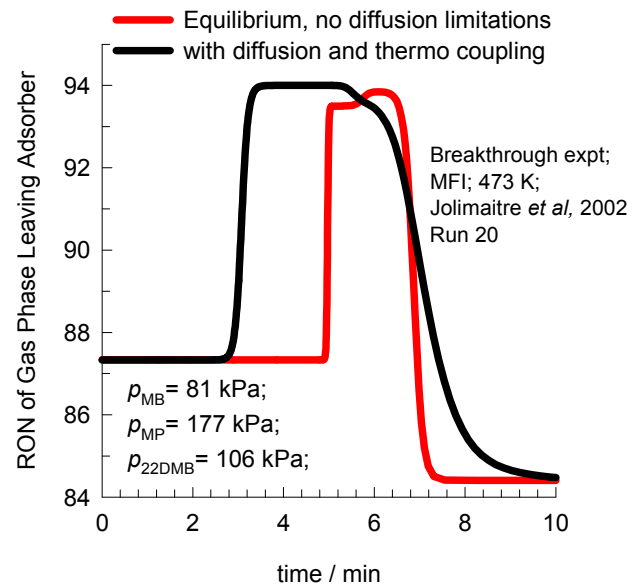








Influence of diffusion on Product RON ^{Figure 119}



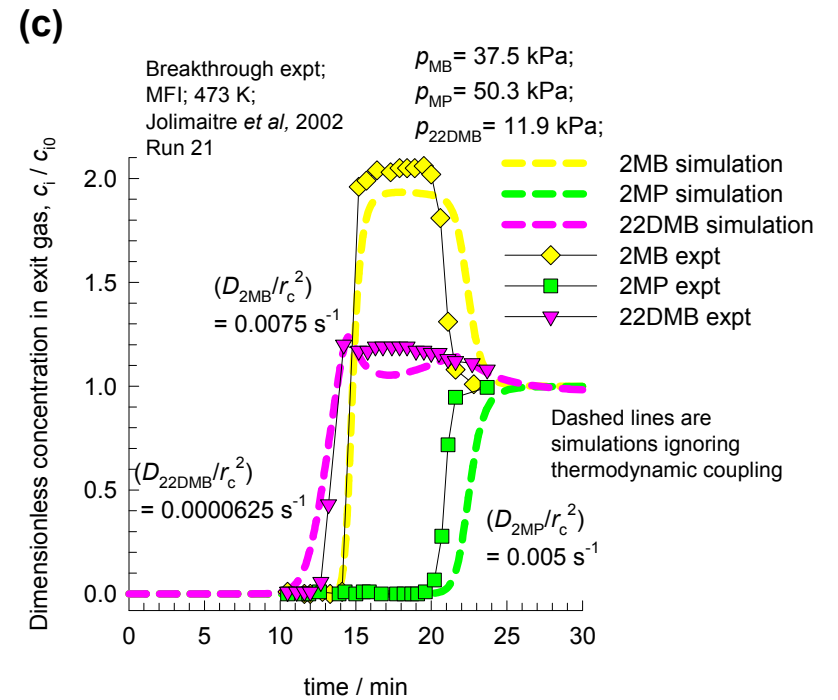
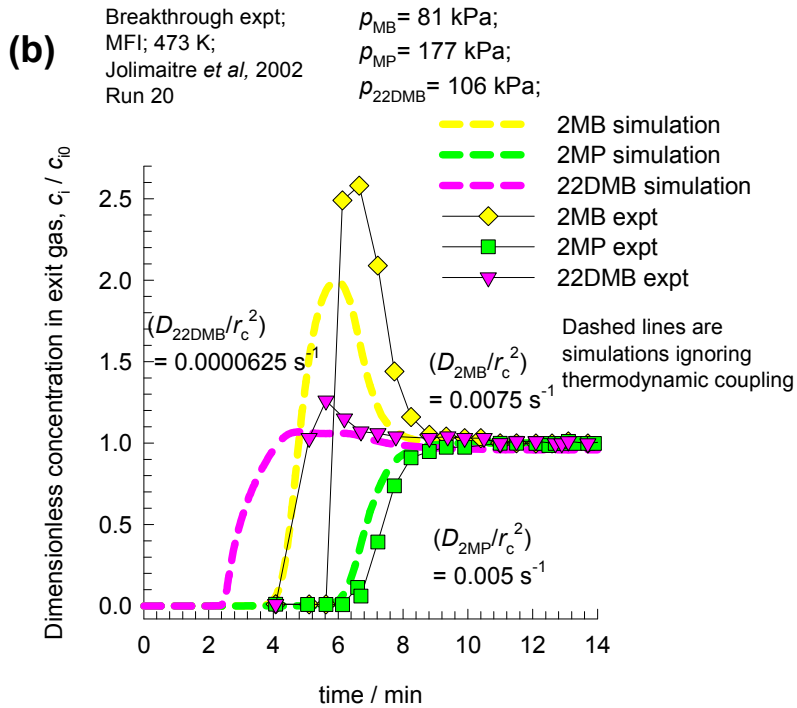
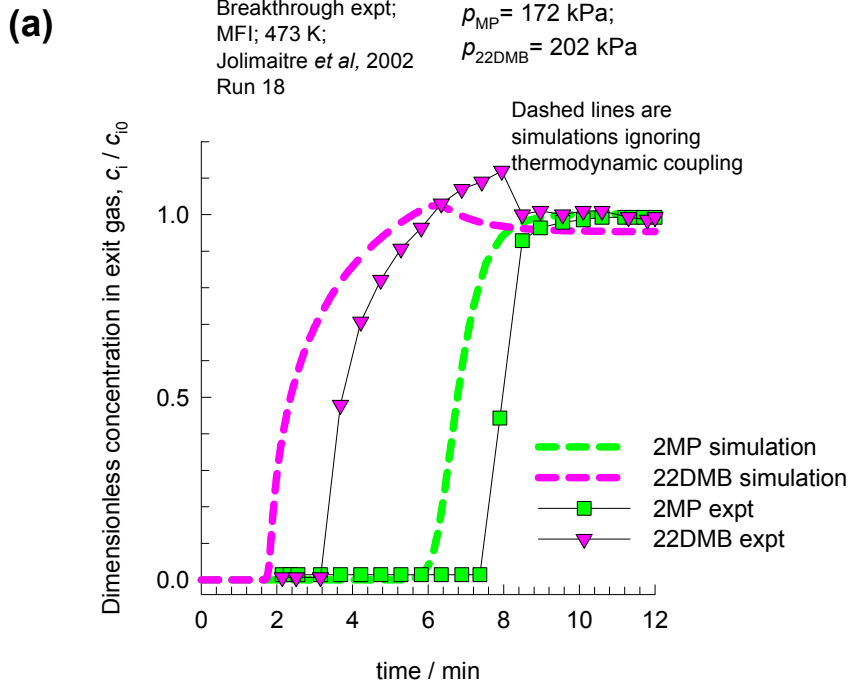
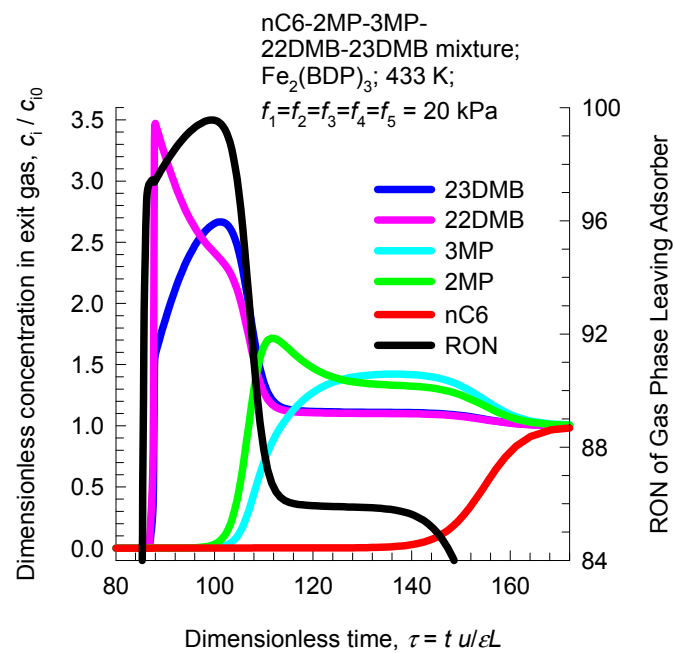
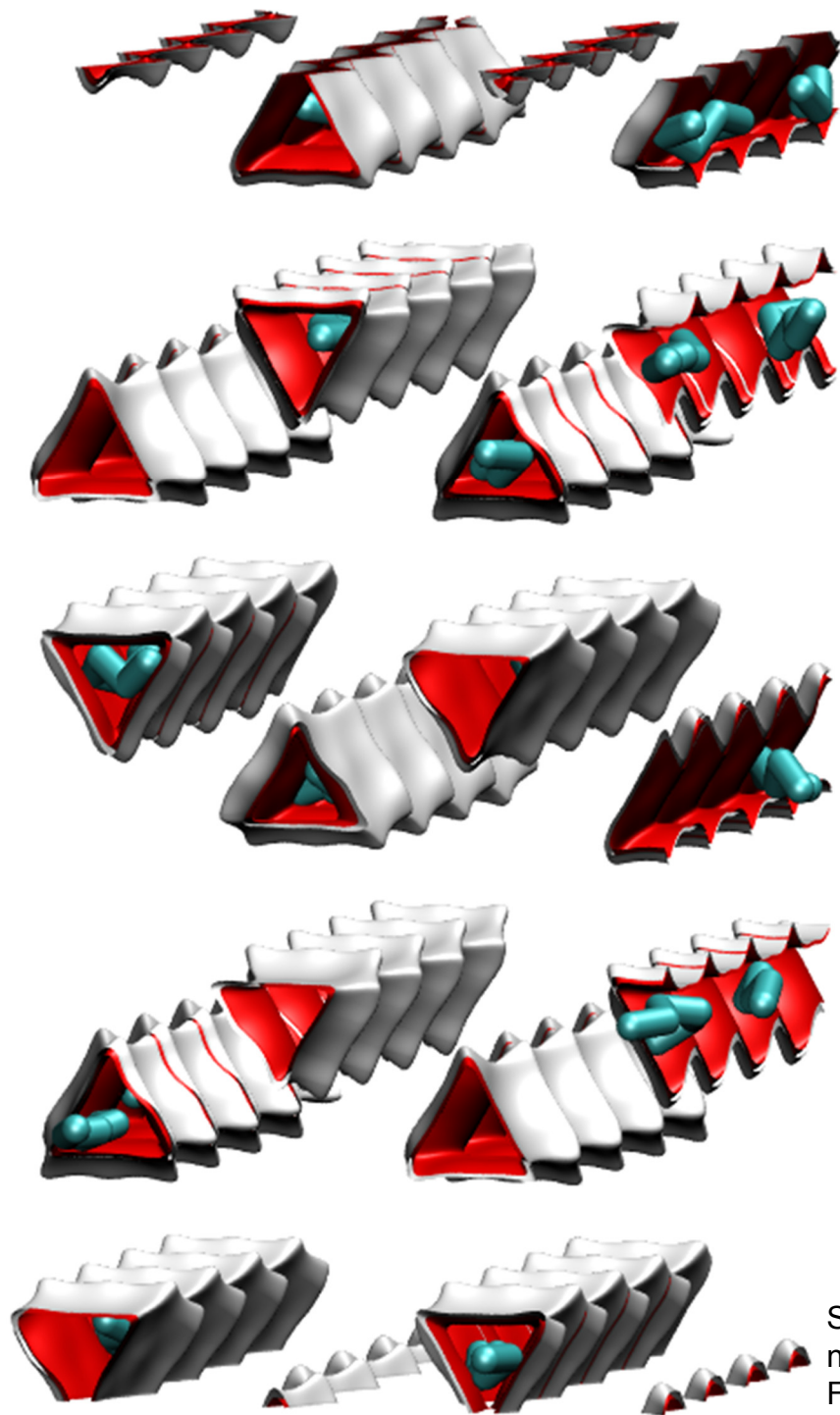
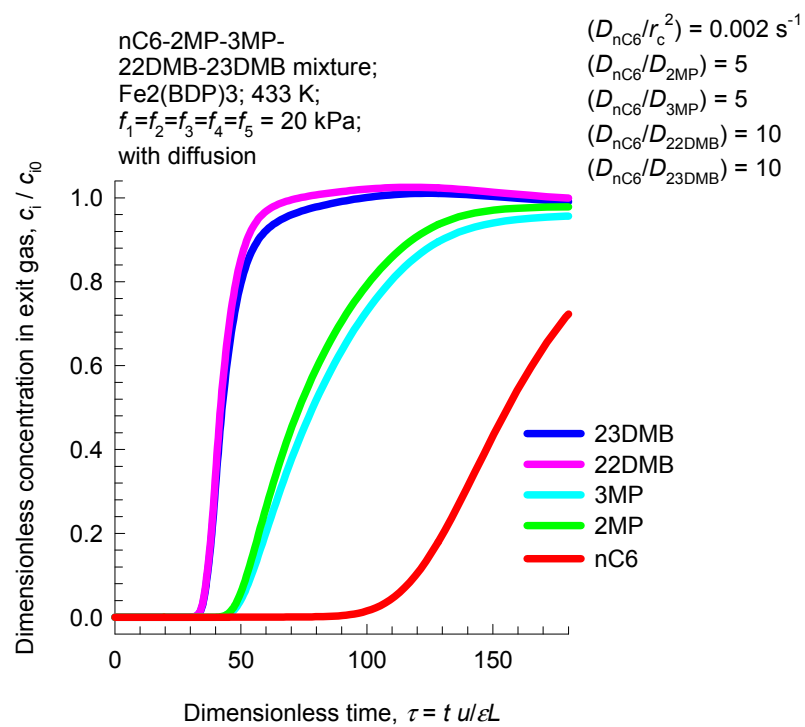
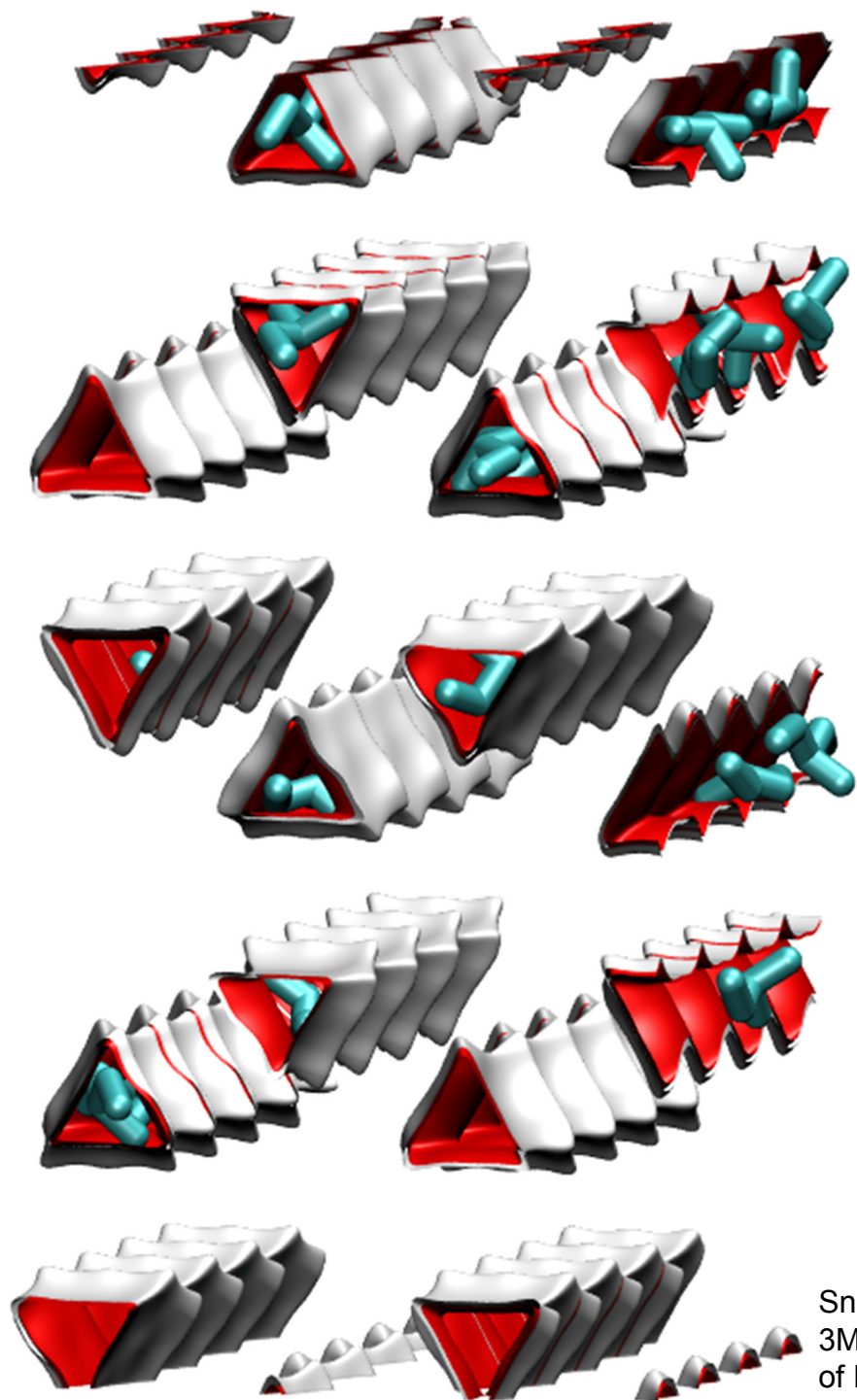


Figure 121



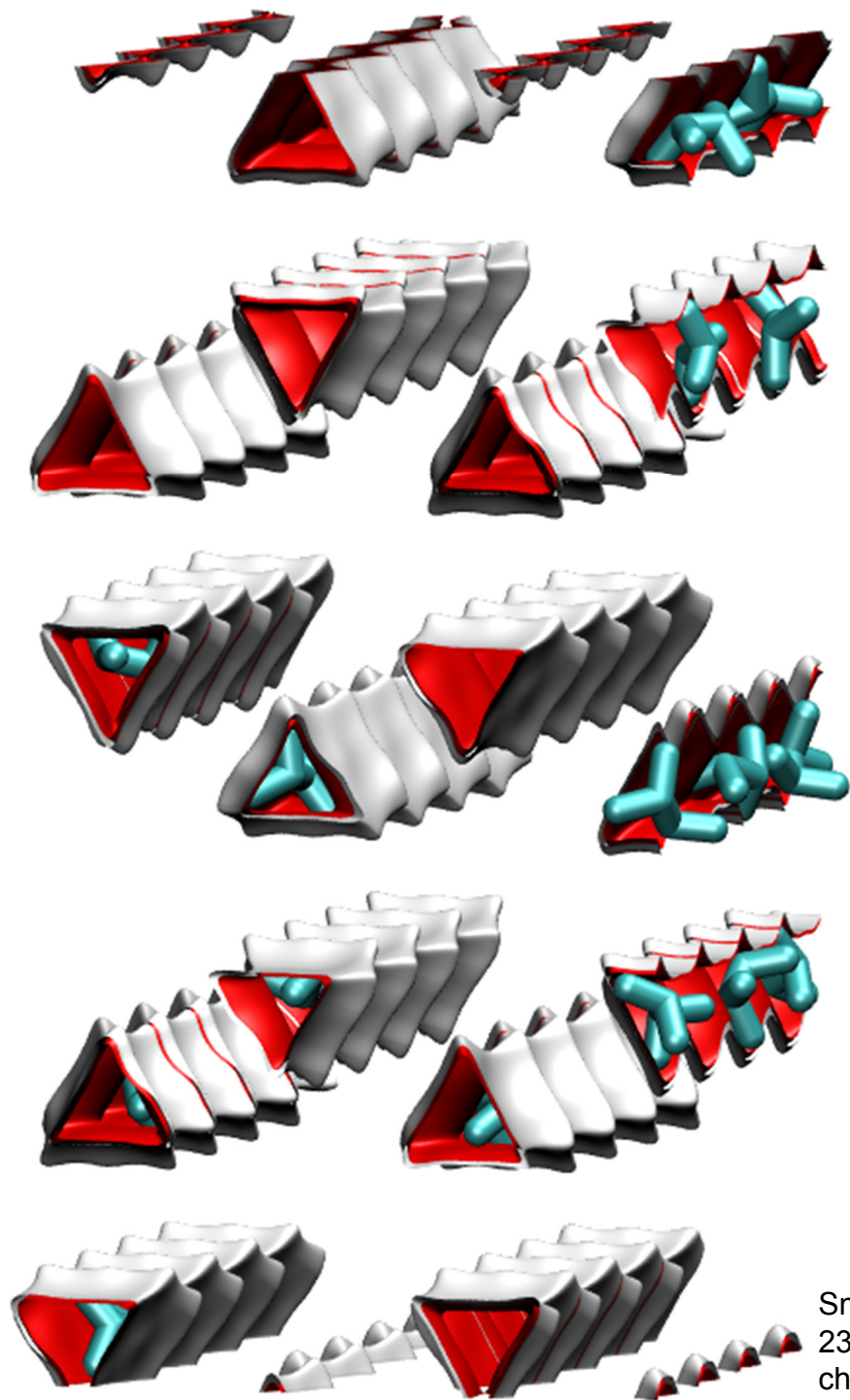
Snapshots showing the location of nC6 within the triangular channels of $\text{Fe}_2(\text{BDP})_3$.

Figure 122

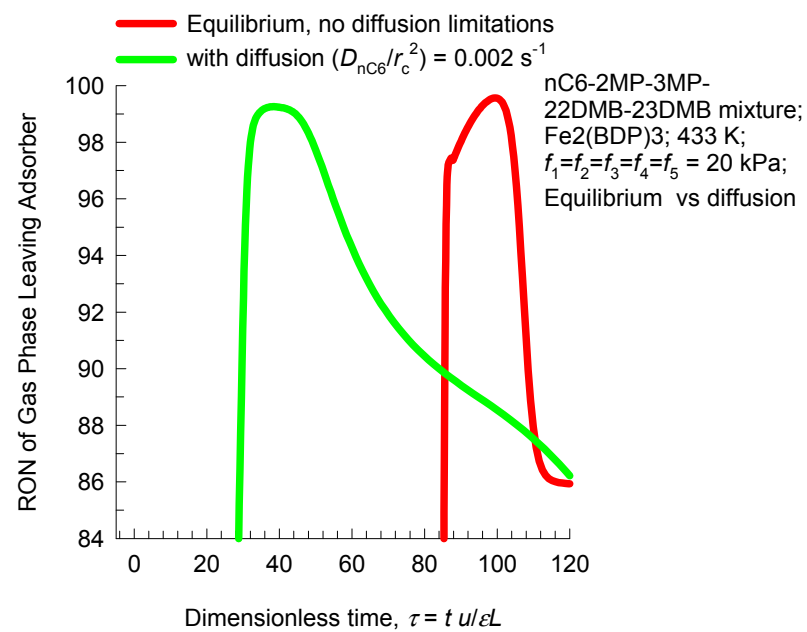


Snapshots showing the location of 3MP within the triangular channels of Fe₂(BDP)₃.

Figure 123

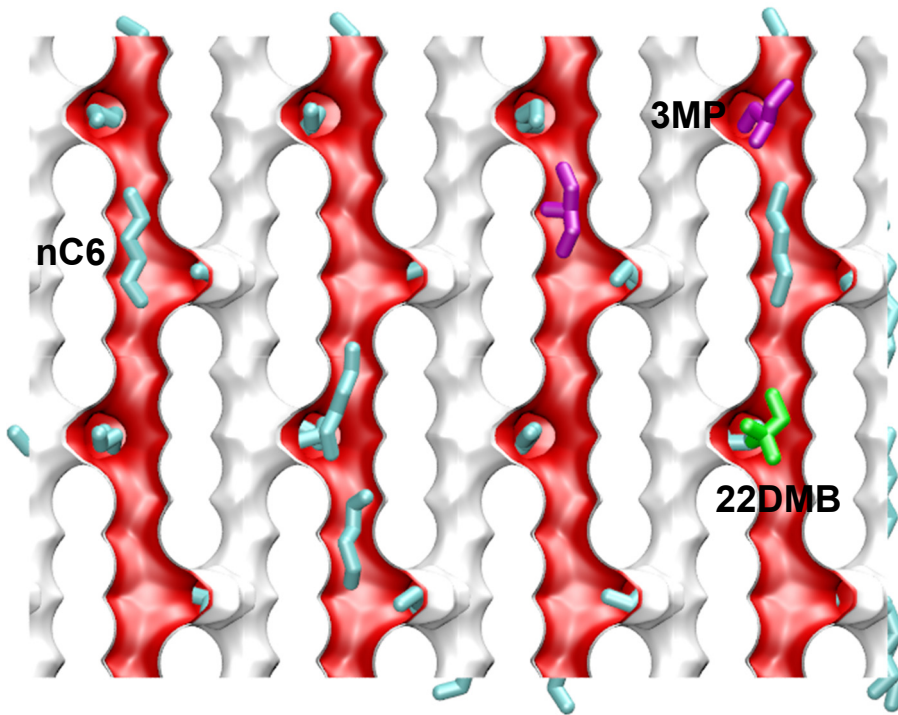


Snapshots showing the location of 23DMB within the triangular channels of $\text{Fe}_2(\text{BDP})_3$.

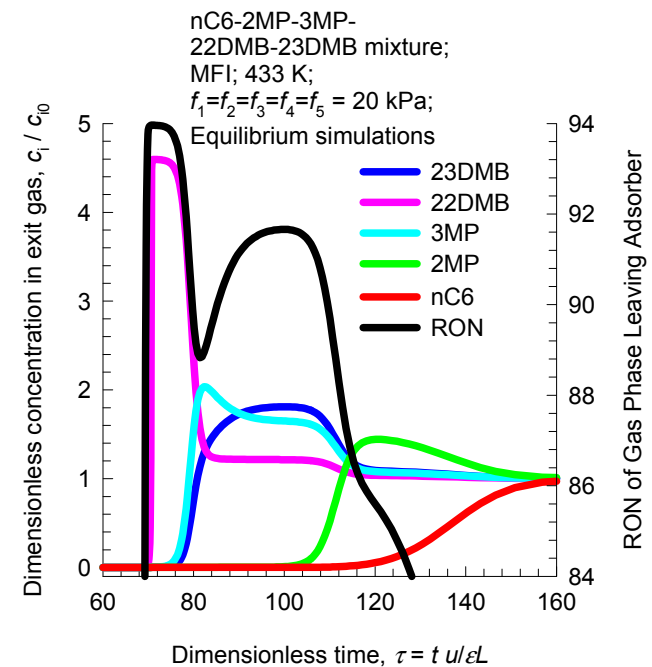


Hexane isomers breakthrough in MFI

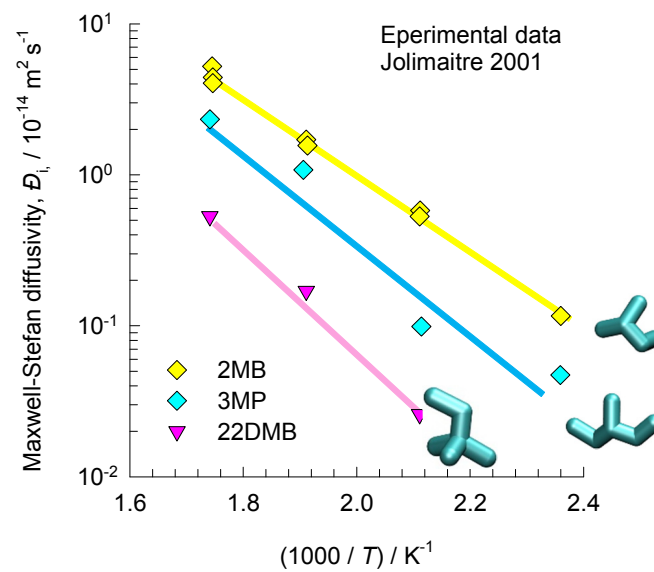
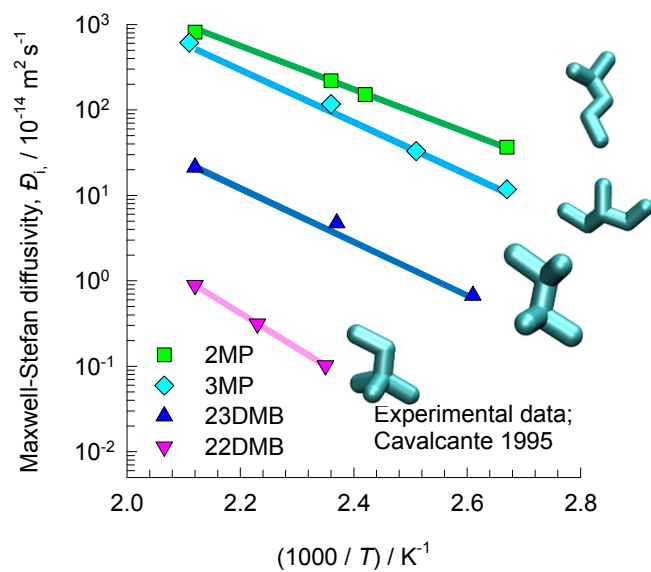
Figure 124



Snapshots showing the location of nC6, 3MP, and 22DMB within the intersecting channels of MFI.

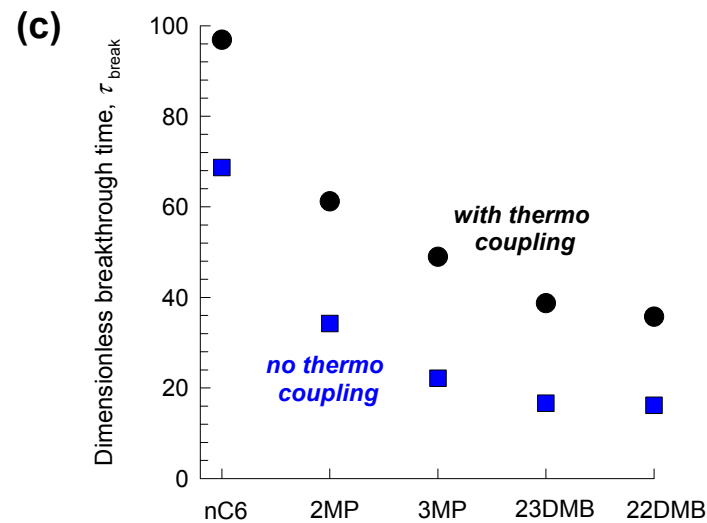
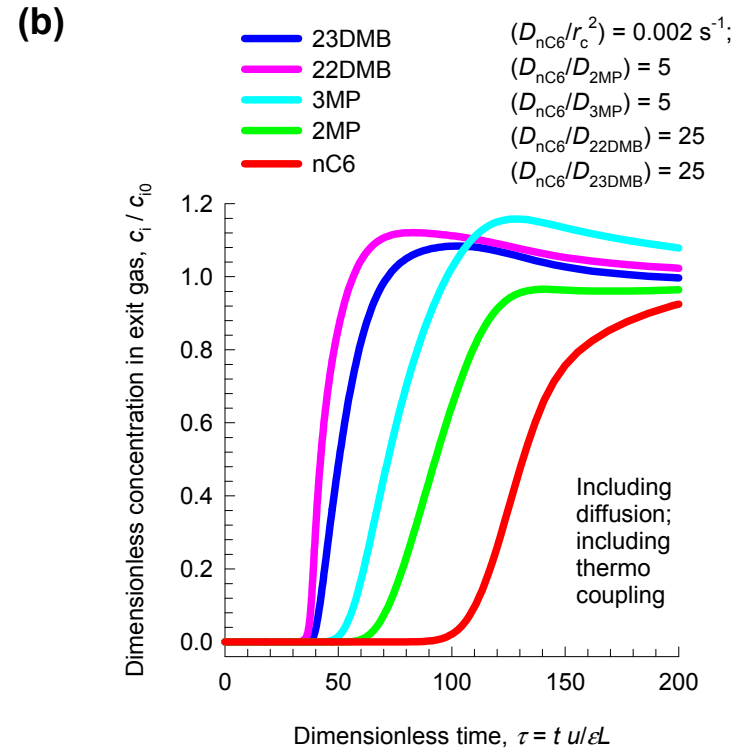
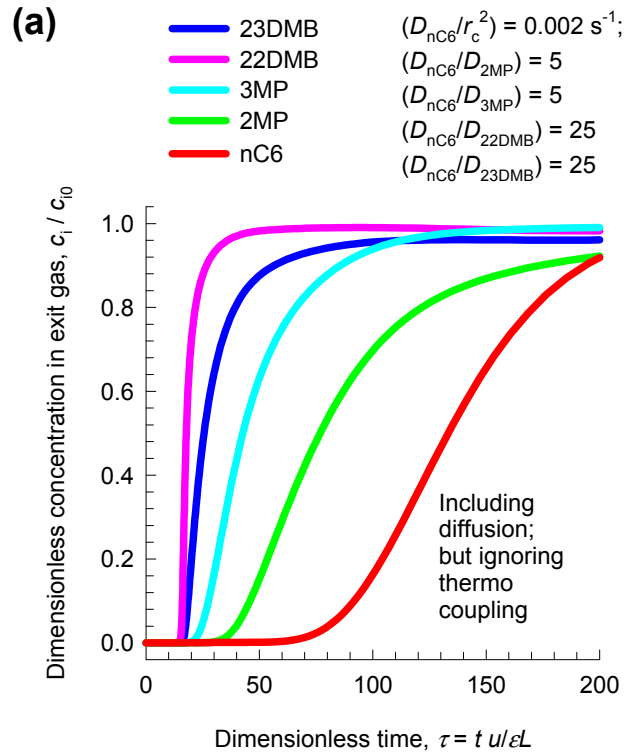


Diffusivities of alkanes in MFI

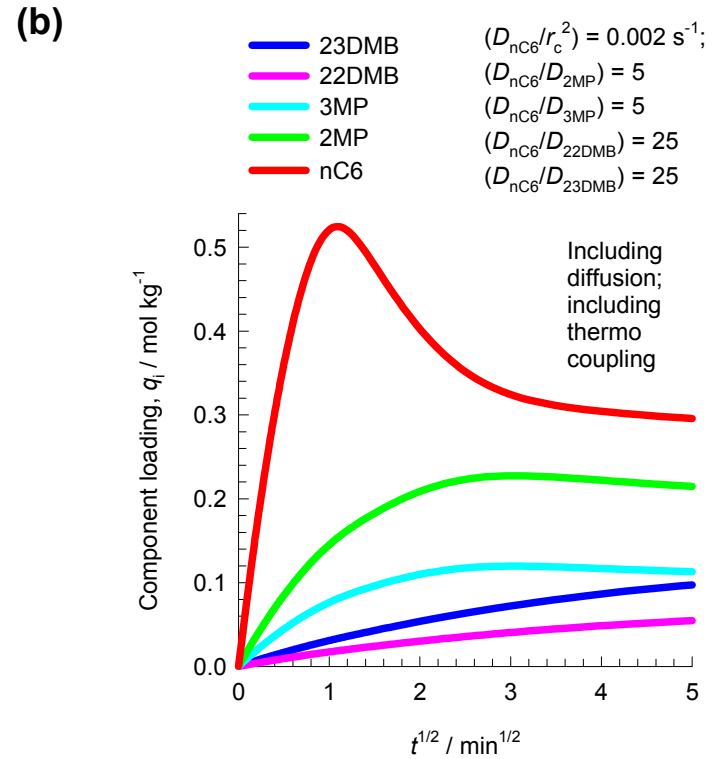
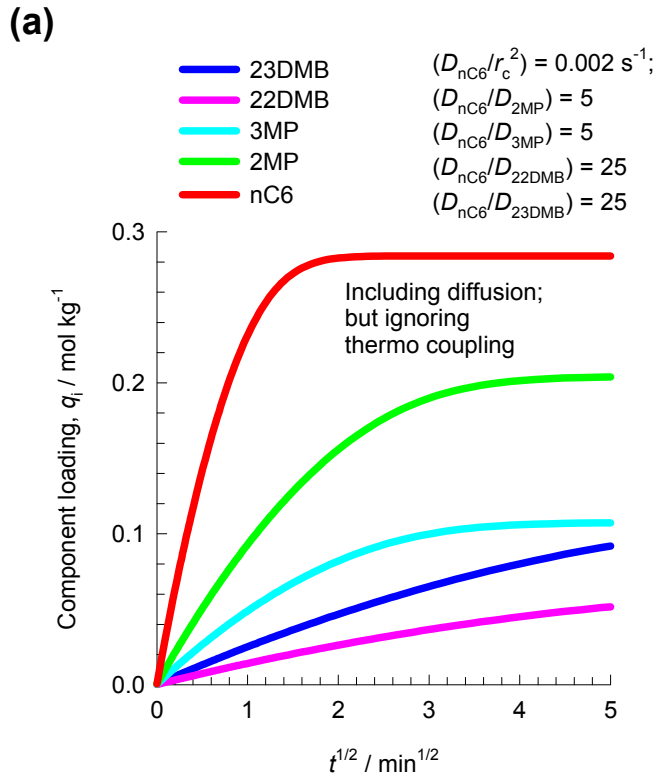


Hexane isomers breakthrough in MFI

Figure 126

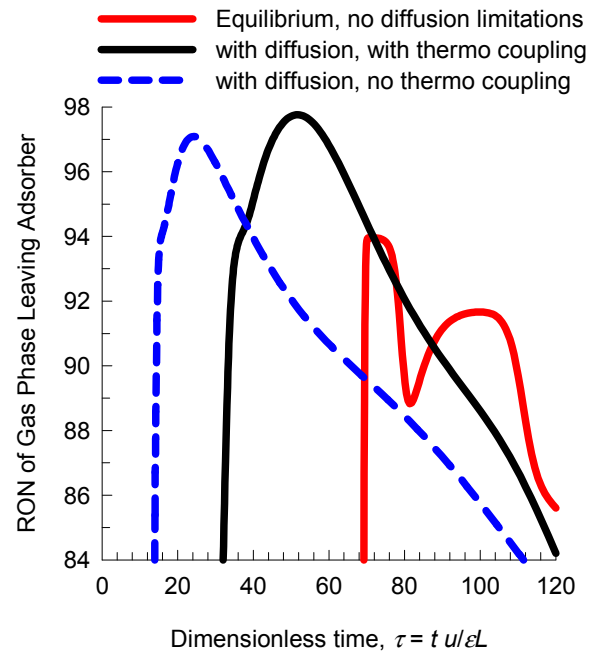


Transient uptake of hexane isomers in MFI crystal

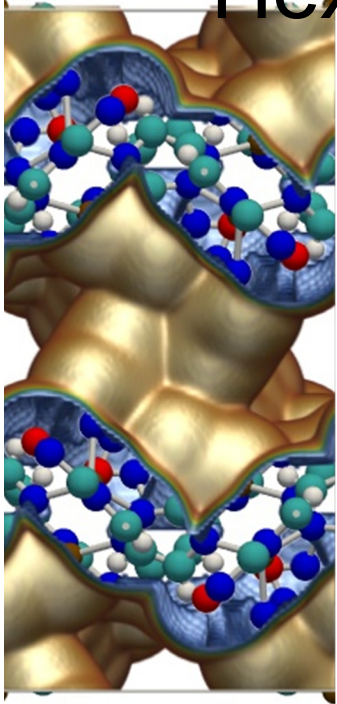


Product RON from MFI adsorber

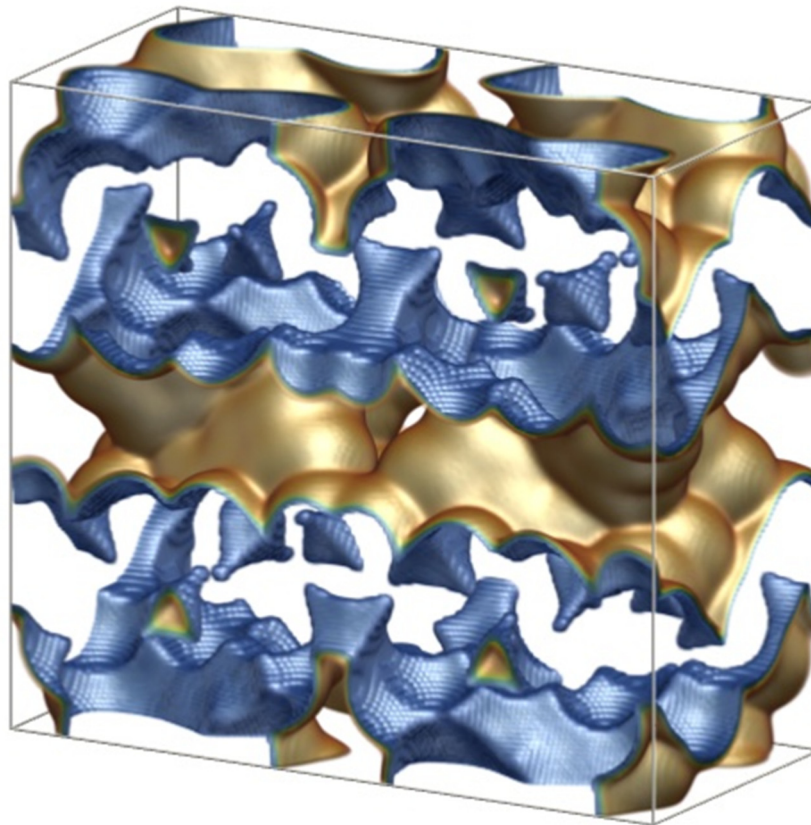
Figure 128



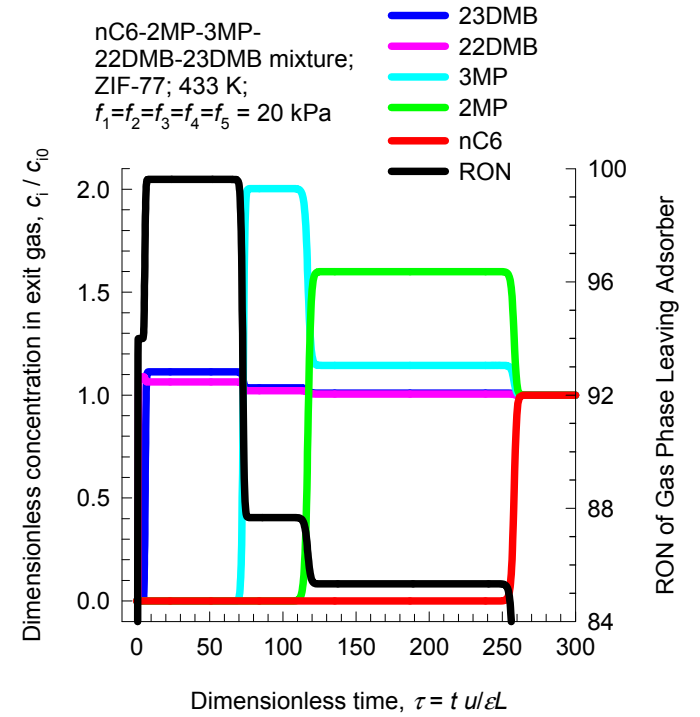
Hexane isomers breakthrough in ZIF-77



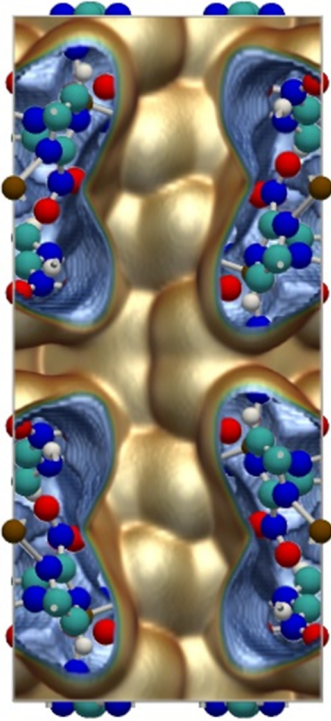
Pore landscape of ZIF-77



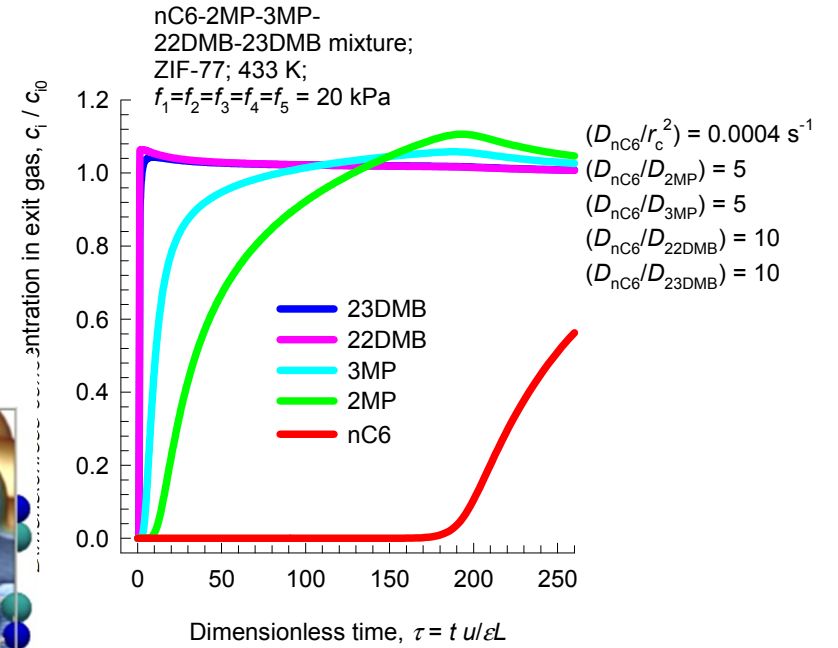
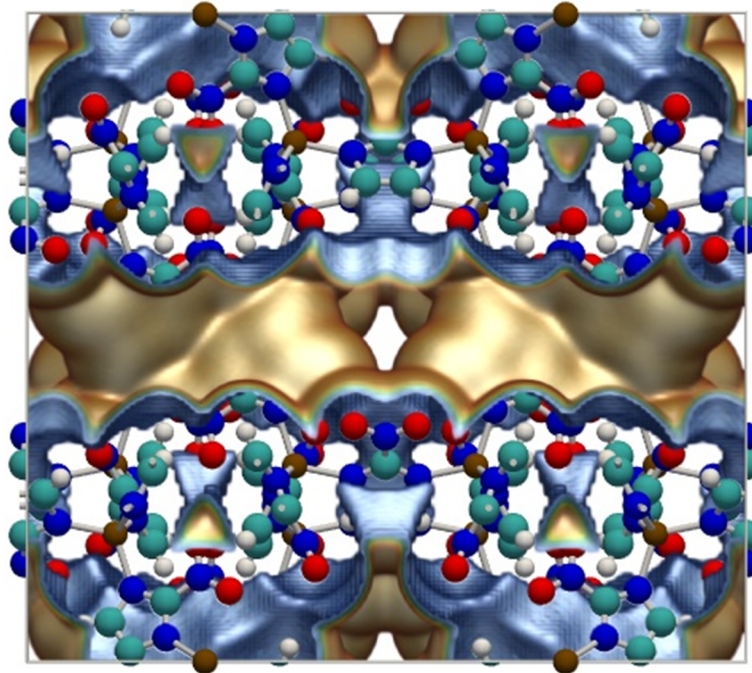
Equilibrium breakthrough simulations



Hexane isomers breakthrough in ZIF-77

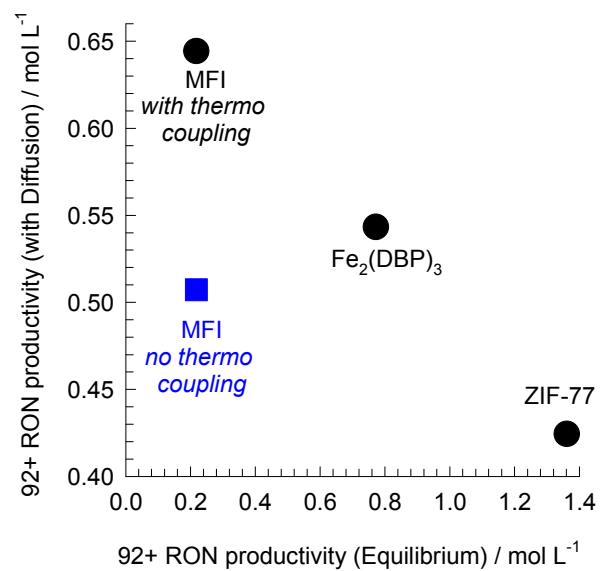


Pore landscape of ZIF-77

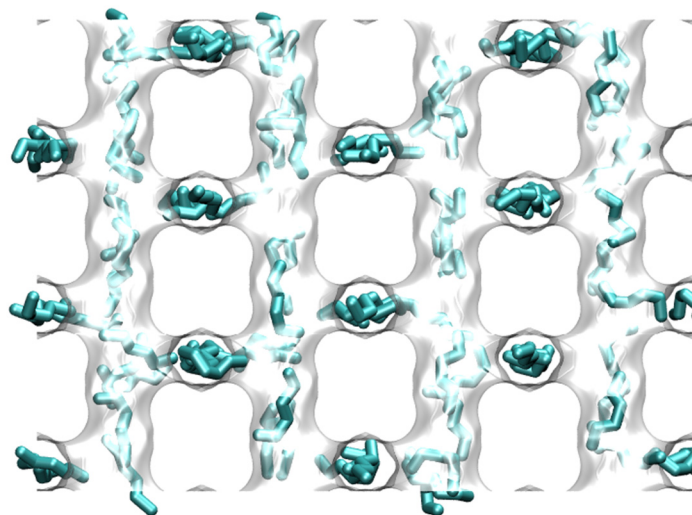
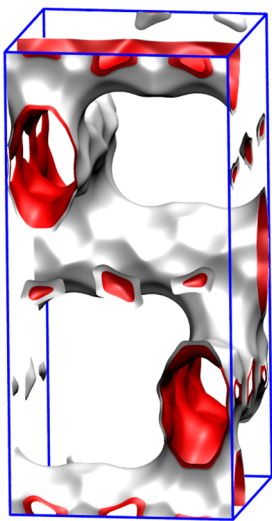


Compare 92+ RON productivities

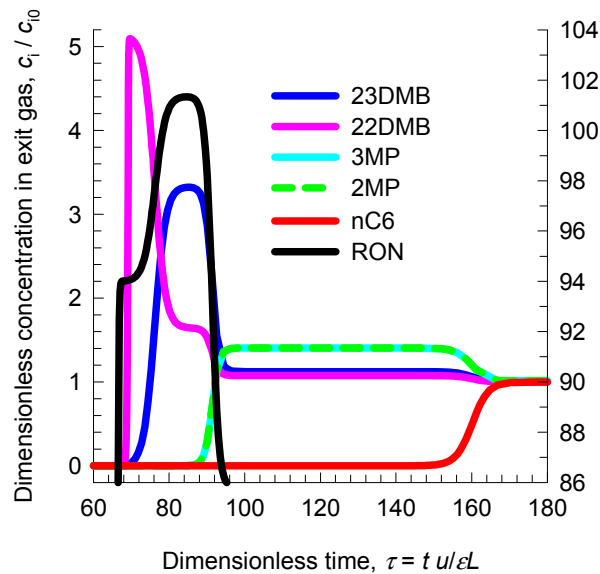
Figure 131



Breakthrough simulations for BEA



Equilibrium breakthrough simulations



Breakthroughs with diffusional limitations

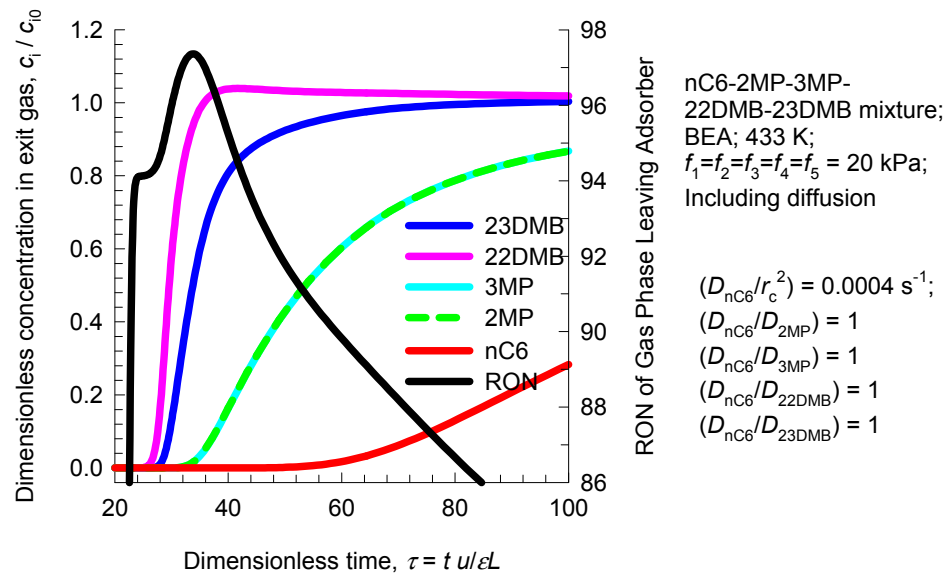
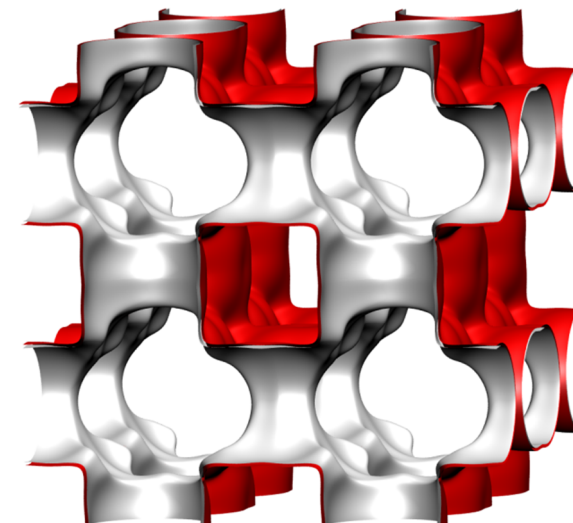
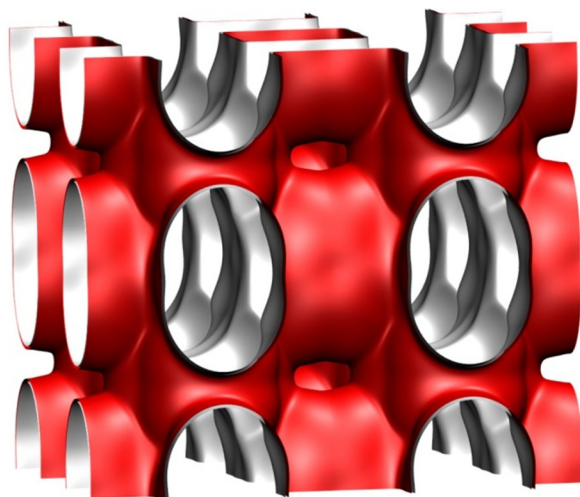
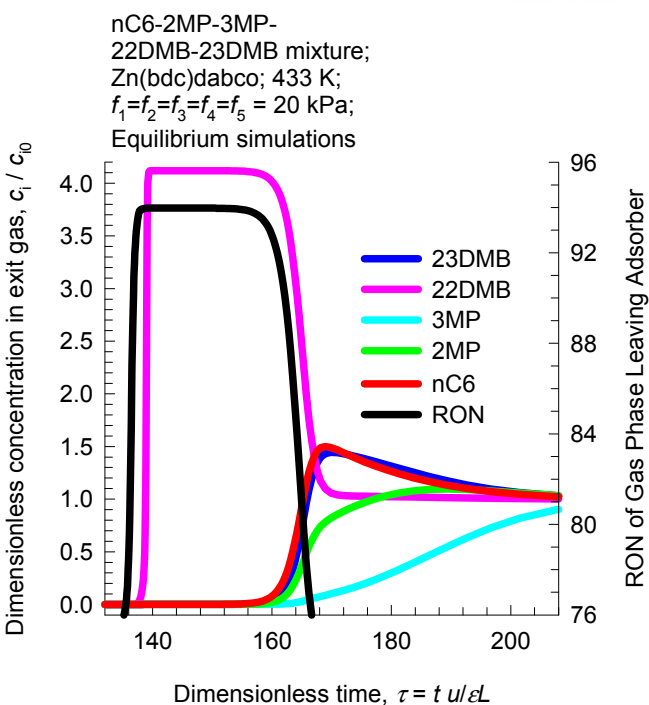


Figure 133

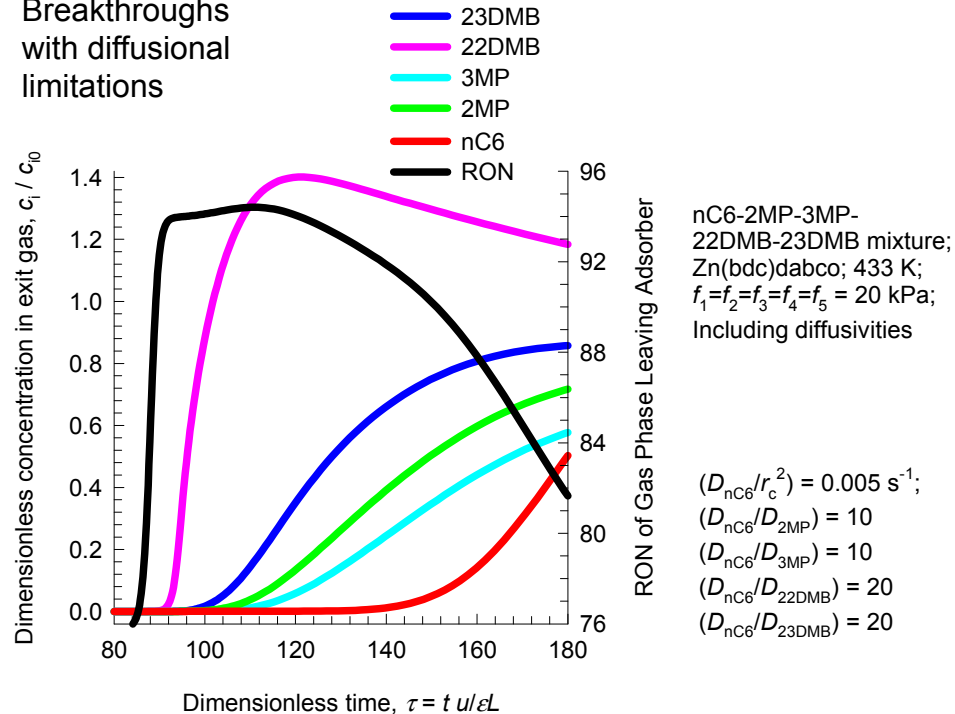
Breakthrough simulations for Zn(bdc)dabco



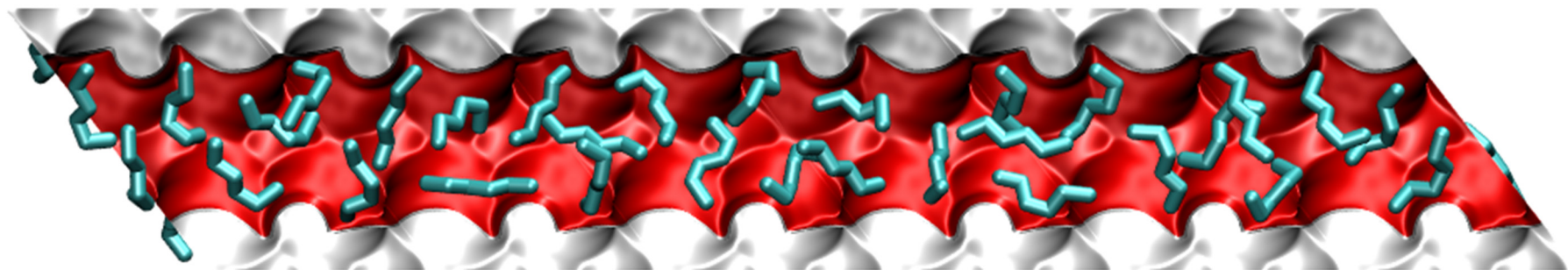
Equilibrium breakthrough simulations



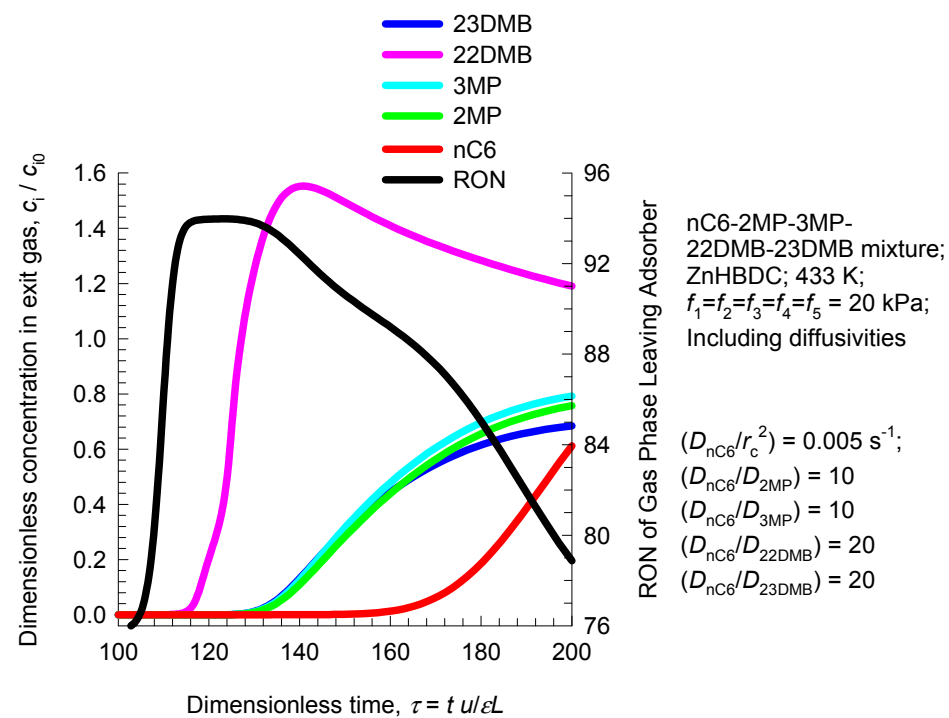
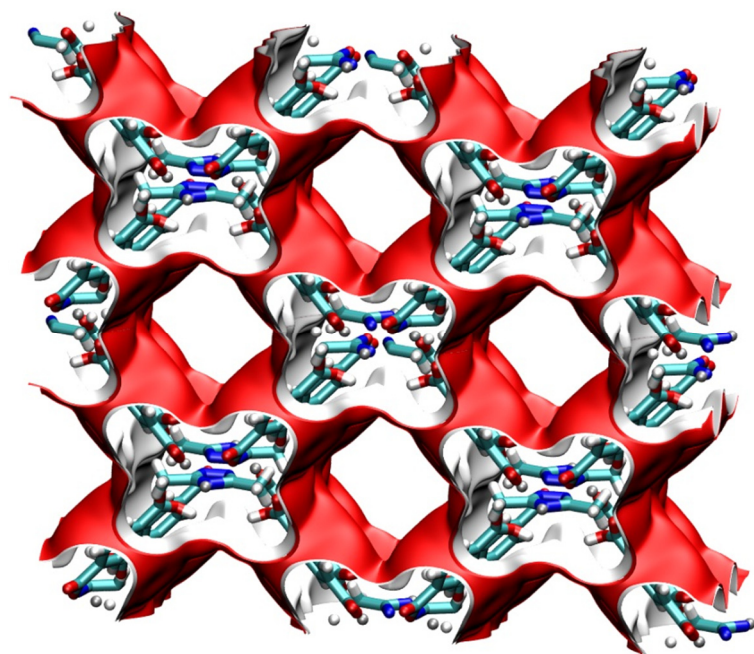
Breakthroughs with diffusional limitations



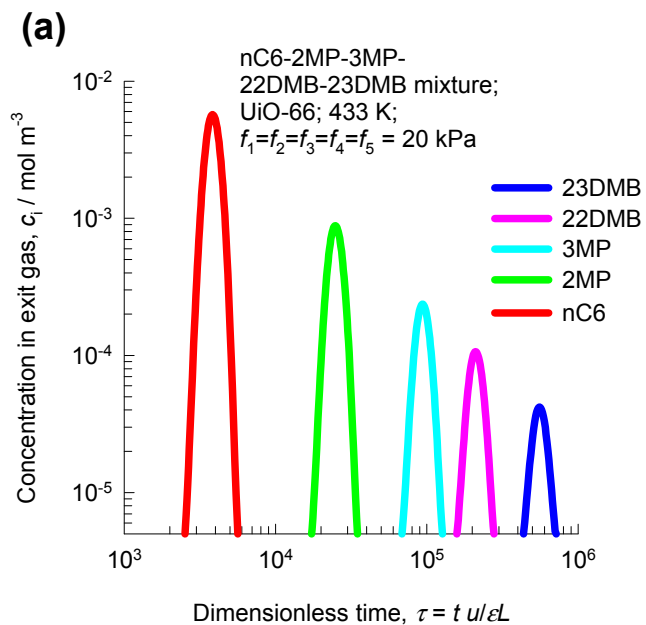
Breakthrough simulations for ZnHBDC



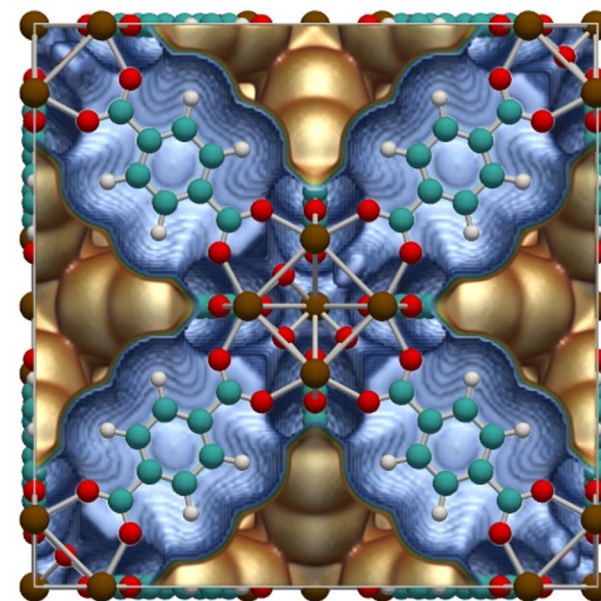
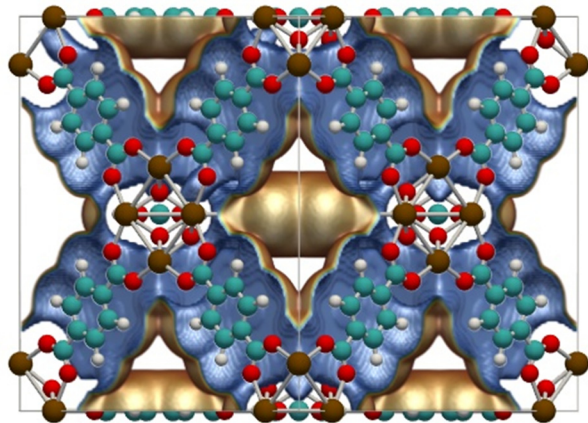
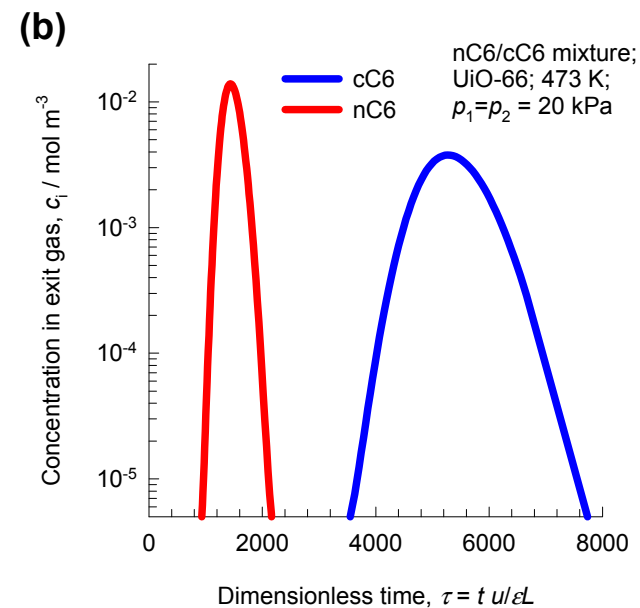
Breakthroughs with diffusional limitations



Pulse chromatographic simulations for UiO-66

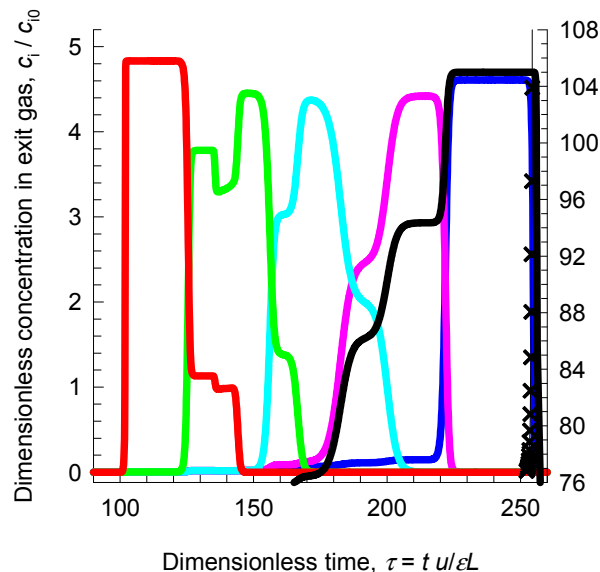


Pulse chromatographic simulations assuming thermodynamic equilibrium

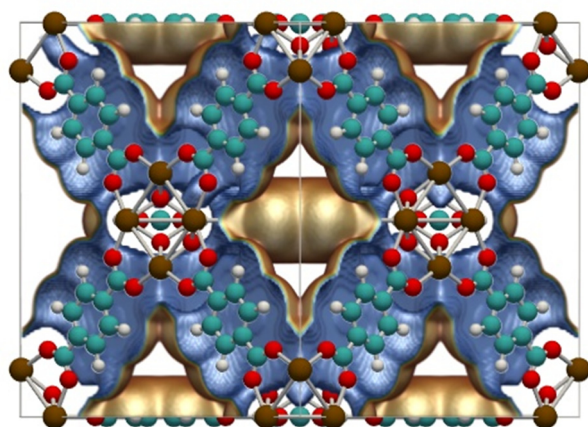
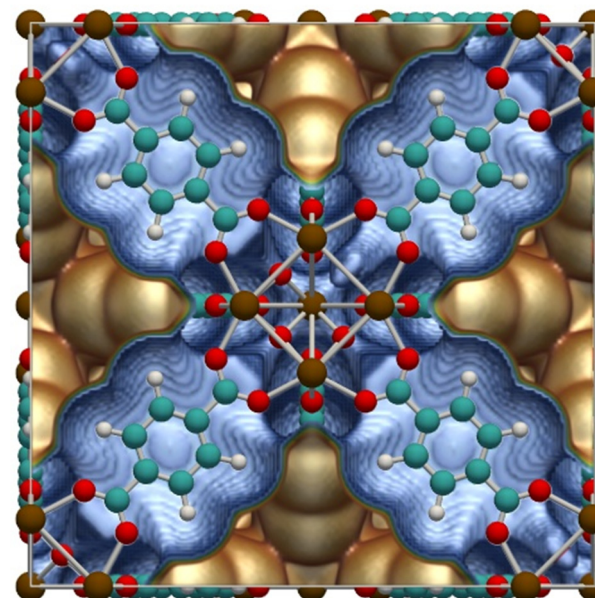


Adsorption/desorption cycles for UiO-66

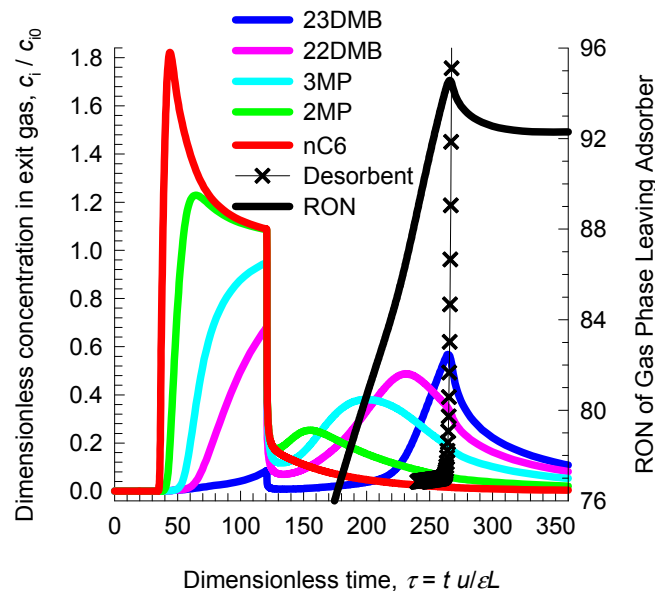
Equilibrium breakthrough simulations



nC6-2MP-3MP-
22DMB-23DMB mixture;
UiO-66; 433 K;
 $f_1=f_2=f_3=f_4=f_5 = 20$ kPa;
Input Desorbent at
 $\tau = 120$;
Equilibrium simulations



Breakthroughs
with diffusional
limitations



nC6-2MP-3MP-
22DMB-23DMB mixture;
UiO-66; 433 K;
 $f_1=f_2=f_3=f_4=f_5 = 20$ kPa;
Input Desorbent at
 $\tau = 120$;
Including diffusion

$$(D_{nC6}/r_c^2) = 0.0004 \text{ s}^{-1};$$

$$(D_{nC6}/D_{2MP}) = 2$$

$$(D_{nC6}/D_{3MP}) = 2$$

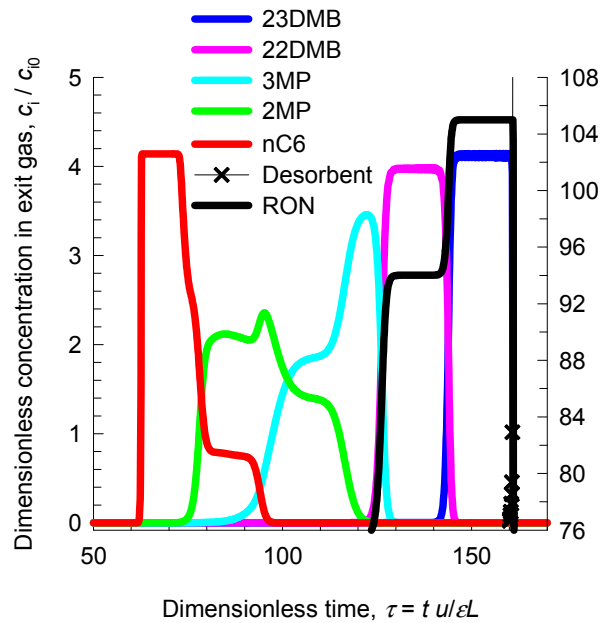
$$(D_{nC6}/D_{22DMB}) = 2$$

$$(D_{nC6}/D_{23DMB}) = 2$$

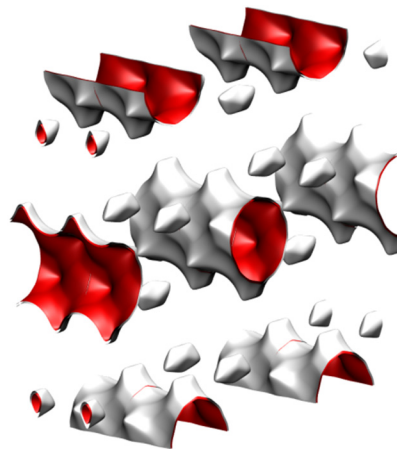
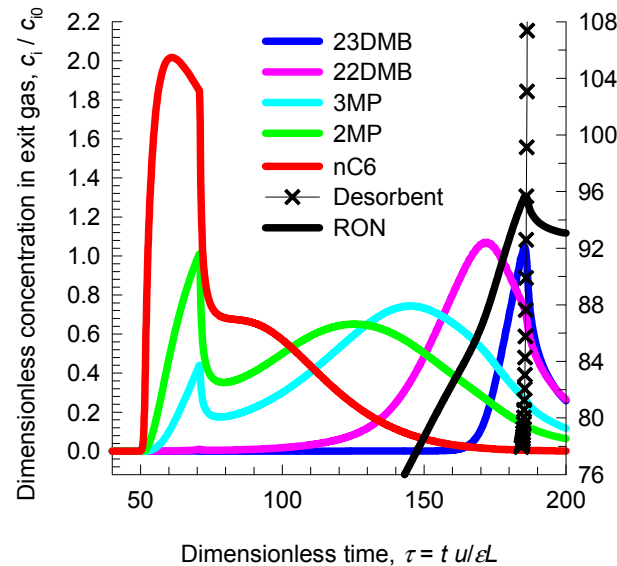
Adsorption/desorption cycles for CFI

Figure 137

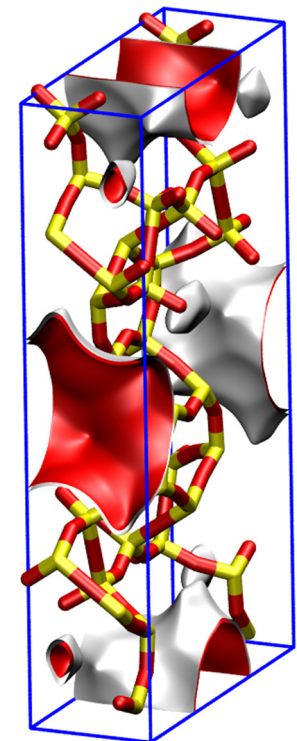
Equilibrium breakthrough simulations



Breakthroughs with diffusional limitations



Length entropy effects cause the reverse adsorption hierarchy



nC6-2MP-3MP-22DMB-23DMB mixture; CFI; 433 K; $f_1=f_2=f_3=f_4=f_5 = 20$ kPa; Input Desorbent at $\tau = 70$; Equilibrium simulations

nC6-2MP-3MP-22DMB-23DMB mixture; CFI; 433 K; $f_1=f_2=f_3=f_4=f_5 = 20$ kPa; Input Desorbent at $\tau = 70$; Including diffusion

$$(D_{nC6}/r_c^2) = 0.0025 \text{ s}^{-1};$$

$$(D_{nC6}/D_{2MP}) = 2$$

$$(D_{nC6}/D_{3MP}) = 2$$

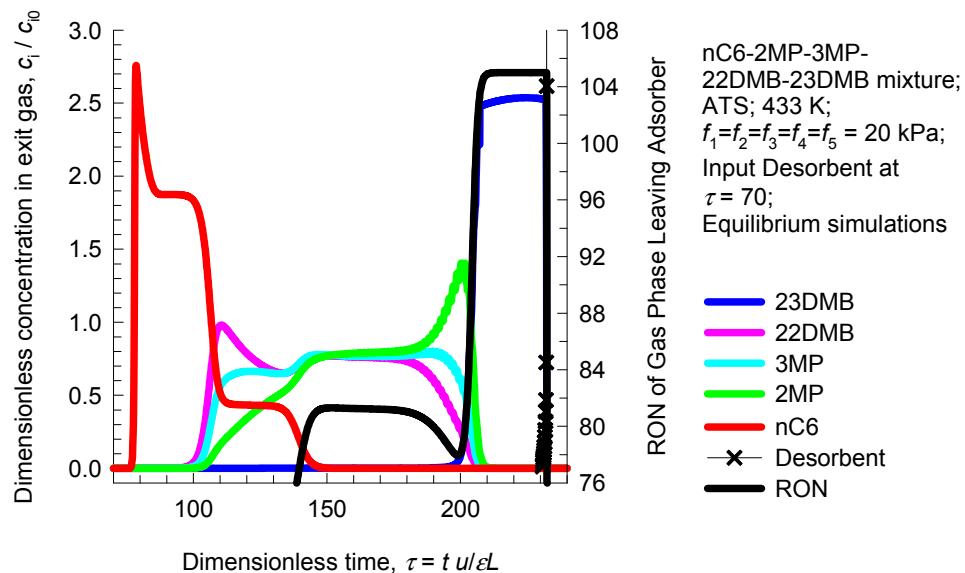
$$(D_{nC6}/D_{22DMB}) = 2$$

$$(D_{nC6}/D_{23DMB}) = 2$$

Adsorption/desorption cycles for ATS

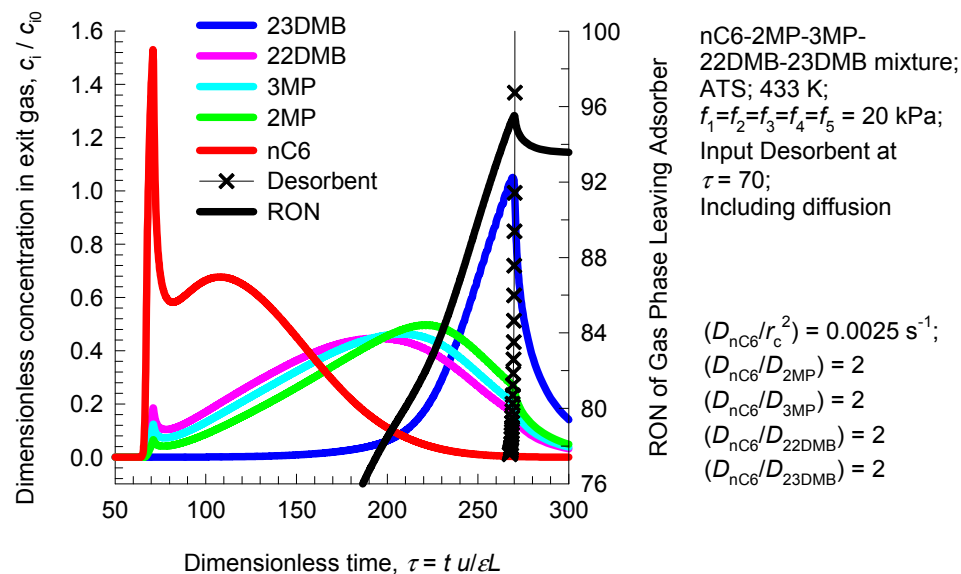
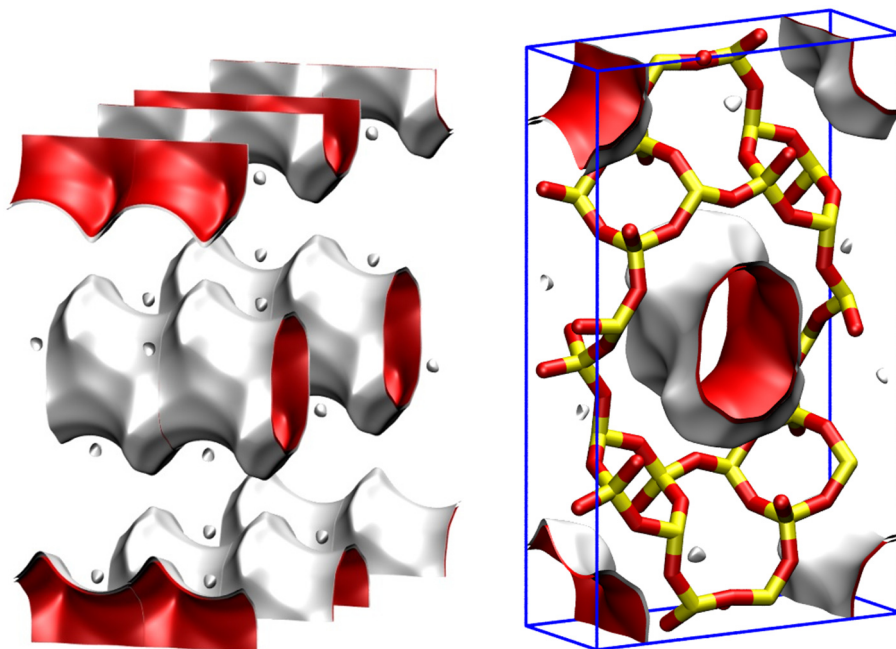
Figure 138

Equilibrium breakthrough simulations



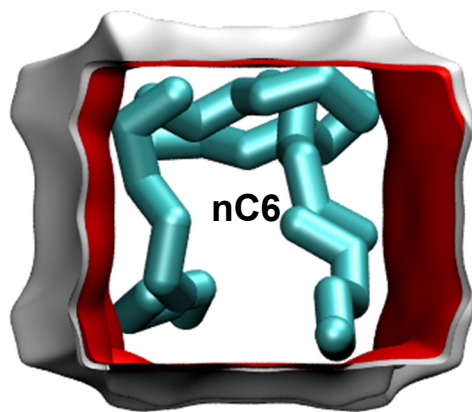
Length entropy effects cause the reverse adsorption hierarchy

Breakthroughs with diffusional limitations

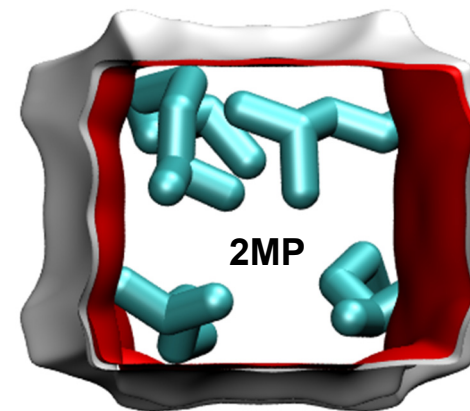
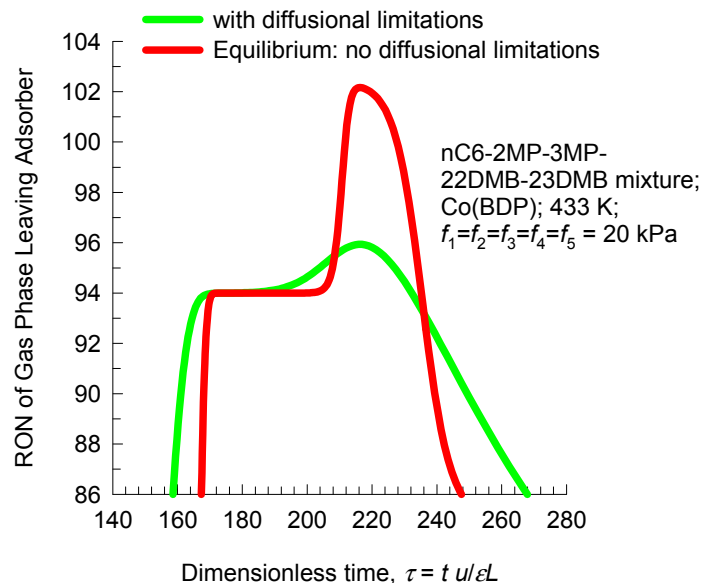


Breakthrough simulations for Co(BDP)

Figure 139



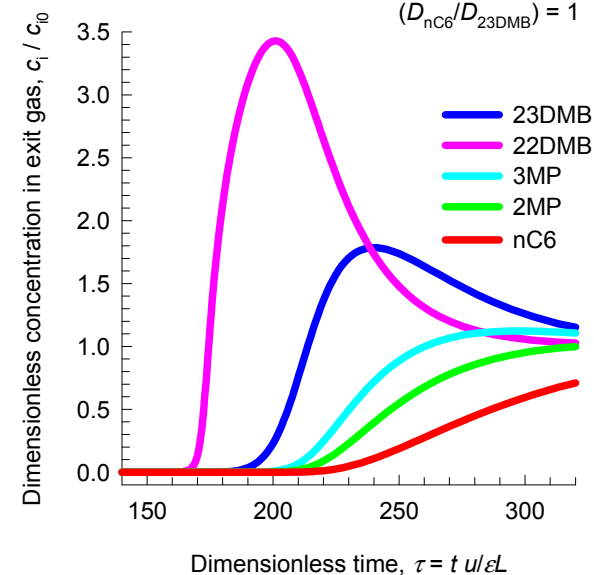
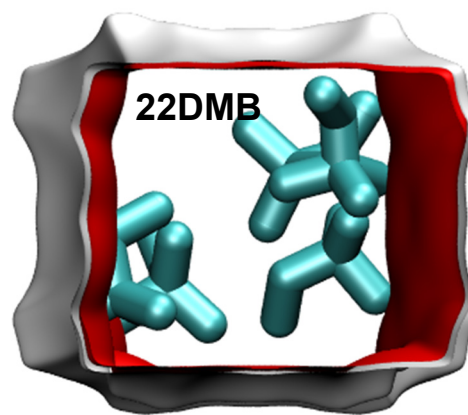
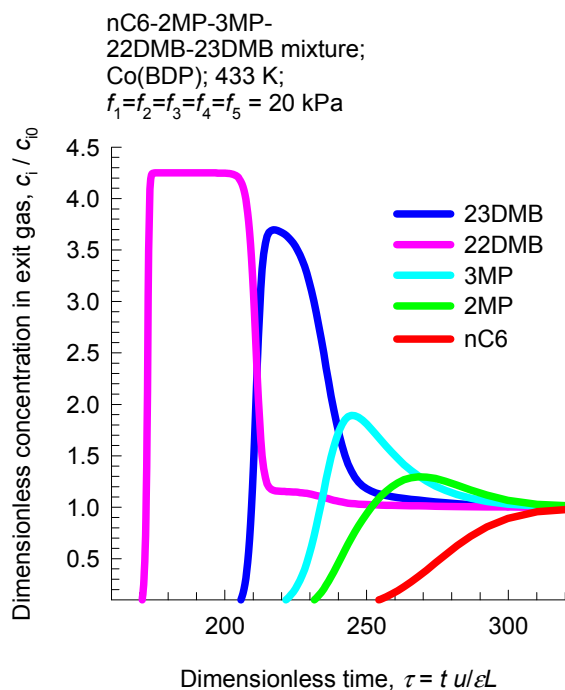
Equilibrium breakthrough simulations



Breakthroughs with diffusional limitations

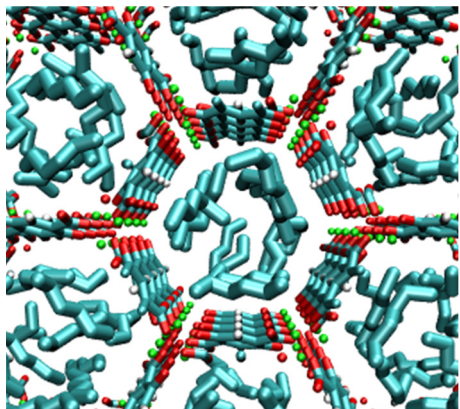
nC6-2MP-3MP-22DMB-23DMB mixture;
Co(BDP); 433 K;
 $f_1=f_2=f_3=f_4=f_5 = 20$ kPa

$(D_{nC6}/r_c^2) = 0.002 \text{ s}^{-1}$;
 $(D_{nC6}/D_{2MP}) = 1$
 $(D_{nC6}/D_{3MP}) = 1$
 $(D_{nC6}/D_{22DMB}) = 1$
 $(D_{nC6}/D_{23DMB}) = 1$

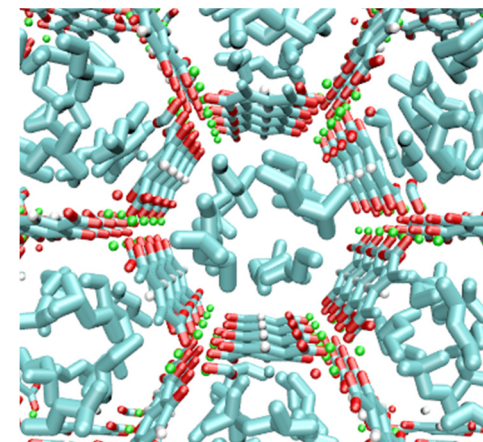
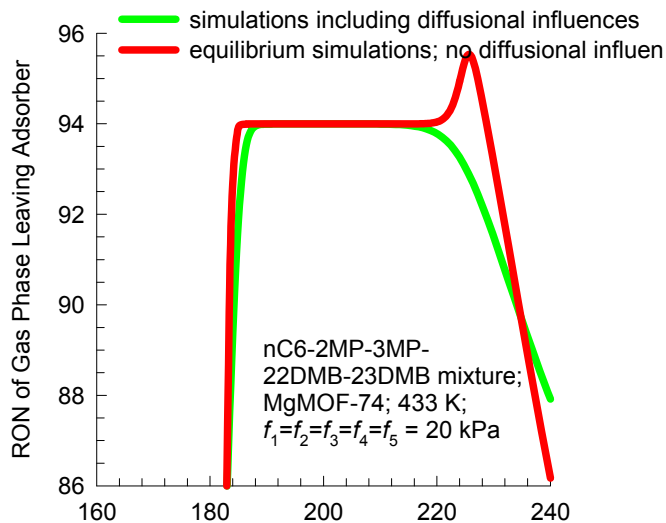


Breakthrough simulations for MgMOF-74 Figure 140

nC6



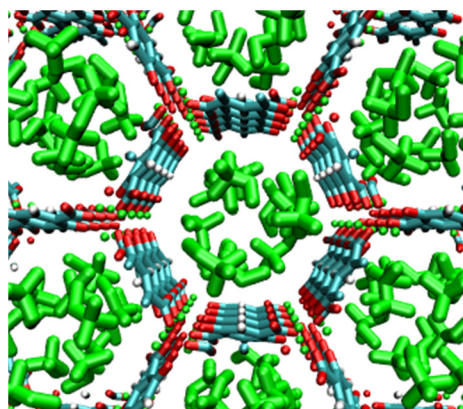
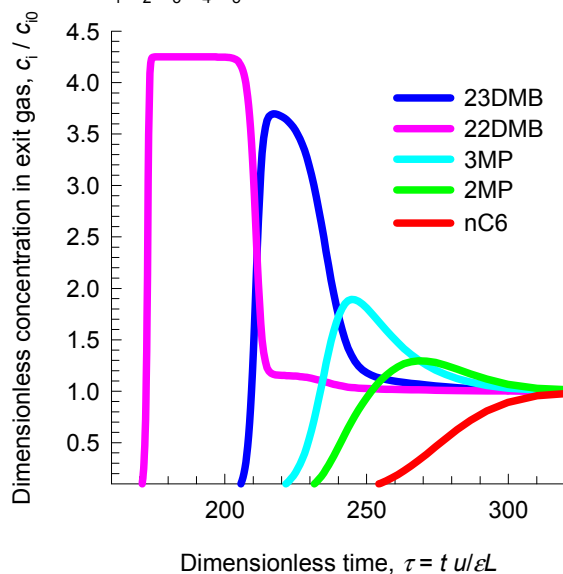
Equilibrium breakthrough simulations



2MP

Breakthroughs with diffusional limitations

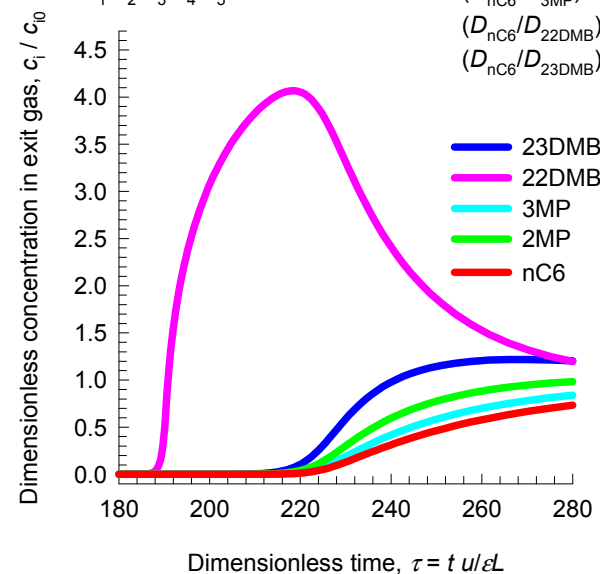
nC6-2MP-3MP-22DMB-23DMB mixture;
Co(BDP); 433 K;
 $f_1=f_2=f_3=f_4=f_5 = 20$ kPa



22DMB

nC6-2MP-3MP-22DMB-23DMB mixture;
MgMOF-74; 433 K;
 $f_1=f_2=f_3=f_4=f_5 = 20$ kPa

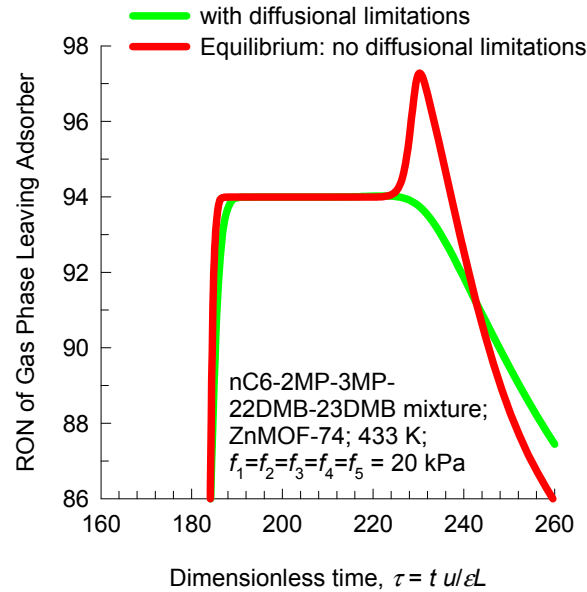
$(D_{nC6}/r_c^2) = 0.002$ s⁻¹;
 $(D_{nC6}/D_{2MP}) = 1$
 $(D_{nC6}/D_{3MP}) = 1$
 $(D_{nC6}/D_{22DMB}) = 1$
 $(D_{nC6}/D_{23DMB}) = 1$



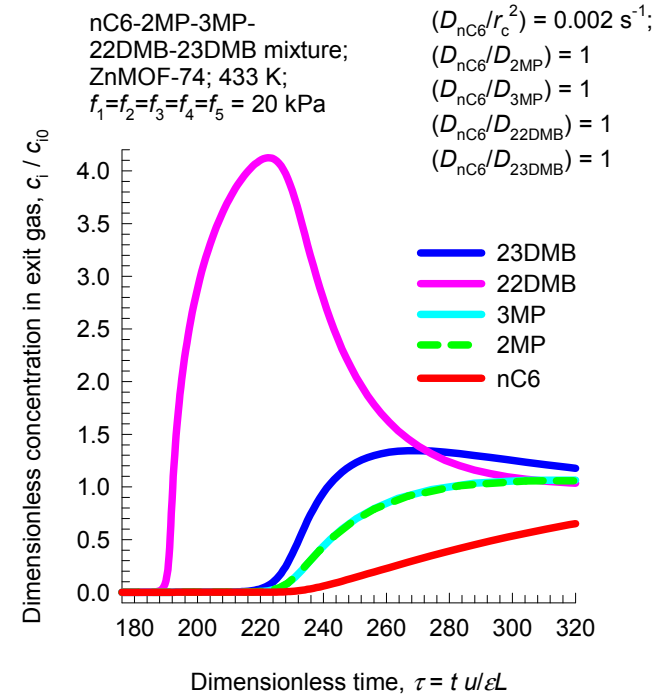
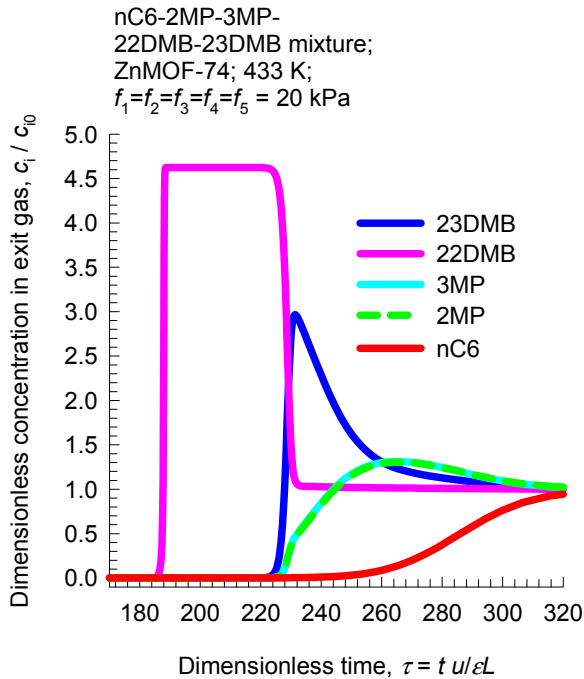
Breakthrough simulations for ZnMOF-74

Figure 141

Equilibrium breakthrough simulations



Breakthroughs with diffusional limitations



Compare 92+ RON productivities

